Journal of Heat Transfer

Published Monthly by ASME

VOLUME 130 • NUMBER 8 • AUGUST 2008

Editor, **YOGESH JALURIA (2010)**
Assistant to the Editor, **S. PATEL**

Associate Editors
Yutaka Asako, Tokyo Metropolitan University, Japan (2010)
Gautam Biswas, Indian Inst. of Tech., Kanpur (2009)
Cho Lik Chan, The University of Arizona (2010)
Louis C. Chow, University of Central Florida (2010)
Minking Chyu, Univ. of Pittsburgh (2009)
Frank J. Cunha, Pratt & Whitney (2011)
Ali Ebadian, Florida International Univ. (2011)
Ofodike A. Ezekoye, Univ. of Texas-Austin (2011)
Satish G. Kandlikar, Rochester Inst. of Tech. (2010)
Sung Jin Kim, KAIST, Korea (2010)
Sai C. Lau, Texas A&M Univ. (2009)
Ben Q. Li, Univ. of Michigan, Dearborn (2009)
Raj M. Manglik, Univ. of Cincinnati (2009)
Jayanthi Y. Murthy, Purdue University (2010)
Pamela M. Norris, Univ. of Virginia (2011)
Patrick E. Phelan, Arizona State Univ. (2011)
Roger R. Schmidt, IBM Corporation (2010)
S. A. Sherif, University of Florida (2010)
Heping Tan, Harbin Institute of Technology (2011)
Peter Vadasz, Northern Arizona University (2010)
Jamal Yagoobi, Illinois Inst. of Tech. (2009)
Walter W. Yuen, Univ. of California–Santa Barbara (2011)

Past Editors
V. DHIR
J. R. HOWELL
R. VISKANTA
G. M. FAETH
K. T. YANG
E. M. SPARROW

HEAT TRANSFER DIVISION
Chair, **C. OH**
Vice Chair, **V. CAREY**
Past Chair, **T. TONG**

PUBLICATIONS COMMITTEE
Chair, **BAHRAM RAVANI**

OFFICERS OF THE ASME
President,
THOMAS M. BARLOW
Executive Director,
THOMAS G. LOUGHLIN
Treasurer,
THOMAS D. PESTORIUS

PUBLISHING STAFF

Managing Director, Publishing
PHILIP DI VIETRO

Manager, Journals
COLIN McATEER

Production Coordinator
JUDITH SIERANT

PHOTOGALLERY

RESEARCH PAPERS

Conduction

(Contents continued on inside back cover)

Transactions of the ASME, Journal of Heat Transfer (ISSN 0022-1481) is published monthly by The American Society of Mechanical Engineers, Three Park Avenue, New York, NY 10016. Periodicals postage paid at New York, NY and additional mailing offices. POSTMASTER: Send address changes to Transactions of the ASME, Journal of Heat Transfer, c/o THE AMERICAN SOCIETY OF MECHANICAL ENGINEERS, 22 Law Drive, Box 2300, Fairfield, NJ 07007-2300. **CHANGES OF ADDRESS** must be received at Society headquarters seven weeks before they are to be effective. Please send old label and new address. **STATEMENT from By-Laws.** The Society shall not be responsible for statements or opinions advanced in papers or ... printed in its publications (B7.1, Para. 3).

COPYRIGHT © 2008 by The American Society of Mechanical Engineers. For authorization to photocopy material for internal or personal use under those circumstances not falling within the fair use provisions of the Copyright Act, contact the Copyright Clearance Center (CCC), 222 Rosewood Drive, Danvers, MA 01923, tel: 978-750-8400, www.copyright.com. Request for special permission or bulk copying should be addressed to Reprints/Permission Department.

Canadian Goods & Services Tax Registration #126148048

This journal is printed on acid-free paper, which exceeds the ANSI Z39.48-1992 specification for permanence of paper and library materials. ∞™
♲ 85% recycled content, including 10% post-consumer fibers.

(Contents continued)

Journal of Heat Transfer Volume 130, Number 8 AUGUST 2008

Evaporation, Boiling, and Condensation

Forced Convection

Heat Exchangers

Melting and Solidification

Micro/Nanoscale Heat Transfer

Radiative Heat Transfer

TECHNICAL BRIEFS

(Contents continued on facing page)

Journal of Heat Transfer Volume 130, Number 8 AUGUST 2008

ERRATA

The ASME Journal of Heat Transfer is abstracted and indexed in the following:

Applied Science and Technology Index, Chemical Abstracts, Chemical Engineering and Biotechnology Abstracts (Electronic equivalent of Process and Chemical Engineering), Civil Engineering Abstracts, Compendex (The electronic equivalent of Engineering Index), Corrosion Abstracts, Current Contents, E & P Health, Safety, and Environment, Ei EncompassLit, Engineered Materials Abstracts, Engineering Index, Enviroline (The electronic equivalent of Environment Abstracts), Environment Abstracts, Environmental Engineering Abstracts, Environmental Science and Pollution Management, Fluidex, Fuel and Energy Abstracts, Index to Scientific Reviews, INSPEC, International Building Services Abstracts, Mechanical & Transportation Engineering Abstracts, Mechanical Engineering Abstracts, METADEX (The electronic equivalent of Metals Abstracts and Alloys Index), Petroleum Abstracts, Process and Chemical Engineering, Referativnyi Zhurnal, Science Citation Index, SciSearch (The electronic equivalent of Science Citation Index), Theoretical Chemical Engineering

Journal of Heat Transfer

Heat Transfer Photogallery

The Twelfth Heat Transfer Photogallery was sponsored by the K-22 Heat Transfer Visualization Committee for the 2007 International Mechanical Engineering Congress and Exhibition (IMECE) held in Seattle, Washington on November 11–16, 2007. The peer-reviewed evaluation process for the presented entries identified the seven entries from 2007 IMECE and two additional entries from 2007 ASME Summer Heat Transfer Conference, held in Vancouver, Canada, for publication in the ASME *Journal of Heat Transfer* August issue of 2008.

The purpose of publishing these entries is to draw attention to the innovative features of optical diagnostic techniques and aesthetic qualities of thermal processes. To focus on visualization images and schematics, the text is kept to a minimum and further details should be found directly from the authors. My wish is that the journal readers enjoy viewing these collections, acquire knowledge of the state-of-the-art features, and also promote their participation in the 2008-IMECE Photogallery [http://www.asmeconferences.org/congress08].

The **Call for Photogallery for 2008-IMECE** is also announced in this issue of *Journal of Heat Transfer*.

Kenneth D. Kihm
Department of Mechanical, Aerospace
and Biomedical Engineering,
University of Tennessee,
Knoxville, TN 37996-2210

Bubble Behavior With and Without Electric Fields

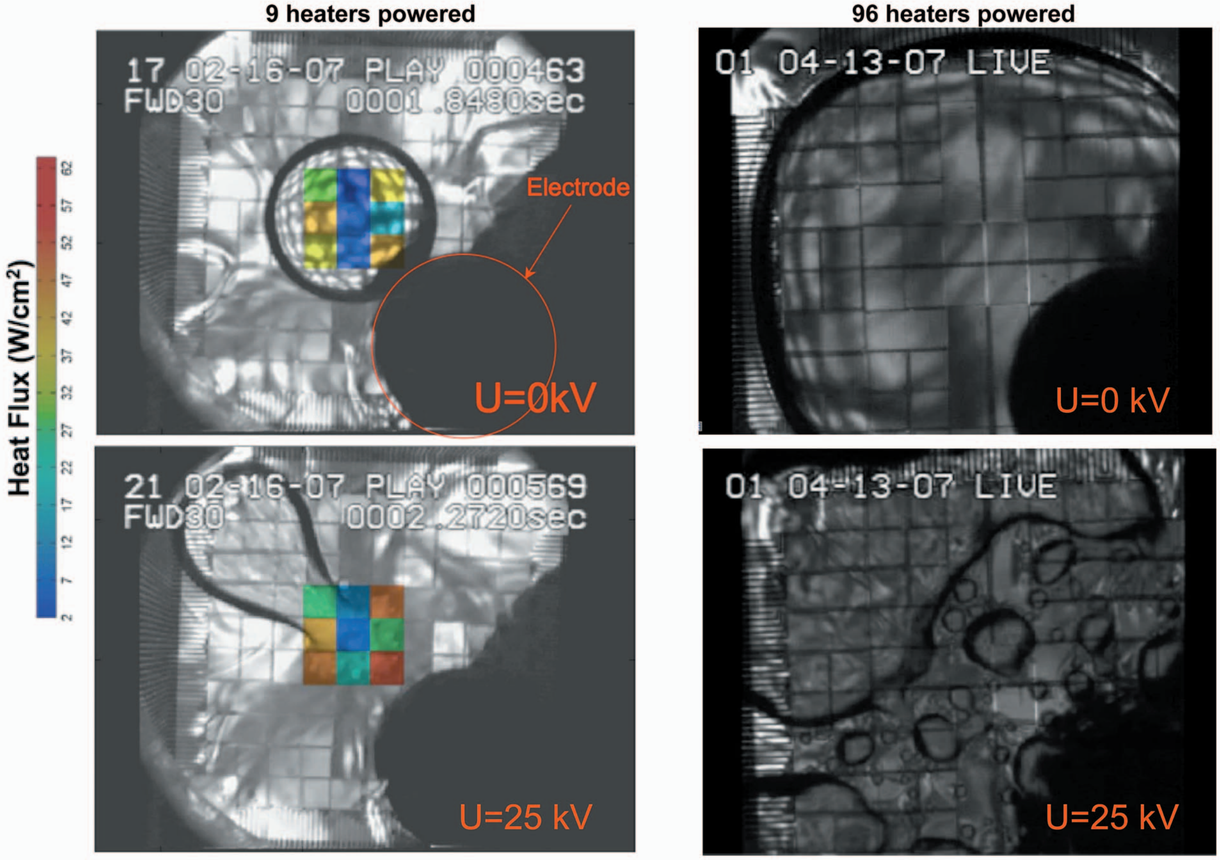
9 heaters powered

96 heaters powered

Heater array

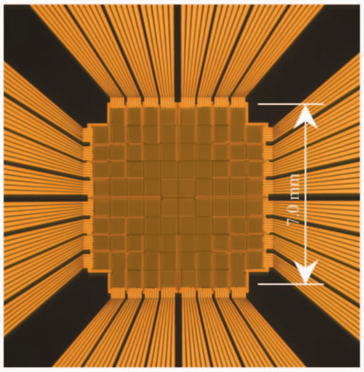

High Voltage Electrode

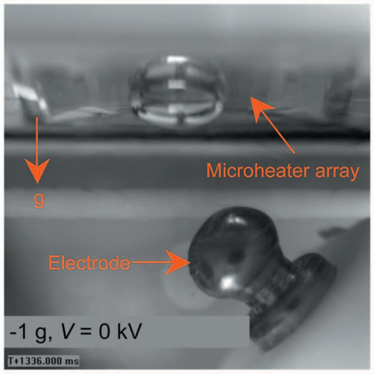

Boiling Curves for 9 Heaters (T_{bulk}=51.6°C)

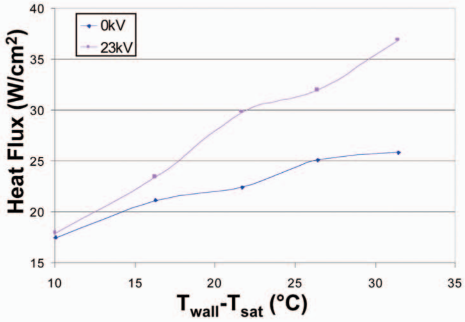

Pool boiling on a downward facing microheater array under the influence of electric fields

C. Herman*, Z. Liu*, and J. Kim**

*Department of Mechanical Engineering, The Johns Hopkins University, Baltimore, MD 21218, USA
**Department of Mechanical Engineering, University of Maryland, College Park, MD 20742, USA

The effects of a nonuniform electric field on vapor bubble detachment and heat transfer rate were studied in pool boiling at different subcooled conditions for various wall temperatures. A dielectric fluid (FC-72) was used as the working fluid at ambient pressure. An array of 3x3 independently controlled microheaters, each 0.7x0.7mm^2 in size, was maintained at constant temperature using electronic feedback loops, enabling the heat transfer from each heater to be determined. An electric field was applied between the horizontal, downward facing microheater array, which was grounded, and a spherical, off-axis top electrode. Boiling heat transfer results with and without the electric field are presented. Without the electric field, a single large "primary" bubble was observed to form due to the coalescence of the individual "satellite" bubbles which nucleated directly from each single heater array. Vapor completely covered the heater due to this primary bubble resulting in a very low heat transfer. With the electric field applied, the primary bubble departed periodcally, enabling new bubbles to grow and transfer much larger amounts of heat. Due to the nonuniformity of the electric field, bubbles moved away from the top electrode (into the region of weaker electric field) during their development.

Acknowledgments: This research was supported by NASA

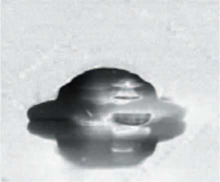
Fig 1: Droplet impact

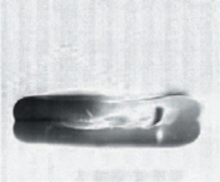
Fig 2: Max. spreading

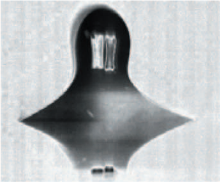
Fig 3: Rebound

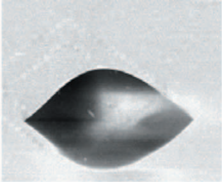
Fig 4: Oscillation

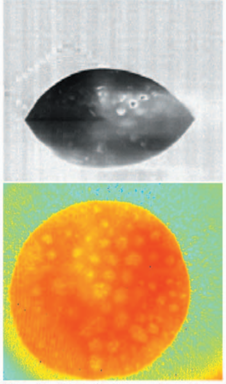
Fig 5: Initial nucleation

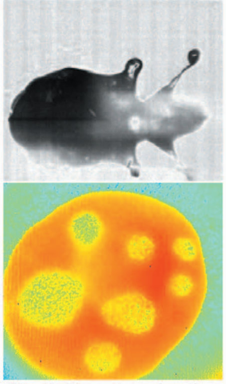
Fig 6: Droplet ejection

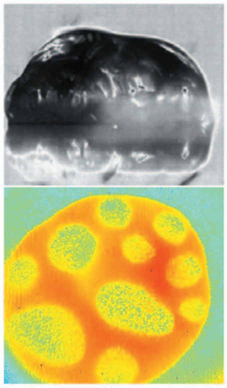
Fig 7: Droplet expansion

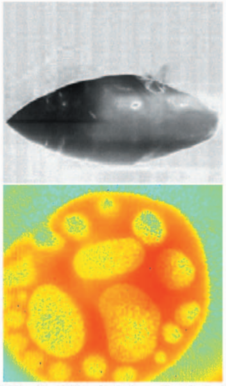
Fig 8: Shrinking height

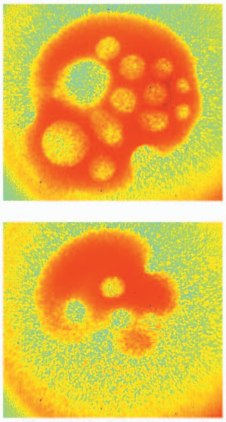
Figs 9 & 10: Dryout

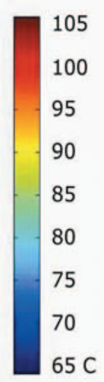

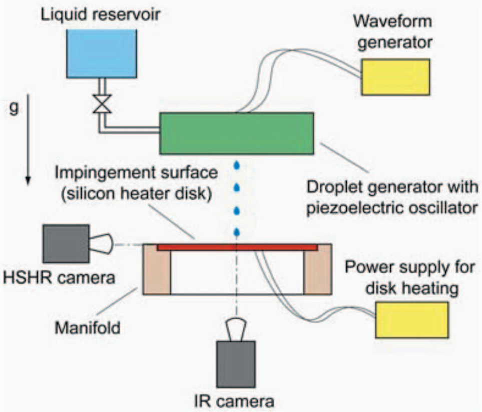

Test facility for high speed and infrared imaging

Simultaneous Droplet Impingement Dynamics and Boiling Heat Transfer

Jian Shen, Christof Graber
Deborah Pence, James Liburdy, Vinod Narayanan
Mechanical Engineering, Oregon State University, USA

Deionized water droplets impinging on a heated, unpolished silicon surface were studied by simultaneously recording the process with a High Speed High Resolution camera (HSHR; 7400 pps; 9 μm/pixel) and an Infrared camera (IR; 120 pps; 10 μm/pixel), as shown above. The HSHR images give information about the impingement dynamics, while the IR images show the heat transfer characteristics of the process. The disk was heated by thin film heaters at the bottom of the disk with a supplied power of 4.7 W. The process is divided into the three stages impingement, boiling, and dryout. During the impingement the droplet impacts on the surface (Fig. 1), spreads out (Fig. 2), rebounds (Fig. 3), and oscillates at a steady diameter (Fig. 4). Boiling involves initial nucleation (Fig. 5) followed by severe boiling including droplet ejection (Fig. 6) and expansion (Fig. 7), and shrinking of the droplet height at constant wetting diameter (Fig. 8). When a critical contact angle is reached, the droplet diameter finally diminishes and dryout occurs (Figs. 9 & 10). The temperatures are based on an intensity-temperature calibration and are the temperatures of the fluid in contact with the surface.

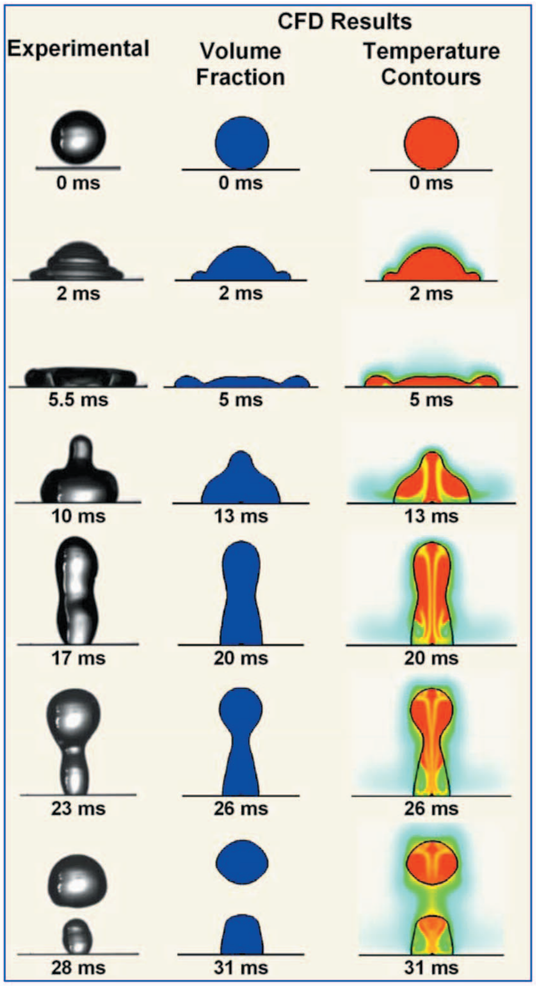

Fig. 1 Water drop impact on Teflon (We ~ 20)

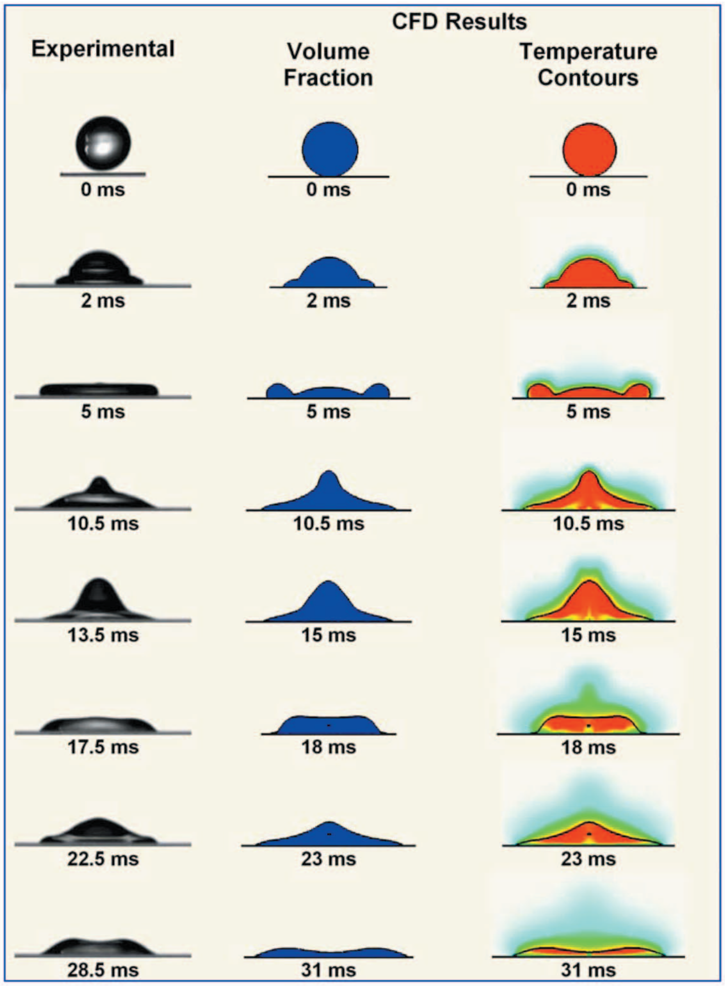

Fig. 2 Water drop impact on glass (We ~ 20)

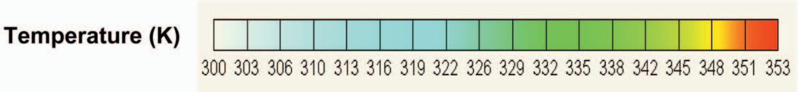

Short Time Impact and Cooling of Water Droplets Impinging on Hydrophobic and Hydrophilic Surfaces

A. Sanjeev, O. Huzayyin, K. P. Gatne, R. M. Manglik and **M. A. Jog**
Department of Mechanical, Industrial, and Nuclear Engineering, University of Cincinnati, Cincinnati, OH 45221-0072

The dynamics and heat transfer characteristics of hot water droplet (initially at 353 K) impinging on cold (at 300 K) hydrophobic (Teflon) and hydrophilic (glass) surfaces in ambient air were simulated using a finite volume scheme with an axisymmetric structured grid. The volume of fluid method was employed to capture the moving air-water interface. The computations were validated by comparing them with photographs of drop impact-spreading-recoil phenomena captured using a digital high-speed video camera operating at 2000 frames per second that was fitted with a 8× zoom lens. The drop diameter and liquid film spread at impact were determined by an image processing software that employs a saturation-intensity pixel-based area-averaging process. Water droplets of diameter ~ 3 mm were generated from a hypodermic needle. The Weber number based on the impact velocity was ~ 20, and the ambient temperature conditions in all experiments were at 300 K.

Figure 1 shows the impact-spreading-recoil/column fracture of a water droplet on a hydrophobic surface. The drop behavior is captured well by the computational model, and a strong recoil is seen that leads to formation of a liquid column and breakup into two unequal droplets. A distinctly different behavior is observed on the hydrophilic surface, where the higher wetting leads to increased spread and weak recoil (Fig. 2). As the droplet spreads, the liquid in contact with the cold surface tends to cool first and then mixes with warmer fluid during recoil. The temperature contours inside the water droplet impacting on a Teflon surface show considerable mixing of hot and cold regions of the fluid. The droplet broken from the liquid column is much warmer than the smaller drop that remains attached to the Teflon surface. The water drop impacting on a glass surface is seen to cool faster as the increased contact area with the glass surface facilitates higher rate of heat transfer.

Saxifrage stolonigera

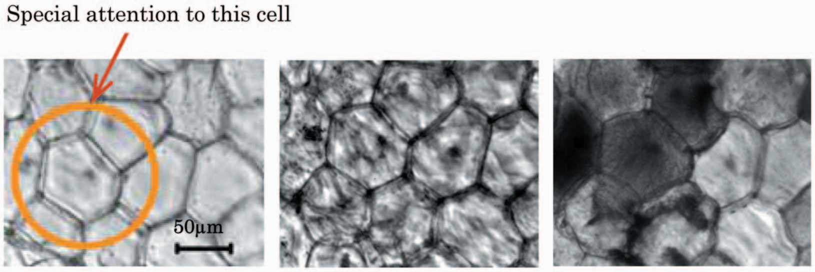

t=0 s (298K) (a) Before Cooling
t=2170 s (263K) (b) Extracellular Freezing
t=2200 s (261.5K) (c) Intracellular Freezing

Microscopic Images of Typical Cooling and Freezing behaviors
(t: Time after the start of cooling)

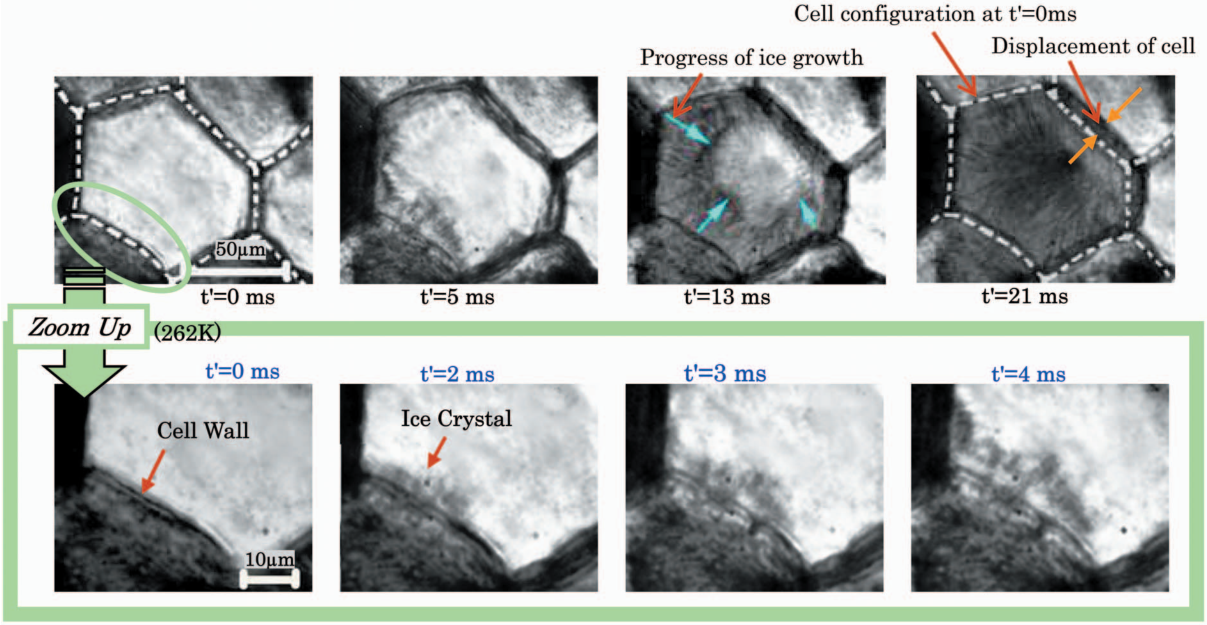

Transition Behaviors from Extracellular Freezing to Intracellular One with High Speed Camera
[t': Time after the beginning of transition, White broken line: cell configuration before transition (at t'=0 ms)]

Freezing Damage of the Plasma Membrane of a Plant Cell

Akemi EGUCHI[1], Akira NARUMI[2] and Yasuhiro IIDA[2]
[1] Undergraduate Student, Kanagawa Institute of Technology, JAPAN
[2] Kanagawa Institute of Technology, JAPAN

It is said that the success of cell freezing depends on the damage of plasma membrane. However, this hypothesis has not been proved yet. The purpose of this research is to clarify how ice crystal injures the plasma membrane. This research paid special attention to the mechanism of transition from extracellular freezing to intracellular one; how ice crystal formed at the outside of cell wall transits to the inside of cell through cell wall. A normal CCD camera, a cooled CCD camera and a high speed video camera attached with a cryomicroscope were utilized to capture the moment of transition and to visualize the damage of plasma membrane. Plant was used for a tissue of a living cell.

The impressive photographs obtained with the tissue on the back side of the leaf surface of *Saxifrage stolonifera* under the condition of cooling rate of -1°C/min are shown. It is found that the photographs of high speed camera clearly catch the drastic moment when ice crystal formed in the intercellular space transits to the inside of cell to cause intracellular freezing just after passing through the cell wall. In comparison between the both cell configurations at t'=0 ms (the white broken line) and at t'=21 ms, the significant deformation is seen due to transition to intracellular freezing. This fact suggests that there is some possibility of estimating the freezing damage of the plasma membrane by measuring the displacement of cell configuration.

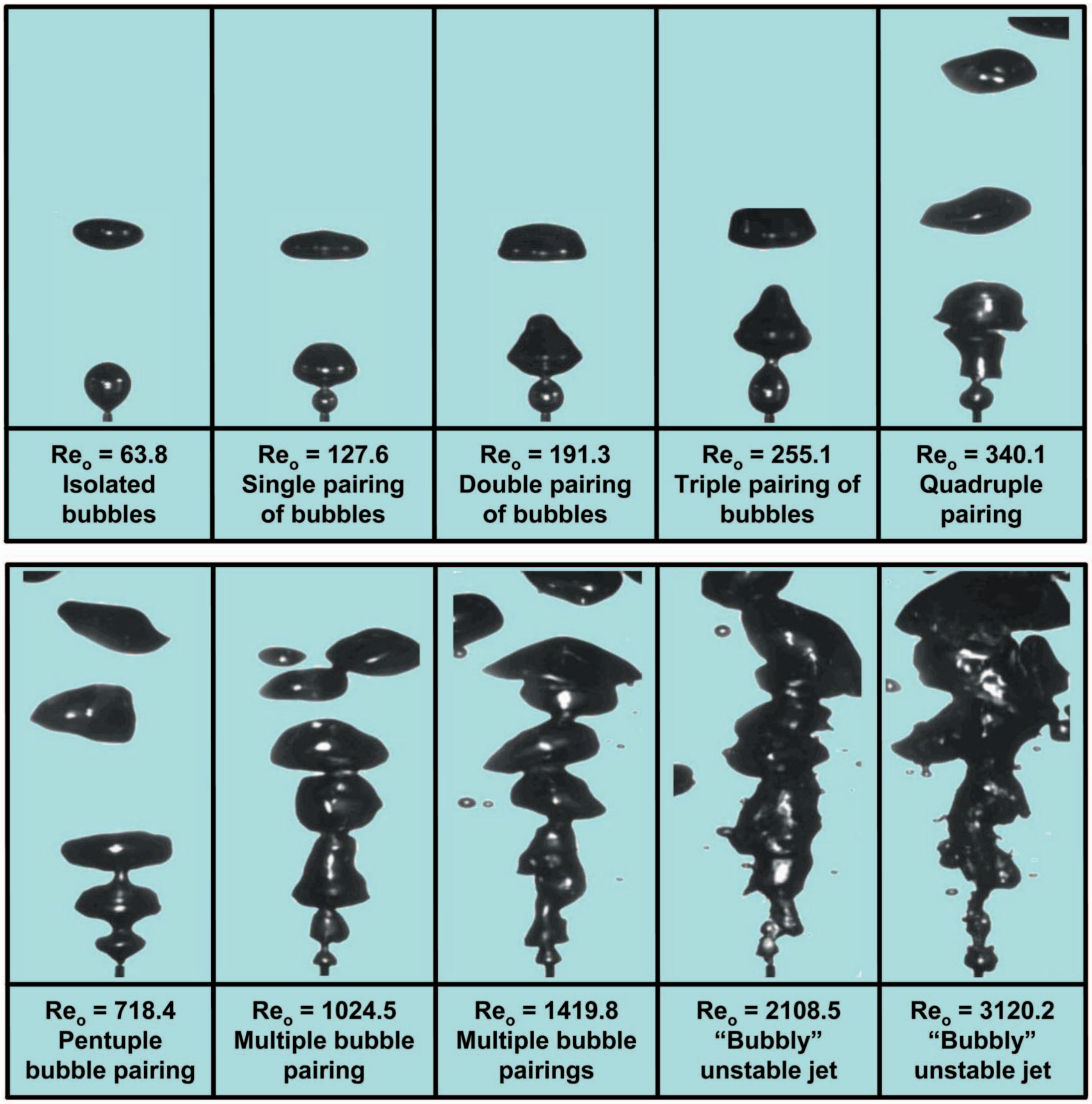

Air-Water Ebullience Systems: Visualizing Single Bubble to Wave Instability Signatures

A. Subramani, **M.A. Jog**, and **R.M. Manglik**
Thermal-Fluids & Thermal Processing Laboratory, University of Cincinnati, Cincinnati, OH 45221-0072

Bubble dynamics and ebullient signatures characterize the fundamental gas-liquid interfacial behavior and primary transport processes in many different applications, including aeration, fermentation, bio-chemical transformation, and phase-change. The air-flow bubbling dynamics at the tip of a vertical capillary-tube orifice (diameter $d_o = 0.32$ mm) in a quiescent water pool with constant volumetric flow rates at room temperature ($T = 25^oC$) are visualized. Images of the millimeter- and millisecond-scale spatial-temporal dynamics of ebullient behavior ranging from isolated single bubbles, to multiple coalescing bubbles and bubble streams, to a jet stream initiating wave or Helmholtz instabilities were acquired as depicted in the photo-stills shown above; here Re_o is based on orifice diameter d_o and air properties. These visuals essentially capture the complex bubble-liquid and bubble-bubble interactions that describe the evolving ebullient structure with increasing air flow rates. Flow visualization were carried out in carefully controlled experiments, using a high-speed (5000 frames per second), high-resolution digital video camera fitted with a 8× optical zoom lens. It was triggered through a computer interface to record continuous high-speed video from which different image frames could be captured by a digital-video-processing software. The steady and fixed volumetric flow-rate air was supplied via a digitally controlled multiple-syringe pump; the lighting for sharp gas-liquid image contrast was controlled using a focusing, single-ended, daylight parabolic aluminized reflector lighting system along with a glossy white reflector that was placed behind the water vessel and bubbling activity.

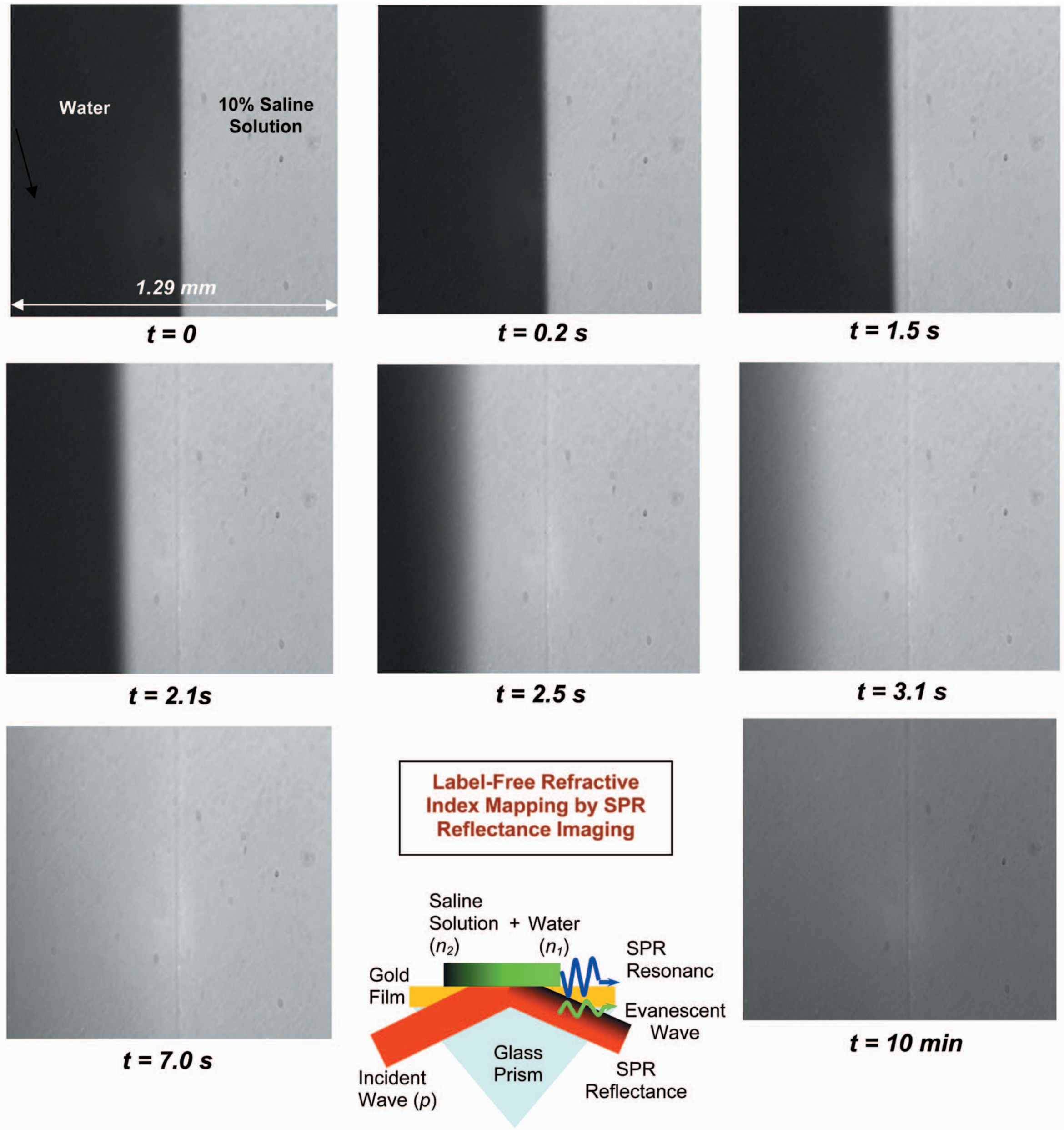

t = 0 *t* = 0.2 s *t* = 1.5 s

t = 2.1s *t* = 2.5 s *t* = 3.1 s

t = 7.0 s *t* = 10 min

Label-Free and Near-Field Mapping of Molecular Diffusion (Saline Solution/Water) Using Surface Plasmon Resonance (SPR) Refractive Index Field Imaging

Il Tai Kim and Kenneth D. Kihm
Department of Mechanical, Aerospace and Biomedical Engineering
University of Tennessee, Knoxville, Tennessee 37996

The near-field (less than a few hundred nanometers) molecular diffusion of saline solution (10%) into water is visualized using the SPR reflectance imaging technique as a label-free, real-time, and full-field refractive index (RI) field mapping tool [I. T. Kim and K. D. Kihm, *Experiments in Fluids* Vol. 41, No. 6, pp. 905-916, 2006]. The slightly heavier saline solution invades the water in the near field and the diffusive region is pushed to the water side during the beginning period of up to 7 seconds. After a considerable amount of time (*t* = 10 min), complete diffusion is reached to show approximately 5 % salinity in the near-field region.

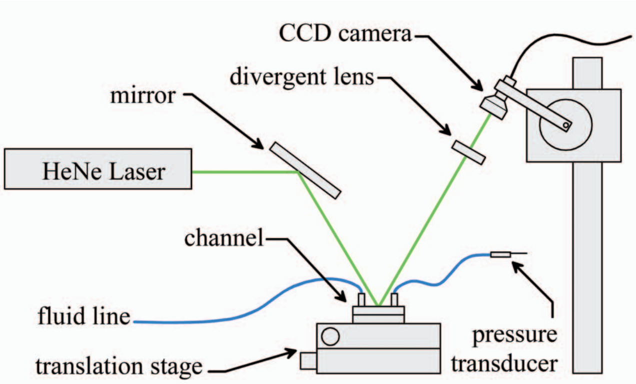

Images processed into binary form using a low pass filter which eliminates all frequencies down to the number of fringes in the image. Interface tracking using the binary images correlates fringe shifts to pressure change.

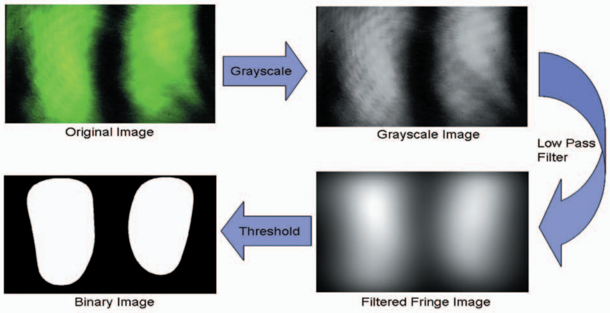

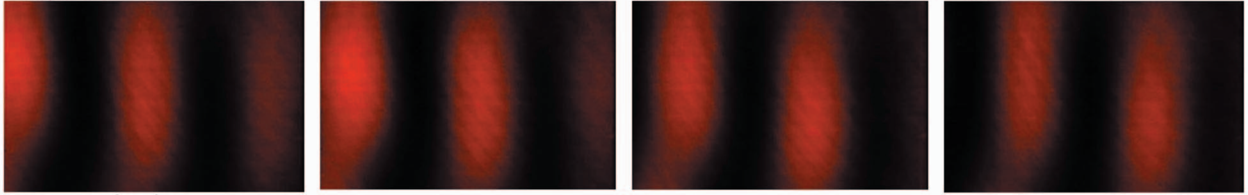
50 μm x 9 mm wide rectangular quartz channel with air – static pressure - raw fringes

atmospheric pressure | 1.84 psig | 2.92 psig | 4.45 psig


50 μm x 9 mm wide rectangular quartz channel with water – static pressure - processed fringes

atmospheric pressure | 1.98 psig | 4.36 psig | 7.09 psig

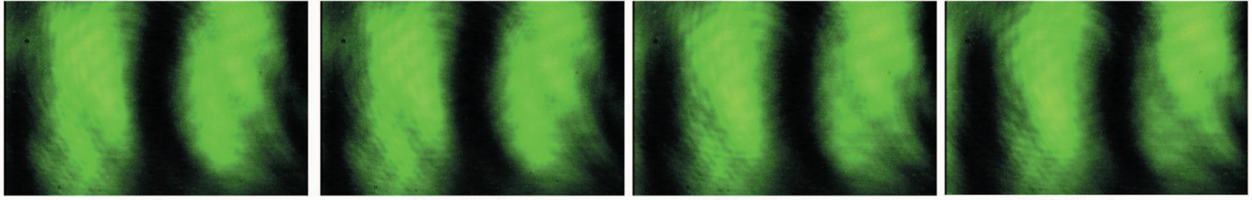
500 μm square glass channel with water – continuous flow – raw fringes

no flow | 19 μl/min | 106 μl/min | 286 μl/min

Visualization of Pressure in Microchannels

Derek Fultz & Jeffrey Allen
Microfluidics and Interfacial Transport Laboratory
Michigan Technological University

The impingement of a glass or PDMS microchannel by an unfocused laser beam has been observed to create high contrast interference fringes which shift due to channel deflection and changes in refractive index (RI) of the fluid within the channel. Since deflection and RI are functions of pressure, fringe movement can be used to visualize and quantify pressure changes within the channel. Through the use of image processing, shift values are obtained and correlated to pressure values which are verified against known RI data for fluids such as air and water. The remaining shift is then due to channel deflection which has been found to match finite element models within 5%. In a 50 μm thick channel using a 752 x 480 CCD array, measurement limits of pressure due solely to RI change are 14.5 psig and 0.8 psig for water and air, respectively. In thin wall channels, such as the 50 μm square channels, the wall deflection acts as an excellent amplification and visualization mechanism for the phenomenon at low pressures providing measurements as low as 0.15 psig and 0.17 psig in water and air, respectively.

Schematic of a phase contrast microscopy for visualizing swarming bacteria

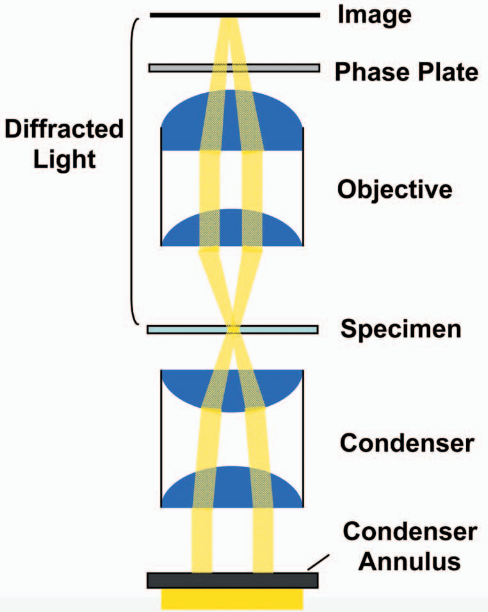

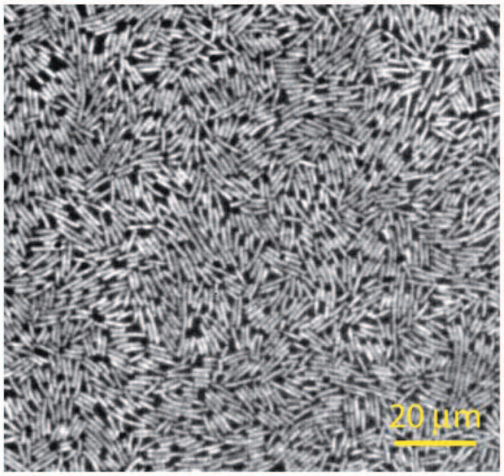

Phase contrast microscopic image of swarming bacteria and their velocity flow field

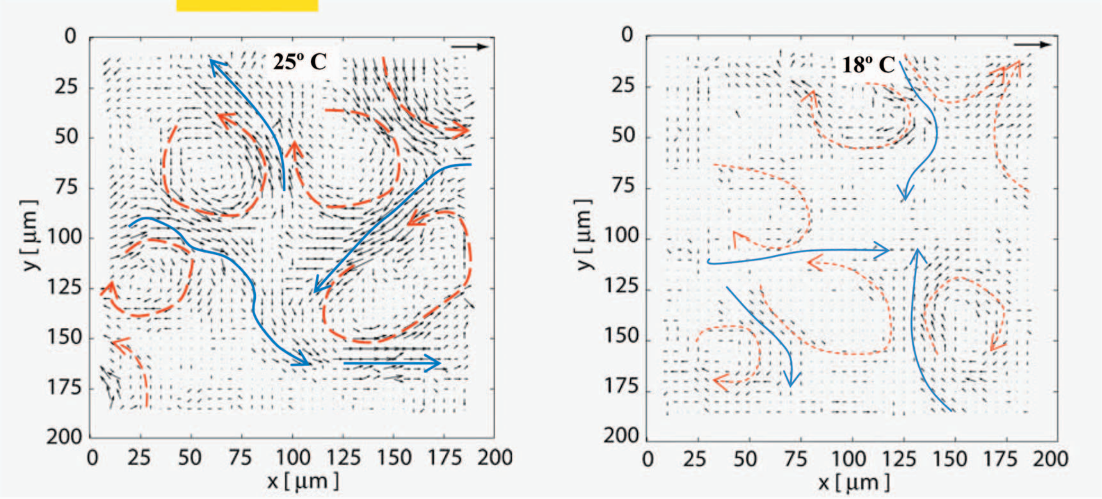

Temperature Effects on Swarming Flagellated Bacteria in Microfluidic Environments

Edward B. Steager, Chang-Beom Kim, and Min Jun Kim
Department of Mechanical Engineering & Mechanics, Drexel University, Philadelphia, PA 19104, U.S.A.

Certain flagellated bacteria exhibit a mode of surface motion known as swarming. It has been reported that this motion is affected by temperature. In order to study this motility we employ phase contrast microscopy. Swarming bacteria are driven by flagella which are powered by biomolecular motors which switch in a clockwise/counter-clockwise sense. The switching frequency and the motor rotation frequency are both temperature sensitive. Swarming bacteria move two-dimensionally in close proximity and may be tracked using a non-labeled cell tracking technique which follows local interrogation windows rather than individual cells. This swarming appears random at first, but average velocity and spatial correlation studies reveal temperature-dependent rotational vortices and translational steams. As temperature falls from 25º C to 18º C, the average velocity is shown to decrease. The arrow (→) denotes a speed of 35 µm/s.

Flow patterns in 400 µm x 400 µm microchannels (8000 fps)

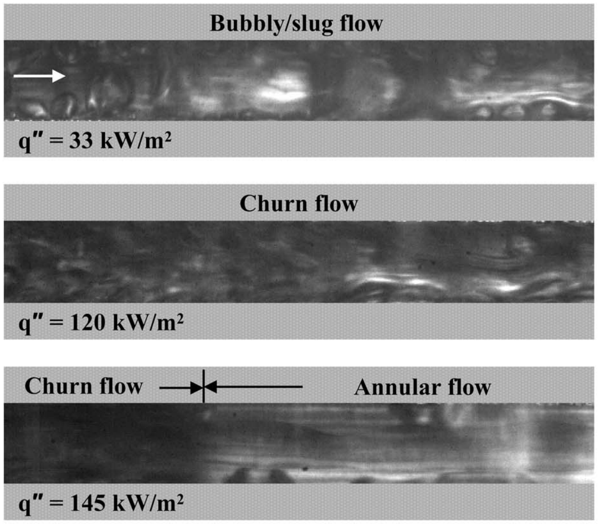

Flow patterns in 2200 µm x 400 µm microchannels (6000 fps)

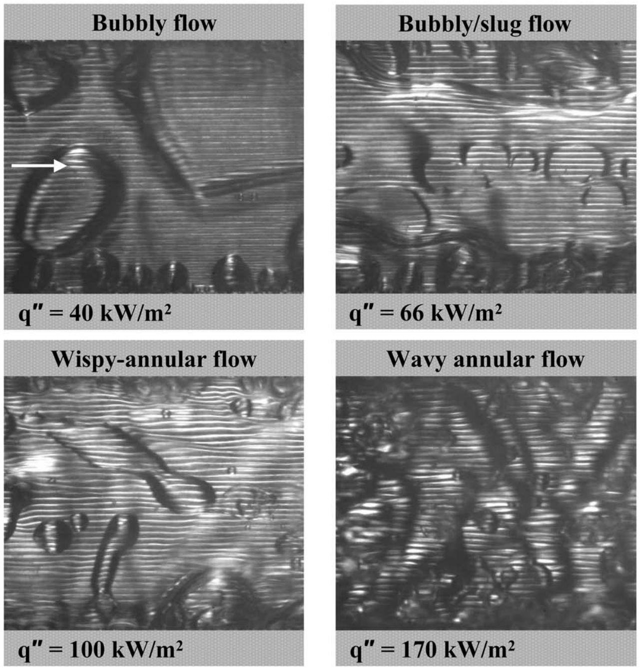

Flow patterns in 5850 µm x 400 µm microchannels (2000-4000 fps)

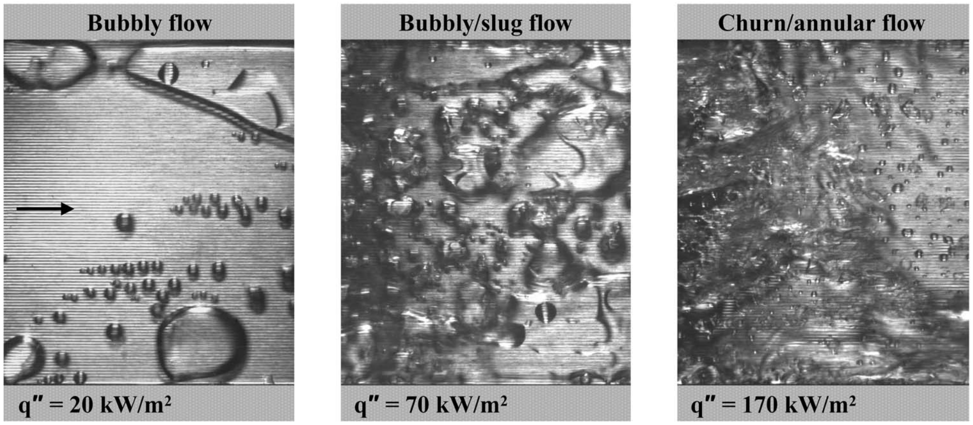

Flow Patterns During Convective Boiling in Microchannels

T. Harirchian and S. V. Garimella
NSF Cooling Technologies Research Center
School of Mechanical Engineering, Purdue University, West Lafayette, IN 47907-2088

To develop a flow regime map for convective boiling in microchannels and to propose flow pattern-based models to predict the corresponding heat transfer coefficients, a thorough understanding of the existing flow patterns and their transitions is necessary. In the present study, high-speed photography is employed to observe the flow patterns in flow boiling of a dielectric liquid, FC-77, in parallel silicon microchannels of depth 400 µm and widths ranging from 100 to 5850 µm. In each test, liquid mass flux and inlet subcooling are fixed at 250 kg/m^{2}s and 5℃, respectively, while the heat flux to the bottom of the heat sink is increased form zero to a value near the critical heat flux. Temperature and pressure are measured at several locations. A high-speed digital video camera is used to observe boiling patterns at frame rates ranging from 2000 to 24000 frames per second (fps). The images presented show a top view of the horizontal microchannels, at a location along the heat sink centerline and near the flow exit.

A Multiscale Model of Thermal Contact Resistance Between Rough Surfaces

Robert L. Jackson

Sushil H. Bhavnani
Fellow ASME

Mechanical Engineering Department,
Auburn University,
201 Ross Hall,
Auburn, AL 36849

Timothy P. Ferguson
Southern Research Institute,
757 Tom Martin Drive,
Birmingham, AL 35211

A new multiscale model of thermal contact resistance (TCR) between real rough surfaces is presented, which builds on Archard's multiscale description of surface roughness. The objective of this work is to construct the new model and use it to evaluate the effects of scale dependent surface features and properties on TCR. The model includes many details affecting TCR and is also fairly easy to implement. Multiscale fractal based models often oversimplify the contact mechanics by assuming that the surfaces are self-affine, the contact area is simply a geometrical truncation of the surfaces, and the pressure is a constant value independent of geometry and material properties. Concern has grown over the effectiveness of frequently used statistical rough surface contact models due to the inadequacies in capturing the true multiscale nature of surfaces (i.e., surfaces have multiple scales of surface features). The model developed in this paper incorporates several variables, including scale dependent yield strength and scale dependent spreading resistance to develop a new model that can be used to evaluate TCR. The results suggest that scale dependent mechanical properties are more influential than scale dependent thermal properties. When compared to an existing TCR model, this very inclusive model shows the same qualitative trend. Results also show the significance of capturing multiscale roughness when addressing the thermal contact resistance problem.
[DOI: 10.1115/1.2927403]

Keywords: contact resistance, heat transfer, nanoscale, roughness, surface

Introduction

Economically improving heat conduction from microelectro mechanical systems (MEMS) and microelectronics is a growing issue in the industry since the size of electronic devices continues to decrease. The decrease in the size of electronic devices reduces the available surface area for heat dissipation, leading to large increases in heat flux. This can yield increases in operating temperatures that exceed design criteria. Thus, the thermal contact resistance (TCR) between these devices and a heat sink is very important, as it limits the rate at which heat can be dissipated. It is well known that the roughness between contacting surfaces can reduce the real area of contact and thus bottleneck the heat flow, which is seen as an increase in the TCR (see Fig. 1).

Although there has been a large amount of work investigating TCR [1–4], there are some severe problems with the current methods used to predict it. Lambert and Fletcher [1] summarized the currently used theoretical and empirical thermal contact resistance models as "these do not agree with most results for an arbitrarily nonflat, rough surface, those usually obtained from common manufacturing processes. Empirical and semiempirical correlations, although many are developed for nonflat, rough surfaces, also suffer from limited applicability."

In addition, these dated theoretical models make use of contact mechanics techniques which have since been proven to have significant pitfalls. For instance, the very popular Greenwood and Williamson (GW) [5] statistical model has been shown to produce results which are dependent on the resolution of the surface profiling device [6–8]. Mikic also developed this methodology further by including the effects of repeated contact and surface deformation [9] (it should be noted that the effect of repeated contact is not included in the current model). Later, Greenwood and Wu [10] stated that the GW model assumption "that 'peaks' on a surface profile—points higher than their immediate neighbors at the sampling interval used correspond to asperities is quite wrong, and gives a false idea of both the number and the radius of curvature of the asperities. Instead we need to return to the earlier Archard concept that roughness consists of 'protuberances on protuberances on protuberances' [11]." In addition, most other models which attempt to correct this issue by using fractal mathematics [12–19] assume that a surface can be characterized as self-affine, or follow a given structure for each scale of roughness, when in reality no real surface is truly self-affine. Sometimes the contact mechanics are also oversimplified so that fractal mathematics can be applied in a practical manner [20]. However, Wang et al. [21] have refined the fractal model to correct some of these concerns. Many of these previous models also use a fundamentally unsound assumption that when the surfaces deform plastically, the pressure is defined by a constant material "hardness." Several researchers have shown that this hardness varies with scale, with the deformed geometry, and with other material properties [8,22–28], and is thus incorrectly employed in the previous models. For these reasons, several researchers have recently developed new multiscale contact models [29–33] to alleviate these problems, although they are still being refined. The work by Li et al. [8] even examined the dependence of the statistical parameters necessary for the GW model to predict TCR and also the scale dependence of the microhardness. The objective of this work is to construct a new inclusive multiscale model and use it to evaluate the effect of scale dependent surface features and properties on TCR.

The current work will consider other important factors that have been neglected in the past, including the scale effects on mechanical [25,28,34–38] and thermal material properties [39–45]. It should be noted that this work does neglect the effect of gas conduction that can occur between the surfaces. There is a

---

Contributed by the Heat Transfer Division of ASME for publication in the Journal of Heat Transfer. Manuscript received January 17, 2007; final manuscript received February 13, 2008; published online May 30, 2008. Review conducted by Yogendra Joshi. Paper presented at the 2006 ASME International Mechanical Engineering Congress (IMECE2006), Chicago, IL, November 5–10, 2006.

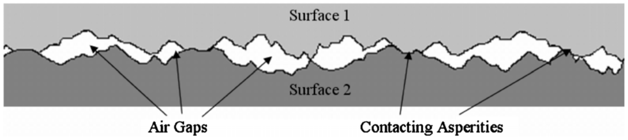

Fig. 1 Schematic of typical rough surface contact (the height of the asperities is exaggerated)

need to resolve these issues and to derive a fundamentally sound model of thermal contact resistance between multiscale rough surfaces. This work develops the new multiscale theory for the thermal contact resistance between rough surfaces and compares it to the existing model by Yovanovich et al. [4].

Existing Models. Following Song and Yovanovich [4,46], a simplified dimensional correlation of the analytical solution for the contact conductance is usually represented as

$$h_c = \frac{1}{R} = 1.25k\frac{m}{\sigma}\left(\frac{P}{H_m}\right)^{0.95} \tag{1}$$

where

$$k = \frac{2k_1k_2}{k_1 + k_2} \tag{2}$$

is the harmonic mean thermal conductivity of the contacting surfaces, $m=[m_1^2+m_2^2]^{1/2}$ is the effective absolute surface slope, $\sigma=[\sigma_1^2+\sigma_2^2]^{1/2}$ is the effective rms surface roughness in microns, k is the effective thermal conductivity, R is the thermal contact resistance, P is the contact pressure in $\mathrm{N/m^2}$, and H_m is the microhardness of the softer material in $\mathrm{N/m^2}$. It should be noted that it can be difficult to find a universally accepted method to calculate m. Equation (1) is also based on the "truncation" model which assumes that the contact area will equal the load, P, divided by the microhardness, H_m. H_m is also dependent on the deformed geometry and the scale of the contact, as discussed previously. The effective microhardness was correlated to the bulk hardness for several metals [28,47]. It was difficult for the authors to find a material that was adequately characterized for both the microhardness theory and for the strain gradient scale dependent properties theory. From Ref. [46], the resulting correlation is

$$\frac{P}{H_m} = \left[\frac{P}{H(1.62\sigma/d_b m)^{c_o}}\right]^{1/1+0.071c_o} \tag{3}$$

where d_b is an empirically measured material constant and c_o is -0.26. These equations will be compared to the new model which considers multiscale effects. Although the model by Song and Yovanovich does not directly consider the effects of multiscale surface features or scale dependent material properties, the use of the empirical microhardness theory appears to have been effective at including these scale effects. This work explores these issues and seeks to illuminate the effect that they have on thermal contact resistance.

Multiscale Rough Surface Contact. The multiscale model [48] uses the same direction of thought as Archard [11], but provides a method that can be easily applied to real surfaces. The model assumptions are given in Ref. [48] which result in the following:

$$A_r = \left(\prod_{i=1}^{i_{\max}} \bar{A}_i\eta_i\right)A_n \tag{4}$$

$$F = \bar{F}_i\eta_i A_{i-1} \tag{5}$$

where A_r is the real area of contact, η is the areal asperity density, F is the contact load, A_n is the nominal contact area, and the subscript i denotes a frequency level, with $i_{\max}$ denoting the highest frequency level considered. Parameters $\bar{A}_i$ and $\bar{F}_i$ are the single asperity contact area and single asperity contact force at a given frequency level, respectively. The total (nominal) area of contact at a given frequency level is denoted by A_i, while η_i is the corresponding areal asperity density.

After selecting the scan length (L), the input surface data are acquired and a fast Fourier transform (FFT) is performed on it. The scan length, L, is limited by the employed surface profile apparatus. However, results from Ref. [48] found that relatively large scales are very important in predicting rough surface contact and therefore a relatively large value of L should be used (ideally a value that is the same order of magnitude as the length of the nominal contact area being considered). From the resulting Fourier series, the asperity areal density, η, and radius of curvature, β, are computed for each frequency level according to

$$\eta_i = 2f_i^2 \tag{6}$$

$$\beta_i = \frac{1}{4\pi^2\Delta_i f_i^2} \tag{7}$$

where f_i denotes the frequency (i.e., the reciprocal of wavelength) and Δ_i is the amplitude corresponding to the given frequency. Equations (6) and (7) are used in the multiscale model framework (Eqs. (4) and (5)) and also in the single asperity models. The nominal contact area (A_n) is then set to be equal to L^2 and is identified with $i=0$.

For a given frequency level, the number of asperities is calculated. The total load is then divided evenly among all of the asperities of the given level. Next, the single asperity area of contact is determined from the given asperity load, the given asperity dimensions, and the material properties, according to the chosen asperity deformation model (e.g., Hertz [49]). Then multiplying by the number of asperities at that level, a provisional total contact area for that frequency level is computed. The result is checked against the contact area predicted by the frequency level below it, and the smaller value is selected as the contact area for the given frequency level. The concept behind this rule is that each frequency level is used to predict the apparent contact area of the next higher frequency level. The iterative procedure continues until all the desired frequencies are considered, resulting in a prediction of the real area of contact at the prescribed load. Additional details of the model can be found in Jackson and Streator [48].

Asperity Deformation. A variety of individual asperity models are available for use within the multiscale framework described above to relate the contact area to the contact force. For a simulation of purely elastic rough surface contact, the Hertzian model [49] may be applied. Alternatively, several models are available that account for elastoplastic deformation of spherically shaped asperities [26,50–52]. A detailed description of several elastoplastic models is given in Kogut and Etsion [52], and Jackson and Green [26]. Brief descriptions of the single asperity models used in the current analysis are provided in the following section.

As the load pressing two rough surfaces together increases, the stresses within the individual asperities also increase. These stresses eventually cause the material within the asperity (modeled as a hemisphere) to yield. The interference at the material yield point is known as the critical interference, ω_c. Jackson and Green (JG) [26] and Chang et al. [50] derived this critical interference analytically using the von Mises yield criterion. The resulting equation from Ref. [26] is

$$\omega_c = \left(\frac{\pi\cdot C\cdot S_y}{2E'}\right)^2\beta \tag{8}$$

where S_y is the yield strength of the material that yields first, E' is the effective modulus of elasticity, β is the radius of the spherical asperity, and C is given by

$$C = 1.295\exp(0.736\nu) \tag{9}$$

and ν is the Poisson ratio of the material that yields first.

The critical force, $\bar{F}_c$, is then calculated at the critical interference, ω_c, to be

$$\bar{F}_c = \frac{4}{3}\left(\frac{\beta}{E'}\right)^2\left(\frac{C}{2}\pi \cdot S_y\right)^3 \tag{10}$$

Similarly, the critical contact area is

$$\bar{A}_c = \pi^3\left(\frac{CS_y\beta}{2E'}\right)^2 \tag{11}$$

In the present study, when the contact is below these critical values the multiscale model uses the Hertzian elastic contact to model individual asperity contact, whereas to model elastoplastic contact, the JG asperity deformation model is used.

The JG model was developed by fitting curves to the results of a finite element model of elastoplastic spherical contact. It predicts the contact force and area between an elastic, perfectly plastic hemisphere and a rigid flat as functions of the ratio of interference (ω) to critical interference (ω_c). (The converse case of a rigid sphere indenting an elastic perfectly plastic half-space is not considered here.) When $0 \leq \omega/\omega_c \leq 1.9$, the JG single asperity model virtually coincides with the Hertzian solution. At interference ratios (ω/ω_c) larger than 1.9, the formulation below is used in the JG model for single-asperity elastoplastic contact:

For $\omega \geq 1.9 \cdot \omega_c$,

$$\bar{A}_{JG} = \pi\beta\omega\left(\frac{\omega}{1.9\omega_c}\right)^B \tag{12}$$

$$\bar{F} = \bar{F}_c\left\{\left[\exp\left(-\frac{1}{4}\left(\frac{\omega}{\omega_c}\right)^{5/12}\right)\right]\left(\frac{\omega}{\omega_c}\right)^{3/2} + \frac{4H_G}{CS_y}\left[1-\exp\left(-\frac{1}{25}\left(\frac{\omega}{\omega_c}\right)^{5/9}\right)\right]\frac{\omega}{\omega_c}\right\} \tag{13}$$

where

$$B = 0.14\exp(23 \cdot e_y) \tag{14}$$

$$e_y = \frac{S_y}{E} \tag{15}$$

For $a/\beta < 0.41$,

$$\frac{H_G}{S_y} = 2.84\left[1-\exp\left(-0.82\left(\frac{a}{\beta}\right)^{-0.7}\right)\right] \tag{16}$$

For $0.41 < a/\beta < 1$,

$$\frac{H_G}{S_y} = 7.32 \cdot \left(\frac{a}{\beta}\right)^3 - 14.12 \cdot \left(\frac{a}{\beta}\right)^2 + 6.28 \cdot \left(\frac{a}{\beta}\right) + 1.52 \tag{17}$$

For $a/\beta > 1$,

$$\frac{H_G}{S_y} = 1 \tag{18}$$

The parameter H_G, referred to as the "hardness geometric limit," represents an asymptote for mean compressive stress, depending on the radius of contact. As the interference (ω) increases past the critical interference (ω_c), Eqs. (12)–(18) depart from the Hertz elastic solution and predict the influence of an enlarging amount of plastic deformation. This causes the contact force to decrease and the contact area to increase in relation to the Hertz contact solution. The predictions of the above equations also compare well with several experimental results [22,53].

Scale Dependent Properties

Mechanical Properties. Scale dependent material properties have been observed for some time. For instance, in the early work by Ling [54], the effect of scale on hardness was included in a rough surface contact model. More recently, Nix and Gao [55] formulated a model which describes the strain gradient effect on the change in material hardness with scale. This model was derived to account for these effects seen during micro- and nanoindentation tests. The strain gradient dependent hardness for Berkovich type indenters is given by Nix and Gao as

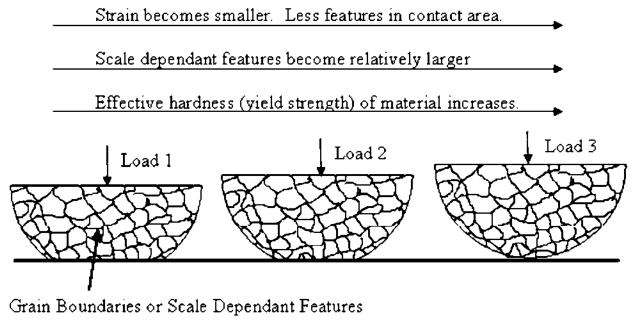

Fig. 2 Schematic showing how scale dependent features can affect material properties

$$H = H_o\sqrt{1+\frac{h^*}{h_p}} \tag{19}$$

where H_o is the macroscopic hardness, H is the corrected scale dependent hardness, h^* is a length scale for the effect, and h_p is the depth of plastic deformation caused by the indentation. Swadener et al. [56] correlate Nix and Gao's results for different shaped indenters, including a Brinell or spherical shape. Figure 2 shows qualitatively how scale dependent features can increase the strain hardening of the material during spherical contact (Note that the strain gradient theory effectively models the change in material yield strength (and hardness) as a function of the magnitude of deformation.) The current work will consider these effects in modeling the contact between multiple scales of rough surfaces by simplifying the asperities as spherical peaks.

As mentioned earlier, it was difficult to find a material that has been evaluated for both microhardness by Yovanovich and Hegazy [28,47] and scale dependent yield strength, but the properties for nickel are available. For nickel surfaces, Lou et al. [57] provided the material length scale required to use Eq. (19). For nickel, the value used is $h^* = 0.343$ μm. From Ref. [46], the corresponding bulk yield strength, $(S_y)_o$, is 0.556 GPa. A theoretical yield strength of the material, $(S_y)_t = 20.7$ GPa (which is E divided by a factor of 10), is used as an upper limit to Eq. (19) [58]. See Table 1 for a complete list of the material properties used in this work.

Next, the value of h_p during contact is required. Jackson et al. modeled the residual stress and deformation of a spherical indenter loaded and unloaded [59]. In the current work, it is as-

Table 1 Material properties for nickel used in this work

Material property	Value
E	207 GPa
v	0.30
$(S_y)_o$	0.556 GPa
H	1.668 GPa
h^*	0.343 μm
$(S_y)_t$	20.7 GPa
k	90.7 W/m k
ρ	8.9 g/cm^3
C	0.44 J/g°C
v_s	4970 m/s

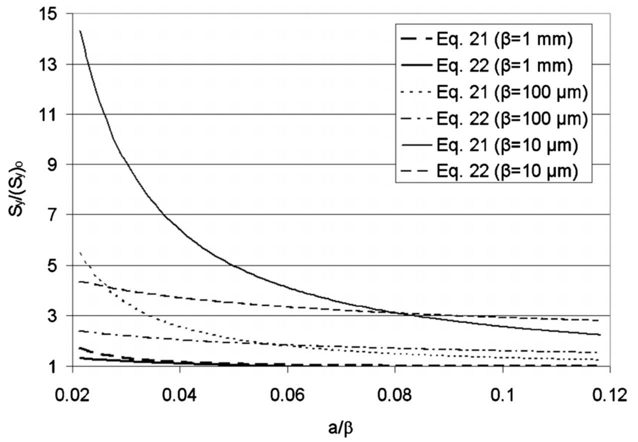

Fig. 3 Comparison of models for scale dependent yield strength

sumed that the residual interference measured in Ref. [59], ω_{res}, will be equal to the residual depth after unloading of a spherical contact, h_p. From Jackson et al. [60],

$$\frac{\omega_{\text{res}}}{\omega_m} = 1.02\left(1 - \left(\frac{(\omega^*)_m + 5.9}{6.9}\right)^{-0.54}\right) \tag{20}$$

This equation is used to approximate h_p.

However, fundamentally the hardness is changing because the strain gradient effect changes the value of the yield strength, S_y. S_y is a parameter in Eqs. (8)–(18) and strain gradient plasticity must also be accounted for in them. Similar to Eq. (19), the strain gradient dependent yield strength can be represented by

$$S_y = (S_y)_o\sqrt{1 + \frac{h^*}{h_p}} \tag{21}$$

where $(S_y)_o$ is the yield strength without strain gradient effects. h_p is found from Eq. (20), which depends on the critical interference, ω_c, among the other parameters. The yield strength predicted by Eq. (21) is inversely proportional to scale. Song and Yovanovich [46] also provided an equation describing the scale dependent hardness:

$$\frac{H_m}{H} = \frac{S_y}{(S_y)_o} = \left(\frac{\sqrt{2}\pi a}{d_b}\right)^{c_o} \tag{22}$$

For nickel d_b is given as 157 μm and from Lou et al. [57] h^* for nickel is given as 243.3 nm. Then, using Eq. (12) to calculate the contact radius a, the predictions for Eqs. (21) and (22) can be compared (see Fig. 3). The results are shown for the contact of three different size spheres against a rigid flat surface. The scale of the contact is represented by the nondimensional quantity a/β. The comparison shows that Eqs. (21) and (22) predict the same general trend (that the strength increases with decreasing scale). However, quantitatively the predictions of the models are quite different. The slope of Eq. (21) appears to be much steeper than the slope of Eq. (22) and so it predicts a more significant change in the strength with scale. It does appear that for β=1 mm, the models make the closest predictions.

It is also important to consider that because ω_c is dependent on S_y, Eqs. (20) and (21) are coupled. Physically this shows that the contact of rough surfaces is dependent on the scale of local asperity surface deformations, which suggests that it cannot be easily described by macroscale global properties. In the current work, Eqs. (12)–(18), (20), and (21) are solved simultaneously using the golden section method.

Although these asperity contact models are mostly continuum based models, they might also be used to consider nanoscale contacts in the multiscale model. This depends on which asperity levels or scales ultimately dictate the area of contact. For very small contacts, the continuum models appear to be effective; however, eventually the nanoscale or atomistic roughness will dominate the problem [61,62]. It would be difficult to incorporate these effects into the current model because the orientation of the lattice and atoms for each asperity in contact would have to be known. Molecular dynamics (MD) models are also very computationally expensive. This is why the current work uses scale dependent modifications to the asperity contact models rather than MD models directly. However, on average, the continuum models are expected to perform adequately. It has also been found that when plastic deformation is included in the multiscale contact model, the smaller asperities (smaller than 1–10 μm) tend to flatten out and have little effect on the total prediction of contact area.

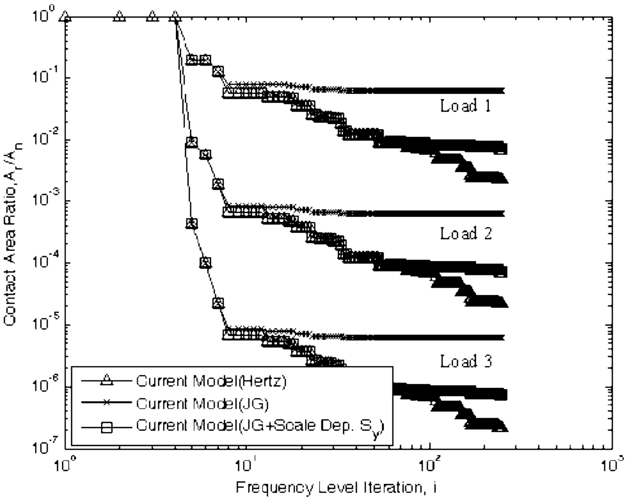

Fig. 4 Progression of the multiscale contact area calculations through the iterative numerical scheme

To help illustrate the predictions made by the multiscale model, the progression of the real area of contact as successive frequency levels are included is shown in Fig. 4. Each curve is for a constant load. Each ledge or drop represents a frequency level which reduces the real area of contact. Note that not all of the frequency levels do so. It can be seen that the single asperity contact model employed also drastically affects the results. The perfectly elastic model underpredicts the real area of contact. Including plastic deformation causes many of the frequency levels to flatten out and not affect the final prediction. This is because they cannot carry much load once significant yielding has occurred. Using the scale dependent yield strength effectively strengthens the asperities, resulting in a prediction of contact area that lies between the elastic and elastoplastic models.

Thermal Properties. A considerable amount of work has been performed by Yovanovich and others in the area of TCR [4]. Generally, the heat conducted between two surfaces can travel either through the asperity contacts or through the gaps, which may be filled with gas or an intermediate material (see Fig. 1). In this work, the effect of heat conducted through the gas is neglected, and so the contacting surfaces are modeled as being in a vacuum. The contact conductance, h, is defined as the heat flux through the contact divided by the change in temperature across the contact:

$$h = q/\Delta T_c \tag{23}$$

where the heat flux, q, is the total heat flow rate divided by the nominal contact area, A_n. The thermal contact resistance, R_c, can then be defined as

$$R_c = (hA_n)^{-1} \tag{24}$$

The value of R over the entire surface can then be found by considering the contact resistance of all N asperities on the contacting surface:

$$R_{\text{total}} = \left(\sum_{i=1}^{N} (hA_n)_i^{-1} \right)^{-1} \tag{25}$$

Around a single asperity contact a "flux tube" is theorized to exist from the contact surface to a depth into the material. The heat transfer between the two surfaces must then pass through the flux tube and thus through the reduced cross-sectional area of the contact. The heat flux will constrict and then expand as it passes through the contact. In past studies, the thermal resistance of the flux tube between the two contacting spheres has been characterized by the Maxwell equation:

$$R_c = \frac{1}{2ka} \tag{26}$$

Then, it has been found that when the scale of contact changes, the governing equations for thermal resistance also change. The work by Prasher [44] provides a simplified form of the scale dependent thermal contact resistance given as

$$R = \frac{(3\pi + 8K)}{6\pi \cdot ak} \tag{27}$$

where K is the Knudsen number defined as λ/a. λ is the phonon free mean path of the material. λ can be calculated from the macroscopic relation:

$$\lambda = \frac{3k}{\rho v_s C} \tag{28}$$

where k is the thermal conductivity, v_s is the solid speed of sound, ρ is the density, and C is the heat capacity. For typical properties of nickel at room temperature (see Table 1), the predicted value of λ is 14 nm. To calculate the phonon free mean path can be difficult as there are several different methods that result in different predictions, as shown by Prasher and Phelan [63].

In addition, if the contact radius of an individual conducting asperity, a, becomes large in relation to the radius of the asperity, β, this will affect the thermal contact resistance through the individual conducting asperity. This effect is accounted for by using the contact alleviation factor, ψ. There are different equations, which can be used to calculate this factor [64]. Cooper et al. [65] provided a simplified equation, which will be used in the current work:

$$\psi = (1 - a/\beta)^{1.5} \tag{29}$$

An alternative form of this function is usually used for the TCR between rough surfaces that is given as

$$\psi = (1 - \sqrt{A_r/A_n})^{1.5} \tag{30}$$

Then the thermal contact resistance for a single asperity is given as

$$R_{\text{asp}} = R \cdot \psi \tag{31}$$

Two different theories are now presented to predict TCR from the multiscale model. First, at the highest frequency level, which reduces contact area (see Fig. 4), the total thermal contact resistance between the surfaces can be calculated from

$$\frac{1}{R_c} = \sum_{n=1}^{N} \left(\frac{1}{R_{\text{asp}}} \right)_n \tag{32}$$

Since all the asperities at this frequency will be identical, Eq. (32) reduces to

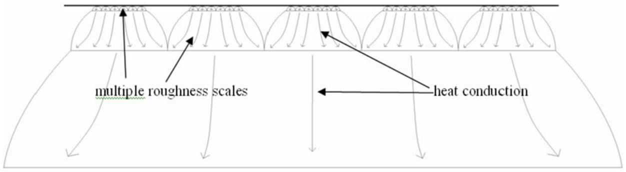

Fig. 5 Schematic illustrating how heat conduction may be influenced by multiple scales of roughness on the surface

$$R_c = \frac{R_{\text{asp}}}{N} = \frac{R_{\text{asp}}}{\eta_i A_{i-1}} \tag{33}$$

where N is the number of asperities at the highest frequency level, which reduces contact area, i, and is calculated as $\eta_i A_{i-1}$ (see section on multiscale model).

Alternatively, the thermal conductance will be calculated by summing the contact resistance from each scale, which reduces the area of contact (see Fig. 5). Recall that each frequency level that reduces contact area is represented as a ledge in Fig. 4. In equation form, this relation is

$$R_{\text{total}} = \sum_{i=1}^{i_{\max}} R_i \eta_i A_{i-1} \tag{34}$$

Both of the above theories (Eqs. (33) and (34)), now dubbed the highest frequency TCR (HFTCR) and multiple frequency TCR (MFTCR), respectively, are considered in the current work. The way in which the contact alleviation factor, ψ, is included in each model is also slightly different. In the HFTCR model, ψ is calculated using the predicted real area of contact over the total nominal area of contact (see Eq. (30)). In contrast, the MFTCR model includes ψ at each frequency level by calculating the ratio of the contact area at the current frequency level to the one below it:

$$\psi_i = (1 - \sqrt{A_i/A_{i-1}})^{1.5} \tag{35}$$

The results of the HFTCR theory are now considered first.

Results

As expected, the trends from the iterative predictions shown in Fig. 4 translate to the final predictions for the real area of contact as a function of load (see Fig. 6). The elastic multiscale model again predicts a contact area much smaller than when plastic deformation is included, and including a scale dependent yield

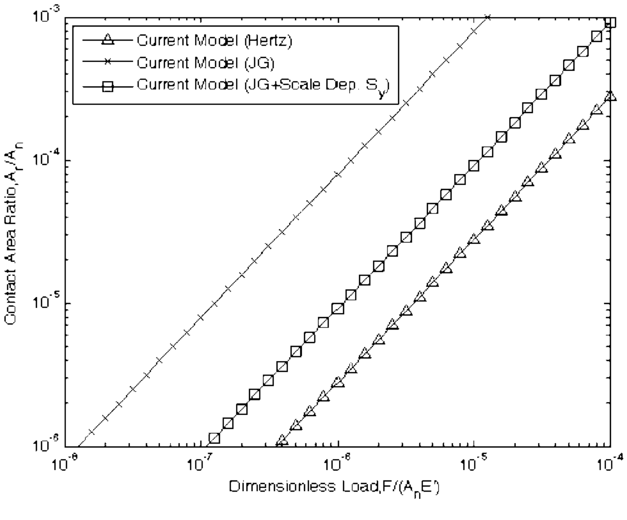

Fig. 6 Multiscale model predicted contact area as a function of load

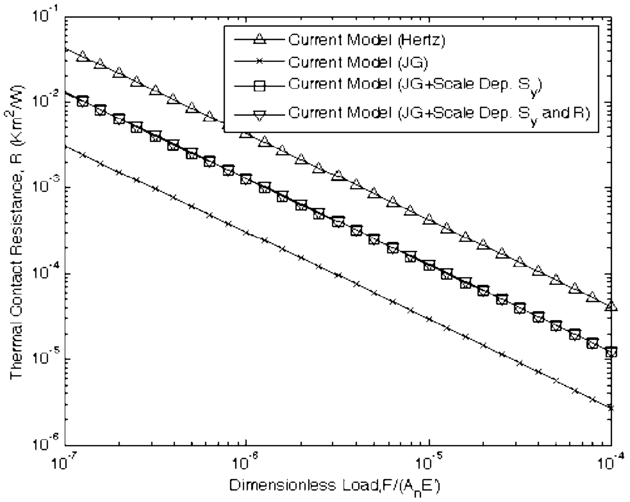

Fig. 7 Multiscale model predicted thermal contact resistance as a function of load considering scale dependent yield strength and resistance

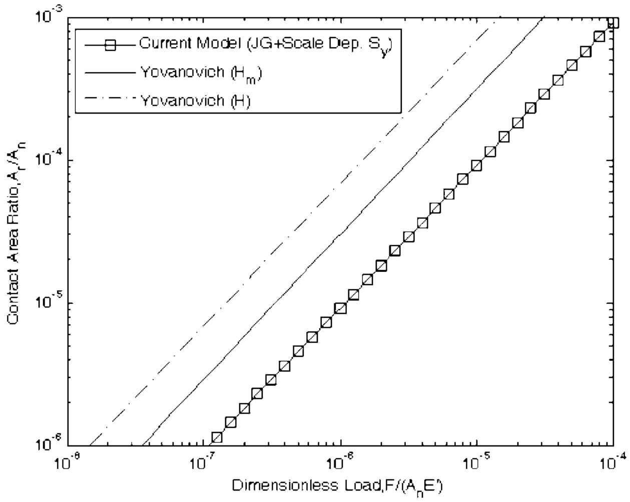

Fig. 8 Comparison of current multiscale contact model to existing models used in TCR

strength results in contact areas in between the other two curves. The contact area also appears to increase nearly linearly on the log-log plot with load. Similar trends are also seen for statistical and fractal models.

Using the HFTCR theory produces the TCR trends shown in Fig. 7 for the contact of rough surfaces. Note that the effect of the contact alleviation factor is also included (Eq. (30)). The real areas of contact predicted by the models appear to not directly correlate to the relative values of the TCR. The reason for this is not obvious, but occurs because the HFTCR theory only uses the highest frequency level to decrease the area of contact in predicting the TCR. Information in this highest frequency level for curvature and the number of asperities may differ between the models. Since TCR is dependent on this information and not on the summed contact area, the predicted relative values of TCR may also differ (see Eqs. (4) and (34)) from the predicted relative values of the area of contact. Partially due to this effect, the MFTCR theory arose.

The results for the multiscale model for rough surface contact including asperity level scale dependent spreading resistance are also shown in Fig. 7 in comparison to the results without considering this scale dependence. The results are almost indiscernible from the results not including this effect. Therefore, it appears that this effect is somewhat negligible in modeling the thermal contact resistance between rough surfaces. Also, Prasher and Phelan [63] showed that there are different methods to calculate λ and that by using Eq. (28), the value may be underpredicted. To consider this possibility, the value of λ was artificially increased by a factor of 10 and the simulation was rerun. The result showed that the effect of the scale dependent spreading resistance did increase slightly by about 16% at all points, but its effect was still significantly smaller than the effect of scale dependent strength.

Next, the contact area predicted by the current multiscale model is compared to that predicted by Yovanovich [4]. See Fig. 8 for this comparison. The current model predicts areas, which are smaller than the those predicted by the Song and Yovanovich's model using the bulk hardness, H, and the truncation model using the microhardness, H_m [28,47]. This agrees with Yovanovich [4] that the bulk hardness alone cannot be used to model contact between rough surfaces accurately. However, it also suggests that it is difficult to predict an effective microhardness value without using empirical relationships. Even though the model predictions are quantitatively different, their slope is almost identical and the predicted qualitative trends are the same. This is very encouraging that two fundamentally very different models predict similar results.

Using HFTCR, the predicted TCR does locate in between Yovanovich's [4] models as the predicted real of contact did (see Fig. 9), but also agrees almost exactly with Yovanovich's model including microhardness. Note that the results shown are for the contact between rough surfaces and not a single asperity contact. This suggests that Yovanovich's microhardness empirical correction does effectively consider the multiscale nature of the surfaces. However, it should be noted that the slope of the TCR for the multiscale model is steeper than that for Yovanovich's models. Perhaps this is because elasticity is also included in the current multiscale model. Again, this is very encouraging that two fundamentally different models (one which includes the scale effect on thermal conductivity) are able to produce very similar results.

Finally, the MFTCR theory is used to predict the TCR from the multiscale model and is also compared to Yovanovich's [4] models (see Fig. 10). All the scale dependent effects on thermal spreading resistance and yield strength are included in the results shown. The predicted TCR using the MFTCR theory is larger than

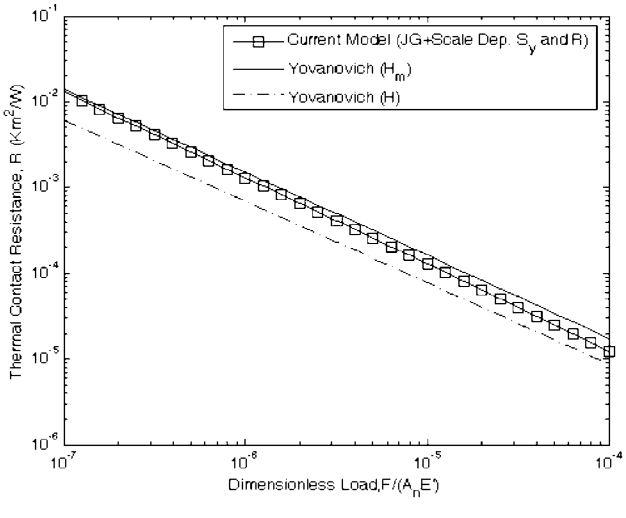

Fig. 9 Comparison of current multiscale contact resistance model (using the HFTCR theory) to existing models used in TCR

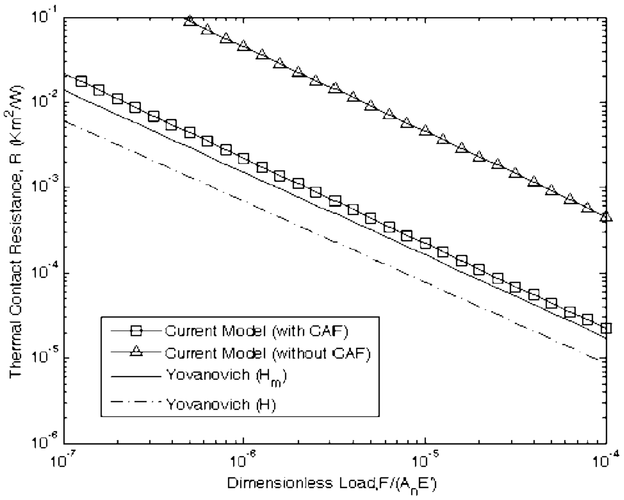

Fig. 10 Comparison of current multiscale contact resistance model (using the MFTCR theory) to existing models used in TCR

the other results. This is, of course, because it considers the resistance accumulated from all the stacked frequencies levels. However, since the contact alleviation factor, ψ, is included at each scale (Eq. (35)), it decreases the TCR significantly, and causes the predicted values to still be fairly close to the values predicted by the Yovanovich model. The predictions of the current multiscale model with and without the contact alleviation factor (CAF) are also shown in Fig. 10. The current multiscale theory also blurs the boundary between the bulk thermal resistance and the TCR from the surface. For instance, if the lowest frequency considered by the multiscale model is close to the size of the sample surface, the resistance resulting from this frequency may sometimes be considered part of the bulk resistance and not the TCR.

Conclusions

A new inclusive multiscale model has been developed, which considers the multiple scales of roughness that exist on a surface and the scale dependence of the mechanical and thermal properties. Therefore, this model theoretically includes more effects and details than most previous models. Scale dependent spreading resistance was found to have virtually no effect on modeling TCR between rough surfaces, while scale dependent yield strength was found to have a more noticeable effect on the TCR results. The predicted TCR results are significantly affected by which frequency levels are considered to reduce TCR. Two theories are presented to calculate TCR from the multiscale model: (1) all frequency levels are considered (MFTCR) and (2) only the highest frequency level that reduces the real area of contact is considered (HFTCR). These two theories produce very different results. Since the MFTCR also considers asperity levels or surface features below, which are in direct contact, it could be said that it starts to incorporate the bulk resistance into the model. This is in contrast to the HFTCR, which only considers the final layer of asperities that are in direct contact. Therefore, these models blur the boundary between the thermal contact resistance at the surface and in the bulk material below it, demonstrating the importance of capturing multiscale effects when evaluating thermal contact resistance.

References

[1] Lambert, M. A., and Fletcher, L. S., 1997, "Review of Models for Thermal Contact Conductance of Metals," J. Thermophys. Heat Transfer, **11**(2), pp. 129–140.

[2] Madhusudana, C. V., and Fletcher, L. S., 1986, "Contact Heat Transfer—The Last Decade," AIAA J., **24**(3), pp. 510–523.

[3] Madhusudana, C. V., Fletcher, L. S., and Peterson, G. P., 1990, "Thermal Conductance of Cylindrical Joints. A Critical Review," J. Thermophys. Heat Transfer, **4**(2), pp. 204–211.

[4] Yovanovich, M. M., 2005, "Four Decades of Research on Thermal Contact, Gap, and Joint Resistance in Microelectronics," IEEE Trans. Compon. Packag. Technol., **28**(2), pp. 182–206.

[5] Greenwood, J. A., and Williamson, J. B. P., 1966, "Contact of Nominally Flat Surfaces," Proc. R. Soc. London, Ser. A, **A295**, pp. 300–319.

[6] Kogut, L., and Jackson, R. L., 2005, "A Comparison of Contact Modeling Utilizing Statistical and Fractal Approaches," ASME J. Tribol., **128**(1), pp. 213–217.

[7] Majumdar, A., and Tien, C. L., 1990, "Fractal Characterization and Simulation of Rough Surfaces," Wear, **136**(2), pp. 313–327.

[8] Li, Y. Z., Madhusudana, C. V., and Leonardi, E., 1998, "Experimental Investigation of Thermal Contact Conductance: Variations of Surface Microhardness and Roughness," Int. J. Thermophys., **19**(6), pp. 1691–1704.

[9] Mikic, B., 1971, "Analytical Studies of Contact of Nominally Flat Surfaces; Effect of Previous Loading," ASME J. Lubr. Technol., **93**(4), pp. 451–456.

[10] Greenwood, J. A., and Wu, J. J., 2001, "Surface Roughness and Contact: An Apology," Meccanica, **36**(6), pp. 617–630.

[11] Archard, J. F., 1957, "Elastic Deformation and the Laws of Friction," Proc. R. Soc. London, Ser. A, **243**, pp. 190–205.

[12] Borri-Brunetto, M., Carpinteri, A., and Chiaia, B., 1999, "Scaling Phenomena Due to Fractal Contact in Concrete and Rock Fractures," Int. J. Fract., **95**(1–4), pp. 221–238.

[13] Borri-Brunetto, M., Chiaia, B., and Ciavarella, M., 2001, "Incipient Sliding of Rough Surfaces in Contact: A Multiscale Numerical Analysis," Comput. Methods Appl. Mech. Eng., **190**(46–47), pp. 6053–6073.

[14] Hyun, S., Pel, L., Molinari, J. F., and Robbins, M. O., 2004, "Finite-Element Analysis of Contact Between Elastic Self-Affine Surfaces," Phys. Rev. E, **70**(22), pp. 026117.

[15] Komvopoulos, K., and Ye, N., 2001, "Three-Dimensional Contact Analysis of Elastic-Plastic Layered Media With Fractal Surface Topographies," ASME J. Tribol., **123**(3), pp. 632–640.

[16] Majumdar, A., and Bhushan, B., 1991, "Fractal Model of Elastic-Plastic Contact Between Rough Surfaces," ASME J. Tribol., **113**(1), pp. 1–11.

[17] Warren, T. L., and Krajcinovic, D., 1995, "Fractal Models of Elastic-Perfectly Plastic Contact of Rough Surfaces Based on the Cantor Set," Int. J. Solids Struct., **32**(19), pp. 2907–2922.

[18] Willner, K., 2004, "Elasto-Plastic Normal Contact of Three-Dimensional Fractal Surfaces Using Halfspace Theory," ASME J. Tribol., **126**(1), pp. 28–33.

[19] Yan, W., and Komvopoulos, K., 1998, "Contact Analysis of Elastic-Plastic Fractal Surfaces," J. Appl. Phys., **84**(7), pp. 3617–3624.

[20] Borodich, F. M., and Persson, B. N. J., 2002, "Comment on Elastoplastic Contact Between Randomly Rough Surfaces," Phys. Rev. Lett., **88**(6), pp. 069601.

[21] Wang, S., Shen, J., and Chen, W. K., 2006, "Determination of the Fractal Scaling Parameter From Simulated Fractal Regular Surface Profiles Based on the Weierstrass-Mandelbrot Function (IJTC2006–12068)," *STLE/ASME International Joint Tribology Conference*, San Antonio, TX.

[22] Chaudhri, M. M., Hutchings, I. M., and Makin, P. L., 1984, "Plastic Compression of Spheres," Philos. Mag. A, **49**(4), pp. 493–503.

[23] Mesarovic, S. D., and Fleck, N. A., 2000, "Frictionless Indentation of Dissimilar Elastic-Plastic Spheres," Int. J. Solids Struct., **37**, pp. 7071–7091.

[24] Kogut, L., and Komvopoulos, K., 2004, "Analysis of Spherical Indentation Cycle of Elastic-Perfectly Plastic Solids," J. Mater. Res., **19**, pp. 3641–3653.

[25] Jackson, R. L., 2006, "The Effect of Scale Dependant Hardness on Elasto-Plastic Asperity Contact Between Rough Surfaces," Tribol. Trans., **49**(2), pp. 135–150.

[26] Jackson, R. L., and Green, I., 2005, "A Finite Element Study of Elasto-Plastic Hemispherical Contact," ASME J. Tribol., **127**(2), pp. 343–354.

[27] Wei, Y., and Hutchinson, J. W., 2003, "Hardness Trends in Micron Scale Indentation," J. Mech. Phys. Solids, **51**, pp. 2037–2056.

[28] Yovanovich, M. M., and Hegazy, A., 1983, "An Accurate Universal Contact Conductance Correlation for Conforming Rough Surfaces With Different Micro-Hardness Profiles," *Proceedings AIAA 18th Thermophysics Conference*, Montreal, QC, Canada.

[29] Jackson, R. L., and Streator, J. L., 2006, "A Multiscale Model for Contact Between Rough Surfaces," Wear, **261**(11–12), pp. 1337–1347.

[30] Almeida, L., Ishikawa, Yu Q., Jackson, R., and Ramadoss, R., "Experimental and Theoretical Investigation of Contact Resistance and Reliability of Lateral Contact Type Ohmic MEMS Relays," *SPIE 2006 Reliability, Packaging, Testing, and Characterization of MEMS/MOEMS, SPIE & Photonics West MOEMS-MEMS MICRO & NANOFABRICATION Symposium*, San Jose, CA.

[31] Bora, C. K., Flater, E. E., Street, M. D., Redmond, J. M., Starr, M. J., Carpick, R. W., and Plesha, M. E., 2005, "Multiscale Roughness and Modeling of MEMS Interfaces," Tribol. Lett., **19**(1), pp. 37–48.

[32] Ciavarella, M., Demelio, G., Barber, J. R., and Jang, Y. H., 2000, "Linear Elastic Contact of the Weierstrass Profile," Proc. R. Soc. London, Ser. A, **456**(1994), pp. 387–405.

[33] Ciavarella, M., Murolo, G., Demelio, G., and Barber, J. R., 2004, "Elastic Contact Stiffness and Contact Resistance for the Weierstrass Profile," J. Mech. Phys. Solids, **52**(6), pp. 1247–1265.

[34] Fleck, N. A., and Hutchinson, J. W., 1993, "A Phenomenological Theory for Strain Gradient Effects in Plasticity," J. Mech. Phys. Solids, **41**, pp. 1825–1857.

[35] Fleck, N. A., Muller, G. M., Ashby, M. F., Hutchinson, J. W., 1994, "Strain

Gradient Plasticity: Theory and Experiment," Acta Metall. Mater., **42**(2), pp. 475–487.
[36] Gao, H., Huang, Y., Nix, W. D., and Hutchinson, J. W., 1999, "Mechanism-Based Strain Gradient Plasticity-I," J. Mech. Phys. Solids, **47**, pp. 1239–1263.
[37] Gao, H., Huang, Y., Nix, W. D., and Hutchinson, J. W., 2000, "Mechanism-Based Strain Gradient Plasticity-II. Analysis," J. Mech. Phys. Solids, **48**, pp. 99–128.
[38] Hutchinson, J. W., 2000, "Plasticity at the Micron Scale," Int. J. Solids Struct., **37**, pp. 225–238.
[39] Saha, S., and Shi, L., 2005, "Molecular Dynamics Simulation of Thermal Transport at Nanometer Size Point Contacts on a Planar Silicon Substrate," San Francisco, CA, United States, American Society of Mechanical Engineers, New York.
[40] Weber, L., Gmelin, E., and Queisser, H. J., 1989, "Thermal Resistance of Silicon Point Contacts," Phys. Rev. B, **40**, pp. 1244–1249.
[41] Weber, L., Lehr, M., and Gmelin, E., 1996, "Investigation of the Transport Properties of Gold Point Contacts," Physica B, **217**(3–4), pp. 181–192.
[42] Little, W. A., 1959, "The Transport of Heat Between Dissimilar Solids at Low Temperatures," Can. J. Phys., **37**, pp. 334–349.
[43] Chen, G., 1996, "Nonlocal and Nonequilibrium Heat Conduction in the Vicinity of Nanoparticles," ASME J. Heat Transfer, **118**, pp. 539–545.
[44] Prasher, R., 2005, "Predicting the Thermal Resistance of Nanosized Constrictions," Nano Lett., **5**(11), pp. 2155–2159.
[45] Chen, G., 2004, "Nanoscale Heat Transfer and Nanostructured Thermoelectrics," *Thermomechanical Phenomena in Electronic Systems-Proceedings of the Intersociety Conference*, Las Vegas, NV, IEEE Inc., Piscataway, NJ.
[46] Song, S., and Yovanovich, M. M., 1988, "Relative Contact Pressure: Dependence on Surface Roughness and Vickers Microhardness," Int. J. Thermophys., **2**(1), pp. 43–47.
[47] Hegazy, A., 1985, "Thermal Joint Conductance of Conforming Rough Surfaces: Effect of Surface Micro-Hardness Variation," Ph.D. thesis, University of Waterloo.
[48] Jackson, R. L., and Streator, J. L., 2005, "A Multiscale Model for Contact Between Rough Surfaces," *World Tribology Conference III* Washington, DC.
[49] Timoshenko, S., and Goodier, J. N., 1951, *Theory of Elasticity*, McGraw-Hill, New York.
[50] Chang, W. R., Etsion, I., and Bogy, D. B., 1987, "An Elastic-Plastic Model for the Contact of Rough Surfaces," ASME J. Tribol., **109**(2), pp. 257–263.
[51] Zhao, Y., Maletta, D. M., and Chang, L., 2000, "An Asperity Microcontact Model Incorporating the Transition From Elastic Deformation to Fully Plastic Flow," ASME J. Tribol., **122**(1), pp. 86–93.
[52] Kogut, L., and Etsion, I., 2002, "Elastic-Plastic Contact Analysis of a Sphere and a Rigid Flat," ASME J. Appl. Mech., **69**(5), pp. 657–662.
[53] Johnson, K. L., 1968, *An Experimental Determination of the Contact Stresses Between Plastically Deformed Cylinders and Spheres in Engineering Plasticity*, Cambridge University Press, Cambridge.
[54] Ling, F. F., 1958, "Some Factors Influencing the Area-Load Characteristics for Semismooth Contiguous Surfaces Under Static Loading," Trans. ASME, **80**, pp. 1113–1120.
[55] Nix, W. D., and Gao, H., 1998, "Indentation Size Effects in Crystalline Materials: A Law for Strain Gradient Plasticity," J. Mech. Phys. Solids, **46**, pp. 411–425.
[56] Swadener, J. G., George, E. P., and Pharr, G. M., 2002, "The Correlation of the Indentation Size Effect Measured With Indenters of Various Shapes," J. Mech. Phys. Solids, **50**, pp. 681–694.
[57] Lou, J., Shrotriya, P., Buchheit, T., Yang, D., and Soboyejo, W. O., 2003, "A Nano-Indentation Study on the Plasticity Length Scale Effects in LIGA Ni MEMS Structures," J. Mater. Sci., **38**, pp. 4137–4143.
[58] Ashby, M., Shercliff, H., and Cebon, D., 2007, *Materials Engineering, Science, Processing and Design*, Elsevier, New York.
[59] Jackson, R. L., Chusoipin, I., and Green, I., 2005, "A Finite Element Study of the Residual Stress and Strain Formation in Spherical Contacts," ASME J. Tribol., **127**(3), pp. 484–493.
[60] Jackson, R. L., Marghitu, D., and Green, I., 2007, "Predicting the Coefficient of Restitution of Impacting Elastic-Perfectly Plastic Spheres," ASME J. Tribol., submitted.
[61] Luan, B., and Robbins, M. O., 2005, "The Breakdown of Continuum Models for Mechanical Contacts," Nature (London) **435**(7044), pp. 929–932.
[62] Gouldstone, A., Chollacoop, N., Dao, M., Li, J., Minor, A. M., and Shen, Y.-L., 2007, "Indentation Across Size Scales and Disciplines: Recent Developments in Experimentation and Modeling," Acta Mater., **55**(12), pp. 4015–4039.
[63] Prasher, R., and Phelan, P. E., 2006, "Microscopic and Macroscopic Thermal Contact Resistances of Pressed Mechanical Contacts," J. Appl. Phys., **100**(6), 063538.
[64] Madhusudana, C. V., 1996, *Thermal Contact Conductance*, Springer-Verlag, New York.
[65] Cooper, M. G., Mikic, B. B., and Yovanovich, M. M., 1969, "Thermal Contact Conductance," Int. J. Heat Mass Transfer, **12**, pp. 279–300.

Inverse Heat Conduction Applied to the Measurement of Heat Fluxes on a Rotating Cylinder: Comparison Between an Analytical and a Numerical Technique

Fabien Volle[1]
Cooling Technologies Research Center,
Purdue University,
West Lafayette, IN 47907-2088
e-mail: vfabien@purdue.edu

Michel Gradeck

Denis Maillet

Arsène Kouachi

Michel Lebouché

Laboratoire d'Energétique et de Mécanique
Théorique et Appliquée,
Vandoeuvre-lès-Nancy, France

A method using either a one-dimensional analytical or a two-dimensional numerical inverse technique is developed for measurement of local heat fluxes at the surface of a hot rotating cylinder submitted to the impingement of a subcooled water jet. The direct model calculates the temperature field inside the cylinder that is submitted to a given nonuniform and time dependent heat flux on its outer surface and to a uniform surface heat source on an inner radius. In order to validate the algorithms, simulated temperature measurements inside the cylinder are processed and used by the two inverse techniques to estimate the wall heat flux. As the problem is improperly posed, regularization methods have been introduced into the analytical and numerical inverse algorithms. The numerical results obtained using the analytical technique compare well with the results obtained using the numerical algorithm, showing a good stable estimation of the available test solutions. Furthermore, real experimental data are used for the estimation, and local boiling curves are plotted and discussed. [DOI: 10.1115/1.2928013]

Keywords: inverse heat conduction, integral transforms, transient, impinging jets, boiling convection

1 Introduction

The direct heat conduction problems are concerned with the determination of temperature at interior points of a region when the initial and boundary conditions, thermophysical properties, and heat generation are specified. In contrast, the inverse heat conduction problem involves the determination of the surface conditions [1], energy generation [2], and/or thermoproperties [3,4] from the knowledge of the temperature measurements taken within the body.

With the improvement of computer capability, use of inverse techniques has in recent decades become a conventional means of resolving heat transfer problems. Important applications of these techniques have been studied in various branches of thermal engineering area: quenching [5], casting and phase-change process [6,7], hot rolling and welding [8], etc.

Recently, a method using a two-dimensional inverse technique has been proposed by Volle et al. [9] for measurement of local heat fluxes at the surface of a rotating cylinder, which experiences boiling convection induced by the impact of a subcooled water jet on its surface. It involves estimating the Fourier boundary condition on the outer surface of the cylinder starting from temperature measurements inside the cylinder, and it has been validated on simulated test cases. The purpose of the present paper is, by comparison with results obtained by a numerical technique, to examine whether a similar linear one-dimensional analytical inverse method can be used to estimate the local boiling curves. Moreover, the experimental setup as well as resulting experimental inversions are presented.

Indeed, numerical methods and computational algorithms for solving IHCPs have been extensively developed over the past decade. Based on finite or boundary elements' techniques, they provide an efficient way to analyze transient heat flow within arbitrarily shaped domains. Most of them are devoted to the determination of transient and/or spatially distributed heat flux on the boundary of the body [10,11]. For example, Hsieh and Su [12] and Bell [13] employed a differential method; Park and Jung [14] and Alhama et al. [15] employed a sequential method to formalize two-dimensional IHCP. Moreover, Huang and Tsai [16] carried out an analysis to arbitrary boundary condition estimation inverse problems by using the conjugate gradient method.

Compared to the numerical computation method, analytical methods to IHCPs could be applied only to samples with simple geometrical configurations [17], for which the solution may be simple and explicit. Nevertheless, they still attract us greatly due to the fact that they have advantages over numerical methods: (1) they supply us with enough information to understand the characteristics of the solution and the effect of the influencing factors, and (2) the time needed for calculation is reduced.

Thus, the results obtained with our one-dimensional analytical technique are compared with results obtained from the same simulated and experimental measurements using a two-dimensional numerical method. The comparison shows that the analytical method is sufficient enough to estimate the extracted heat fluxes, even though variation of the cylinder conductivity with temperature is not taken into account.

---

[1] Corresponding author.

Contributed by the Heat Transfer Division of ASME for publication in the JOURNAL OF HEAT TRANSFER. Manuscript received February 23, 2007; final manuscript received January 11, 2008; published online June 10, 2008. Review conducted by A. Haji-Sheikh.

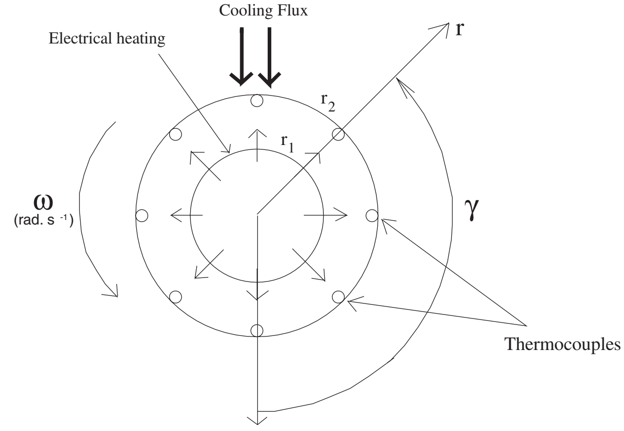

Fig. 1 Model geometry

2 Direct Heat Transfer Problem

2.1 Modeling. In the direct problem, the exact temperature T at a point M inside a rotating cylinder—composed of two layers of radii r_1 and r_2—is sought as a function of polar coordinates (r,γ), as shown in Fig. 1. A uniform surface heat source $P(W)$ is dissipated at radius r_1 and a heat flux density φ_2, which varies with angle γ and with time t, is given on the outer radius r_2. We were interested in cases where φ_2 shows a symmetry with respect to the plane $\gamma=\pi$.

For each domain i (where subscript i designates temperature T in the central layer $(0\leq r<r_1;i=1)$ and in the outer layer $(r_1<r\leq r_2;i=2)$) of the rotating homogeneous cylindrical sample, assuming constant thermophysical properties, the mathematical formulation of the two-dimensional heat conduction problem can be written in the laboratory coordinates system as

$$\frac{\partial^2 T_i}{\partial r^2}+\frac{1}{r}\frac{\partial T_i}{\partial r}+\frac{1}{r^2}\frac{\partial^2 T_i}{\partial \gamma^2}-\frac{\omega}{a}\frac{\partial T_i}{\partial \gamma}=\frac{1}{a}\frac{\partial T_i}{\partial t} \tag{1}$$

where a is the thermal diffusivity of the material and ω is the angular velocity.

The associated boundary and interface conditions are

$$T_i(r,\gamma+2\pi,t)=T_i(r,\gamma,t)$$

$$\text{finite temperature } T_1(r=0,\gamma,t)$$

$$T_1(r=r_1,\gamma,t)=T_2(r=r_1,\gamma,t) \tag{2}$$

$$\frac{P}{2\pi r_1 l}-\lambda\frac{\partial T_1}{\partial r}(r=r_1,\gamma,t)=-\lambda\frac{\partial T_2}{\partial r}(r=r_1,\gamma,t)$$

$$-\lambda\frac{\partial T_2}{\partial r}(r=r_2,\gamma,t)=\varphi_2(\gamma,t)$$

and the initial condition

$$T_i(r,\gamma,t=0)=T^{SS}(r,\gamma) \tag{3}$$

The linear direct problem that is considered can then be solved by expressing temperature T in terms of the function $\varphi_2(\gamma,t)$. It can be considered as the superposition of different problems that are independently solved [9]. We will only consider here the cooling temperature T^{cool}, solution of Eq. (1) associated with the boundary conditions:

$$T(r,\gamma+2\pi,t)=T(r,\gamma,t)\ \text{(periodicity conditions)}$$

$$-\lambda\frac{\partial T}{\partial r}(r=r_2,\gamma,t)=\varphi_2(\gamma,t),\quad \frac{\partial T}{\partial r}(r=0,\gamma,t)=0 \tag{4}$$

$$T(r,\gamma,t=0)=0$$

A semianalytical solution has been proposed by Volle et al. [9]. This solution utilizes Laplace (parameter p) and Fourier (parameter n) transforms, the temperature being given in the Fourier domain by the relation

$$\tilde{T}(r,n,t)=-\frac{1}{\lambda}\int_0^t[\tilde{\varphi}_2(n,\tau)][e^{-jn\omega(t-\tau)}Z_n(t-\tau)]d\tau \tag{5}$$

with

$$\bar{Z}_n(r,p)=\frac{I_n\left(\sqrt{\frac{p}{a}}r\right)}{\sqrt{\frac{p}{a}}I'_n\left(\sqrt{\frac{p}{a}}r_2\right)} \tag{6}$$

This bidimensionnal solution has been used to elaborate an inversion algorithm that has been successfully tested on simulated measurements.

The idea of the present paper is to use a 1D analytical solution (similar to Eq. (5)) in order to propose a 1D analytical inversion algorithm. This algorithm can then be validated by comparison with results obtained with a 2D numerical algorithm applied to the same experimental data.

2.2 One-Dimensional Analytical Solution. Using the classical Laplace transformation of temperature T (noted " ¯"),

$$\bar{T}(r,p)=\int_0^\infty T(r,t)e^{-pt}dt$$

and considering an initial temperature equal to 0, the 1D analytical solution for temperature T is in the time domain

$$T(r,\gamma,t)=-\frac{1}{\lambda}\int_0^t[\varphi_2(\gamma,\tau)][Z_0(r,t-\tau)]d\tau \tag{7}$$

with

$$\bar{Z}_0(r,p)=\frac{I_0\left(\sqrt{\frac{p}{a}}r\right)}{\sqrt{\frac{p}{a}}I_1\left(\sqrt{\frac{p}{a}}r_2\right)} \tag{8}$$

The temporal inversion of Eq. (8) is made using Stehfest's numerical algorithm [18]:

$$Z_0(r,t)=\frac{\ln 2}{t}\sum_{j=1}^{10}V_j\bar{Z}_0\left(r,p=\frac{j\ln 2}{t}\right) \tag{9}$$

where V_j's are the tabulated Stehfest coefficients:

$$V_1=1/12,\quad V_2=-385/12,\quad V_3=1279,\quad V_4=-46871/3$$

$$V_5=505{,}465/6,\quad V_6=-473{,}915/2,\quad V_7=1{,}127{,}735/3$$

$$V_8=-1{,}020{,}215/3,\quad V_9=328{,}125/2,\quad V_{10}=-65{,}625/2$$

Moreover, as $Z_0\to\infty$ when $t\to\tau$, we use an asymptotic behavior $\check{Z}_0(r,t-\tau)$ for $Z_0(r,t-\tau)$ and we obtain with $t_{\lim}=i_{\lim}\Delta t$ ($i_{\lim}=1$ in our case),

$$T(r,\gamma,t)=-\frac{1}{\lambda}\left[\int_0^{t-t_{\lim}}\varphi_2(\gamma,\tau)Z_0(r,t-\tau)d\tau+\int_{t-t_{\lim}}^{t}\varphi_2(\gamma,\tau)\check{Z}_0(r,t-\tau)d\tau\right] \tag{10}$$

with

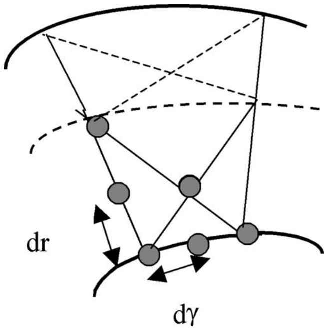

Fig. 2 Mesh

$$\breve{Z}_0(r,t) = \sqrt{\frac{a}{\pi t}\frac{r_2}{r}}\, e^{-(r_2-r)^2/4at} + \frac{1}{2}\frac{a}{\sqrt{r r_2}}\,\mathrm{erfc}\left[\frac{r_2-r}{2\sqrt{at}}\right] \qquad (11)$$

2.3 Two-Dimensional Numerical Technique. The technique is based on the Galerkin finite element method. 1140 meshes have been considered for the grid, the reference mesh (composed of six nodes with $dr=1$ mm and $d\gamma=3°$) being represented in Fig. 2.

The temperature field can be obtained by decomposition on the interpolation functions Ψ at each nose

$$T = \Sigma_m \Psi_m T_m \qquad (12)$$

For the temporal discretization, we use an implicit scheme

$$\frac{\partial T}{\partial t} = \frac{T^{n+1} - T^n}{\Delta t} \qquad (13)$$

Table 1 Parameters used in the study

Parameter	Value
λ	90.7 W m^{-1} K^{-1}
ρc	3.919.520 J K^{-1} m^{-3}
r_1, r_2, l	0.049 m, 0.0875 m, 0.2 m
P, ω	6000 W, 6 rad s^{-1}

2.4 Direct Model Results. The analytical direct model was tested for a given heat flux imposed at radius $r=r_2$. This heat flux $\varphi_2(\gamma,t)$ decreases exponentially in time and has a triangular shape in γ. It is equal to

$$\begin{aligned}
&\frac{P}{2\pi r_2 l} \quad \text{for } 0<\gamma<\frac{3\pi}{4}\\
&\left[\frac{4K_t}{\pi}\gamma - 3K_t\right]e^{(-t/t_c)} + \frac{P}{2\pi r_2 l} \quad \text{for } \frac{3\pi}{4}<\gamma<\pi\\
&\left[-\frac{4K_t}{\pi}\gamma + 5K_t\right]e^{(-t/t_c)} + \frac{P}{2\pi r_2 l} \quad \text{for } \pi<\gamma<\frac{5\pi}{4}\\
&\frac{P}{2\pi r_2 l} \quad \text{for } \frac{5\pi}{4}<\gamma<2\pi
\end{aligned} \qquad (14)$$

where parameter K_t allows to choose the heat flux level. As we wish to simulate industrial cooling heat fluxes, a value of 10^6 W m^{-2} is chosen for this parameter. The other parameters used for the simulations are given in Table 1.

The excitation $\varphi_2(\gamma(t),t)$, given by Eq. (14), as well as the temperature response of a point located at angle $\gamma=\pi$ at $t=0$, obtained by the analytical solution (10) for a radius $r_{\mathrm{TC}}=r_2$, are plotted in Fig. 3 in the moving coordinates system related to the cylinder (with $K_t=10^6$ W m^{-2} and $t_c=1$ s).

In this figure, we also plotted the temperature response calculated with the 2D analytical model (Eq. (5)). We see that the two models are equivalent, which justifies the use of a 1D analytical method for the inversion.

The temperature profile obtained from the numerical solution was very similar to the previous one. The difference stems from the tangential conductive transfer at the wall.

3 Inverse Problem

In the inverse problem, the condition relative to the flux φ_2 (which is now unknown) is replaced by a measured temperature condition, the transient measurements being made by $N_{\mathrm{TC}}=24$ temperature sensors located at radius $r=r_{\mathrm{TC}}$. All other quantities appearing in the formulation of the physical problem (thermophysical properties, etc.) are assumed to be exactly known, but the measurements may contain random errors.

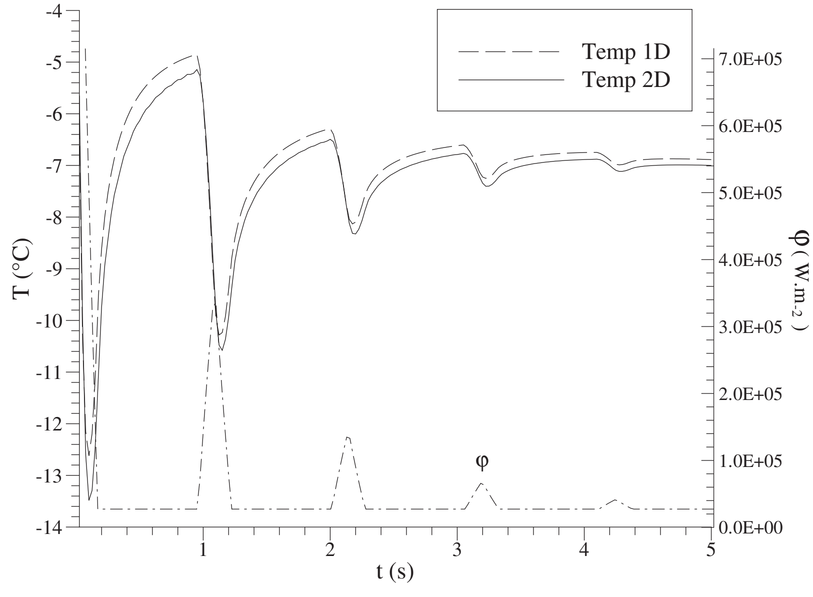

Fig. 3 Variations of $T(t)$ for $r=r_2$ and $\gamma(t=0)=\pi$

3.1 Analytical Method.

In practice, the problem is solved in the particular case where $\varphi_2(\gamma,t)$ is a piecewise constant function of time t:

$$\varphi_2(\gamma,t) = \varphi_{2,k}(\gamma) \quad \text{for } t_k \leqslant t \leqslant t_{k+1} \tag{15}$$

with $t_k = k\Delta t$ and $k \geq 0$, where Δt is both a discretization time step for φ_2 and a calculation time step for temperature T.

It yields for $t_i = i\Delta t$ $(i \geq 2)$ and with $t_0 = 0$:

$$T(r,\gamma,t_i) = -\frac{1}{\lambda}\left[\sum_{k=0}^{i-2}\varphi_{2,k}\int_{t_k}^{t_{k+1}} Z_0(r,t_i-\tau)d\tau + \varphi_{2,(i-1)}\int_{t_i-t_{\lim}}^{t_i}\breve{Z}_0(r,t_i-\tau)d\tau\right] \tag{16}$$

Temperature $T\ (r,\gamma,t_i)$ is thus a linear combination of the $\varphi_{2,k}$:

$$T(r,\gamma,t_i) = \sum_{k=0}^{i-1} X_{i,k+1}\varphi_{2,k} \tag{17}$$

where the coefficients $X_{i,k+1}$ are

$$X_{i,k+1} = -\frac{1}{\lambda}\int_{t_k}^{t_{k+1}} L^{-1}\left[\frac{I_0\left(\sqrt{\frac{p}{a}}r\right)}{\sqrt{\frac{p}{a}}I_1\left(\sqrt{\frac{p}{a}}r_2\right)}\right]_{t_i-\tau} d\tau \tag{18}$$

or

$$X_{i,k+1} = -\frac{1}{\lambda}\int_{t_k}^{t_{k+1}}\breve{Z}_0(r,t_i-\tau)d\tau \tag{19}$$

depending on the value of k $(k < i - i_{\lim}$ or $k \geq i - i_{\lim})$.

This yields in a matrix form

$$\mathbf{T} = \begin{pmatrix} T(r,t_1) \\ \vdots \\ T(r,t_i)\end{pmatrix} = \begin{pmatrix} X_{11} & \dots & 0 \\ \vdots & \ddots & \vdots \\ X_{i1} & \dots & X_{ii}\end{pmatrix}\begin{pmatrix}\varphi_{2,0} \\ \vdots \\ \varphi_{2,i-1}\end{pmatrix} = \mathbf{X}\boldsymbol{\varphi}_2 \tag{20}$$

where matrix $\mathbf{X}$ is the *sensitivity matrix*, which defines the relationship between a change in the surface heat flux and the corresponding change in the computed temperature response.

If $\mathbf{T}(r_{\mathrm{TC}},\gamma_m(t),t)$ is the vector of exact temperatures measured by the mth thermocouple, Eq. (20) can be solved to find vector $\boldsymbol{\varphi}_2$. Actually, experimental measurements always present some uncertainty, and the above method is no longer valid. We call $\mathbf{Y}(r_{\mathrm{TC}},\gamma_m(t),t)$ the value of $\mathbf{T}(t)$ measured at radius r_{TC} and angle $\gamma_m(t)$. Assuming an additive random error, we have

$$Y_m(t_i,\varphi_2) = T_m(t_i,\varphi_2) + \epsilon_{mi} \tag{21}$$

where ϵ_{mi} $(m=1$ to N_{TC}, $i=1-i_f)$ is an uncorrelated, zero mean and identically distributed normal noise of constant standard deviation σ.

To take this noise into account, it is possible to use an ordinary least squares (OLS) method [19], which consists in minimizing the sum S of the square errors between computed and measured values

$$S_m = (Y_m - \mathbf{X}\boldsymbol{\varphi}_2)^t(Y_m - \mathbf{X}\boldsymbol{\varphi}_2) \tag{22}$$

with respect to the unknown heat flux vector $\boldsymbol{\varphi}_2$. Thus, $\partial S_m/\partial\boldsymbol{\varphi}_2$ must vanish as a necessary condition for minimization

$$\frac{\partial S_m}{\partial\boldsymbol{\varphi}_2} = 0 \tag{23}$$

which can be put into the form

$$\hat{\varphi}_2 = (\mathbf{X}^t\mathbf{X})^{-1}\mathbf{X}^tY_m \tag{24}$$

However, the inverse problem is inherently ill posed, and experimental error will have an impact on the solution. Indeed, this ill posedness results in high sensitivity to data errors due to the poor conditioning of the $\mathbf{X}^t\mathbf{X}$ matrix. The process of converting an ill-posed problem to a well-posed one is termed regularization: The idea is to make the problem "regular" by changing the original problem slightly. In our case, the temporal regularization is afforded by using Beck's future time step method [20].

3.2 Numerical Technique.

The method used here is the function specification method proposed by Blanc et al. [21], with Beck's future time step regularization. Moreover, to assure a certain regularity to the angular variation of φ_2, a regularization term is added to the error function (Tikhonov's regularization [22]). A second-order term, which represents, under a discrete form, the second derivative of function $\varphi_2(\gamma)$, has been chosen here. It smoothes the flux fluctuations and stabilizes the problem

$$S = \sum_{i=1}^{N_{\mathrm{TC}}}\left[\sum_{j=1}^{N_{tf}}\left(T_{\exp_i}^{k+j} - T_i^{k+j}(\varphi_1^{k+1},\ldots,\varphi_l^{k+1},\ldots,\varphi_{N_{\mathrm{TC}}}^{k+1})\right)^2\right] + \alpha\sum_{m=2}^{N_{\mathrm{TC}}-1}(\varphi_{m-1}^{k+1} - 2\varphi_m^{k+1} + \varphi_{m+1}^{k+1})^2 \tag{25}$$

Thus, if temperature T^k and surface heat flux density φ^k are known at time t^k, the heat flux density $\varphi^{k+1}(\varphi_1^{k+1},\ldots,\varphi_l^{k+1},\ldots,\varphi_{N_{\mathrm{TC}}}^{k+1})$ at time t^{k+1} is obtained by minimization of the error function $S(\varphi_1^{k+1},\ldots,\varphi_l^{k+1},\ldots,\varphi_{N_{\mathrm{TC}}}^{k+1})$, where $T_{\exp_i}^k$ is the measured temperature at point i and at time k, T_i^k is the calculated temperature (solution of the direct problem), and α is the regularization coefficient (α is about $10^{-10}\ \mathrm{K}^2\ \mathrm{W}^{-2}\ \mathrm{m}^4$).

3.3 Inversions From Simulated Measurements.

In order to test the two inverse algorithms, we have implemented them on simulated measurements. These simulated measurements come from the temperature profile $T(r_{\mathrm{TC}},\gamma(t),t)$, the output of the bidimensional direct model (see Eq. (5)), which was modified by a random additive noise ϵ, of standard deviation σ, according to Eq. (21). The outputs $\hat{\varphi}_2$ of the analytical and numerical inverse algorithms were estimates of the heat flux φ_2, the input of the direct model. The results are presented in Fig. 4, with $r_{\mathrm{TC}} = 86.5$ mm.

For this value of r_{TC}, knowing that the discretization time step Δt is as $0.005\ \mathrm{s} \leq \Delta t \leq 0.01\ \mathrm{s}$ (depending on the studied cases), the dimensionless time step Δt_i, defined by

$$\Delta t_i = \frac{a}{(r_2 - r_{\mathrm{TC}})^2}\Delta t \tag{26}$$

is always as $\Delta t_i \geq 0.11$, which is greater than the critical value of 5×10^{-2}: The inversion is then possible for the discretization time step size is large enough when compared with the size of the characteristic time of the system $(r_2 - r_{\mathrm{TC}})^2/a$.

We see in Fig. 4 that the two inverse methods seem to be reliable for in each case, agreement between $\hat{\varphi}_2$ and φ_2 is quite good. However, it appears that a degradation of estimation accuracy is observed near the discontinuity points, which is due to the smoothing imposed by the regularizations. Lastly, it should be noted that the time needed for calculation is significantly reduced when the analytical model is used (no grid). Other simulations showed that neglecting the two-dimensional effects had tendency, as one could expect it, to overestimate the heat flux.

A point of very practical importance is the selection of proper value for the regularization parameter α: Its level must be adjusted as a function of the noise in the data. In this work, we have chosen to minimize the following norm based on the estimated and exact heat flux densities:

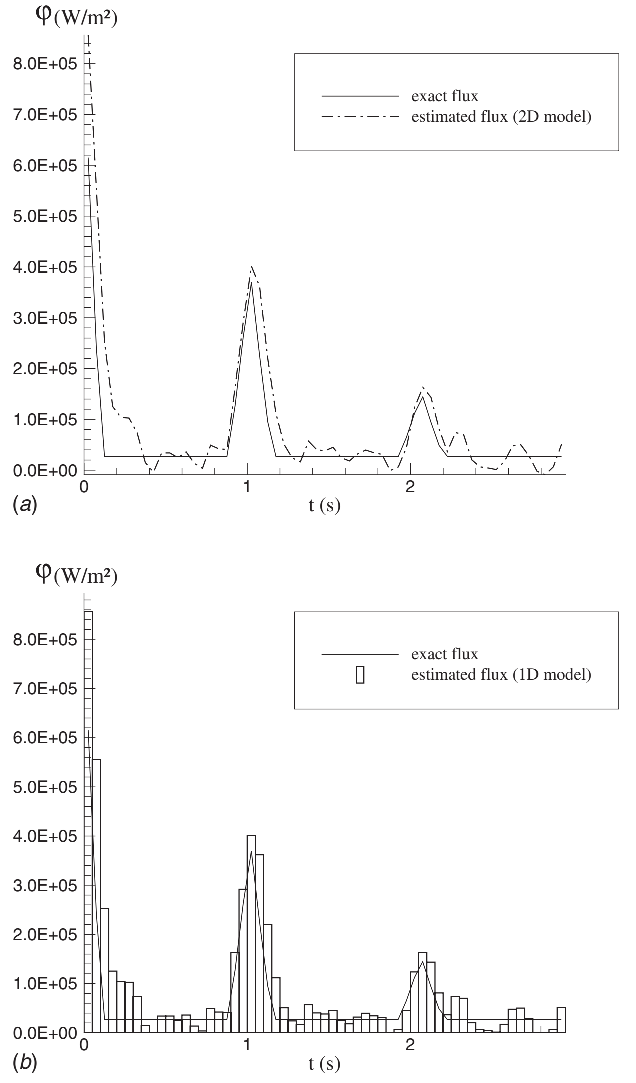

Fig. 4 Exact and estimated heat flux for simulated temperature measurements at $r_{\mathrm{TC}}=86.5$ mm, with $\gamma(t=0)=0$, $\sigma=0.5°\mathrm{C}$, $N_{\mathrm{fts}}=3$, and $\alpha=7\times10^{-10}$ $\mathrm{m^4\,K^2\,W^{-2}}$

$$e_{\varphi_2}=\sqrt{\frac{1}{N}\sum_{i=1}^{n}(\varphi_2-\hat{\varphi}_2)^2} \tag{27}$$

For a noise ϵ of standard deviation $\sigma=0.5°\mathrm{C}$, the adjusted value of α that minimized e_{φ_2} is $\alpha=7\times10^{-10}$ $\mathrm{m^4\,K^2\,W^{-2}}$.

Another approach would have been to invoke the "discrepancy principle," whose idea is to select α as small as possible and such that the temperature residual

$$R=\sqrt{\frac{1}{N}\sum_{i=1}^{n}(\mathbf{Y}-\mathbf{X}\hat{\varphi}_2)^2} \tag{28}$$

is consistent with the measurement error in the data. This recommendation, made by Tikhonov and Arsenin [22], has been verified during our simulations.

4 Experimental Measurements

4.1 Experimental Setup. A rotating cylindrical pipe made out of nickel of 200 mm length, 49 mm inside radius, and 87.5 mm outside radius was built at LEMTA. 24 thermocouples of 0.12 mm diameter, used to measure local transient temperature near the surface, were embedded parallel to the cylinder axis. Their junctions were located in the transverse plane of symmetry of the cylinder. A nominal radius of implantation was $r_{\mathrm{TC}}=86.5$ mm.

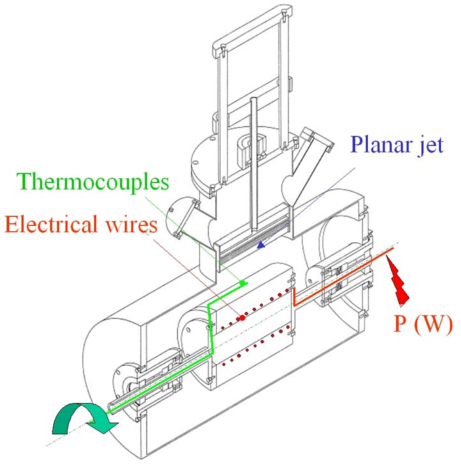

Fig. 5 Experimental setup (not to scale)

A uniform and time-constant surface heat source $P(W)$ was dissipated through three electrical wires inserted into grooves machined in the internal surface of the external cylinder in order to reach the desired initial surface temperature.

The measurement cylinder, see Fig. 5, was submitted to the impingement of a subcooled water jet whose temperature and velocity were known. The nozzle/surface distance was also known, and it consisted in another parameter, which could influence the cooling rates.

4.2 Experimental Procedure. The experimental procedure was as follows: When the surface temperature had reached the desired value, the jet cooling started and transient temperatures were measured by the thermocouples. Measurements were made for different jet velocities, jet temperatures, initial surface temperatures, and for different cylinder's angular velocities.

Then, these measurements were used as inputs for the two inverse algorithms in order to estimate the heat flux extracted by the subcooled water jet. The advantage of the method resides in the fact that it is a nonintrusive method, which allows to quantify the effect of different parameters on the cooling rates and on the boiling phenomena that can occur at the surface of the cylinder.

It should be noted that the question of whether or not the temperature dependence of the conductivity has in our experimental conditions a significant effect on the estimated heat flux has not been considered. Indeed, as nickel's conductivity varies slightly with temperature, we chose to consider the linear problem and to use a mean value for conductivity.

5 Inversion From Experimental Measurements

5.1 Comparison of Techniques. Both techniques—analytical and numerical—were used to estimate surface heat fluxes starting from the same experimental temperature profiles. Regularization coefficients of $\alpha=7\times10^{-10}$ $\mathrm{m^4\,K^2\,W^{-2}}$ (for the numerical technique) and $N_{\mathrm{fts}}=3$ (for the analytical method) and a constant value of 90.7 W/m K for conductivity were used for the inversions.

5.1.1 Static Cylinder ($\omega=0$ rad/s). Results for both techniques are presented in Figs. 6 and 7 in the case of a static cylinder. Figure 6 shows the experimental temperature and the corresponding estimated boiling curve (heat flux variations with respect to surface superheat ΔT_{sat}) at 3.2 cm from the impinging point in convection regime ($T_{\mathrm{wall}}(t=0)<100°\mathrm{C}$). Figure 7 concerns cooling at the impinging point in boiling regime ($T_{\mathrm{wall}}(t=0)$

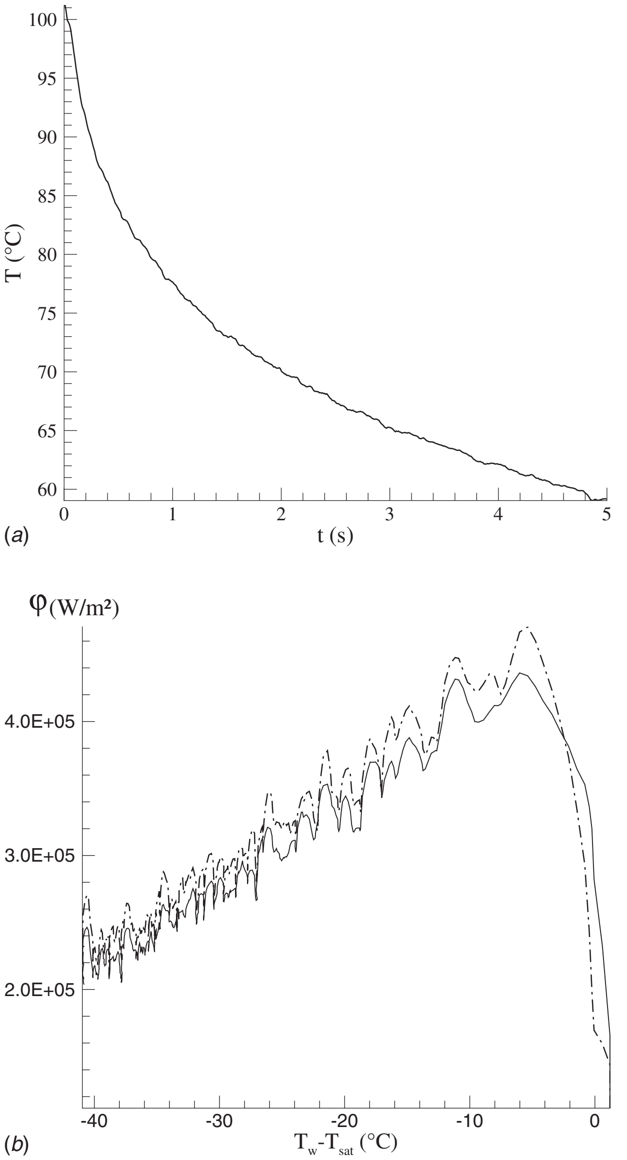

Fig. 6 Experimental temperature and boiling curves for the static case in convection regime (——: 2D model; —·—: 1D model)

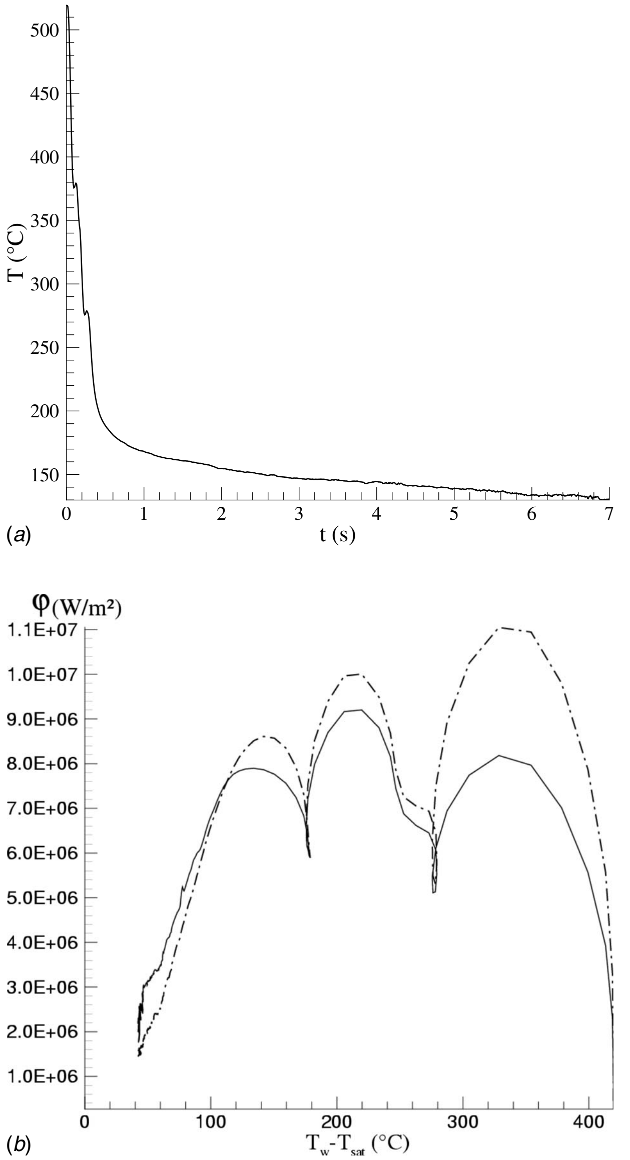

Fig. 7 Experimental temperature and boiling curves for the static case in boiling regime (——: 2D model ;—·—: 1D model)

$\gg 100°C$).

In Fig. 6, we see a good agreement in the results obtained with the two techniques. When compared in boiling regime (Fig. 7), the results are close for $\Delta T_{sat} < 300°C$. There is a higher dispersion for highest values of ΔT_{sat}, even if the general shape is the same. This must be due to the constriction of the lines of flux, which makes the two-dimensional heat transfers important, especially in the impinging area.

5.1.2 Rotating Cylinder ($\omega \neq 0$ rad/s). Although it is impossible to give a clear explanation of the influence of the surface motion on boiling regimes yet, Fig. 8 shows the feasibility of the estimation in the case of a rotating cylinder.

Plotted in this figure are the temporal variations of the estimated surface heat flux when the cylinder rotates at $\omega \approx 15$ rad/s and for a temperature of the jet T_{jet} equal to 36 °C. We can see that the results obtained using the 1D analytical technique compare well with the results obtained using the 2D numerical algorithm, the calculation being much faster in the case of the analytical algorithm.

We also see in Fig. 8 the different boiling regimes ((1) film boiling, (2) transition boiling, (3) nucleate boiling, and (4) forced convection) with a maximum heat flux (corresponding to the critical heat flux) of about 4 MW/m^2.

It should be noted that, when the cylinder rotates, the dispersion between the results obtained with the two methods tends to decrease: The rotation seems to standardize the surface phenomena.

6 Advantages and Disadvantages of the Inverse Method

The advantages of this inverse method for the calculation of the angular and temporal evolutions of the local surface heat fluxes on a cylinder are the following.

1. The method is comparable to a nonintrusive fluxmeter: It allows to plot local boiling curves, including for the transition boiling regime, without perturbing the phenomena of interest.
2. The method does not depend on the physical phenomenon that creates the surface heat flux: It is therefore applicable in many branches of mechanics.
3. There is no need for heat loss estimation.

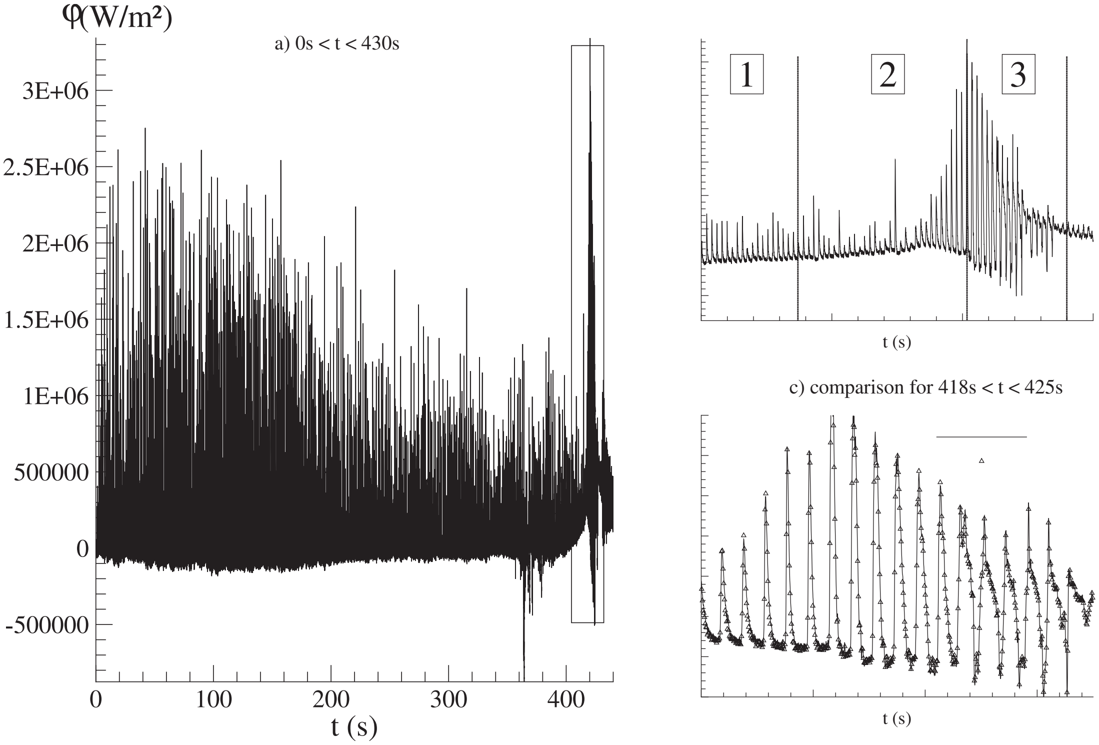
a) 0s < t < 430s

c) comparison for 418s < t < 425s

Z_0 = transfer function
α = parameter for Tikhonov regularization
γ = polar angle
λ = thermal conductivity
σ = noise standard deviation
φ = heat flux
ω = angular velocity

References

[1] Alifanov, O. M., 1974, "Solution of an Inverse Problem of Heat Conduction by Iteration Methods," J. Eng. Phys., **26**, pp. 471–476.
[2] Lin, D. T. W., and Yang, C., 2007, "The Estimation of the Strength of the Heat Source in the Heat Conduction Problems," Appl. Math. Model., **31**, pp. 2696–2710.
[3] Adjali, M. H., and Laurent, M., 2007, "Thermal Conductivity Estimation in Non-Linear Problems," Int. J. Heat Mass Transfer, **50**, pp. 4623–4628.
[4] Huang, C. H., and Ozisik, M. N., 1991, "A Direct Integration Approach for Simultaneously Estimating Temperature Dependent Thermal Conductivity and Heat Capacity," Numer. Heat Transfer, Part A, **20**, pp. 95–110.
[5] Hammad, J., Mitsutake, Y., and Monde, M., 2004, "Movement of Maximum Heat Flux and Wetting Front During Quenching of Hot Cylindrical Block," Int. J. Therm. Sci., **43**, pp. 743–752.
[6] Nowak, I., Nowak, A. J., and Wrobel, L. C., 2003, "Inverse Analysis of Continuous Casting Processes," Int. J. Numer. Methods Heat Fluid Flow, **13**, pp. 547–564.
[7] Peneau, S., Humeau, J. P., and Jarny, Y., 1996, "Front Motion and Convective Heat Flux Determination in a Phase Change Process," Inverse Probl. Eng., **4**, pp. 53–91.
[8] Huang, C. H., Ju, T. M., and Tseng, A. A., 1995, "The Estimation of Surface Thermal Behavior of Working Roll in Hot Rolling Process," Int. J. Heat Mass Transfer, **38**, pp. 1019–1031.
[9] Volle, F., Maillet, D., Gradeck, M., and Lebouché, M., 2007, "Semi-Analytical Inverse Heat Conduction on a Rotating Cylinder With Laplace and Fourier Transforms," Inverse Problems in Science and Engineering, to be published.
[10] Alifanov, O. M., 1994, *Inverse Heat Transfer Problems*, Springer, Berlin.
[11] Chen, C.-K., Wu, L.-W., and Yang, Y.-T., 2006, "Estimation of Time-Varying Inlet Temperature and Heat Flux in Turbulent Circular Pipe Flow," ASME J. Heat Transfer, **128**(1), pp. 44–52.
[12] Hsieh, C. K., and Su, K. C., 1980, "A Methodology of Predicting Cavity Geometry Based on Scanned Surface Temperature Data—Prescribed Surface Temperature at the Cavity Side," ASME J. Heat Transfer, **102**(2), pp. 324–329.
[13] Bell, G. E., 1984, "An Inverse Solution for the Steady Temperature Field Within a Solidified Layer," Int. J. Heat Mass Transfer, **27**(12), pp. 2331–2337.
[14] Park, H. M., and Jung, W. S., 2001, "On the Solution of Multidimensional Inverse Heat Conduction Problems Using an Efficient Sequential Method," ASME J. Heat Transfer, **123**(6), pp. 1021–1029.
[15] Alhama, F., Zueco, J., and Gonzalez Fernandez, C. F., 2003, "An Inverse Determination of Unsteady Heat Fluxes Using a Network Simulation Method," ASME J. Heat Transfer, **125**(6), pp. 1178–1182.
[16] Huang, C. H., and Tsai, C. C., 1998, "An Inverse Heat Conduction Problem of Estimating Boundary Fluxes in an Irregular Domain With Conjugate Gradient Method," Heat Mass Transfer, **34**, pp. 47–54.
[17] Monde, M., and Mitsutake, Y., 2000, "Analytical Method in Inverse Heat Transfer Problem Using Laplace Transform Technique," Int. J. Heat Mass Transfer, **43**(21), pp. 3965–3975.
[18] Stehfest, H., 1970, "Algorithm 368: Numerical Inversion of Laplace Transforms," Commun. ACM, **13**, pp. 47–49.
[19] Beck, J.-V., and Arnold, K. J., 1977, *Parameter Estimation in Engineering and Science*, Wiley, New York.
[20] Beck, J.-V., Blackwell, B., and St-Clair, C.-R., 1985, *Inverse Heat Conduction-Ill-Posed Problems*, Wiley, New York.
[21] Blanc, G., Raynaud, M., and Chau, T. H., 1998, "A Guide for the Use of Function Specification Method for 2D Inverse Heat Conduction Problems," Rev. Gen. Therm., **37**, pp. 17–30.
[22] Tikhonov, A. N., and Arsenin, V. Y., 1977, *Solutions of Ill-Posed Problems*, Winston, Washington, DC.

Heat Transport Capability in an Oscillating Heat Pipe

H. B. Ma
Associate Professor
e-mail: mah@missouri.edu

B. Borgmeyer
Graduate Research Assistant

P. Cheng
Graduate Research Assistant

Y. Zhang
Associate Professor

Department of Mechanical and Aerospace Engineering,
University of Missouri-Columbia,
Columbia, MO 65211

A mathematical model predicting the oscillating motion in an oscillating heat pipe is developed. The model considers the vapor bubble as the gas spring for the oscillating motions including effects of operating temperature, nonlinear vapor bulk modulus, and temperature difference between the evaporator and the condenser. Combining the oscillating motion predicted by the model, a mathematical model predicting the temperature difference between the evaporator and the condenser is developed including the effects of the forced convection heat transfer due to the oscillating motion, the confined evaporating heat transfer in the evaporating section, and the thin film condensation in the condensing section. In order to verify the mathematical model, an experimental investigation was conducted on a copper oscillating heat pipe with eight turns. Experimental results indicate that there exists an onset power input for the excitation of oscillating motions in an oscillating heat pipe, i.e., when the input power or the temperature difference from the evaporating section to the condensing section was higher than this onset value the oscillating motion started, resulting in an enhancement of the heat transfer in the oscillating heat pipe. Results of the combined theoretical and experimental investigation will assist in optimizing the heat transfer performance and provide a better understanding of heat transfer mechanisms occurring in the oscillating heat pipe. [DOI: 10.1115/1.2909081]

Introduction

Because of the rapid development of the electronic industry, with chips packed closer together and the continuing decrease in the size of electronic packages, heat flux levels continue to increase. For example, the new design of high-density computer chips for the next generation of desktop computers may reach a heat flux level of over 80 $\mathrm{W/cm^2}$. Metal oxide semiconductor controlled thyristors generate heat fluxes from 100 $\mathrm{W/cm^2}$ to 200 $\mathrm{W/cm^2}$. Moreover, some laser diode applications have reached a heat flux level of 500 $\mathrm{W/cm^2}$. Conventional heat sinks or spreaders become severely inadequate at these high levels of heat fluxes. While the conventional heat pipe can significantly push the border of cooling power, the heat transfer limitations in the heat pipe restrict the applications for these high levels of heat fluxes.

Oscillating heat pipe (OHP) is a new type of two-phase heat transfer devices that rely on oscillatory flow of liquid slug and vapor plug in a long miniature tube bent into many turns. Compared to the conventional heat pipe, the OHP has the following features: (1) Because most or all of working fluid does not flow through the wick structure, there is a low pressure drop of working fluid. (2) Because the vapor flow direction is the same as liquid flow, there is no vapor flow influence on the liquid flow. (3) Because the tube is so small, the vapor plugs can be formed in the OHP. The thermally driven, oscillating flow inside the capillary tube will effectively sweep the surface and produce some "blank" surfaces to significantly enhance evaporating and condensing heat transfer. (4) Due to the oscillating motion in the capillary tube, the heat added on the evaporating area can be distributed by the forced convection in addition to the phase-change heat transfer. Clearly, the OHP has a potential to remove an extra high level of heat flux.

Extensive experimental investigations [1–6] and theoretical analysis [7–15] have been conducted, and show that there exist oscillating or/and circulating motions in an OHP, which depend on working fluids [2–4,10], tilt angles [5–7], dimensions [2,6,9,10,13], filling ratio [5,9,14], number of turns [2,4,13], and heat flux levels [2,4,7,14]. While these investigations have provided an insight into the mechanisms of oscillating motions occurring in the OHP, the primary factors affecting the heat transport capability have not been fully understood. As mentioned above, the OHP transfers heat through forced convection in addition to phase-change heat transfer. Although it is expected that the heat transport capability occurring in the OHP should be much higher than the convectional heat pipe, the available experimental data show that the effective thermal conductivity of the OHP is low. In this investigation, a mathematical model predicting the temperature difference from the evaporating section to the condensing section is developed to determine the primary factors affecting the heat transport capability in the OHP, which includes the oscillating motion occurring in the OHP, confined convection boiling, and film condensation. An experimental investigation will also be conducted to verify the model presented in this paper.

Theoretical Analysis

To simplify the problem and find the primary factors affecting the heat transfer performance in an OHP, an OHP, as shown in Fig. 1, is considered. The OHP consists of an evaporating section, an adiabatic section, and a condensing section. As heat is added on the evaporating section in the OHP, the liquid is vaporized, causing the vapor volume expansion. Vapor in the condensing section is condensed into liquid, causing the volume contraction. The volume expansion and contraction excite an oscillation motion of the liquid plugs and vapor bubbles in the miniature channels. Through the forced convection and phase-change heat transfer, heat is transferred from the evaporating section to the condensing section. Clearly, heat transfer in the OHP involves the evaporating heat transfer in the evaporating section, condensing heat transfer in the condensing section, and oscillating motions in the whole heat pipe.

Heat Transfer in the Evaporating Section. When applying a heat source to the external circumference of the evaporator section, as shown in Fig. 1, heat is transported by radial conduction through the evaporator wall and reaches the working fluid, resulting in vaporization. The vapor volume expansion in the evaporating section combined with the vapor volume contraction in the

---

Contributed by the Heat Transfer Division of ASME for publication in the Journal of Heat Transfer. Manuscript received April 25, 2007; final manuscript received July 24, 2007; published online May 29, 2008. Review conducted by Louis C. Chow.

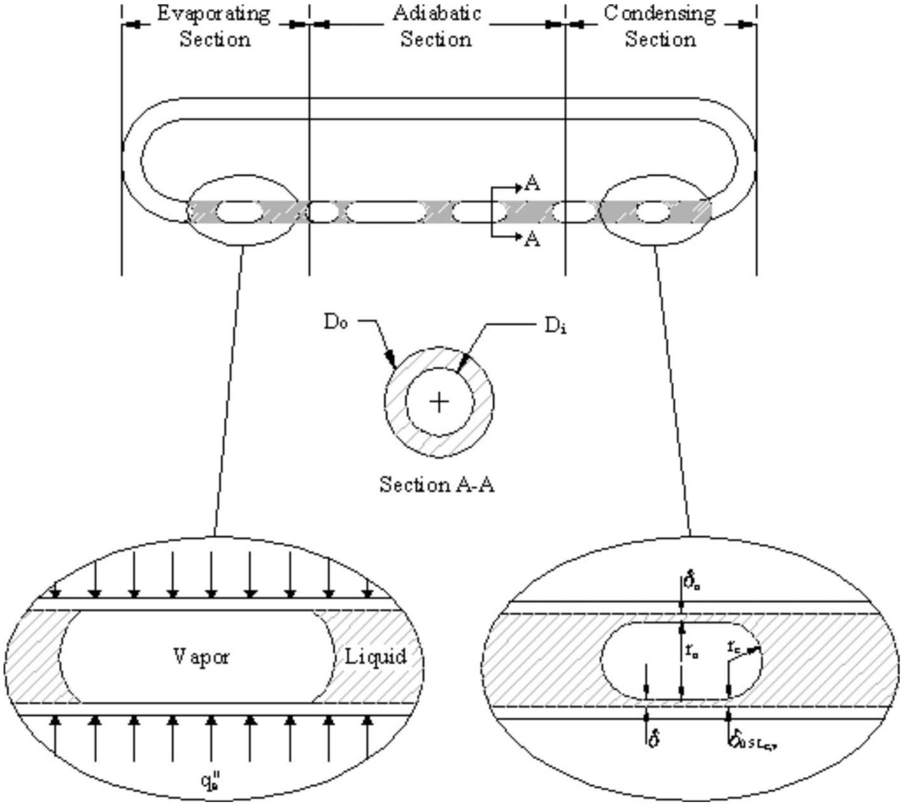

Fig. 1 Schematic of an OHP

condensing section generates the forced convection in the OHP. If the tube structuring the evaporating section is smooth, i.e., no wick structures on the inside surface of tube, the heat transfer process occurring in the evaporating section is similar to convection boiling heat transfer, which has been extensively investigated [16–23]. The heat transfer in the evaporating section of the OHP can be described by a combination of nucleate boiling (microscopic) and bulk convection (macroscopic). The total heat transfer coefficient h can be expressed as

$$h = h_{\text{mic}} + h_{\text{mac}} \tag{1}$$

where h_{mic} is due to the nucleate boiling heat transfer and h_{mac} due to the bulk convection caused by oscillating motions. Chen [16] developed a model describing the nucleate boiling heat transfer, where the microscopic nucleate boiling portion of the heat transfer coefficient could be found by

$$h_{\text{mic}} = 0.00122\left[\frac{k_l^{0.79} c_{pl}^{0.45} \rho_l^{0.49}}{\sigma^{0.5} \mu_l^{0.29} h_{lv}^{0.24} \rho_v^{0.24}}\right][T_w - T_{\text{sat}}(P_l)]^{0.24} \times [P_{\text{sat}}(T_w) - P_l]^{0.75} S \tag{2}$$

where S is a suppression factor and a function of the two-phase Reynolds number, i.e.,

$$S = (1 + 2.56 \times 10^{-6}\,\text{Re}_{\text{tp}}^{1.17})^{-1} \tag{3}$$

The two-phase Reynolds number in Eq. (3) can be determined by

$$\text{Re}_{\text{tp}} = \text{Re}_l [F(X_{tt})]^{1.25} \tag{4}$$

where the liquid Reynolds number and the Martinelli parameter X_{tt} are defined by

$$\text{Re}_l = \frac{G(1-x)D_i}{\mu_l} \tag{5}$$

$$X_{tt} = \left(\frac{1-x}{x}\right)^{0.9}\left(\frac{\rho_v}{\rho_l}\right)^{0.5}\left(\frac{\mu_l}{\mu_v}\right)^{0.1} \tag{6}$$

respectively. The function $F(X_{tt})$ shown in Eq. (4) depends on the Martinelli parameter, i.e.,

$$F(X_{tt}) = 1 \quad \text{for } X_{tt}^{-1} \le 0.1 \tag{7}$$

$$F(X_{tt}) = 2.35\left(0.213 + \frac{1}{X_{tt}}\right)^{0.736} \quad \text{for } X_{tt}^{-1} > 0.1 \tag{8}$$

With a given liquid filling ratio ϕ the quality x shown in Eq. (6), can be determined by

$$x = \frac{\rho_v - \phi\rho_v}{\bar{\rho}} \tag{9}$$

where the average density of working fluid in the system may be calculated by the following relation of

$$\frac{1}{\bar{\rho}} = \frac{x}{\rho_v} + \frac{1-x}{\rho_l} \tag{10}$$

Utilizing the Martinelli parameter for a two-phase flow, the heat transfer coefficient due to the forced convection caused by oscillating motions can be readily determined by

$$h_{\text{mac}} = F(X_{tt}) h_l \tag{11}$$

where h_l is the liquid-phase heat transfer coefficient defined as

$$h_l = 0.023\left(\frac{k_l}{D}\right)\text{Re}_l^{0.8}\,\text{Pr}_l^{0.4} \tag{12}$$

Oscillating Motions. Examining the oscillating phenomena occurring in an OHP, there exist four kinds of forces, i.e., the thermally driven force, the capillary force, the frictional force, and the elastic restoring force. Based on Newton's laws, $\Sigma^{F}=md^2x/d\tau^2$, Ma et al. [14] established a mathematical model describing the motion of the working fluid in an OHP as

$$(L_l\rho_l + L_v\rho_v)A\frac{d^2x}{d\tau^2} + \left[(f_l\,\mathrm{Re}_l)\left(\frac{\mu_l L_l}{2D_h^2}\right) + (f_v\,\mathrm{Re}_v)\left(\frac{\mu_v L_v}{2D_h^2}\right)\right]A\frac{dx}{d\tau} + \frac{A\rho_v RT}{L_v}x = \left(\frac{Ah_{fg}\rho_{v,c}}{T_e}\right)\left(\frac{\Delta T_{\max}-\Delta T_{\min}}{2}\right)[1+\cos(\omega\tau)] \tag{13}$$

Utilizing Laplace transforms, the exact solution can be readily obtained,

$$x(\tau) = \frac{B}{m}\left\{\frac{(\sqrt{\zeta^2-1})\sin(\omega\tau) - e^{-\zeta\omega\tau}\sinh[\omega(\sqrt{\zeta^2-1})\tau]}{2\zeta\omega^2\sqrt{\zeta^2-1}} + \frac{1 - e^{-\zeta\omega\tau}\left[\cosh((\sqrt{\zeta^2-1})\omega\tau) + \dfrac{\zeta\sinh((\sqrt{\zeta^2-1})\omega\tau)}{\sqrt{\zeta^2-1}}\right]}{\omega^2}\right\} \tag{14}$$

where

$$m = A(\rho_L L_L + \rho_V L_V) \tag{15}$$

$$c = A\left[(f_l\cdot\mathrm{Re}_l)\left(\frac{\mu_l L_l}{2D_h^2}\right) + (f_v\,\mathrm{Re}_v)\left(\frac{\mu_v L_v}{2D_h^2}\right)\right] \tag{16}$$

$$k = \frac{A\rho_V RT}{L_V} \tag{17}$$

$$B = \left(\frac{Ah_{fg}\rho_{v,c}}{T_e}\right)\left(\frac{\Delta T_{\max}-\Delta T_{\min}}{2}\right) \tag{18}$$

For the system described by Eq. (14), the undamped natural frequency ω_0 and a damping ratio ζ can be, respectively, written as

$$\omega_0 = \sqrt{\frac{k}{m}} \tag{19}$$

$$\zeta = \frac{c}{2m\omega_0} \tag{20}$$

The model considers the thermal energy from the temperature difference between the evaporator and condenser as the driving force for the oscillating motion. For a given temperature difference between the evaporator and condenser, the average velocity of oscillating motions occurring in the system can be readily calculated.

During the derivation of Eq. (13), it was assumed that x is small relative to L_v; the pressure variation at the time interval of $\Delta\tau$ in the vapor phase between the evaporator and condenser was based on

$$\Delta p_v = \frac{\rho_v RT}{L_v}x \tag{21}$$

As shown in Eq. (21), the vapor pressure is linearly dependent on x. For a given vapor volume, if the length of total vapor bubble is much longer than x, the assumption of linear relation between Δp_v and x is reasonable. Experimental results show that when the heat flux is higher, the aptitude and frequency significantly increase. If the total volume occupied by vapor at the time τ is V_v, i.e., L_vA, and vapor is assumed as an ideal gas, the vapor pressure at the time τ can be found as

$$p_{v,\tau} = \frac{m_v RT}{L_v A} \tag{22}$$

At the time $\tau+\Delta\tau$, after heat is added to the evaporating section and evaporation occurs, the increase in the pressure will result in a decrease in the vapor volume by $-xA$, and the pressure in the vapor space yields

$$p_{v,\tau+\Delta\tau} = \frac{m_v RT}{(L_v - x)A} \tag{23}$$

The pressure variation at the time interval of $\Delta\tau$ can be approximately written as

$$\Delta p_v = \frac{\rho_v RT}{L_v}\left(x + \frac{x^2}{L_v} + \frac{x^3}{L_v^2} + \ldots + \frac{x^n}{L_v^{n-1}}\right) \tag{24}$$

Considering Eq. (24), Eq. (13) can be rewritten as

$$(L_l\rho_l + L_v\rho_v)A\frac{d^2x}{d\tau^2} + \left[(f_l\,\mathrm{Re}_l)\left(\frac{\mu_l L_l}{2D_h^2}\right) + (f_v\,\mathrm{Re}_v)\left(\frac{\mu_v L_v}{2D_h^2}\right)\right]A\frac{dx}{d\tau} + \frac{A\rho_v RT}{L_v}\left(x + \frac{x^2}{L_v} + \frac{x^3}{L_v^2} + \ldots + \frac{x^n}{L_v^{n-1}}\right) = \left(\frac{Ah_{fg}\rho_{v,c}}{T_e}\right)\left(\frac{\Delta T_{\max}-\Delta T_{\min}}{2}\right)[1+\cos(\omega\tau)] \tag{25}$$

Heat Transfer in the Condensing Section. The vapor generated in the evaporating section is condensed in the condensing section if the phase-change driving force exists, and the condensate in the thin film region will flow into the liquid-slug region due to the capillary force. Because the film thickness in the condensing film region is very thin compared to the meniscus thickness in the liquid slug, most of the condensing heat transfer will occur in the thin film region, as shown in Fig. 1. In this region, the Reynolds number of the condensate is very small; hence the inertial terms can be neglected and based on conservation of momentum in the thin film, the pressure drop due to the viscous flow can be found as

$$\frac{dP_l}{ds} = \frac{f\,\mathrm{Re}_\delta\,\mu_l D_o q_c'' s}{2\delta^3 D_i \rho_l h_{fg}} \tag{26}$$

where

$$\mathrm{Re}_\delta = \frac{\bar{U}_{l,c}\delta\rho_l}{\mu_l} \tag{27}$$

By integrating Eq. (26) from $s=0$ to $L_{c,v}/2$, the total pressure drop along half of the vapor bubble length can be found as

$$\Delta P_l = \int_o^{L_{c,v}/2}\left(\frac{f\cdot\mathrm{Re}_\delta\,\mu_l D_o q_c''}{2\delta^3 D_i\rho_l h_{fg}}\right)s\,ds \tag{28}$$

There exist numerous vapor slugs in the OHP including the condensing section. Although the vapor slug distributions, i.e., vapor bubble number, in the OHP is unpredictable, the total vapor space remains constant for a given liquid filling ratio ϕ, which is defined as

$$\phi = \frac{V_l}{V} \tag{29}$$

where V_l is the volume occupied by liquid, and V is the total volume throughout the heat pipe. It is assumed that all of the vapor slugs in the condensing region are combined into one large slug with condensation occurring on its perimeter. Assuming a uniform distribution of vapor throughout the entire length of the heat pipe, the length of the idealized single vapor slug in the condenser may be found by

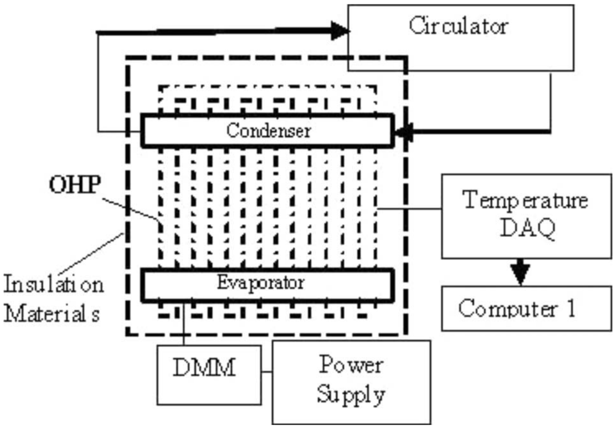

Fig. 2 Schematic of experimental system

$$L_{c,v} = L_c(1-\phi) \tag{30}$$

The capillary pressure along the condensate film can be found as

$$\frac{dP_c}{ds} = 2\sigma \frac{dK}{ds} \tag{31}$$

Integrating Eq. (31) from $K=1/r_o$ to $K=1/r_c$, the total capillary pressure can be found as

$$\Delta P_c = \sigma\left(\frac{2}{r_c} - \frac{1}{r_o}\right) \tag{32}$$

where r_o is the meniscus radius of the liquid-vapor interface at the line of symmetry, $s=0$, and r_c is the meniscus radius of the liquid-vapor interface at the liquid slug, $s=L_{c,v}$, which can be, respectively, found by

$$r_0 = \frac{1}{2}(D_i - 2\delta_0) \tag{33}$$

and

$$r_c = \frac{1}{2}(D_i - 2\delta_{0.5L_{c,v}}) \tag{34}$$

Considering Eqs. (33) and (34), the total capillary pressure can be rewritten as

$$\Delta P_c = \sigma\left(\frac{2}{\left(\frac{D_i}{2} - \delta_{0.5L_{c,v}}\right)} - \frac{1}{\left(\frac{D_i}{2} - \delta_o\right)}\right) \tag{35}$$

For the steady-state condensation process of the thin film, the capillary pressure defined by Eq. (35) should be equal to the pressure drop determined by Eq. (28). With a given heat flux level, i.e., q_c'', Eqs. (35) and (28) can be readily solved and the condensation film thickness determined.

Experimental System

In order to verify the analytical model predicting the heat transfer performance, experimental investigations were conducted. The experimental system, as shown in Fig. 2, consisted of a test section including an OHP, a cooling bath, a power supply, and a data acquisition system. The OHP shown in Fig. 3 was made of copper tube. The inner and outer diameters of the tube were 1.65 mm and 3.175 mm, respectively. Aluminum cooling block connected to the cooling bath provided a constant temperature condenser. The evaporating section of the OHP was a strip resistance heater that spanned the copper plate. The OHP was surrounded with fiberglass insulation to reduce the heat loss. Based on the insulation surface temperature, the calculated heat loss is less than 1.5% of the total heat added on the OHP. Twelve thermocouples were used to measure the temperature distributions along the heat pipe. Multiple thermocouples were placed in the evaporator, adiabatic, and condenser regions to determine the temperature drop across the sections. The temperature data were directly sent to a data acquisition system (National Instruments) connected to a personal computer for data recording and analysis. The OHP was backfilled to a 50% filling ratio with HPLC grade water.

Prior to the start of the experiment, the system was allowed to equilibrate and reach steady state such that the steady-state operating temperature was achieved and a uniform temperature distribution with no heater power input was observed throughout the OHP. Once the experimental system reached the equilibrium, the input power was increased in 50 W increments up to a maximum heat input of 350 W. The steady-state condition was defined as the mean temperature in the evaporator with a change of less than 0.5°C in 5 min. To obtain the data for the next successive power level, the power was approximately incremented every 30 min. During the tests, the input power and temperature data, including the ambient temperature, were simultaneously recorded through the data acquisition system.

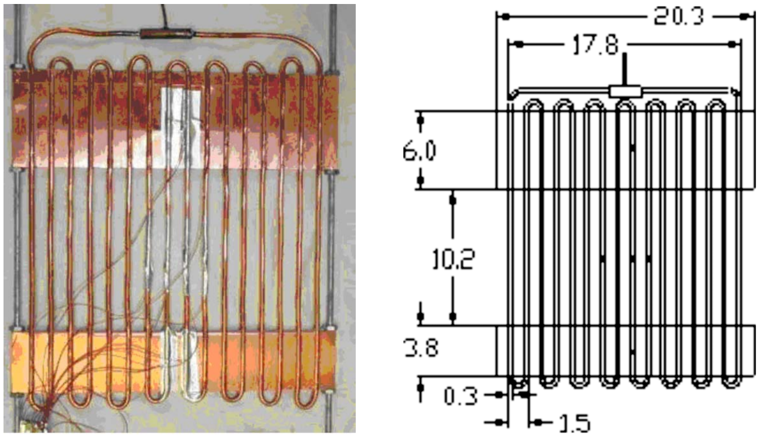

(*a*) (*b*)

Fig. 3 Experimental heat pipe and dimensioned drawing: (*a*) photo; (*b*) dimensions (cm)

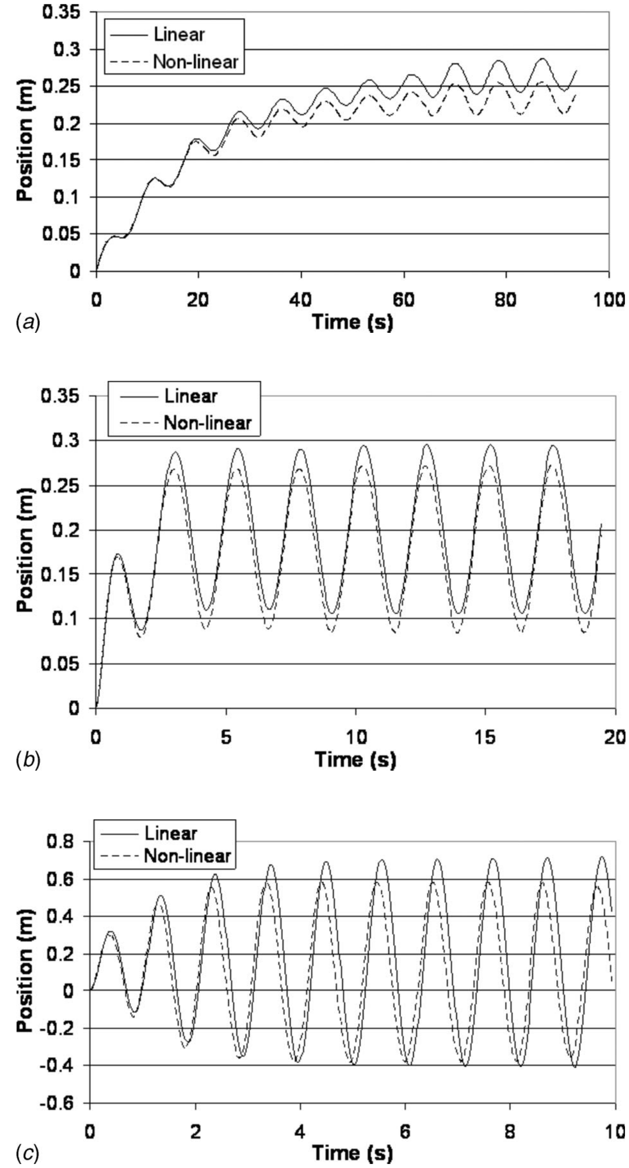

Fig. 4 Slug position versus time for linear and nonlinear equations at operating temperatures of (*a*) 20°C; (*b*) 60°C; (*c*) 100°C

Results and Discussion

The model for the fluid motion with the added nonlinear terms has different results from those originally presented by Ma et al. [14]. Figures 4(*a*)–4(*c*) show the difference between the nonlinear model and the previously developed linear model for operating temperature of 20°C, 60°C, and 100°C, respectively. Because the operating temperature of the heat pipe depends on the cooling bath temperature, the coolant temperature flowing through the condenser section is defined as the operating temperature. It can be seen that the amplitude and frequency of the fluid motion obtained by the present nonlinear model are lower than those obtained by the linear model. The effect of the nonlinear terms on the frequency is more prominent with increasing operating temperature. Figure 5 shows the effect of temperature difference on the fluid motion obtained from the current model. It can be seen that increasing temperature difference does not have an effect on frequency; however, the amplitude is greatly increased with a temperature difference increase.

Figures 6(*a*) and 6(*b*) show the theoretical contribution of heat transfer in the micro- and macroregions of the evaporator to the overall heat transfer coefficient for an operating temperature of 20°C and 60°C, respectively. The contribution in the microregion, which is due to the convective evaporation, is much less than the heat transfer due to the forced convection (i.e., macroregion). This means that the heat transfer in an OHP is mainly due to the exchange of sensible heat, which agrees with the results presented by Khandekar et al. [7,8] and Zhang and Faghri [12,13]. The role of phase-change heat transfer is sustaining the pressure difference between the evaporating and condensing sections that is the driving force for oscillatory flow. Figures 7(*a*) and 7(*b*) display the theoretical evaporator, condenser, and total temperature differences in the specified OHP for operating temperatures of 20°C and 60°C, respectively. The temperature difference in the evaporator section contributes more to the total temperature difference than that in the condenser.

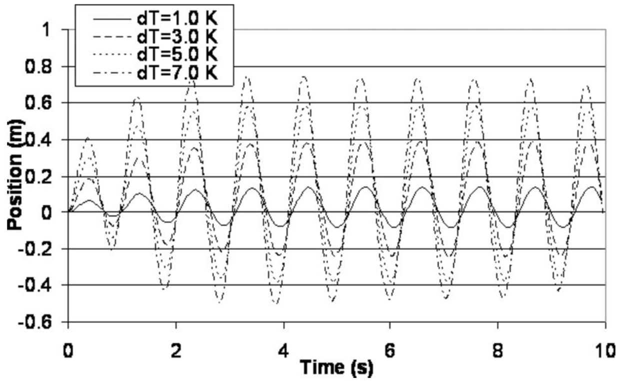

Fig. 5 Slug position versus time for nonlinear equations at an operating temperature of 100°C and varied temperature difference

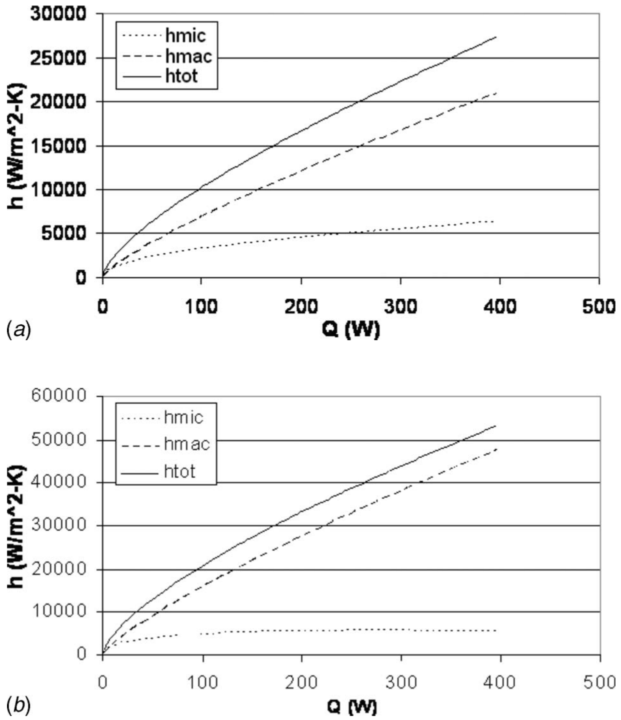

Fig. 6 Micro-, macro-, and total heat transfer coefficients versus heat input at operating temperatures of (*a*) 20°C and (*b*) 60°C

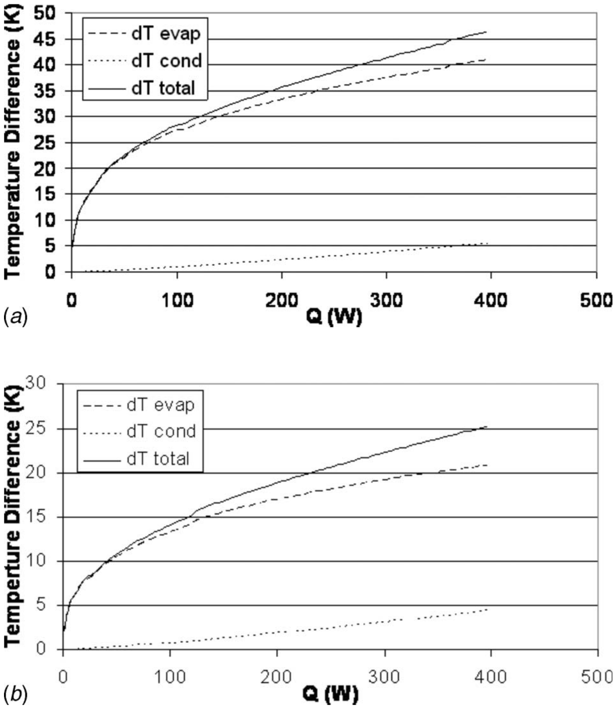

Fig. 7 Evaporator, condenser, and total temperature differences versus heat input at operating temperatures of (*a*) 20°C and (*b*) 60°C

Experiments on the heat transfer performance of the OHP shown in Fig. 3 were performed and the results are presented in terms of the temperature difference from the evaporator to the condenser ΔT_t and heat input Q. Temperature differences were based on the difference between the average recorded temperatures in the evaporator and condenser sections. It is apparent that the oscillating motions generated in the heat pipe enhanced the heat transfer. When the input power was higher than 30 W, the oscillating motions started and the increase in temperature drop with respect to heat input was reduced. It can be concluded from experiments that there exist an onset temperature difference for the start of oscillating motions and a range of temperature differences for the steady-state oscillating motion. Figure 8 shows the comparison between the experimental results obtained from the specified OHP and the temperature drops determined with the theoretical model proposed herein. The results showed that the agreement between the predicted and measured temperature drops agreed very well for the operating temperature of 20°C. When the operating temperature is increased to 60°C, the predicted temperature drop for the case of low heat input is lower than the experimental results. As the heat input increases, the discrepancy between the predicted and measured temperature drops significantly decreases and excellent agreement is obtained. Considering the facts that the pressure drop in the turns of the OHP and possible circulation of working fluid were not taking into account in the theoretical model, the agreement between the theoretical and experimental results is very good.

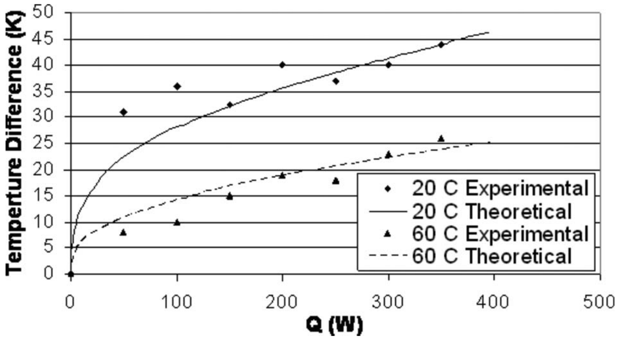

Fig. 8 Experimental and theoretical total temperature differences versus heat input at operating temperatures of 20°C and 60°C

Conclusions

A mathematical model predicting the fluid motion and temperature drop in an OHP has been developed. The model includes the forced convection heat transfer due to the oscillating motions, the confined evaporating heat transfer in the evaporating section, and thin film condensation heat transfer in the condensing section. The numerical results indicate that the oscillating motions occurring in the OHP significantly enhances the heat transfer in the OHP. An experimental investigation of temperature drops occurring in an OHP was also conducted. Experimental results indicated that there exists an onset temperature difference for the excitation of oscillating motions in an OHP, i.e., when the input power or the temperature difference from the evaporating section to the condenser was higher than this onset value the oscillating motion started, resulting in an enhancement of the heat transfer. Results of the investigation will assist in optimizing the heat transfer performance and provide a better understanding of heat transfer mechanisms occurring in the OHP.

Acknowledgment

The work presented in this paper was funded by the Office of Naval Research Grant No. N00014-06-1-1119, under the direction of Dr. Mark Spector.

Nomenclature

A = cross-sectional area, m^2
c = specific heat, J/kg K
D = tube diameter, m
f = friction factor
G = mass flux, kg/s m^2
h = heat transfer coefficient, W/m^2 K
h_{fg} = latent heat, kJ/kg
k = thermal conductivity, W/m K; stiffness, N/m
K = curvature, 1/m
L = length, m
m = mass, kg
p = pressure, N/m^2
Pr = Prandtl number
q'' = heat flux, W/m^2
r = radius, m
R = gas constant, J/(kg K)
Re = Reynolds number
s = location, m
S = suppression factor
T = temperature, K
u_a = average oscillation velocity, m/s
x = coordinate, m; quality
X = Martinelli parameter
z = direction, m

Greek Symbols

δ = film thickness, m
ϕ = filling ratio
ρ = density, kg/m^3
$\bar{\rho}$ = average density, kg/m^3
σ = surface tension, N/m
μ = viscosity, N s/m^2
ζ = damping ratio
τ = time, s

ω = frequency, Hz

Subscripts

e = evaporator
c = condenser
h = hydraulic
i = inside
l = liquid
mac = macro
max = maximum
mic = micro
min = minimum
p = pressure
sat = saturated
tp = two phase
v = vapor
w = wall

References

[1] Akachi, H., 1990, "Structure of a Heat Pipe," U.S. Patent No. 4,921,041.

[2] Ma, H. B., Wilson, C., Yu, Q., Choi, U. S., and Tirumala, M., 2006, "An Experimental Investigation of Heat Transport Capability in a Nanofluid Oscillating Heat Pipe," ASME J. Heat Transfer, **128**, pp. 1213–1216.

[3] Zhang, X. M., Xu, J. L., and Zhou, Z. Q., 2004, "Experimental Study of a Pulsating Heat Pipe Using FC-72, Ethanol, and Water as Working Fluids," Exp. Heat Transfer, **17**, pp. 47–67.

[4] Park, K., and Ma, H. B., 2007, "Nanofluid Effect on the Heat Transport Capability in a Well-Balanced Oscillating Heat Pipe," J. Thermophys. Heat Transfer, **21**(2), pp. 443–445.

[5] Kim, J. H., Lee, W. H., Jung, H. S., and Kim, J. S., 2000, "Characteristics of Pressure Oscillation in Self-Excited Oscillating Heat Pipe Based on Experimental Study," *Sixth International Heat Pipe Symposium*, Chiang Mai, Thailand, pp. 263–272.

[6] Borgmeyer, B., and Ma, H. B., 2007, "Experimental Investigation of Oscillating Motions in a Flat Plate Pulsating Heat Pipe," J. Thermophys. Heat Transfer, **21**(2), pp. 405–409.

[7] Khandekar, S., and Groll, M., 2003, "An Insight into Thermo-Hydrodynamic Coupling in Closed Loop Heat Pipes," Int. J. Therm. Sci., **43**(1), pp. 13–20.

[8] Khandekar, S., Nanyam, S., and Groll, M., 2004, "Two-Phase Flow Modeling in Closed Loop Pulsating Heat Pipes," *13th International Heat Pipe Conference*, Sept. 19–25.

[9] Zuo, J., North, M. T., and Wert, K. L., 2001, "High Heat Flux Heat Pipe Mechanism for Cooling of Electronics," IEEE Trans. Compon. Packag. Technol., **24**(2), pp. 220–225.

[10] Lin, L., Ponnappan, R., and Leland, J., 2001, "Experimental Investigation of Oscillating Heat Pipes," J. Thermophys. Heat Transfer, **15**(4), pp. 395–400.

[11] Qu, W., and Ma, H. B., 2007, "Theoretical Analysis of Start-up of a Pulsating Heat Pipe," Int. J. Heat Mass Transfer, **50**, pp. 2309–2316.

[12] Zhang, Y., and Faghri, A., 2003, "Oscillatory Flow in Pulsating Heat Pipes With Arbitrary Numbers of Turns," J. Thermophys. Heat Transfer, **17**(3), pp. 340–347.

[13] Zhang, Y., and Faghri, A., 2002, "Heat Transfer in an Oscillating Heat Pipe With Open End," Int. J. Heat Mass Transfer, **45**(4), pp. 755–764.

[14] Ma, H. B., Hanlon, M. A., and Chen, C. L., 2006, "An Investigation of Oscillating Motions in a Miniature Pulsating Heat Pipe," Microfluid. Nanofluid., **2**(2), pp. 171–179.

[15] Wong, T. N., Tong, B. Y., Lim, S. M., and Ooi, K. T., 1999, "Theoretical Modeling of Oscillating Heat Pipe," *Proceedings of 11th International Heat Pipe Conference*, Tokyo, Japan, pp. 159–163.

[16] Chen, J. C., 1966, "Correlation for Boiling Heat Transfer to Saturated Fluids in Convective Flow," Ind. Eng. Chem. Process Des. Dev., **5**(3), pp. 322–339.

[17] Zhao, T. S., and Cheng, P., 1998, "Heat Transfer in Oscillatory Flows," *Annual Review of Heat Transfer*, C. L. Tien, ed., Begell House, Inc., Redding, CT, Vol. IX, No. 9, pp. 359–420.

[18] Wallis, G. B., 1969, *One-Dimensional Two-Phase Flow*, McGraw-Hill Book Company, New York.

[19] Peterson, G. P., 1994, *An Introduction to Heat Pipe: Modeling, Testing, and Applications*, Wiley, New York.

[20] Yuan, H., Oguz, H. N., and Prosperetti, A., 1999, "Growth and Collapse of a Vapor Bubble in a Small Tube," Int. J. Heat Mass Transfer, **42**(19), pp. 3643–3657.

[21] Thomas, K. J., and Kim, C. J., 1998, "Valveless Pumping Using Traversing Vapor Bubbles in Microchannels," J. Appl. Phys., **83**(11), pp. 5658–5664.

[22] Kurzweg, U. H., 1985, "Enhanced Heat Conduction in Fluids Subjected to Sinusoidal Oscillations," ASME J. Heat Transfer, **107**(3), pp. 459–462.

[23] Kurzweg, U. H., and Zhao, L. D., 1984, "Heat Transfer by High-Frequency Oscillations: A New Hydrodynamic Technique for Achieving Large Effective Thermal Conductivities," Phys. Fluids, **27**(11), pp. 2624–2627.

Yao-Hsien Liu

Michael Huh

Je-Chin Han
e-mail: jc-han@tamu.edu

Turbine Heat Transfer Laboratory,
Department of Mechanical Engineering,
Texas A&M University,
College Station, TX 77843-3123

Sanjay Chopra
Siemens Power Company,
4400 Alafaya Trail,
Orlando, FL 32826

Heat Transfer in a Two-Pass Rectangular Channel (AR=1:4) Under High Rotation Numbers

This paper experimentally investigated the rotational effects on heat transfer in a two-pass rectangular channel (AR=1:4), which is applicable to the channel near the leading edge of the gas turbine blade. The test channel has radially outward flow in the first passage through a redirected sharp-bend entrance and radially inward flow in the second passage after a 180 deg sharp turn. In the first passage, rotation effects on heat transfer are reduced by the redirected sharp-bend entrance. In the second passage, under rotating conditions, both leading and trailing surfaces experienced heat transfer enhancements above the stationary case. Rotation greatly increased heat transfer enhancement in the tip region up to a maximum Nu ratio (Nu/Nu_s) of 2.4. The objective of the current study is to perform an extended parametric study of the low rotation number (0–0.3) and low buoyancy parameter (0–0.2) achieved previously. By varying the Reynolds numbers (10,000–40,000), the rotational speeds (0–400 rpm), and the density ratios (inlet density ratio=0.10–0.16), the increased range of the rotation number and buoyancy parameter reached in this study are 0–0.67 and 0–2.0, respectively. The higher rotation number and buoyancy parameter have been correlated very well to predict the rotational heat transfer in the two-pass, 1:4 aspect ratio flow channel. [DOI: 10.1115/1.2909615]

Keywords: heat transfer, rotating rectangular channel, rotation number, buoyancy parameter, internal cooling

Introduction

Internal cooling techniques for gas turbine blades have been studied for several decades. Gas Turbine Heat Transfer and Cooling Technology [1] provides in-depth information about updated cooling techniques. The internal cooling techniques of the gas turbine blade include jet impingement, rib turbulated cooling, and pin-fin cooling. Advanced internal cooling techniques are needed to prevent overheating of the turbine blade. The internal cooling of the gas turbine blade is influenced by the channel aspect ratio, rib turbulator configurations, and rotational and flow parameters.

Coolant is circulated through serpentine passages fabricated on the inside of the gas turbine blade in order to remove heat from the blade surface. Different aspect ratio channels are applicable to different parts of the turbine blade, as shown in Fig. 1. The narrow aspect ratio of 1:4 simulates channels near the leading edge, while the wide aspect ratio of 4:1 channel is applicable to the channels near the trailing edge. Rib turbulators are used inside the cooling passages to enhance the heat transfer.

Han [2] measured the heat transfer and friction factor in a square duct with several rib configurations. Afterwards, Han [3] extended the study to five aspect ratio channels (AR=4:1, 2:1, 1:1, 1:2, and 1:4). He concluded that ribs enhanced the heat transfer for every aspect ratio channel. Park et al. [4] also conducted an experimental study on five different aspect ratio channels with angled ribs under stationary conditions. They concluded that the low aspect ratio channels (1:2 and 1:4) provide better heat transfer performance when compared to the high aspect ratio channels. Guidez [5] experimentally studied the convective heat transfer in rectangular rotating channel with an aspect ratio of 1:2. Furthermore, he theoretically analyzed rotation effects with a 3D Navier–Stokes turbulant mixing length model. He concluded that Coriolis acceleration has a beneficial influence on the mean heat transfer. Agarwal et al. [6] studied the heat/mass transfer in a 1:4 aspect ratio rotating rectangular channel with smooth and ribbed walls. The rotation number varied from 0.0 to 0.12. They concluded that the 1:4 channel, when compared to a 1:1 channel, provides less heat transfer enhancement. Fu et al. [7] experimentally studied the heat transfer and pressure drop inside the 1:2 and 1:4 aspect ratio channels under stationary and rotating conditions with smooth and ribbed walls. They concluded that rotation has a relatively small effect in the second passage due to the large distance between the leading and trailing surfaces. Fu et al. [8] further extended their studies to five different aspect ratio channels (AR=4:1, 2:1, 1:1, 1:2, and 1:4) with two channel orientations (90 deg and 45 deg or 135 deg). The rotation numbers varied from 0.0 to 0.3. Their results showed that the overall levels of heat transfer enhancement for all ribbed channels were comparable. Su et al. [9] performed a Computational Fluid Dynamics (CFD) study using a Reynolds stress model for rotating rectangular channels (AR=1:1, 1:2, and 1:4). The rotation number ranged from 0.0 to 0.28 with the channel at an orientation of 90 deg relative to the axis of rotation. They concluded that for large Reynolds and rotation numbers, the effect of rotation continuously decreases with decreasing aspect ratio.

In the turn region, the secondary flow is generated by the turn geometry and turbulence enhancement. The secondary flow augments the heat transfer, especially at the first part of the second passage. Liou and Chen [10] investigated the 180 deg turn effects in a rectangular channel with a width to height ratio of 1.25. The rotation number ranged from 0.0 to 0.44 with a Reynolds number from 5000 to 50,000. They showed that the unsteadiness of separation bubbles downstream of the sharp turn significantly augments the heat transfer in the first part of the second passage. Liou et al. [11] also used laser doppler velocimetry (LDV) to measure the turbulent flow field inside a rotating two-pass square duct. The flow field and the kinetic energy distribution near the 180 deg turn were measured. The rotation number was varied from 0.0 to 0.2. They concluded that as the rotation number is increased, the tur-

---

Contributed by the Heat Transfer Division of ASME for publication in the Journal of Heat Transfer. Manuscript received June 15, 2007; final manuscript received October 11, 2007; published online June 2, 2008. Review conducted by Gautam Biswas.

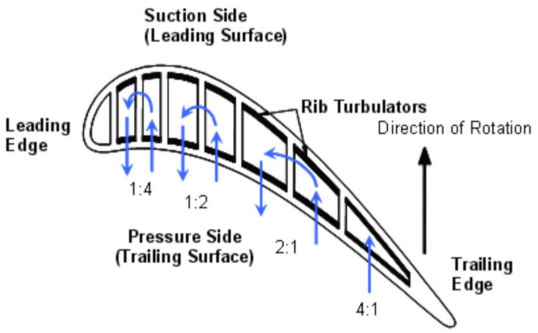

Fig. 1 Gas turbine blade internal cooling channels and their applicable aspect ratios

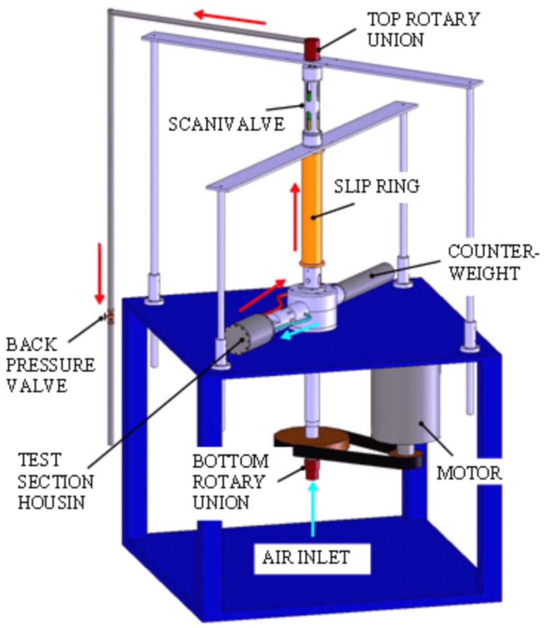

Fig. 2 Rotating arm assembly used to perform heat transfer experiments with the 1:4 aspect ratio test section

bulence intensity level increases exponentially. The increased turbulence intensity and Coriolis force by the increased rotation number enhance the heat transfer in the turn region. Numerous studies have focused on internal heat transfer in rotating channels under fully developed flow conditions. However, the internal flow channel of the gas turbine blade in engines experiences strong effects due to the entrance geometry. The heat transfer enhancement differs from that of fully developed flow when entrance effects are present. Wright et al. [12] conducted a survey of rectangular channels with aspect ratios of 4:1 and 8:1. They studied three different entrance geometries and concluded that the entrance effects will greatly enhance the heat transfer. They showed that as the rotation number increases, the effect of the entrance geometry decreases. The entrance enhancement will decrease as the rotation number increases. The influence of the entrance geometry on the heat transfer is more apparent in the smooth channels than in the ribbed channels.

Wagner et al. [13] performed heat transfer measurements inside a square channel with radial outward flow in the first passage. The rotation number ranged from 0.00 to 0.48 in their studies. Wagner et al. [14] continued to investigate the heat transfer inside the second and third passages of the square channel. The results from Refs. [13,14] showed that both the rotation number and density ratio caused large changes in heat transfer for radially outward flow but relatively small changes for radially inward flow. They also pointed out that the heat transfer was relatively unaffected by the buoyancy parameter for the radially inward flow on the leading surface. Zhou et al. [15] investigated the rotation effects in a 4:1 aspect ratio channel. The rotation number ranged from 0.0 to 0.6. They concluded that on the destabilized surfaces in the first passage and second passage, rotation enhances the heat transfer up to a certain Ro, beyond which the enhancement is flat or reduced.

Currently in the available open literature, heat transfer data at high rotation numbers for internal cooling channels are very limited. The maximum rotation number for the 1:4 aspect ratio channel studied by previous researchers was 0.3 at a Reynolds number of 5000. The range of the rotation number for the current study was from 0.0 to 0.67. The buoyancy parameter in the current study ranged from 0.0 to 2.0. The objective of the current study is to investigate the heat transfer enhancement in a rotating two-pass rectangular channel ($\mathrm{AR}=1:4$) at high rotation numbers and high buoyancy parameters. The Reynolds number, the rotational speed, and the density ratio are varied in order to obtain a thorough understanding of the effects of the rotation number and buoyancy parameter. Through this study, a detailed set of base line data has been established for a smooth walled 1:4 aspect ratio channel, with parameters near to those of aircraft engines. In addition, this study focuses on the effect of inlet geometry on the first-passage radially outward flow heat transfer distributions.

Experimental Facility

Typical rotation numbers for aircraft engines are near 0.25 with Reynolds numbers close to 50,000. One method to achieve similar conditions in the laboratory is to use air at high pressures. As the pressure of the air increases, so will the density. For a fixed mass flow rate (Reynolds number) and hydraulic diameter, an increase in density will result in a decrease in velocity. A lower velocity will, in turn, increase the rotation number. In order to achieve larger rotation numbers at higher Reynolds numbers, the experiments for the present study were conducted with air at a pressure of 5 bars. For the current study, a rotation number of 0.17 can be achieved at a Reynolds number of 40,000.

Rotating Facility. Figure 2 shows the rotating facility used to conduct the experiments for the current study. A steel table is used as the support structure. A 25 hp electric motor is used to drive the shaft, which in turn spins the arm. Counterweights, located opposite of the test section housing, are used to balance the arm so that minimal vibrations are experienced during rotation. The local radius of rotation R_x ranges from 603 mm to 730 mm. The cooling air from the compressor enters an ASME square-edge orifice meter (not shown), where the mass flow rate is measured. Cooling air enters the rotating assembly at the bottom of the shaft via a rotary union. A chiller is hooked up to the flow loop before the rotary union to cool the air at the inlet. The air then passes through the hub and into the bore of the arm. A rubber hose is used to direct the flow from the arm to the test section housing. After the air flows through the test section, it exits the housing. The hot exhaust air is then directed, by means of a rubber hose, to the slip ring. A 12.7 mm diameter copper tube, which passes through the bore of the slip ring, is used to direct the air to the top rotary union. A Steel pipe is connected to the top rotary union and a valve is used to adjust the back pressure of the system.

Test Section ($\mathbf{AR=1:4}$). The entrance geometry with a redirected sharp bend is shown in Fig. 3. The coolant air goes through a 9.525 mm inlet hose into the curved plenum region. After direct impingement on the plenum region, the flow is redirected into the 1:4 aspect ratio test section. Two screens were placed prior to the first copper plate region of the test section to help spread the flow at the entrance. A nylon substrate, with a low thermal conductiv-

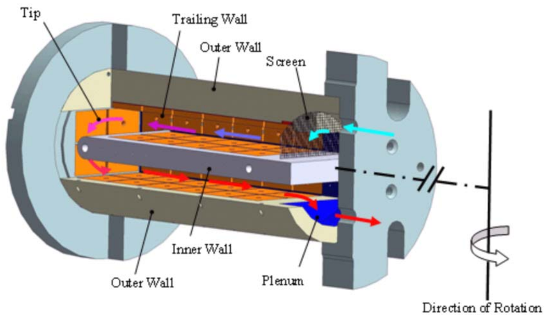

Fig. 3 Drawing showing redirected sharp-bend entrance and the flow channel geometry of the 1:4 aspect ratio test section

ity, is used to support the copper plates and heaters. Between each copper plate is an insulator strip of nylon, which prevents conduction between copper plates. The copper plates on the leading and trailing walls are rectangular in shape and measure 23.81 $\times$11.11 mm^2. The outer and inner wall copper plates are square and measure 23.81$\times$23.81 mm^2. The tip copper plates are rectangular with dimensions of 23.81$\times$17.46 mm^2. The flow channel width is 50.8 mm and has a height of 12.70 mm, resulting in a hydraulic diameter of 20.32 mm. The test section consists of two passes. The flow in the first passage is radially outward, and after a 180 deg turn, radially inward in the second passage. Figure 4 shows that each passage is divided into six regions. The screens were instrumented before the first copper plate, as shown in the figure. There are a total of 12 regions in the test section. The overall test section length is 190.50 mm. The heated channel length of each passage is 154.50 mm and the plenum depth is 19.05 mm. One thermocouple is placed at the inlet to measure the air temperature as it enters the test section. At the exit of the test section, two thermocouples are used to measure the air temperature. The air passing through the test section is heated using prefabricated heaters that are placed beneath the copper plates. A total of 12 heaters are used for the outer, inner, leading, and trailing walls. An additional heater is used for the tip. A thermally conductive paste is used between the heaters and the copper plates in order to reduce contact resistance. Blind holes with a diameter of 1.59 mm are drilled 1.59 mm deep on the back side of each copper plate. Thermocouples are placed inside of the blind holes and are affixed to the copper plates using highly conductive epoxy. Temperature measurements were taken on all of the leading, trailing, and cap copper plates. On the outer and inner walls, only the temperatures of the copper plates at Regions 4 and 10 were measured due to limited slip ring channels.

For the present study, the test section was oriented 90 deg to the direction of rotation. The air pressure was maintained at 5 bars for all cases studied. The Reynolds numbers under investigation were 10,000, 15,000, 20,000, 30,000, and 40,000. At each Reynolds number, the rotational speed was varied from 0 rpm to 400 rpm with an increment of 100 rpm.

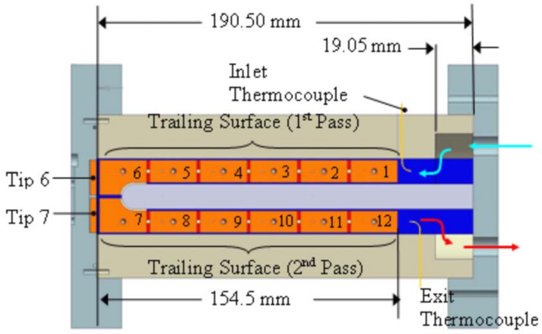

Fig. 4 Test section view showing the copper plate region numbering convention

Data Reduction

Heat Transfer Enhancement. This study investigates the regionally averaged heat transfer coefficient (h) at various locations within the rotating duct. The heater is designed to supply uniform heat flux along the streamwise direction. The uniform wall temperature of 65°C ($(\Delta\rho/\rho)_{\text{in}}=0.10$) in the circumferential direction is maintained through the entire tests. Two additional wall temperatures of 70°C ($(\Delta\rho/\rho)_{\text{in}}=0.14$) and 80°C ($(\Delta\rho/\rho)_{\text{in}}=0.16$) are tested specifically under the highest rotational speed to study the buoyancy parameter effects. The regionally averaged heat transfer coefficient is calculated using the net heat transferred from the heated copper plate (Q_{net}), the projected surface area of each copper plate segment (A), the regionally averaged temperature of the plate ($T_{w,x}$), and the local bulk mean temperature of the air flow in the channel ($T_{b,x}$). Therefore, the regionally averaged heat transfer coefficient is given as

$$h = (Q_{\text{net}}/A)/(T_{w,x} - T_{b,x}) \tag{1}$$

The net heat transfer is calculated as

$$Q_{\text{net}} = (VI)\frac{A}{A_h} - Q_{\text{loss}} \tag{2}$$

The voltage (V) is measured with a multimeter and the current (I) is supplied to each heater by variac transformers. The power input to each heater is multiplied by the ratio of the copper plate area (A) to the total heater area (A_h).

In order to determine the external heat losses (Q_{loss}) escaping from the test section during the experiment, two heat loss calibration tests are performed. The first heat loss calibration test is performed at a lower wall temperature than the experiment wall temperature. Similarly, a second heat loss calibration test is performed at a higher wall temperature than the experiment wall temperature. During the heat loss calibration tests, the wall temperature is maintained by supplying power to each heater with the variac transformers. A successful heat loss calibration test is achieved when the total power input to the test section reaches equilibrium with the environment. The heat loss, which occurs during the experiment, is then determined by interpolating between the two sets of heat loss data. It is noted that heat loss calibration tests were performed at all rotational speed conditions considered in the present study and the stationary case as well. In order to minimize natural convection effects during the heat loss calibration tests, an insulating material was placed inside of the flow channels.

The copper plate surface area used in this study is the projected surface area of the channel. The regionally averaged wall temperature ($T_{w,x}$) is directly measured using the thermocouple installed in the blind hole on the back side of each copper plate. Because the plates are made of copper, which has a high thermal conductivity, the temperature of each plate is assumed uniform. One thermocouple at the inlet and two thermocouples at the outlet of the test section measure the inlet and outlet bulk temperatures, respectively. Therefore, the bulk temperature at any location in the test section can be calculated using linear interpolation. The results presented from this study are based on the linear interpolation method. Although linear interpolation was chosen for determining the coolant temperature at various locations in the channel, the coolant temperature can also be calculated using the conservation of energy principle. For the present study, both methods compare very well. The energy balance equation is

$$T_{b,x} = T_{b,i} + \sum_i Q_{\text{net}}/mc_p \tag{3}$$

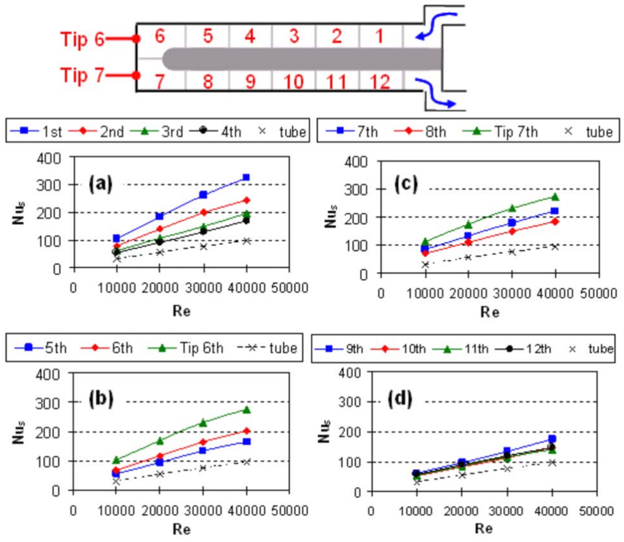

Fig. 5 Stationary Nusselt number distribution in each region of the channel

The Dittus–Boelter/McAdams correlation for heating ($T_{w,x} > T_{b,x}$) is used in this study to provide a basis of comparison. The Dittus–Boelter/McAdams correlation from Kays et al. [16] is used to calculate the Nusselt number for fully developed turbulent flow through a smooth stationary pipe. Therefore, the Nu ratio is given as

$$\frac{\mathrm{Nu}}{\mathrm{Nu}_0} = \left(\frac{hD_h}{k}\right)\left(\frac{1}{0.023\,\mathrm{Re}^{0.8}\,\mathrm{Pr}^{0.4}}\right) \tag{4}$$

where h is calculated by Eq. (1). All air properties are taken based on the bulk air temperature with a Prandtl number (Pr) for air of 0.71.

Experimental Uncertainty. An uncertainty analysis was performed based on the method described by Kline and McClintock [17]. Air properties were taken based on the mean bulk air temperature. The estimated uncertainty for the temperature measurements is 0.5°C. The uncertainty of the Nu ratio is approximately 6.0% for the highest Reynolds number. For the lowest Reynolds number (Re=10,000), the maximum uncertainty is approximately 9.7% on the low heat flux wall under rotating conditions.

Results and Discussion

Stationary Results With Entrance Geometry Effects. Before explaining the rotating results, the stationary flow behavior inside the channel needs to be discussed. The cooling air enters the plenum and is then redirected into the 1:4 test region. This redirected sharp-bend entrance significantly alters the heat transfer, especially in the regions near the plenum. Figure 5 shows the stationary Nusselt number in different locations of the channel. The data for the fully developed turbulent flow in a smooth circular tube are also plotted for comparison. The nondimensional Nusselt number is chosen to study the heat transfer enhancement. In Regions 3, 4, 9, and 10, the results are the average of six copper plates along the circumferential direction; while in the other regions, the results are the average of the leading and trailing surfaces only. Near the entry region of the channel, the Nusselt number is higher than the fully developed flow case in the smooth tube. It decreases along the streamwise direction from Region 1 to Region 4 as shown in Fig. 5(*a*). Figures 5(*b*) and 5(*c*) are the regions near the 180 deg turn portion. The direct impingement in the tip region produces the highest Nusselt number.

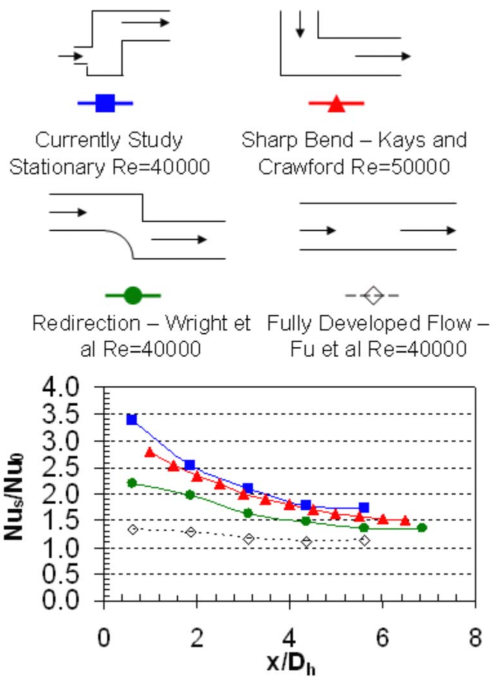

Fig. 6 Nu ratio ($\mathrm{Nu}/\mathrm{Nu}_0$) comparisons for different entrance geometries in a smooth channel

In the second pass, as shown in Fig. 5(*d*), although the stationary Nusselt number is still higher than the smooth tube, the magnitude of the heat transfer enhancement is smaller than the first pass and the turn region. The difference between the four regions is also smaller, which indicates that the flow is approaching the fully developed condition.

Figure 6 shows the Nu ratio comparisons inside the stationary channel from several open literature sources. The Nu ratio has been considered in order to eliminate the Reynolds number effects. Only first few data points of the current study, in the first passage with redirected sharp bend, were compared to eliminate the effects from the 180 deg turn. The sharp-bend geometry presented by Kays et al. [16] in the circular tube and the redirection geometry by Wright et al. [12] in the 4:1 channel clearly show that the entrance geometry significantly augments the Nu ratio, especially when x/D_h is small. The fully developed flow inside a 1:4 stationary channel by Fu et al. [8] shows the lowest Nu ratio. As x/D_h increases, the Nu ratios of the four curves converge along the streamwise direction. The flow does not achieve the fully developed flow behavior in the first passage because the passage is short (L/D_h=7.5).

Rotating Results. When there is no rotation, Coriolis and rotation-induced buoyancy forces are not present, and thus the flow can be considered to be symmetric. Heat transfer enhancement is therefore similar on the leading and trailing surfaces in each respective passage. As the Reynolds number increases, the magnitude of heat transfer (Nu) will increase; however, the magnitude of the enhancement only slightly decreases because a ratio is being considered. The conceptual view of the rotation-induced secondary flow is shown in Fig. 7(*a*). In the first passage, the rotation-induced secondary flow impinges onto the trailing surface, and the rotation-induced buoyancy force further thins the boundary layer on the trailing surface. In the second passage, the Coriolis forces change direction, due to radially inward flow, and impingement occurs on the leading surface. This secondary-flow behavior has been predicted by Su et al. [9].

In general, in the first passage, the heat transfer enhancement begins to decrease due to the boundary layer growth along the streamwise direction. At the turn region, the heat transfer en-

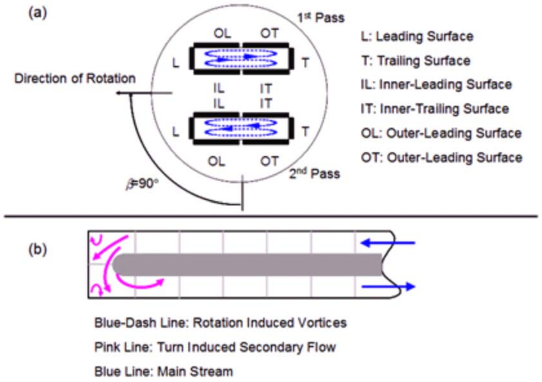

Fig. 7 Conceptual view of (*a*) rotation-induced secondary flow inside a two-passage rectangular channel (AR=1:4), and (*b*) turn-induced secondary flow

hancement increases because the conceptual view of the turn-induced secondary flow, as shown in Fig. 7(*b*). The main flow impinges onto the tip. As the flow is redirected into the second passage, the flow impinges on the outer wall. Small vortices develop in the corner regions of the turn. The flow separates on the inner wall in the second passage near the turn region, but reattaches further downstream. In the second passage, the boundary layer begins to grow once again, and thus the heat transfer decreases in the streamwise direction.

Figure 8 shows the heat transfer enhancement at various rotational speeds at Reynolds numbers of 10,000 and 20,000. The effect of increasing the rotational speed is observed. The effect of rotation near the entrance, on the leading surface, is clearly shown in Fig. 8. At a Reynolds number of 10,000, as the rotation number increases, it is seen that the effect of rotation becomes stronger than the entrance effect. The leading surface exhibits degradation at smaller x/D_h values with increasing rotation number. This behavior has been observed in a square channel by Wagner et al. [13]. For example, at a rotation number of 0.34, degradation begins to occur at an x/D_h greater than 4.375. For a rotation number of 0.67, degradation occurs at $x/D_h=1.875$. However, at a Reynolds number of 20,000, near the entrance region, the entrance effect is larger than the rotation effect. The heat transfer enhancement for the rotating case is similar to the stationary case near the entrance. In the turn region, at a rotation number of 0.67, the Nu ratio reaches a maximum of 6.8, which is two to three times more than the stationary case. This is due to the effect of rotation.

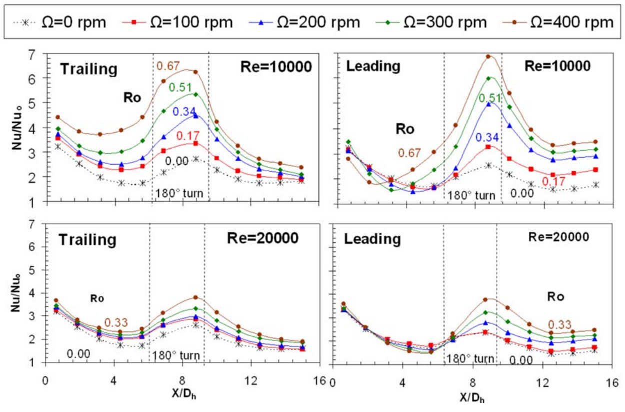

Fig. 8 Streamwise Nu ratio (Nu/Nu_0) distributions for different rotational speeds

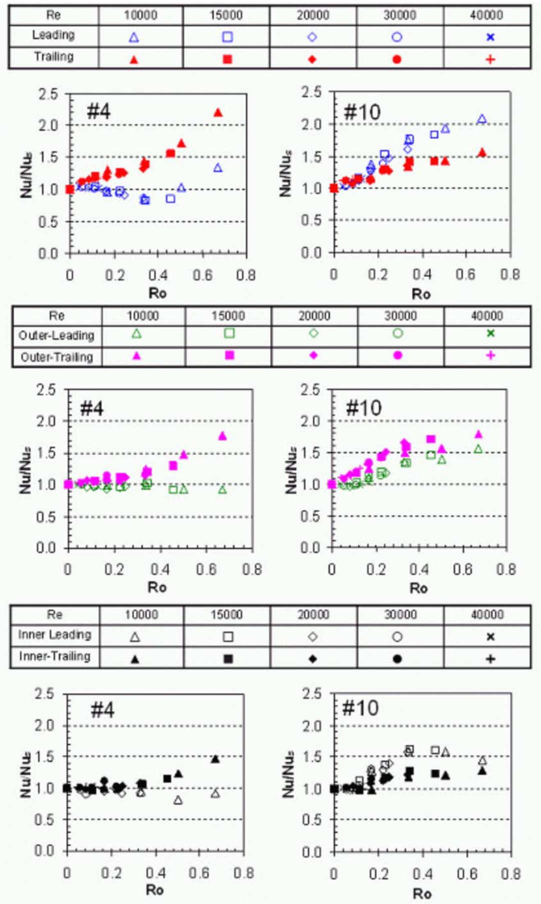

Fig. 9 Nu ratio (Nu/Nu_s) distribution with respect to the rotation number in Regions 4 and 10

Rotation Number Effects. The rotation number is a relative measure of the rotational Coriolis force and bulk flow inertia force [Han et al. [1]]. In the current study, the rotation number is varied by the Reynolds number and the rotational speed. The rotation number in this study varied from 0 to 0.67. The data presented here are based on the wall temperature of 65°C (the inlet density ratio=0.10). Figure 9 shows the effect of the rotation number on the Nu ratio (Nu/Nu_s) in the first passage at Region 4. The stationary Nusselt number is chosen as the denominator of the Nu ratio (Nu/Nu_s) so that the effect of rotation on heat transfer can be compared. In the first passage, the Coriolis force pushes the core coolant toward the trailing surface. The Nu ratio increases on the trailing surface as the rotation number increases. On the leading surface, the Nu ratio decreases up to a rotation number of 0.3. The Nu ratio then increases with the rotation number up to Ro=0.67. The increase of the Nu ratio is due to the development of large-scale reverse flow cells (Wagner et al. [13]). However, in a square channel (AR=1:1), the heat transfer ratio continues to decrease until the rotation number is 0.2 at the downstream location in the first passage, as reported by Wagner et al. [13]. The Nu ratio on the inner/outer trailing surfaces also increases with increasing rotation number, as shown in Fig. 9. The heat transfer enhancement due to rotation in the inner and outer regions is smaller because of the orientation of the rotating channel. The effect of the rotation-induced secondary-flow pattern on these regions is weaker. The radially inward flow in the second passage reverses the direction of the Coriolis forces. Figure 9 also shows the effect of rotation on the Nu Ratio in Region 10. No significant difference in Nu ratios for the leading and trailing surfaces is observed when rotation number is smaller than 0.12. Afterwards, the leading surface Nu

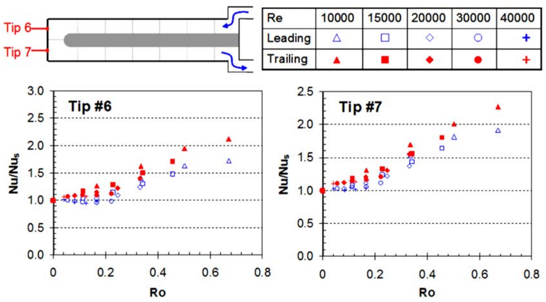

Fig. 10 Nu ratio $(\mathrm{Nu}/\mathrm{Nu}_s)$ with respect to the rotation number in the tip region

ratios are greater than the trailing. At Outer Region 10, it is interesting to note that the outer trailing surface has greater heat transfer than the outer leading surface. The Nu ratios at Inner Region 10 on the leading and trailing surfaces increase up to a rotation number of 0.33. Afterwards, the trailing surface Nu ratios remain level at approximately a Nu ratio of 1.2. The Nu ratio on the leading surface begins to decrease after a rotation number of 0.3.

The tip region is located at the end of the test section, where the 180 deg turn connects the first passage and the second passage (cf. Figs. 3 and 4). The incoming flow impinges on the tip region and creates the highest heat transfer throughout the entire channel. Impingement of the mainstream flow occurs on both Tip Regions 6 and 7, and enhances the heat transfer significantly in the tip region. The Nu ratio distribution with respect to the rotation number for the tip region is shown in Fig. 10. The rotation also enhances the heat transfer in the tip region. The heat transfer enhancement in this region is due to the combined effects of Coriolis force and the turn-induced secondary flow. The largest Nu ratio of 2.2 for Tip 6 occurs on the trailing surface at a rotation number of 0.67. At Tip 7, the largest Nu ratio of approximately 2.4 occurs at a rotation number of 0.67. The heat transfer on the trailing surface is higher than the leading surface in the tip region. Liou et al. [11] reported that as the rotation number increases, the magnitude of the secondary-flow velocity increases linearly and the magnitude of turbulence intensity level increases exponentially in the 180 deg turn region. This explains why the heat transfer ratio also enhances in the tip region.

Buoyancy Parameter Effects. The buoyancy parameter due to the centrifugal force and the temperature difference is important because of the high rotating speed and large temperature differences in the actual engines. For the radial outward flow, the rotation-induced buoyancy force aids the inertia force. This force opposes the inertia force in the second passage because the main flow direction is reversed. The buoyancy parameter, as defined by Wagner et al. [13], is used to present the combined effects of the Coriolis and buoyancy forces.

$$\mathrm{Ro}=\frac{\Omega D_h}{U_b} \tag{5}$$

The local buoyancy parameter can be rewritten by incorporating the measured wall and coolant temperatures, as shown in Eq. (7).

$$\mathrm{Bo}_x=\left(\frac{\Delta\rho}{\rho}\right)_x(\mathrm{Ro})^2\frac{R_x}{D_h} \tag{6}$$

$$\mathrm{Bo}_x=\frac{T_{w.x}-T_{b,x}}{T_{f,x}}(\mathrm{Ro})^2\frac{R_x}{D_h} \tag{7}$$

The local film temperature is the average of the local wall and the local coolant temperatures.

$$T_{f,x}=(T_{w,x}+T_{b,x})/2 \tag{8}$$

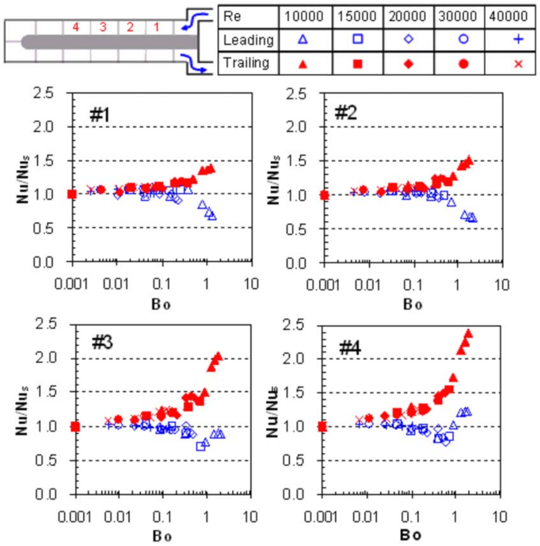

Fig. 11 Nu ratios $(\mathrm{Nu}/\mathrm{Nu}_s)$ with respect to buoyancy parameter from Regions 1 to 4

Five Reynolds numbers, each at four rotational speeds, are presented at corresponding buoyancy parameters. In addition to the inlet density ratio of 0.10, the results of two additional density ratios of 0.14 and 0.16 are also presented. The rotation buoyancy effects, on the Nu ratio $(\mathrm{Nu}/\mathrm{Nu}_s)$, caused by the radially outward flow in the first passage, are shown in Fig. 11. In the first passage, the Nu ratio on the trailing surface increases with an increase of the buoyancy parameter. In Region 1, the entrance effects dominate over the rotation effects and the Nu ratios are close to 1.1. The Nu ratio on the leading surface continues to decrease in Regions 1 and 2 because of the turbulence decay near the wall. However, the large-scale development of the recirculation flow will enhance the heat transfer at high buoyancy parameters. Therefore, Regions 3 and 4 show that the Nu ratio on the leading surface decreases, and then increases with an increase of the buoyancy parameter. The recirculation flow starts to develop near a buoyancy parameter of 0.8 in Regions 3 and 4. Fu et al. [8] showed a similar trend but at a buoyancy parameter of 0.08. The recirculation effect enhances the heat transfer ratio on the leading surface above that of the stationary case in Region 4. The heat transfer ratio is about 2.2 times higher than the stationary case at a buoyancy parameter of 2.0 in Region 4. The Nu ratio difference between the leading surface and trailing surface is small until the buoyancy parameter is larger than 0.3 in Region 1. However, the Nu ratio difference between the leading surface and trailing surface becomes larger when the buoyancy parameter is larger than 0.01 in Region 4. It also shows that the entrance effect decreases along the streamwise direction.

Figure 12 shows the effect of the buoyancy parameter on the Nu ratio $(\mathrm{Nu}/\mathrm{Nu}_s)$ in the regions near the 180 deg turn in the test section. In Region 5, the heat transfer ratio on the leading surface decreases slightly up to a buoyancy parameter of 0.3, where then it begins to increase. In Region 6, the heat transfer increases as the buoyancy parameter increases on both the leading and trailing surfaces. The heat transfer enhancement on the trailing surface in Region 6 is about 2.7 times greater than the stationary case. The trailing surface experiences higher heat transfer augmentation than the leading surface at the other regions in the first passage. At Tips 6 and 7, the radially outward flow directly impinges on the surface. In this region, the heat transfer is considerably higher than any other surfaces in the test section. However, the heat transfer ratio is smaller when compared to Regions 6 and 7. This shows that the rotation effect is smaller due to the flow impingement. The heat transfer increases when the buoyancy parameter

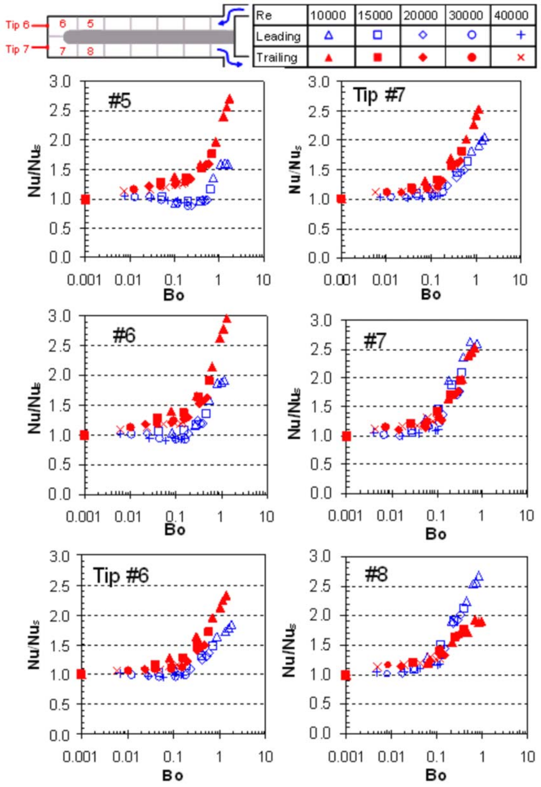

Fig. 12 Nu ratios (Nu/Nu_s) against buoyancy parameter from Regions 5 to 8

increases. At low buoyancy parameters, the strong turbulence mixing near the turn dominates over the rotation effects. The heat transfer ratio in the tip region is slightly greater on the trailing surface than the leading surface. Regions 7 and 8 are strongly affected by the turn-induced secondary flow and the radially inward flow in the second passage. The Nu ratio is slightly higher on the leading surface than the trailing surface for both Regions 7 and 8 at higher buoyancy parameters. Figure 13 shows the effect of the buoyancy parameter on the Nu ratio in Regions 9–12 in the second passage. In the second passage, the combination of the rotation-induced buoyancy force, the inertia force, and the Coriolis force serves to show the effects of rotation. In these four regions, radially inward flow moves the core coolant toward the leading surface. Therefore, higher Nu ratios are observed on the leading surface when compared to the trailing surface. Heat transfer increases with the buoyancy parameter on both the leading and trailing surfaces. Close to the exit of the channel, the effects of the 180 deg turn are reduced. The difference in heat transfer ratios between the leading and trailing surfaces increases in the streamwise direction.

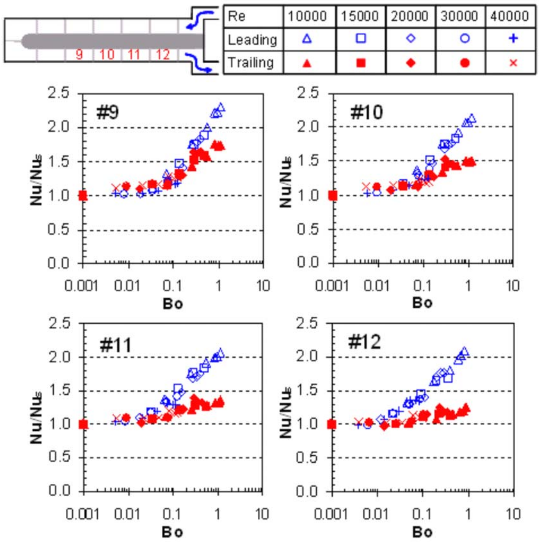

Fig. 13 Nu ratios (Nu/Nu_s) with buoyancy parameter from Regions 9 to 12

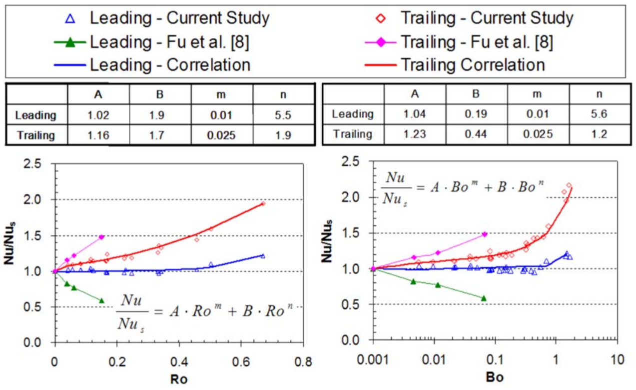

Fig. 14 Average Nu ratios (Nu/Nu_s) (six points) in the first pass

Average Heat Transfer Ratio. The average Nu ratios (Nu/Nu_s) in the first passage are presented in Fig. 14. The results are based on the six copper plates on the leading surface and the six copper plates on the trailing surface. Results from the current study show a smaller enhancement on the trailing surface and smaller degradation on the leading surface than that of the fully developed flow. The data from Fu et al. [8] are with an unheated entrance length to provide a hydrodynamically fully developed flow condition. The effect of rotation in the current study is greatly reduced because of the entrance geometry with redirected sharp bend in the first passage. The two sets of data show similar trends and the heat transfer ratio on the trailing surface is higher than the leading surface. The average Nu ratio on the trailing surface from Fu et al. [8] and the current study increases with the rotation number and buoyancy parameter. For the current study, the maximum average Nu ratio of 1.95 occurs at a rotation number of 0.67 and buoyancy parameter of approximately 1.2 on the trailing surface in the first passage. The Nu ratio is correlated to both the rotation number and buoyancy parameter with a power-law function. The experimental Nu ratio results are within $\pm 10\%$ of the correlation curve for both the rotation number and buoyancy parameter.

In Fig. 15, the average Nu ratio for the second passage is presented. The average Nu ratios on both the leading and trailing surfaces increase with the rotation number and the buoyancy parameter. The results of the current study and those of Fu et al. [8] in the second passage have similar trends and levels because both of them have the same 180 deg sharp turn. The experimental results can be correlated by a power-law function and the discrepancy is about $\pm 12\%$. The buoyancy parameter effect on heat transfer in the second passage is strongly affected by the 180 deg turn geometry. The average heat transfer ratios on the leading and trailing surfaces increase with the rotation number as well as the buoyancy parameter. The maximum Nu ratio of 2.3 occurs at a rotation number of 0.67 and buoyancy parameter 1.0 on the leading surface in the second passage. The above results show that the rotation number can be used to correlate the data from different rotational speeds and Reynolds numbers. The buoyancy parameter

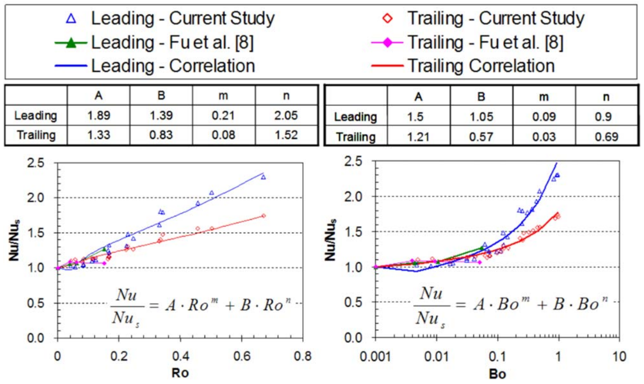

	A	B	m	n
Leading	1.89	1.39	0.21	2.05
Trailing	1.33	0.83	0.08	1.52

	A	B	m	n
Leading	1.5	1.05	0.09	0.9
Trailing	1.21	0.57	0.03	0.69

Fig. 15 Average Nu ratios ($\mathrm{Nu}/\mathrm{Nu}_s$) (six points) in the second pass

is capable of quantifying the effects of rotation even with the contribution from different density ratios, rotational speeds, and Reynolds numbers.

Conclusions

This study further increases the understanding of the effects of the entrance geometry and rotation on heat transfer in a two-pass rectangular (AR=1:4) rotating channel. The range of the rotation number and buoyancy parameter was extended to values above those in current open literature sources. The rotation and buoyancy parameters in this study reached 0.67 and 2.0, respectively. Previous studies only reported results for the leading and trailing walls of the flow channel, and this study has provided new insight to the heat transfer behavior in the tip region of the flow channel. Listed below are the important findings from the research work performed.

1. The rotation effect on heat transfer on the leading and trailing surfaces in the first passage is dramatically reduced by the redirected sharp-bend entrance. As the rotation number increases, the rotation effect begins to dominate over the entrance effect in the first passage. The effect of the entrance geometry is diminished in the second passage due to the strong 180 deg turn effect.
2. Heat transfer increases on the trailing surface in the first passage as the rotation number increases. On the leading surface, in the first passage (x/D_h of 4.375), the heat transfer initially decreases but begins to increase when the rotation number reaches a critical value of 0.3. This phenomenon is due to the formation of large-scale rotating buoyancy generated reverse flow cells.
3. The increased range of the buoyancy parameter and rotation number, reached in this study, can be used to predict the heat transfer enhancement from different rotational speeds, Reynolds numbers, and density ratios.
4. The tip region experiences the highest heat transfer ratio over the entire channel because of the direct impingement of the main flow, 180 deg sharp turn-induced secondary flow, and rotation. Rotation increases the heat transfer ($\mathrm{Nu}/\mathrm{Nu}_s$) by 2–2.5 times in the tip portion. The largest Nu ratio ($\mathrm{Nu}/\mathrm{Nu}_0$) observed was between 6.0 and 8.0 in the tip region.
5. As the rotation number increases, the heat transfer increases on both the leading and trailing surfaces in the second passage. This trend is different from both the square (AR=1:1) and AR=1:2 channels. The difference is attributed to the geometrical effects of the 1:4 aspect ratio channel with 180 deg sharp turn on the Coriolis-induced secondary flow in the second passage.

Acknowledgment

This work has been funded through the Marcus Easterling Endowment Fund.

Nomenclature

A = projected surface area of a copper plate segment
A_h = total heater surface area
AR = channel aspect ratio, $W:H$
Bo_x = local buoyancy parameter, $(\Delta\rho/\rho)_x \mathrm{Ro}^2 (R_x/D_h)$
D_h = channel hydraulic diameter
H = channel height
h = regionally averaged heat transfer coefficient
I = current
k = thermal conductivity of the coolant
L = length of the heated portion of the test section
Nu = regionally averaged Nusselt number
Nu_0 = Nusselt number for fully developed turbulent flow in nonrotating smooth pipe
Nu_s = regionally averaged Nusselt number under stationary condition
Pr = Prandtl number of the coolant
Q_{net} = net heat transfer
Q_{loss} = external heat loss
R = mean radius of rotation
R_x = local radius of rotation
Re = Reynolds number
Ro = rotation number, $\Omega D_h/U_b$
$T_{w,x}$ = regionally averaged wall temperature
$T_{b,x}$ = local coolant bulk temperature
$T_{f,x}$ = local film temperature
U_b = bulk velocity in streamwise direction
V = voltage
W = channel width
β = angle of channel orientation with respect to the axis of rotation
μ = viscosity of the coolant
ρ = density of the coolant
$(\Delta\rho/\rho)_{\mathrm{in}}$ = inlet coolant-to-wall density ratio, $(T_w - T_{bi})/T_w$
$(\Delta\rho/\rho)_x$ = local coolant-to-wall density ratio
Ω = rotational speed

References

[1] Han, J. C., Dutta, S., and Ekkad, S. V., 2000, *Gas Turbine Heat Transfer and Cooling Technology*, Taylor and Francis, New York.
[2] Han, J. C., 1984, "Heat Transfer and Friction in Channels With Two Opposite Rib-Roughened Walls," ASME J. Heat Transfer, **106**, pp. 774–781.
[3] Han, J. C., 1988, "Heat Transfer and Friction Characteristics in Rectangular Channels With Rib Turbulators," ASME J. Heat Transfer, **110**, pp. 321–328.
[4] Park, J. S., Han, J. C., Huang, Y., and Ou, S., 1992, "Heat Transfer Performance Comparisons of Five Different Rectangular Channels With Parallel Angled Ribs," Int. J. Heat Mass Transfer, **35**(11), pp. 2891–2903.
[5] Guidez, J., 1989, "Study of the Convective Heat Transfer in a Rotating Coolant Channel," ASME J. Turbomach., **111**, pp. 43–50.
[6] Agarwal, P., Acharya, S., and Nikitopoulos, D. E., 2003, "Heat/Mass Transfer in 1:4 Rectangular Passages With Rotation," ASME Paper No. GT 2003-38615.
[7] Fu, W. L., Wright, L. M., and Han, J. C., 2004, "Heat Transfer in Two-Pass Rotating Rectangular Channels (AR=1:2 and AR=1:4) With 45° Angled Rib Turbulators," ASME Paper No. GT 2004-53261.
[8] Fu, W. L., Wright, L. M., and Han, J. C., 2005, "Buoyancy Effects on Heat Transfer in Five Different Aspect-Ratio Rectangular Channels With Smooth Walls and 45-Degree Ribbed Walls," ASME Paper No. GT 2005-68493.
[9] Su, G., Chen, H. C., Han, J. C., and Heidmann, D., 2004, "Computation of Flow and Heat Transfer in Two-Pass Rotating Rectangular Channels (AR=1:1, AR=1:2, AR=1:4) With 45-Deg Angled Ribs by a Reynolds Stress Turbulence Model," ASME Paper No. GT 2004-53662.
[10] Liou, T.-M., and Chen, C. C., 1999, "Heat Transfer in a Rotating Two-Pass Smooth Passage With a 180° Turn," Int. J. Heat Mass Transfer, **42**, pp. 231–247.

[11] Liou, T. M., Chen, C. C., and Chen, M. Y., 2003, “Rotating Effect on Fluid Flow in Two Smooth Ducts Connected by a 180-Degree Bend,” J. Fluids Eng., **125**, pp. 138–148.

[12] Wright, L. M., Fu, W. L., and Han, J. C., 2005, “Influence of Entrance Geometry on Heat Transfer in Rotating Rectangular Cooling Channels (AR=4:1) With Angled Ribs,” J. Heat Transfer, **127**, pp. 378–387.

[13] Wagner, J. H., Johnson, B. V., and Hajek, T. J., 1991, “Heat Transfer in Rotating Passage with Smooth Walls and Radial Outward Flow,” ASME J. Turbomach., **113**, pp. 42–51.

[14] Wagner, J. H., Johnson, B. V., and Kopper, F. C., 1991, “Heat Transfer in Rotating Serpentine Passages With Smooth Walls,” ASME J. Turbomach., **113**, pp. 321–330.

[15] Zhou, F., Lagrone, J., and Acharya, S., 2004, “Internal Cooling in 4:1 AR Passages at High Rotation Numbers,” ASME Paper No. GT 2004-53501.

[16] Kays, W., Crawford, M., and Weigand, B., 2005, *Convective Heat and Mass Transfer*, McGraw Hill, New York.

[17] Kline, S. J., and McClintock, F. A., 1953, “Describing Uncertainty in Single-Sample Experiments,” Mech. Eng. (Am. Soc. Mech. Eng.), **75**, pp. 3–8.

Ashis K. Mazumder
Department of Applied Mechanics and Drawing,
Bengal Engineering and Science University,
Shibpur, Howrah 711 103,
West Bengal, India
e-mail: ashis.mazumadar@rediffmail.com

Sujoy K. Saha[1]
Mechanical Engineering Department,
Bengal Engineering and Science University,
Shibpur, Howrah 711 103,
West Bengal, India
e-mail: sujoy_k_saha@hotmail.com

Enhancement of Thermohydraulic Performance of Turbulent Flow in Rectangular and Square Ribbed Ducts With Twisted-Tape Inserts

The thermohydraulic performance of turbulent flow of air through rectangular and square ribbed ducts with twisted-tape inserts has been experimentally studied. The performance is influenced by the twisted-tape-generated swirl flow and the boundary layer separation, reattachment, and flow recirculation due to the ribs. Correlations developed for friction factor and Nusselt number satisfactorily predict the experimental data. The performance of the ribbed ducts with full-length twisted-tape inserts is found to be better than only ribbed ducts and ducts with only twisted-tape inserts. The regularly spaced twisted-tape elements in specific cases significantly perform better than their full-length counterparts. However, the short-length twisted-tape performance is worse than the full-length twisted tapes. [DOI: 10.1115/1.2909611]

Keywords: forced convection, turbulent flow, twisted-tape, transverse ribs, heat transfer augmentation, uniform wall heat flux

Introduction

References [1–12] give information on friction and heat transfer in channels having ribs. Han [9] identified that the heat transfer performance in a stationary ribbed channel primarily depends on the channel aspect ratio, the rib configuration, and the flow Reynolds number.

Webb et al. [13] studied the repeated rib heat transfer in circular cross-sectioned tubes. Taslim et al. [14] studied the coolant channel shapes that are relevant for the leading edge of an airfoil. Ekkad and Han [15] used a transient liquid crystal technique to measure the detailed heat transfer coefficient profile in a smooth, sharp 180 deg turn. Though there are several fundamental studies on rib turbulated surfaces, in Acharya et al. [16,17], the results related to turbine applications are addressed. Acharya et al. [18] reported detailed measurement of the velocity, temperature, and heat transfer in both developing and periodically developed regions of a ribbed duct. Ekkad and Han [19] studied different rib configurations in a two pass channel. Ekkad et al. [20] studied the detailed heat transfer coefficient distributions with different rib orientations in a two pass channel with film cooling bleed holes. More recent works on ribs [21–39] deal with rotation of the channel and the angled ribs.

Twisted tapes are useful for some turbulent duct flow applications [40–44]. Kieda et al. [45] investigated the single-phase water flow and heat transfer in a rectangular cross-sectioned twisted channel. Zhang et al. [46] used twisted-tape inserts and ribs in a circular tube. Later, Zhang et al. [47] used different types of inserts to study the combined rib and twisted-tape inserts in square ducts.

Figure 1(*a*) shows the layout of a duct containing a full-length twisted tape. Figure 1(*b*) shows the layout of a duct containing regularly spaced twisted-tape elements.

It is clear from the literature review that no results of systematic experimental study of heat transfer and pressure drop characteristics of turbulent flow through square and rectangular ribbed ducts with twisted-tape inserts are available.

The following major tasks have, therefore, been undertaken in the present investigation:

1. To study the heat transfer and pressure drop characteristics of the above mentioned flow situation.
2. To study the effects of twisted-tape length, space ratio, Reynolds number, rib heights, rib spacing, and duct aspect ratio on friction factor and Nusselt number.
3. To develop correlations for prediction of friction factor and Nusselt number.
4. To evaluate the performance of the combined use of transverse ribs and twisted tapes.

Figure 1(*c*) shows the duct cross section having ribs in opposite walls and twisted tapes centrally placed in the duct cross section. Twisted tapes are axially placed inside the duct. The objective of the present work is to see whether the ribs can be made useful for turbulent flow when they are used in combination with twisted tapes. Many heat exchangers use square and rectangular ducts.

Experimental Setup, Operating Procedure, and Data Reduction

Three (one square and two rectangular) channels for heat transfer measurements were constructed. Also three (one square and two rectangular) acrylic channels (for pressure drop measurements) of same dimensions as those of heat transfer channels were constructed. The square channel with $\mathrm{AR}=1$ had $13\times 13\ \mathrm{mm}^2$ cross section. Rectangular channels with $\mathrm{AR}=0.5$ and 0.333 had $13\times 26\ \mathrm{mm}^2$ and $13\times 39\ \mathrm{mm}^2$ cross sections, respectively. The hydraulic diameters of the channels were 13 mm, 17.33 mm, and 19.50 mm, respectively. An acrylic plenum was connected to the inlet of the test channel to provide uniform inlet velocity to the test channel by smooth bell-shaped transition. The sketch of the test channel and the associated plenum is shown in Fig. 2(*a*). The values of (*a*, *b*, and *l*) were (39 mm, 39 mm, 195 mm), (39 mm, 78 mm, 260 mm), and (78 mm, 117 mm, 487 mm) for $\mathrm{AR}=1$,

---

[1] Corresponding author.

Contributed by the Heat Transfer Division of ASME for publication in the JOURNAL IN HEAT TRANSFER. Manuscript received May 15, 2007; final manuscript received August 18, 2007; published online June 3, 2008. Review conducted by Anthony M. Jacobi.

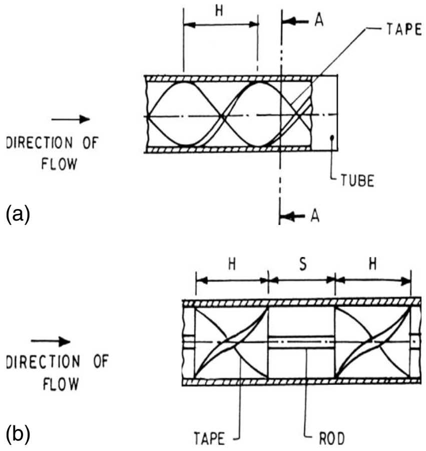

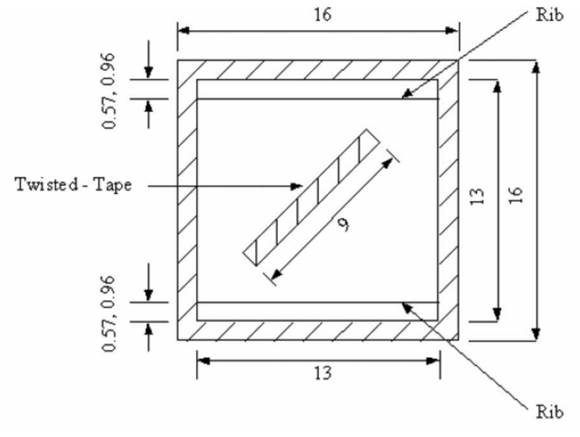

(i) AR = 1 - Square Duct

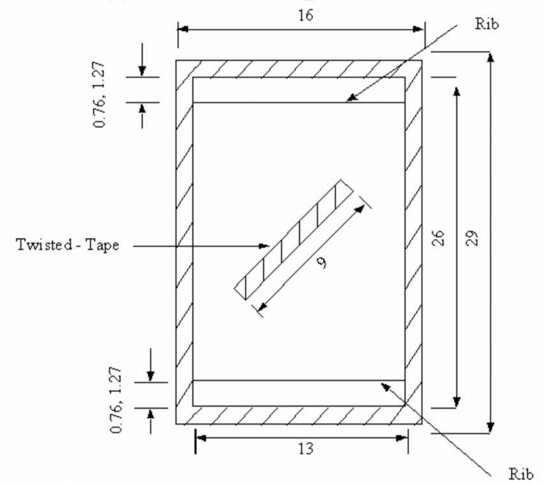

(ii) AR = 0.5 - Rectangular Duct I

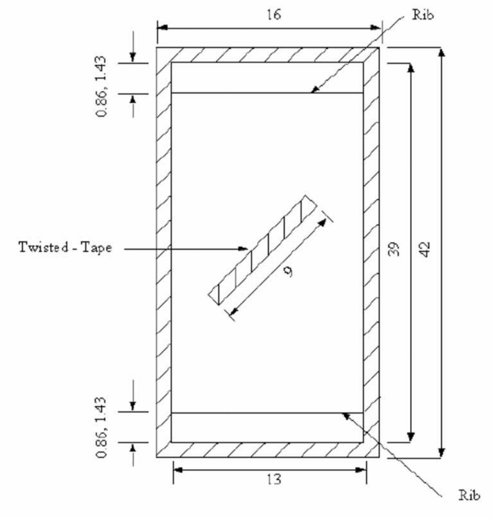

(iii) AR = 0.333 - Rectangular Duct II

ALL DIMENSIONS ARE IN MM (NOT TO SCALE)

(c)

Fig. 1 (***a***) **Layout of a duct containing a full-length twisted-tape; (*b*) layout of a duct containing regularly spaced twisted-tape elements; (*c*) duct cross sections showing rib and twisted-tape inside the ducts**

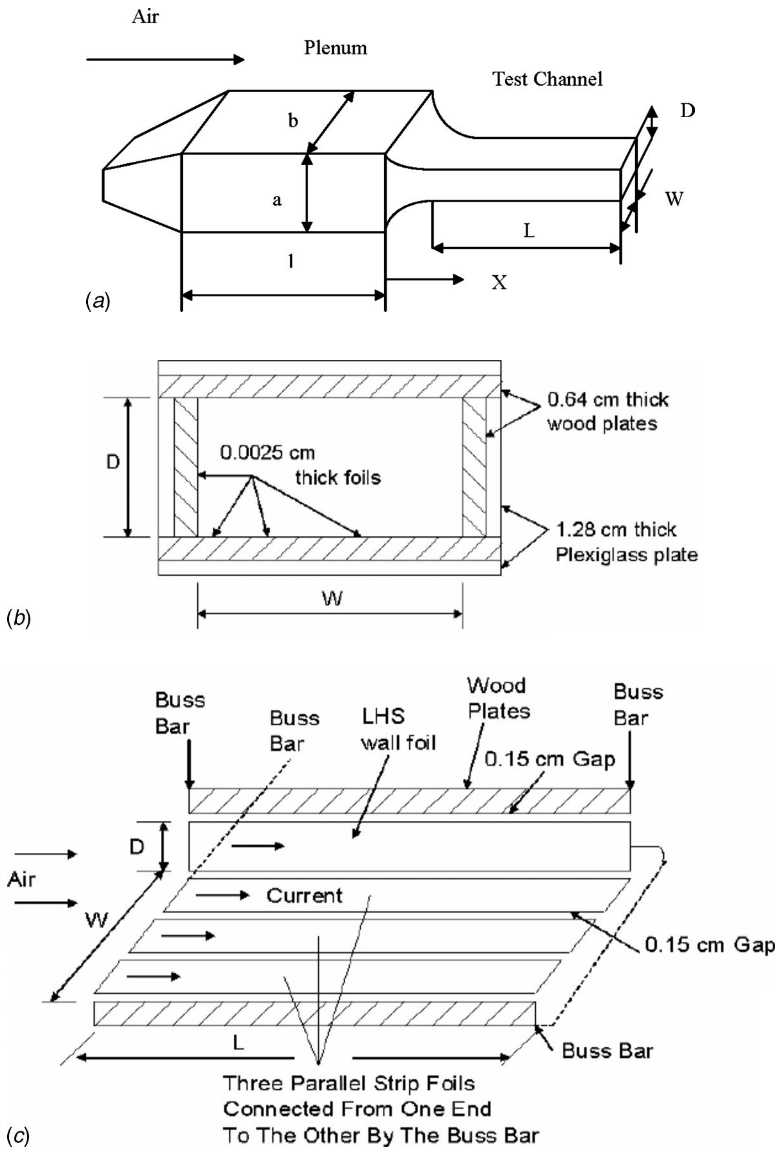

Fig. 2 (***a***) **Sketch of the test channels and plenums;** (***b***) **test channel cross section;** (***c***) **distributions of electrical foil heaters**

AR=0.5, and AR=0.333 ducts, respectively. For all cases of pressure drop as well as heat transfer measurements, *L* was 1275 mm.

Each wall of the heat transfer test channel was made of nonconductive material. The nonconductive wall was constructed by the combination of a 1.5 mm thick wood board and a 12.8 mm thick acrylic plate. Thin ceramic foils were placed on the inner side of the wood board surface for electrical and thermal insulation. Then 0.025 mm thick stainless steel foils were cemented to the inner face (ceramic surface) of each wall, individually controlled by a Variac transformer, for controllable electrical heating to the test channel. The cross section of the test channel and the distributions of electrical foil heaters are sketched in Figs. 2(*b*) and 2(*c*).

For ribbed channel heat transfer tests, transverse brass ribs with a square cross section were periodically fixed in line on the top and bottom walls of the foil heated channels in a required distribution. Brass ribs were not in electrical contact with the stainless steel foil heaters. Mica sheet insulation with adhesive was given to the rib surface in contact with the heater foils. Each heat transfer test channel had 28 (36 gauge copper Constantan) thermocouples, at seven axial locations and 4 thermocouples at each axial location (1 in the middle of each edge along the periphery). The axial positions of the thermocouples from the onset of heating along the downstream direction were 0.025 m, 0.225 m, 0.425 m, 0.625 m, 0.825 m, 1.025 m, and 1.225 m respectively. The thermocouples were connected to a 36 point selector switch box, which in turn was connected to a digital multimeter and a single cold junction at 0°C. The mass flow rate of air was calculated by measuring the pressure drops across the orifice meter. The power supplied to each heat transfer test channel was measured by digital voltmeter and ammeter. The inlet and outlet bulk fluid temperatures to the test sections were measured by thermocouples placed 5 cm upstream from the inlet and 20 cm downstream from the outlet of each test section.

In each pressure drop test channel with transverse acrylic ribs, 12 pressure taps along the top ribbed wall were used for the static pressure drop measurement. Pressure drops in the test channel were measured by using vertical U-tube water manometer. Air was forced through the test channel by a blower. The twisted tapes were made from (δ=0.37 mm) thick stainless steel strip. Pieces of stainless steel rods of ($d.D_h$=1.5 mm) diameter were used to make the tape rod assembly. Only one twisted tape was axially and centrally placed in the plane of the cross section in each duct and steel lugs kept the tapes in place.

In an experimental run, the blower was switched on and the heat input to the test section was set to the required value by adjusting the autotransformers. The air flow rate was controlled to the desired value. The air mass flow rate was calculated by noting the pressure drop across the orifice meter.

The bulk temperature of the fluid at any axial position at a distance z from the inlet was computed by assuming a linear temperature variation along the length. The duct inner wall temperatures were determined from the measured values of the outer wall temperature by applying the one dimensional heat conduction equation. There was only 3–5% of maximum wall temperature variation in peripheral outside wall temperature measured at four locations in an axial station. The circumferentially averaged inner wall temperature (T_{wi}) at any axial position was taken as the arithmetic mean of the inner wall temperatures at that axial position. The heat transfer coefficient (h) at any axial position was determined from the heat flux based on the inner surface area; the average inner wall temperature and the calculated fluid bulk mean temperature at that axial position. The local Nusselt numbers were axially averaged by trapezoidal rule. The properties of the fluid were evaluated at the mean bulk temperature.

The values of the parameters investigated were as follows:

(a) Mass flow rate, $\dot{m}=0.722-6.851$ kg/min
(b) Reynolds number, $\mathrm{Re}=11{,}543<\mathrm{Re}<108{,}166$
(c) Prandtl number, $\mathrm{Pr}=0.7$
(d) Heat flux, $q''=956-8923\ \mathrm{W/m^2}$
(e) $\Delta T_b=T_{\mathrm{bo}}-T_{\mathrm{bi}}=5.280-20.697\,^\circ\mathrm{C}$
(f) $\Delta T=T_{\mathrm{wi}}-T_b=72.265-145.587\,^\circ\mathrm{C}$

An uncertainty analysis as suggested by Kline and McClintock [48] showed that uncertainties involved in the estimation of friction factors were within +4% and those involved in the estimation of Nusselt number were within +7.5%. Detailed calculations of uncertainty analysis are shown in Ref. [49].

More information about this section can be obtained from Ref. [50].

Results and Discussion

Manner of Presentation of Results. The pressure drop results are presented in terms of f, where f is given by

$$f=\varphi(\mathrm{DP},\mathrm{RP},\mathrm{TTP},\mathrm{Re}) \tag{1}$$

and the heat transfer results are presented in terms of Nu, where Nu is given by

$$\mathrm{Nu}=\vartheta(\mathrm{DP},\mathrm{RP},\mathrm{TTP},\mathrm{Re},\mathrm{Pr},\mathrm{BC}) \tag{2}$$

where DP=duct parameter, RP=rib parameters, TTP=twisted-tape parameters, Re=Reynolds number, Pr=Prandtl number, and BC=thermal boundary condition imposed on the duct wall. The test section was subjected to uniform wall heat flux (UWHF) thermal boundary condition.

The short-length twisted-tape (TTP) results will be presented first and regularly spaced twisted-tape elements (TTP) results will follow. Different types of parameters will be referred to, as and when these are discussed.

Validation of the Experimental Setup. The present experimental setup was validated by carrying out pressure drop experiments in plain rectangular duct (DP) with aspect ratio AR=0.333 and comparing the present friction factor data with Blasius correlation ($f=0.079\,\mathrm{Re}^{-0.25}$) with the circular tube diameter replaced by the hydraulic diameter of the duct. The present experimental data was within +8.5% of the Blasius correlation. The experimental setup was further validated by carrying out heat transfer measurements in the rectangular duct (DP) (AR=0.333) with only transverse ribs and comparing the present Nusselt number data with those predicted by the correlation given in Ref. [9]. The present experimental data were within +10% of that predicted by the correlation given in Ref. [9].

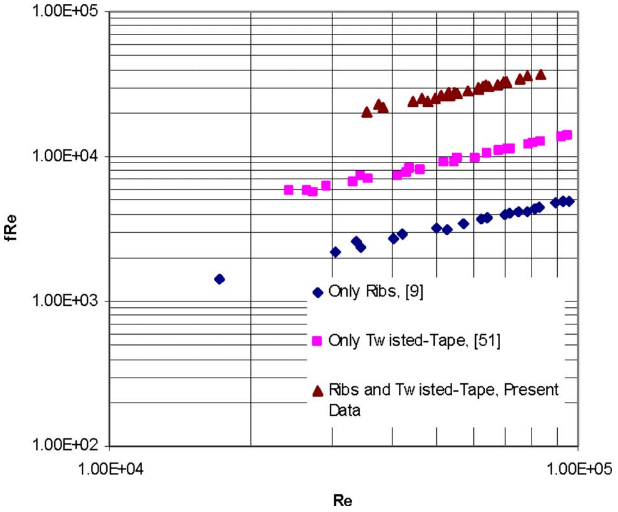

Fig. 3 Comparison of present friction factor data with other data, AR=0.333; only twisted tape (full-length twisted tape); only ribs, *e*/*D*$_h$=0.0735, *P*/*e*=10; ribs and short-length twisted tape; l=0.9, *e*/*D*$_h$=0.0735, *P*/*e*=10; for all cases, *Y*=2.5

Comparison of Present Data With Other Data. Figure 3 shows the present short-length twisted-tape (TTP) friction factor data and Figure 4 shows the present regularly spaced twisted-tape elements (TTP) friction factor data. These figures also show data for only twisted tapes [51] and for only transverse ribs [9]. Figures 5 and 6 show the corresponding Nusselt number data. Figures 3–6 show that the present duct configurations are having maximum pressure drop and heat transfer. This observation is particularly true for Re>50,000 in the case of heat transfer because of the flatter temperature profiles at higher Reynolds number. Only the ribs are having the lowest heat transfer and pressure drop and only the twisted tapes lie in-between in terms of heat transfer and pres-

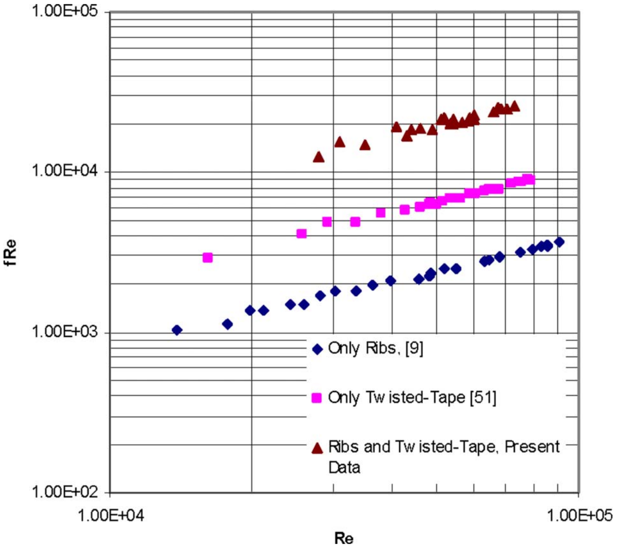

Fig. 4 Comparison of present friction factor data with other data, AR=0.333; only regularly spaced twisted-tape elements, *s*=2.5; only ribs, *e*/*D*$_h$=0.0735, *P*/*e*=10; ribs and regularly spaced twisted-tape elements; *s*=2.5, *e*/*D*$_h$=0.0735, *P*/*e*=10; for all cases, *Y*=2.5

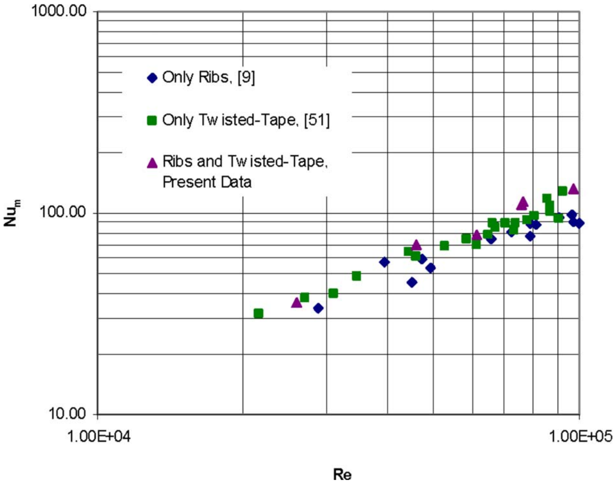

Fig. 5 Comparison of present Nusselt number data with other data, AR=0.333; only twisted tape (full-length twisted tape); only ribs, e/D_h=0.0735, P/e=10; ribs and short-length twisted tape; l=0.9, e/D_h=0.0735, P/e=10; for all cases, Y=2.5

sure drop. These results are expected since ribs affect only near-wall flow and they do not affect the main body of flow through the duct. Therefore, momentum and thermal energy diffusion are influenced by the ribs only in the near-wall region. However, twisted-tape-generated flow is the helical faster flow with rapid momentum and thermal energy diffusion. Combined twisted-tape and ribs cause additional momentum loss and thermal energy diffusion due to the inertia as well as boundary layer separation and reattachment and flow recirculation.

Short-Length Twisted-Tape (TTP) Results

Friction Factor Results. Only the isothermal friction factor data have been generated. Nonisothermal friction factor data can be derived using the well-known correction factor. Following the observation made in Ref. [51], twist ratio, y=2.5, only has been considered. Performance of the short-length twisted tape has been compared to the full-length twisted tape (TTP).

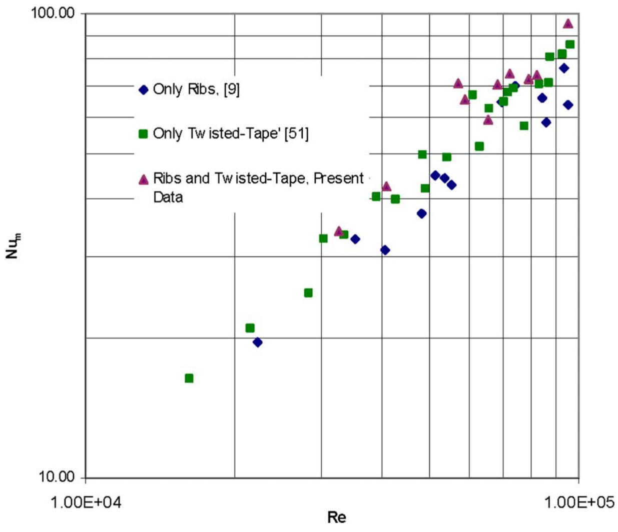

Fig. 6 Comparison of present Nusselt number data with other data, AR=0.333; only regularly spaced twisted-tape elements, s=2.5; only ribs, e/D_h=0.0735, P/e=10; ribs and regularly spaced twisted-tape elements; s=2.5, e/D_h=0.0735, P/e=10; for all cases, Y=2.5

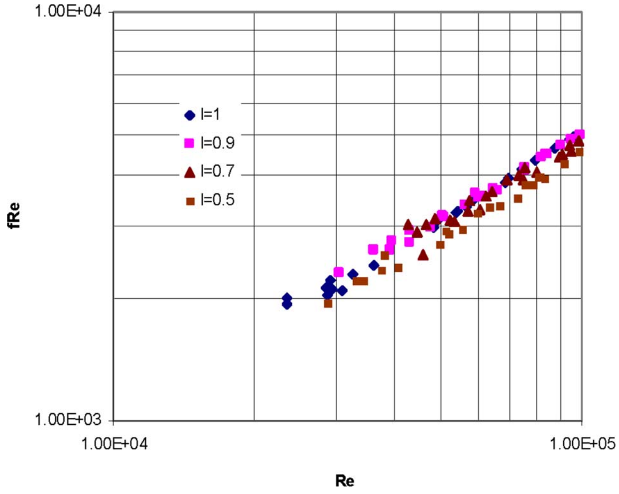

Fig. 7 Effect of twisted-tape length (TTP)—friction versus Reynolds number—AR=1, e/D_h=0.0441, P/e=10; for all cases, Y=2.5

Effect of Twisted-Tape Length (TTP). $l=1$ refers to the full-length twisted tape and $l<1$ is the short-length twisted tape. As shown in Fig. 7, the friction factor decreases as the twisted-tape length (TTP) decreases; this is particularly true for $l<0.9$. For $l=1$ and $l=0.9$, the results are not much different. However, Mazumder [50] has shown that twisted tapes with $l<0.5$ do not generate sufficient swirl effect in the flow. The reason of decreasing friction factor with decreasing l is the decrease in friction surface area and the early decay of the swirl; there is straight flow in the downstream. The swirl intensity created by the twisted tape is more important than the amount of tape surface area; this is the reason why the friction factor does not continue to monotonically decrease as the tape length continues to decrease beyond a certain point.

Effect of Duct Aspect Ratio (DP). Figure 8 shows the effect of aspect ratio (DP) of duct on friction factor. As the aspect ratio ($\leqslant 1$) decreases, the friction factor increases. This is because the lower the aspect ratio, the more the mixing of the more asymmetric velocity profiles and the secondary motion and loss of momentum.

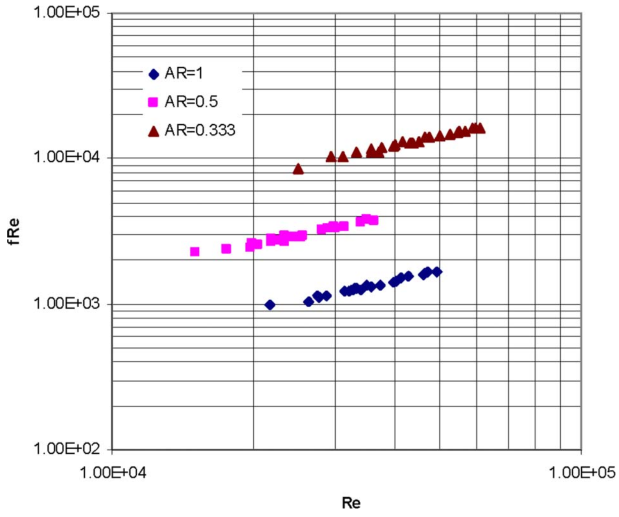

Fig. 8 Effect of duct aspect ratio (DP)—friction versus Reynolds number—l=0.7, e/D_h=0.0441, P/e=20; for all cases, Y=2.5

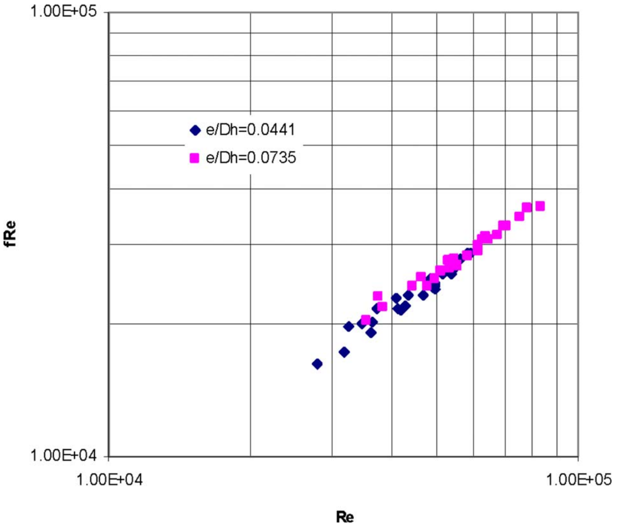

Fig. 9 Effect of rib height (RP)—friction versus Reynolds number—l=0.9, AR=0.333, $P/e=10$; for all cases, $Y=2.5$

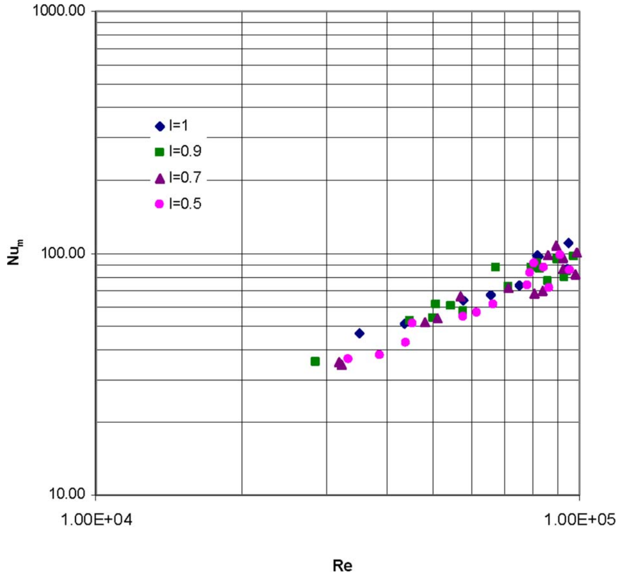

Fig. 11 Effect of twisted-tape length (TTP)—Nusselt number versus Reynolds number—AR=1, $e/D_h=0.0441$, $P/e=10$; for all cases, $Y=2.5$

Effect of Rib Heights (RP). Figure 9 shows that the friction factor increases with the increase of rib heights (RP). As the rib height increases, the asymmetric velocity profiles in the fluid mix locally more vigorously due to the stronger secondary flow and more recirculation. With higher blockage of the channel, pressure drop increases with no significant increase in heat transfer. The optimum value of (e/D_h) is somewhere between 0.05 and 0.15; although >10% blockage of the channel is not generally used.

Effect of Rib Spacing (RP). As the rib spacing (RP) increases, the friction factor decreases (Fig. 10); with the increased rib spacing, there is less number of occasions of boundary layer separation and reattachment on the wall. Also, for wider rib spacing, a thicker boundary layer is developed after flow reattachment between the ribs. However, for wider rib spacing, there will be poorer enhancement in heat transfer also due to the smaller contribution of the rib-top Nusselt number. On the other hand, with more ribs packed per unit surface area, there will be very high pressure drop due to the additional momentum loss. P/e is seldom <10 or >20; there is no exact optimum value, either.

Nusselt Number Results. Figures 11–14 show the effects of twisted-tape length (TTP), duct aspect ratio (DP), rib height (RP), and rib spacing (RP) on Nusselt number. In Fig. 11, $l=1$ refers to the full-length twisted tape and $l<1$ refers to short-length twisted tape. The thermal behavior is similar to the hydrodynamic behavior. However, the effect of duct aspect ratio (DP) is not as strong as it was in the case of pressure drop measurements, thus defying the Reynolds analogy. Here, the Prandtl analogy and Karman–Boelter–Martinelli analogy are applicable, turbulent and molecular transport being equally important. It is conjectured here that the duct aspect ratio (DP) does not have significant effect on thermal boundary layer thickness and the consequent convective thermal resistance.

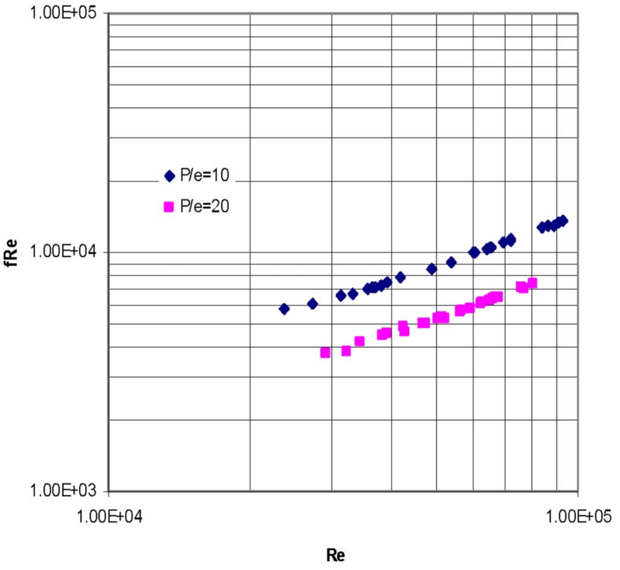

Fig. 10 Effect of rib pitch (RP)—friction versus Reynolds number—l=0.9, AR=0.5, $e/D_h=0.0441$; for all cases, $Y=2.5$

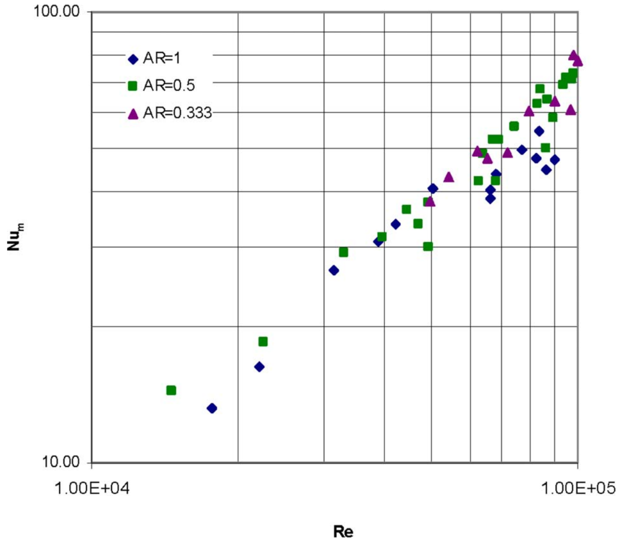

Fig. 12 Effect of duct aspect ratio (DP)—Nusselt number versus Reynolds number—l=0.7, $e/D_h=0.0441$, $P/e=20$; for all cases, $Y=2.5$

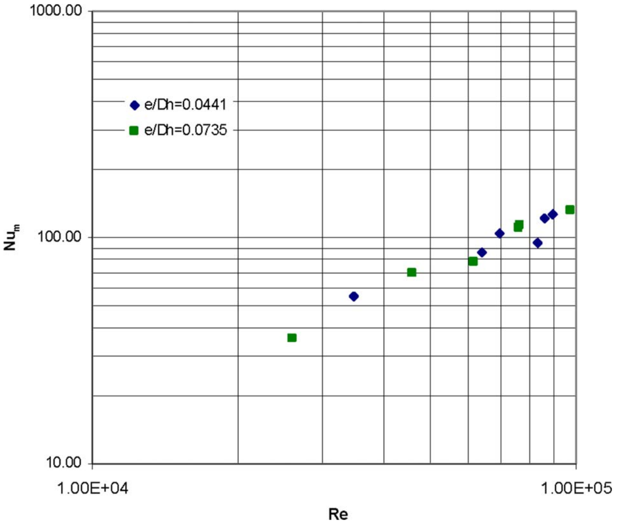

Fig. 13 Effect of rib height (RP)—Nusselt number versus Reynolds number—l=0.9, AR=0.333, *P*/*e*=10; for all cases, *Y*=2.5

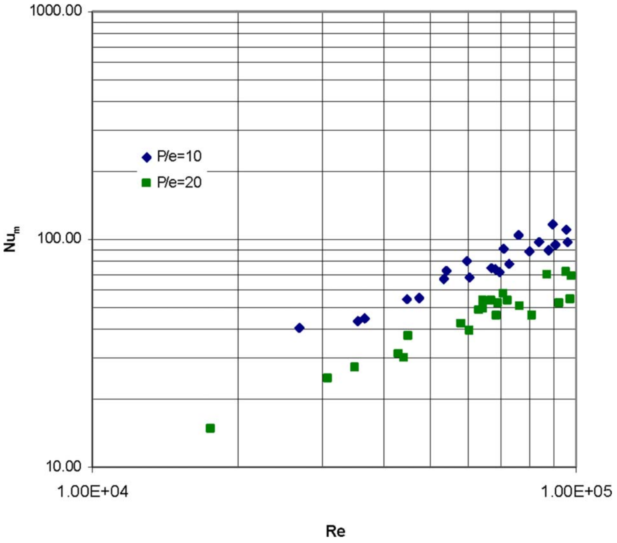

Fig. 14 Effect of rib pitch (RP)—Nusselt number versus Reynolds number—l=0.9, AR=0.5, *e*/*D$_h$*=0.0441; for all cases, *Y*=2.5

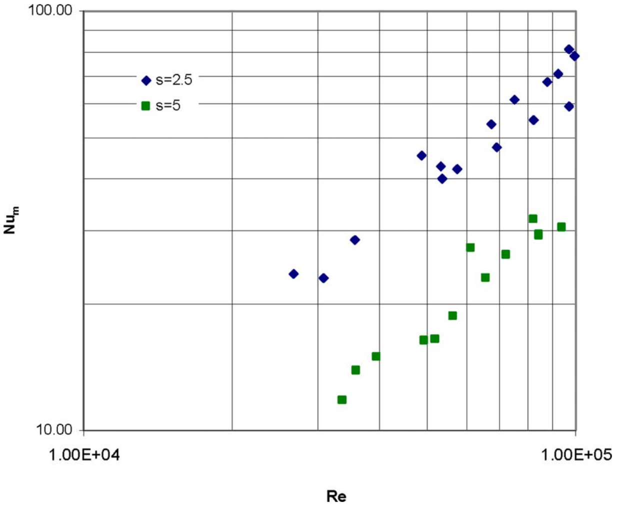

Fig. 15 Effect of space ratio (TTP)—friction versus Reynolds number—AR=1, *e*/*D$_h$*=0.0441, *P*/*e*=10; for all cases, *Y*=2.5

Regularly Spaced Twisted-Tape Element Results

Friction Factor Results

Effect of space ratio, s (TTP). Figure 15 shows that the friction factor increases as *s* decreases since there is more frequent mixing and momentum loss. Also, small *s* means more number of twisted-tape elements and more friction surface and attendant pressure loss.

Effect of duct aspect ratio (DP), rib height (RP), and rib spacing (RP). The behavior of the regularly spaced twisted-tape elements is similar to the behavior of short-length twisted tapes.

It is generally true in all friction factor results that the boundary layer separates at the ribs and reattaches further downstream; there is also recirculation and associated momentum loss increasing pressure drop due to the fluid mixing.

Nusselt Number Results. All observations for heat transfer measurement are similar to those for pressure drop measurements.

The buoyancy effect in the plain duct portion in the case of short-length twisted tape and in the annular space region in the case of regularly spaced twisted tape elements has been reflected in the Nusselt number correlations. The swirl flow inertia forces were persistent in the twisted-tape region.

Effect of Compressibility of Air. Aerodynamic heating of the thermal boundary layer is manifested in the dissipation of heat due to the viscous stress related shear work causing adiabatic temperature rise $T_{\mathrm{ad,r}}$ of air given by

$$T_{\mathrm{ad,r}} = R_f \times \mathrm{Vel} \times \mathrm{Vel} \times 0.5C_p^{-1}$$

where R_f is the recovery factor and $R_f = \mathrm{Pr}^{0.3333}$, for turbulent flow.

In the present investigation, the maximum temperature of air was limited to 40°C; the maximum air velocity was 123 m/s and maximum $T_{\mathrm{ad,r}}$ was likely to be 6.68°C.

For this compressibility effect of air, the Nu values presented in the figures could be 1–3% higher. However, the performance ratios R_1 and R_2 calculated considering this compressibility effect of air did not give any qualitatively different result and the conclusions drawn in this investigation are correct.

Correlations and Performance Evaluation

Correlations. All the correlations have been developed by log-linear regression analysis. The correlation of friction factor for internal rib turbulators with short-length twisted tapes has been found to be

$$f\,\mathrm{Re} = K\left(1 + 10^{-6}\left(\left(\frac{\mathrm{Re}^2}{y}\right)\left(\frac{\pi}{\pi - \left(\frac{4\delta}{D_h}\right)}\right) \times \left(1 + \left(\frac{\pi}{2y}\right)^2\right)^{0.5}\right)^{2.67}\right)^{1/7} \frac{\left(\frac{e}{D_h}\right)^{0.0343} l^{0.178}}{\left(\frac{P}{e}\right)^{0.739} (\mathrm{AR})^{1.52}} \qquad (3)$$

where

$$K = 17.355\frac{\left(\pi + 2 - 2\left(\frac{\delta}{D_h}\right)\right)^2}{\left(\frac{\pi}{\pi - 4\left(\frac{\delta}{D_h}\right)}\right)}\left(1 + \left(\frac{\pi}{2y}\right)^2\right) \qquad (4)$$

The correlation of friction factor for internal rib turbulators with regularly spaced twisted-tape elements has been found to be

$$(f\,\mathrm{Re})_{\mathrm{Sw}} = K\left(1 + 10^{-6}\left(\left(\frac{\mathrm{Re}^2}{y}\right)\left(\frac{\pi}{\pi - \left(\frac{4\delta}{D_h}\right)}\right)\times\left(1+\left(\frac{\pi}{2y}\right)^2\right)^{0.5}\right)^{2.67}\right)^{1/7}\frac{\left(\frac{e}{D_h}\right)^{0.135}\frac{d^{0.108}}{s^{1.075}}}{\left(\frac{P}{e}\right)^{0.157}(\mathrm{AR})^{1.49}} \quad (5)$$

where K is as above in Eq. (4). The correlation of Nusselt number for internal rib turbulators with short-length twisted tapes has been found to be

$$\mathrm{Nu} = 0.023(\text{Term 1} + \text{Term 2})\left(\frac{1}{\mathrm{AR}} + 0.1\right)^{0.15}\times\frac{\left(\frac{e}{D_h}\right)^{0.0541} l^{0.182}}{\left(\frac{P}{e}\right)^{0.754}}, \quad \mathrm{AR} \leqslant 1 \quad (6)$$

where Term 1 and Term 2 given below refer to the forced and free convections, respectively.

$$\text{Term 1} = 1.1978\mathrm{Pr}^{0.4}\left[\frac{(4y^2+\pi^2)^{0.25}\left(\pi - 4\left(\frac{\delta}{D_h}\right)\right)^{0.5}\left(\left(\frac{\mathrm{Re}^2}{y}\right)\left(\frac{\pi}{\pi-4\left(\frac{\delta}{D_h}\right)}\right)\left(1+\left(\frac{\pi}{2y}\right)^2\right)^{0.5}\right)^{0.5} y^2}{\left(\pi + 2 - 2\left(\frac{\delta}{D_h}\right)\right)}\right]^{0.8} \quad (7)$$

and

$$\text{Term 2} = 0.5044\mathrm{Pr}^{0.33}\left[\Delta T_w\beta\frac{\left(\pi - 4\left(\frac{\delta}{D_h}\right)\right)\left(\frac{\mathrm{Re}^2}{y}\right)\left(\frac{\pi}{\pi - 4\frac{\delta}{D_h}}\right)\left(1+\left(\frac{\pi}{2y}\right)^2\right)^{0.5}}{\left(\pi+2-2\left(\frac{\delta}{D_h}\right)\right)(4y^2+\pi^2)^{0.5}}\right]^{0.33}, \quad \Delta T_w = T_{\mathrm{wi}} - T_b \quad (8)$$

The correlation of Nusselt number for internal rib turbulators with regularly spaced twisted-tape elements has been found to be

$$\mathrm{Nu} = 0.023(\text{Term 1} + \text{Term 2})\times\left(\frac{1}{\mathrm{AR}} + 0.1\right)^{0.15}\frac{\left(\frac{e}{D_h}\right)^{0.1561}\frac{d^{0.122}}{s^{1.129}}}{\left(\frac{P}{e}\right)^{0.136}}, \quad \mathrm{AR} \leqslant 1 \quad (9)$$

where Term 1 and Term 2 are as above in Eqs. (7) and (8), respectively. f and Nu are strong functions of P/e for short-length twisted tape since the swirl is weak and decaying in the downstream past the twisted tape and the fluid strongly experiences the effect of ribs. Whereas, for the regularly spaced twisted-tape elements, the swirl is very strong throughout the test duct and as such the effect of ribs on the flow is weak. Exponential coefficient for d was suggested in Ref. [52].

All correlations predict the experimental data within +17%.

Performance Evaluation. The performance of the present geometry has been evaluated on the basis of the following two important criteria:

- Criterion 1. Basic geometry fixed, pumping power fixed—increase heat transfer—Performance ratio R_1
- Criterion 2. Basic geometry fixed, heat duty fixed—reduce pumping power—Performance ratio R_2

$$R_1 = \frac{\mathrm{Nu}_{\mathrm{slt,rst}}}{\mathrm{Nu}_{\mathrm{flt}}}$$

$\mathrm{Nu}_{\mathrm{slt,rst}}$ at a given Re, $\mathrm{Re}_{\mathrm{slt,rst}}$ is obtained from the correlation for short-length twisted-tape or regularly spaced twisted-tape elements. $\mathrm{Nu}_{\mathrm{flt}}$ for full-length twisted-tape is taken at the Re, $\mathrm{Re}_{\mathrm{flt}}$, where $\mathrm{Re}_{\mathrm{flt}}$ is calculated from the constant pumping power consideration as

$$\mathrm{Re}_{\mathrm{flt}} = \left[\left(\frac{f_{\mathrm{slt,rst}}}{f_{\mathrm{flt}}}\right)\left(\frac{A_{o,\mathrm{slt,rst}}}{A_{o,\mathrm{flt}}}\right)\mathrm{Re}^3_{\mathrm{slt,rst}}\right]^{1/3}$$

where

$$A_{o,\mathrm{slt}} = l(WD - \delta D_h) + (1-l)WD$$

(neglecting rib cross section area)

$$A_{o,\mathrm{rst}} = \left((WD - \delta D_h)y + \left(WD - \frac{\pi d^2}{4}\right)s\right) \Big/ (y+s)$$

×(neglecting rib cross section area)

$$A_{o,\mathrm{flt}} = WD - \delta D_h$$

$$R_2 = \frac{(f\,\mathrm{Re}^3 A_o)_{\mathrm{slt,rst}}}{(f\,\mathrm{Re}^3 A_o)_{\mathrm{flt}}}$$

For a given Re, $\mathrm{Re}_{\mathrm{slt,rst}}$, the $\mathrm{Nu}_{\mathrm{slt,rst}}$ is obtained from the correlation. $\mathrm{Re}_{\mathrm{flt}}$ corresponding to $\mathrm{Nu}_{\mathrm{slt,rst}}$ is obtained from the correlation for full-length twisted tape.

Based on these R_1 and R_2 criteria, full-length twisted tape in combination with transverse ribs performs better than the cases with only ribs and only full-length twisted tapes. From the performance ratio, it has been observed that short-length twisted tapes perform worse than their full-length counterparts and, therefore, these are not recommended.

The performance ratios R_1 and R_2 for regularly spaced twisted-tape elements have been evaluated for $s=2.5$ and $s=5.0$. Zhang et al. [46,47] have shown that both heat transfer and pressure drop are higher with the addition of ribs in the pipe fitted with full-length twisted tape. Present experimental data corroborate this.

However, it is observed that regularly spaced twisted-tape elements significantly perform better than their full-length counterparts for small as well as large transverse ribs with large spacing for closely spaced twisted-tape elements ($s \leqslant 2.5$) and these are recommended; there is an 11–31% increase in heat duty at constant pumping power and 12–45% reduction in pumping power at constant heat duty, the benefit being more as the duct becomes shallower with decrease in aspect ratio.

Conclusions

The heat transfer and pressure drop characteristics for turbulent flow through ribbed rectangular and square ducts having twisted-tape inserts have been experimentally investigated.

The present experimental data and the performance evaluation show that the full-length twisted-tape inserts in combination with transverse ribs in square and rectangular ducts, through which turbulent flow occurs under constant wall heat flux boundary condition, perform better than both the cases when twisted tapes and ribs act alone.

The most important finding of the present investigation is that regularly spaced twisted-tape elements significantly perform better than the full-length twisted tapes when they act in conjunction with transverse ribs for small as well as large transverse ribs with large spacing for closely spaced twisted-tape elements ($s \leqslant 2.5$).

However, the short-length twisted tapes perform worse than the full-length twisted tape. Correlations useful to designers have been developed. The buoyancy effect has been observed in the plain duct portion in the case of short-length twisted tape and in the annular space region in the case of regularly spaced twisted-tape elements. This has been taken care of in the Nusselt number correlations. The swirl flow inertia forces were persistent in the twisted-tape region.

Acknowledgment

The authors gratefully acknowledge the financial support given to this present research by Government of India through its funding agencies DST, CSIR, and AICTE, Ministry of Human Resource and Ministry of Science & Technology.

Nomenclature

A = heat transfer area, m^2
A_o = plain duct flow cross-sectional area, $=W.D$, m^2
AR = aspect ratio$=W/D$, dimensionless
C_p = constant pressure specific heat, J/kg K
CR = contraction ratio, dimensionless
D = depth of the duct cross section, m
D_h = hydraulic diameter of the test duct, $=4A_o/P$, m
d = nondimensional diameter of the rod connecting two successive tape elements
d^* = actual diameter of the rod$=d \cdot D_h$, m
e = rib height, m
f = fully developed Fanning friction factor$=(1/2) \times [\Delta P/(\rho V_0^2)](D_h/z)$, dimensionless
H = pitch for 180 deg rotation of twisted tape, m
h_z = axially local heat transfer coefficient, W$/($m^2 K$)$
k = fluid thermal conductivity, W/(m K)
L = axial length, length of the duct, m
L_T = length of twisted tape, m
l = nondimensional twisted-tape length$=L_T/L$, dimensionless
$\dot{m}$ = mass flow rate, kg/min
Nu$_m$ = axially averaged Nusselt number$=1/L\int_0^L h_z D_h dz/k$, dimensionless
ΔP = pressure drop, N$/$m^2
P = wetted perimeter in the particular cross section of the duct, rib spacing, m
Pr = fluid Prandtl number$=\mu C_p/k$, dimensionless
Re = Reynolds number based on plain duct diameter $=(\rho V_0 D_h)/\mu$, dimensionless
S = space between two successive tape elements, m
s = space ratio$=S/D_h$, dimensionless
T = temperature, K
ΔT_w = wall to fluid bulk temperature difference, K
V_o = mean velocity based on plain duct diameter $=\dot{m}/\rho A_0$, m/s
W = width of the duct, m
Y = twist ratio$=H/D_h$, dimensionless
z = axial length, the distance between the measuring pressure taps, m

Greek Symbols

α = rib angle of attack, deg
β = coefficient of isobaric thermal expansion, K^{-1}
δ = tape thickness, m
μ = fluid dynamic viscosity, kg/ms
ρ = density of the fluid, kg$/$m^3

Subscripts

b = at bulk fluid temperature
flt = full-length twisted tape
h = hydraulic diameter
i = inlet
o = outlet
rst = regularly spaced twisted tape elements
slt = short-length twisted-tape
w = duct wall
z = local value

References

[1] Goldstein, R. J., 1971, "Film Cooling," *Advances in Heat Transfer*, Academic, New York, Vol. 7, pp. 321–379.
[2] Morris, W. D., 1981, *Heat Transfer and Fluid Flow in Rotating Coolant Channels*, Research Studies, England, pp. 1–228.
[3] Elovic, E., and Koffel, W. K., 1983, "Some Considerations in the Thermal Design of Turbine Airfoil Cooling Systems," Int. J. Turbo Jet Engines, **1**(1), pp. 45–65.
[4] Hennecke, D. K., 1984, "Heat Transfer Problems in Aero-Engines," *Heat Transfer and Fluid Flow in Rotating Machinery* D. E. Metzger and N. H. Afgan, eds., Hemisphere, Washington, DC, pp. 353–379.
[5] Harasgama, S. P., 1995, "Aero-Thermal Aspects of Gas Turbine Flows: Turbine Blading Internal Cooling and External Effects," *VKI Lecture Series 1995-05*, T. Arts, ed.
[6] Han, J. C., and Dutta, S., 1995, "Internal Convection Heat Transfer and Cooling: An Experimental Approach," *VKI Lecture Series 1995-05*, T. Arts, ed.
[7] Lakshminarayana, B., 1996, "Turbine Cooling and Heat Transfer," *Fluid Dynamics and Heat Transfer of Turbomachinery*, Wiley, New York, Chap. 7, pp. 597–721.
[8] Simoneau, R. J., and Simon, F. F., 1993, "Progress Towards Understanding and Predicting Convection Heat Transfer in the Turbine Gas Path," Int. J. Heat Fluid Flow, **142**(2), pp. 106–127.
[9] Han, J. C., 1988, "Heat Transfer and Friction Characteristics in Rectangular Channels With Rib Turbulators," ASME J. Heat Transfer, **100**, pp. 321–328.
[10] Park, J. S., Han, J. C., Huang, Y., Ou, S., and Boyle, R. J., 1992, "Heat Transfer Performance Comparisons of Five Different Rectangular Channels With Parallel Angled Ribs," Int. J. Heat Mass Transfer, **35**(11), pp. 2891–2903.
[11] Han, J. C., Park, J. S., and Lei, C. K., 1989, "Augmented Heat Transfer in Rectangular Channels of Narrow Aspect Ratios With Rib Turbulators," Int. J. Heat Mass Transfer, **32**(9), pp. 1619–1630.
[12] Han, J. C., and Park, J. S., 1988, "Developing Heat Transfer in Rectangular Channels With Rib Turbulators," Int. J. Heat Mass Transfer, **31**(1), pp. 183–195.
[13] Webb, R. L., Eckert, E. R. G., and Goldstein, R. J., 1971, "Heat Transfer and Friction in Tubes With Repeated Rib Roughness," Int. J. Heat Mass Transfer, **14**(4), pp. 601–617.
[14] Taslim, M. E., Li, T., and Spring, S. D., 1997, "Measurements of Heat Transfer Coefficients and Friction Factors in Rib Roughened Channels Simulating Leading Edge Cavities of a Modern Turbine Blade," ASME J. Turbomach., **119**, pp. 601–609.
[15] Ekkad, S. V., and Han, J. C., 1995, "Local Heat Transfer Measurements Near a Sharp 180° Turns of a Two Pass Smooth Square Channel With a Transient Liquid Crystal Image Technique," J. Flow Visualization Image Process., **2**, pp.

285–297.

[16] Acharya, S., Dutta, S., Myrum, T. A., and Baker, R. S., 1993, “Periodically Developed Flow and Heat Transfer in a Ribbed Duct,” Int. J. Heat Mass Transfer, **36**(8), pp. 2069–2082.

[17] Acharya, S., Dutta, S., Myrum, T. A., and Baker, R. S., 1994, “Turbulent Flow Past a Surface Mounted Two Dimensional Rib,” ASME J. Fluids Eng., **116**(2), pp. 238–246.

[18] Acharya, S., Myrum, T. A., Qiu, X., and Sinha, S., 1997, “Developing and Periodically Developed Flow, Temperature and Heat Transfer in a Ribbed Duct,” Int. J. Heat Mass Transfer, **40**(2), pp. 461–479.

[19] Ekkad, S. V., and Han, J. C., 1997, “Detailed Heat Transfer Distributions in Two Pass Square Channels With Rib Turbulators,” Int. J. Heat Mass Transfer, **40**(11), pp. 2525–2537.

[20] Ekkad, S. V., Huang, Y., and Han, J. C., 1998, “Detailed Heat Transfer Distributions in Two Pass Smooth and Turbulated Square Channels With Bleed Holes,” Int. J. Heat Mass Transfer, **41**(13), pp. 3781–3791.

[21] Viswanathan, A. K., and Tafti, D. K., 2007, “Investigation of Detached Eddy Simulations in Capturing the Effects of Coriolis Forces and Centrigugal Buoyancy in Ribbed Ducts,” ASME J. Heat Transfer, **129**(7), pp. 778–789.

[22] Saha, A. K., and Acharya, S., 2007, “Turbulent Heat Transfer in Ribbed Coolant Passages of Different Aspect Ratios: Parametric Effects,” ASME J. Heat Transfer, **129**(4), pp. 449–463.

[23] Chang, S. W., Lion, T. M., Hung, J. H., and Yeh, W. H., 2007, “Heat Transfer in a Radially Rotating Square-Sectioned Duct With Two Opposite Walls Roughened by 45° Staggered Ribs at High Rotation Numbers,” ASME J. Heat Transfer, **129**(2), pp. 188–199.

[24] Fu, W. L., Wright, L. M., and Han, J. C., 2006, “Rotational Buoyancy Effects on Heat Transfer in Five Different Aspect Ratio Rectangular Channels With Smooth Walls and 45 Degree Ribbed Walls,” ASME J. Heat Transfer, **128**(11), pp. 1130–1141.

[25] Tyagi, M., and Acharya, S., 2005, “Large Eddy Simulations of Flow and Heat Transfer in Rotating Ribbed Duct Flows,” ASME J. Heat Transfer, **127**(5), pp. 486–498.

[26] Wright, L. M., Fu, W. L., and Han, J. C., 2005, “Influence of Entrance Geometry on Heat Transfer in Rotating Rectangular Cooling Channels (AR=4:1) With Angled Ribs,” ASME J. Heat Transfer, **127**(4), pp. 378–387.

[27] Jia, R., Sunden, B., and Faghri, M., 2005, “Computational Analysis of Heat Transfer Enhancement in Square Ducts With V-Shaped Ribs: Turbine Blade Cooling,” ASME J. Heat Transfer, **127**(4), pp. 425–433.

[28] Won, S. Y., Burgess, N. K., Peddicord, S., and Ligrani, P. M., 2004, “Spatially Resolved Surface Heat Transfer for Parallel Rib Turbulators With 45 deg Orientations Including Test Surface Conduction Analysis,” ASME J. Heat Transfer, **126**(2), pp. 193–201.

[29] Mahmood, G. I., Ligrani, P. M., and Chen, K., 2003, “Variable Property and Temperature Ratio Effects on Nusselt numbers in a Rectangular Channel With 45 deg Angled Rib Turbulators,” ASME J. Heat Transfer, **125**(5), pp. 769–778.

[30] Al-Hadhrami, L., Griffith, T., and Han, J. C., 2003, “Heat Transfer in Two-Pass Rotating Rectangular Channels (AR=2) With Five Different Orientations of 45 deg V-Shaped Rib Turbulators,” ASME J. Heat Transfer, **125**(2), pp. 232–242.

[31] Al-Qahtani, M., Chen, H. C., and Han, J. C., 2003, “A Numerical Study of Flow and Heat Transfer in Rotating Rectangular Channels (AR=4) With 45 deg Rib Turbulators by Reynolds Stress Turbulence Model,” ASME J. Heat Transfer, **125**(1), pp. 19–26.

[32] Griffith, T. S., Al-Hadhrami, L., and Han, J. C., 2002, “Heat Transfer in Rotating Rectangular Cooling Channels (AR=4) With Angled Ribs,” ASME J. Heat Transfer, **124**(4), pp. 617–625.

[33] Murata, A., and Mochizuki, S., 2001, “Large Eddy Simulation of Turbulent Heat Transfer in an Orthogonally Rotating Square Duct With Angled Rib Turbulators,” ASME J. Heat Transfer, **123**(5), pp. 858–867.

[34] Kiml, R., Mochizuki, S., and Murata, A., 2001, “Effects of Rib Arrangements on Heat Transfer and Flow Behaviour in a Rectangular Rib-Roughened Passage: Application to Cooling of Gas Turbine Blade Trailing Edge,” ASME J. Heat Transfer, **123**(4), pp. 675–681.

[35] Jang, Y. J., Chen, H. C., and Han, J. C., 2001, “Computation of Flow and Heat Transfer in Two-Pass Channels With 60 deg Ribs,” ASME J. Heat Transfer, **123**(3), pp. 563–575.

[36] Lin, Y. L., Shih, T. I. P., Stephens, M. A., and Chyu, M. K., 2001, “A Numerical Study of Flow and Heat Transfer in a Smooth and Ribbed U-Duct With and Without Rotation,” ASME J. Heat Transfer, **123**(2), pp. 219–232.

[37] Hwang, G. J., Tzeng, S. C., Mao, C. P., and Soong, C. Y., 2001, “Heat Transfer in a Radially Rotating Four-Pass Serpentine Channel With Staggered Half-V Rib Turbulators,” ASME J. Heat Transfer, **123**(1), pp. 39–50.

[38] Acharya, S., Hibbs, R. G., Chen, Y., and Nikitopoulos, D. E., 2000, “Mass/Heat Transfer in a Ribbed Passage With Cylindrical Vortex Generators: The Effect of Generator-Rib Spacing,” ASME J. Heat Transfer, **122**(4), pp. 641–652.

[39] Webb, R. L., Narayanamurthy, R., and Thors, P., 2000, “Heat Transfer and Friction Characteristics of Internal Helical-Rib Roughness,” ASME J. Heat Transfer, **122**(1), pp. 134–142.

[40] Smithberg, E., and Landis, F., 1964, “Friction and Forced Convection Heat Transfer Characteristics in Tubes With Twisted-Tape Swirl Generators,” ASME J. Heat Transfer, **86**, pp. 39–49.

[41] Thorsen, R., and Landis, F., 1968, “Friction and Heat Transfer Characteristics in Turbulent Swirl Flow Subjected to Large Transverse Temperature Gradients,” ASME J. Heat Transfer, **90**, pp. 87–97.

[42] Watanabe, K., Taira, T., and Mori, Y., 1983, “Heat Transfer Augmentation in Tubular Flow by Twisted Tapes at High Temperatures and Optimum Performance,” Heat Transfer-Jpn. Res., **12**(3), pp. 1–31.

[43] Date, A. W., 1973, “Flow in Tubes Containing Twisted Tapes,” Heating and Ventilating Engineering, **47**, pp. 240–249.

[44] Zhuo, N., Ma, Q. L., Zhang, Z. Y., Sun, J. Q., and He, J., 1992, “Friction and Heat Transfer Characteristics in a Tube With a Loose Fitting Twisted-Tape Insert,” Multiphase Flow and Heat Transfer, Second International Symposium, X. J. Chen, T. N. Veziroglu, and C. L. Tien, eds., Hemisphere, New York, Vol. 1, pp. 657–661.

[45] Kieda, S., Torii, T., and Fujie, K., 1984, “Heat Transfer Enhancement in a Twisted Tube Having a Rectangular Cross Section With or Without Internal Ribs,” ASME Paper No. 84-HT-75.

[46] Zhang, Y. M., Han, J. C., and Lee, C. P., 1997, “Heat Transfer and Friction Characteristics of Turbulent Flow in Circular Tubes With Twisted-Tape Inserts and Axial Interrupted Ribs,” J. Enhanced Heat Transfer, **4**, pp. 297–308.

[47] Zhang, Y. M., Azad, G. M., Han, J. C., and Lee, C. P., 2000, “Turbulent Heat Transfer Enhancement and Surface Heating Effect in Square Channels With Wavy, and Twisted Tape Inserts With Interrupted Ribs,” J. Enhanced Heat Transfer, **7**, pp. 35–49.

[48] Kline, S. J., and McClintock, F. A., 1953, “Describing Uncertainties in Single Sample Experiments,” Mech. Eng. (Am. Soc. Mech. Eng.), **75**(1), pp. 3–8.

[49] Saha, S. K., and Mallick, D. N., 2005, “Heat Transfer and Pressure Drop Characteristics of Laminar Flow in Rectangular and Square Plain Ducts and Ducts With Twisted-Tape Inserts,” ASME J. Heat Transfer, **127**, pp. 966–977.

[50] Mazumder, A. K., 2005, “Flow and Heat Transfer Characteristics of Turbulent Flow in Rectangular and Square Channels With Rib Turbulators and Twisted Tapes,” Ph.D. Thesis, Bengal Engineering and Science University, Shibpur.

[51] Saha, S. K., Gaitonde, U. N., and Date, A. W., 1990, “Heat Transfer and Pressure Drop Characteristics of Turbulent Flow in a Circular Tube With Regularly Spaced Twisted-Tape Elements,” Exp. Therm. Fluid Sci., **3**(6), pp. 632–640.

[52] Date, A. W., and Saha, S. K., 1990, “Numerical Prediction of Laminar Flow and Heat Transfer Characteristics in a Tube Fitted With Regularly Spaced Twisted-Tape Elements,” Int. J. Heat Fluid Flow, **11**(4), pp. 346–354.

Numerical Heat Transfer Optimization in Modular Systems of Y-Shaped Fins

Giulio Lorenzini[1]
e-mail: giulio.lorenzini@unibo.it

Simone Moretti

Department of Agricultural Economics and Engineering,
Alma Mater Studiorum-University of Bologna,
viale Fanin No. 50,
40127 Bologna, Italy

This paper analyses the heat exchange behavior in systems characterized by Y-shaped fins through a numerical approach based on a CFD software. Starting from individual Y profiles, as optimized in a previous work in relation to the dimensionless conductance and to the performance parameter of efficiency, it has been here investigated the advantage of a modular use of profiles. The analysis has been performed by superimposing some dimensional constraints to make immediately comparable the results obtained in the different configurations faced. Each module considered has a number of fins depending on the angle α between the two arms of the Y profile. This number depends therefore also on the horizontal width occupied by the whole system and it is upperly limited by the value allocated to the best performing individual fin. The results showed a significant increase of the dimensionless conductance and therefore of the exchanged thermal power for those multifin configurations with low values of α. This result validates the new optimization criterion proposed. [DOI: 10.1115/1.2927396]

1 Introduction

The requirements of the modern industry give an ever more important role to heat exchanging systems. In fact, each performance increase of any device always involves a higher heat flux produced that, if not removed, could damage the device itself. This is the case of the electronic industry and, more generally, of the heat exchangers industry. In many applications, in fact, the thermal load generated during the activity of the systems causes so important technical malfunctioning to remarkably reduce the performances of the systems involved. In some cases, this problem can also lead to the physical destruction of certain components [1]. A classic example is that of the CPU. In every computer, in fact, both for domestic and for professional use, it is employed a cooling device based on forced convection modules aimed at refrigerating the core of the data processing system. Those heat exchangers utilize fans and highly conductive bars opportunely shaped to remove in an effective way the thermal power internally generated. An increase of temperature following a not suitably dissipated heat flux could cause a burnout or a fusion of the working components. The classical approaches to design these auxiliary systems are based on the physical realization of the models and their successive testing in laboratory, so to define the performance parameters of interest [2,3]. The experimental method, however, immediately appears expensive, both in time and in financial terms. Moreover, it also generally results to be just partially effective because of the number of possible combinations among the geometrical parameters that characterize a component. In addition, the experimental error also affects the quality of the results. Modern industry is ever more oriented to find more performing systems, subjected, at the same time, to a growing request of volume reduction. This factor obviously introduces the necessity of an increased designing freedom, limited in the classical approaches by budget and time requirements. These problems have given therefore growing importance to the numerical approaches, which seem to match such requirements. References [4,5] adopt this technique to define and analyze some geometric configurations for heat exchangers to be used in electronics. However, the problem here faced starts from that in Ref. [6]: Through the analytical approach typical of the Constructal theory, it was obtained an optimal T-shaped fin able to maximize the dimensionless thermal conductance through its root. The same problem in Ref. [6], faced and solved positively through a simplified approach easily applicable to practical cases, has already been studied in Ref. [7] by the same authors of this paper. The aim was to propose and validate a method based on a CFD code. This research team made one step ahead in Ref. [8], using the same approach to examine Y-shaped fins. The results obtained justified a new formulation of optimization, based also on efficiency assessment. The work presented in this paper is based again on the methodology applied in Ref. [7] and in Ref. [8], which is implementing a geometrical model with a CFD code. The purpose is that of evolving the results obtained in Ref. [8] by taking advantage of the efficiency considerations made on that occasion for the Y fins. This allows for a full coupling of the classical concept of optimization, proposed in Refs. [6,7] and based on the attainment of the highest value of conductance, with that of efficiency and horizontal width occupied (“space factor”) [8]. The space factor becomes so essential for a new general definition of optimization because, as it has been seen in Ref. [8], the Y-shaped fin results less optimized (in relation to conductance) but more efficient than the T shape. Useful information for the present work were also available in recent publications related to heat transfer in different situations [9–11].

2 Model Definition

The geometrical definition of Y shapes has been presented in Ref. [8]. Three general cases were defined, presented in Figs. 1–3.

Case I: 180 deg$<\alpha<\alpha_{\text{lim}}$ The whole set of values for α lying within the cited interval gives to the fin a shape of arrow and its lower limit is a value equal to 180 deg, corresponding to a T shape. The α_{lim} angle represents the upper limit realizing the contact between the arms of the profile and the support the fin is linked with. Bigger values of α would correspond to the arms going under the root of the system.

CASE II: $\alpha_{\text{lim }2}<\alpha<180$ deg In this case, as in Case III, the values assumed by α give the fin a Y shape. Their lower limit is $\alpha_{\text{lim }2}$, where the intersection between the two arms touches the

---

[1] Corresponding author.

Contributed by the Heat Transfer Division of ASME for publication in the JOURNAL OF HEAT TRANSFER. Manuscript received June 8, 2006; final manuscript received August 31, 2006; published online May 29, 2008. Review conducted by Yogesh Jaluria.

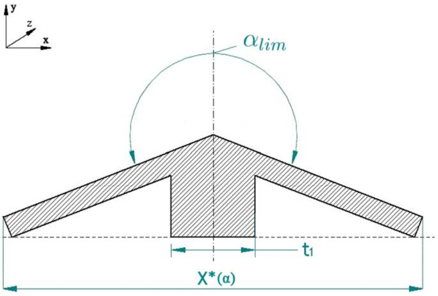

Fig. 1 Case I: 180 deg$<\alpha<\alpha_{\mathrm{lim}}$.

horizontal support with its lowest part. The upper limit, equal to 180 deg, is instead typical of a T-shape configuration.

Case III: $\alpha_{\mathrm{lim}\,3}<\alpha<\alpha_{\mathrm{lim}\,2}$ A further reduction of α leads the virtual intersection between the two lowest surfaces of the arms to happen below the root level.

Analyzing the results obtained in relation to the maximization of the dimensionless conductance q_1^*, as defined at the end of this section, it was observed [8] that its highest value is that obtained in correspondence to an angle α approximately equal to 180 deg: This means for a T-shape configuration. The efficiency of thermal exchange is defined as the ratio between the thermal power exchanged and the highest thermal power exchangeable if the whole surface of the profile were at the root temperature. The dependence of the efficiency on α proved that the former is higher when the latter is lower [8]. In particular, the thermal exchange efficiency reached a value in the vicinity of 1 for α getting close to 78 deg, as shown in Fig. 4. A general exam of this result suggests the possibility of a modular use of Y-shaped fins, each one with a small value of α, that is, with a limited horizontal width occupied in relation to the device to be cooled. This hypothesis seems supported by the analysis of the horizontal dimensionless width $X^*(\alpha)$ of each single profile, which is directly proportional to the angle α. $X^*(\alpha)$, with respect to the dimensional width $X(\alpha)$, was made dimensionless as follows:

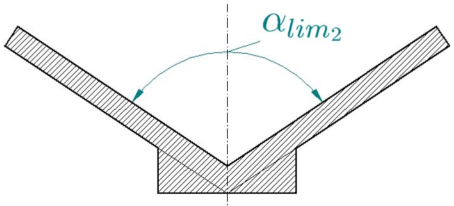

Fig. 2 Case II: $\alpha_{\mathrm{lim}\,2}<\alpha<$180 deg

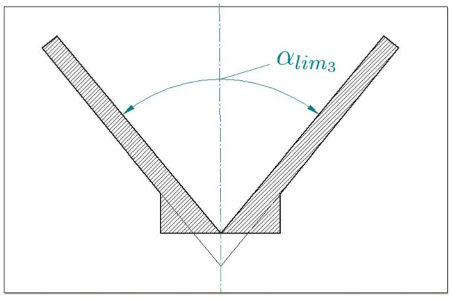

Fig. 3 Case III: $\alpha_{\mathrm{lim}\,3}<\alpha<\alpha_{\mathrm{lim}\,2}$

$$X^*(\alpha)=\frac{X(\alpha)}{t_1} \tag{1}$$

where t_1 is the width of the vertical stem, as shown in Fig. 1. See also Fig. 5.

The reference term to obtain dimensionless values is t_1, held constant in the whole set of domains analyzed in this research, and equal to the optimum value obtained in Refs. [7,8].

Further testing has implied the insertion of a number of fins equal to i within the same horizontal width X', typical of the case with highest dimensionless conductance q_1^* (α=180 deg). The number i is an integer number, upperly limited by the value n, integer part of n (α), defined as follows:

$$n(\alpha)=\frac{X'^*}{X^*(\alpha)} \tag{2}$$

As just anticipated, X'^* is constant and it corresponds to the horizontal width typical of the T-shaped fin, which has proved to maximize the dimensionless conductance [7]. Its value is equal to 33.57142. Plotting the trend of $n(\alpha)$, one obtains the curve of Fig. 6, from which it can be evicted that the highest number of profiles that can be inserted within a width X'^* is 5, once the constraint of Y-shape geometry has been set. Further reducing the amplitude of α, with respect to the minimum of 78 deg previously identified, would determine meaningless profiles. In fact, the intersection between the arms of the fin would entirely lie below the root and the corresponding profile would not be Y shaped anymore.

It is then necessary to show the relationship that defines d, horizontal distance between the fins in a modular system (Fig. 7). This parameter is defined so to make the single fin a modular element for the system, as clarified in Fig. 7. Modularity is fundamental to allow that more systems could be located one close another with periodical setting.

The expression for the length d is

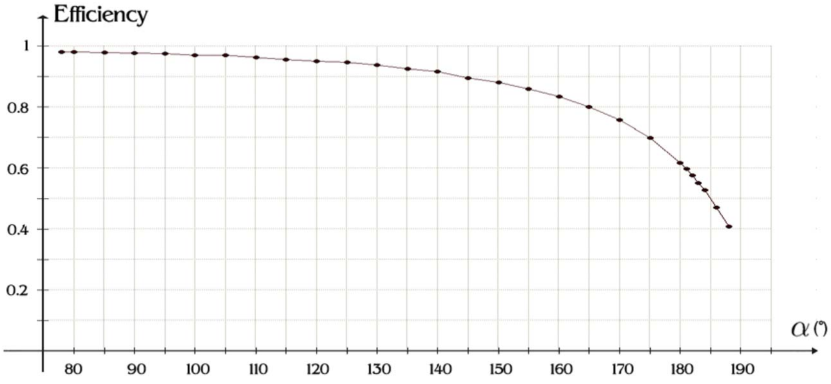

Fig. 4 Heat exchange efficiency for Y-shaped fins [8]

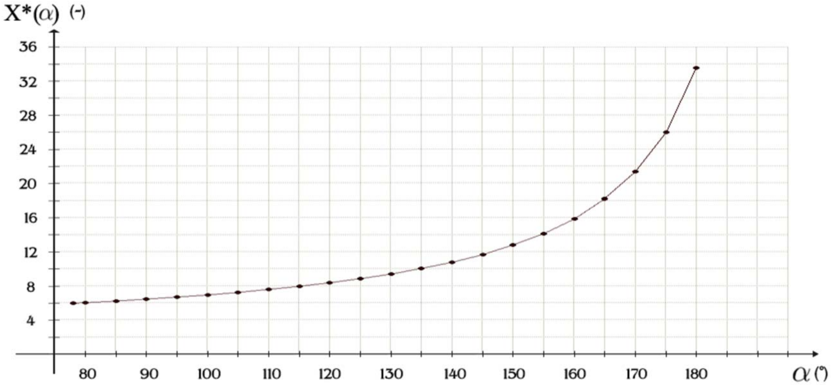

Fig. 5 Dimensionless width of the fin in function of α

$$d = \frac{X'^*}{i} - 1 \tag{3}$$

The parameter X'^*, as already explained, represents the horizontal width of the best performing fin with respect to the dimensionless conductance (α=180 deg) [8]. The variable i is the number of fins used in each case: It can vary from 1 to 5 and its value can be obtained by the curve in Fig. 6, choosing the integer part of $n(\alpha)$ for each considered α. The value of t_1 gives the width of the vertical stem of each fin considered. In analogy with Refs. [6–8], the boundary conditions are here defined starting from a convection coefficient h variable in function of the geometry:

$$h = \frac{a^2\lambda}{2\sqrt{A}} \tag{4}$$

where A is the surface subtended by the arms of the fin, as represented in the example of Fig. 8.

The other parameters are the thermal conductivity λ and the dimensionless parameter a that allows for the variation of h, independently from the other parameters involved in the definition [6]. The value of a is assumed equal to 0.1 [6–8]. Moreover, the analysis has been made in the hypothesis of "ideal" forced convection, which could be schematized by an air flow flowing along the z axis (Fig. 1) with a velocity high enough to keep its temperature constant. CONSOL MULTIPHYSICS requires dimensional values in input to the solver: The temperature T_1 at the root of the fin and the environmental one T_∞ are set equal to 100°C and 20°C, respectively. This does not affect the generality of the present study because of the conductance being expressed in dimensionless terms, as follows:

$$q_1^* = \frac{q_1}{\lambda W(T_1 - T_\infty)} \tag{5}$$

where q_1 is the thermal power through the root of the fin and W is the width of the fin in the z axis (Fig. 1). For the same reason, it is not a limit to consider, as in Ref. [6], the thermal conductivity λ equal to 200 W/(m°C), value typical of aluminium, much used in thermal-fluid dynamics applications. Once the effect of W on the use of computational resources was assessed, W itself was assigned equal to the minimum value able to make negligible the checkerboard effects. The depth of the systems under exam so assumes a hemi-infinite nature, in analogy with Refs. [6,7].

3 Methods and Tests

The numerical computations have been realized with the code CONSOL MULTIPHYSICS 3.3 that, using a simple graphical interface, also allows the creation of simple geometrical models. However, in the cases here faced, it was preferred a CAD modeling approach, choosing the IGES file format as sharing tool between the two informatics applications. Once imported the model in the CFD environment, it has been generated an opportune mesh (Fig. 9 reports the case of a module with four fins). Its number of elements is a function of the angle α and of the number of fins inserted in each module. It has been obtained a minimum of 63,468 elements for the configuration with a single fin and α equal to 165 deg; a maximum of 266,115 elements for a system containing five finned profiles and an angle α equal to 78 deg. The mesh has been generated with particular care to the critical zones. Among them are the intersections between the vertical stem and the arms of the fin, characterized by high temperature gradients.

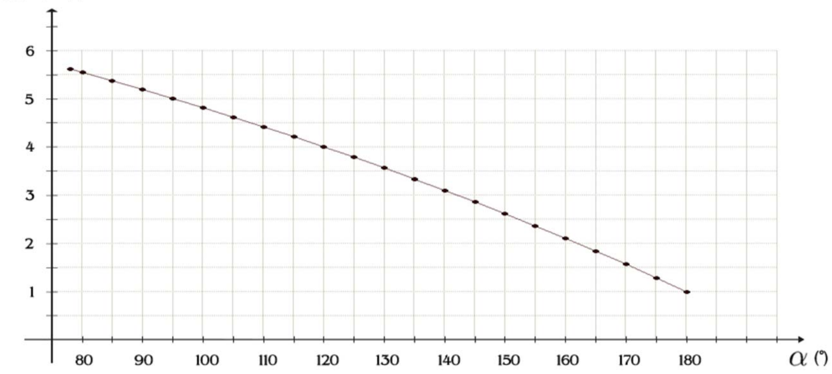

Fig. 6 Number of profiles $n(\alpha)$ function of α, given X'^*

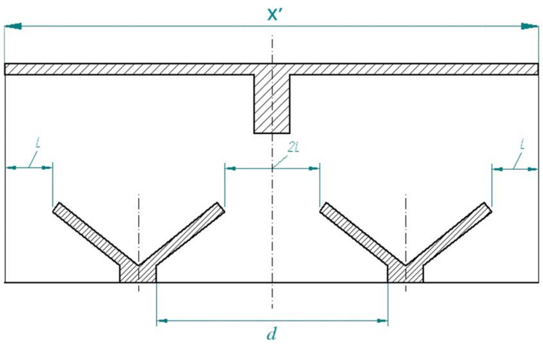

Fig. 7 Modular system of Y-shaped fins

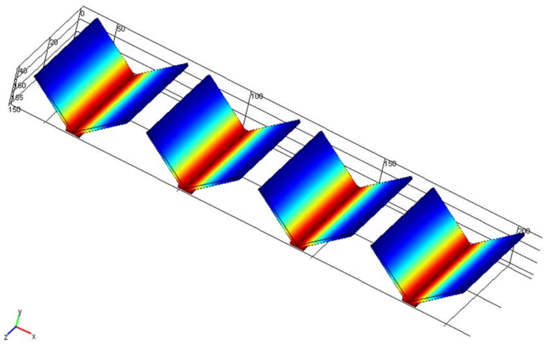

Fig. 10 Temperature trend: four-fin module

4 Results and Comments

The aim of this investigation is to apply those characteristics of efficiency observed in Ref. [8] (Fig. 4) for single Y-shaped fins, to a multifin module that, based on the same horizontal dimensional constraint of an optimized T-shaped fin, could offer better thermal performances than the latter. In fact, an increase of efficiency is accompanied by a horizontal dimensional reduction, typical of the Y-shaped fins, with respect to the T-shape case. Such evidence has suggested the possibility to use more single Y profiles in a space of the same horizontal width occupied by an optimal T-shaped fin. It results therefore fundamental to characterize the trend of the conductance in this new kind of configurations, evaluating each case in function of the number of profiles and of the angle α (Fig. 6).

Consequently, the system offering the best performances could be considered the result of this novel approach, aimed at reaching a new formulation of optimization, once the fundamental space factor has also been considered. The numerical analysis has supplied, for all the cases, trends of temperature similar to the ones in Fig. 10, describing the case of a four-fin module. The figure shows trends in good agreement with those presented in Refs. [6,8]. Representing in a Cartesian diagram the trend of the dimensionless conductance with the angle α and with the number of profiles n, one can obtain the pattern of Fig. 11. In the punctual values represented in Fig. 11, a proportionality between the value of the dimensionless conductance of the single fin and that of the n-fin system has been observed. This means that the value of q^* observed for a n-fin module is very close to the one obtainable multiplying n for the conductance of the single fin, with the same value for α. As it has been assumed an ideal forced convection condition, where the fluid flows along the z direction (Fig. 10) with a so high velocity to keep constant its temperature, this result was expected. The effects of the mutual thermal affections of the fins are, in fact, negligible.

From the numerical comparisons made between the characteristics of the reference profile and the results obtained in the multifin configurations, a noticeable increase of performance relatively to the dimensionless conductance q_1^* has been observed. As it can be seen in the plot of Fig. 11, the performance in the modular systems increase considerably, even just adding a second profile, with respect to the case $n=1$ and $\alpha=180$ deg. The case analyzed that gave the best performances was that with $n=5$ and $\alpha=78$ deg, which compared to the reference case resulted 4.034 times more performing. For the given definition of the dimensionless conductance q_1^*, the thermal conductivity λ, the depth in the z direction W (Fig. 1), the temperature at the root of the fin T_1 and the environmental temperature T_∞ have been held constant for each case analyzed. So, under these conditions, the plot of Fig. 11 also represents in a qualitative way the trend of the thermal power q_1 through the root of the system.

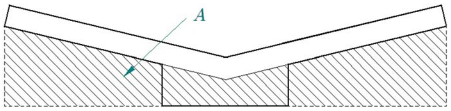

Fig. 8 Area subtended by the arms of a fin

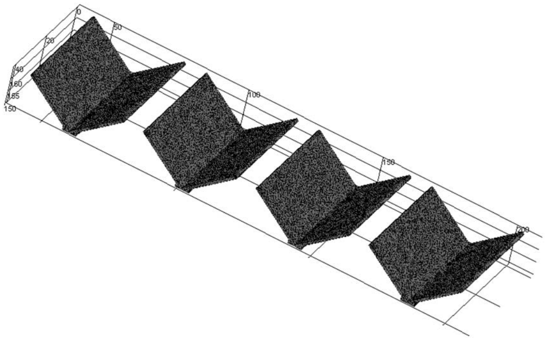

Fig. 9 Mesh generation: case of the four-fin module

5 Conclusions

The optimization research presented in this paper deepens the knowledge of performance efficiency of Y-shaped fins, starting from the results obtained in previous works. It was, in particular, known that a variation of the angle between the two arms of a fin induces a small reduction of conductance, with respect to the T-shaped fin case. This effect was, however, associated with a relevant increase of efficiency of the fin itself. All these considerations have led to studying the effect of a modular system of fins with the purpose of employing, with the new device, the same horizontal width previously allocated to simpler systems. This led to a new assessment of the thermal performances of heat exchangers, also in relation to the dimension of the module. It has been held, as a start for the realization of new models, the same geometrical constraints tested in the reference papers, choosing the best performing geometries in relation to the dimensionless conductance of the single-fin systems, and this made the results fully comparable to the reference ones. The results showed that the configuration with the best performances ($n=5$, $\alpha=78$ deg) guarantees a global conductance value 4.034 times higher than the reference case with $n=1$ and $\alpha=180$ deg. Then, a relevant increase of conductance and of thermal power exchanged, with the same "space occupation" of the reference T-shaped configuration can be observed. This result can be promising for all those thermal exchange applications that need better performances with little space available, as it happens in many technical fields.

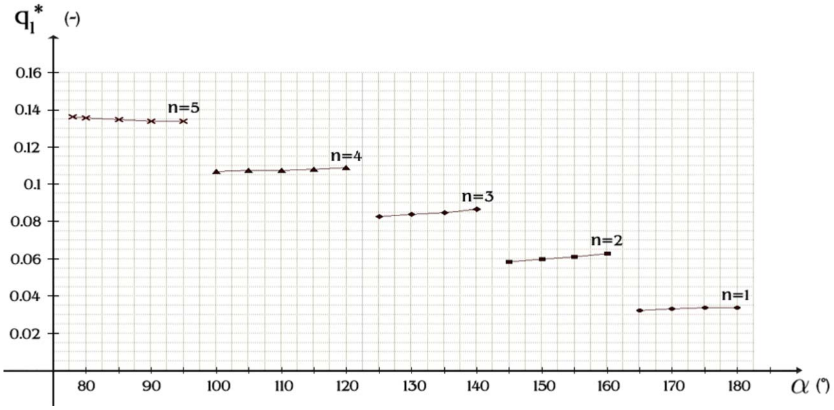

Fig. 11 **Conductance q_1^* in the modular system**

Nomenclature

a = dimensionless parameter, Eq. (4)
A = area (m^2)
d = space between two fin in the array (m)
h = heat transfer coefficient ($W\ m^{-2}\ K^{-1}$)
i = number of modules
$n(\alpha)$ = dimensionless ratio, Eq. (2)
q = heat flux (W)
t = thickness (m)
T = temperature (K)
W = width (m)
$X(\alpha)$ = length of the Y-shaped fin (function of α) (m)
X' = length of the optimal T-shaped fin (m)

Greek Letters

α = angle (deg)
λ = fin thermal conductivity ($W\ m^{-1}\ K^{-1}$)

Subscripts

1 (one) = root
∞ = local environment

Superscript

(*) = dimensionless variables

References

[1] Lall, P., Pecht, M., and Hakim, E., 1997, *Influence of Temperature on Microelectronics and System Reliability: A Physics of Failure Approach*, CRC Press, Boca Raton, FL.

[2] Upton, T. D., and Watt, D. W., 1997, "Experimental Study of Transient Natural Convection in an Inclined Rectangular Enclosure," Int. J. Heat Mass Transfer, **40**(11), pp. 2679–2690.

[3] Jubran, B. A., Swiety, S. A., and Hamdan, M. A., 1996, "Convective Heat Transfer and Pressure Drop Characteristics of Various Array Configurations to Simulate the Cooling of Electronic Modules," Int. J. Heat Mass Transfer, **39**(16), pp. 3519–3529.

[4] Horvat, A., and Catton, I., 2003, "Numerical Technique for Modeling Conjugate Heat Transfer in an Electronic Device Heat Sink," Int. J. Heat Mass Transfer, **46**(12), pp. 2155–2168.

[5] Kandasamy, R., and Subramanyam, S., 2005, "Application of Computational Fluid Dynamics Simulation Tools for Thermal Characterization of Electronic Packages," Int. J. Heat Mass Transfer, **15**(1), 61–72.

[6] Bejan, A., and Almogbel, M., 2000, "Constructal T-Shaped Fins," Int. J. Heat Mass Transfer, **43**, pp. 2101–2115.

[7] Lorenzini, G., and Moretti, S., 2007, "A CFD Application to Optimise T-Shaped Fins: Comparisons With Constructal Theory's Results," ASME J. Electron. Packag., **129**(3), pp. 324–327.

[8] Lorenzini, G., and Moretti, S., 2007, "Numerical Analysis on Heat Removal From Y-shaped Fins: Efficiency and Volume Occupied for a New Approach to Performance Optimisation," Int. J. Therm. Sci., **46**(6), pp. 573–579.

[9] Zdanski, P. S. B., Ortega, M. A., Fico, N. G. C. R. Jr., 2005, "Heat Transfer Studies in the Flow Over Shallow Cavities," ASME J. Heat Transfer, **127**(7), pp. 699–712 2005.

[10] Burgess, N. K., and Ligrani, P. M., 2005, "Effects of Dimple Depths on Channel Nusselt Numbers and Friction Factors," ASME J. Heat Transfer, **127**(8), pp. 839–847.

[11] Barbosa Saldana, J. G., Anand, N. K., Sarin, V., 2005, "Numerical Simulation of Mixed Convective Flow Over a Three-Dimensional Horizontal Backward Facing Step," ASME J. Heat Transfer, **127**(9), pp. 1027–1036.

Phase Change Heat Transfer Enhancement Using Copper Porous Foam

Ali Siahpush
e-mail: ali.siahpush@inl.gov

James O'Brien
e-mail: james.obrien@inl.gov

Idaho National Laboratory,
P.O. Box 1625,
Idaho Falls, ID 83415-3760

John Crepeau
University of Idaho,
1776 Science Center Drive,
Idaho Falls, ID 83402
e-mail: crepeau@uidaho.edu

A detailed experimental and analytical study has been performed to evaluate how copper porous foam (CPF) enhances the heat transfer performance in a cylindrical solid/liquid phase change thermal energy storage system. The CPF used in this study had a 95% porosity and the phase change material (PCM) was 99% pure eicosane. The PCM and CPF were contained in a vertical cylinder where the temperature at its radial boundary was held constant, allowing both inward freezing and melting of the PCM. Detailed quantitative time-dependent volumetric temperature distributions and melt/freeze front motion and shape data were obtained. As the material changed phase, a thermal resistance layer built up, resulting in a reduced heat transfer rate between the surface of the container and the phase change front. In the freezing analysis, we analytically determined the effective thermal conductivity of the combined PCM/CPF system and the results compared well to the experimental values. The CPF increased the effective thermal conductivity from 0.423 W/m K to 3.06 W/mK. For the melting studies, we employed a heat transfer scaling analysis to model the system and develop heat transfer correlations. The scaling analysis predictions closely matched the experimental data of the solid/liquid interface position and Nusselt number. [DOI: 10.1115/1.2928010]

Keywords: porous media, phase change, scale analysis

Introduction

In recent years, there has been an increased interest in the proposed use of phase change processes for the storage of thermal energy. A survey of the experimental literature [1] reveals a strong concentration on melting and freezing outside of heated or cooled cylinders embedded either vertically or horizontally in a phase change medium. The solution of moving boundary problems with phase change has been of special interest due to the inherent difficulties associated with the nonlinearity of the interface conditions and the unknown locations of the moving boundaries. Exact closed-form solutions of solid/liquid phase change, also known as the Stefan problem, are available only for a limited number of cases [2].

Majumdar et al. [3] performed an experimental study of melting in a vertical cylinder. Data were obtained for a mixture of paraffin, which melts over a wide range of temperatures. The heat transfer data were confined to the case of an initially subcooled solid. Finite-difference solutions for melting of a phase change medium contained in a vertical cylinder were presented by Pannu et al. [4] for a restricted range of the governing parameters. Fundamental heat transfer experiments were performed for freezing of an initially superheated and nonsuperheated liquid in a cooled vertical cylindrical container (inward freezing) by Sparrow and Broadbent [5]. They concluded that although the latent heat is the major contributor to the total extracted energy, the total sensible energies could make a significant contribution, especially with large tube-wall subcooling, large liquid superheating, and short freezing times. Natural convection effects in the superheated liquid were modest and were confined to short freezing times. Lunardini [6] and Poulikakous [7] investigated the melting and freezing of a phase change material (PCM) contained in a vertical cylinder. Akgün et al. [8] studied the melting and solidification characteristics of paraffin as a PCM and found that it is ideal because of its high latent heat storage capabilities and relative ease of handling.

The use of porous materials to enhance heat transfer has been investigated by a number of researchers. Filling the flow passage with steel particles, Koh and Stevens [9], was able to increase the effectiveness of regenerative devices. Weaver and Viskanta [10,11] have investigated melting of ice and freezing of water in porous media experimentally and analytically for horizontal and vertical cylindrical capsules. Quantitative results of the temperature distribution and solid/liquid interface shape were obtained for inward melting and freezing with different sizes and types of spherical beads used as the porous media. Tong and Khan [12] demonstrated the increase in the heat transfer rate during outward freezing of a PCM with a low thermal conductivity by inserting a high-porosity metal matrix into the PCM contained in a cylinder. They presented the numerical results in the form of solid/liquid interface movements, isotherms, streamlines, and heat transfer rates. Py et al. [13] investigated the behavior of paraffin impregnated by capillary forces into a compressed expansed natural graphite matrix. They found that the thermal conductivity of the composite system closely matched that of the sole graphite matrix. Using a porous aluminum matrix as a thermal energy storage system, Trelles and Dufly [14] numerically simulated thermoelectric cooling. Their models showed that the metal matrix in the PCM greatly improved the cooling performance. Mesalhy et al. [15] used volume averaged conservation equations to model phase change in a porous metal matrix and found that to enhance the response of the PCM, a matrix with high porosity and high thermal conductivity is optimal.

In convection heat transfer, scale analysis has been shown to be a powerful tool to produce order-of-magnitude results and trends [16]. Scale analysis is a relatively simple technique to give correct dimensionless forms, which can guide more exact results. Bejan [17] has used this technique to study convection in porous media as well. Kim and Kim [18] derived a scale relation for the Nusselt number as a function of the Rayleigh number for turbulent natural convection in a porous layer. They found good correlation be-

---

Contributed by the Heat Transfer Division of ASME for publication in the Journal of Heat Transfer. Manuscript received February 19, 2007; final manuscript received February 21, 2008; published online May 30, 2008. Review conducted by Jamal Seyed-Yagoobi. Paper presented at the 2005 ASME Heat Transfer Summer Conference (HT2005), San Francisco, CA, July 15–22, 2005.

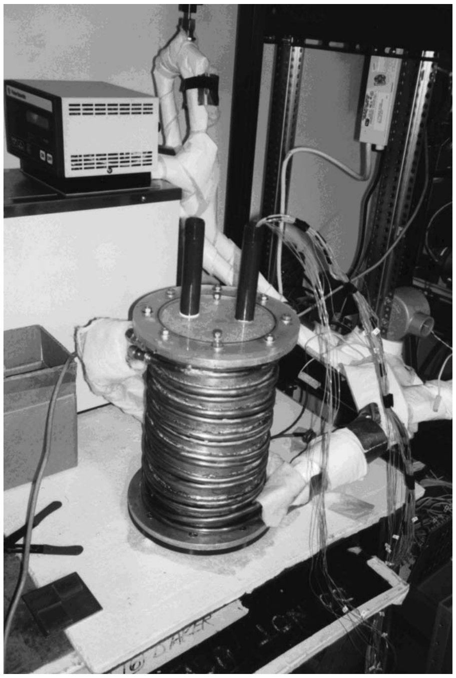

Fig. 1 Photograph of experimental apparatus showing the copper cylinder with the copper metal foam inserted

tween their analysis and experimental results. Scale analysis of natural convection has been compared to numerical studies for rectangular tanks heated from below by Sarris et al. [19]. Their scale analysis led to behavior that was confirmed by their numerical results.

The present study compares the experimental results with a scale analysis for melting and freezing of a PCM embedded in a vertical, cylindrical copper metal foam matrix.

Experimental Setup and Procedure

The experiments were performed in a copper test vessel. In order to provide a controlled, constant wall temperature thermal boundary condition, a pair of copper tubes was wrapped and soldered around the outside of the copper test vessel, with two tube inlets, each at opposite ends of the test vessel. In this manner, the double-wrapped tubing acted like a counterflow heat exchanger to provide a uniform wall temperature boundary condition around the outer periphery of the test vessel. A photograph of the test vessel with the copper tubes mounted on the tank and locations of the external thermocouples is shown in Fig. 1. The test vessel was fabricated from a large copper tube with an inside diameter of 15.55 cm (6.125 in.), an outside diameter of 16.19 cm (6.375 in.), and a height of 30.48 cm (12 in).

Lids made of acrylic plastic sealed the test vessel on the top and bottom. The thermal conductivity of acrylic is much lower than the thermal conductivity of the PCM and the copper test vessel, which helped reduce the end effects. Two small vertical copper tubes were placed in the top cap to enable removal of excess PCM during melting and to prevent overflowing, as well as to provide a passage of the thermocouple wires. The test vessel system was insulated using 10 cm (4.0 in.) thick fiberglass fitted around the entire vessel and caps. A constant temperature bath was selected to supply cooling/heating fluid to the copper heat exchange tubes that kept the outer wall of the container at constant temperature.

For these experiments, 99% pure eicosane ($C_{20}H_{42}$) was chosen as the PCM. Eicosane was desirable because it has a single fusion temperature (36.5°C), which is just slightly higher than ambient temperature, making it convenient for phase change experimentation. Low-temperature heating can be used to melt the PCM and ambient-temperature cooling can be used to refreeze it. In addition, the proximity of the melting point to ambient temperature results in reduced heat losses to the environment. The thermophysical properties of eicosane are reasonably well established, and the thermal conductivity of the solid eicosane is given as 0.423 W/m K [20].

For the initial series of base line tests without any copper porous foam (CPF) installed in the test section, a plastic tree was fabricated to hold the thermocouples (TCs) in place. Four additional TCs deployed along the outside height of the copper test vessel measured the wall temperature.

For testing with the CPF in place, cylindrical disks of copper foam were machined to fit securely in the tank. The porous material selected for these experiments was copper metal foam with 95% porosity. It had an open-celled structure composed of dodecahedronlike cells, with 12–14 pentagonal or hexagonal faces and the pore sizes ranged from 2.54 mm (0.10 in.) down to about 0.127 mm (0.005 in.). The edges of these cells were composed of copper fibers and typically there was a lumping of material at points where the fibers intersect. TCs were positioned in the gap region between adjacent porous disks providing several layers of TCs to monitor the progression of the phase change front. The TCs were covered with a small amount of rubber to prevent electrical contact with the CPF. The rubber was about 0.2 mm thick and did not affect the temperature measurements. Eighty-one TCs at uniform radial and vertical locations were installed in the tank for the tests using the CPF. The test apparatus internal volume was then filled with eicosane. The size of the TCs was comparable to the copper foam filaments, so there was minimal flow interference. It should be noted that in the testing with the CPF, less eicosane was utilized due to the volume occupied by the CPF. This decrease in volume of the eicosane was measured and considered in the analysis.

Numerous freezing and melting tests were performed at various wall temperatures. At the termination of the tests, all of the TCs indicated that the entire eicosane volume was in thermal equilibrium with the constant temperature water bath.

Experimental Results

Freezing. Freezing tests were conducted to determine the effects of the high-conductivity CPF material on the freezing process and corresponding heat transfer rates, and to calculate the effective thermal conductivity of the combined PCM/CPF system. The initial and boundary conditions of the experiment were established to reduce the eicosane temperature from an initial value of 50°C to a final value of 10°C.

Figure 2 shows the temperature-time history at the radial location $r=33$ mm and height $h=165$ mm for the phase change process with and without the CPF. The figure clearly shows that the CPF significantly accelerates the freezing process. After 20 min of freezing, the effect of natural convection disappeared and the heat transfer mechanism became pure conduction. The combined system achieved thermal equilibrium at 10°C after about 150 min, whereas the time duration required to achieve thermal equilibrium was about 600 min for the case without CPF under the same initial and boundary conditions.

Figure 2 also shows that the freezing front passes the TC location significantly earlier for the CPF case (85 min) than without the CPF (220 min). In addition, the introduction of the CPF gives rise to a significant increase in the effective thermal conductivity of the solid eicosane. The rate of change of the temperature profile for the CPF case after passage of the freezing front shows this effect.

Based on the vertical and radial TC locations, a time history of the freezing front locations was developed. This history is presented in Fig. 3, where phase change interface locations are shown for the systems without the CPF (Fig. 3(*a*)) and with the CPF (Fig. 3(*b*)). On the left of each front is liquid eicosane and on its right

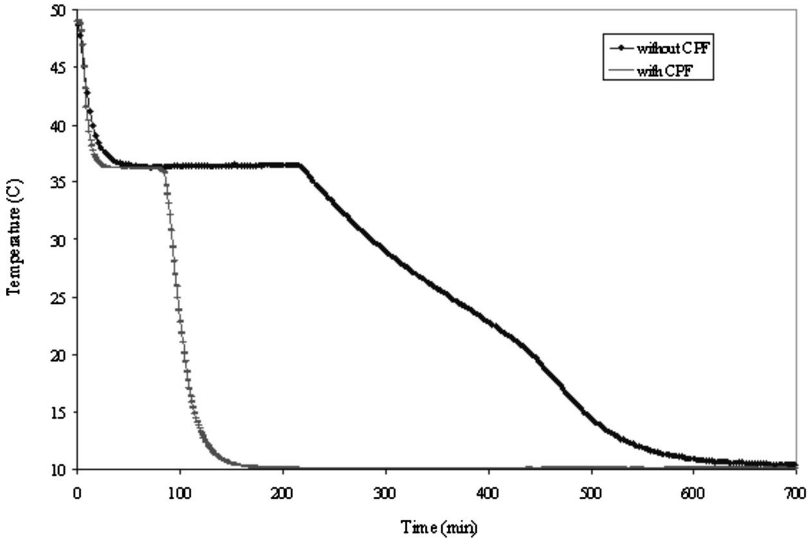

Fig. 2 Temperature history during the freezing of eicosane at $r=33$ mm and $h=165$ mm with and without the CPF.

the solid eicosane. For the system without the CPF, the figure shows how slowly the phase change front moves in comparison to the system with the CPF.

Once the superheat decayed to zero, natural convection ceased. In addition, there was no further heat conduction from the liquid to the freezing front since there was no longer a temperature difference to drive it. The effect of the initial superheat vanished after 20 min. As expected, the freezing front moved steadily inward with time and the frozen layer adjacent to the wall grew thicker. At 30 min into the experiment, a thin layer of frozen eicosane also formed along the top, indicating a heat leak, most likely due to the trapped air layer. As the solid layer grew inward, the thermal resistance associated with the solid eicosane increased, and the heat transfer rate out of the system decreased. This decrease in heat transfer rate is reflected in Fig. 3 by the closer spacing of the large-time interface locations.

Based on the overall TC data, we found that with the CPF in place, the eicosane in the entire tank reached the fusion temperature after approximately 20 min, whereas without the CPF, the system required about 45 min to achieve the fusion temperature. The system completely froze within 85 min with the CPF compared to 370 min without. With the CPF, the system reached the equilibrium set point of 10°C after 150 min, and without the CPF, the system reached the equilibrium temperature of 10°C after 650 min.

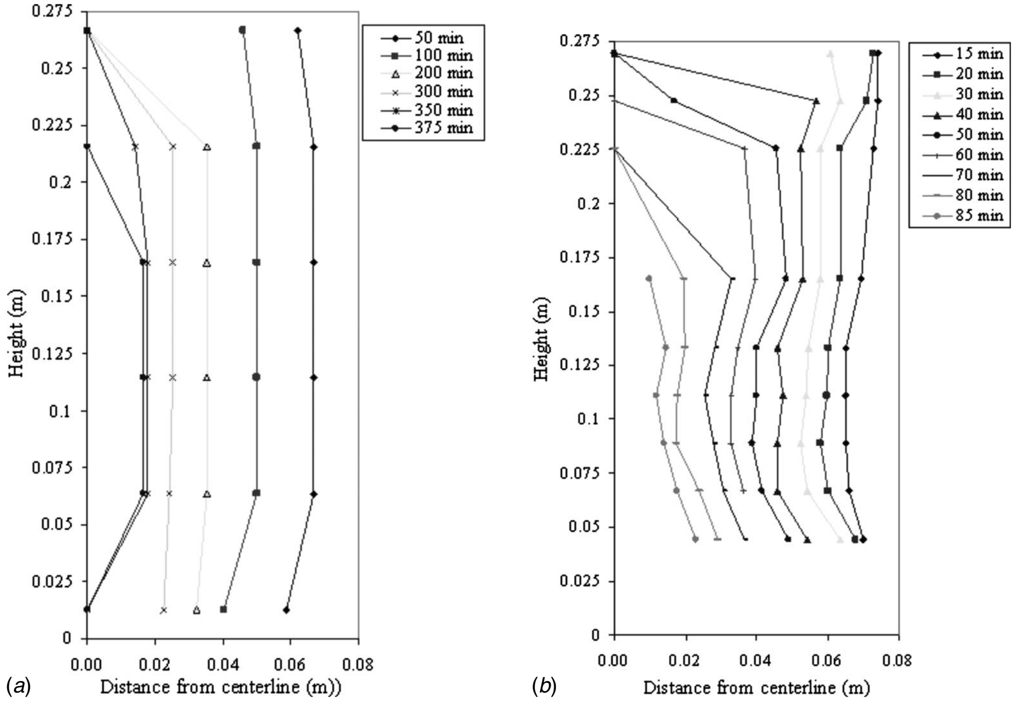

Fig. 3 Experimental data showing the location of the solid-liquid phase change front in time during freezing of the eicosane: (*a*) without the CPF and (*b*) with the CPF

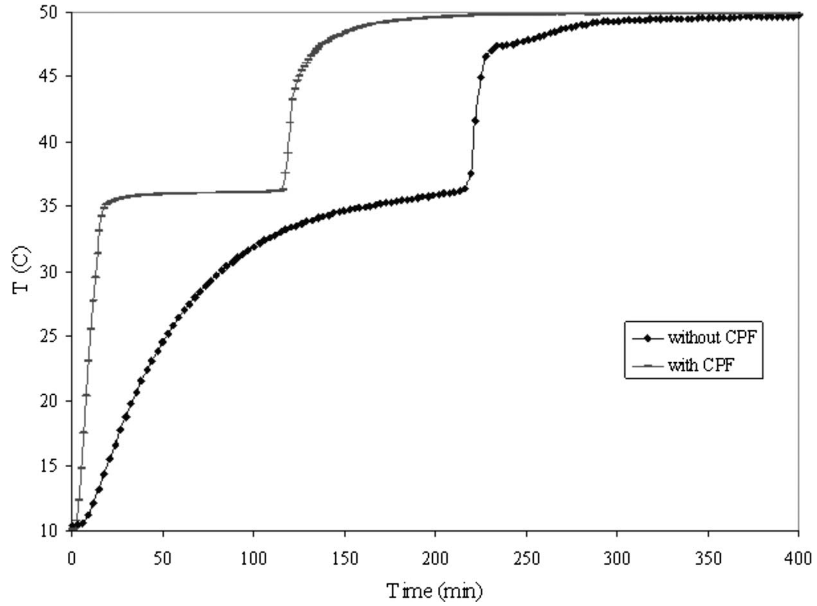

Fig. 4 Temperature history during melting of the eicosane at $r=33$ mm and $h=165$ mm with and without the CPF

Melting. We then compared the melting behavior of the PCM both with and without the CPF. Here, the initial temperature was 10°C and the wall boundary temperature was 50°C. Figure 4 gives the temperature versus time plots at the same location as those in Fig. 2, $r=33$ mm and $h=165$ mm. With the CPF in place, the temperature reached the fusion temperature after about 20 min, 125 min sooner than for the case without the CPF. The plot shows that the melt front passed this location at about 117 min, compared to 218 min for the non-CPF case. These results indicate significantly higher heat transfer rates for the CPF case, due to the increased effective thermal conductivity of the combined PCM/CPF system.

Figure 5 shows a comparison of the melting fronts both with and without the CPF. Based on the vertical and radial locations of the TCs, and the values of elapsed time at which each TC was observed to exceed the fusion temperature, a comprehensive time history of the melting process was developed. One such representative time history of melt fronts without the CPF in place is presented in Fig. 5(*a*), where cross-sectional views of the melt fronts are shown at eight different times (50 min, 75 min, 100 min, 150 min, 200 min, 250 min, 275 min, and 300 min).

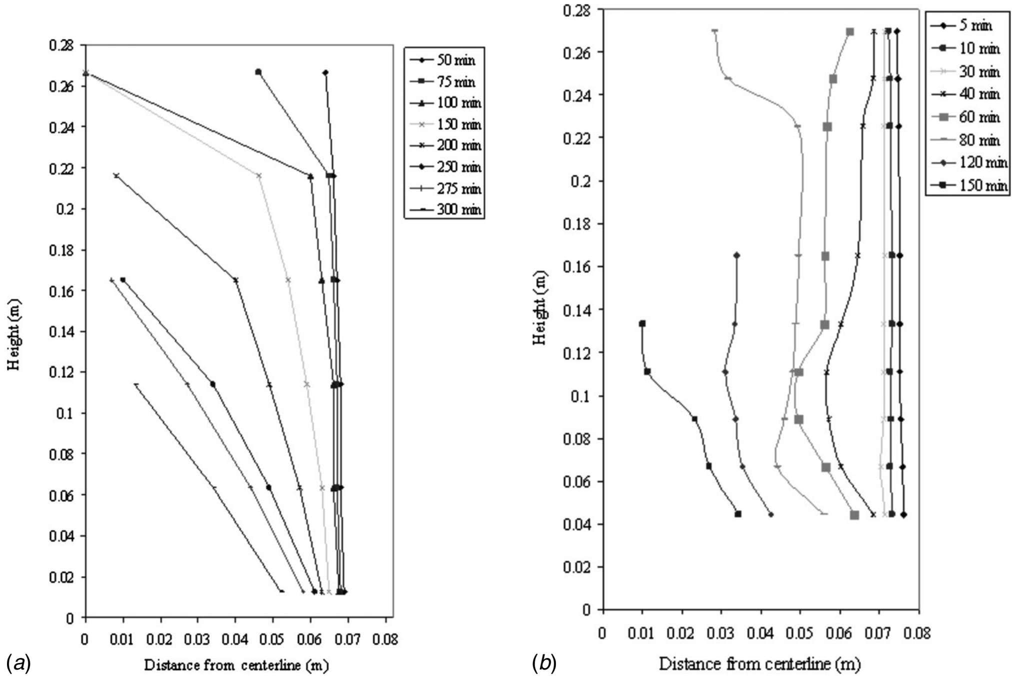

Fig. 5 Data showing the location of the solid-liquid phase change front during the melting of eicosane: (*a*) without the CPF and (*b*) with the CPF

The melt front progressed inward from right to left in the figure. On the left side of each front is solid eicosane and on its right side is liquid eicosane.

Without the CPF, the melt front was almost parallel to the hot wall for the first 20 min, indicating a conduction-dominated melting process. After this initial period, approximately 75 min into the experiment, a transition regime began where the natural convection flow carved out its own zone in the upper part of the liquid region, while the lower part remained conduction dominated.

At 150 min, the melt front gradually exhibited a shape typical of convection-dominated melting. The interface moved faster near the top where the liquid, heated by the hot wall, impinged on the solid eicosane. The melt rate decreased toward the bottom, since the liquid cooled down as it descended along the interface. At 200 min, the height of the solid/liquid interface decreased steadily until the solid region disappeared entirely.

There were two factors that contributed to the departure of the actual behavior of the melt front from that of pure conduction. First was the density decrease that accompanies melting. The liquid phase must seek additional volume into which to expand, and this caused an upward flow of liquid from the melt layer into the free space above the solid. The displaced liquid caused melting to occur at the upper surface of the solid as well as at the adjacent side surface. It is this volume change driven motion that is believed to be responsible for the initial departures of the melt front from that of pure conduction.

Second, as time passed, natural convection motion developed in the melt layer, with an upward flow adjacent to the tank wall and a downward flow adjacent to the melt front. This circulation pattern delivered relatively hot liquid to the upper reaches of the solid, where its presence accelerated the rate of inward and downward melting. Natural convection and the aforementioned volume change driven motions are mutually aiding, but natural convection is the dominant factor during most of the melting period.

From Fig. 5(*b*), it can be seen that for the initial 30 min, the melting front was almost parallel to the hot wall indicating a conduction-dominated melting process. Approximately 80 min into the experiment, the lower portion of the melt front was roughly parallel to the wall, while the rate of melting is much higher in the upper region. The flow carved out its own convection-dominated zone in the upper part of the liquid region, while the lower part was dominated by conduction. After 80 min, the height of the unmelted solid shrunk rapidly, and the melt front exhibited a shape typical of convection-dominated melting. The interface moved faster near the top where the liquid, heated by the hot wall, melted the solid. The melt rate decreased toward the bottom, since the liquid cooled down as it descended along the interface. As was observed in the non-CPF case, the local melting rate is slowest at the bottom of the cylinder and progressively increased upward.

During the course of the experiments with the CPF in place, the melt front behaved differently compared to the non-CPF case and the curvature of the interface was not as pronounced as what was encountered during melting without the CPF. This was expected because of the high effective conductivity of the combined PCM/CPF system. The porosity and the permeability of the porous material also have a direct effect on the convection heat transfer suppression mechanism. As the porosity and permeability of the porous media decrease, the importance of convection heat transfer is reduced.

Analytical Modeling

Effective Thermal Conductivity Modeling During Freezing. A general form of the energy conservation equation for a homogeneous system in cylindrical coordinates, $T=T(r,t)$, with constant thermal conductivity, no change in the azimuthal direction and no internal heat generation, is given as [21]

$$\frac{1}{r}\frac{\partial}{\partial r}\left(r\frac{\partial T}{\partial r}\right)+\frac{\partial^2 T}{\partial z^2}=\frac{1}{\alpha}\frac{\partial T}{\partial t} \tag{1}$$

Equation (1) may also be adopted as the heat equation for a porous material saturated with a fluid, if the PCM thermal properties are replaced by "effective" properties. During the freezing process, it was assumed that the porous media were isotropic and homogeneous, with uniform porosity. Based on these assumptions, the resulting time-dependent energy equation, with no changes in the vertical direction for a saturated porous media, i.e., the combined PCM/CPF system, is

$$\frac{1}{r}\frac{\partial}{\partial r}\left(r\frac{\partial T}{\partial r}\right)_i=\frac{1}{\alpha_{\text{eff}-i}}\left(\frac{\partial T}{\partial t}\right)_i \tag{2}$$

The subscript i represents either the solid or liquid phase of the eicosane. The initial and boundary conditions are

$$\begin{gathered} T_l(r,0)=T_i, \quad T_s(r_w,t)=T_w \\ \frac{\partial T(0,t)}{\partial r}=0, \quad T_s(r_{\text{fus}},t)=T_l(r_{\text{fus}},t)=T_{\text{fus}} \end{gathered} \tag{3}$$

The energy balance at the interface yields [22]

$$\phi\rho_s\Delta h_{\text{fus}}\left(\frac{\partial r}{\partial t}\right)_{\text{fus}}+k_{\text{eff}-l}\left(\frac{\partial T}{\partial r}\right)_{\text{pl}}-k_{\text{eff}-s}\left(\frac{\partial T}{\partial r}\right)_{\text{ps}}=0 \quad \text{at } r=r_{\text{fus}} \tag{4}$$

Effective or average properties are used, which are based on the fraction of solid and liquid phases and the porosity of the CPF [23] as follows:

$$(\phi\rho c_p)_{\text{eff}-i}=\phi(\rho c_p)_i+(1-\phi)(\rho c_p)_{\text{por}} \tag{5}$$

$$\alpha_{\text{eff}-i}=\frac{k_{\text{eff}-i}}{(\phi\rho c_p)_{\text{eff}-i}} \tag{6}$$

The heat conduction equation (2) in the solid region can be integrated using the boundary conditions in Eq. (3), yielding the temperature distribution $T_s(r)$ as

$$T_s(r)=T_w+\frac{(T_{\text{fus}}-T_w)}{\ln(r_{\text{fus}}/r_w)}\ln(r/r_w) \tag{7}$$

Substituting $T_s(r)$ from Eq. (7) into the interface energy balance equation (4) and solving the resulting differential equation, the location of the phase change interface, r_{fus}, can be evaluated from [6]

$$\begin{aligned} 2\left(\frac{r_{\text{fus}}}{r_w}\right)^2\ln\left(\frac{r_{\text{fus}}}{r_w}\right)-\left(\frac{r_{\text{fus}}}{r_w}\right)^2+1 &= 4\left(\frac{\alpha_{\text{eff}-s}t}{r_w^2}\right)\frac{c_{\text{ps}}(T_{\text{fus}}-T_w)}{h_{\text{fus}}} \\ &= 4\text{Fo}_s\text{St}_s \end{aligned} \tag{8}$$

where Fo_s is the Fourier number of solid eicosane, a dimensionless time parameter that represents the ratio of the heat conduction rate to the rate of thermal energy storage in a solid, and St_s is the Stefan number of the solid eicosane that represents the ratio of sensible heat to latent heat during solidification. Given an effective value of the thermal diffusivity, Eq. (8) may be solved iteratively for the phase change interface location, r_{fus}, at any time.

Siahpush [22] has extensively reviewed the effective thermal conductivity literature and has shown that the model of Calmidi and Mahajan [24] gave the most accurate agreement with the experimental data. They modeled a metal foam consisting of dodecahedronlike cells with 12–14 pentagonal or hexagonal faces. The edges of the cells in the model are formed by individual fibers, as shown in Fig. 6. The lumping of material at the points of intersection of the fibers is taken into account in the structure by a square region. Since the structure shown in Fig. 6 is periodic, it is convenient to consider it a unit cell.

Based on this geometry, Calmidi and Mahajan expressed the effective thermal conductivity as

$$k_{\text{eff}-s}=\left(\frac{2}{\sqrt{3}}\left(\frac{r\frac{\ell}{L}}{k_s+\left(1+\frac{\ell}{L}\right)\frac{k_{\text{por}}-k_s}{3}}+\frac{(1-r)\frac{\ell}{L}}{k_s+\frac{2}{3}\left(\frac{\ell}{L}\right)(k_{\text{por}}-k_s)}+\frac{\frac{\sqrt{3}}{2}-\frac{\ell}{L}}{k_s+\frac{4r}{3\sqrt{3}}\left(\frac{\ell}{L}\right)(k_{\text{por}}-k_s)}\right)\right)^n \tag{9}$$

In Eq. (9), the value of n depends on the porosity of the porous material as well as the type of fluid. Its value varies between -1 and $-1/4$. For the copper foam used in these experiments, the dimensions based on Fig. 6 are given as $\ell=0.096$ cm and $L=0.198$ cm, where $2L$ is the total distance between two intersections.

Calculation of the Effective Thermal Conductivity. If the fusion radius is known from the experimental results, Eq. (8) may be utilized to estimate the effective thermal conductivity of the combined PCM/CPF. Results are shown in Fig. 7. The apparent effective thermal conductivity values are initially quite low, then approach a plateau between 60 min and 100 min, and then finally fall off again after 100 min. For short times, a portion of the heat transfer out of the eicosane is associated with the loss of sensible heat out of the liquid eicosane and CPF in cooling them from 50°C to the fusion temperature, 36.5°C. An additional portion is associated with the loss of sensible heat from the solid eicosane and CPF in cooling them from the fusion temperature to the wall temperature of 10°C. This loss of sensible heat is not included in the analysis that was presented in the development of Eq. (8). In Fig. 7, based on the analytical results, the theoretical model was corrected to account for the sensible heat leaving the eicosane.

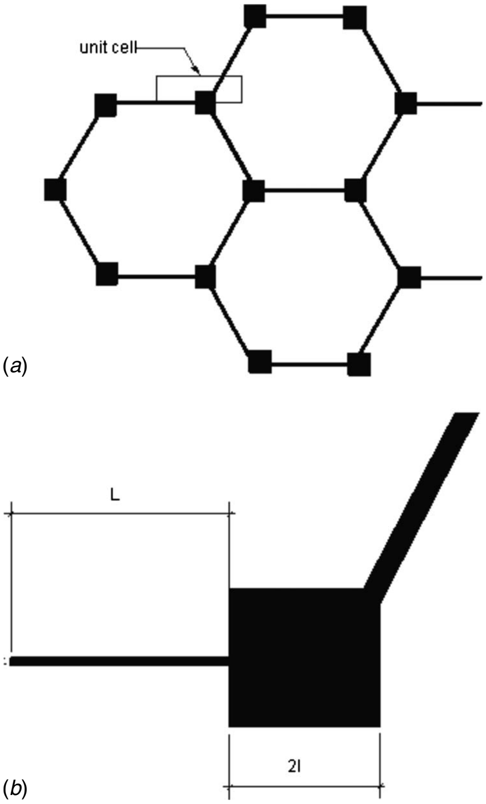

Fig. 6 (*a*) Hexagonal structure of the metal matrix and (*b*) representative unit cell according to the model of Calmidi and Mahajan [24]

Also, although the entire tank system was externally insulated, heat was removed much faster from the eicosane adjacent to the top airspace due to natural convection in the air than from the bulk liquid eicosane and CPF. This cold air caused the top layer of eicosane to freeze prematurely. As time passed, a skin of frozen eicosane formed atop the liquid. Inward and downward cooling of eicosane continued, as presented previously in Fig. 3. This figure shows the convection cooling of the top layer due to the trapped air between eicosane and the lid. This cooling caused downward freezing of eicosane. The one-dimensional model does not ac-

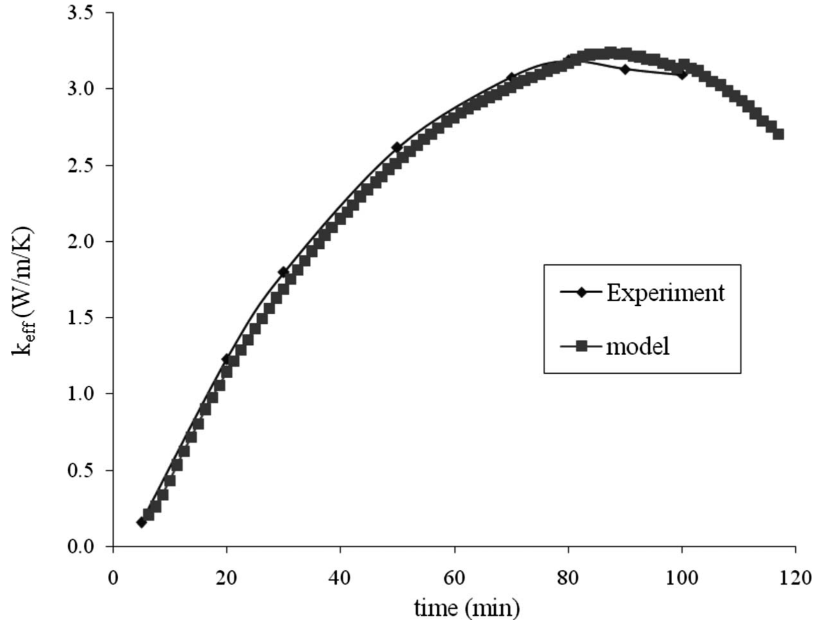

Fig. 7 Theoretical and experimental values of the effective thermal conductivity of the combined eicosane/CPF system

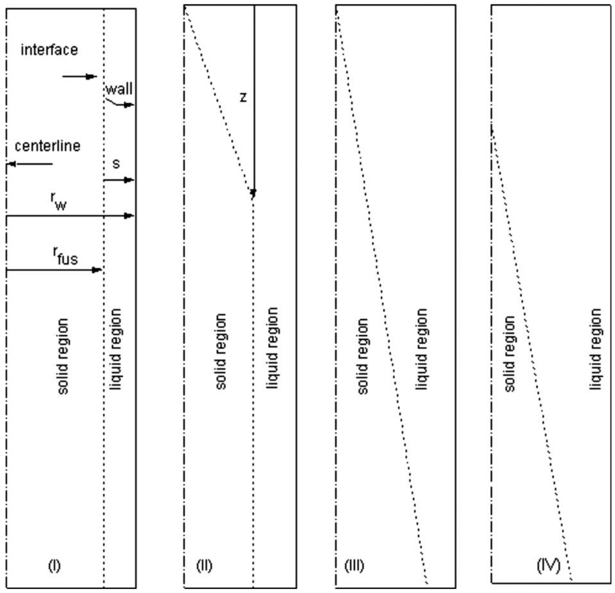

Fig. 8 Four regimes of melting based on the scale analysis of Jany and Bejan [26]

count for this two dimensionality of the experiment. These effects cause the apparent thermal conductivity based on Eq. (8) to be low for short times.

For times greater than 60 min, the temperature everywhere in the system is at or below the fusion temperature and the rate of solidification is relatively low. Based on the procedure described earlier, the apparent thermal conductivity presented in Fig. 7 for times between 60 min and 100 min is selected for the effective thermal conductivity. For large times, the apparent thermal conductivity decreased as the top portion of the freezing front reached the test section centerline. The "best" value was judged to be the value near the peak of the apparent conductivity curve, observed at about 85 min, with a value of 3.06 W/mK. The shift downward of the theoretical values is due to the fact that the theoretical evaluations were based on the fusion temperature of the eicosane, whereas the calculations using the experimental data were based on the initial set point temperature of 50°C.

In the effective thermal conductivity model, a value of $n=-0.31$ resulted in the best match to the experimental average value. The discrepancy between this model (3.14 W/mK) and the value of the effective thermal conductivity (3.06 W/m K) is less than 3%. This model considered not only the porosity but also the geometry of the porous material.

The uncertainty in the effective thermal conductivity values was dependent on the measurement errors in the mass flow rate of the cooling water, temperature differences in the inlet and outlet of the cooling water, and the TCS. These uncertainties were taken from the manufacturer's specifications for each device. By incorporating these error values, and using standard analysis [25], the uncertainty in the effective thermal conductivity was determined to be less than 3.1% [22].

Scale Analysis of Melting Eicosane. During the melting experiments, four regimes, based on the vertical and radial locations of the TCS of melting heat transfer, were observed. These regimes and their main characteristics are presented schematically in Fig. 8 [26]. In this figure, the dashed line represents the phase change interface front. On the right of the dashed line is the liquid region and on its left, the solid region. The melt progresses from the right toward the centerline on the left. The "conduction regime" (I) is dominated strictly by thermal diffusion. The "transition regime" (II) occurs when a natural convection flow carves its own convection-dominated zone in the upper part of the liquid region, while the lower part remains dominated by conduction. The "quasisteady natural convection regime" (III) begins when the convection-dominated zone of the preceding regime fills the entire height of the cylinder. Finally, the arrival of the solid-liquid interface at the centerline marks the beginning of the "variable-height regime" (IV). From this time, the height of the solid/liquid interface decreases steadily until the solid region disappears entirely.

The object of scale analysis is to use the basic principles of convection heat transfer in order to produce order-of-magnitude estimates for quantities of interest (in our case Nusselt number and radius of fusion). When used in conjunction with experimental data, the scale analysis can also be used as a framework for the development of correlations, relating the independent and dependent variables associated with the phenomena. The key to the correct correlation of natural convection melting is the identification of the proper scales of the phenomena in order to construct appropriate correlations for the heat transfer and the melting rate. Jany and Bejan [27,28] have explored and solved several scale analysis cases for melting in an enclosure in Cartesian coordinates. Their approach was adopted and modified to reflect our case of inward melting in a cylindrical coordinate system.

A number of assumptions are made for this analysis. We assumed that the PCM was a pure substance and that the solid/liquid interface was clearly defined, i.e., the PCM had a well-defined fusion temperature; the liquid was Newtonian and incompressible; the fluid flow was laminar and two dimensional (r,z) and had no end effect; the liquid had a Prandtl number greater than 1; the properties were all constant, with the exception of the linear density-temperature relation assumed in the buoyancy term of the momentum equation (the Boussinesq approximation); the porous media were isotropic and homogeneous; the overall volume change due to phase change was negligible; there was no heat source or generation; the porous media were uniform, isotropic, and homogeneous; and finally, the local temperatures of the phase in the voids and porous medium were the same.

Conduction Regime (I). If we can assume that the components and the solid PCM are initially at the fusion temperature, then immediately after $t=0$, the melting process is governed strictly by conduction heat transfer. The heat transfer across the very thin liquid film is absorbed by the latent heat of fusion at the solid-liquid interface. An approximation of the interface equation in cylindrical coordinates can be expressed as [22]

$$2\pi r_{\mathrm{fus}} k_{\mathrm{eff}} H \frac{T_w - T_{\mathrm{fus}}}{r_w - r_{\mathrm{fus}}} \approx \Delta h_{\mathrm{fus}} \frac{dm}{dt} = \Delta h_{\mathrm{fus}} \frac{d}{dt}(\phi \rho_{\mathrm{liq}} \pi (r_w^2 - r_{\mathrm{fus}}^2) H) \tag{10}$$

Integrating Eq. (10) yields the following solution for the radius of fusion in the conduction regime:

$$r_{\mathrm{fus}_{\mathrm{I}}} \approx r_w - H\theta^{1/2} \tag{11}$$

where θ is the dimensionless time defined by

$$\theta = \frac{k_{\mathrm{eff}}(T_w - T_{\mathrm{fus}})}{\phi \rho_l \Delta h_{\mathrm{fus}} H^2} t = \mathrm{St}_l \mathrm{Fo} \tag{12}$$

In Eq. (12), St_l is the liquid Stefan number (for the porous melting case) and is defined as

$$\mathrm{St}_l = \frac{c_{\mathrm{pl}}(T_w - T_{\mathrm{fus}})}{\phi \Delta h_{\mathrm{fus}}} \tag{13}$$

The Nusselt number based on the height is defined as [26]

$$\mathrm{Nu}_{\mathrm{I}} = -\frac{1}{H}\frac{dr_{\mathrm{fus}}}{d\theta} \tag{14}$$

Substitution of Eq. (11) into Eq. (14) yields the Nusselt number for Regime I,

$$\text{Nu}_{\text{I}} \approx \frac{1}{H}\frac{d}{d\theta}(H\theta^{1/2}) \approx \frac{1}{2}\theta^{-1/2} \tag{15}$$

The conduction regime disappears in a relatively short time after the beginning of the experiment. From Eq. (11), we can evaluate the melt thickness (or fusion radius), then evaluate the Nusselt number corresponding to the conduction regime from Eq. (15). In order to validate these parameters, the Nusselt number and the liquid thickness must be evaluated from the data.

Transition/Mixed Regime (II). In the fluid mechanics of porous media, the momentum equations are accompanied by the numerous experimental observations summarized mathematically as Darcy's law [29]. The pressure terms can be eliminated by taking the difference of the cross derivatives, and by using the Boussinesq approximation, $\rho=\rho_0(1-\beta(T-T_0))$, so for a slender thermal boundary layer, Darcy's law can be expressed as [22]

$$\frac{\partial^2\Phi}{\partial r^2} = -\frac{Kg\beta}{\nu_l}\frac{\partial T}{\partial r} \tag{16}$$

where K is the Blake–Kozeny model for the relationship between the permeability and the porosity and d is the metal matrix characteristic pore diameter [12],

$$K = \frac{d^2\phi^3}{175(1-\phi)^2} \tag{17}$$

and Φ is the streamfunction,

$$u = \frac{\partial\Phi}{\partial z}$$

$$w = -\frac{\partial\Phi}{\partial r} \tag{18}$$

Introducing the streamfunction into the energy equation and considering steady-state conditions for negligible kinetic energy, body forces, and no heat generation, the energy equation becomes [22]

$$\frac{\partial\Phi}{\partial z}\frac{\partial T}{\partial r} + \frac{\partial\Phi}{\partial r}\frac{\partial T}{\partial z} = \alpha_{\text{eff-}l}\left(\frac{1}{r}\frac{\partial T}{\partial r} + \frac{\partial^2 T}{\partial z^2}\right) \tag{19}$$

In the thermal boundary layer (upper convection region of the mixed regime), the scale of Eqs. (16) and (19) may be expressed, respectively, as

$$\frac{\Phi}{\delta_z^2} = \frac{Kg\beta}{\nu_l}\frac{\Delta T}{\delta_z} \tag{20}$$

$$\frac{\Phi}{z}\frac{\Delta T}{\delta_z}, \frac{\Phi}{\delta_z}\frac{\Delta T}{z} \approx \alpha_{\text{eff-}l}\left(\frac{\Delta T}{\delta_z^2}, \frac{\Delta T}{z^2}\right) \tag{21}$$

where δ_z is the thickness of the thermal boundary layer. Comparing the terms on the right side of Eq. (21) reveals that the second term is much smaller than the first term and it can be ignored. The streamfunction may be evaluated from Eq. (21) and then substituted into Eq. (20). The result is

$$\delta_z \approx z\text{Ra}_z^{-1/2} \tag{22}$$

$$\text{Ra}_z = \frac{Kg\beta z\Delta T}{\upsilon_{\text{liq}}\alpha_{\text{eff}}} \quad \text{and } \text{Ra}_z = \frac{z}{H}\text{Ra}_H \tag{23}$$

where Ra_z and Ra_H are the Rayleigh numbers based on z and the total height of the cylinder H, respectively.

Substituting Eq. (23) into Eq. (22) yields

$$\delta_z \approx \left(\frac{zH}{\text{Ra}_H}\right)^{1/2} \tag{24}$$

In the lower portion of the melt region during Regime II (the conduction region), the scale of the melt thickness is given as Eq. (11).

The upper convection zone expires at its lower extremity, where δ_z is of the same order of magnitude as the melt thickness of the lower part (conduction zone), $\delta_z \approx r_w - r_{\text{fus}}$, at the conduction-convection level. Equating Eqs. (24) and (11) establishes the height of the convection-dominated regime, z,

$$z \approx H\text{Ra}_H\theta \tag{25}$$

The Nusselt number for Regime II, Nu_{II}, has two components. The first is convection over the z height, and the second is conduction over the remainder of the height $(H-z)$, which was expressed in Eq. (15). For the lower region, the Nusselt number in the convection zone may be expressed as

$$\text{Nu}_{\text{II-conv}} = \frac{q_{\text{cond}}}{2\pi r_{\text{fus}}k_{\text{eff-}l}(T_w - T_{\text{fus}})} \tag{26}$$

where the q_{cond} is the conduction heat transfer across the liquid gap in the lower region of Regime II and is given by

$$q_{\text{cond}} \approx 2\pi r_w k_l(H-z)\frac{T_w - T_{\text{fus}}}{\delta_z} \tag{27}$$

Substituting the q_{cond} definition from Eq. (27) into the Nusselt number expression of Eq. (26), and utilizing Eqs. (15), (24), and (25), produces the transition-regime Nusselt number (Nu_{II}).

$$\text{Nu}_{\text{II}} \approx H\theta^{-1/2} + \text{Ra}_H\theta^{1/2} \tag{28}$$

The Nusselt number for Regime II is made up of two components, one due to conduction in the lower region, the first term on the right of Eq. (28), and the other due to convection, the last term on the right of Eq. (28). This heat transfer scaling law holds at $\theta=0$ until the convection height (z) extends all the way to the bottom of the tank ($z \approx H$).

Next, our attention is directed toward defining the scale of the melt radius for Regime II. At the interface, the convection heat transfer rate (q_{conv}) balances the rate at which latent heat (q_{fus}) is released from the interface. This relation may be expressed as

$$(q_{\text{conv}} = hA\Delta T) \approx \left(q_{\text{fus}} = \phi\rho_{\text{liq}}\Delta h_{\text{fus}}\frac{dV}{dt}\right) \tag{29}$$

The left side of Eq. (29) expresses a relation for the convection heat transfer rate and is expressed as

$$q_{\text{conv}} = \text{Nu}_{\text{II}}k_{\text{eff-}l}(T_w - T_{\text{fus}}) \tag{30}$$

where q_{conv} is the heat transfer per unit height. Substitution of Eq. (10) into Eq. (29) yields

$$q_{\text{fus}} = \phi\pi H\rho_l\Delta h_{\text{fus}}(-2r_{\text{fus}})\frac{dr_{\text{fus}}}{dt} \tag{31}$$

Substituting the value of the Nu_{II} from Eq. (28) into Eq. (30), equating, and then integrating Eq. (31) results in an equation that describes the average position of the interface with respect to the dimensionless time,

$$r_{\text{fus}_{\text{II}}} \approx \sqrt{r_w^2 - H(\theta^{1/2} + \text{Ra}_H\theta^{3/2})} \tag{32}$$

Convection Regime (III). Once the transition/mixed regime ends, the quasisteady convection zone fills the entire liquid space of height H, which is the onset of Regime III. In this regime, the heat transfer and location of the melting front are controlled by the convection contribution of Eq. (28). The conduction term of Eq. (28) disappears, and this Nusselt number scale is the minimum value for Regime III,

$$\text{Nu}_{\text{III}} = \text{Ra}_H^{1/2} \tag{33}$$

In this regime, we can ignore the conduction contribution of Eq. (32), so that the radius of fusion for Regime III can be given by

$$r_{\text{fus}_{\text{III}}} \approx \sqrt{r_w^2 - H\text{Ra}_H\theta^{3/2}} \tag{34}$$

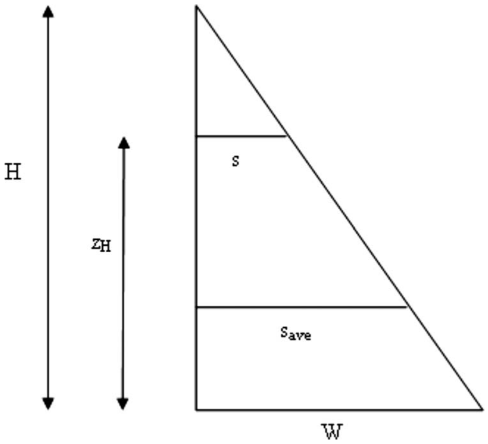

Fig. 9 Idealized interface slope for the variable-height regime (IV) based on the scale analysis of Jany and Bejan [26]

Variable-Height Regime (IV). The onset of Regime IV is defined as the time at which the height of the solid-liquid interface z_H decreases steadily until the solid phase disappears entirely. Therefore, the vertical length scale in the effective Rayleigh number Ra_z decreases with time, so the Nusselt number for this regime may be given by

$$\mathrm{Nu}_{\mathrm{IV}} \approx \mathrm{Ra}_z^{1/2} = \frac{z}{H}\mathrm{Ra}_H^{1/2} \tag{35}$$

Referring to Fig. 9 in Regime IV, the average melt-front position is evaluated based on the assumption that the base of the solid region always has a length of order W (until the solid region disappears entirely). This figure represents the idealized cross section of the interface shape for Regime IV. (To the right of the triangle, the eicosane is melted.) In this figure, z_H is the idealized height of the solid eicosane, s is the actual width of the solid, and s_{ave} is the average width of the solid eicosane. Note that the average nonmelt regime height is assumed to be $z_H/2$.

Based on the geometry of Fig. 9, s_{ave} may be defined as

$$s_{\mathrm{ave}} = r_w - r_{\mathrm{fus}} \approx W\left(\frac{H - \frac{1}{2}z_H}{H}\right) \tag{36}$$

Substituting Eq. (36) into the definition of the Nusselt number from Eq. (14), and comparing it to Eq. (35), yields a relation for z_H,

$$z_H \approx H\sqrt{1 - \frac{H}{W}\mathrm{Ra}_H^{1/2}\theta} \tag{37}$$

Substitution of the z_H value from Eq. (37) into Eqs. (35) and (36) results in expressions for the average melt radius, and the Nusselt number for Regime IV:

$$r_{\mathrm{fus}_{\mathrm{IV}}} \approx r_w - L\left(1 - \frac{1}{2}\left(1 - \frac{H}{W}\mathrm{Ra}_H^{1/2}\theta\right)^2\right) \tag{38}$$

$$\mathrm{Nu}_{\mathrm{IV}} \approx \mathrm{Ra}_z^{1/2} - \frac{H}{W}\mathrm{Ra}_H\theta \tag{39}$$

Figures 10 and 11 show the comparisons between the experimental data and the predictions using scale analysis, for all four regimes, of the radii of fusion, Eqs. (11), (32), (34), and (38) and the Nusselt number, Eqs. (15), (28), (33), and (39), respectively.

The Nusselt number of Regimes I and II started at infinity at the beginning of the experiment. As time progressed, the Nusselt numbers decreased proportionally to $\theta^{1/2}$. The Nusselt number predicted by the scale analysis reached a local minimum value, as the relative importance of conduction decreased and the importance of convection increased. The experimental data show that the Nusselt number decreases monotonically with time.

As the conduction contribution, Regime I disappeared around $\theta = 0.0045$, the transition regime began, introducing a convection cell until its effect eventually dominated the heat transfer mode. Regime II disappeared at about $\theta = 0.0055$. The scale analysis results indicated that in Regime III, the Nusselt number is constant

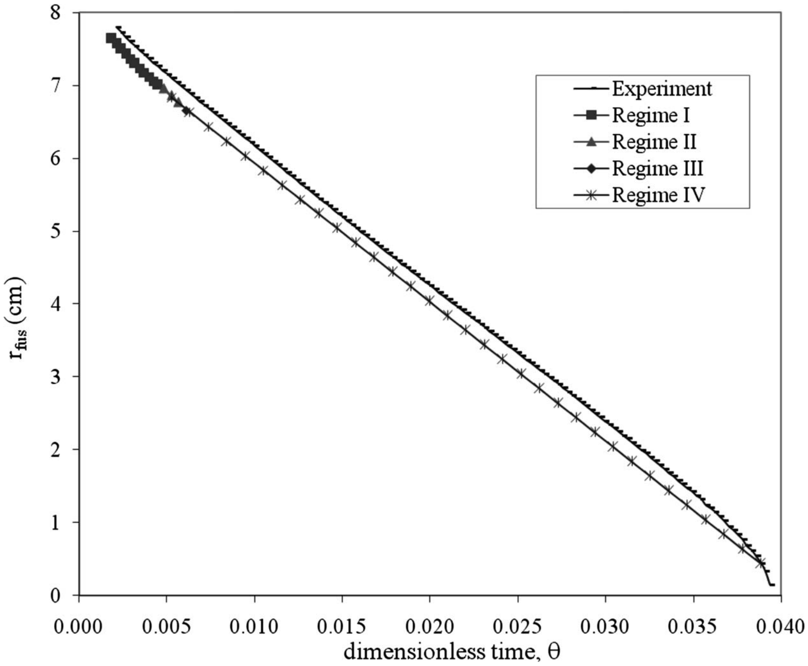

Fig. 10 Comparison of the experimentally determined values of the radius of fusion with the scale analysis predictions over all four melting regimes

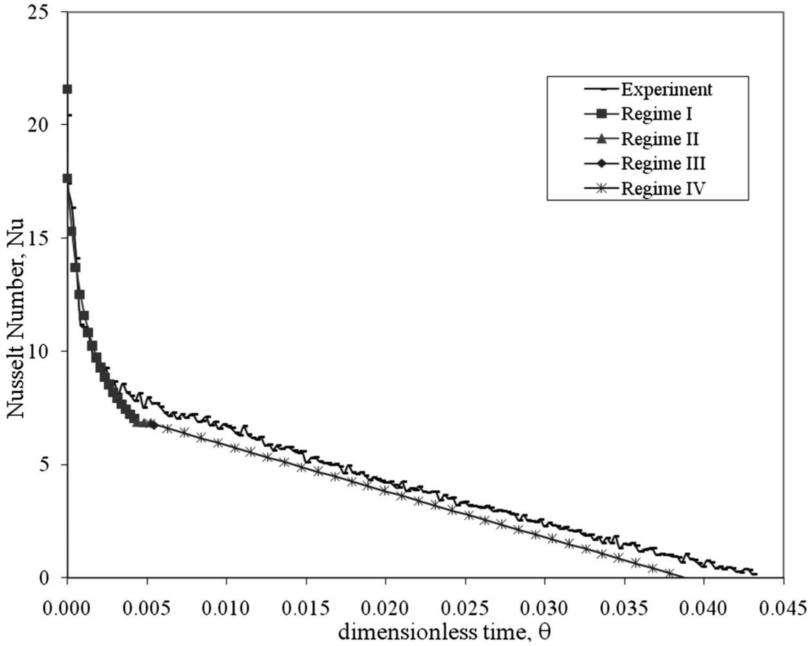

Fig. 11 Comparison of the experimental values of the Nusselt number with the scale analysis predictions over all four melting regimes

with respect to time. Jany and Bejan [28] refer to this as the boundary layer regime, where fluid motion is confined to distinct boundary layers that form distinctly along the heated wall and along the interface front. Most of the core cavity fluid is relatively stagnant and thermally stratified. The convection regime ended at about $\theta=0.006$. From this figure, it can be seen that Regimes II and III disappear after a very short time. This observation is confirmed by the behavior of the melt fronts with CPF shown in Fig. 5(*b*).

Next, the variable-height regime, Regime IV, began. In Regime IV, the Nusselt number decreased monotonically as a function of θ. Experimental results indicated a monotonically decreasing Nusselt number for the rest of the experiment. These figures show that the Regime IV predictions for the Nusselt number and the radius of fusion follow the data closely to the end of the data run.

The uncertainty in the radius of fusion for both freezing and melting was dependent on the relative uncertainty for the mass flow rate of water, the uncertainty of the temperature difference between inlet and outlet of the water flow, and the uncertainty of the temperature differences measured with TCs. The uncertainty in the radius of fusion measurements was determined to be less than 7.8%. The only experimental uncertainty associated with the measured Nusselt number was the instantaneous heat transfer to the eicosane (q_{cond}). The analysis indicated that the error in the Nusselt numbers was typically less than 6.2% [22].

5 Conclusions

A detailed experimental study has been carried out to evaluate the heat transfer performance of a solid/liquid phase change thermal energy storage system, which comprised of eicosane as the PCM and CPF of 95% porosity. The CPF increased the effective thermal conductivity from 0.423 W/m K to 3.06 W/m K. By increasing the effective thermal conductivity, the time to completely freeze the PCM decreased from 375 min to 85 min, and the time to melt decreased from 500 min to 250 min. Detailed quantitative time-dependent volumetric temperature distributions and melt-front motion and shape data were obtained, which showed the effect that the CPF had on the phase change process.

An analytical model of the freezing process was developed, and predictions obtained from the analytical model results were compared to the experimentally measured radius of fusion values. We showed that the Calmidi and Mahajan model for the effective thermal conductivity of the combined PCM/CPF system agreed to within 3% of the experimentally determined value. Their model considered not only the porosity but also the geometric structure of the porous material.

For melting with and without the CPF, we found, using a scale analysis, that it could be characterized by four heat transfer regimes, each with its own melt location scaling rules and Nusselt numbers. The melting process for the porous case clearly showed that the CPF had a significant effect in enhancing the heat transfer process, despite the attenuation of natural convection due to the flow resistance. The curvature of the phase change interface was not as pronounced as what was encountered during melting without the CPF, which is expected because of the high effective conductivity of the combined PCM/CPF system. The scaling model predictions were compared to the experimentally measured radius of fusion values and the results were within 10% of the data measurements in the worst case.

Nomenclature

A = area
c_p = specific heat at constant pressure
d = matrix characteristic pore diameter
Fo = Fourier number, $\alpha t/(2r_w)^2$
g = gravitational constant
Δh_{fus} = latent heat of fusion
H = vertical length scale of cylinder
k = thermal conductivity
K = permeability
ℓ = length dimension in metal matrix
L = length dimension in metal matrix
m = mass
n = modeling exponent
Nu = Nusselt number
r = radial distance
Ra = Rayleigh number
s = solid thickness variable
St = Stefan number, $c_p\Delta T/\Delta h_{\mathrm{fus}}$

t = time
T = temperature
u, w = velocity variables
V = volume of tank
W = width dimension in Regime IV
z = lengthwise coordinate

Subscripts

ave = average
cond = conduction
conv = convection
eff = effective property
fus = fusion
H = height
i = phase
l = liquid
por = porous media
pl = liquid portion of saturated porous media
ps = solid portion of saturated porous media
s = solid
w = wall
0 = initial value
I, II, III, IV = convection regimes

Greek

α = thermal diffusivity
β = isothermal compressibility
δ_z = thermal boundary layer thickness
ϕ = porosity
Φ = streamfunction
ν = kinematic viscosity
ρ = density
θ = dimensionless time

References

[1] Viskanta, R., Bathelt, R., and Hale, N. W., 1980, "Latent Heat-of-Fusion Energy Storage: Experiments on Heat Transfer During Solid-Liquid Phase Change," *Alternative Energy Sources III: Proceedings of the Third Miami Conference on Alternative Energy Sources*, Hemisphere, Washington, DC.

[2] Carslaw, H. S., and Jaeger, J. C., 1959, *Conduction of Heat in Solids*, Clarendon, Oxford, England.

[3] Majumdar, A. S., Ashraf, F. A., and Weber, M. E., 1979, "PMC Thermal Energy Storage in Cylindrical Containers of Various Configurations," *Proceedings of the Second International Conference on Alternative Energy Sources*, Miami, Dec.

[4] Pannu, J., Joglekar, G., and Rice, P. A., 1980, "Natural Convection Heat Transfer to Cylinders of Phase Change Material Used for Thermal Storage," AIChE Symp. Ser., **76**(198), pp. 47–55.

[5] Sparrow, E. M., and Broadbent, J. A., 1983, "Freezing in a Vertical Tube," ASME J. Heat Transfer, **105**, pp. 217–225.

[6] Lunardini, V. J., 1991, *Heat Transfer With Freezing and Thawing*, Elsevier Science, New York.

[7] Poulikakous, D., 1994, *Conduction Heat Transfer*, Prentice-Hall, Englewood Cliffs, NJ.

[8] Akgün, M., Aydın, O., and Kaygusuz, K., 2007, "Experimental Study on Melting/Solidification Characteristics of a Paraffin as PCM," Energy Convers. Manage., **48**, pp. 669–678.

[9] Koh, J. C. Y., and Stevens, R. L., 1976, "Enhancement of Cooling Effectiveness by Porous Material in Coolant Passage," ASME J. Heat Transfer, **97**, pp. 309–311.

[10] Weaver, J. A., and Viskanta, R., 1986, "Freezing of Liquid-Saturated Porous Media," ASME J. Heat Transfer, **108**, pp. 654–659.

[11] Weaver, J. A., and Viskanta, R., 1986, "Melting of Frozen, Porous Media Contained in a Horizontal or Vertical Cylinder Capsule," Int. J. Heat Mass Transfer, **29**, pp. 1943–1951.

[12] Tong, X., and Khan, J. A., 1996, "Enhancement of Heat Transfer by Inserting a Metal Matrix Into a Phase Change Material," Numer. Heat Transfer, Part A, **30**, pp. 125–141.

[13] Py, X., Olives, R., and Mauran, S., 2001, "Paraffin/Porous-Graphite-Matrix Composite as a High and Constant Power Thermal Storage Material," Int. J. Heat Mass Transfer, **44**, pp. 2727–2737.

[14] Trelles, J. P., and Dufly, J. J., 2003, "Numerical Simulation of Porous Latent Heat Thermal Energy Storage for Thermoelectric Cooling," Appl. Therm. Eng., **23**, pp. 1647–1664.

[15] Mesalhy, O., Lafdi, K., Elgafy, A., and Bowman, K., 2005, "Numerical Study for Enhancing the Thermal Conductivity of Phase Change Material (PCM) Storage Using High Thermal Conductivity Porous Matrix," Energy Convers. Manage., **46**, pp. 847–867.

[16] Bejan, A., 1995, *Convection Heat Transfer*, 2nd ed., Wiley, New York.

[17] Bejan, A., 2003, "Simple Methods for Convection in Porous Media: Scale Analysis and the Intersection of Asymptotes," Int. J. Energy Res., **27**, pp. 859–874.

[18] Kim, S., and Kim, M. C., 2002, "A Scale Analysis of Turbulent Heat Transfer Driven by Buoyancy in a Porous Layer With Homogeneous Heat Sources," Int. Commun. Heat Mass Transfer, **29**, pp. 127–134.

[19] Sarris, I. E., Lekakis, I., and Vlachos, N. S., 2004, "Natural Convection in Rectangular Tanks Heated Locally From Below," Int. J. Heat Mass Transfer, **47**, pp. 3549–3563.

[20] Hale, D. V., Hoover, M. J., and O'Neill, M. J., 1971, "Phase Change Handbook," NASA Contractor Report No. NASA-CR-61363.

[21] Incropera, F. P., and Dewitt, D. P., 1990, *Fundamentals of Heat and Mass Transfer*, Wiley, New York.

[22] Siahpush, A., 2002, "Performance of Solid/Liquid Phase-Change Thermal Energy Storage Systems Through the Use of a High Conductivity Porous Metal Matrix," Ph.D. thesis University of Idaho, Idaho.

[23] Beckermann, C., and Viskanta, R., 1988, "Natural Convection Solid/Liquid Phase Change in Porous Medium," Int. J. Heat Mass Transfer, **31**, pp. 35–46.

[24] Calmidi, V. V., and Mahajan, R. L., 1999, "The Effective Thermal Conductivity of High Porosity Fibrous Metal Foams," ASME J. Heat Transfer, **121**, pp. 466–471.

[25] Coleman, H. W., and Steele, W. G., 1989, *Experimentation and Uncertainty Analysis for Engineers*, Wiley, New York.

[26] Jany, P., and Bejan, A., 1988, "Scale of Melting in the Presence of Natural Convection in a Rectangular Cavity Filled With Porous Medium," ASME J. Heat Transfer, **110**, pp. 526–528.

[27] Jany, P., and Bejan, A., 1988, "Scaling Theory of Melting With Natural Convection in an Enclosure," Int. J. Heat Mass Transfer, **31**(6), pp. 1221–1235.

[28] Jany, P., and Bejan, A., 1987, "Melting in Presence of Natural Convection in a Rectangular Cavity Filled With Porous Medium," Department of Mechanical Engineering and Material Science, Duke University, Report No. DU-AB-4.

[29] Burmeister, L. C., 1993, *Convective Heat Transfer*, Wiley, New York.

Variable Physical Properties in Natural Convective Gas Microflow

Huei Chu Weng

Cha'o-Kuang Chen[1]
e-mail: ckchen@mail.ncku.edu.tw

Department of Mechanical Engineering,
National Cheng Kung University,
Tainan 701, Taiwan, R.O.C

Anisothermal flow prevails in a heated microchannel. It is desirable to understand the influence of temperature-dependent physical properties on the flow and heat transfer characteristics for natural convective gas microflow. In this study, formulas for the shear viscosity, thermal conductivity, constant-pressure specific heat, density, and molecular mean free path are proposed in power-law form and validated through experimental data. Natural convective gas flow with variable physical properties in a long open-ended vertical parallel-plate microchannel with asymmetric wall temperature distributions is further investigated. The full Navier–Stokes equations and energy equation combined with the first-order slip/jump boundary conditions are employed. Analysis process shows that the compressibility and viscous dissipation terms in balance equations are negligible. Numerical solutions are presented for air at the standard reference state with complete accommodation. It is found that the effect of variable properties should be considered for hotter-wall temperatures greater than 306.88 K. The effect is to advance the velocity slip and temperature jump as well as the velocity symmetry and temperature nonlinearity. Moreover, it tends to reduce the mass flow rate and the local heat transfer rate excluding on the cooler-wall surface where the temperature-jump effect prevails over the temperature-nonlinearity effect. Increasing the cooler-wall temperature magnifies the effect on flow behavior but minifies that on thermal behavior. [DOI: 10.1115/1.2927400]

1 Introduction

Natural convective gas microflow, encountered in many engineering fields, e.g., microelectrochemical cell transport, microheat exchanging, and microchip cooling, is an attractive branch of microfluidics [1] due to its reliability, simplicity, and cost effectiveness in flow and heat transfer mechanism. Chen and Weng [2] initiated the analytical study of steady fully developed natural convection for air in an open-ended vertical parallel-plate microchannel with asymmetric temperature distributions. In this work, the Navier–Stokes equations and energy equation subject to the first-order slip/jump boundary conditions were solved. The effects of rarefaction and fluid-wall interaction were shown to increase the flow rate and to decrease the heat transfer rate. Haddad et al. [3] later reported implicit finite-difference simulations of the developing natural convection in an isothermally heated microchannel filled with porous media. Chen and Weng [4] further investigated the importance of thermal creep and high-order slip/jump in the developing region for both symmetric- and asymmetric-heating cases. Recently, Avci and Aydin [5] analytically investigated the effect of pressure gradient on the gas microflow obtained by Chen and Weng [2], the so-called mixed convective gas microflow.

Previous studies have been done using the Boussinesq approximation [6] to simplify the solutions of practical problems. The usual approximation is based on two principles.

1. Variation of fluid density is considered only in the buoyancy term of the momentum balance equation.
2. Other physical properties are assumed constant.

Ignoring the importance of physical property variation in convective flow with large temperature difference between the hotter wall and the ambient fluid or the cooler wall could cause considerable deviation from the accurate estimation of flow and thermal fields as well as the corresponding characteristics. Natural convective gas microflow with variable physical properties should be studied extensively.

In the present work, the natural convective gas flow in a long open-ended parallel-plate microchannel with asymmetric wall temperature distributions is studied. The main goal is to predict the effect of variable physical properties in the anisothermal microflow. The shear viscosity, thermal conductivity, constant-pressure specific heat, density, and molecular mean free path are assumed to vary with absolute temperature according to a simple power law. Experimental data are used to validate these power-law models. Based on a perturbation analysis, the full Navier–Stokes equations and energy equation are simplified, and the simplified equations subject to the first-order slip/jump boundary conditions are numerically solved by using an implicit finite-difference procedure. The validation of the mathematical model and the numerical code is established by comparing our results with available theoretical and experimental results. The effect of variable physical properties on the flow and thermal fields as well as the corresponding characteristics for different values of the hotter-wall temperature parameter and Knudsen number at different ratios of the wall-ambient temperature differences is then investigated.

2 Basic Equations

The field equations derived from the balance principles for mass, momentum, and energy [7] are

$$\frac{d\rho}{dt} + \rho \nabla \cdot \mathbf{u} = 0 \tag{2.1}$$

$$\rho \frac{d\mathbf{u}}{dt} = -\nabla p - \frac{2}{3}\nabla(\mu \nabla \cdot \mathbf{u}) + \nabla \cdot (\mu((\nabla \mathbf{u})^T + \nabla \mathbf{u})) + \rho \mathbf{f} \tag{2.2}$$

$$\rho c_p \frac{dT}{dt} = \nabla \cdot (k \nabla T) + \beta T \frac{dp}{dt} + \mu \Phi + \rho h \tag{2.3}$$

where d/dt is the material derivative, $\mathbf{u}$ is the velocity vector, p is the pressure, T is the temperature, $\mathbf{f}$ is the body force vector, h is

---

[1] Corresponding author.

Contributed by the Heat Transfer Division of ASME for publication in the JOURNAL OF HEAT TRANSFER. Manuscript received January 6, 2007; final manuscript received March 11, 2008; published online May 29, 2008. Review conducted by Ben Q. Li.

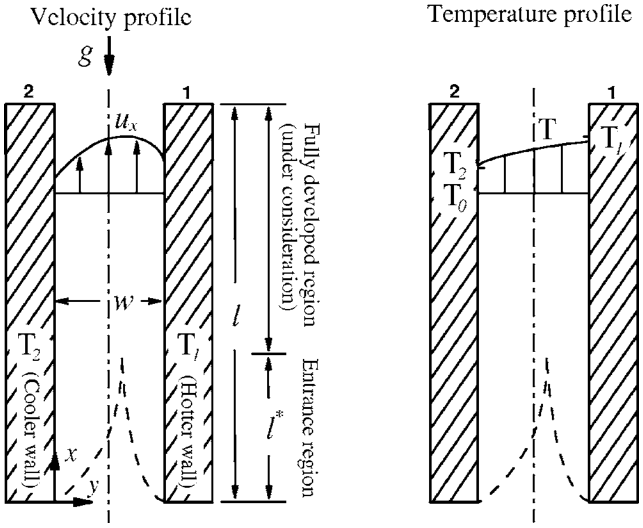

Fig. 1 Geometric sketch and parameters of natural convection in the microchannel

the internal heat generation rate, ρ is the density, μ is the shear viscosity, c_p is the constant-pressure specific heat, k is the thermal conductivity, β is the thermal expansion coefficient, and Φ is a function characterizing the viscous dissipation, defined in index notation as

$$\Phi=(u_{i,j}u_{i,j}+u_{i,j}u_{j,i})-\frac{2}{3}(u_{i,i})^2 \tag{2.4}$$

where u_i is the velocity in index notation. Recognizing the ideal gas law $p=\rho RT$, where R is the specific gas constant, gives $\beta=1/T$. Furthermore, let the pressure p be characterized by the "pressure defect" $\hat{p}=p-p_h$, where p_h is the hydrostatic pressure. Then, Eqs. (2.2) and (2.3) become

$$\rho\frac{d\mathbf{u}}{dt}=-\nabla\hat{p}+(\rho-\rho_0)\mathbf{g}-\frac{2}{3}\nabla(\mu\nabla\cdot\mathbf{u})+\nabla\cdot(\mu((\nabla\mathbf{u})^T+\nabla\mathbf{u})) \tag{2.5}$$

$$\rho c_p\frac{dT}{dt}=\nabla\cdot(k\nabla T)+\frac{d\hat{p}}{dt}+\rho_0\mathbf{g}\cdot\mathbf{u}+\mu\Phi \tag{2.6}$$

where $\mathbf{g}$ is the gravitational field vector and the subscript 0 denotes the inlet values. Here, we have replaced the body force with the gravitational force and neglected the internal heat generation.

Consider a vertical duct formed between two parallel plates (an open-ended vertical parallel-plate channel). The plates are kept at a distance w apart and maintained at uniform temperatures T_1 and T_2 ($T_1\geq T_2$). Let x and y denote the usual rectangular coordinates, let u_x and u_y denote the components of velocity field, and assume that the channel is parallel to the direction of the gravitational body force with $\mathbf{g}=(g_x,g_y)=(-g,0)$, as shown in Fig. 1. The field equations described by Eqs. (2.1), (2.5), and (2.6) for two-dimensional steady flow are

$$\frac{\partial(\rho u_x)}{\partial x}+\frac{\partial(\rho u_y)}{\partial y}=0 \tag{2.7}$$

$$\rho\left(u_x\frac{\partial u_x}{\partial x}+u_y\frac{\partial u_x}{\partial y}\right)=-\frac{\partial\hat{p}}{\partial x}+(\rho_0-\rho)g-\frac{2}{3}\frac{\partial}{\partial x}\left(\mu\left(\frac{\partial u_x}{\partial x}+\frac{\partial u_y}{\partial y}\right)\right)+2\frac{\partial}{\partial x}\left(\mu\frac{\partial u_x}{\partial x}\right)+\frac{\partial}{\partial y}\left(\mu\left(\frac{\partial u_y}{\partial x}+\frac{\partial u_x}{\partial y}\right)\right) \tag{2.8}$$

$$\rho\left(u_x\frac{\partial u_y}{\partial x}+u_y\frac{\partial u_y}{\partial y}\right)=-\frac{\partial\hat{p}}{\partial y}-\frac{2}{3}\frac{\partial}{\partial y}\left(\mu\left(\frac{\partial u_x}{\partial x}+\frac{\partial u_y}{\partial y}\right)\right)+2\frac{\partial}{\partial y}\left(\mu\frac{\partial u_y}{\partial y}\right)+\frac{\partial}{\partial x}\left(\mu\left(\frac{\partial u_y}{\partial x}+\frac{\partial u_x}{\partial y}\right)\right) \tag{2.9}$$

$$\begin{aligned}\rho c_p\left(u_x\frac{\partial T}{\partial x}+u_y\frac{\partial T}{\partial y}\right)&=\frac{\partial}{\partial x}\left(k\frac{\partial T}{\partial x}\right)+\frac{\partial}{\partial y}\left(k\frac{\partial T}{\partial y}\right)+\left(u_x\frac{\partial\hat{p}}{\partial x}+u_y\frac{\partial\hat{p}}{\partial y}\right)\\&\quad-\rho_0 g u_x+\mu\left(2\left(\left(\frac{\partial u_x}{\partial x}\right)^2+\left(\frac{\partial u_y}{\partial y}\right)^2\right)\right.\\&\quad\left.+\left(\frac{\partial u_x}{\partial y}+\frac{\partial u_y}{\partial x}\right)^2-\frac{2}{3}\left(\frac{\partial u_x}{\partial x}+\frac{\partial u_y}{\partial y}\right)^2\right)\end{aligned} \tag{2.10}$$

Anisothermal flow prevails in a heated microchannel. It becomes necessary to have realistic formulas for temperature-dependent physical properties. For air, the effect of temperature on the shear viscosity and thermal conductivity can be closely approximated using the Sutherland-law forms [8]:

$$\mu=\mu_0\left(\frac{T}{T_0}\right)^{1.5}\left(\frac{T_0+107.9}{T+107.9}\right) \tag{2.11}$$

$$k=k_0\left(\frac{T}{T_0}\right)^{1.5}\left(\frac{T_0+202.2}{T+202.2}\right) \tag{2.12}$$

Such expressions are still complicated. Schlichting [9] proposed a simple expression for μ written as

$$\mu=\mu_0\left(\frac{T}{T_0}\right)^{\omega} \tag{2.13}$$

According to the power-law form, the expression for k can be written as

$$k=k_0\left(\frac{T}{T_0}\right)^{\varpi} \tag{2.14}$$

Here, ω and ϖ are the viscosity and conductivity indices, respectively. Shang and Wang [10] provided a possible approximation for the constant-pressure specific heat:

$$c_p=c_{p0}\left(\frac{T}{T_0}\right)^{\varpi-\omega} \tag{2.15}$$

However, the model predicts a convex curve that is different from the actual one (a concave curve). We propose a new model as follows:

$$c_p=c_{p0}\left(2+s\left(\frac{T}{T_0}-1\right)-\left(\frac{T}{T_0}\right)^{\varpi-\omega}\right) \tag{2.16}$$

where s is a coefficient. If the shear viscosity, thermal conductivity, and specific heat are known at two temperatures, one can determine the values of ω, ϖ, and s. In Table 1, 300 K and 600 K are used for the constant determination of common gases. In addition, the approximation for the density can be expressed as

$$\rho=\rho_0\left(\frac{T}{T_0}\right)^{-1} \tag{2.17}$$

In Fig. 2, we verify the present formulas (2.13), (2.14), (2.16), and (2.17) for air. The calculated results compare very well with the experimental data listed by Suryanarayana [11]. The percentage absolute errors for μ, k, c_p, and ρ over $300\leq T\leq 600$ are less than 0.88, 0.39, 0.31, and 0.11, respectively. Results also show that formulas (2.12) and (2.15) cause the more apparent disagreements.

The average distance between molecular collisions is called the molecular mean free path. It plays an important role in microflow behavior, related to the temperature and pressure of gases by

Table 1 Physical properties of common gases at the standard reference state [11]

Parameters	Air	Nitrogen (N_2)	Helium (He)	Argon (Ar)
Viscosity (μ) (kg/s m)$\times 10^{-5}$	1.842	1.774	1.982	2.259
Thermal conductivity (k) (W/m K)	0.0261	0.0258	0.149	0.0176
Constant-pressure specific heat (c_p) (J/K kg)	1007	1041	5197	521.6
Density (ρ) (kg/m^3)	1.185	1.131	0.164	1.634
Mean free path (λ) (m)$\times 10^{-7}$	0.666	0.657	1.928	0.696
Ratio of specific heats (γ)	1.399	1.406	1.664	1.663
Prandtl number (Pr)	0.712	0.717	0.689	0.669
Viscosity index (ω)	0.712	0.707	0.685	0.755
Conductivity index (ϖ)	0.799	0.784	0.720	0.766
Specific-heat coefficient (s)	0.1059	0.0882	0.0246	0.00574

$$\lambda = \frac{\sqrt{\pi RT/2}\mu}{p} \tag{2.18}$$

For the microflow considered here, the closed form is

$$\lambda = \lambda_0\left(\frac{T}{T_0}\right)^{\omega+1/2} \tag{2.19}$$

3 Analysis

The study of fully developed flow is useful and instructive because it yields the closed form solutions in the channel as the limiting conditions for the developing flow. A detailed study for pressure-driven flow was performed by Arkilic et al. [12] by using a perturbation analysis. Following the analysis, we introduce the following dimensionless parameters:

$$X = \frac{x}{l}, \quad Y = \frac{y}{l_c}, \quad U = \frac{u_x}{u_c}, \quad V = \frac{u_y}{u_c}, \quad \Theta = \frac{T - T_0}{T_1 - T_0}, \quad P = \frac{\hat{p}}{p_c}$$

$$\chi = \beta_0(T_1 - T_0), \quad \Lambda_1 = \frac{\rho_0^2 g^2 \beta_0 l_c^4}{k_0 \mu_0}, \quad \Lambda_2 = \frac{\mu_0 g \beta_0 l_c}{k_0}$$

$$\mathrm{Pr} = \frac{c_{p0}\mu_0}{k_0}, \quad \delta = \frac{l_c}{l} \tag{3.1}$$

where χ is the hotter-wall temperature parameter, Λ_1, Λ_2 are the parameters reflected the size effect, Pr is the Prandtl number, and δ is the perturbation variable. Here, the characteristic length, velocity, and pressure are, respectively, defined as

$$l_c = w, \quad u_c = \frac{\rho_0 g \beta_0 (T_1 - T_0) l_c^2}{\mu_0}, \quad p_c = \rho_0 u_c^2 \tag{3.2}$$

Substituting Eq. (3.1) into Eqs. (2.7)–(2.10) gives

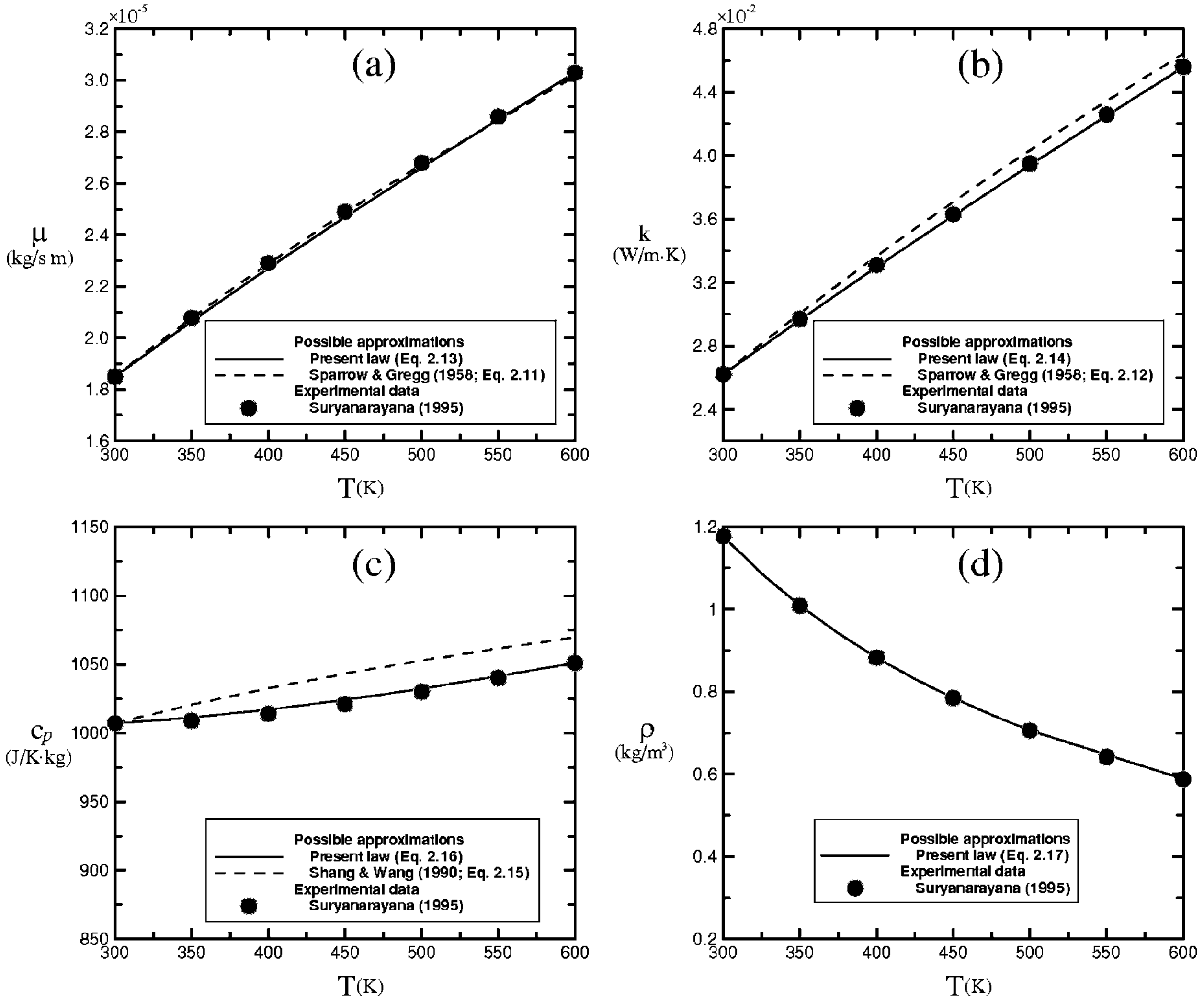

Fig. 2 [(*a*)–(*d*)] Possible approximations of the experimental property data listed by Suryanarayana [11]; T_0=298.15 K

$$\delta\frac{\partial}{\partial X}\left(\frac{U}{1+\chi\Theta}\right)+\frac{\partial}{\partial Y}\left(\frac{V}{1+\chi\Theta}\right)=0 \tag{3.3}$$

$$\begin{aligned}\frac{1}{1+\chi\Theta}\left(\delta U\frac{\partial U}{\partial X}+V\frac{\partial U}{\partial Y}\right)
&= -\delta\frac{\partial P}{\partial X}+\frac{\Lambda_2}{\Lambda_1\chi}\left(\frac{\Theta}{1+\chi\Theta}\right)\\
&\quad -\frac{2}{3}\frac{\Lambda_2}{\Lambda_1\chi}\frac{\partial}{\partial X}\left((1+\chi\Theta)^{\omega}\left(\delta^2\frac{\partial U}{\partial X}+\delta\frac{\partial V}{\partial Y}\right)\right)\\
&\quad +2\frac{\Lambda_2}{\Lambda_1\chi}\frac{\partial}{\partial X}\left((1+\chi\Theta)^{\omega}\delta^2\frac{\partial U}{\partial X}\right)\\
&\quad +\frac{\Lambda_2}{\Lambda_1\chi}\frac{\partial}{\partial Y}\left((1+\chi\Theta)^{\omega}\left(\delta\frac{\partial V}{\partial X}+\frac{\partial U}{\partial Y}\right)\right)\end{aligned} \tag{3.4}$$

$$\begin{aligned}\frac{1}{1+\chi\Theta}\left(\delta U\frac{\partial V}{\partial X}+V\frac{\partial V}{\partial Y}\right)
&= -\frac{\partial P}{\partial Y}-\frac{2}{3}\frac{\Lambda_2}{\Lambda_1\chi}\frac{\partial}{\partial Y}\left((1+\chi\Theta)^{\omega}\left(\delta\frac{\partial U}{\partial X}+\frac{\partial V}{\partial Y}\right)\right)\\
&\quad +2\frac{\Lambda_2}{\Lambda_1\chi}\frac{\partial}{\partial Y}\left((1+\chi\Theta)^{\omega}\frac{\partial V}{\partial Y}\right)\\
&\quad +\frac{\Lambda_2}{\Lambda_1\chi}\frac{\partial}{\partial X}\left((1+\chi\Theta)^{\omega}\left(\delta^2\frac{\partial V}{\partial X}+\delta\frac{\partial U}{\partial Y}\right)\right)\end{aligned} \tag{3.5}$$

$$\begin{aligned}\frac{2+s\chi\Theta-(1+\chi\Theta)^{\varpi-\omega}}{1+\chi\Theta}\left(\delta U\frac{\partial \Theta}{\partial X}+V\frac{\partial \Theta}{\partial Y}\right)
&= \frac{\Lambda_2}{\mathrm{Pr}\,\Lambda_1\chi}\frac{\partial}{\partial X}\left((1+\chi\Theta)^{\varpi}\delta^2\frac{\partial \Theta}{\partial X}\right)\\
&\quad +\frac{\Lambda_2}{\mathrm{Pr}\,\Lambda_1\chi}\frac{\partial}{\partial Y}\left((1+\chi\Theta)^{\varpi}\frac{\partial \Theta}{\partial Y}\right)+\frac{\Lambda_1\chi}{\mathrm{Pr}}\left(\delta U\frac{\partial P}{\partial X}+V\frac{\partial P}{\partial Y}\right)\\
&\quad -\frac{\Lambda_2}{\mathrm{Pr}\,\chi}U+\frac{\Lambda_2}{\mathrm{Pr}}(1+\chi\Theta)^{\omega}\left(2\left(\delta^2\left(\frac{\partial U}{\partial X}\right)^2+\left(\frac{\partial V}{\partial Y}\right)^2\right)\right.\\
&\quad \left.+\left(\frac{\partial U}{\partial Y}+\delta\frac{\partial V}{\partial X}\right)^2-\frac{2}{3}\left(\delta\frac{\partial U}{\partial X}+\frac{\partial V}{\partial Y}\right)^2\right)\end{aligned} \tag{3.6}$$

The two terms in continuity equation (3.3) must be of the same order of magnitude; moreover, the buoyancy term in the momentum equation (3.4) will be of the same order of magnitude as the largest of the other terms. Hence, we expand U, V, P, and Θ in powers of δ as follows:

$$U=U_0+\delta U_1,\quad V=\delta V_0,\quad P=P_0+\delta P_1,\quad \Theta=\Theta_0+\delta\Theta_1 \tag{3.7}$$

Substituting Eq. (3.7) into Eqs. (3.3)–(3.6) and considering the usual fully developed limit (i.e., $\delta \ll 1$, a sufficiently long channel), we obtain the reduced forms

$$\frac{\partial}{\partial X}\left(\frac{U}{1+\chi\Theta}\right)+\frac{\partial}{\partial Y}\left(\frac{V}{1+\chi\Theta}\right)=0 \tag{3.8}$$

$$\frac{\partial}{\partial Y}\left((1+\chi\Theta)^{\omega}\frac{\partial U}{\partial Y}\right)=-\frac{\Theta}{1+\chi\Theta} \tag{3.9}$$

$$\frac{\partial}{\partial Y}\left((1+\chi\Theta)^{\varpi}\frac{\partial \Theta}{\partial Y}\right)-\Lambda_1 U+\Lambda_1\chi(1+\chi\Theta)^{\omega}\left(\frac{\partial U}{\partial Y}\right)^2=0 \tag{3.10}$$

Here, the characters U_0, V_0, and Θ_0 have been replaced with U, V, and Θ, respectively. For convective gas microflow ($l_c < 1$ mm), the value of the size-dependent parameter Λ_1 is always less than 10^{-6}, e.g., $\Lambda_1 < 9.44\times 10^{-7}$ for air and $\Lambda_1 < 2.93\times 10^{-9}$ for helium at the standard reference state. We can, therefore, omit the last two terms (compressibility and viscous dissipation terms) in Eq. (3.10). Reduced energy equation with isothermally heated boundary conditions implies $\Theta(Y)$. A solution of Eq. (3.9) in the form $\Theta(Y)$ is only possible if U is a function of Y position only, i.e., $\partial U/\partial X=0$. The normalized field equations then become

$$V=0 \tag{3.11}$$

$$\frac{d}{dY}\left((1+\chi\Theta)^{\omega}\frac{dU}{dY}\right)=-\frac{\Theta}{1+\chi\Theta} \tag{3.12}$$

$$\frac{d}{dY}\left((1+\chi\Theta)^{\varpi}\frac{d\Theta}{dY}\right)=0 \tag{3.13}$$

The normalized boundary conditions, which describe velocity slip and temperature-jump conditions at the fluid-wall interface, are

$$\begin{aligned}U(0)&=\frac{2-\sigma_v}{\sigma_v}\mathrm{Kn}(0)\frac{\partial U(0)}{\partial Y}\\
U(1)&=-\frac{2-\sigma_v}{\sigma_v}\mathrm{Kn}(1)\frac{\partial U(1)}{\partial Y}\end{aligned} \tag{3.14}$$

$$\begin{aligned}\Theta(0)&=\xi+\frac{2-\sigma_t}{\sigma_t}\frac{2\gamma}{\gamma+1}\frac{1}{\mathrm{Pr}}\mathrm{Kn}(0)\frac{\partial\Theta(0)}{\partial Y}\\
\Theta(1)&=1-\frac{2-\sigma_t}{\sigma_t}\frac{2\gamma}{\gamma+1}\frac{1}{\mathrm{Pr}}\mathrm{Kn}(1)\frac{\partial\Theta(1)}{\partial Y}\end{aligned} \tag{3.15}$$

where

$$\mathrm{Kn}=\frac{\lambda}{l_c}=\frac{\lambda_0}{l_c}\left(\frac{T}{T_0}\right)^{\omega+1/2}=\mathrm{Kn}_0(1+\chi\Theta)^{\omega+1/2},\qquad \xi=\frac{T_2-T_0}{T_1-T_0} \tag{3.16}$$

For simplicity, we have considered the first-order slip/jump law of Maxwell [13]. Here, γ is the ratio of specific heats, σ_v and σ_t are the tangential momentum and thermal accommodation coefficients, respectively, Kn is the Knudsen number, and ξ is the wall-ambient temperature difference ratio. It should be noted that σ_v and σ_t are the parameters that describe the fluid-wall interaction (related to the material and quality of channel wall, i.e., its type and roughness). The two accommodation coefficients range from near 0 to 1, where the two values, respectively, represent specular accommodation and complete (or diffuse) accommodation.

An important parameter for microflow is the mass flow rate $\dot{m}$. The dimensionless mass flow rate is

$$\dot{M}=\frac{\dot{m}}{\rho_0 u_c l_c}=\int_0^1\frac{U}{1+\chi\Theta}dY \tag{3.17}$$

An important parameter for microheat transfer is the heat transfer rate q. The dimensionless local heat transfer rate, expressed as the Nusselt number, is

$$\mathrm{Nu}_i=\frac{q_i l_c}{(T_1-T_0)k_0}=\begin{cases}(1+\chi\Theta)^{\varpi}\dfrac{d\Theta_i}{dY} & \text{for } i=1\\ -(1+\chi\Theta)^{\varpi}\dfrac{d\Theta_i}{dY} & \text{for } i=2\end{cases} \tag{3.18}$$

where $i=1$ and $i=2$ refer to the hotter-wall and cooler-wall surfaces, respectively. Here, we have assumed that the channel walls are made of materials of low emissivity, so that the effect of thermal radiation is excluded.

The momentum and energy equations (3.12) and (3.13) subject to the boundary conditions (3.14) and (3.15) have been numerically solved by using an implicit finite-difference method. For numerical analysis, Eqs. (3.12) and (3.13) are replaced by the following difference equations:

$$a_j^v U_{j-1} + b_j^v U_j + c_j^v U_{j+1} = d_j^v \tag{3.19}$$

$$a_j^t \Theta_{j-1} + b_j^t \Theta_j + c_j^t \Theta_{j+1} = d_j^t \tag{3.20}$$

where

$$a_j^v = \frac{(1+\chi\Theta_j)^{\omega}}{(\Delta Y)^2}, \quad b_j^v = -\frac{2(1+\chi\Theta_j)^{\omega}}{(\Delta Y)^2}, \quad c_j^v = \frac{(1+\chi\Theta_j)^{\omega}}{(\Delta Y)^2}$$

$$d_j^v = -\chi\omega(1+\chi\Theta_j)^{\omega-1}\left(\frac{U_{j+1}^g - U_{j-1}^g}{2\Delta Y}\right)^2 - \frac{\Theta_j}{1+\chi\Theta_j}$$

$$a_j^t = \frac{(1+\chi\Theta_j^g)^{\varpi}}{(\Delta Y)^2}, \quad b_j^t = -\frac{2(1+\chi\Theta_j^g)^{\varpi}}{(\Delta Y)^2}, \quad c_j^t = \frac{(1+\chi\Theta_j^g)^{\varpi}}{(\Delta Y)^2}$$

$$d_j^t = -\chi\varpi(1+\chi\Theta_j^g)^{\varpi-1}\left(\frac{\Theta_{j+1}^g - \Theta_{j-1}^g}{2\Delta Y}\right)^2, \quad j = 2,3,4,\ldots,M \tag{3.21}$$

The corresponding slip/jump difference conditions obtained from Eqs. (3.14) and (3.15) are

$$U_1 = \frac{2-\sigma_v}{\sigma_v}\mathrm{Kn}_0(1+\chi\Theta_1)^{\omega+1/2}\frac{-U_3^g + 4U_2^g - 3U_1^g}{2\Delta Y}$$

$$U_{M+1} = -\frac{2-\sigma_v}{\sigma_v}\mathrm{Kn}_0(1+\chi\Theta_{M+1})^{\omega+1/2}\frac{3U_{M+1}^g - 4U_M^g + U_{M-1}^g}{2\Delta Y} \tag{3.22}$$

$$\Theta_1 = \xi + \frac{2-\sigma_t}{\sigma_t}\frac{2\gamma}{\gamma+1}\frac{1}{\mathrm{Pr}}\mathrm{Kn}_0(1+\chi\Theta_1^g)^{\omega+1/2}\frac{-\Theta_3^g + 4\Theta_2^g - 3\Theta_1^g}{2\Delta Y} \tag{3.23}$$

$$\Theta_{M+1} = 1 - \frac{2-\sigma_t}{\sigma_t}\frac{2\gamma}{\gamma+1}\frac{1}{\mathrm{Pr}}\mathrm{Kn}_0(1 + \chi\Theta_{M+1}^g)^{\omega+1/2}\frac{3\Theta_{M+1}^g - 4\Theta_M^g + \Theta_{M-1}^g}{2\Delta Y}$$

Here, the superscript g denotes the guess values. Numerical solutions are obtained by first selecting values for Kn_0, Pr, ξ, χ, γ, σ_v, σ_t, ω, and ϖ. Then, by using the tridiagonal-matrix algorithm (TDMA), the variables U and Θ are obtained by the following steps.

1. Guess the velocity Θ^g and the velocity U^g at each grid point.
2. Solve the energy equation (Eq. (3.20)) subject to the jump conditions (Eq. (3.23)) to find the new corrected temperature Θ.
3. Replace the previous intermediate value (Θ^g) with the new corrected value (Θ), and return to Step 2. Repeat this process until the solution converges.
4. Solve the momentum equation (Eq. (3.19)) subject to the slip conditions (Eq. (3.22)) to find the new corrected velocity U.
5. Replace the previous intermediate value (U^g) with the new corrected value (U), and return to Step 4. Repeat this process until the solution converges.

The grid size for simulating the slip flow is used with 0.0025. The solution in each process is declared convergent when the maximum normalized residual becomes smaller than a chosen convergence criterion of $\varepsilon = 1\times10^{-4}$. The grid size and the convergence criterion have been validated by comparison with available theoretical and experimental results.

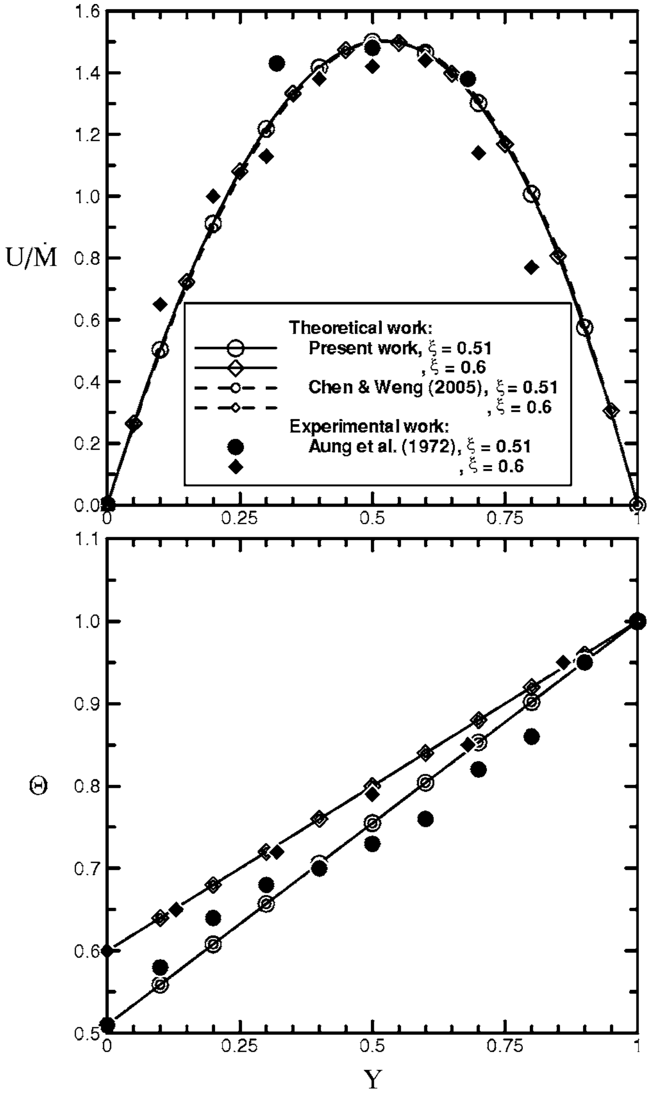

Fig. 3 Comparison of the results of the present study with those of available work: ξ=0.51: χ=0.1813, Kn_0=1.38×10^{-5} (w=5.119 mm, T_0=312.57 K); ξ=0.6: χ=0.0409, Kn_0=1.48×10^{-5} (w=4.775 mm, T_0=312.57 K)

4 Results and Discussion

In Fig. 3, we check the results in terms of the velocity $U/\dot{M}$ and the temperature Θ with those of Chen and Weng [2] and Aung et al. [14]. The theoretical work of Chen and Weng is the case where the Boussinesq approximation is applied, the so-called constant-property case. The experimental work of Aung et al. is a macroscale case near w=5 mm. Our macroscale results compare very well with the theoretical data. It seems that the effect of variable physical properties on the velocity and temperature fields is negligible at low hotter-wall temperatures (for small values of χ). However, theoretical results are in a little disagreement with the experimental data in detail. The disagreement may result from the difficulty in making precise measurements or the influence of channel geometry (l=d=17.78 cm in the experimental setup, where l and d are the channel length and depth, respectively). In fact, to ensure that results are suitable for comparisons, a long and high-aspect channel should be used for experimental studies.

Air is used in most engineering application fields. We pay attention to the influence of variable physical properties on the microflow for air at the standard reference state: 298.15 K and 1 atm. Physical properties at the chosen reference state are shown

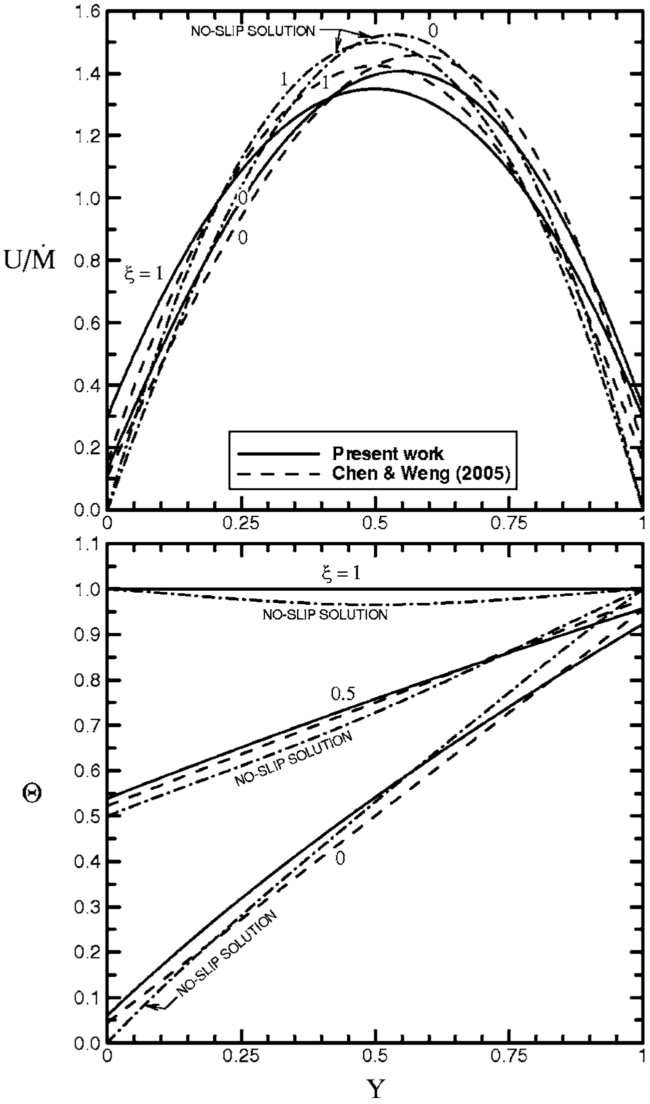

Fig. 4 Velocity and temperature distributions for different values of ξ with $\mathrm{Kn}_0=0.03$ and $\chi=1$

in Table 1. The present parametric study has been performed over the ranges: $0 \leq \mathrm{Kn}_0 \leq 0.1$ (the minimum size: 0.67 μm) and $0 \leq \chi \leq 2$ (the maximum wall temperature: 894.45 K). For simplicity, we have conducted calculations for complete accommodation (i.e., $\sigma_v=1$ and $\sigma_t=1$). Note that Kn_0 characterizes the effect of channel size and that χ represents a measure of the departure from the inlet temperature.

In Fig. 4, we plot the variable-property effect on the velocity and temperature fields based on the symmetric-heating case ($\xi=1$) and the asymmetric-heating case ($\xi=0.5$, $\xi=0$). The solid line denotes the variable-property case, and the dashed line denotes the constant-property case. The chosen reference values of Kn_0 and χ for the analysis are 0.03 ($w=2.22$ μm) and 1 ($T_1=596.30$ K), respectively. The no-slip solution (dashed-dotted line) is also shown to provide a fundamental understanding of the deviation from macroscale behavior. It is clear from the plot that the consideration of variable properties leads to an additional velocity slip and temperature jump on wall surfaces except for the symmetric-heating case in the temperature field; moreover, it furthers the symmetry in the velocity profile and the convex nonlinearity in the temperature profile. Due to the additional slip and jump obtained, we also observe smaller variations of $U/\dot{M}$ and Θ with Y. By increasing the cooler-wall temperature (increasing ξ), the effect of variable physical properties can be magnified on the velocity field but minified on the temperature field. In addition, a comparison of the velocity fields of slip and no-slip flows shows that the effect of rarefaction (a finite value of Kn_0) is to reduce the maximum value and to shift the asymmetric profile to the hotter-wall side ($Y=1$). A comparison of temperature fields shows that, in opposition to a slip flow, the no-slip flow exhibits the behavior of concave profile and the nonlinearity increases with increasing ξ.

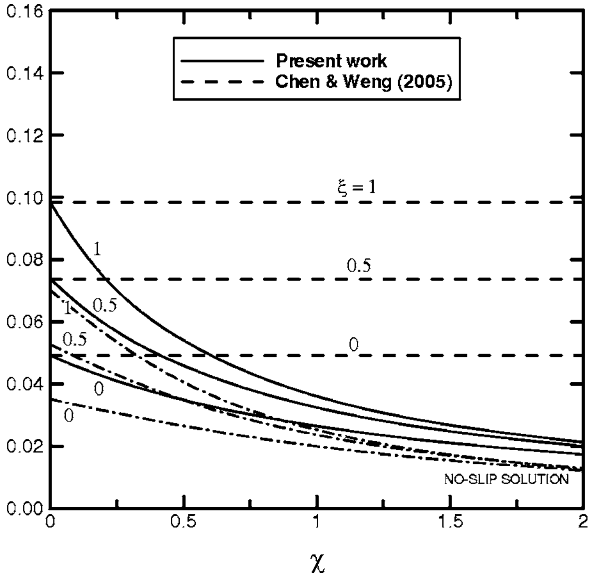

Fig. 5 Mass flow rate versus χ for different values of ξ with $\mathrm{Kn}_0=0.03$

Figure 5 illustrates the variation of the mass flow rate $\dot{M}$ with χ. The symmetric-heating case $\xi=1$ and two asymmetric-heating cases $\xi=0.5$ and $\xi=0$ are presented. It is observed that $\dot{M}$ parabolically decreases with the hotter-wall temperature parameter χ and then approaches zero, so that the difference with the constant-property solution (dashed line) parabolically increases. When the cooler-wall temperature parameter ξ increases, the variable-property effect increases. Figure 5 also illustrates the no-slip solution. It is seen that the variational tendency is similar to that of the slip solution. The effects of increasing χ and ξ seem smaller than those of the slip solution. Figure 6 illustrates the variations of the local heat transfer rates Nu_1 and Nu_2 with χ. It shows that, except for the symmetric-heating case, variable physical properties may have a significant effect. Due to the convex nonlinearity in the temperature profile, as shown in Fig. 4, we can predict smaller values than those in the constant-property case. However, the temperature jump has a countereffect on Nu_2. Greater values may therefore be obtained on the cooler-wall surface, e.g., for $\xi=0.5$ with $\chi>1.42$, where the temperature-jump effect prevails over the temperature-nonlinearity effect. The variable-property effect can be minified by increasing the value of ξ. Note that unlike the slip solution, Nu_1 and Nu_2 of the no-slip flow always parabolically decrease with χ. Due to the concave nonlinearity in the no-slip temperature profile, as shown in Fig. 4, we can obtain positive values of Nu_2 for large values of ξ.

Finally, to provide a criterion for determining whether the importance of variable physical properties should be stressed, we classify a flow as constant property if

$$\frac{|\dot{M}_{\mathrm{cp}}-\dot{M}|}{\dot{M}} < 0.05 \tag{4.1}$$

where the subscript cp denotes the constant-property value obtained from the work of Chen and Weng [2]. For a given value of

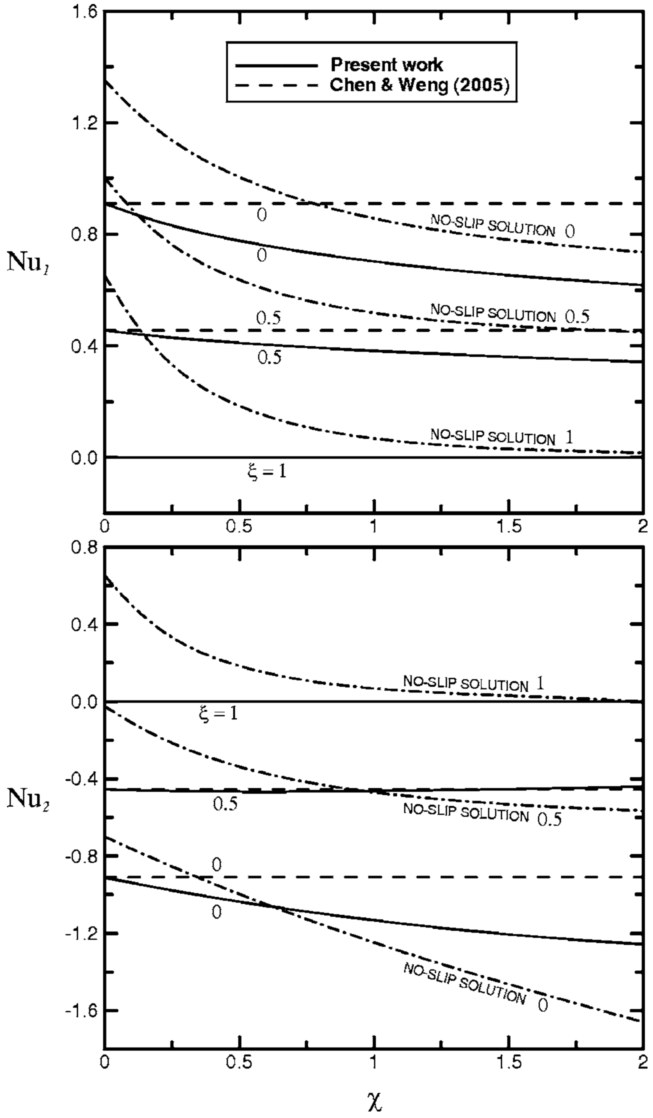

Fig. 6 Local heat transfer rate versus χ for different values of ξ with $\mathrm{Kn}_0=0.03$. The subscript 1 denotes the hotter-wall surface, and the subscript 2 denotes the cooler-wall surface.

ξ, we seek the critical value of χ for all values of Kn_0. In the plane (χ, Kn_0), the locus divides the plane into variable-property and constant-property regions. From Fig. 7, it is observed that critical χ is a monotone increasing function of Kn_0 and that the variable-property region is enlarged by the increase in ξ. Because the minimum value of critical χ is 0.02928, corresponding to $T_1 = 306.88$ K, we conclude that the effect of variable physical properties should be considered for hotter-wall temperatures greater than 306.88 K.

5 Conclusions

Realistic formulas for the shear viscosity, thermal conductivity, constant-pressure specific heat, density, and molecular mean free path have been provided and employed to study the effect of variable physical properties on natural convective gas microflow. A long open-ended vertical parallel-plate microchannel with uniform but not necessarily symmetric wall temperature distributions was used in the analysis. The full Navier–Stokes equations and energy equation subject to the first-order slip/jump boundary conditions were numerically solved. Results show that ignoring the importance of physical property variation at hotter-wall temperatures greater than 306.88 K may cause significant deviation from the estimation of flow and thermal characteristics. The variable-property effect results in the increases in the velocity symmetry and temperature nonlinearity as well as the decreases in the mass flow rate and the local heat transfer rate except for the cooler-wall surface where the temperature-jump effect prevails over the temperature-nonlinearity effect. By increasing the cooler-wall temperature, the effect on flow behavior is magnified, but the effect on thermal behavior is minified. In addition to the understanding of rarefied-gas transport behavior, the present study may benefit the designs and fabrications of microfluidic system devices in need of high-temperature heated channels.

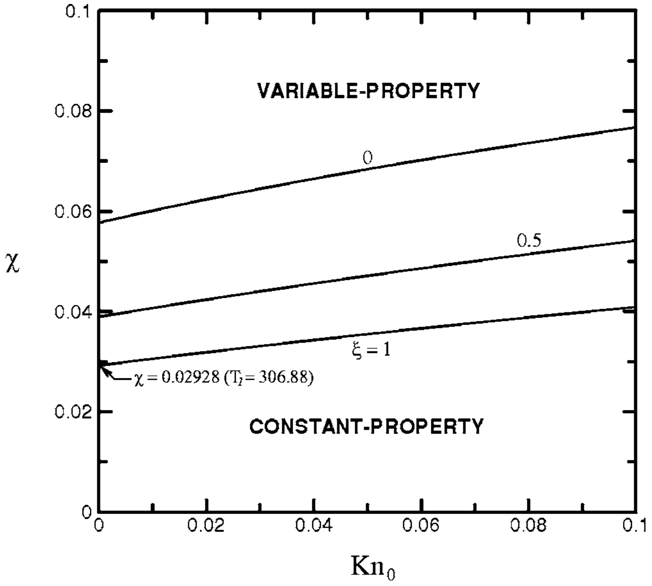

Fig. 7 Critical hotter-wall temperature parameter versus Kn_0 for different values of ξ

Acknowledgment

This research was supported by the National Science Council of Taiwan under Grant No. NSC 95-2221-E-006-249. The authors are grateful to the reviewers for their helpful comments and suggestions.

Nomenclature

c_p, c_v = specific heats at constant pressure and constant volume, respectively
d = channel depth
$\mathbf{f}$ = body force vector
g = gravitational field strength
$\mathbf{g}$ = gravitational field vector
h = internal heat generation rate
j = number index in y directions
k = thermal conductivity
Kn = Knudsen number, Eq. (3.16)
l = channel length
l^* = development length
$\dot{m}$ = mass flow rate
$\dot{M}$ = dimensionless mass flow rate, Eq. (3.17)
Nu = dimensionless local heat transfer rate, Eq. (3.18)
p = pressure
P = dimensionless pressure defect, Eq. (3.1)
$\hat{p}$ = pressure defect, $p - p_h$
p_h = hydrostatic pressure
Pr = Prandtl number, Eq. (3.1)

q = local heat transfer rate
R = local curvature radius of the streamline
s = specific heat coefficient
T = temperature
$\mathbf{u}$ = velocity vector
u = velocity
u_i = velocity in index notation
u_x, u_y = velocity components in x, y directions
U, V = dimensionless velocity components in x, y directions, Eq. (3.1)
w = channel width
x, y = rectangular coordinate system
X, Y = dimensionless rectangular coordinate system, Eq. (3.1)

Greek Letters

β = thermal expansion coefficient
γ = ratio of specific heats, c_p/c_v
δ = perturbation variable
ε = convergence criterion
λ = molecular mean free path
ξ = wall-ambient temperature difference ratio, Eq. (3.16)
Θ = dimensionless temperature, Eq. (3.1)
Λ_1, Λ_2 = size-dependent parameters, Eq. (3.1)
μ = shear viscosity
ρ = density
σ_t, σ_v = thermal and tangential momentum accommodation coefficients, respectively
χ = hotter-wall temperature parameter
ω, ϖ = viscosity and conductivity indices, respectively
Φ = viscous dissipation function

Subscripts

1 = hotter-wall values
2 = cooler-wall values
0 = inlet properties of the fluid
c = characteristic values
cp = constant-property values

Superscript

g = guess values

Special Symbols

d/dt = material derivative

References

[1] Weng, H. C., and Chen, C. K., 2008, "Fully Developed Thermocreep-Driven Gas Microflow," Appl. Phys. Lett., **92**, p. 094105.
[2] Chen, C. K., and Weng, H. C., 2005, "Natural Convection in a Vertical Microchannel," ASME J. Heat Transfer, **127**, pp. 1053–1056.
[3] Haddad, O. M., Abuzaid, M. M., and Al-Nimr, M. A., 2005, "Developing Free-Convection Gas Flow in a Vertical Open-Ended Microchannel Filled With Porous Media," Numer. Heat Transfer, Part A, **48**, pp. 693–710.
[4] Chen, C. K., and Weng, H. C., 2006, "Developing Natural Convection With Thermal Creep in a Vertical Microchannel," J. Phys. D, **39**, pp. 3107–3118.
[5] Avci, M., and Aydin, O., 2007, "Mixed Convection in a Vertical Parallel Plate Microchannel," ASME J. Heat Transfer, **129**, pp. 162–166.
[6] Boussinesq, J., 1903, *Theorie Analytique de la Chaleur Heat Dissipation of Parallel Plates by Free Convection*, Gauthier-Villars, Paris.
[7] Bejan, A., 1995, *Convection Heat Transfer*, Wiley, New York.
[8] Sparrow, E. M., and Gregg, J. L., 1958, "The Variable Fluid Property Problem in Free Convection," Trans. ASME, **80**, pp. 879–886.
[9] Schlichting, H., 1979, *Boundary-Layer Theory*, McGraw-Hill, New York.
[10] Shang, D. Y., and Wang, B. X., 1990, "Effect of Variable Thermophysical Properties on Laminar Free-Convection of Gas," Int. J. Heat Mass Transfer, **33**, pp. 1387–1395.
[11] Suryanarayana, N. V., 1995, *Engineering Heat Transfer*, West Publishing Company, New York.
[12] Arkilic, E. B., Schmidt, M. A., and Breuer, K. S., 1997, "Gaseous Slip Flow in Long Microchannels," J. Microelectromech. Syst., **6**, pp. 167–178.
[13] Maxwell, J. C., 1879, "On Stress in Rarefied Gases From Inequalities of Temperature," Philos. Trans. R. Soc. London, **170**, pp. 231–256.
[14] Aung, W., Fletcher, L. S., and Sernas, V., 1972, "Developing Laminar Free Convection Between Vertical Plates With Asymmetric Heating," Int. J. Heat Mass Transfer, **15**, pp. 2293–2308.

Neil Zuckerman
e-mail: zuckermn@seas.upenn.edu

Jennifer R. Lukes
e-mail: jrlukes@seas.upenn.edu

Department of Mechanical Engineering and
Applied Mechanics,
University of Pennsylvania,
Philadelphia, PA 19104

Atomistic Visualization of Anisotropic Wave Propagation in Crystals

Presented here is a new molecular dynamics simulation approach for visualizing multidimensional acoustic wave-packet propagation in anisotropic materials. This approach allows examination of longitudinal wave propagation in a selected frequency range and may also be extended to track transverse motions. The obtained results agree with analytical predictions and experimental measurements of quasilongitudinal wave front propagation in the literature. Additionally, spectral analysis reveals minor levels of frequency redistribution as the wave packet propagates, which is indicative of phonon-phonon scattering. The present approach provides new capabilities for phonon-focusing studies and offers an alternative to existing experimental and Monte Carlo techniques used for these studies. [DOI: 10.1115/1.2909608]

Keywords: elastic waves, phonon focusing, heat transfer, molecular dynamics

1 Introduction

The transfer of heat within nonmetallic solids primarily occurs by the propagation of elastic waves associated with the displacement of atoms from their lattice sites. These traveling vibrational waves occur in quantized units called phonons. In single crystals at low temperatures, the phonons may ballistically travel, meaning they persist along straight-line trajectories for long distances without scattering. The elastic anisotropy of crystals causes directional variation in this ballistic heat flux, channeling higher numbers of phonons along specific directions. Understanding how a material preferentially channels vibrational energy in different directions will provide a better understanding of heat transfer in crystals and material properties, with increased utility for applications involving short heat pulses, small dimensions, and/or low temperatures. The visualization of this heat propagation can also improve understanding and modeling of low-temperature heat transfer at greater length and time scales when material properties yield different speeds of heat propagation in different directions, as these directional variations influence the mesoscale transport of phonons.

The phonon-focusing behavior of crystals has been experimentally investigated for a limited selection of materials in laboratory settings, such as Si, GaAs, LiF, InSb, Ge, and other semiconductors [1]. The techniques measure heat pulse intensity at various positions on a crystal surface following excitation of phonons from a point source on the opposite side. The point source is commonly excited by a narrow electron beam or a laser briefly impinging on a metal surface film. The material sample is maintained at a low temperature (e.g., 2 K) to suppress phonon-phonon collisions and diffusive transport of heat. The signal on the crystal surface is commonly picked up by superconducting detectors, which change resistance in response to temperature increases [1,2]. Input pulse durations are on the order of 10 ns, which requires careful tracking of time or phase differences between the heat pulse input and signal output. The equipment and high-quality material samples necessary for this method make a numerical method a desirable alternative.

The nonuniform propagation of heat in the materials can be explained using principles of elasticity for crystalline lattice structures. In general, the wave vector and the group velocity vector (propagation direction) of an elastic wave in a crystal will have different directions. Due to the crystal anisotropy, two separate phonons with wave vectors possessing different magnitudes and directions may have parallel group velocity vectors. This is illustrated in Fig. 1, which shows a slowness contour (line of constant ω) in a two-dimensional momentum space, corresponding to inverse phase velocities of a type of transverse oscillating mode in a (100) face plane of a cubic crystal [3]. Group velocity vectors will be perpendicular to this slowness surface. The two different wave vectors ($\mathbf{k}$) shown in the figure have identical group velocity vectors ($\mathbf{v_g}$). A collection of phonons of a given polarization with uniform density in wave vector space will have real-space group velocity vectors with a nonuniform distribution, resulting in real-space directions with higher- and lower-than-average phonon fluxes, as shown in Fig. 2. The aspherical ray surface surrounding a point source of phonons may feature "caustics," which are directions or surfaces that have been experimentally observed to have very high phonon fluxes (phonon focusing). Up to three distinct acoustic vibrational eigenmodes will be present in any given direction. The mode with the highest velocity (and lowest "slowness" k/ω) is labeled quasilongitudinal, and along crystal axes will have the form of a pure longitudinal vibration. Similarly, the other two vibrational modes are labeled quasislow transverse and quasifast transverse based on their velocities, and along certain axes of crystal symmetry will be degenerate, pure transverse vibrations. In other directions, a vibrational eigenmode will be a mixed mode. Each of the distinct vibrational eigenmodes of the lattice will have a different group velocity (a function of direction) and thus a different wave front or ray surface.

The most common method of numerical investigation uses a Monte Carlo model of phonon transport to simulate the experimental technique [4]. The Monte Carlo simulation performs calculations for many phonons in a selected range of wave vector and of selected polarizations to determine their position and time of arrival on the crystal surface corresponding to the image plane. Many individual phonon transport calculations are required to span the necessary time interval, densely sample all relevant modes, wave numbers, and wave vector directions, and accumulate enough phonons on the image plane within a given time window to provide clear contrast (dynamic range and signal resolution). The more detailed versions of these Monte Carlo models incorporate the full three-dimensional dispersion relations to calculate phonon group velocities.

Contributed by the Heat Transfer Division for publication in the JOURNAL OF HEAT TRANSFER. Manuscript received May 4, 2007; final manuscript received September 13, 2007; published online May 30, 2008. Review conducted by Jayathi Murthy.

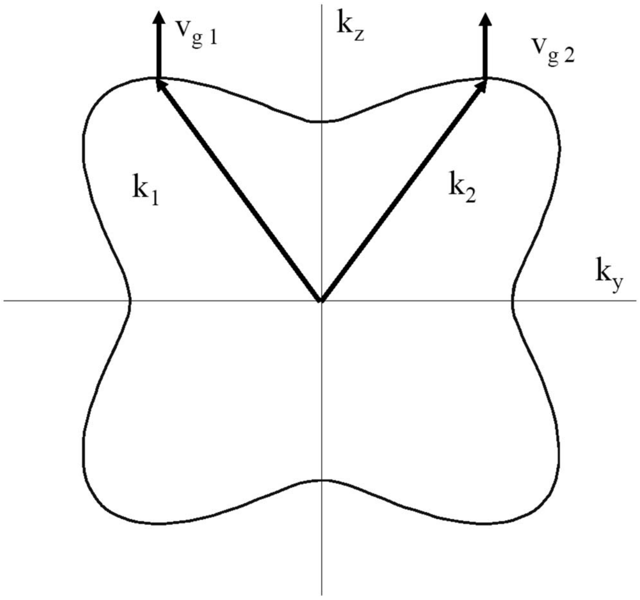

Fig. 1 Slowness surface for quasitransverse mode in (100) plane, plotted in *k*-space with sample wave and group velocity vectors

In this study, molecular dynamics (MD) is explored as a tool for visualizing spatially nonuniform propagation of heat in crystal lattices. It serves as an alternative to the Monte Carlo method and other numerical models. Unlike the Monte Carlo approach, the established MD models of various materials incorporate potential energy functions to describe their atomic interactions. This means that the user need not compute dispersion relations or material elastic stiffness constants, because these properties are natural results of the selected potential function.

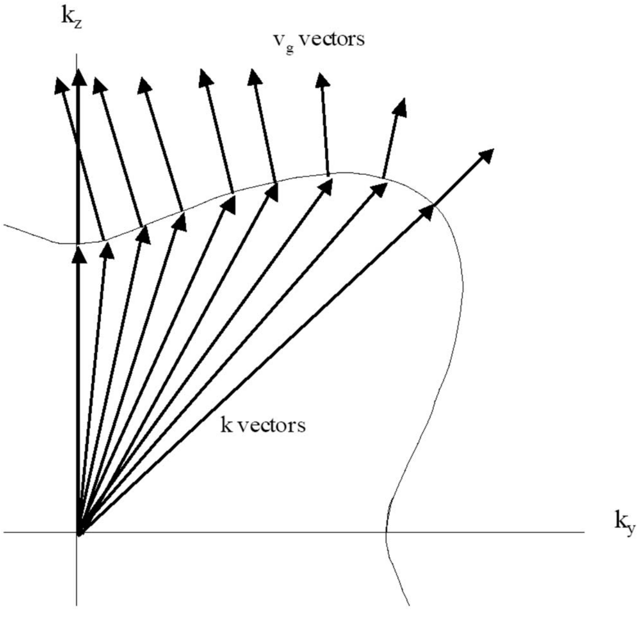

Fig. 2 Schematic depiction of nonuniform distribution of group velocity vectors resulting from uniform distribution of wave vectors

Table 1 Ratios of material stiffness constants for Ar and similar cubic crystals

Material	$a=C_{11}/C_{44}$	$b=C_{12}/C_{44}$	$\Delta=a-b-2$ anisotropy factor
Ar, 12-6 LJ	1.7	1.0	−1.2
GaAs	1.9	1.0	−1.1
Ge	1.9	0.7	−0.8
Si	2.1	0.8	−0.7

2 Simulation Method

The simulation approach is to model a block of atoms, impose a point-source vibration into the atomic lattice to create traveling waves, and then monitor atoms on a selected crystal plane to determine their kinetic energy as a function of position and time. This method is selected because of its similarity to the experimental technique in its use of a point-source excitation and its monitoring of signals on a plane.

The MD model used is based on program code of Lukes and Tien [5], which uses a Lennard–Jones (LJ) 12-6 potential function with parameters $\sigma=0.34$ nm and $\varepsilon=1.67\times10^{-21}$ J [6]. The model simulates a solid argon crystal in a face-centered cubic lattice, which, due to its single atom basis, supports acoustic modes only. LJ 12-6 argon was selected based on its speed of computation, but has the added benefit that its cubic stiffness constants are close to those of Ge, Si, and GaAs, as shown in Table 1. The elastic constant ratios of LJ 12-6 argon are $a_{\mathrm{Ar}}=C_{11}/C_{44}=1.7$, and $b_{\mathrm{Ar}}=C_{12}/C_{44}=0.96$, per Barker et al. [7]. Ge, Si, and GaAs have wave fronts with similar qualitative characteristics. One of the most important characteristics is that as the longitudinal-mode wave vector departs farther from the [100] direction, the group velocity and phase velocity increase. This behavior is also predicted by acoustic theory [3]. For these materials, the longitudinal-mode wave front intersects a (100) plane in a form resembling a "rounded square," similar to that shown for germanium in Fig. 6 of Ref. [8]. As Ar is more anisotropic than Ge, the shape of the wave front is even less circular.

The lattice is configured as a large box-shaped domain with rigid walls on two opposite sides and periodic boundaries on the other four sides (Fig. 3). All sides of the domain are ⟨100⟩ planes. The simulation domain typically contains between 5000 and 340,000 atoms, with side lengths of up to 26 nm, based on 50 unit cells sized at 0.53 nm each.

An image plane could be selected at any place within the crystal with any orientation. To match a number of experimental

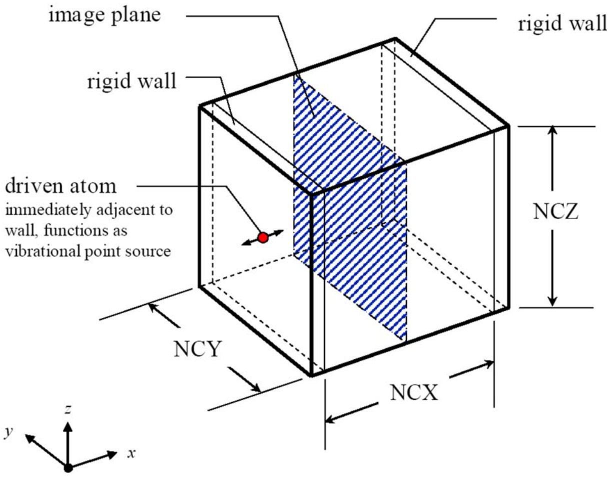

Fig. 3 Schematic of simulation domain

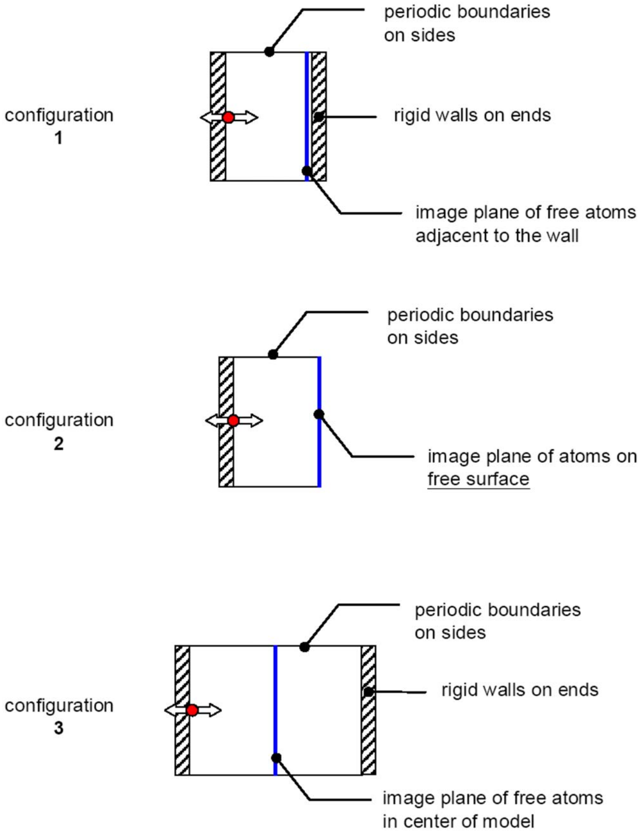

Fig. 4 Various boundary conditions investigated in the simulations

samples, we use a (100) image plane, and as part of the model investigation we examined results from three different configurations of the boundary conditions, shown in Fig. 4. Configuration 1 uses a plane of atoms adjacent to a rigid far wall. Configuration 2 uses a far wall with a free surface, matching the experimental configuration (though not the length scale). Configuration 3 uses a longer model with rigid walls on both ends, and samples data at an image plane in the center of the model.

In Configuration 1, the wave reflects off of the far wall and the reflected portion may interfere with incoming portions of the same wave, but this does not change the fundamental shape(s) of the ray surfaces or those of the resulting contours, so Configuration 1 can give meaningful results. Configuration 2 gives unsatisfactory results due to its free surface. A free surface causes local static relaxation of the lattice, a scale-dependent effect resulting from image plane atoms having a different number of neighbor atoms from which they may feel forces. This local relaxation changes the lattice constant as well as the ratios of stiffness constants, which for our purposes means changing the simulated material. The Molecular Statics process of relaxation is conducted with the method of steepest descent, which leaves a small amount of residual thermal noise. Unfortunately, in our models, this noise is the same order of magnitude as the signal reaching the image plane, resulting in an image with the proper recognizable contours but nonuniform or unclear details.

Configuration 3 gives results similar to those of Configuration 1, but without the issue of reflection from the far wall boundary causing phase inversion and wave interference. The images from Configuration 3 are collected well before any waves have encountered the far wall. All of the images presented in this paper come from models with Configuration 3, as shown in Fig. 3.

The position and velocity of each atom in the image plane are tracked over time. In the computations described below, these data are recorded at intervals of 10 or 50 time steps, where each time step represents 1 fs. To provide very high time resolution, they could be sampled every time step, which would generate a very large data set for postprocessing. The recorded velocity of each atom is used to compute the kinetic energy at the image plane as a function of position. The KE data are used to create contour maps of kinetic energy on the image plane at selected instants, plotted with a cubic spline curve fit. Using this method, one could also track and plot momentum, if desired, for comparison versus experimental sensors that respond to local atomic momentum rather than energy.

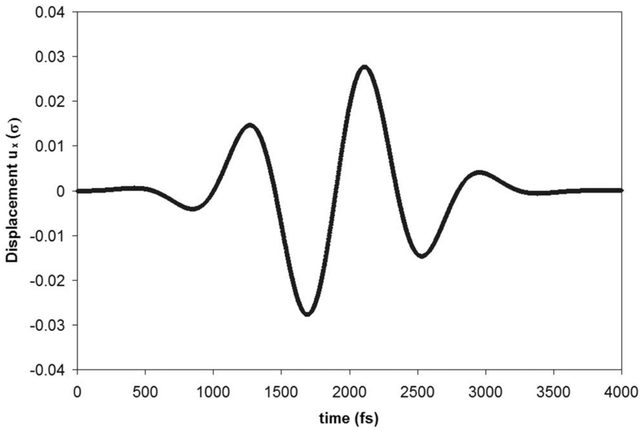

Fig. 5 Typical narrow wave-packet shape, ω=0.007 rad/fs

The lattice in the model is first initialized at a temperature of 0 K. A point source of heat is generated by moving a single atom in a lattice position centered adjacent to one wall of the model. This generates disturbances in the positions of neighboring atoms, which travel in a wavelike fashion radially away from the point source. By moving the atom in particular directions, one can generate waves or combinations of waves with strong polarizations in particular directions. The most successful point-source motions we have used thus far are temporally narrow wave-packet oscillations. Figure 5 shows an example shape of one of these input wave packets. The packet amplitude represents displacement of the driving atom from its equilibrium position, and the time derivative of the packet is proportional to the magnitude of the local atomic velocity. The kinetic energy of the moving atom then varies over time, as shown in Fig. 6, with individual peaks in kinetic energy at successive time intervals. This pattern of peaks is preserved as the excited wave travels away from the source and

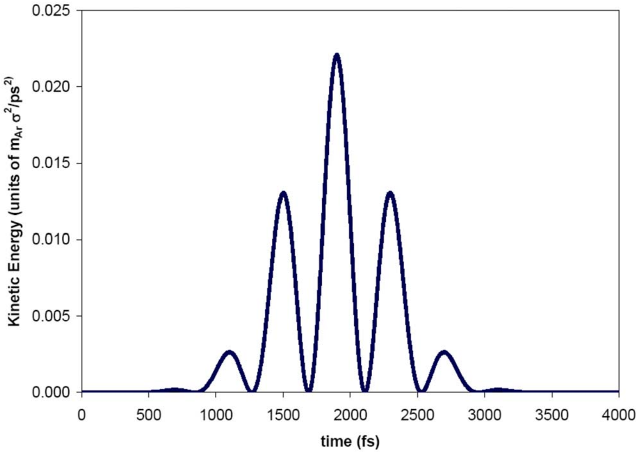

Fig. 6 Kinetic energy time history of wave packet (source signal), ω=0.007 rad/fs

reaches the image plane. At each point in space, the local displacement along a modal eigenvector resembles a wave packet.

Each point (each atom) on the image plane has a sequence of kinetic energy peaks resembling those in Fig. 6, and will return to a low-temperature state after the wave passes through its position. As different points on the image plane have different distances from the source, and due to the directional variation of group velocity, the observed effect is that of a series of pulses arriving at the center of the *y*-*z* image plane and radially traveling outward in a series of rings.

The use of a temporal wave packet allows the input to be set at or around a selected frequency ω, which is a useful numerical model feature not available in the experimental method. The direction of the particle velocity is chosen and the resulting wave numbers and group velocities of excited vibrations are generated within the model as a consequence of the crystal stiffness constants, determined by the lattice structure and potential function. To extract information about the longitudinal mode, the displacements of the driven atom are aligned with the x axis, though this motion will generate all three modes of acoustic waves. The individual modes propagate as separate wave packets that travel at different speeds but may overlap in space. Input displacement amplitude should be kept small to keep the material response in the linear elastic regime, meaning several percent of a lattice constant. Due to the $1/r^2$ decay of vibrational energy propagating from a point source in three dimensions [3], excessively small displacements will be difficult to distinguish at the image plane. The conflicting desires for both a linear response and strong signal levels limit the range of input displacements capable of generating useful images. Because the wave amplitude quickly decreases with a $1/r$ dependence as it travels from the point source, high-amplitude initial pulses may be tolerable, with some corresponding decrease in packet quality as discussed in Sec. 3. In addition, we use images generated by the early peaks of the packet, which have smaller amplitudes than those of the packet center and thus less distortion. Our clearest images result from packets with maximum source atom displacement amplitudes in the range of 1–7% of a lattice constant, measured at the packet center, corresponding to early pulse amplitudes on the order of 0.02σ at the source atom.

3 Results and Discussion

3.1 Phonon-Phonon Scattering. Because multiple modes may be generated by the point-source motion, which travel in various directions, the packet does not represent a single phonon. It instead represents a collection of phonons forming a heat pulse. The wave packets generated by the atomic point motion experience some degradation as they travel across the crystal, primarily due to the atomic bond anharmonicity, which allows phonon-phonon interactions. Phonon-phonon interactions, in general, result in distribution of energy to different frequencies, and the appearance of new frequencies not originally excited at the source is a strong indication that phonon-phonon scattering is occurring.

The transport from the source to the image plane is seen by tracking displacement pulses at various atoms with different distances from the source. A packet-shaped disturbance propagates outward at constant, finite speed and maintains the same shape over the propagation distance (typically 10–20 lattice cells). The transport is not purely ballistic, but in those regions with small displacement amplitudes it approaches the ballistic transport that comes from harmonic wave motion. The majority of energy in the packet remains around the selected driving frequency ω. To examine the frequency content of the wave packet, the x-direction displacements of selected atoms along the x axis are monitored over time and a Fourier transform is performed on each displacement time history to obtain the frequency spectrum at each position.

Figure 7 shows the amplitude-frequency characteristics of the longitudinal-mode vibration at the source atom, at the center of the image plane, and at a position between the two, with a wave-packet input centered at 1.1 THz. Due to the presence of point masses rather than a continuum, the vibrational wave number has an upper limit, which corresponds to a frequency of 2.1 THz on the argon dispersion relation (Fig. 8). Inputs above this frequency will not propagate in a wavelike fashion.

From comparison of the frequency spectra in Fig. 7, we see that the longitudinal pulse arriving at the image plane has frequency characteristics that are similar but not identical to the input. As the hemispherical wave amplitude decreases in proportion to $1/r$, the figure includes spectra scaled by a factor of r to permit comparison of scaled amplitudes. The scaled amplitudes at different locations are not exactly equal, as energy may be scattered into or out of other (transverse) modes. From the signal at the image plane, we see that the majority of the wave energy lies in a large peak surrounding the input frequency, with a pulse full width at half maximum (FWHM) value of 0.4 THz, one-third of the driving center frequency. The motion of the source is not necessarily the same as the response of the surrounding atoms. All neighboring atoms feel the influence of the source motion, and stronger atomic force interactions occur in the directions of closer atomic spacing, such as the close-packed [111] direction. As the wave propagates toward the image plane, it degrades in quality, and wave energy is redistributed to other frequencies. This effect has been observed to grow stronger for very long domains (NCX > 20). Additionally, the use of higher input wave amplitudes ($u_{\text{input}} > 0.1\sigma$) increases this effect.

The influence of wave amplitude upon packet characteristics can be seen when using a plane wave of high amplitude. In the case of the point source, the high-amplitude motion is present only in a small region of space near the source, as energy spreads out over an expanding wave front. In contrast, the plane wave packet maintains its high amplitude as it travels because its wave fronts have constant surface area. This causes strongly nonlinear elastic effects, which continue through the complete path of motion of the plane wave. Figure 9 shows the resulting frequency spectrum caused by sending a longitudinal plane wave packet through ten lattice cells (15σ). This boundary-driven case uses a displacement amplitude of 0.03σ and a driving frequency of 0.007 rad/fs (1.1 THz), and may be compared to Fig. 7. We see that the continuous strong anharmonic effects cause a dramatic redistribution of the wave energy into vibrations of other frequencies, with more energy being distributed into the lower-frequency vibrations. This observation is consistent with the conclusions of Ref. [9]. It is expected that further redistribution will occur as the packet continues to propagate, ultimately leading to an equilibrium (Planck-like) frequency distribution.

To minimize phonon-phonon scattering effects, it is beneficial to keep wave-packet amplitudes small and thus permit the packet to travel with less distortion. It is important to note that reduction of pulse amplitude, while reducing anharmonic interactions, also reduces the signal-to-noise levels on the image plane. In terms of phonon motion, minimal packet distortion is equivalent to a condition of near-ballistic phonon transport through a region at low temperature, as in the experiments, with low phonon population and a low probability of phonon-phonon scattering. With a larger domain, the wave packet may be elongated in space, reducing the width of the packet on the amplitude-frequency diagram. Due to the scaling relations discussed in Sec. 5, achieving low bandwidth packets can quickly become computationally expensive.

Figure 10 shows an amplitude-frequency spectrum at the image plane for a longer, lower-frequency packet (0.74 THz) than those previously applied (1.1 THz). Interestingly, this lower frequency packet exhibits less high-frequency redistribution, indicating that less phonon-phonon scattering is occurring for this case.

The inclusion of periodic boundaries on the sides of the model could potentially clutter the image plane signal with periodic “duplicates” of the initial pulse, formed by wave fronts that travel to one periodic boundary, wrap around to the opposing periodic

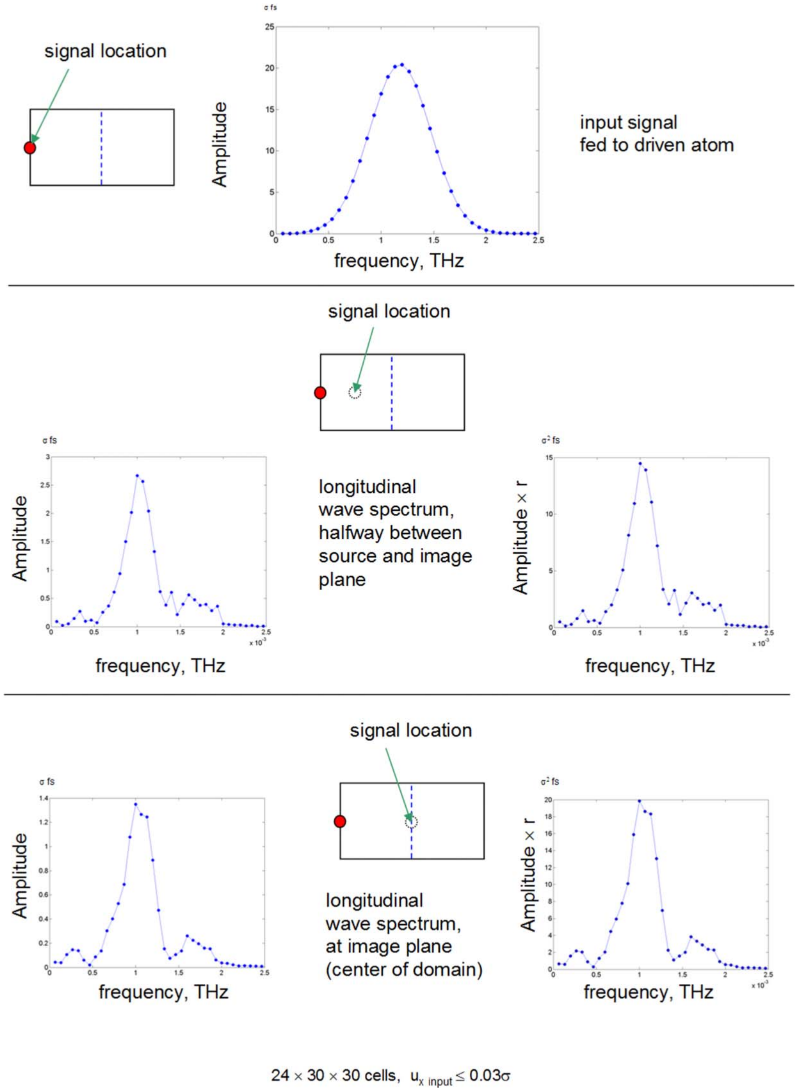

Fig. 7 Frequency spectra of wave packet at various locations, $\omega = 0.007$ rad/fs

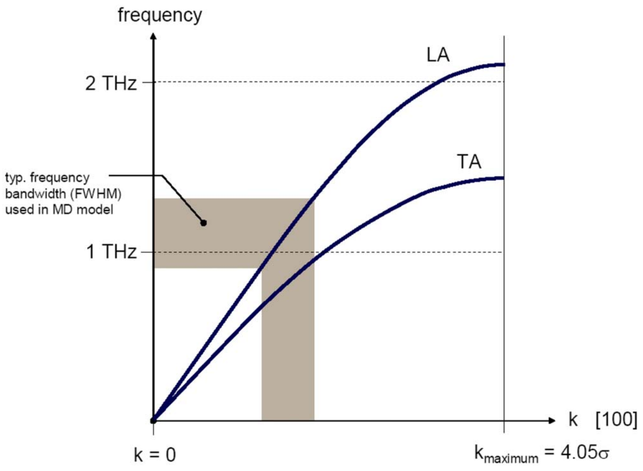

Fig. 8 12-6 argon dispersion relation for [100] direction, based on Barker et al. [8]

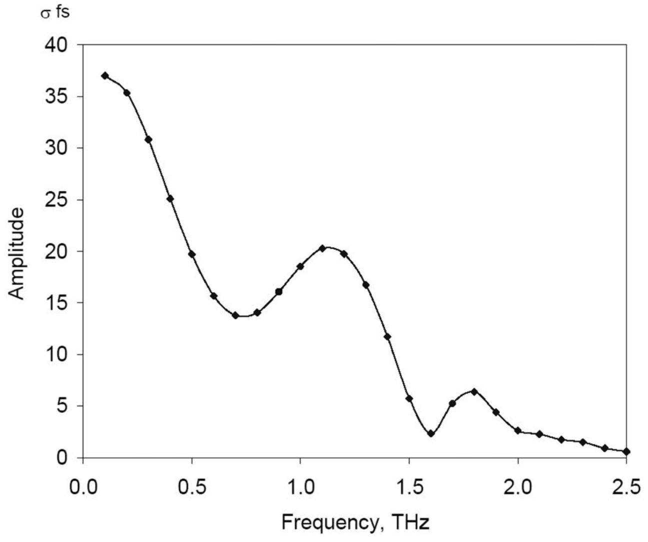

Fig. 9 Frequency spectrum of high-amplitude plane wave arriving at image plane, $\omega_{\text{input}} = 0.007$ rad/fs

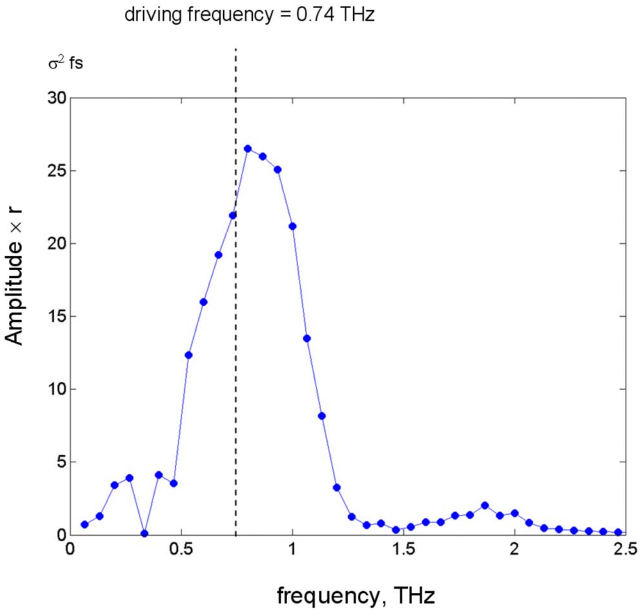

Fig. 10 Frequency spectrum for wave packet at center of image plane, scaled by radius, ω=0.00465 rad/fs

boundary, and eventually arrive at the image plane. A two-dimensional schematic of this behavior is shown in Fig. 11. To prevent this confusing effect, the model is constructed such that the distance between the fixed walls in the x direction is in the range of 60–120% of the distance between opposing periodic boundaries in the y and z directions, and data are collected at a position halfway between the two x-plane walls. Data are sampled for a limited time and over a limited span of the image plane to filter out any stray signals that may have passed through periodic boundaries on their way to the image plane. The image plane will show the arrival of waves with quasilongitudinal and both quasitransverse polarizations, and by selecting early times we may observe the arrival of longitudinal pulses prior to the arrival of transverse wave energy.

3.2 Visualization of the Longitudinal Mode at the Image Plane. The motion of the point-source atom results in multiple bands of kinetic energy appearing on the image plane, corresponding to peaks and valleys of the wave packet. The patterns on the image plane are examined to isolate those associated with the quasilongitudinal waves. Figure 12(*b*) shows the patterns generated by this longitudinal displacement packet at different times. The squared-off rather than circular shape is a direct consequence of the directional variation of the speed of sound. This pattern is repeatable for simulation domains with differing ratios of NCY and NCZ. The wave-packet nature of the driving vibration results in a pulse that is spread out in space on the image plane. The outline of the wave front on the image plane is that of a circle stretched in the y-z diagonal directions, with a greater kinetic energy level seen in the diagonal corners. There is a physically correct anisotropy in both the group velocity and the energy density. This matches the analytical prediction of the ray surface shape, as shown in Fig. 6 of Ref. [8]. The shape generated by the MD model matches that of the experimentally measured quasilongitudinal wave front shown in Figure 19(a) of Ref. [8] as well as the phonon image video provided in [10]. The cubic spline interpolation introduces some noise in the MD image of the wave front, but does not substantially change the shape. In addition, the MD wave fronts are wider at these particular instants, which ultimately results from the MD model's that need to simulate a crystal with lengths on the order of 10 nm while preserving the proper (unscaled) vibrational wavelengths.

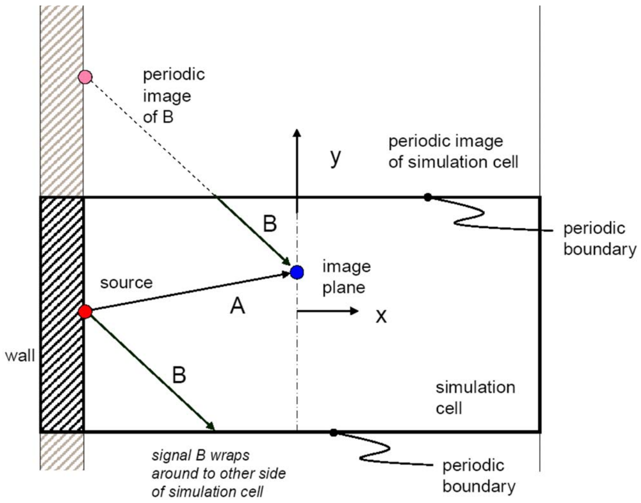

Fig. 11 Schematic depiction of signal passing through periodic boundary to reach image plane

In Fig. 12, the time history of the expanding front of the longitudinal-driven pulse as it moves across the image plane corresponds to the arrival of peaks of the wave packet. As seen in the experiments, the pulse appears to emerge from a central point, and then appears to radially travel outward in the y-z plane, forming the rounded-square shape. The intensity of the contours gives the local atomic kinetic energy, analogous to energy density per unit of area. Points or features on the wave fronts are not actually traveling in a lateral direction in the y-z plane, but rather along radial lines emanating from the point source of energy on the opposite side of the crystal. The motion of this image occurs because as the wave front grows in the radial direction, its intersection with the fixed image plane grows as well. In addition to this growth, the image may change shape as the image plane slices through a different part of the roughly hemispherical wave front. So the radial motion apparent in the y-z plane is the motion of the intersection of this front and the y-z plane, and thus the velocity of an image feature in this plane is only a projection of the propagation velocity of the image feature on the expanding front. This is further illustrated in the two-dimensional schematic of Fig. 13, showing a section cut through a crystal, with an expanding aspherical front contacting a fixed image plane at successive times. In this figure, the wave is shown reflecting off of the far wall of the crystal, as occurs in an experiment. From the images seen in Fig. 12, we can see that the energy traveling from a point source propagates at higher speeds as the direction varies farther from [100], in accordance with acoustic theory for cubic crystals with stiffnesses matching or close to those of LJ solid argon.

4 Simulation Artifacts Present at Late Times

At sufficiently late times in narrow-domain models, the wave fronts will travel through periodic boundaries. At late times, the signal will contain both directly transmitted waves and indirect waves (as in Fig. 11). As wave interference occurs, the planar images of the packet-shaped pulse in this case contain multiple "islands" of high kinetic energy, rather than continuous streaks. The signal on the image plane can and should be tested to verify its invariance with changes in domain shape. Figure 14 shows signals collected at late times in domains with different proportions in the y and z directions. Here, the proportions are deliberately chosen to be narrow to demonstrate the problems associated with signals in narrow domains at late times. At first inspection, the image shown on the square image plane shows a series of energy peaks in an interesting pattern that suggests some physical meaning. A sample feature is circled in the central image, as well as the corresponding location in the adjacent images. Comparison

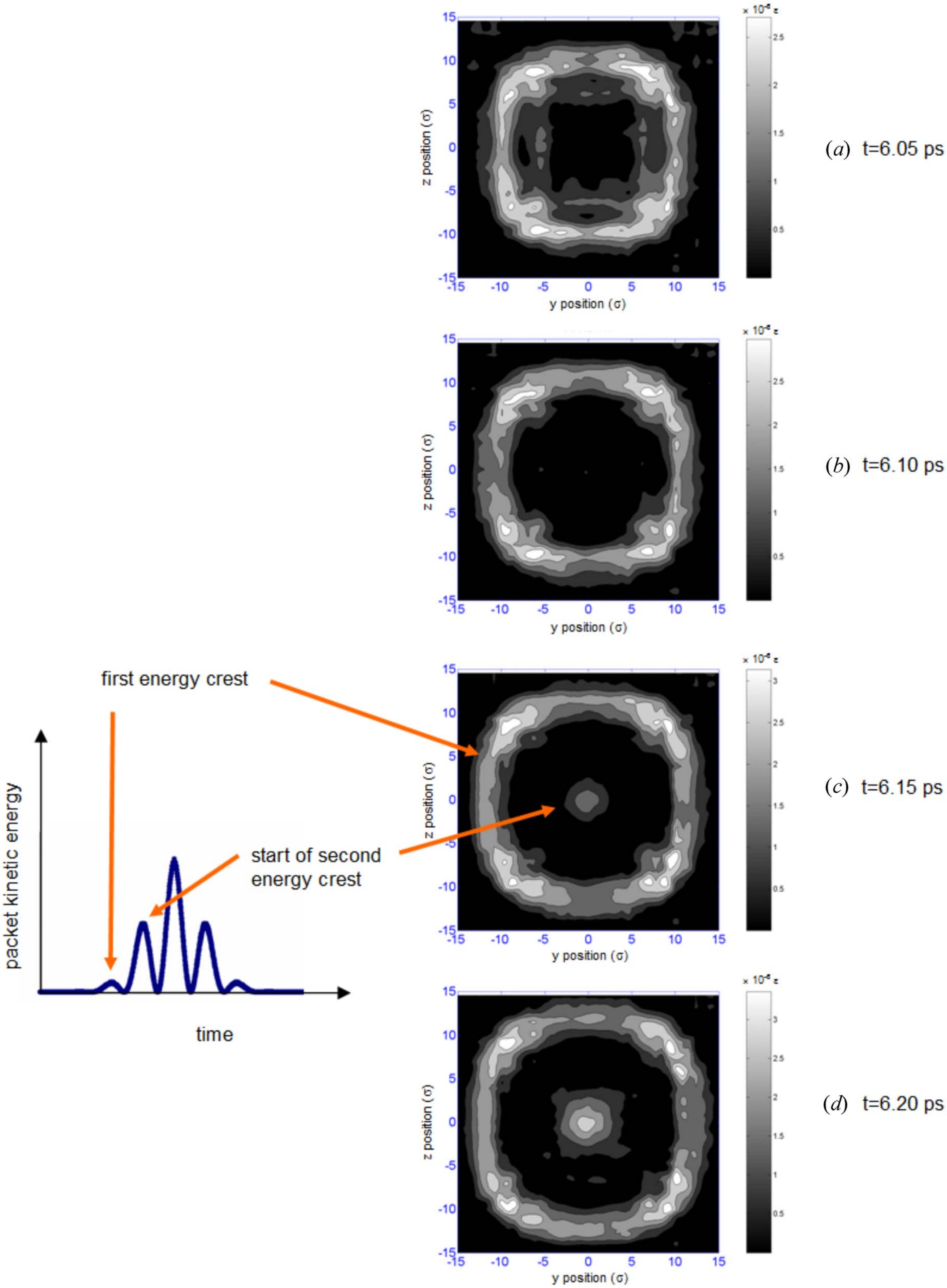

Fig. 12 ((*a*)–(*d*)) Kinetic energy contours—progressive time images of expanding longitudinal pulse

with the other adjacent figures, representing the same case run with domains of differing proportions, shows that the patterns disappear or change with domain shape. This indicates that the patterns result from wave overlap and interference following transmission through the periodic boundaries, and do *not* represent proper wave propagation patterns. In addition, at sufficiently late time steps, the model may display pulses that have reflected off of both fixed walls and returned to the image plane a second time. In contrast, the previously shown contours (Fig. 12) do not vary with domain proportions. These transmission and reflection

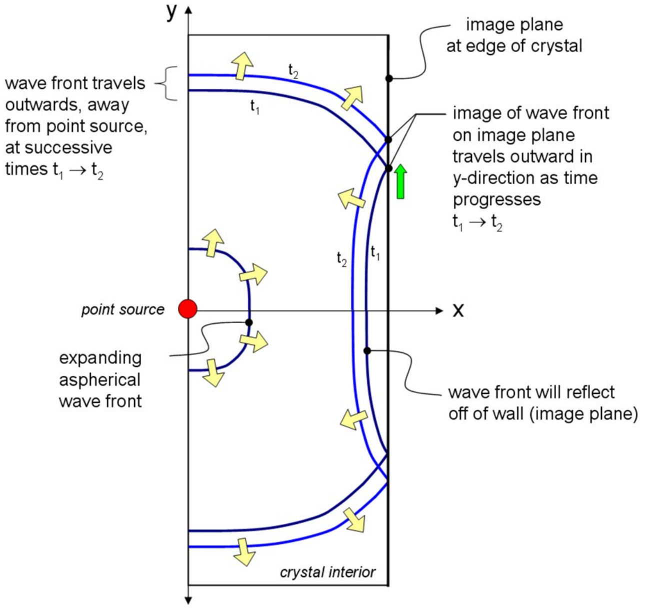

Fig. 13 Two-dimensional schematic of wave fronts intersecting image plane at successive times

effects limit the total simulation time over which meaningful images will be presented. For the method to produce proper results, the patterns must be shown to be invariant to lateral extensions of the simulation domain, and time windows must be chosen to avoid picking up the overlapping periodic signals. In practice, the model has to be run with various simulation domain shapes to verify that the patterns of interest are not domain dependent.

5 Advantages and Limitations of the Method

A key advantage of the present approach is its elimination of the task of directly calculating the dispersion relation or vibrational eigenvectors and eigenvalues for every possible direction. Instead, this information naturally results from the choice of potential function and crystal structure. With a sufficiently large domain, the various eigenmodes will separate into independent packets that arrive at the image plane at distinct times, as seen in experiment. Our computational ability limits our domain size, so the desired longitudinal wave packet partly overlaps the transverse mode vibrations that are incidentally generated. By examining images at sufficiently early simulation times, we are able to sense the arrival of the early pulses of the quasilongitudinal mode packet.

The modeling technique relies on selection of domain size in the *y*-*z* plane (NCY × NCZ, as shown in Fig. 3) to provide sufficient resolution of the images. This feature is also common to the Monte Carlo model, where the image plane is sampled into bins, which collect incident phonons. This model resolves signal level as a scalar value inherent at every step of the calculation, so runs containing many separate vibrations may not be necessary, unlike the Monte Carlo approach. Instead, the MD approach requires selection of simulation cell length in the *x* direction to provide the proper angular span of group velocity vector directions, and this translates the *y*-*z* resolution into an angular resolution. As the length of the model increases in the *x* direction (NCX), the computation time rises in proportion to NCX^2, due to a linear increase in the number of atoms modeled combined with a linear increase in the simulated time required for a pulse to traverse the simulation domain, traveling from the source to the image plane. This scaling relation makes the MD model computationally expensive for high resolution/large domain simulations.

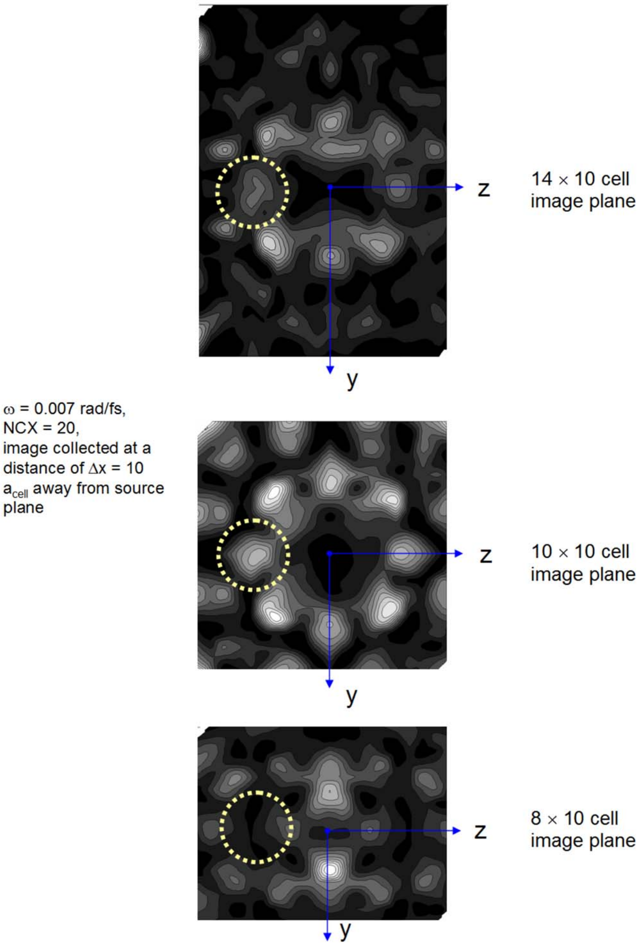

Fig. 14 Kinetic energy contours on image planes, example images after signals have passed through periodic boundaries

In the Monte Carlo approach, a large number of phonons and hence individual computations are necessary to ensure sufficient *y* resolution, *z* resolution, time resolution (via window selection), and image contrast or relative intensity. Increasing any one of these can proportionally increase computation time. Increasing the number of points in the Monte Carlo model's *y*-*z* plane fourfold while maintaining the same angular spread will require four times the computation time. In the MD model, maintaining a given angular span of group velocity vectors while increasing the *y*-*z* plane's pixel count (resolution) fourfold will require doubling NCX, NCY, NCZ, and simulated time, ultimately requiring 16 times the computation time. This potentially high cost of the MD model is somewhat compensated for by the collection of data with very high time resolution, and with very high signal level resolution in the image plane by using floating-point values for kinetic energy levels.

The images in this study were taken from runs using domains of 32 × 46 × 36 and 24 × 30 × 20 unit cells. Smaller computational domains gave indistinct patterns due to the poor resolution. Computations for these domains were completed on a single processor in less than 24 h. A model of this type using 12-6 argon potential functions could produce results for a 60 × 100 × 100 cell case in less than a month using a single processor available today. While increased domains will provide higher resolution, they also result in decreased pulse amplitude at the image plane, thus lower signal-to-noise levels. As the pulse propagates over a longer distance, it is subjected to increased scattering due to the anharmonic potential functions, and raising the initial pulse amplitude to increase signal levels will distort the pulse by increasing the anharmonic scattering.

Given a sufficiently large model, one could select a multiple-atom region of the material to serve as the point source of phonons. In this surface region, the atoms could be given initial velocities based on a chosen energy distribution, and then allowed to interact over time and redistribute the energy by generating waves. This approach would more closely match that of the experiment. To maintain the ratio of the heated region diameter to material sample size found in the experiment, the model would have to incorporate many millions of atoms. This desirable but computationally expensive signal generation method is beyond the scope of the present calculations. A pulse driven using multiple atoms could improve the signal-to-noise level. This would also permit the driven input to have a uniform distribution of $\mathbf{k}$, potentially yielding transverse mode caustics as seen in experiments. In its present form, the model will not properly resolve caustics, a clear drawback.

Our method for identification of the quasilongitudinal wave front is by arrival time. Due to our computational limits, any quasitransverse wave packets present will overlap with the trailing portion of the quasilongitudinal packet. In phonon-focusing experiments, the pulses are short enough and the length scale large enough that the individual modes separate in space into distinct pulses for the quasilongitudinal, quasifast transverse, and quasislow transverse pulses. With MD models which are an order of magnitude larger than those we use, the wave packets will separate as well, and allow separate visualization of the quasitransverse modes in the fashion of the experiment.

6 Conclusions

A new MD method was developed to observe wave-packet propagation in crystals. This method revealed anisotropic propagation of wave fronts associated with point-source energy inputs using narrow wave packets. These images showed wave front patterns associated with the quasilongitudinal mode. This method may serve as an alternative to experimental and other numerical methods due to its high time resolution, high signal intensity resolution, and ability to simulate vibrations of a specific frequency range.

Acknowledgment

This work was supported by National Science Foundation CAREER Grant No. CBET-0547588.

Nomenclature

a = crystal elastic stiffness ratio, C_{11}/C_{44}
b = crystal elastic stiffness ratio, C_{12}/C_{44}
k = wave number
$\mathbf{k}$ = wave vector
KE = kinetic energy
PE = potential energy
NCX = number of lattice cells used in x direction
NCY = number of lattice cells used in y direction
NCZ = number of lattice cells used in z direction
r = radial distance from source
t = time
u = displacement
$\mathbf{v_g}$ = group velocity vector
x = coordinate direction
y = coordinate direction, lateral
z = coordinate direction, lateral
Δ = elastic anisotropy factor, $\Delta = a - b - 2$
ε = model parameter—energy value corresponding to minimum potential energy of a pair of atoms (distance below 0 PE), equivalent to maximum binding energy
σ = potential function length parameter spacing at which the atomic pair has energy matching that of a pair at infinite separation
ω = vibrational angular frequency

References

[1] Wolfe, J. P., 1998, *Imaging Phonons: Acoustic Wave Propagation in Solids*, Cambridge University Press, Cambridge, UK.
[2] Shields, J. A., Tamura, S., and Wolfe, J. P., 1991, "Elastic Scattering of Acoustic Phonons in Si," Phys. Rev. B, **43**(6), pp. 4966–4975.
[3] Auld, B. A., 1973, *Acoustic Fields and Waves in Solids*, Vol. I, Wiley, New York.
[4] Gańcza, W. M., and Paszkiewicz, T., 1995, "Phonon Focussing Patterns: Monte Carlo Simulation of the Motion of Ballistic Phonon Beams in Cubic Crystals," Comput. Phys. Commun., **85**, pp. 423–436.
[5] Lukes, J. R., and Tien, C.-L., 2004, "Molecular Dynamics Simulation of Thermal Conduction in Nanoporous Thin Films," Microscale Thermophys. Eng., **8**, pp. 341–359.
[6] Allen, M. P., and Tildesley, D. J., 1987, *Computer Simulation of Liquids*, Oxford University Press, Oxford.
[7] Barker, J. A., and Klein, M. L., 1970, "Elastic Constants and Phonon Dispersion Curves for Solid Argon near 0°K," Phys. Rev. B, **2**(10), pp. 4176–4179.
[8] Wolfe, J. P., and Hauser, M. R., 1995, "Acoustic Wavefront Imaging," Ann. Phys. (N.Y.), **4**, pp. 99–126.
[9] Maris, H. J., and Tamura, S., 1993, "Anharmonic Decay and the Propagation of Phonons in an Isotropically Pure Crystal at Low Temperatures: Application to Dark-Matter Detection," Phys. Rev. B, **47**(2), pp. 727–739.
[10] Wolfe, J. P., July 2007, "Phonons, UIUC Physics," ⟨http://www.physics.uiuc.edu/Education/Graduate/phon_1.mpg⟩ and ⟨http://www.physics.uiuc.edu/people/Wolfe/2movies.html⟩

Size Effect on the Thermal Conductivity of Thin Metallic Films Investigated by Scanning Joule Expansion Microscopy

Siva P. Gurrum
Semiconductor Packaging Technology Research,
Texas Instruments Incorporated,
Dallas, TX 75243

William P. King
Department of Mechanical Science and Engineering,
University of Illinois,
Urbana-Champaign,
Urbana, IL 61801

Yogendra K. Joshi
G.W. Woodruff School of Mechanical Engineering,
Georgia Institute of Technology,
Atlanta, GA 30332

Koneru Ramakrishna
Package Material Technology Development,
Analog & Mixed Signal Technologies,
Technology Solutions Organization,
Freescale Semiconductor, Inc.,
Austin, TX 78735

A technique to extract in-plane thermal conductivity of thin metallic films whose thickness is comparable to electron mean free path is described. Microscale constrictions were fabricated into gold films of thicknesses 43 nm and 131 nm. A sinusoidal voltage excitation across the constriction results in a local temperature rise. An existing technique known as scanning joule expansion microscopy, measures the corresponding periodic thermomechanical expansion with a 10 nm resolution and determines the local temperature gradient near the constriction. A three-dimensional finite-element simulation of the frequency-domain heat transfer fits the in-plane thermal conductivity to the measured data, finding thermal conductivities of 82 ± 7.7 *W/mK for the 43 nm film and* 162 ± 16.7 *W/mK for the 131 nm film, at a heating frequencies of 100 kHz and 90 kHz, respectively. These values are significantly smaller than the bulk thermal conductivity value of 318 W/mK for gold, showing the electron size effect due to the metal-dielectric interface and grain boundary scattering. The obtained values are close to the thermal conductivity values, which are derived from electrical conductivity measurements after using the Wiedemann–Franz law. Because the technique does not require suspended metal bridges, it captures true metal-dielectric interface scattering characteristics. The technique can be extended to other films that can carry current and result in Joule heating, such as doped single crystal or polycrystalline semiconductors.*
[DOI: 10.1115/1.2928014]

Keywords: thermal conductivity, metallic thin films, size effects, surface scattering, atomic force microscopy

Introduction

Thermal and electrical properties of thin films are important for performance and reliability design of future microelectronic and nanoelectronic systems. Electrical connections in these systems consist of metal wiring of size 100 nm or less. When the size of a metal interconnect is comparable to electron mean free path, electron transport is dominated by scattering with the metal-dielectric interface, which can reduce the electrical and thermal conductivities to less than half the bulk value [1–6]. This conductivity reduction has been explained by the Fuchs–Sondheimer model [1,2] and subsequently more refined models [3–6]. Grain boundary electron scattering can also be greatly enhanced for such thin films due to the much smaller grain sizes observed in thin films, when compared to the bulk [7]. A number of techniques have been proposed to measure the thermal conductivity of thin films [8–14]. There are significant challenges that need to be overcome at the nanometer scale. These include spot size limitations that restrict laser-based techniques to spatial resolution no better than 100 nm [8–10], and infrared techniques to the diffraction limit of a few microns. One technique suitable for nanostructures uses resistance thermometry in a suspended bridge [11–15]. However, this technique has a low sensitivity if the substrate is not etched away [15]. This etch alters electron interface scattering properties and skews the measurement. There is a need for improved thermal characterization techniques that preserve the interface between the heated nanostructure and its surroundings.

A number of previous reports have described thermal conductivity measurements using scanning thermal microscopy (SThM) [16], in which a temperature-sensing element is fabricated onto a scanning probe [17–20]. Thermal conductivity measurement using SThM faces several challenges. In either steady-state [17–19] or periodic [20] measurements, heat flow from the probe into the sample is deduced by calibration with samples of known thermal conductivity. A significant drawback of these techniques is that heat transfer between the probe and sample has sensitive dependence on tip-sample contact, which can be modulated by the sample hardness, contact force, or wear [21]. Small changes in tip-sample contact can lead to large changes in measured temperature values, reducing the usefulness of SThM for quantitative property measurement.

This article describes a technique to measure the in-plane thermal conductivity of thin metallic films and interconnects using scanning joule expansion microscopy (SJEM) developed by Varesi and Majumdar [22]. SJEM measures the periodic thermal expansion amplitude at the sample surface, which corresponds to the periodic temperature at the surface. A solution to the periodic heat diffusion equation is compared with the measured temperature distribution. The thermal conductivity is used as a fitting parameter to match simulation and experiment, and the fit thermal conductivity is close to the independently deduced value, obtained by using the electrical conductivity measurements and by using the Wiedemann–Franz law [23]. The SJEM technique originally developed by Varesi and Majumdar [22] does not rely upon tip-sample heat flow, and thus overcomes several drawbacks associ-

---

Contributed by the Heat Transfer Division of ASME for publication in the JOURNAL OF HEAT TRANSFER. Manuscript received March 7, 2007; final manuscript received February 5, 2008; Review conducted by Cholik Chan. Paper presented at the 2005 ASME International Mechanical Engineering Congress (IMECE2005), Orlando, FL, November 5–11, 2005.

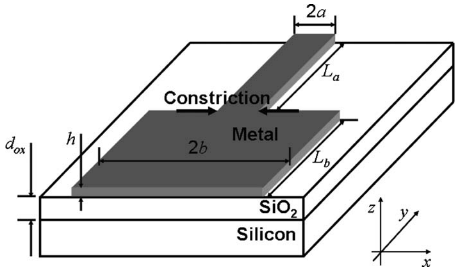

Fig. 1 A schematic of the constriction in a metal thin film

Table 1 Dimensions of constrictions investigated in the present work

	Constriction A	Constriction B
Shorter width $(2a)$	7.01 μm	6.2 μm
Longer width $(2b)$	200 μm	200 μm
Metal thickness (h)	43.4 nm	131.3 nm
Oxide thickness (d_{ox})	849 nm	7.72 μm

ated with SThM. The novelty of the present technique is in using a constriction to measure the temperature amplitude variation due to the current crowding and using detailed frequency space simulations to extract the in-plane thermal conductivity of metallic films.

Measurement Technique and Experimental Details

The test structure consists of a constriction between the two metal lines of different widths. Figure 1 shows a schematic of the constriction and the different layers underneath the metal film. The described technique can also be applied on other electrically conducting films such as doped semiconductors. A periodic current through this structure results in a periodic expansion of the surface. Due to the current continuity, the current density is much higher near the constriction and in the narrow line than in the wide interconnect. Higher current density causes higher heat generation per unit volume, and if the thermal conductivity of the metal film is not too high, this heat generation variation results in a sensible temperature amplitude gradient near the constriction. The temperature amplitude gradient becomes steeper as the heating frequency is increased. This temperature amplitude gradient is measured using SJEM at several different frequencies. Thermal conductivity of the film is then extracted by fitting these curves with detailed numerical simulations. The width of the constriction is made small compared to the length of the electrical interconnects, so that the local temperature amplitude distribution in the vicinity of the constriction is independent from the rest of the structure.

The test structure in the present study includes metal lines made of gold films. Both the shorter $(2a)$ and longer $(2b)$ width lines in the test structure extend to more than 2 mm in length (Fig. 1). The metal line was deposited using electron beam evaporation of gold and patterned by the lift-off technique. The silicon dioxide layer underneath was deposited by plasma enhanced chemical vapor deposition (PECVD) process. It is important that there be a good contact between the metal lines and the underlying silicon dioxide. The expansion amplitude deteriorates considerably when there is a delamination between the metal line and the oxide layer. Two structures, Constriction A and Constriction B, of different thicknesses were investigated. All the dimensions of these structures are given in Table 1.

The thermal conductivity of silicon dioxide underneath the metal lines is important in the numerical model, and was independently measured using the 3ω method [24]. The thermal conductivity of silicon dioxide was measured in Constriction A wafer to be 1.16 ± 0.035 W/mK, and in Constriction B wafer to be 1.00 ± 0.019 W/mK. These values are typical for chemical vapor deposited silicon dioxide films [25].

A closed-loop atomic force microscope (AFM) (Asylum Research—MFP-3D) was used along with a digital and a RF lock-in amplifier (Stanford Research Systems—SR830 and SR844). The AFM scan rates varied from 0.25 Hz to 2 Hz. These were adjusted such that for each data point (pixel in the x-y plane of the film), at least ten surface oscillations were detected by the AFM tip. Most of the measurements are in the few 100 oscillations/data point range. This allowed sufficient time for the lock-in to detect the particular frequency component.

Numerical Modeling

Thermal Model in Frequency Space. A sinusoidal voltage signal in an interconnect results in a steady (DC) and a periodic (AC) heat generation. Since SJEM measures only the AC temperature amplitude, significant computational effort can be saved by transforming the heat conduction equation into frequency or complex space. Consider the transient heat conduction equation

$$\rho c \frac{\partial T(\mathbf{r},t)}{\partial t} = k\nabla^2 T(\mathbf{r},t) + \dot{q}'''(\mathbf{r},t) \tag{1}$$

with a time varying volumetric heat generation. If ω_h is the frequency of heat generation ($\omega_h = 2\omega$, where ω is the frequency of input voltage signal), periodic components of heat generation and temperature can be written as

$$T(\mathbf{r},t) = (X(\mathbf{r}) + iY(\mathbf{r}))e^{i\omega_h t}, \quad \dot{q}'''(\mathbf{r},t) = q_o(\mathbf{r})e^{i\omega_h t} \tag{2}$$

where $X(\mathbf{r})$ and $Y(\mathbf{r})$ are, respectively, the real and imaginary parts of temperature amplitude, $q_o(\mathbf{r})$ is the spatially varying heat generation amplitude and $i = \sqrt{-1}$. With these substitutions, Eq. (1) leads to two steady coupled partial differential equations:

$$k\nabla^2 X(\mathbf{r}) + \rho c \omega_h Y(\mathbf{r}) + q_o(\mathbf{r}) = 0$$

$$k\nabla^2 Y(\mathbf{r}) - \rho c \omega_h X(\mathbf{r}) = 0 \tag{3}$$

These equations are solved using an in-house developed code based on the traditional finite-element method (FEM) [26]. In the numerical simulations, lengths L_a and L_b along the metal line, shown in Fig. 1, are made long enough so that the results near the constriction are independent of these lengths. The temperature amplitude reaches a constant value further from the constriction, corresponding to a two-dimensional case. Specifically, $L_a = 20$ μm and $L_b = 40$ μm for Constriction A, and $L_a = 30$ μm and $L_b = 60$ μm for Constriction B. The numerical model also includes the entire oxide film thickness, and a portion of silicon substrate (100 μm for Constriction A and 60 μm for Constriction B). These thicknesses for silicon capture the transient behavior accurately at the heating frequencies used in the current study.

Heat Generation Model. In steady-state conditions, electric field can be obtained from a solution of Poisson's equation for electric potential with a zero space charge. Ohm's law gives a relationship between the electric field and current density, once the electrical resistivity is known. Heat generation can then be calculated using the electric field and current density. The following set of equations fully describes a steady-state scenario:

$$\nabla^2 V(\mathbf{r}) = 0$$

$$\mathbf{E}(\mathbf{r}) = -\nabla V(\mathbf{r})$$

$$\mathbf{j}(\mathbf{r}) = \mathbf{E}(\mathbf{r})/\rho_e$$

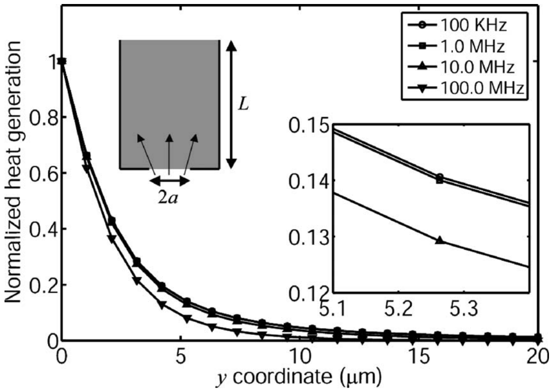

Fig. 2 Effect of skin depth on heat generation profiles is shown for different frequencies. The inset zooms a portion of the plot to resolve lower frequencies. For the frequencies considered in this work, the skin effect can be neglected. It is assumed that $L \rightarrow \infty$.

$$\dot{q}'''(\mathbf{r}) = \mathbf{j}^2(\mathbf{r})\rho_e \tag{4}$$

where $V(\mathbf{r})$ is the electric potential, $\mathbf{E}(\mathbf{r})$ is the electric field, $\mathbf{j}(\mathbf{r})$ is the current density, and ρ_e is the electrical resistivity. For an accurate description of transient cases, the complete set of Maxwell's electromagnetic equations should be considered [27]. These equations are coupled and are difficult to solve for an arbitrary conductor. For small frequencies, this may not be necessary, as the skin depth becomes very large. Skin depth δ_s is given by [27]

$$\delta_s = \sqrt{\frac{2\rho_e}{\mu\omega}} \tag{5}$$

where ω is the frequency of the input voltage signal. The effect of magnetic fields on current density and heat generation are negligible if the skin depth is much larger than the conductor diameter. For a typical $\rho_e = 2.2\ \mu\Omega$ cm for gold, the skin depth is 333.8 μm at $\omega = 50$ kHz and 105.6 μm at $\omega = 500$ kHz. Skin effect may then be neglected for the smaller linewidth interconnect (7 μm wide). The discussion in the following paragraph shows that it can also be neglected in the wider line (200 μm wide).

An analytical solution available for a related geometry is used to identify the effect of skin depth in the wider line. Ney [28] obtained an analytical solution for a constriction type structure including skin effect. The geometry is shown in the inset of Fig. 2. It is assumed that the thickness into the plane of the paper is much smaller than all other dimensions and skin depth, which allows for a two-dimensional analysis. Normalized heat generation profiles for this structure are plotted in Fig. 2 for several frequencies. Due to the fitting procedure used in thermal property extraction, normalized heat generation is sufficient for analysis. It is clear that significant deviations appear at very high frequencies, but there is little difference between the profiles for 100 kHz and 1.0 MHz. The maximum frequency used in the present work is 500 kHz, and it can thus be concluded that the effects of skin depth can be ignored. Heat generation can now be calculated by assuming that the amplitudes of various quantities are governed by steady-state equations given in Eq. (4). It is important to solve for precise current density and heat generation profile near the constriction using Eq. (4). A simple one-dimensional model, in which the current density is assumed to be constant in each line, but the total current is kept the same, leads to very different temperature amplitude profiles near the constriction. Far from the constriction, the temperature amplitude reduces to that of a two-dimensional geometry with an infinitely long metal line of the same width.

Thermomechanical Model for Expansion Amplitude. SJEM measures only the expansion amplitude of the surface. This amplitude is in general a complex function of temperature, thermophysical, and mechanical properties. It is assumed in the thermal conductivity extraction procedure that the expansion amplitude is linearly proportional to temperature amplitude. This assumption is examined by performing a detailed deformation analysis of a two-dimensional structure. It is convenient to use Einstein notation to describe the governing dynamical equation (see Ref. [29] for a detailed derivation of the equations). Let $\mathbf{u}_i$ be the displacement vector (i takes the values 1, 2, and 3 corresponding to x, y, and z directions). The strain tensor components ε_{ij} are given as

$$\varepsilon_{ij} = \frac{1}{2}(u_{i,j} + u_{j,i}) \tag{6}$$

where $u_{i,j}$ stands for the partial derivative of $\mathbf{u}_i$ with respect to j coordinate. Within the framework of linear thermoelasticity, a constitutive equation between the stress tensor σ_{ij} and strain tensor is given by

$$\sigma_{ij} = \frac{E}{(1+\nu)(1-2\nu)}[\nu\delta_{ij}\varepsilon_{kk} + (1-2\nu)\varepsilon_{ij}] - \frac{E}{(1-2\nu)}\alpha(T - T_o)\delta_{ij} \tag{7}$$

where E is Young's modulus, ν is Poisson's ratio, α is the coefficient of thermal expansion (CTE), T is the temperature, T_o is the reference temperature, and δ_{ij} is the Kronecker delta. The dynamical equation is derived by applying Newton's second law to a differential volume element:

$$\rho\ddot{u}_i = \sigma_{ij,j} + \rho b_i \tag{8}$$

where ρ is the density, b_i is a volumetric body force such as that due to the gravity, and the dots denote the second order partial derivative with respect to time. Using Eq. (7) for the stress tensor results in the following dynamical equation, known as the Navier's equation.

$$\rho\ddot{u}_i = \frac{E}{2(1+\nu)}u_{i,jj} + \frac{E}{2(1+\nu)(1-2\nu)}u_{j,ij} - \frac{E\alpha}{(1-2\nu)}T_{,i} + \rho b_i \tag{9}$$

The above equation is transformed into frequency space since only the expansion amplitude is required. Assuming $u_i = u_i^* \exp(i\omega_h t)$ and $T = T^* \exp(i\omega_h t)$, where the superscript "*" implies a complex function of space, and ignoring body forces results in

$$-\rho\omega_h^2\ddot{u}_i^* = \frac{E}{2(1+\nu)}u_{i,jj}^* + \frac{E}{2(1+\nu)(1-2\nu)}u_{j,ij}^* - \frac{E\alpha}{(1-2\nu)}T_{,i}^* \tag{10}$$

If the temperature field is known, this equation can be solved for the expansion amplitude u_i^*.

A two-dimensional analysis of a long metal line was performed to verify the validity of a linear relation between the expansion amplitude and temperature amplitude. In this case, a plane strain assumption was made to reduce the computational cost. In a plane strain and linear elasticity assumption, ε_{yy}, ε_{yx}, and ε_{yz} are assumed to be zero. A schematic of the simulated half metal line structure is shown in the inset of Fig. 3(a) (half metal line is sufficient due to symmetry). The vertical plane at $x = 0$ was constrained to move only in the vertical direction. The problem was solved in FEMLAB, which allows for coupling of different equations. The temperature amplitude was calculated by the solution of heat conduction equation in the frequency space, which was then used as an input for deformation modeling. Tables 2(a) and 2(b) list the thermomechanical properties [30–33] and thermal properties used in the simulation.

Expansion and temperature amplitudes on the surface of the structure are plotted in Fig. 3(a) for $\omega_h = 100$ kHz from the center of the metal line to its edge. If the relationship between them is

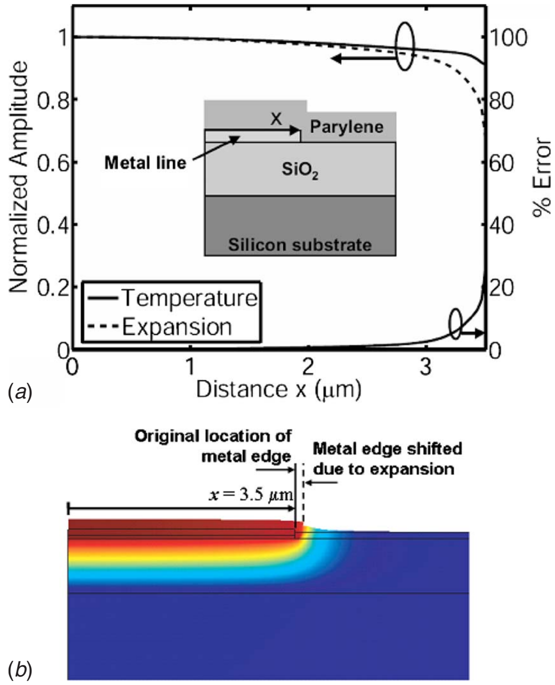

Fig. 3 (*a*) Comparison of expansion amplitude and temperature amplitude over the metal line. The two-dimensional structure modeled under the plane strain assumption is shown in the inset. (*b*) Deformation amplitude is shown by the displaced structure. Temperature amplitude is plotted using color shading. The deformation is artificially scaled by a large factor for clarity.

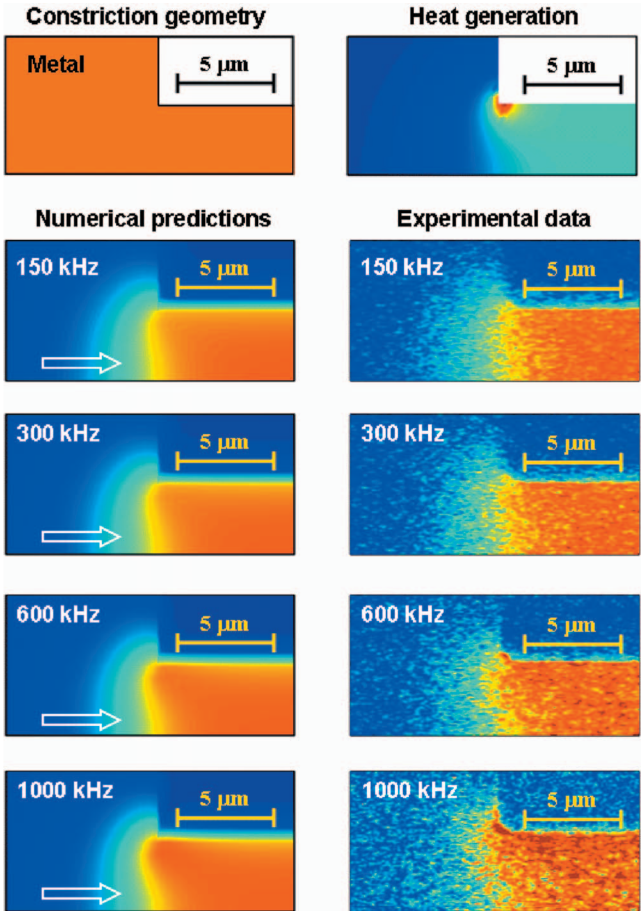

Fig. 4 A comparison of numerical and experimental expansion amplitudes as the frequency is varied. The block arrows in the left column figures show the viewing direction. Viewing in this direction shows that the temperature amplitude surface gradually becomes more concave (for example, look at the yellow band of contours), which is a clear signature of in-plane thermal penetration depth.

linear, the two curves should coincide. It is apparent that the linearity assumption fails, as one approaches the edges of the metal line. This is primarily due to the large CTE mismatch between the metal and underlying oxide layer. The percentage error is also shown in the same plot. This is not a serious concern since the thermal conductivity extraction procedure uses expansion amplitude only along the centerline of the metal line. The deformation of the structure is depicted in Fig. 3(*b*) along with the temperature amplitude over the cross section. The deformation is arbitrarily scaled to a much larger value for clarity. Due to the large heating frequency, the temperature amplitude is appreciable only in the oxide layer close to the metal line.

Table 2 (*a*) Mechanical properties used for thermomechanical simulation and (*b*) thermal properties used in thermal conductivity extraction

(*a*)	Material	Young's modulus E (GPa)	Poisson's ratio ν	CTE α (ppm/K)	Density ρ (kg/m^3)
	Silicon	97.68	0.278	2.62	2329
	Silicon dioxide	59.0	0.24	1.0	2185
	Gold	80.12	0.423	14.20	18880
	Parylene	3.2	0.4	35.0	1289

(*b*)	Material	Density (kg/m^3)	Specific heat (J/kg K)	Thermal conductivity (W/mK)
	Silicon dioxide	2185	744	Measured
	Silicon	2329	712	148
	Gold	18880	128	Extracted

Experimental Results and Thermal Conductivity Extraction

In a periodic heating case, the temperature amplitude at the heating source gradually reduces as the heating frequency is increased. Temperature oscillations are felt only within a small region surrounding the heat source, the extent of which continuously reduces with increasing frequency. The size of this region is characterized by the frequency dependent thermal penetration depth, which also depends on the thermal properties of the medium. Thermal conductivity can be extracted if the temperature amplitude measurements are sufficiently accurate to observe in-plane thermal penetration depth, assuming the heat capacity is known. This effect in the constriction is shown in Fig. 4 as the frequency is increased. Even though the spatial variation in heat generation is the same for all the cases, both predicted and measured amplitudes clearly show a frequency dependent structure. As the frequency increases, in-plane thermal penetration depth within the gold film reduces, and the amplitude drops much more steeply near the constriction. In the limit that the penetration depth is zero, the expansion amplitude will be similar to the heat generation amplitude. This effect is clearly seen at 1000 kHz. Noise levels gradually increase as the frequency is increased to 1000 kHz. Thermal expansion amplitude continuously reduces as the frequency increases. This investigation shows that frequency dependent structure can be captured by SJEM on a constriction.

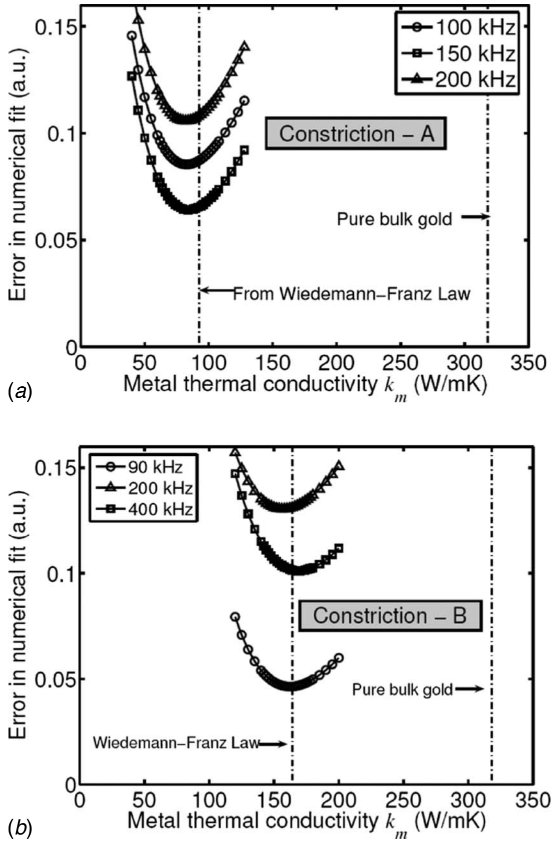

Fig. 5 Error in numerical fit at different frequencies as the thermal conductivity of metal film is varied for Constriction A (*a*) and Constriction B (*b*)

This can allow for thermal conductivity extraction of thin films, which is described in the following section. In a strict sense, it is the thermal diffusivity that determines the thermal penetration depth. We present the discussion in terms of thermal conductivity since it is a more common quantity, assuming the density and specific heat can be approximated by its bulk values.

Ideally, the calculation of expansion amplitude requires thermomechanical properties of the underlying layers. In order to deduce temperature amplitude from the expansion amplitude, the CTE and thickness of all the underlying layers that contribute to the expansion signal must be known. In the present structure, the CTEs of metal line and parylene are much larger than the underlying oxide and silicon substrate. Since the thermal diffusivity of gold is high, temperature across the thickness of the metal line is constant. It can be assumed that the temperature across parylene is also constant, since the thickness ($\sim$100 nm) is much smaller than the thermal penetration depth (thermal penetration depth for parylene is $\sim\sqrt{k/\rho c_P f}=669$ nm, where thermal conductivity $k=0.082$ W/mK, density $\rho=1289$ kg/m^3, specific heat $c_P=711$ J/kg K, and heating frequency $f=200$ kHz). If one ignores temperature dependence of properties, then the temperature amplitude and expansion signal are linearly proportional. The contribution of the underlying layers (silicon dioxide and silicon substrate) to the expansion signal diminishes as the frequency increases. Higher frequencies diminish the effect of far-field conditions. The validity of these assumptions was verified using a detailed thermomechanical analysis of the structure, as described in the section "Thermomechanical Model for Expansion Amplitude" in the previous section titled "Numerical Modeling." Thermomechanical analysis, which includes the parylene film, demonstrates that the expansion amplitude and temperature amplitude are linearly related at the center of the metal film. With this linearity assumption, only the thermal properties are required in the extraction procedure and are listed in Table 2(*b*). The extraction procedure has also been applied to Constriction B, which does not have any parylene layer.

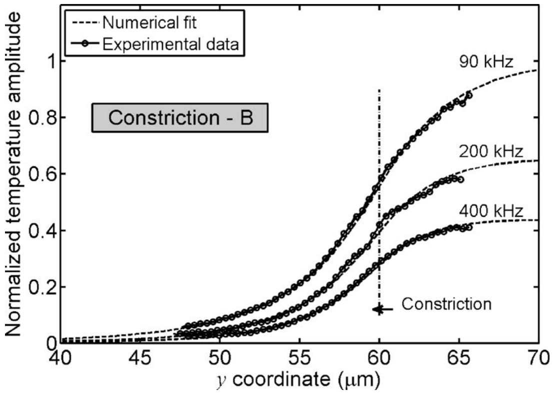

Fig. 6 Comparison of experimental and numerical temperature amplitude profiles along the centerline near the constriction after minimizing the error in numerical fit

A simple minimization procedure was used to find the proportionality constant between the expansion signal and temperature amplitude. If $E(x,y)$ is the expansion signal, then $T_{\text{exp}}(x,y)=CE(x,y)$, where C is the unknown proportionality constant. For a given temperature amplitude $T_{\text{num}}(x,y)$ obtained from numerical simulations, C was obtained by minimizing the mean square error. Temperature amplitude profile on the centerline of metal lines was averaged over a micron across the width and was used in this fitting procedure. Phase lag information between the heating voltage signal and expansion signal will also depend on thermal properties of the films in the stack. In this work, we only consider the expansion amplitude and plan to investigate phase lag in future work.

The error after obtaining the best C for different values of metal thermal conductivity is shown in Fig. 5(*a*) for 100 kHz, 150 kHz, and 200 kHz heating frequencies. It is clear that a good fit is obtained for metal thermal conductivity near 82.0 W/mK. Although gold has a bulk thermal conductivity of 318 W/mK at room temperature, thin films of thickness comparable to mean free path are known to have much lower thermal conductivity due to enhanced electron surface and grain boundary scattering [1–7]. The fit value of thermal conductivity thus appears reasonable for the 43 nm thick film (Constriction A) used in the present investigation.

Measurements were also made on Constriction B and the errors are shown in Fig. 5(*b*). This structure lacks parylene coating, but the signal-to-noise ratio is still good due to the large oxide layer underneath the metal layer. Thicker oxide resulted in larger temperature amplitude. The thickness of this structure is 131 nm and is about three times the mean free path of electrons. The best fit thermal conductivity is 162 W/mK, and is about twice that of Constriction A film. The obtained temperature profiles at the best fit are compared with measurements in Fig. 6. These agree with the measurements very closely over the entire range.

It is well known that electrical and thermal conductivity of bulk metals are approximately related by the Wiedemann–Franz Law [23], according to which

$$\frac{\kappa_{\text{film}}}{\sigma_{\text{film}}T}=L_o \qquad (11)$$

where σ_{film} is the electrical conductivity, κ_{film} is the thermal conductivity, T is the temperature, and L_o is the Lorenz number [23]. Based on the electrical resistance measurements, the electrical re-

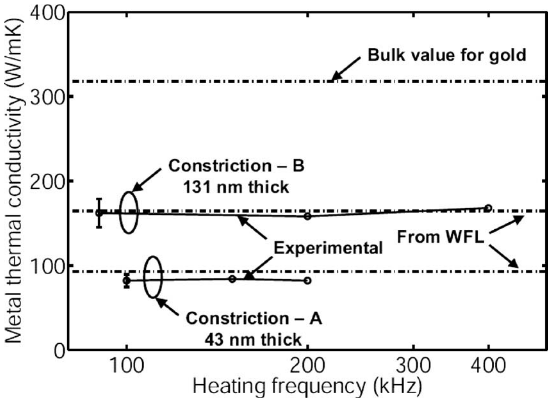

Fig. 7 A summary of the extracted thermal conductivities for two constrictions and their comparison with bulk value and WFL predictions

sistivity of the line was found to be 7.52 $\mu\Omega$ cm. Using 2.32×10^{-8} WΩ/K^2 for the Lorenz number of gold resulted in a thermal conductivity of 92.55 W/mK for the metal line. This value is close to the extracted value of 82 W/mK as generally expected. Some recent measurements by Zhang et al. [34] suggest that Weidemann–Franz law (WFL) may not be applicable for thin films. They measured a thermal conductivity to electrical conductivity ratio of 1.4×10^{-5} W Ω/K for a 28 nm platinum thin film, as compared to a bulk value of 7.5×10^{-6} W Ω/K, both at 300 K. The deviation here is more than 50%. The authors did not provide any concrete reason for the deviation, and pointed out that material type, fabrication method, and film size should be considered in applying WFL. Figure 7 summarizes all our measurements made along with the predicted values from WFL, and bulk thermal conductivity of gold. It thus appears that a constriction in a thin metal film characterized through SJEM in conjunction with the 3ω method can enable in-plane thermal conductivity measurements of thin films and interconnects in the sub-100 nm range. The technique does not require extensive microfabrication since freestanding metal films are not necessary. The absence of freestanding films captures the true electron surface scattering characteristics.

Uncertainty Analysis

The extracted thermal conductivity values depend on several parameters, such as metal linewidth, metal thickness, and silicon dioxide thermal conductivity. Uncertainties in these parameters propagate into the measured thermal conductivity of the metal line. The uncertainties can be accounted for by the procedure described in Ref. [35]. The analysis for oxide thermal conductivity measurements for both structures is shown in Tables 3(*a*) and 3(*b*). Metal linewidths were measured using the AFM, oxide thicknesses were measured using AFM scan on trenches etched in the samples from the same wafers, and TCR was calibrated in an oven between room temperature and 80°C. The uncertainty in oxide thermal conductivity is then used as an input for uncertainty calculations for extracted metal thermal conductivities. These analyses for Constriction A structure at 100 kHz heating frequency and Constriction B structure at 90 kHz heating frequency are shown in Tables 4(*a*) and 4(*b*), respectively. The uncertainty in both cases is about ±10%. Figure 7 shows these uncertainty bars for the two constriction structures.

Conclusions

This article proposes a novel technique to extract in-plane thermal conductivity of thin metallic films whose thickness is comparable to electron mean free path. The technique uses SJEM to map temperature amplitude gradient near a constriction between wide and narrow metal lines. Thermal conductivity is extracted by using a numerical fit to measurements. Extracted thermal conductivities of thin gold films show consistency with predictions from Wiedemann–Franz for the 43 nm and 131 nm gold films investigated in this study.

Table 3 Uncertainty analysis for oxide thermal conductivity measurements in (*a*) Constriction A and (*b*) Constriction B

(*a*)	Parameter	Nominal value	Deviation	% change in k_{ox} for $+u_i$
	Metal half width (a)	3.5 μm	±0.5 μm	−1.3
	Oxide thickness (d_{ox})	849 nm	±5 nm	+0.5
	TCR (α_T)	1.678×10^{-3}/°C	$\pm 0.035 \times 10^{-3}$/°C	+2.3
	Input voltage (V_{in})	4.246 V	±1 mV	+0.1
	Silicon thermal conductivity (k_{Si})	148 W/mK	±7.4 W/mK	−0.4
	Silicon heat capacity (C_{Si})	1.66×10^6 J/m^3	$\pm 0.08 \times 10^6$ J/m^3	−0.1
	3ω voltage ($V_{3\omega}$)	2.68 mV	±0.03 mV	−1.1
	Oxide thermal conductivity k_{ox}	1.16 W/mK	±0.035 W/mK	±3%
(*b*)	Parameter	Nominal value	Deviation	% change in k_{ox} for $+u_i$
	Metal half width (a)	3.1 μm	±0.07 μm	−1.1
	Oxide thickness (d_{ox})	7.72 μm	±10 nm	+0.1
	TCR (α_T)	2.176×10^{-3}/°C	$\pm 0.022 \times 10^{-3}$/°C	+1.1
	Input voltage (V_{in})	4.05 V	±1 mV	+0.1
	Silicon thermal conductivity (k_{Si})	148 W/mK	±7.4 W/mK	−0.4
	Silicon heat capacity (C_{Si})	1.66×10^6 J/m^3	$\pm 0.08 \times 10^6$ J/m^3	<−0.1
	3ω voltage ($V_{3\omega}$)	6.985 mV	±0.07 mV	−1.0
	Oxide thermal conductivity k_{ox}	1.00 W/mK	±0.019 W/mK	±1.9%

Table 4 Uncertainty analysis for extracted metal thermal conductivity in (*a*) Constriction A at 100 kHz heating frequency and (*b*) Constriction B at 90 kHz heating frequency

(*a*)	Parameter	Nominal value	Deviation	% change in k_m for $+u_i$
	Metal half width (a)	3.5 μm	$\pm$0.05 μm	4.9
	Metal thickness (h)	43.4 nm	$\pm$1.2 nm	2.4
	Oxide thermal conductivity k_{ox}	1.16 W/mK	$\pm$0.035 W/mK	2.4
	Constriction location	—	$\pm$0.06 μm	7.3
	Metal thermal conductivity k_m	82 W/mK	$\pm$7.7 W/mK	$\pm$9.4%

(*b*)	Parameter	Nominal value	Deviation	% change in k_m for $+u_i$
	Metal half width (a)	3.1 μm	$\pm$0.07 μm	8.6
	Metal thickness (h)	131.3 nm	$\pm$3.5 nm	4.9
	Oxide thermal conductivity k_{ox}	1.00 W/mK	$\pm$0.019 W/mK	1.2
	Constriction location	—	$\pm$0.04 μm	2.5
	Metal thermal conductivity k_m	162 W/mK	$\pm$16.7 W/mK	$\pm$10.3%

The technique clearly captures the conductivity reduction due to the electron size effect. Unlike other methods, this technique does not require suspended metal films for good accuracy. The measurements thus capture true metal-dielectric interface scattering characteristics. Due to the high resolution possible by AFM, the technique can potentially be used for sub-100 nm width metal lines. The technique can easily be extended to other films that can carry current and result in Joule heating, such as doped single crystal or polycrystalline semiconductors. It can also be suitably extended to metallic films at intermediate temperatures (few K to few hundred K), where Wiedemann–Franz Law breaks down.

Acknowledgment

The authors acknowledge support for this work by the Semiconductor Research Corporation through Task 1179.001 customized by Freescale Semiconductor, Inc.

Nomenclature

E = Young's modulus (Pa)
$\vec{E}$ = electric field vector (V/m)
T = temperature (°C)
V = voltage (V)
X = real part of temperature amplitude (°C)
Y = imaginary part of temperature amplitude (°C)
a = half width of shorter metal line (m)
b = half width of wider metal line (m)
c = specific heat (J/kg K)
$\vec{j}$ = current density vector (A/m^2)
L_o = Lorenz number (W Ω/K^2)
$\dot{q}'''$ = volumetric heat generation (W/m^3)
u_i = displacement vector (m)

Greek Letters

α = coefficient of thermal expansion (/°C)
δ_s = skin depth (m)
ε_{ij} = strain tensor
κ = thermal conductivity (W/mK)
μ = magnetic permeability (N/A^2)
ν = Poisson's ratio
ρ = density (kg/m^3)
ρ_e = electrical resistivity (Ω m)
σ_{ij} = stress tensor (Pa)
ω = frequency of voltage input signal (Hz)
ω_h = frequency of heat generation and temperature amplitude

References

[1] Fuchs, K., 1938, "The Conductivity of Thin Metallic Films According to the Electron Theory of Metals," Proc. Cambridge Philos. Soc., **34**, pp. 100–108.
[2] Sondheimer, E. H., 1952, "The Mean Free Path of Electrons in Metals," Adv. Phys., **1**, pp. 1–42.
[3] Ziman, J. M., 1960, *Electrons and Phonons*, Oxford University Press, New York.
[4] Soffer, S. B., 1967, "Statistical Model for the Size Effect in Electrical Conduction," J. Appl. Phys., **38**, pp. 1710–1715.
[5] Namba, Y., 1970, "Resistivity and Temperature Coefficient of Thin Metal Films With Rough Surface," Jpn. J. Appl. Phys., **9**, pp. 1326–1329.
[6] Gurrum, S. P., Joshi, Y. K., King, W. P., and Ramakrishna, K., 2004, "Numerical Simulation of Electron Transport Through Constriction in a Metallic Thin Film," IEEE Electron Device Lett., **25**, pp. 696–698.
[7] Mayadas, A. F., and Shatzkes, M., 1970, "Electrical-Resistivity Model for Polycrystalline Films: The Case of Arbitrary Reflection at External Surfaces," Phys. Rev. B, **1**, pp. 1382–1389.
[8] Hatta, I., Sasuga, Y., Kato, R., and Maesono, A., 1985, "Thermal Diffusivity Measurement of Thin Films by Means of an AC Calorimetric Method," Rev. Sci. Instrum., **56**, pp. 1643–1647.
[9] Kemp, T., Srinivas, T. A. S., Fettig, R., and Ruppel, W., 1995, "Measurement of Thermal Diffusivity of Thin Films and Foils Using a Laser Scanning Microscope," Rev. Sci. Instrum., **66**, 176–181.
[10] Langer, G., Hartmann, J., and Reichling, M., 1997, "Thermal Conductivity of Thin Metallic Films Measured by Photothermal Profile Analysis," Rev. Sci. Instrum., **68**, 1510–1513.
[11] Boiko, B. T., Pugachev, A. T., and Bratsychin, V. M., 1973, "Method for the Determination of the Thermophysical Properties of Evaporated Thin Films," Thin Solid Films, **17**, pp. 157–161.
[12] Volklein, F., and Kessler, E., 1984, "A Method for the Measurement of Thermal Conductivity, Thermal Diffusivity, and Other Transport Coefficients of Thin Films," Phys. Status Solidi A, **81**, pp. 585–596.
[13] Lu, L., Yi, W., and Zhang, D. L., 2001, "3ω Method for Specific Heat and Thermal Conductivity Measurements," Rev. Sci. Instrum., **72**, 2996–3003.
[14] Zhang, X., Xie, H., Fujii, M., Ago, H., Takahashi, K., Ikuta, T., Abe, H., and Shimizu, T., 2005, "Thermal and Electrical Conductivity of a Suspended Platinum Nanofilm," Appl. Phys. Lett., **86**(1–3), 171912.
[15] Yang, Y., and Asheghi, M., 2004, "A Novel Technique for In-Plane Thermal Conductivity Measurements of Electrically Conductive Interconnects and Nanostructures," *Proceedings of 2004 Inter Society Conference on Thermal Phenomena-ITHERM*, IEEE, Piscataway, NJ, pp. 564–569.
[16] Majumdar, A., 1999, "Scanning Thermal Microscopy," Annu. Rev. Mater. Sci., **29**, pp. 505–585.
[17] Ruiz, F., Sun, W. D., Pollak, F. H., and Venkatraman, C., 1998, "Determination of the Thermal Conductivity of Diamond-Like Nanocomposite Films Using a Scanning Thermal Microscope," Appl. Phys. Lett., **73**, pp. 1802–1804.
[18] Gorbunov, V. V., Fuchigami, N., Hazel, J. L., and Tsukruk, V. V., 1999, "Probing Surface Microthermal Properties by Scanning Thermal Microscopy," Langmuir, **15**, pp. 8340–8343.
[19] Fischer, H., 2005, "Quantitative Determination of Heat Conductivities by Scanning Thermal Microscopy," Thermochim. Acta, **425**, pp. 69–74.
[20] Fiege, G. B. M., Altes, A., Heiderhoff, R., and Balk, L. J., 1999, "Quantitative Thermal Conductivity Measurements With Nanometre Resolution," J. Phys. D, **32**, pp. L13–L17.
[21] Pollock, H. M., and Hammiche, A., 2001, "Micro-Thermal Analysis: Techniques and Applications," J. Phys. D, **34**, pp. R23–R53.
[22] Varesi, J., and Majumdar, A., 1998, "Scanning Joule Expansion Microscopy at Nanometer Scales," Appl. Phys. Lett., **72**, pp. 37–39.
[23] Ashcroft, N. W., and Mermin, N. D., *Solid State Physics*, Holt, Rinehart, and Winston, Philadelphia, PA.
[24] Cahill, D. G., 1990, "Thermal Conductivity Measurement From 30 to 750 K: The 3ω Method," Rev. Sci. Instrum., **61**, pp. 802–808.
[25] Ju, Y. S., and Goodson, K. E., 1999, "Process-Dependent Thermal Transport Properties of Silicon-Dioxide Films Deposited Using Low-Pressure Chemical Vapor Deposition," J. Appl. Phys., **85**, pp. 7130–7134.
[26] Segerlind, L. J., 1984, *Applied Finite Element Analysis*, 2nd ed., Wiley, New York.
[27] Jackson, J. D., 1998, *Classical Electrodynamics*, 3rd ed., Wiley, New York.
[28] Ney, M. M., 1991, "Striction and Skin Effects on the Internal Impedance Value of Flat Conductors," IEEE Trans. Electromagn. Compat., **33**, pp. 321–327.
[29] Mase, G. T., and Mase, G. E., 1999, *Continuum Mechanics for Engineers*, 2nd ed., CRC Press, Boca Raton, FL.
[30] Nikanorov, S. P., Burenkov, Yu. A., and Stepanov, A. V., 1971, "Elastic Properties of Silicon," Sov. Phys. Solid State, **13**, pp. 2516–2518.

[31] Zhao, J.-H., Ryan, T., Ho, P. S., McKerrow, A. J., and Shih, W.-Y., 1999, "Measurement of Elastic Modulus, Poisson Ratio, and Coefficient of Thermal Expansion of On-Wafer Submicron Films," J. Appl. Phys., **85**, pp. 6421–6424.
[32] Nandanpawar, M. I., and Rajagopalan, S., 1978, "Wachtman's Equation and Temperature Dependence of Bulk Moduli in Solids," J. Appl. Phys., **49**, pp. 3976–3979.
[33] Zhou, J. W. L., Chan, H.-Y., To, T. K. H., Lai, K. W. C., and Li, W. J., 2004, "Polymer MEMS Actuators for Underwater Micromanipulation," IEEE/ASME Trans. Mechatron., **9**, pp. 334–342.
[34] Zhang, X., Xie, H., Fujii, M., Ago, H., Takahashi, K., Ikuta, T., Abe, H., and Shimizu, T., 2005, "Thermal and Electrical Conductivity of a Suspended Platinum Nanofilm," Appl. Phys. Lett., **86**, 171912.
[35] Kline, S. J., and McClintock, F. A., 1953, "Describing Uncertainties in Single Sample Experiments," Mech. Eng. (Am. Soc. Mech. Eng.), **75**, pp. 3–8.

Infrared Radiative Properties of Submicron Metallic Slit Arrays

Y.-B. Chen[1]

B. J. Lee

Z. M. Zhang[2]
e-mail: zhuomin.zhang@me.gatech.edu

George W. Woodruff School of Mechanical Engineering,
Georgia Institute of Technology,
Atlanta, GA 30332

Submicron metallic slit arrays with different geometry were designed and fabricated on silicon substrates. Their infrared radiative properties (transmittance, reflectance, and absorptance) were investigated both experimentally and theoretically. The normal transmittance of three fabricated Au slit arrays was measured at wavelengths between 2 μm and 15 μm using a Fourier-transform infrared spectrometer. The experimental results were compared to the values calculated from the rigorous coupled-wave analysis. The applicability of the effective medium theory for modeling radiative properties was also examined. The agreement between the measurement and modeling results demonstrates the feasibility of quantitative tuning of the radiative properties by employing periodic micro/nanostructures. [DOI: 10.1115/1.2909614]

Keywords: electromagnetic, grating, microscale, nanoscale, radiative properties, slit array

1 Introduction

Materials with wavelength-selective and/or polarization-dependent radiative properties play a significant role in modern technologies, including energy conversion, radiation detectors, spectroscopy, and liquid-crystal display [1–4]. One of the methods used to modify the radiative properties is by creating periodic micro/nanostructures, such as periodic metallic slit arrays and microcavities [4]. Metallic slit arrays with a period less than 1 μm exhibit unique radiative properties and thus have been employed in a large number of applications. An example is the wire-grid infrared polarizers, which utilize the broadband polarization-dependent transmittance of the periodic metallic wire grid [5]. According to Carr et al. [6], subangstrom lateral movement could be detected based on the change in reflectance at the wavelength close to the slit period for a pair of slit arrays that can shift position relative to each other. Moreover, the period variation of slit arrays may be used to tune the wavelength of maximum diffraction efficiency at specific directions for micro-optical instruments [7]. Another application of metallic slit arrays is in near-field nanolithography since gratings facilitate the excitation of surface plasmon polaritons [8,9]. Indeed, the study of the radiative properties of submicron slit arrays has become a dynamic research area.

Most studies about the radiative properties of metallic slit arrays with submicron period dealt with numerical modeling [3,10,11]. Recently, Lee et al. [12] systematically investigated the mechanisms of transmission enhancement through metallic slit arrays using the rigorous coupled-wave analysis (RCWA). Depending on the wavelength region, the enhanced transmittance may be attributed to surface plasmon polaritons, Wood's anomaly, cavity resonance, and the effective medium behavior [4,12]. For the effective medium behavior, the periodic structures can be approximated as a homogeneous medium, whose optical constants are polarization dependent. This results in an enhanced transmittance that is insensitive to wavelength in the midinfrared. Lee et al. [13] further illustrated a strong confinement of the infrared radiation in the near-field regime, i.e., at the slit exit. The electromagnetic energy can be localized to the slit width of $\lambda/400$ in the midinfrared. Here, λ is the wavelength in vacuum. It should be noted that laser ablation through metallic slit arrays has been demonstrated in the near infrared [14]. With energy confinement and transmission enhancement, submicron metallic slit arrays may be used as a localized heating source for thermal manufacturing, laser ablation, or polymer curing at the nanometer scale. However, very few measurements were made along with rigorous modeling on the radiative properties of submicron metallic slit arrays in a large spectral region from near- to midinfrared.

The objective of the present work is to experimentally and numerically investigate the infrared transmittance through submicron metallic slit arrays. Several samples were fabricated with the assistance of electron-beam (e-beam) lithography and physical vapor deposition, resulting in Au/Ti strips on Si substrates with a period $\Lambda = 800$ or 1000 nm. The transmittance of the fabricated samples was measured for each polarization in the spectral region between approximately 1.67 μm and 15 μm at normal incidence. RCWA is used to calculate the transmittance, and the calculated results are compared to the measurement data. The applicability of the effective medium theory (EMT) is also evaluated. Furthermore, absorptance and reflectance are calculated for incidence either on the slit side or on the plain Si side of the sample to examine the wavelength- and polarization-dependent radiative properties of metallic slit arrays on dielectric substrate in a broad spectral region.

2 Experiments

Metallic slits were designed and fabricated on double-side-polished, (111) oriented single-crystal Si wafers of 400 μm thickness. Si was selected as the substrate to support the metallic strips because of its low absorption in the infrared region. The main steps of the fabrication process are illustrated in Fig. 1. The first step was to coat a 0.5-μm-thick e-beam resist on the Si substrate of 25×25 mm^2 area, which was diced from a 100-mm-diameter wafer. The resist was then exposed to the e-beam after soft baking at 130°C for 1 min. A JEOL JBX-9300FS e-beam lithography system was employed due to its high resolution, flexibility, and repeatability in pattern generation [15]. The e-beam was generated at 100 kV and 2 nA with 4–9 nm beam diameter. The resulting spatial resolution is better than 20 nm. The pattern was created on a 200×200 μm^2 field each time. The sample was then translated in both the x and y directions to duplicate the pattern 20×20 times. The fabricated metallic slit array has an area of 4×4 mm^2 near the center of the Si substrate.

---

[1] Current address: Department of Mechanical Engineering, National Cheng Kung University, Taiwan 701, Taiwan.

[2] Corresponding author.

Contributed by the Heat Transfer Division of ASME for publication in the JOURNAL OF HEAT TRANSFER. Manuscript received May 29, 2007; final manuscript received August 9, 2007; published online June 4, 2008. Review conducted by Ben Q. Li.

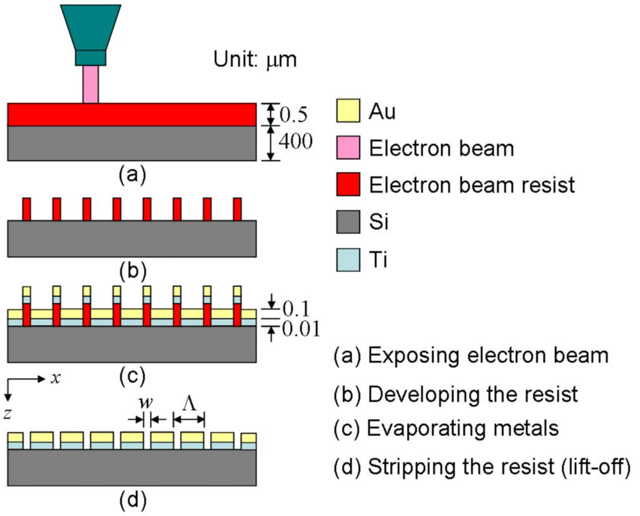

Fig. 1 Illustration of the fabrication process for periodic submicron metallic slit arrays (not to scale): (*a*) exposing e-beam, (*b*) developing the resist, (*c*) evaporating metals, and (*d*) stripping the resist

The next step was to develop the exposed resist to form the patterns on the Si substrate, as shown in Fig. 1(*b*). Afterward, 10 nm Ti and 100 nm Au were subsequently coated on top of the structure, as shown in Fig. 1(*c*). The thin Ti film acts as an adhesive layer between Au and Si. The metal deposition was done using a CVC SC 5000 evaporator without breaking its vacuum chamber. A quartz crystal microbalance monitors the thickness such that the deposition thickness is within 10% variation [16]. Metals were evaporated on either the resist or the substrate without connections. The final step of sample fabrication was the lift-off process, which removes the unwanted metal coatings by stripping the resist below them. During the lift-off, the metal strips directly coated on Si substrate remained. Figure 1(*d*) shows the schematic of the sample, although the dimensions are not to scale.

The images of fabricated samples were taken by a scanning electron microscope (SEM), as shown in Fig. 2. The samples described in the present work are numbered 1, 2, and 3 with different lateral dimensions. The slit arrays are characterized by metal strip width (l), slit width (w), and the period ($\Lambda = l + w$). The lateral parameters of the three fabricated samples are listed in Table 1. Note that the filling ratio is defined as $f = l/\Lambda$. Samples 1 and 2 were fabricated according to the same pattern during the e-beam exposure. In the lift-off, Samples 1 and 2 were soaked in N-methyl-2-pyrrolidone at 70°C for 10 h and 8 h, respectively. The longer soaking time for Sample 1 may be responsible for its slightly wider slits.

Although the fabrication of each sample took several hours and the strips were formed by connecting sections in each field, the whole slit array exhibits very uniform patterns. The period is determined by the original patterns, with the designed values of 800 nm for Samples 1 and 2 and 1000 nm for Sample 3. Figure 2(*a*) is the enlarged SEM image of top view for Sample 2. The measurement of the strip width relative to the period in an enlarged SEM image determines the filling ratio f. The filling ratios are larger than 0.63, and the slit widths are close to 300 nm. The uncertainty of the SEM measurement is less than 5 nm. Figure 2(*b*) shows the SEM image of Sample 3 in an oblique angle to demonstrate the sides and edges of several metal strips on top of the Si substrate. From the contrast, one can see a thin Ti adhesive film located underneath each Au strip. The top surface profile of the Au strip is nearly flat, except that the edges show some Au residue from the lift-off process. Some small warps at the end of the metal strip can be seen; however, most metal strips are flat and straight, especially in the middle sections of the slit arrays.

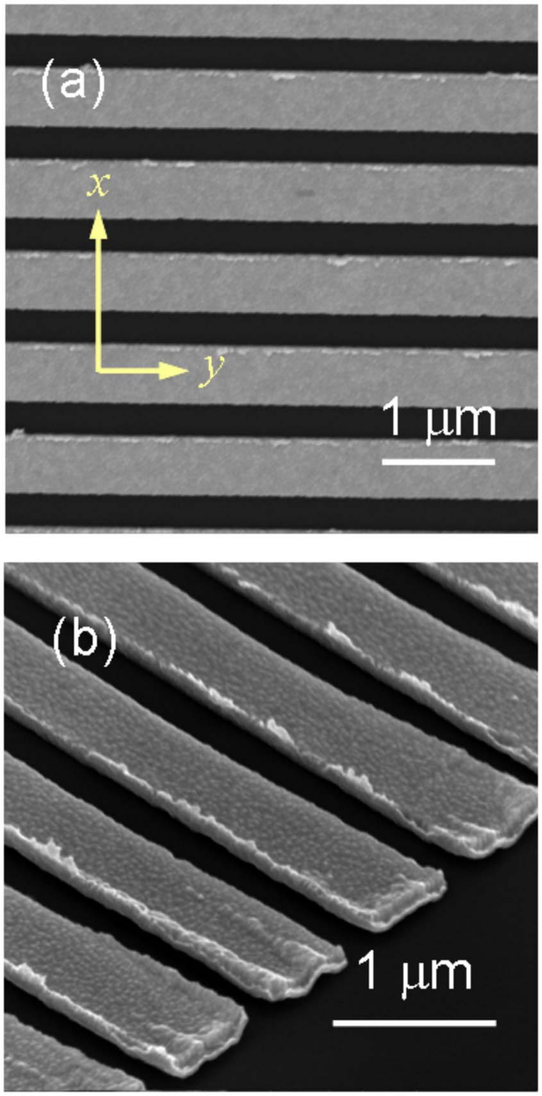

Fig. 2 SEM images of two fabricated structures: (*a*) Sample 2 and (*b*) Sample 3

An ABB FTLA2000 Fourier-transform infrared (FTIR) spectrometer [17] was used to measure the transmittance (T) for both transverse electric (TE) and transverse magnetic (TM) waves at near normal incidence. The convention to define the grating geometry and polarization of the incident radiation is the same as that previously used by Chen et al. [18]. For a TE wave, the electrical field is polarized parallel to the strips (i.e., the y direction as shown in Fig. 2). For a TM wave, magnetic field is parallel to the strips. The spectrometer is equipped with a Globar source and a pyroelectric detector to measure the transmittance spectrum in the wave number ($1/\lambda$) range from 500 cm^{-1} to 6000 cm^{-1} ($1.67\ \mu\text{m} < \lambda < 20\ \mu\text{m}$). All measurements in the present work

Table 1 Lateral dimensions of submicron metallic slit arrays

Sample No.	Period, Λ (nm)	Slit width, w (nm)	Metal filling ratio, f
1	800	296	0.630
2	800	284	0.645
3	1000	285	0.715

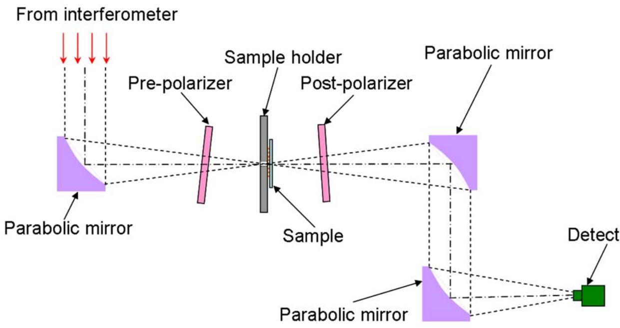

Fig. 3 Schematic of the optical setup for measuring the polarized infrared transmittance

were conducted with a resolution of 8 cm^{-1} to avoid the effect of interference in the Si substrate. The cosine truncation function was used for the apodization, and the cosine function was used for phase correction [19]. Figure 3 is a schematic of the transmittance measurement setup. In order to produce pure linearly polarized radiation, two infrared polarizers, made of wire grid on ZnSe substrate, were employed: one in front of the aperture and the other behind the sample. The two polarizers were intentionally positioned unparallel to each other to eliminate multiple reflections. Moreover, neither polarizer was parallel to the sample. The extinction ratio of each polarizer is 130 at $\lambda=3$ μm and is 350 at $\lambda=8$ μm. The extinction ratio is defined as the ratio of the maximum transmitted power to the minimum transmitted power of the polarizer for a plane polarized incident beam [20]. By using two polarizers, the effective extinction ratio exceeds 10,000 for the whole measured wavelength region. However, the polarizers have also significantly reduced the signal-to-noise ratio and limited the measured wavelength up to 15 μm. For all measurements, an average of 800 scans was used to improve the signal-to-noise ratio. Another drawback for the insertion of the polarizers is the absorption by H_2O and CO_2 since it is difficult to purge the optical compartment between the two polarizers with the N_2 gas. When the transmittance is close to 0.5, the expanded uncertainty is estimated to be 0.03 in the measurements due to various sources of error. When the transmittance is less than 0.1, a relative uncertainty of 30% is estimated. The measurement error may come from beam divergence, phase correction, and possible misalignment of the sample with respect to the aperture [21].

The normal transmittance of a plain Si substrate was measured to study the effect of orientation of the polarizers. Figure 4 shows the measured transmittance for three spectrophotometry setups including no polarizer, two untilted polarizers, and two tilted polarizers in the spectral range from 2 μm to 15 μm. The transmittance calculated using optical constants from Ref. [22] agrees well with the measurements without polarizers. Note that the spectral averaging of transmittance was applied to remove fringes when calculating the transmittance [4,17]. The difference in transmittance from the calculated and the measured is within 0.005 in the regions without significant absorption by the gas or by lattice vibrations in Si. Hence, the calculated results are not shown in Fig. 4. If the polarizers are not tilted, multiple reflections exist between the sample and polarizers such that the measured transmittance exceeds the actual values. By tilting the polarizers, the measured transmittance is not affected by the introduction of the polarizers. Because the sample compartment was not purged in all three measurements, the transmittance spectra are influenced by the absorption by the CO_2 gas around $\lambda=4.3$ μm and by H_2O vapor around $\lambda=6.3$ μm, and by both CO_2 and H_2O at $\lambda=2.7$ μm, respectively [23]. The absorption beyond $\lambda=7$ μm is mainly due to lattice vibrations in Si [4].

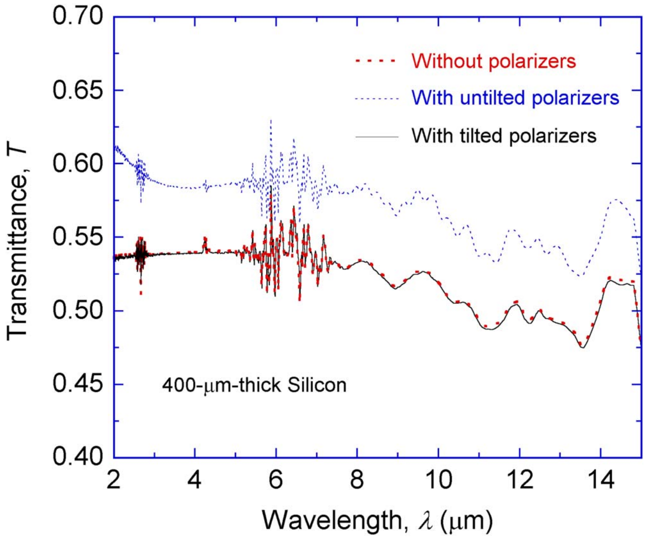

Fig. 4 Measured normal transmittance spectra for a plain 400-μm-thick Si substrate

3 Calculation of the Radiative Properties

The cross section view of the studied metallic slit arrays is shown in Fig. 1(*d*). The wavelength-dependent dielectric function $\varepsilon=(n+i\kappa)^2$ of each material is needed for the numerical modeling, where n is the refractive index and κ is the extinction coefficient. The optical constants of Ti and Si are available from the tabulated data in Ref. [22] at the wavelength region of interest (1.67 μm $<\lambda<15$ μm). Interpolation of the optical constants is used for data point between two neighboring values. Since optical constants of Au listed in Ref. [22] are available up to 9.9 μm, the Drude model is employed and extended to the whole spectral range [24]. In the Drude model, the dielectric function ε is expressed as [4]

$$\varepsilon(\omega)=\varepsilon_\infty-\frac{\omega_p^2}{\omega^2+i\omega\gamma} \tag{1}$$

where ω is the angular frequency, γ is the scattering rate, ω_p is the plasma frequency, and ε_∞ is the constant that accounts for high-frequency contributions. The scattering rate and plasma frequency of Au are taken from Ref. [24] as $\gamma=216$ cm^{-1} and $\omega_p=7.25\times10^4$ cm^{-1}. In the present study, ε_∞ is set to 1. The change in the dielectric function at wavelengths longer than 2 μm is negligible when ε_∞ is varied from 1 to 2. At short wavelengths, the radiative properties are also calculated using optical constants from the tabulated values from Ref. [22] for comparison with the Drude model.

RCWA is a commonly used method for solving the Maxwell equations in periodic structures [12,18]. Within the computational capacity, RCWA can achieve sufficient accuracy by increasing the Fourier terms in the expansions of the dielectric function and the electromagnetic fields in the grating region. The convergence of RCWA is very rapid when the method of handling the product of two functions is employed [25]. Detailed discussion about the RCWA formulations for 1D gratings can be found in Ref. [12]. The jth diffraction order satisfies the Floquet condition [18]

$$k_{x,j}=k_{x,\text{inc}}+j2\pi/\Lambda \tag{2}$$

where k_x is the x component of the wave vector and the subscript "inc" denotes the incidence. Note that $j=0,\pm1,\pm2,\ldots$. In the calculation, the refractive index of air is assumed to be 1 and its absorption is neglected. Equation (2) can be rearranged and expressed in terms of the angle of incidence and angles of diffraction as follows:

$$n \sin \theta_j = \sin \theta_{\text{inc}} + j\lambda/\Lambda \tag{3}$$

where θ_j is the zenith angle of the jth order diffraction and θ_{inc} is the zenith angle of incidence. Note that n is the refractive index of the material above or below the grating for the reflected or transmitted diffractions, respectively. Hence, the diffraction angle in the Si substrate is different from that in air. The refractive index of Si varies from 3.45 at $\lambda = 2\ \mu$m to 3.42 at 15 μm [22].

Alternatively, EMT is a simple method that may provide a first-order approximation of the radiative properties of periodic structures, when the period is much shorter than the wavelength. In the EMT formulation, the periodic structure is treated as a homogeneous material with an effective dielectric function ε_{eff}, which depends on the polarization of the incident radiation [5,26]. The effective dielectric functions of the grating region for TE waves ($\varepsilon_{\text{eff,TE}}$) and TM waves ($\varepsilon_{\text{eff,TM}}$) are expressed in the following simplified forms, respectively:

$$\varepsilon_{\text{eff,TE}} = f\varepsilon_m + (1-f)\varepsilon_a \tag{4a}$$

$$\varepsilon_{\text{eff,TM}} = [f/\varepsilon_m + (1-f)/\varepsilon_a]^{-1} \tag{4b}$$

where ε_m and ε_a are the dielectric functions of the metal and air, respectively, and f is the filling ratio. With known thickness and effective dielectric functions, the radiative properties of periodic structures can be calculated using thin-film optics [4], which is much faster than the rigorous numerical methods. The calculated results from both RCWA and EMT algorithms are compared to the measured transmittance of the fabricated slit arrays.

4 Results and Discussion

Figure 5 shows the normal transmittance spectra of Sample 1, obtained from experiments (solid line) and the RCWA modeling (dashed line), at wavelengths between 1.67 μm and 15 μm for both TE and TM waves. The transmittance is the same regardless of whether the incidence is on the slit side or on the substrate side. The measurement was performed when the radiation after passing the aperture is incident on the slit sides. In the calculation, the wavelength interval is 0.05 μm for $\lambda < 4\ \mu$m and is 0.2 μm for $\lambda > 4\ \mu$m. In the RCWA modeling, the fringes due to interference in the Si substrate are removed by averaging the transmittance over a free spectral range using the fringe-average method [17]. It can be seen from Fig. 5 that the RCWA prediction is in good agreement with the spectrometric data. The TE wave spectra monotonically decrease toward the long wavelength, and the transmittance value is less than 0.01 at $\lambda > 4\ \mu$m. Furthermore, the measured transmittance shows a negative value near $\lambda = 14\ \mu$m due to the artifacts in the inverse Fourier transform of truncated interferogram. For the TM wave, the transmittance is close to that of plain Si for $\lambda > 6\ \mu$m, although the measured values are slightly lower than those predicted by RCWA for $8\ \mu\text{m} < \lambda < 11\ \mu$m. At short wavelengths, there is a deep valley in the transmittance spectra near $\lambda = 3\ \mu$m. It should be emphasized that no adjustable parameters were used in the modeling because the optical constants of materials and the dimensions are predetermined, as discussed in the previous sections. Variation of the thickness of Au by 10% does not significantly alter the predicted transmittance. In the RCWA modeling, the dielectric function of Au was calculated using the Drude model [24], while the values of the optical constants tabulated in Ref. [22] are somewhat different from those predicted by the Drude model, especially at shorter wavelengths. However, the transmittance calculated using the optical constants from Ref. [22] exhibits negligible difference from that calculated using the Drude model for $2.0\ \mu\text{m} < \lambda < 9.8\ \mu$m. Hence, the Drude model is appropriate for the transmittance calculation.

The transmittance spectra can be modified by a phenomenon called Wood's anomaly [27], which happens when a diffracted wave propagates at the grazing angle, i.e., when the normal component of the wave vector $k_{z,j}$ becomes zero. The wavelength can be predicted from the grating equation, Eq. (3), with $\sin \theta_j = \pm 1$. For Samples 1 and 2, the corresponding wavelength is $\lambda = 0.8n \approx 2.75\ \mu$m for the +1 and −1 diffraction orders inside Si ($n \approx 3.44$) to propagate in the positive and negative x directions, respectively. The diffracted wave switches between an evanescent mode and a propagating mode as the wavelength is slightly changed about 2.75 μm. For TE waves, Wood's anomaly is manifested as a discontinuity in the transmittance at $\lambda \approx 2.75\ \mu$m. On the other hand, Wood's anomaly can affect the radiative properties of shallow metallic gratings in a more significant way and in a much broader spectral region for TM waves. This is the reason why the TM wave transmittance begins to decrease at $\lambda = 6\ \mu$m down to a minimum of nearly zero at $\lambda = 2.81\ \mu$m and then increases towards shorter wavelengths. The transmittance starts to decrease again at $\lambda = 1.7\ \mu$m due to another Wood's anomaly expected at $\lambda \approx 1.4\ \mu$m for the ± 2 diffraction orders. In fact, Wood's anomaly can significantly deteriorate the performance of polarizers [28]. Before discussing the discrepancy of the RCWA prediction and the experiments for $\lambda < 2.8\ \mu$m, let us take a look at the transmittance of Sample 2 and examine the validity of EMT.

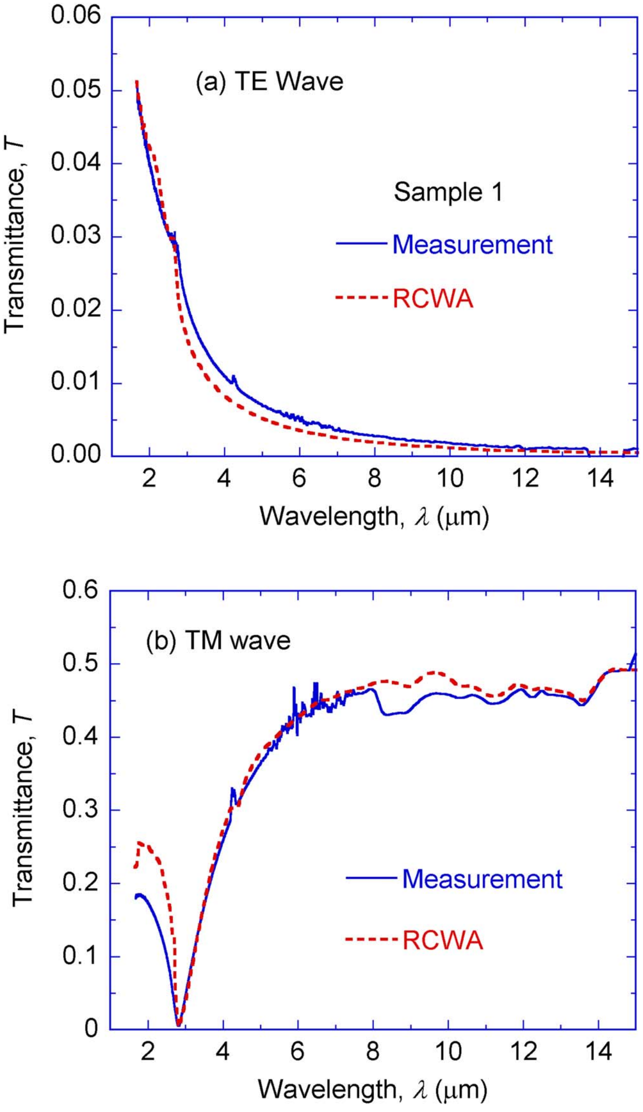

Fig. 5 Transmittance of a submicrometer metallic slit array identified as Sample 1: (*a*) TE wave and (*b*) TM wave

As shown in Fig. 6, the transmittance of Sample 2 is very close to that of Sample 1 because of the similar geometry. For clarity, the transmittance for TE wave is plotted in logarithmic scale. For

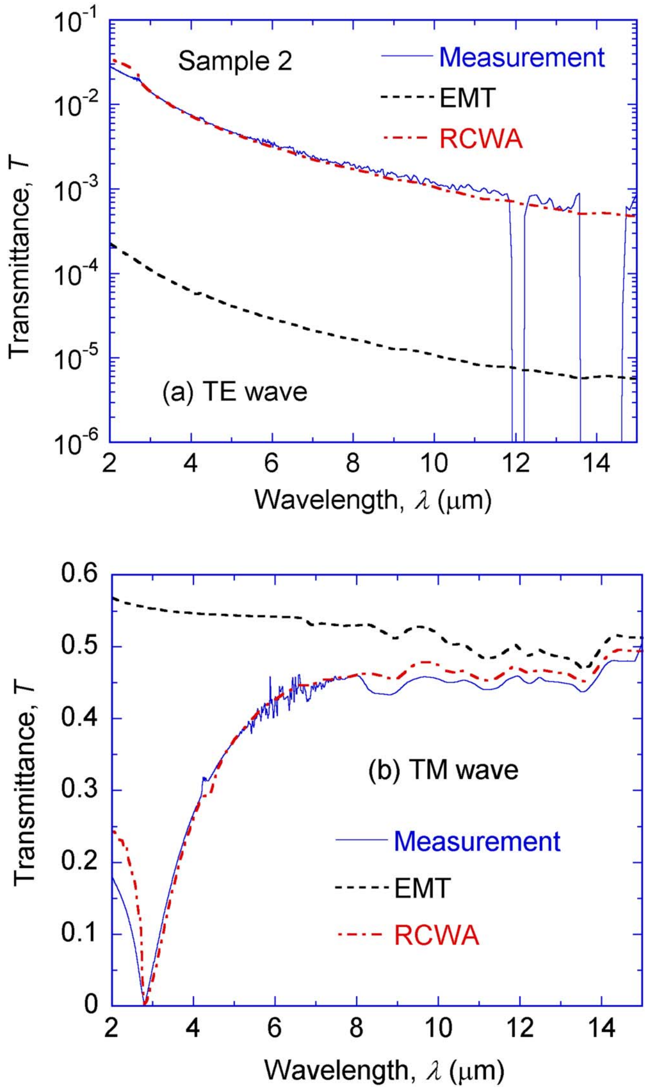

Fig. 6 Comparison of the transmittance spectra between experiments and modeling results from both RCWA and EMT for Sample 2: (*a*) TE wave and (*b*) TM wave

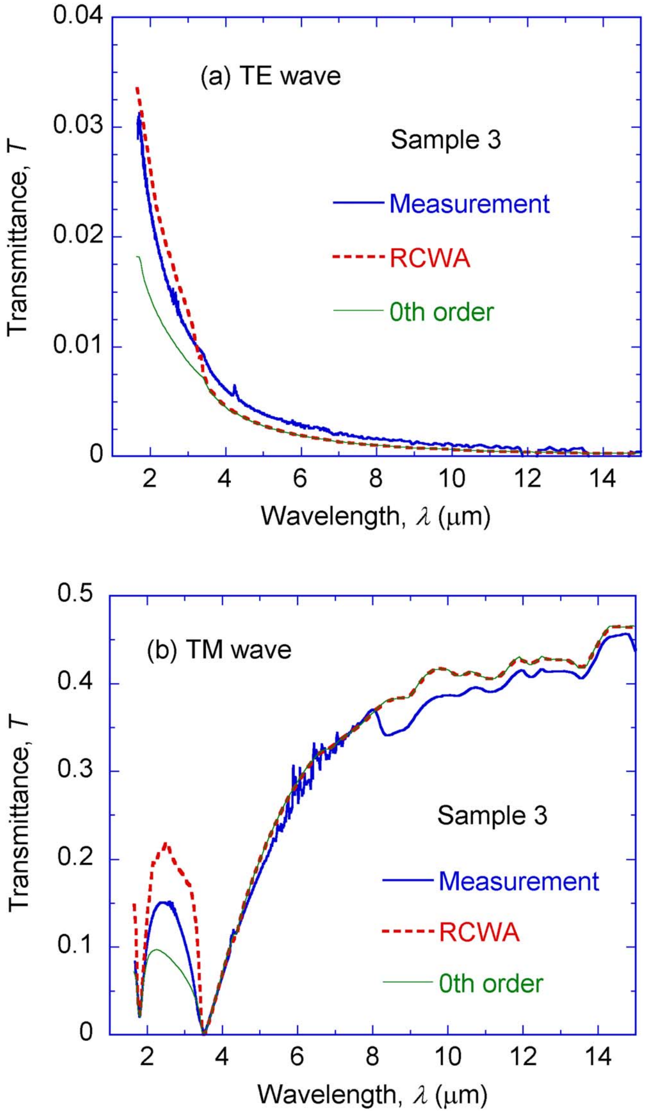

Fig. 7 Measured transmittance of Sample 3 and comparison with RCWA prediction considering all diffraction orders or only the zeroth order: (*a*) TE wave and (*b*) TM wave

Sample 2, the spectrometer artifacts resulted in a negative value near $\lambda = 12$ μm and $\lambda = 14$ μm. In general, the agreement between RCWA and the experiment is slightly better for Sample 2 than for Sample 1. The transmittance calculated using EMT is also shown for comparison. The Au and Ti strips are treated as two homogeneous layers of thin films on the Si substrate using the effective medium formulation. Although the wavelength-to-period ratio λ/Λ is greater than 3 at $\lambda > 2.4$ μm, EMT failed to predict the transmittance by nearly two orders of magnitude for the TE wave. For the TM wave at $\lambda > 8$ μm, EMT slightly overpredicts the transmittance, as shown in Fig. 6(*b*). Because EMT cannot properly account for Wood's anomaly, it significantly overpredicts the transmittance at shorter wavelengths. It should be noted that the transmittance variation near $\lambda = 6.3$ μm is due to water vapor. The transmittance bump at $\lambda = 4.3$ μm is because the CO_2 concentration is actually lower during the sample measurement than that during the reference measurement. However, the transmittance calculated using RCWA exhibits a slight drop near $\lambda = 4.3$ μm due to the absorption by Ti; this will become clear later when the absorptance spectra are discussed.

The transmittance spectra of Sample 3 for both TE and TM waves are shown in Fig. 7. Since the filling ratio is the highest among three samples, the transmittance is the lowest. Because the grating period is $\Lambda = 1$ μm, Wood's anomaly occurs at $\lambda = 3.43$ μm and 1.73 μm, resulting in two observable transmittance valleys whose minima are at 3.52 μm and 1.79 μm, respectively. For all three samples, the RCWA overpredicts the transmittance at shorter wavelengths. When the wavelength is slightly shorter than that of Wood's anomaly, the $j = \pm 1$ diffraction orders become a propagating wave inside Si. The angle of propagation decreases from 90 deg but is much greater than the critical angle between Si and air, which is about 17 deg. As a result, the diffracted waves are guided inside the Si and can travel a lateral distance longer than a few millimeters, which may exceed the diameter of the aperture or the area of the slit array. Therefore, the infinitely extended grating model may not accurately agree with the measured transmittance because only part of the diffracted waves can be collected by the detector of the spectrometer. For this reason, the transmittance is also calculated by ignoring all the diffracted waves inside Si, except the zeroth order. The thin line in Fig. 7 represents the transmittance obtained by tracing the energy of zeroth-order diffracted waves inside the Si substrate, which is assumed to be thick so that interference effect can be neglected [4]. For $\lambda \geqslant 3.43$ μm, the only propagating wave is the zeroth-order diffraction, and the predicted transmittance using the zeroth

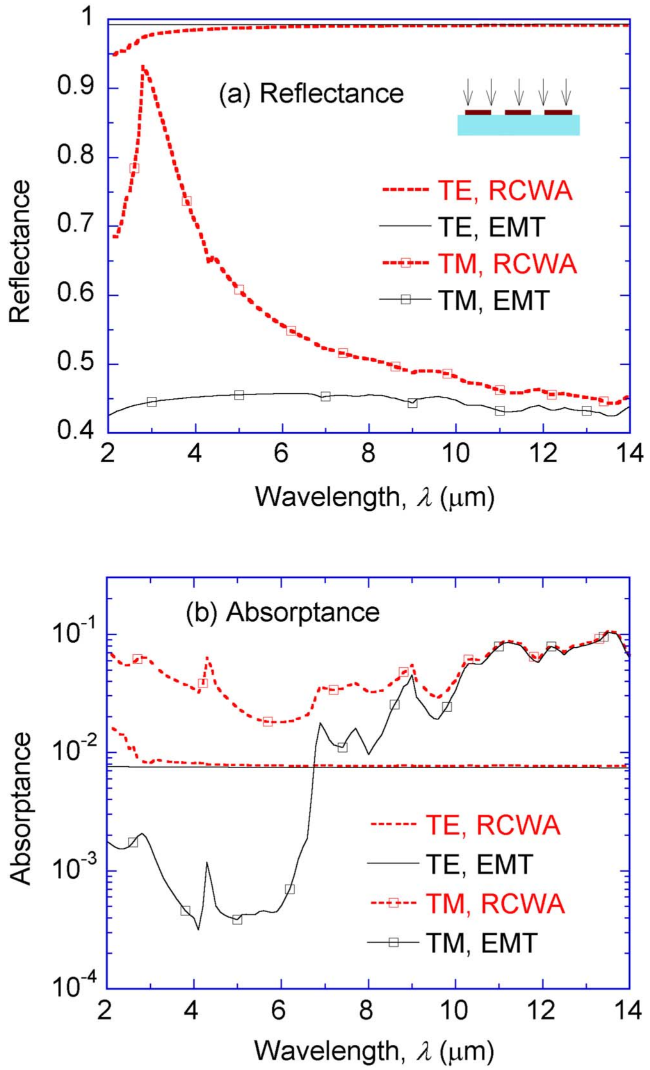

Fig. 8 Calculated reflectance and absorptance using the geometry of Sample 2 for radiation incident on the metallic slits: (*a*) reflectance and (*b*) absorptance. The solid and dashed lines indicated the results from EMT and RCWA, respectively. The lines with square marks are for TM waves.

order is the same as that from RCWA. However, ignoring the higher diffraction orders results in an underprediction of the transmittance for $\lambda \leqslant 3.43$ μm. This is because the $j = \pm 1$ diffraction can be reflected by the Si-air interface back to the grating region, and the subsequent diffraction can result in propagating waves in the normal direction that will contribute to the transmitted energy. Because of the lateral shift and the finite beam size and grating area, not all of the diffracted waves are fully accounted for in the measurements. The above discussion qualitatively explains why the experimental transmittance is within the values predicted by RCWA and that by considering the zeroth-order diffraction only. It is interesting to note that the separation of the three spectra appears at the exact wavelength of Wood's anomaly for the TM wave.

To thoroughly understand the radiative properties of metallic slit arrays, the reflectance and absorptance for the geometry of Sample 2 are calculated using both RCWA and EMT, as shown in Fig. 8 in the spectral region from 2 μm to 14 μm. The inset indicates that the radiation is incident on the gratings because the reflectance and absorptance strongly depend on which side the radiation is incident [29]. For the TE wave, the reflectance is very high, greater than 0.99 at longer wavelengths, while the absorptance is approximately 0.01. EMT is in excellent agreement with RCWA for $\lambda > 3$ μm, because the effective dielectric functions of Au are metal-like with a very small penetration depth. At $\lambda < 3$ μm, Wood's anomaly enhances the absorptance and reduces the reflectance. The absorption at short wavelength is mainly due to Ti, coupled with the grating structure. This is validated by calculating the absorptance with Au gratings without Ti. EMT could not predict the absorptance by Ti because of the low transmittance of the effective medium in the Au grating region. The reason why EMT underpredicts the transmittance, as suggested in Fig. 6(*a*), cannot be explained based on the reflectance and absorptance characteristics. There seems to be a limitation of EMT in quantitatively predicting the transmittance at very low levels.

For the TM wave, the reflectance has a sharp peak near the anomaly wavelength and gradually decreases toward longer wavelengths. At longer wavelengths, EMT is in excellent agreement with RCWA in absorptance and good agreement in reflectance. It should be noted that absorption at $\lambda \geqslant 6$ μm mainly comes from Si due to lattice vibrations. It can be seen from Fig. 8 that EMT fails to predict both the reflectance and absorptance at short wavelengths due to Wood's anomaly as discussed earlier in the comparison of transmittance spectra. The effective dielectric functions of Au and Ti for TM waves are dielectric-like with slight absorption (small κ values). Besides, the absorption coefficient of Si is negligibly small at short wavelengths. Hence, EMT predicts little absorption with distinct features due to the absorption peak of Ti at $\lambda = 4.3$ μm and another at $\lambda = 2.9$ μm. On the other hand, due to Wood's anomaly, a significant rise in absorptance inside Ti is predicted by RCWA, as shown in Fig. 8(*b*) for the TM wave between 2 μm and 8 μm. It is interesting to notice that between 6 μm and 8 μm, the absorption due to Ti exceeds that due to Si, resulting in a somewhat flatter and higher absorption band. Throughout the spectral region, RCWA predicts a much higher absorptance for TM waves than for the TE waves. This is associated with the lower reflectance and higher transmittance for TM waves than for TE waves.

Figure 9 shows the reflectance and absorptance for radiation incident on the plain Si side. Because the radiation first penetrates into the Si substrate, the reflectance is significantly reduced, whereas the absorption by Si and Ti is greatly enhanced. This is particularly true for TE waves since the gratings act like a good reflector (metallic behavior). Multiple reflections inside Si result in a large increase in the absorptance for TE waves at longer wavelengths. It can be seen from Fig. 9(*b*) that the absorptance for TE waves significantly increases in the whole spectrum, compared to Fig. 8(*b*). Furthermore, the absorptance for TE waves exceeds that for TM waves at longer wavelengths. For TM waves, the reflection peak is reduced, resulting in enhanced absorptance at shorter wavelengths. At longer wavelengths, the changes in reflectance and absorptance are very small for TM waves. Due to the dielectric behavior of the grating regions for TM waves, the reflectance and absorptance predicted by EMT are insensitive to which side the radiation is incident on.

For TE waves, EMT fails to predict the reflectance and absorptance between 2 μm and 3 μm for incidence on the grating side as noted in Fig. 8, due to the screening of the effective medium of the Au grating region. On the contrary, as shown in Fig. 9, the EMT prediction is in excellent agreement with that of RCWA in terms of the absorptance and reflectance for TE waves in the whole spectral region when the incidence is on the substrate side. This is because the absorption of the Ti grating region can be fully accounted when the incidence is on the dielectric substrate. Moreover, the small absorption peak at $\lambda \approx 4.3$ μm due to Ti has been shifted toward shorter wavelengths in the TE wave spectra. It is surprising to see that EMT exactly predicts the same absorption peak location and magnitude as those of RCWA. Hence, EMT has its merit not only in providing a first-order approximation of the

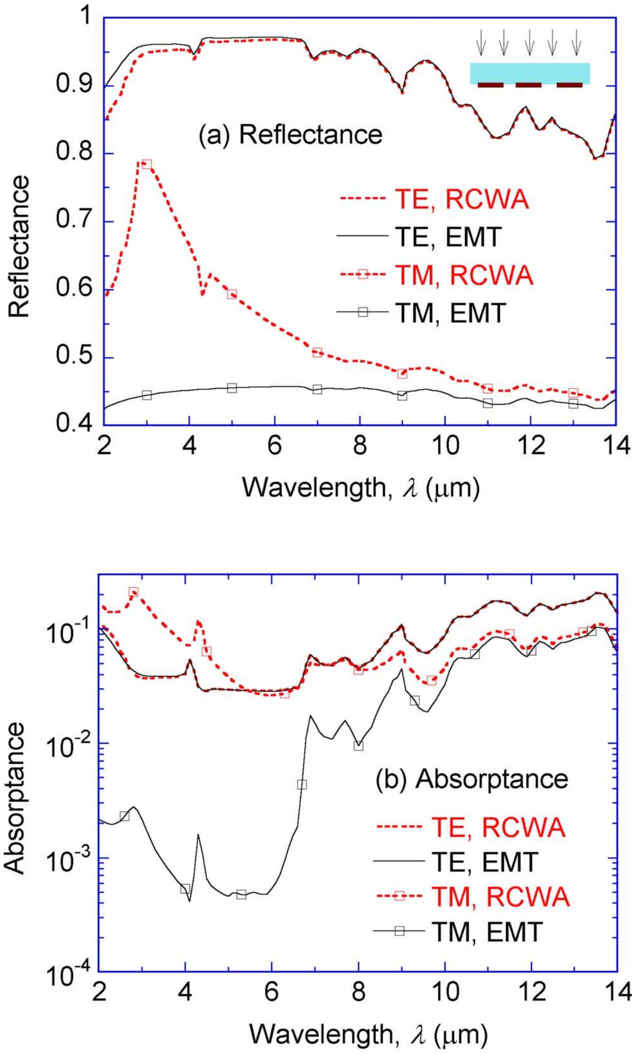

Fig. 9 Calculated reflectance and absorptance using the geometry of Sample 2 for radiation incident on the Si substrate: (*a*) reflectance and (*b*) absorptance

radiative properties but also in offering some reasonable interpretations of the underlying physical mechanisms of electromagnetic wave interaction with micro/nanostructures.

5 Conclusions

We have fabricated submicron metallic slit arrays and measured their transmittance in the near- and midinfrared. These slit arrays have a period of 800–1000 nm with a slit width about 300 nm. The measurement results compare well to those from the RCWA modeling in the wavelength range from 2 μm to 15 μm for both TE and TM waves. The effects of polarization and Wood's anomaly on the radiative properties have been observed. While the EMT provides a good approximation of the radiative properties for the TM wave at long wavelengths, it may underpredict the transmittance by two orders of magnitude for the TE wave. Hence, caution must be taken when applying the EMT in modeling the radiative properties. On the positive side, EMT does offer some plausible explanations of the absorption and reflection characteristics for TE waves. The present study clearly demonstrates the feasibility of tailoring infrared radiative properties using micro/nanostructures. The quantitative comparison with measurements presented in this work will help design optical devices, such as infrared filters and polarizers, and will also facilitate the application of slit arrays in nanoscale thermal manufacturing.

Acknowledgment

The authors thank Mr. Devin Brown of Georgia Tech's Microelectronics Research Center for assistance in the operation of e-beam lithography. This work was supported by the National Science Foundation (CTS-0500113).

Nomenclature

f = filling ratio
i = $\sqrt{-1}$
j = diffraction order
k = wave vector, m^{-1}
l = strip width, m
n = refractive index
T = transmittance
w = slit width, m

Greek Symbols

γ = scattering rate, rad/s
ε = dielectric function
θ = zenith angle, deg
κ = extinction coefficient
Λ = period of metallic slit arrays, m
λ = wavelength, m
ω = angular frequency, rad/s
ω_p = plasma frequency, rad/s

References

[1] Basu, S., Chen, Y.-B., and Zhang, Z. M., 2007, "Microscale Radiation in Thermophotovoltaic Devices—A Review," Int. J. Energy Res., **31**, pp. 689–716.
[2] Kim, S. H., Park, J.-D., and Lee, K.-D., 2006, "Fabrication of a Nano-Wire Grid Polarizer for Brightness Enhancement in Liquid Crystal Display," Nanotechnology, **17**, pp. 4436–4438.
[3] Crouse, D., and Keshavareddy, P., 2007, "Polarization Independent Enhanced Optical Transmission in One-Dimensional Gratings and Device Applications," Opt. Express, **15**, pp. 1415–1427.
[4] Zhang, Z. M., 2007, *Nano/Microscale Heat Transfer*, McGraw-Hill, New York.
[5] Yeh, P., 1978, "A New Optical Model for Wire Grid Polarizers," Opt. Commun., **26**, pp. 289–292.
[6] Carr, D. W., Sullivan, J. P., and Friedmann, T. A., 2003, "Laterally Deformable Nanomechanical Zeroth-Order Gratings: Anomalous Diffraction Studied by Rigorous Coupled-Wave Analysis," Opt. Lett., **28**, pp. 1636–1638.
[7] Tung, Y. C., and Kurabayashi, K., 2005, "Nanoimprinted Strain-Controlled Elastomeric Gratings for Optical Wavelength Tuning," Appl. Phys. Lett., **86**, p. 161113.
[8] Luo, X. G., and Ishihara, T., 2004, "Surface Plasmon Resonant Interference Nanolithography Technique," Appl. Phys. Lett., **84**, pp. 4780–4782.
[9] Liu, Z. W., Wei, Q. H., and Zhang, X., 2005, "Surface Plasmon Interference Nanolithography," Nano Lett., **5**, pp. 957–961.
[10] Porto, J. A., García-Vidal, F. J., and Pendry, J. B., 1999, "Transmission Resonances on Metallic Gratings With Very Narrow Slits," Phys. Rev. Lett., **83**, pp. 2845–2848.
[11] Astilean, S., Lalanne, P., and Palamaru, M., 2000, "Light Transmission through Metallic Channels Much Smaller Than the Wavelength," Opt. Commun., **175**, pp. 265–273.
[12] Lee, B. J., Chen, Y.-B., and Zhang, Z. M., 2008, "Transmission Enhancement Through Nanoscale Metallic Slit Arrays From the Visible to Mid-Infrared," J. Comput. Theor. Nanosci., **5**, pp. 201–213.
[13] Lee, B. J., Chen, Y.-B., and Zhang, Z. M., 2008, "Confinement of Infrared Radiation to Nanometer Scales Through Metallic Slit Arrays," J. Quant. Spectrosc. Radiat. Transf., **109**, pp. 608–619.
[14] Moroki, A., Kitano, R., Obara, M., and Tsuda, H., 2005, "Femtosecond Laser Processing Using Subwavelength Thin Metal Slit Arrays," Jpn. J. Appl. Phys., Part 1, **44**, pp. 8753–8758.
[15] Groves, T. R., Pickard, D., Rafferty, B., Crosland, N., Adam, D., and Schubert, G., 2002, "Maskless Electron Beam Lithography: Prospects, Progress, and Challenges," Microelectron. Eng., **61**, pp. 285–293.
[16] Lee, H. J., Chen, Y.-B., and Zhang, Z. M., 2006, "Directional Radiative Properties of Anisotropic Rough Silicon and Gold Surfaces," Int. J. Heat Mass Transfer, **49**, pp. 4482–4495.
[17] Lee, B. J., Khuu, V. P., and Zhang, Z. M., 2005, "Partially Coherent Spectral Radiative Properties of Dielectric Thin Films With Rough Surfaces," J. Thermophys. Heat Transfer, **19**, pp. 360–366.
[18] Chen, Y.-B., Zhang, Z. M., and Timans, P. J., 2007, "Radiative Properties of Patterned Wafers With Nanoscale Linewidth," ASME J. Heat Transfer, **129**, pp. 79–90.

[19] Griffiths, P. R., and De Haseth, J. A., 1986, *Fourier Transform Infrared Spectrometry*, Wiley, New York.

[20] Kim, D., 2005, “Polarization Characteristics of a Wire-Grid Polarizer in a Rotating Platform,” Appl. Opt., **44**, pp. 1366–1371.

[21] Kaplan, S. G., Hanssen, L. M., and Datla, R. U., 1997, “Testing the Radiometric Accuracy of Fourier Transform Infrared Transmittance Measurements,” Appl. Opt., **36**, pp. 8896–8908.

[22] Palik, E. D., 1998, *Handbook of Optical Constants of Solids*, Academic, San Diego, CA, Vols. I and II.

[23] Siegel, R., and Howell, J. R., 2002, *Thermal Radiation Heat Transfer*, 4th ed., Taylor & Francis, New York.

[24] Ordal, M. A., Long, L. L., Bell, R. J., Bell, S. E., Bell, R. R., Alexander, R. W., and Ward, C. A., 1983, “Optical Properties of the Metals Al, Co, Cu, Au, Fe, Pb, Ni, Pd, Pt, Ag, Ti, and W in the Infrared and Far Infrared,” Appl. Opt., **22**, pp. 1099–1119.

[25] Li, L. F., 1996, “Use of Fourier Series in the Analysis of Discontinuous Periodic Structures,” J. Opt. Soc. Am. A, **13**, pp. 1870–1876.

[26] Lalanne, P., and Lemercier-Lalanne, D., 1996, “On the Effective Medium Theory of Subwavelength Periodic Structures,” J. Mod. Opt., **43**, pp. 2063–2085.

[27] Hessel, A., and Oliner, A. A., 1965, “A New Theory of Wood’s Anomalies on Optical Gratings,” Appl. Opt., **4**, pp. 1275–1297.

[28] Lochbihler, H., and Depine, R., 1993, “Highly Conducting Wire Gratings in the Resonance Region,” Appl. Opt., **32**, pp. 3459–3465.

[29] Kumar, A. R., Zhang, Z. M., Boychev, V. A., and Tanner, D. B., 1999, “Temperature-Dependent Far-Infrared Absorptance of Thin $YBa_2Cu_3O_{7-\delta}$ Films in the Normal State,” Microscale Thermophys. Eng., **3**, pp. 5–15.

Friction Numbers and Viscous Dissipation Heating for Laminar Flows of Water in Microtubes

Mohamed S. El-Genk[1]
Regents Professor
e-mail: mgenk@unm.edu

In-Hwan Yang

Chemical and Nuclear Engineering Department,
and Institute for Space and Nuclear Power
Studies,
University of New Mexico,
Albuquerque, NM 87131

The friction numbers for laminar flows of water in microtubes, determined from the temperature rise due to the viscous dissipation heating assuming a velocity slip, show a strong dependence on the diameter and aspect ratio. The calculated values compare well with those determined from experimental data for water flows in glass and diffused silica microtubes (16–101 μm in diameter D and aspect ratios $L/D=499-1479$). With a slip, the friction number almost exponentially decreases as D decreases and, to a lesser extent, as L/D increases. For $D>400$ μm, the friction number approaches the theoretical Hagen–Poiseuille for macrotubes (64) when $L/D>\sim 1500$, but higher values at smaller L/D. The developed semiempirical analytical expression for calculating the friction number is in good agreement with the numerical and experimental results. The results suggest the presence of a velocity slip in the experiments and the plausible presence of a thin nanolayer at the walls of the microtubes. For $D>200$ μm, this layer, if exists, is estimated to be ~18.9 nm, but increases to ~21.5 nm for $D<200$ μm, when $\bar{Re}=800$ and $L/D=1479$. [DOI: 10.1115/1.2909617]

Keywords: microtubes and microchannels, slip, friction number, viscous heat dissipation, laminar flow

Introduction

In recent years, there has been a growing interest in fluid flow and heat transfer in microtubes and microchannels for a host of potential applications. Examples include cooling of electronics and microsatellites, biomedical procedures, and microelectromechanical systems (MEMSs). A key challenge in these applications is to accurately predict the pumping requirements and the amount of viscous dissipation heating. In biomedical applications, an increase in fluid temperature by a few °C could be detrimental to living tissues.

Significant work has been reported on laminar flow of liquids and gases in microchannels and microtubes [1–34]. The focus of reported work has been to investigate the applicability of the Navier–Stokes equations in predicting the friction number in microtubes and microchannels. Some have measured the rise in the flowing liquid temperature due to the viscous heat dissipation, others have investigated the effect of surface roughness on the friction number, and a few reported both the friction numbers determined from pressure drop measurements and the measured rise in the liquid temperature due to the viscous heat dissipation. For fully developed laminar flows in macrochannels ($D_h>1$ mm), some reports have suggested that a relative roughness less than 5% insignificantly affects the value of the friction number and others have shown that roughness has a measurable effect on the friction number. In microtubes and microchannels, the effect of surface roughness is important because of the very small flow area, the significantly large surface to volume ratio and the stressed nature of the flow, increasing the rise in temperature due to the viscous heat dissipation and hence, the value of the friction number. Although negligible in macrochannel and macrotube flows, viscous heat dissipation becomes increasingly important in microtubes and microchannels as D or D_h decreases. This is because of the significant increase in the wall surface area per unit volume of flowing fluid to as much as 10^4-10^6 m^{-1} compared to $0.01-1$ m^{-1} for macrotubes and macrochannels. Viscous heat dissipation decreases the liquid viscosity at the walls, which may decrease the friction numbers below the Hagen–Poiseuille values for macrochannels and macrotubes. Conversely, the viscosities of gases increase with temperature, thus increasing the friction number and viscous heat dissipation for gas flows in microtubes and microchannels.

There has been a large scattering in the reported values of the friction number, $C_{f,\mathrm{exp}}$, determined from the pressure drop measurements by various investigators for liquid flows in microchannels and microtubes (Figs. 1(*a*)–1(*c*)). Some has reported higher, while others reported lower values than those of the Hagen–Poiseuille, $C_{f,\mathrm{tho}}$ (Figs. 1(*a*)–1(*c*)). The inconsistencies are reduced somewhat, but not completely eliminated, when accounting for the decrease in the dynamic viscosity of the flowing liquid at wall due to the viscous heat dissipation. The corresponding changes in the liquid heat capacity and density are insignificantly small to affect the temperature rise in microchannel or microtube flows in the experiments.

Investigators have attributed the differences between the friction numbers determined from the pressure drop measurements, $C_{f,\mathrm{exp}}$, for microtubes and microchannel and those of the Hagen–Poiseuille to experimental uncertainties and a potential effect of surface roughness. Experimental uncertainties include those in the flow and the pressure drop measurements, dimensions and geometry, and due to the entrance effects. Accounting for effect of the surface roughness on the reported values of the friction number for liquid flows in microchannels and microtubes did not fully resolve the large inconsistencies in the reported values by various investigators (Figs. 1(*a*)–1(*c*)). Another important consideration is the potential departure from Navier–Stokes formulation due to the effect of viscous heating on the fluid properties and the highly stressed flow condition. The applied pressure in some of the water flow experiments in microtubes exceeds 120 MPa [1–8].

Figure 1(*a*) shows that the reported values of the friction number for liquid flows in microtubes, determined from the pressure

---

[1] Corresponding author.

Contributed by the Heat Transfer Division of ASME for publication in the JOURNAL OF HEAT TRANSFER. Manuscript received July 2, 2007; final manuscript received October 3, 2007; published online June 4, 2008. Review conducted by Yogesh Jaluria.

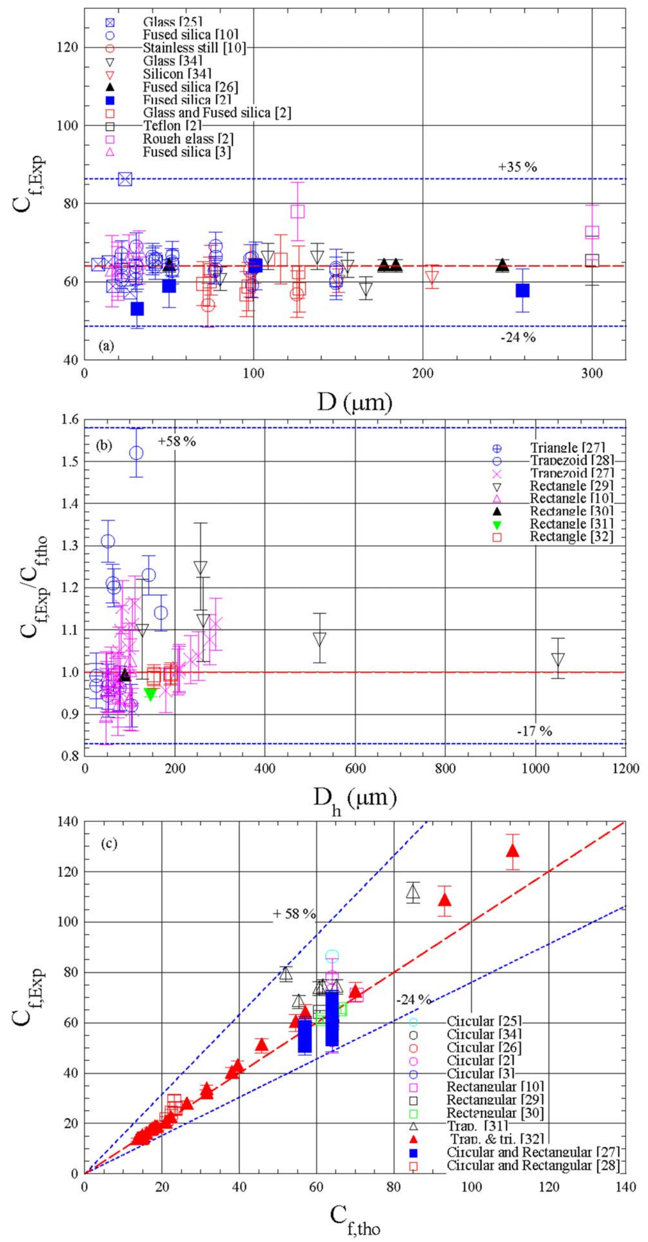

Fig. 1 Friction numbers for microtubes and microchannels

drop measurements, are as much as 35% higher and 24% lower than the Hagen–Poiseuille for smooth macrotubes (64). For microchannel liquids flows, the reported values of the friction number are as much as 58% higher and 17% lower than the Hagen–Poiseuille [4] (Fig. 1(*b*)). As shown in Fig. 1(*c*), the reported friction numbers for microtube and microchannel flows, determined from pressure drop measurements, are within +58% and −24% of those of the Hagen–Poiseuille.

Xu et al. [5] have carried out experiments with de-ionized water in rectangular microchannels that were etched into aluminum and silicon substrates. The microchannels varied in length from 0.01 m to 0.05 m and had a hydraulic diameter D_h from 30 μm to 334 μm. The inlet Reynolds number $\mathrm{Re}_{\mathrm{in}}$ in the experiments varied from 20 to 4000. The measured surface roughness using a laser interferometer microscope was ~0.5 μm and less than 20 nm for the aluminum and silicon channels. Xu et al. [5] did not report any measurements for quantifying the effect of surface roughness on the values of the friction number, but performed theoretical analysis showing that this effect could be neglected. The reported uncertainties in the values of the friction number and Reynolds number were <12% in the experiments of Xu et al. [5].

Kandilkar et al. [6] have performed experiments and measured the pressure drop in microtubes, 620 μm and 1067 μm in diameter with a relative roughness of 0.321–0.71%. Results indicated that the effect of roughness on the value of the friction number is insignificant for the large diameter but could be important for the small diameter microtubes. For stainless steel microtubes with diameters of 128.76 μm and 179.8 μm and a relative surface roughness of 3–4%, the experimental measurements by Li et al. [34] have shown that the friction number could be as much as 37% and 15% higher than the Hagen–Poiseuille of 64 for smooth macrotubes [9].

Hetsroni et al. [33] suggested that there is no difference in the flow behavior in microchannels and microtubes with hydraulic diameters down to 50 μm. This suggestion was based on extensive theoretical analysis and the reported measurements by numerous investigators for flows in smooth (glass and silicon) microtubes and rough microchannels (stainless steel). The microtubes and the rectangular, triangular, and trapezoidal microchannels had hydraulic diameters of 1.01–4010 μm. Test liquids investigated in the reviewed experiments included, among others, tap, distilled, and de-ionized water, R134a, methanol, and isopropanol.

In their experiments using trapezoidal silicon, microchannels with a relative surface roughness of 3.5–5.7%, Qu et al. [8], have reported friction numbers that were higher than those of the Hagen–Poiseuille. The reported friction numbers for microchannels with D_h=51.3 μm and 64.9 μm were 30% higher than those of the Hagen–Posieuille and 15–18% higher for the larger microchannels with D_h of 114.5 μm to 168.9 μm.

For water flows in a rectangular microchannel with a smooth bottom surface, depth of 521 μm, and high aspect ratio (119.19:1), the experimental data of Pfund et al. [29] (Fig. 1(*c*)) have shown that the friction number (24.2+1.3) determined from the pressure drop measurements is more than 10% higher than its Hagen–Poiseuille value, $C_{f,\mathrm{tho}}$=22.4 [4] (Fig. 1(*b*)). Similar results have been reported by the same authors for 263 μm deep microchannel with a smooth bottom. The reported friction number for this microchannel (26.1+2.3) was more than 12.5% higher than its Hagen–Posieuille value (23.2). For roughened microchannels, the reported friction numbers were close to the Hagen–Poiseuille value. However, the large scattering in the reported data made it difficult to quantify, with confidence, the individual effects of microchannel dimensions and surface roughness on the values of the friction number.

Li et al. [34] have experimentally investigated water flows in smooth glass and silicon microtubes with diameters from 79.9 μm to 166.3 μm and from 100.25 μm to 205.3 μm, and in stainless steel microtubes with diameters from 128.76 μm to 179.8 μm and relative roughness of 3–4%. The reported friction number for the smooth microtubes was approximately the same as the Hagen–Poiseuille of 64 for smooth macrotubes, but 15–17% higher for the roughened microtubes (Figs. 1(*a*) and 1(*c*)).

Celata et al. [2] have investigated the effects of wall roughness and hydrophobicity on the pressure drop and temperature rise due to the viscous heat dissipation in adiabatic flows of degassed water in untreated, smooth microtubes with diameters from 31 μm to 259 μm. The reported friction numbers for the microtubes with diameters >31 μm were within +10% of the Hagen–Poiseuille value (64), but as much as 19% lower for the 31 μm diameter microtube (Figs. 1(*a*) and 1(*c*)). The experimental data for the siliconated (hydrophobic) microtubes with diameters of 70 μm to 326 μm showed that the slip at the wall had no effect on the value of the friction number, which came to within +10% of the Hagen–Posieuille of 64. For the roughed glass microtubes with diameters of 126 μm and 299 μm, the reported friction numbers determined from the pressure drop measurements in the experiments were >20% higher than the Hagen–Poiseuille for smooth macrotubes of 64 (Figs. 1(*a*) and 1(*c*)).

Celata et al. [2] have attributed the large variation in the reported values of the friction numbers to a deviation in the cross section of the microtubes used in the experiments from a perfectly circular geometry. In order to minimize side heat losses from the walls of the microtubes by natural convection, Celata [1] and Celata et al. [2] placed their test sections in vacuum. They estimated the side heat losses by radiation in the experiments with the highest temperature rise of the water flow in the microtubes ($D=50$ μm and $\bar{\mathrm{Re}}=700$) due to the viscous heating to be in the order of 1%, and thus considered negligible. Similarly, the side heat losses to natural convection of ambient air in the experiments of Judy et al. [10], calculated in this work using COMSOL MULTIPHYSICS 3.2A software, is found to be negligible. These losses are estimated to introduce less than 0.01 K error in the measured temperature rise of laminar water flows ($\mathrm{Re}<800$) in a microchannel ~10 cm long.

Rands et al. [3] have conducted their water flow experiments in fused silica microtubes with a circular cross section accurate to within +1 μm and diameters of 16.6 μm, 19.7 μm, 26.3 μm, and 32.2 μm. The lengths of the microtubes varied from 1 cm to 3 cm (or $L/D>625$). The reported friction numbers were consistent with the Hagen–Poiseuille for smooth macrotubes (64) (Figs. 1(*a*) and 1(*c*)). However, the overall uncertainties in the pressure drop data used to determine the friction numbers were 16–29%, with the highest value for the smallest microtube diameter. Rands et al. [3] have used similar setup to that of Judy et al. [10]; thus it is save to assume that the side heat losses in their experiments to natural convection of ambient air were negligibly small to affect the measured rise in the water flow temperature due to the viscous heat dissipation.

A potential effect of surface roughness in microchannels and microtubes on the friction number is that caused by a potential slip at the wall due to the presence of a thin layer of gas, separating the liquid flow from the wall, e.g., Refs. [11–14]. Tretheway and Meinhart [15] have measured the velocity profiles of water flows in extruded glass, rectangular channels measuring 30×300 μm in cross section and 8.25 cm long. The microchannel wall was covered with a 2.3 nm thick monolayer of a hydrophobic coating. The measured velocity profile with a micron-resolution, particle image velocimetry in the clean microchannel was consistent with the solution of the Navier–Stokes equation for fully developed laminar flow with a nonslip boundary. However, they reported a slip of approximately 10% of the freestream velocity, just at the hydrophobic wall of the microchannel.

Similarly, Baudry et al. [11] in their studies of the hydrodynamic forces between a sphere and a plane immersed in glycerol using a surface force apparatus (SFA) have reported that the drainage of the thin liquid film is different on hydrophobic and hydrophilic planes. Such a difference was attributed to the existence of a slip at the interface between the liquid film and the hydrophobic plane. For this surface, the reported slip length was ~65 glycerol molecular diameters.

Assuming a nonslip at the walls of macrochannels and macrotubes has shown good agreement of the friction number values determined from the pressure drop measurements for fully developed laminar flows with those of the classical Hagen–Poiseuille. The slip at the wall, however, could be important for liquid flows in microchannels and microtubes, even those with hydrophilic walls. This may partially explain the inconsistencies in the reported values of the friction number by various investigators for laminar flows of liquids in microchannels and microtubes (Figs. 1(*a*)–1(*c*)). The presence of a slip at the wall of microtubes and microchannels depends on many factors including wettability and surface roughness [11–14,16] and had been the subject of considerable debate and discussion.

Experimental results have shown that slip is a predictable and measurable effect for flow of highly confined liquids. Since liquid flow in microtubes and microchannels is highly confined, then it is appropriate to hypothesize that the same effect could be present when the applied pressure exceeds a certain critical value [13,17–21]. Experiments involving liquid flows in microtubes with hydrophobic walls have shown a reduction in pressure losses by as much as 20–40%. The obvious reason in this case is the lake of wetting of the wall, resulting in a slip, which reduces the pressure losses and viscous heating. This effect has been quantified in terms of an apparent liquid viscosity at the wall. Reported results for hydrophobic surfaces have shown this viscosity to be lower than that of the bulk liquid. In the case of a hydrophilic wall, however, the wetting of the liquid to the wall precludes the slip, except when the liquid is highly stressed.

This paper examines the experimental measurements in Refs. [1–3] in an attempt to quantify the effect of a potential slip on the reported values of the friction number, also known as Poiseuille number, determined from the pressure drop measurements in the experiments. The values of the friction number for laminar water flows in microtubes of various diameters and aspect ratios are determined from the reported measurements in the experiments of the temperature rise, rather than the pressure drop measurements (Figs. 1(*a*)–1(*c*)). Numerical calculations are also performed at the same condition in the experiments, namely, hydrodynamically fully developed but thermally developing inlet flow, adiabatic wall, and temperature dependent water viscosity. The numerical simulation using COMSOL MULTIPHYSICS 3.2A software calculates the temperature rise due to the viscous dissipation heating in the experiments and deduces the values of the friction numbers, both for nonslip and slip at the walls of the microtubes. The values of the friction numbers are compared to those determined from the reported measurements of the rise in the temperatures of the laminar water flows in glass and diffused silica microtubes [1–3]. A semiempirical analytical expression is also developed, which calculates the temperature rise in liquid flows in microtubes due to the viscous heat dissipation and the friction number for nonslip and slip conditions at the microtube walls. This expression also accounts for the effect of thermal development of the flow at the inlet of the microtubes. The calculated temperature rise and the determined values of the friction number using this expression, as functions of the diameter D and L/D of the microtubes, are compared to those obtained from the numerical calculations and from the reported experimental data.

Effect of Slip at Microtube Wall

To account for a potential slip at the microtube wall, the steady-state, Navier–Stokes momentum balance equation

$$\frac{\bar{\mu}_\ell}{r}\left[\frac{d}{dr}\left(r\frac{d\nu_{z,\ell}}{dr}\right)\right]=\frac{dP_\ell}{dz} \tag{1}$$

is solved subject to the boundary condition that the fluid velocity at the wall ($r=R$) is not zero, but proportional to the shear stress [22,23] as

$$\nu_{z,\ell}(r=R)=\beta(d\nu_{z,\ell}/dr),\qquad (d\nu_{z,\ell}/dr)\big|_{r=0}=0 \tag{2}$$

In this equation, the slip length β is the distance behind the wall at which the liquid velocity extrapolates to zero. The fully developed radial velocity profile derived from the solution of Eq. (1), subject to the slip boundary in Eq. (2), can be expressed as

$$\nu_{z,\ell}(r)=\frac{D^2\Delta P}{16\bar{\mu}L}(1-(2r/D)^2+(4\beta/D)) \tag{3a}$$

The average flow velocity in the microtube is then given as

$$\bar{\nu}_{z,\ell}=\frac{D^2\Delta P}{32\bar{\mu}L}(1+8(\beta/D)) \tag{3b}$$

and the corresponding average Reynolds number is

$$\bar{\mathrm{Re}} = \left(\frac{\rho D \bar{\nu}_{z,\ell}}{\bar{\mu}}\right) = \frac{\rho D^3 \Delta P}{32 \bar{\mu}^2 L}(1 + 8(\beta/D)) \tag{3c}$$

The steady-state energy balance equation for fluid flow in the microtubes is expressed as

$$\rho C_p \nu_{z,\ell}(r)\left(\frac{\partial T}{\partial z}\right) = \bar{\mu}\left(\frac{\partial \nu_{z,\ell}}{\partial r}\right)^2 \tag{4}$$

The right hand side of Eq. (4) is evaluated using Eq. (3*a*). When integrating Eq. (4) over the total volume of the liquid in the microtube, the rearranged results can be expressed in terms of the average flow velocity as

$$\frac{8\pi\bar{\mu}L}{(1 + 8(\beta/D))^2}\bar{\nu}_{z,\ell}^2 = \left(\frac{\pi}{4}D^2\right)\rho\bar{\nu}_{z,\ell}C_p\Delta T \tag{5}$$

Substituting for the average flow velocity from Eq. (3*b*) and rearranging the results give the following expression for the rise in the liquid temperature due to the viscous heat dissipation in the microtube as

$$\Delta T = \frac{64}{(1 + 8(\beta/D))^2}\left(\frac{\bar{\mu}^2}{2\rho^2 L^2 C_p}\right)\left(\frac{L^3 \bar{\mathrm{R}}e}{D^3}\right) \tag{6}$$

Equation (6) can be used to determine the friction number, $C_{f,\mathrm{tho}}$, in terms of the modified average Reynolds number, $\bar{\mathrm{Re}}^*$ and dimensionless temperature rise ΔT^* in the microtube, as

$$\Delta T^* = \frac{64}{(1 + 8(\beta/D))^2}\bar{\mathrm{Re}}^* = C_{f,\mathrm{tho}}\bar{\mathrm{Re}}^* \tag{7}$$

The friction number, $C_{f,\mathrm{tho}}$, can also be obtained from a similar equation written in terms of the dimensionless pressure drop and the modified average Reynolds number for laminar flow in a smooth microtube as

$$\Delta P^* = \frac{64}{(1 + 8(\beta/D))^2}\bar{\mathrm{Re}}^* = C_{f,\mathrm{tho}}\bar{\mathrm{Re}}^* \tag{8}$$

Therefore, the friction number, $C_{f,\mathrm{tho}}$, can be obtained from either the pressure drop or the temperature rise measurements in microtubes using Eq. (7) or (8). In the microtube experiments, it is not possible to determine the exact pressure drop because of the entrance and exit effects and the physical difficulties of mounting the pressure transducer taps at the inlet and the exit of the microtube. On the other hand, the measurements of the temperature rise due to the viscous dissipation heating in microtubes are relatively more accurate because of the relative ease with which to mount thermocouples or temperature sensors at the inlet and exit of the microtubes.

The comparison of Eqs. (7) and (8) gives the following relationship between the pressure drop and the temperature rise due to the viscous dissipation heating in microtubes as

$$\Delta P^* = \Delta T^* \quad \text{or } \Delta P = \rho C_p \Delta T \tag{9}$$

Equations (7)–(9) assume hydrodynamically and thermally fully developed laminar flows in microtubes with adiabatic wall and constant fluid physical properties evaluated at the average temperature in the microtubes. In macrotube flows, viscous dissipation heating is infinitesimally small to measure, thus determining the friction number from the pressure drop measurements using Eq. (8) had been used and is quite accurate.

With a nonslip at the wall of the microtubes (or $\beta = 0\ \mu$m), the friction numbers, $C_{f,\mathrm{tho}}$ from Eqs. (7) and (8) are the same as the classical Hagen–Posieuille for smooth macrotubes (64). On the other hand, with a slip at the wall ($\beta > 0$), the friction numbers for the microtube flows are lower than that of the Hagen–Poiseuille for smooth macrotubes; almost exponentially decreasing as the diameter of the microtube decreases (Eqs. (7) and (8)). It approaches that of the Hagen–Poiseuille when the macrotube diameter is large enough such that $8\beta/D$ is $\ll 1$. For example, with a slip length $\beta = 0.5\ \mu$m, the friction numbers for fluid flows in microtubes with diameters of 30 μm and 50 μm are 21.1% and 13.8% lower than the Hagen–Poiseuille of 64. Increasing the microtube diameter to 500 μm increases the friction number to 98.43% of the Hagen–Poiseuille.

Equations (7)–(9) do not account for the effect of the thermal development of the flow at the entrance of the microtubes in the experiments; thus only valid for large L/D where the contribution of the thermal entrance effect is negligible. Also, the liquid physical properties used in these equations are evaluated at the average temperature in the microtube, while in the experiments they change along the microtube as the fluid temperature rises due to the viscous heat dissipation. The form of Eq. (7) is used in this work to determine the friction numbers from the numerical calculations and the experimental data of the temperature rise due to the viscous heat dissipation in water flows in microtubes [1–3]. The values of the friction number obtained from the numerical calculations, assuming different slip lengths, are compared to those determined from the reported water flow data. The agreement reveals the value of the slip length, if any, at the wall of the microtubes in the experiments.

Results and Discussion

The values of the friction number, $C_{f,\mathrm{Exp}}$ for the water flows in the microtubes are directly determined from plotting the dimensionless temperature rise in the microtubes, ΔT^*, versus the modified Reynolds number $\bar{\mathrm{Re}}^*$ in the experiments [1–3]. The slop of the linear best fit of the data equals the friction number. Similarly, the friction number is obtained from the results of the numerical calculations of the temperature rise in the water flows in microtubes with wide ranges of diameters ($D > 10\ \mu$m) and $L/D = 300-1479$, and inlet Reynolds number $\mathrm{Re}_{\mathrm{in}}$ from 100 to 800, and assuming different slip lengths ($\beta \geq 0\ \mu$m). The numerical calculations for laminar water flows in microtubes are performed at typical conditions in the experiments, e.g., hydrodynamically fully developed, but thermally developing inlet flow, adiabatic wall, and temperature dependent liquid properties. The values of the friction number obtained from the experimental data and from the numerical calculations with different slip lengths, $\beta \geq 0$, are compared to determine the plausible slip length, if any, in the experiments [1–3].

As indicated earlier, the side heat losses in these experiments are negligible and their effect on the reported rise in the temperature of the water flows due to the viscous heat dissipation is insignificantly small. On the other hand, the thermal development of the flow at the entrance of the microtubes with small aspect ratio ($L/D < 400$) can cause the rise in the water flow temperature due to the viscous heating to increase by an additional 10–15%, depending on the aspect ratio and the value of Reynolds number (e.g., Figs. 2(*a*) and 2(*b*)).

Effect of Thermally Developing Inlet Flow. As indicated earlier, Eq. (7) assumes thermally and hydrodynamically fully developed flow at the inlet of the microtubes and constant physical properties evaluated at the average temperature in the microtube. In addition, it assumes an adiabatic wall and incompressible flow. Thus, the increase in the liquid temperature due to the viscous dissipation heating in the microtubes is linear with distance from the entrance. To account for the effect of the thermal developing condition at the inlet of the microtubes in the experiments and in the numerical calculations, Eq. (7) can be rewritten as

$$\Delta T^* = C_{f,\mathrm{mod}}\bar{\mathrm{Re}}^* = C_{f,\mathrm{tho}}(1 + f)\bar{\mathrm{Re}}^* \tag{10}$$

The thermal entrance correction factor ($0 \leqslant f < 1$) in Eq. (10) is empirically correlated in terms of D and L/D using the values of the friction numbers determined from the present numerical calculations and from the reported experimental data for water flows in glass and diffused silica microtubes [1–3].

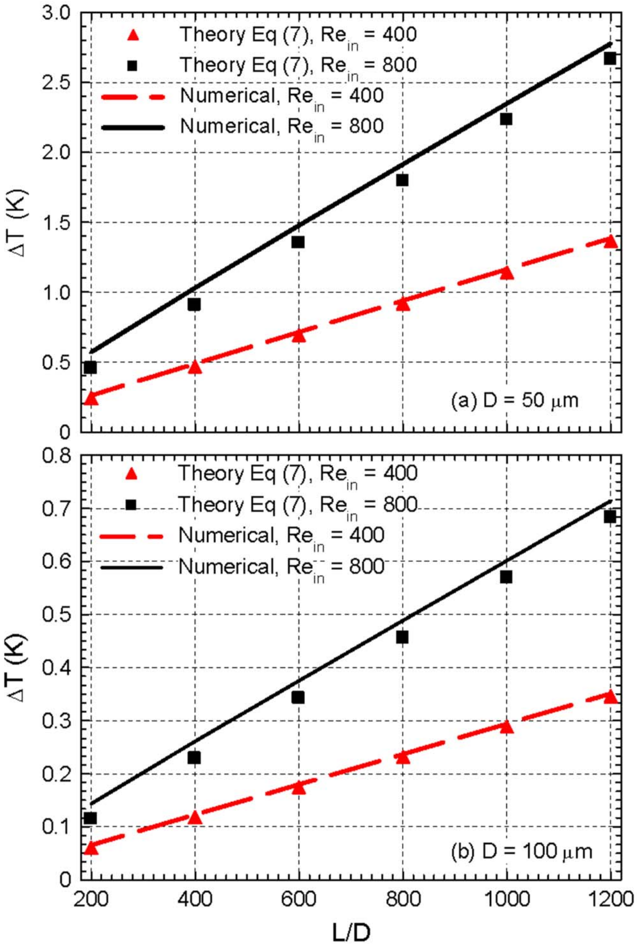

Fig. 2 Effect of entrance condition on viscous heating of water flow in microtubes

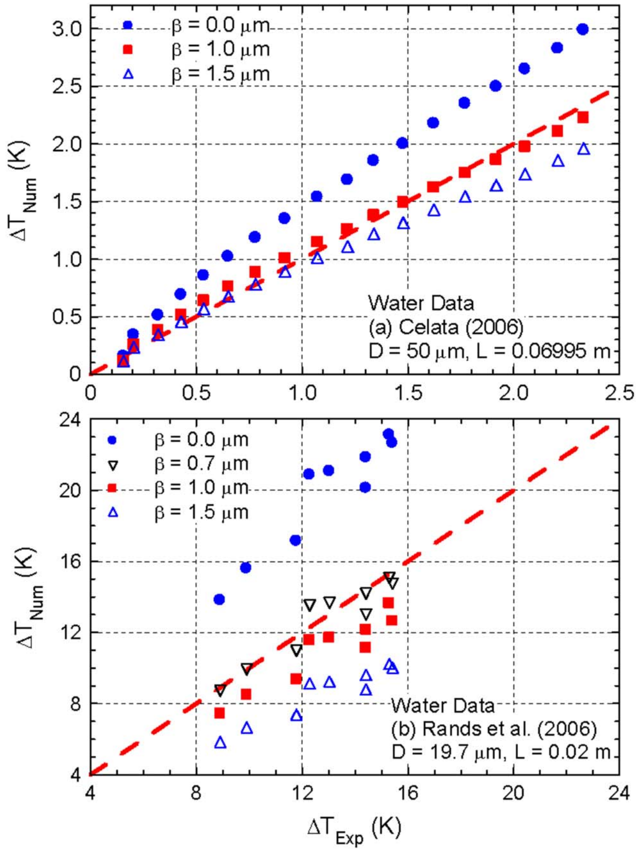

Fig. 3 Effect of slip length on viscous heating of water flow in microtubes

Numerical Calculations. The numerical calculations for laminar water flows in microtubes are performed using COMSOL MULTIPHYSICS 3.2A software, both with nonslip and slip condition at the wall ($\beta \geq 0$). The calculated liquid velocity $v(\mathbf{r},z)$, and temperature $T(\mathbf{r},z)$, account for the viscous dissipation heating at the wall of the microtubes. The liquid dynamic viscosity is taken to be temperature dependent; however, the changes in the density, thermal conductivity, and heat capacity are negligible. The numerical calculations used grids of different sizes for the different microtube diameters. The number of the nodes in the radial direction varied from 20 to 25 and from 185 to 200 in the axial direction of the flow. Finer numerical grids insignificantly changed the predictions of the temperature rise in the water flows due to the viscous dissipation heating and of the pressure drop in the microtubes. The calculations are performed for inlet Reynolds numbers up to 800, and for different values of D and L/D and at the inlet temperatures given by Celata [1] in the water flow experiments. For the experiments by Rands et al. [3], the water inlet temperature in the numerical calculation is taken constant at 295 K.

The predictions using Eq. (7) of the temperature rise in the microtubes and from the numerical calculations are compared in Figs. 2(*a*) and 2(*b*) at two different inlet Reynolds numbers and microtube diameters. Unlike Eq. (7), the numerical calculations allow the dynamic viscosity of the liquid to change with temperature along the microtube. As shown in these figures, neglecting the thermal development at the entrance of the microtubes (Eq. (7)) underestimates the rise in the water flow temperature due to the viscous dissipation heating and hence the friction number by as much as 10–15%, depending on the diameter and the aspect ratio of the microtube. The smaller the microtube diameter and aspect ratio the larger is the deviation between the predicted temperature rise by Eq. (7) and the numerical calculation. The difference between the analytical and numerical predictions of the temperature rise in microtubes diminishes as L/D increases and/or the inlet Reynolds number decreases (Figs. 2(*a*) and 2(*b*)).

Slip Lengths in the Experiments. Figures 3(*a*) and 3(*b*) compares the values of the temperature rise determined from the numerical calculations with those measured in recent experiments for water flows in glass and diffused silica microtubes [1–3]. The results and the comparisons in these figures are strongly suggestive of a plausible slip at the wall of the microtubes in these experiments. The comparison in Fig. 3(*a*) suggests that the slip length, β, in the experiments of Celata [1] and Celata et al. [2] could be ~ 1.0 μm. Similarly, the comparison of the results in Fig. 3(*b*) suggests that the slip length in the experiments of Rands et al. [3] could be ~ 0.7 μm.

These deductions are solely based on the comparison with the experimental measurements of the temperature rise in the microtubes due to the viscous heat dissipation in laminar water flows. Neglecting the effect of a slip at the microtube walls overpredicts the temperature rise in the experiments and the value of the friction number. This issue, a subject of ongoing discussion, invites future investigations using a combination of molecular dynamics and continuum flow calculations and carefully instrumented experiments to determine the nature of the slip in microtubes and microchannels. These investigations may also determine, from first principles, the diameter below which a slip and other nonequilibrium effects at the wall begin to affect the liquid flows in microtubes and microchannels.

Nagayama and Cheng [19] have recently performed nonequilibrium molecular dynamic simulations investigating the effect of interface wettability on the pressure-driven flow of a Lennard–Jones fluid in a nanochannel. The results suggested that the non-slip boundary condition may break down when the driving force caused by the applied pressure overcomes the interfacial resistance. The corresponding critical shear stress rate indicates the point at which the solid no longer impart momentum to the flowing liquid in microtubes or microchannels [16,21,22]. Thus, it may be argued that the velocity slip at a hydrophilic interface, as in the experiments [1–3], could have been caused by the driving force overcoming the interfacial resistance. This view is consistent with those of other investigators for highly confined flows; however, it needs further and thorough investigations.

The results in Figs. 3(*a*) and 3(*b*) clearly show that neglecting the slip at the wall ($\beta=0$) overestimates the temperature rise due to the viscous dissipation heating, compared to the reported measurements in the experiments, by as much as 50%. Conversely, assuming a large slip length of 1.5 μm underestimates the rise in the water flow temperature due to the viscous dissipation heating by as much as 50% compared to the experimental values. With a slip length of 1.0 μm, the reported experimental values of the temperature rise in the microtubes by Celata and Celata et al. [1,2] are in excellent agreement with the values determined from the numerical calculations (Figs 3(*a*) and 4–6). In Figs. 4–6, the friction number, C_f, equals the slope indicated by the linear fit of the reported experimental data using the form depicted by Eq. (7).

Figures 4–6 show that neglecting the slip at the wall of the microtubes overestimates the values of the friction number by significant amounts. Theses figures also show that the friction number strongly depends on the microtube diameters and is independent of their length. The friction number increases as the microtube diameter increases. Similar results are obtained from the experimental data reported by Rands et al. [3] for water flows in microtubes of different diameters and lengths (Figs. 3(*b*) and 7). These figures confirm the plausible presence of a slip at the walls of the microtubes in the experiments (a slip length of 0.7 μm).

The friction numbers determined from the slopes of the experimental data in Figs. 7(*a*)–7(*c*) confirm that the friction number increases as the microtube diameter increases. The friction numbers determined from the results of the numerical calculations with slip lengths of 1.0 μm and 0.7 μm (indicated by the dashed lines in Figs. 4–7) are in excellent agreement with those determined from the reported experimental data for water flows in microtubes [1–3]. The results presented in Figs. 4–7 also show that determining the friction number for water flows in microtubes from the measurements of the temperature rise due to the viscous dissipation heating is an effective and preferred approach. This is because the uncertainties in the temperature measurements caused by the placement of the thermocouples in the microtubes experiments are typically much smaller than those caused by the placements of the probes for the pressure drop measurements.

The results in Figs. 4–7 are strongly suggestive that in the experiments in Refs. [1–3] the slip length at the wall of microtubes could have been ~1.0–1.5 μm and 0.7 μm, respectively. The plausible existence of a slip at the walls of the microtubes in the water flow experiments is also supported by the results presented in Fig. 8. This figure plots the values of the friction number obtained from the numerical calculations assuming a slip at the wall versus those determined from the measured temperature rise in the experiments (Figs. 4–7).

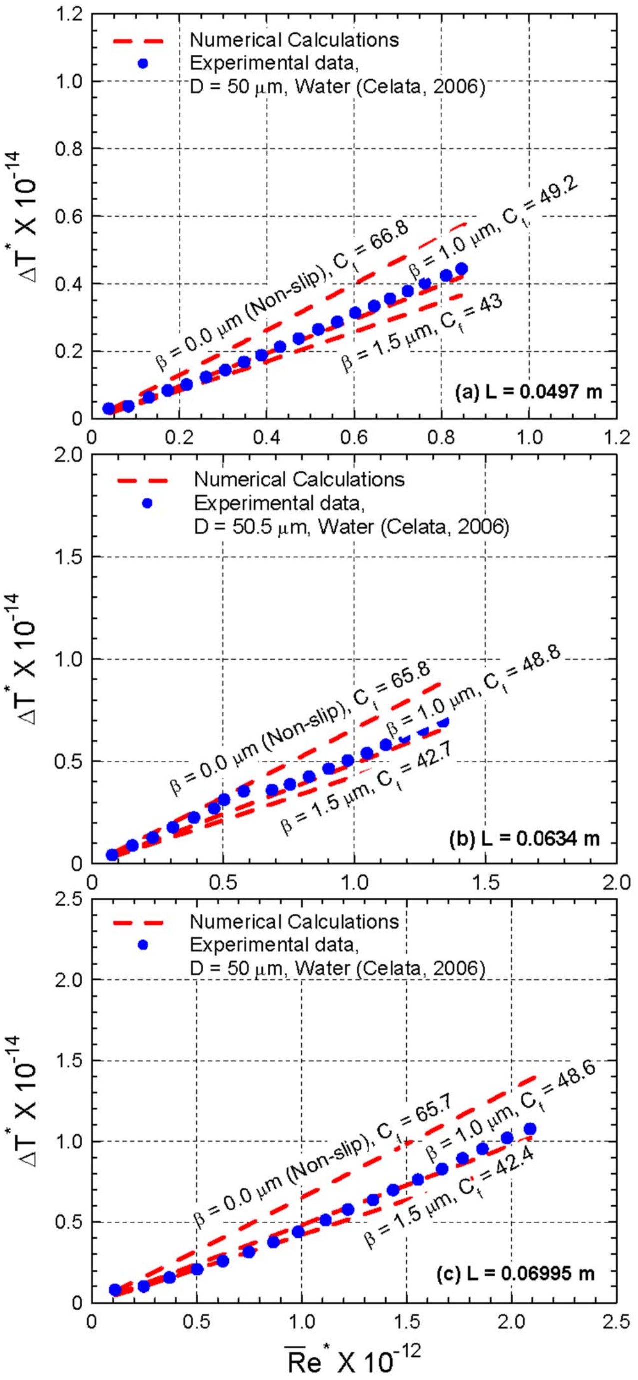

Fig. 4 Experimental measurements confirming slip at the wall of 50 μm diameter microtube

Additional Discussion of the Effect of Slip. Except for neglecting a plausible slip at the wall, the theory by Morini [24] is identical to that presented in this paper in terms of assuming thermally and hydrodynamically fully developed flow at the entrance of the microtubes, adiabatic walls, and constant liquid properties. For a nonslip condition ($\beta=0$), the predictions of the gradient of the temperature rise in the microtubes due to the viscous heat dissipation (Eq. (6)) are identical to those of Morini's (Figs. 9(*a*)–9(*d*)). As shown in these figures, both predictions, however, are higher than the experimental results reported by Celata and Celata et al. [1,2]. When the analytical calculations using Eq. (6) assume a slip length of $\beta=1$ μm, the analytical results of the friction number are in good agreement with those determined from the experimental data. These agreements support the argument for the plausible presences of a slip at the walls of the microtubes in the experiments (Celata [3]), in which the flow is highly confined and stressed as the applied pressure exceeded 120 MPa.

Effects of Microtube Diameter and Aspect Ratio. To examine the effect of the microtube diameter D and aspect ratio L/D on the friction number, the values determined from the numerical

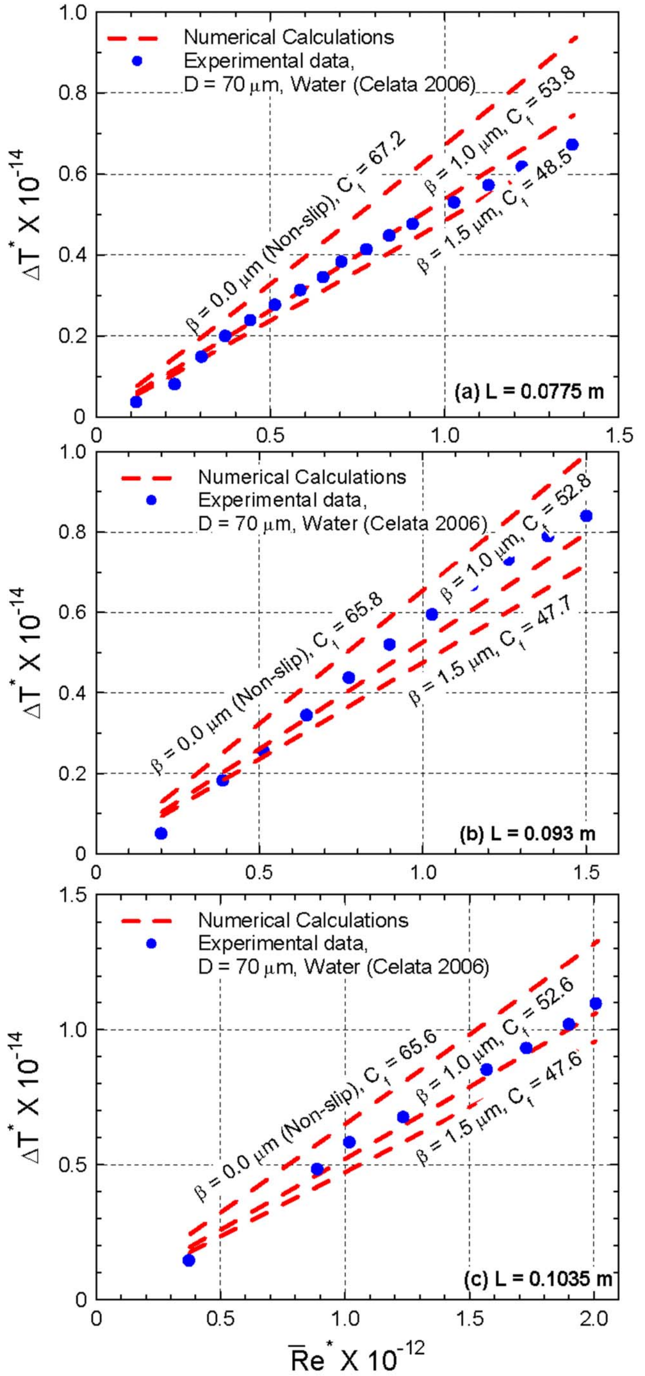

Fig. 5 Experimental measurements confirming slip at the wall of 70 μm diameter microtube

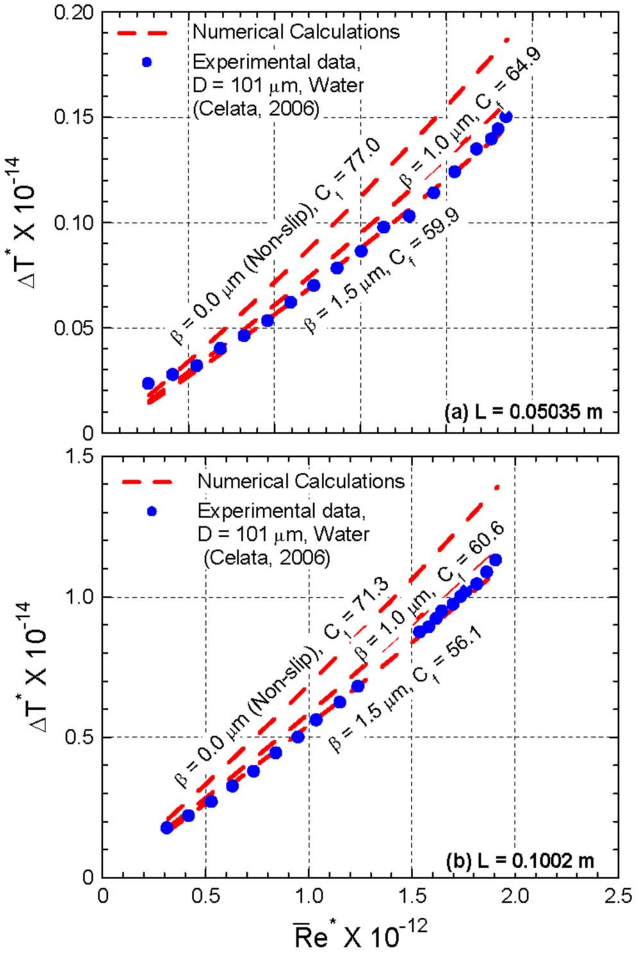

Fig. 6 Experimental measurements confirming slip at the wall of 101 μm diameter microtube

calculations with slip lengths β=1.0 μm and 0.7 μm are compared in Figs. 10(*a*) and 10(*b*) to those obtained from the experimental data [1–3]. The solid curves in these figures are those obtained from Eq. (7) with the same slip lengths. These figures show that the friction number almost exponentially increases as the microtube diameter increases and, to a much lesser extent, as the aspect ratio L/D decreases.

Although the aspect ratio is part of the modified Reynolds number $\bar{\mathrm{Re}}^*$, Eq. (7) could not be used to explicitly determine the separate effect of L/D on the friction number, $C_{f,\mathrm{tho}}$. Unlike the experiments and the numerical calculations, Eq. (7) assumes thermally fully developed inlet flows. Such an assumption has been shown in Fig. 2 to underestimate the temperature rise due to the viscous dissipation heating in water flows in microtubes. Thus, the friction number from Eq. (7), $C_{f,\mathrm{tho}}$, is expected to be lower than in the experiments because of neglecting the thermal developing effect at the inlet of the microtubes. The numerical calculations with the same slip lengths, but for thermally developing inlet flow condition as in the experiments, show that the dependence of the friction number for water flows on the microtube diameter is similar to that given by Eq. (7), but the friction numbers at small L/D values are higher than those given by Eq. (7) (Figs. 10(*a*) and 10(*b*)).

The results delineated in these figures indicate that the effect of L/D on the friction number for microtube water flows is negligible when $D < 20$ μm, but becomes increasingly important as the diameter of the microtubes increases. The dependence of the friction number on L/D is also confirmed by the experimental data for microtubes of the same diameters, but different values of L/D (Celata [1], Rands et al. [3]).

Figures 10(*a*) and 10(*b*) show that the friction numbers determined from the reported temperature rise in the microtube experiments and from the numerical calculations increase as L/D decreases. They approach those predicted by Eq. (7) as L/D approaches 1479, suggesting that for large aspect ratios the effect the thermal development of the water flow at the inlet of the microtubes on viscous dissipation heating and hence, the friction umber can be neglected.

The numerical values of the friction number, $C_{f,\mathrm{num}}$ (the dashed curves in Figs. 10(*a*) and 10(*b*)) show a similar dependency on the

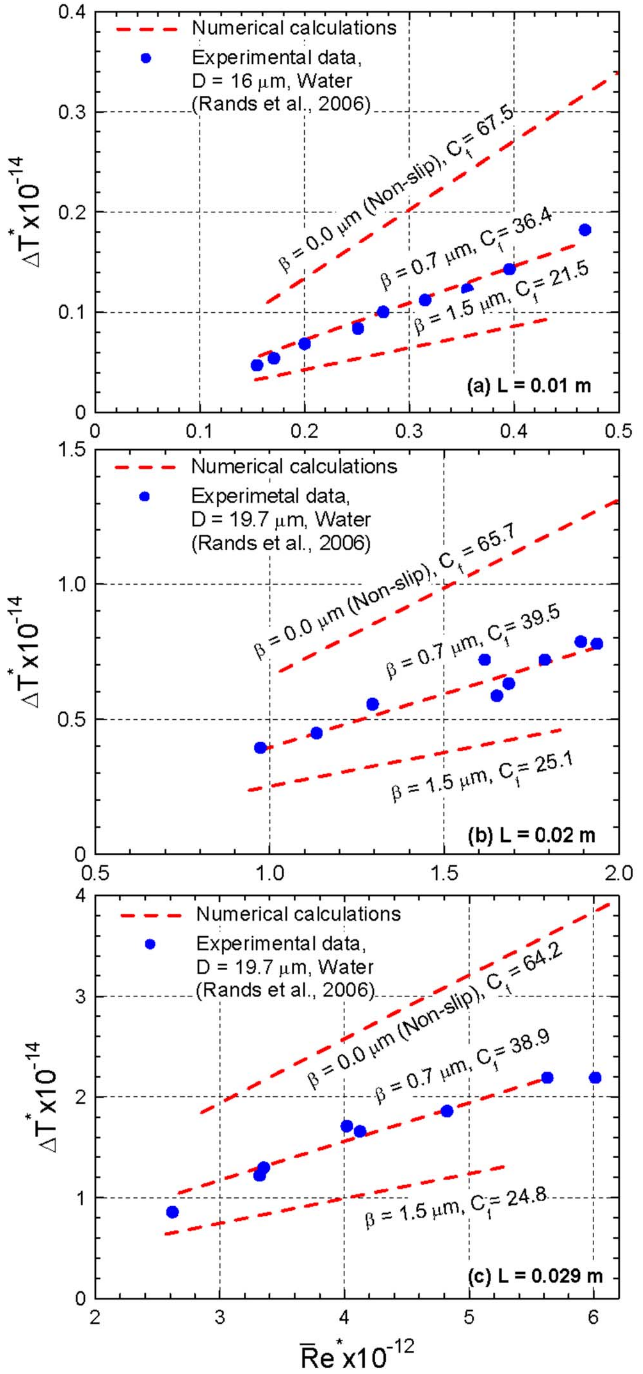

Fig. 7 Additional measurements confirming slip at the wall of microtubes

microtube diameter as indicated by Eq. (7) (the solid curves). The friction numbers determined from the numerical calculations are in excellent agreement with those obtained from the experimental data, for the same microtube diameter, L/D, and with the slip lengths determined earlier (Figs. 11(*a*) and 11(*b*)). Such an agreement confirms the soundness of the numerical calculations and is strongly suggestive of the plausible presence of slip at the wall of the microtubes in the experiments of Celata [1] and Celata et al. [2] ($\beta \simeq 1.0$ μm) and Rands et al. [3] ($\beta \simeq 0.7$ μm). The results in Figs. 10(*a*) and 10(*b*) also show that for large L/D, the friction numbers for microtube flows are lower than the classical Hagen–Poiseuille of 64. However, for $L/D \geqslant 1479$ and $D > 400$ mm, the friction numbers for the water flows in microtubes approach that

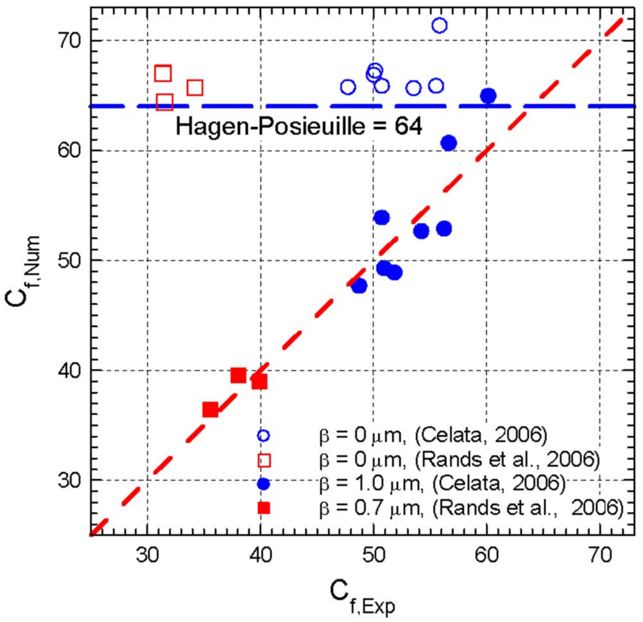

Fig. 8 Effect of slip length on friction number for water flows in microtubes

of Hagen–Poiseuille for smooth macrotubes (64). Results also show that for smaller L/D, the thermal entrance effect could cause the friction number in the microtubes to exceed that of the Hagen–Poiseuille for smooth macro-tubes (64).

Thermal Entrance Effect. Equation (7) accurately predicts the dependency of the friction number, $C_{f,\text{tho}}$, on the diameter of the microtubes with and without slip at the wall. However, the calculated values using Eq. (7) are consistently lower by $>14\%$ than those obtained from the experimental measurements [1–3] and the numerical calculations performed for the same inlet conditions in the experiments and assuming slip lengths of 1.0 μm and 0.7 μm (Figs 11(*a*) and 11(*b*)). This difference is because Eq. (7) assumes thermally fully developed inlet flow, while in both the experiments and the numerical calculations the liquid flow at the inlet of the microtubes is thermally developing, which explains the higher values of the friction number.

The results in Figs. 10(*a*) and 10(*b*) suggest that for $L/D \geqslant 1479$ the effect of the flow thermal development at the entrance of the microtubes on the friction number can be neglected. Thus, Eq. (7) can be used to accurately determine the friction number for laminar flow in microtubes as a function of the diameter and the slip length at the wall, β. In order to account for the effect of the thermally developing inlet flow in microtubes with small L/D; Eq. (7) is modified to the form given by Eq. (10).

Effect of L/D. In Eq. (10), the entrance thermal correction factor f is introduced to account for the effect of L/D (or the thermal development of the flow at the inlet of the microtubes). It has the following form:

$$f = a[1 - \exp(-D/\ell)] \tag{11}$$

The coefficient a and characteristic length ℓ are functions of the aspect ratio of the microtubes, L/D. These coefficients are determined from the best fit of the numerical calculations of the temperature rise in the water flows in microtubes of different diameters and L/D and for inlet Reynolds number from 100 to 800. The obtained empirical expressions for a and ℓ are

$$a = 25.4(L/D)^{-0.91}, \quad \ell = 2.18(L/D)^{0.415} \tag{12}$$

The empirical expression for the entrance thermal correction factor f given by Eq. (11) is in excellent agreement with the nu-

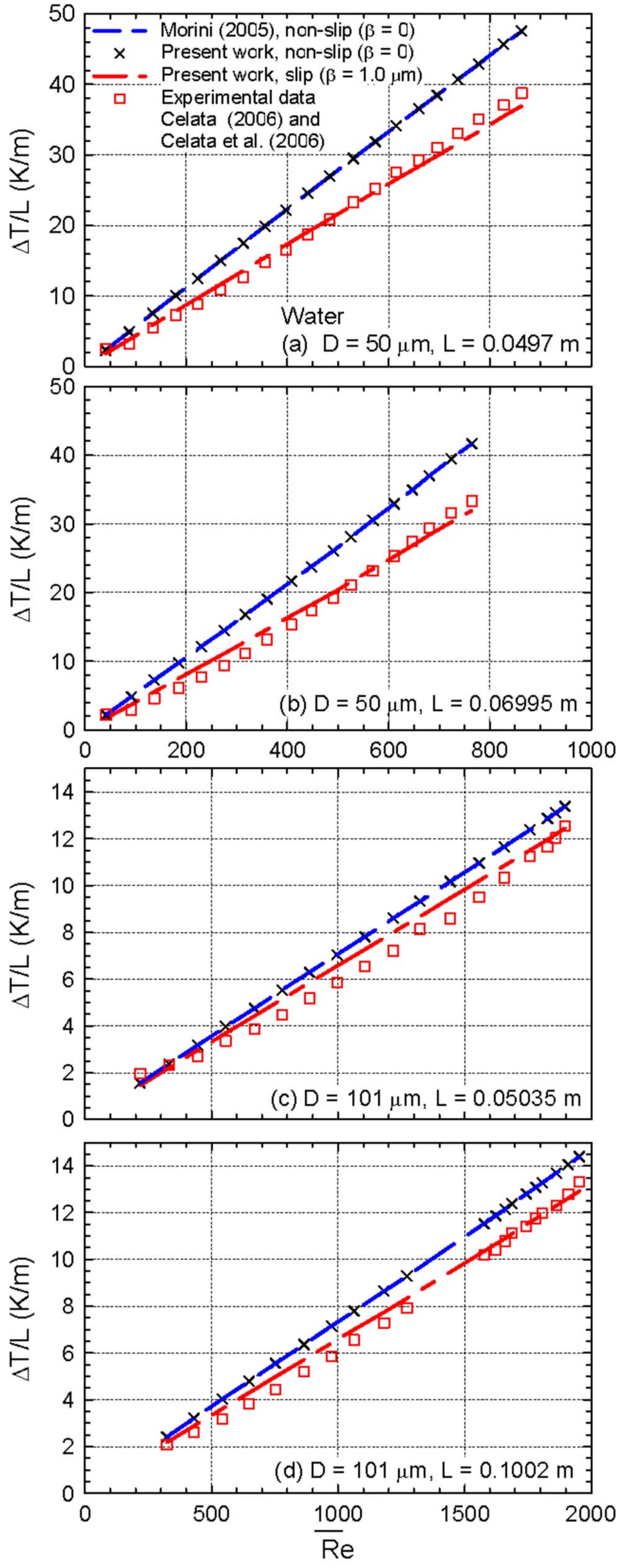

Fig. 9 Comparisons of theory with experimental data of Celata [1] and Celata et al. [2]

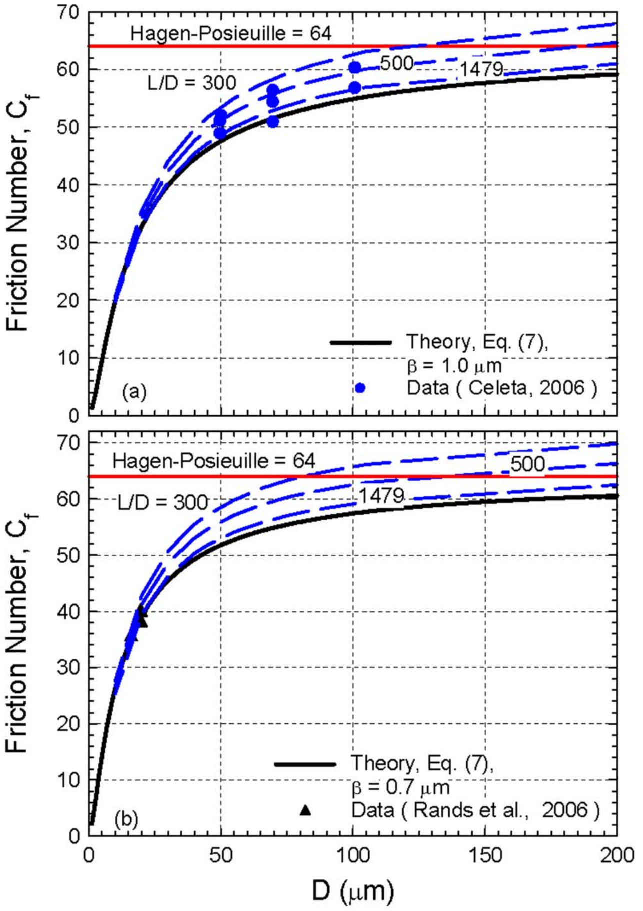

Fig. 10 Effects of *D* and *L/D* on friction number for laminar flow of water in microtubes

merical predictions (Fig. 12). This figure shows that f increases as the diameter of the microtube increases, but becomes almost independent of the microtube diameter, when $D > 200$ μm. It is also a strong function of L/D, with a gradually diminishing effect as L/D increases approaching 1500. For this L/D, the effect of thermal development at the inlet of microtubes is negligible, as f becomes infinitesimally small and the predictions of Eq. (10) of the friction number become identical to those of Eq. (7) ($f \sim 0$).

The values of the modified friction number, $C_{f,\mathrm{mod}}$, calculated using Eq. (10), which accounts for the effect of thermal development of the flow at the inlet of microtubes (Eqs. (11) and (12)), are compared in Figs. 13(*a*) and 13(*b*) with those obtained from the reported measurements for water flows in microtubes [1–3]. The results in Figs. 13(*a*) and 13(*b*) show that the predictions of the friction number using Eq. (10) are within +5% and +1 to −3% of the values determined from the reported experimental data by Celata [1] and Rands et al. [3], respectively. The analytical predictions are also in excellent agreement with the friction numbers determined from the numerical calculations performed at same conditions in the experiments and assuming slip lengths, $\beta = 1.0$ μm and 0.7 μm.

Slip at Microtube Wall. Figure 14 presents a line diagram for the velocity profile for laminar flow in a microtube with assumed slip at the wall. It hypothesizes that with a slip, the flowing liquid is separated from the wall of the microtube by a very thin layer, δ, of gas or liquid vapor. The velocity at the interface between this layer and the flowing liquid $((R\text{-}\delta), z)$ is v_{slip} and the boundary between the thin gas layer and the wall (R, z) is that of nonslip (β=0 μm). The slip velocity at the liquid-gas layer interface, v_{slip}, increases as the slip length, β, increases. The one-dimensional momentum equation for laminar liquid flow in the microtube (Fig. 13), Eq. (1), is solved subject to the boundary conditions:

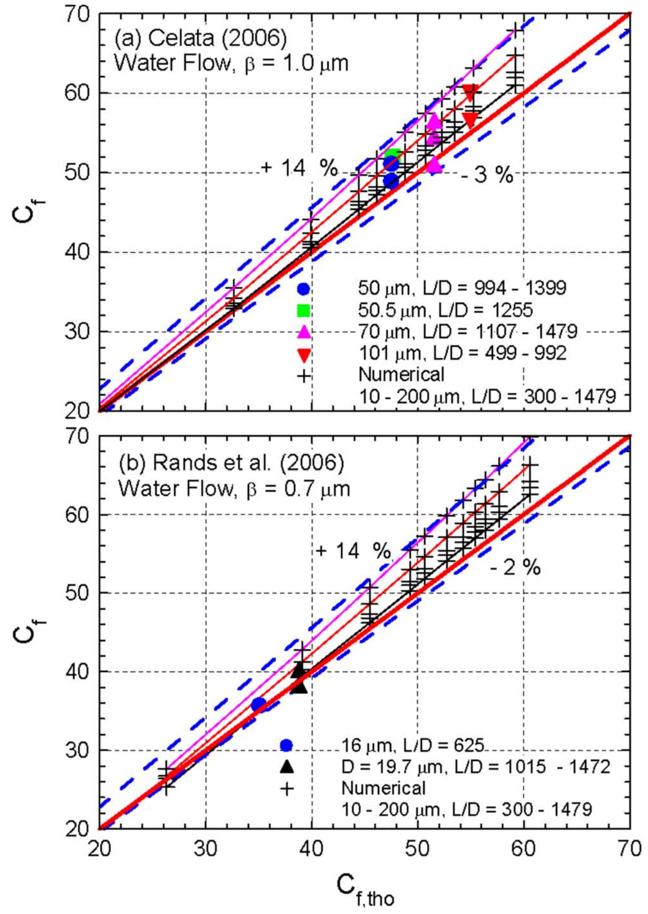

Fig. 11 Effect of neglecting entrance thermal development on friction number

$$\nu_{z,\ell}(R-\delta) = -\beta \frac{d\nu_{z,\ell}}{dr}(R-\delta), \quad \frac{d\nu_{z,\ell}}{dr}(r=0) = 0 \tag{13}$$

Similarly, the one-dimensional momentum equation in the thin gas layer at the microtube wall (Fig. 14) is given as

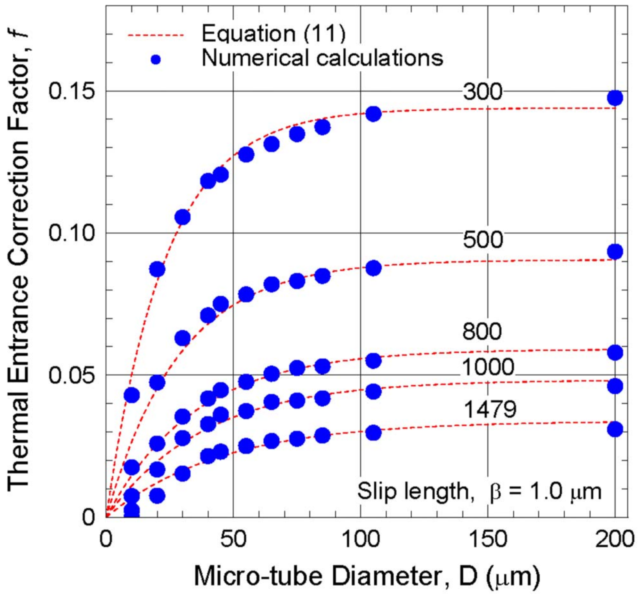

Fig. 12 Correction factor for thermal flow development at inlet of microtubes

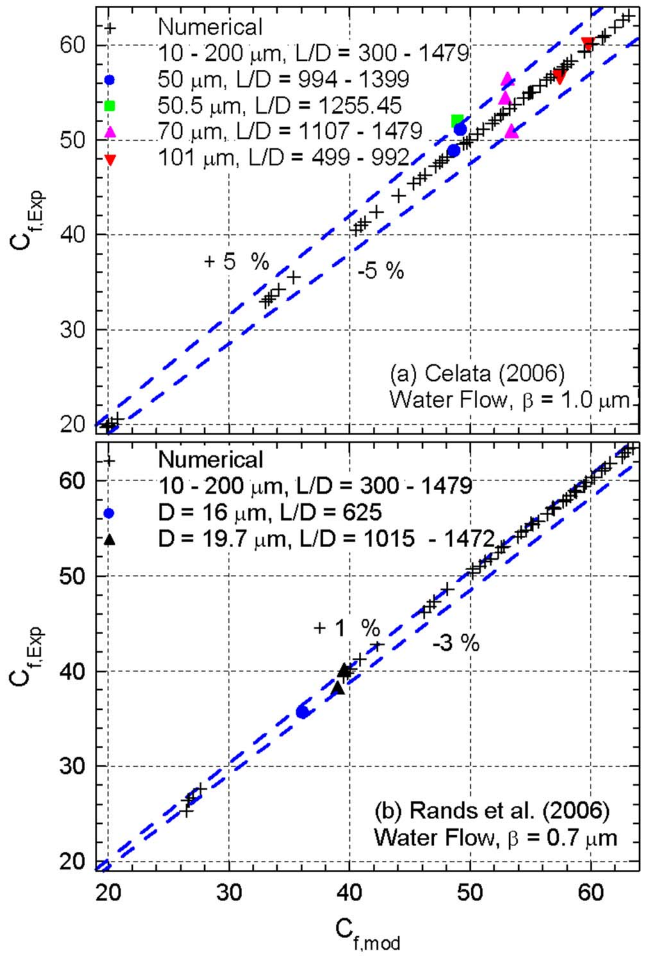

Fig. 13 Effect of accounting for thermal development at inlet of microtubes

$$\frac{\mu_g}{r}\left[\frac{d}{dr}\left(r\frac{d\nu_z}{dr}\right)\right] = \frac{dP}{dz} \tag{14}$$

This equation is subject to the boundary conditions:

$$\nu_{z,g}(R-\delta) = \nu_{z,\ell}, \quad \nu_{z,g}(R) = 0 \tag{15}$$

The solution of Eqs. (1) and (14) gives the following expression for the thickness of the thin gas layer, δ, in terms of the dynamic viscosities of the liquid and the gas and the assumed slip length, β, as

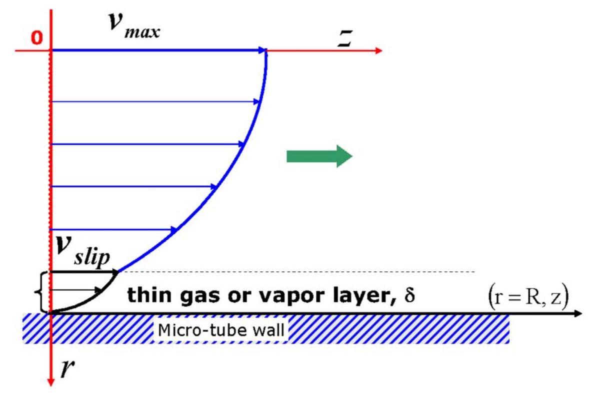

Fig. 14 Velocity profile for laminar flow in a microtube with a slip at the wall

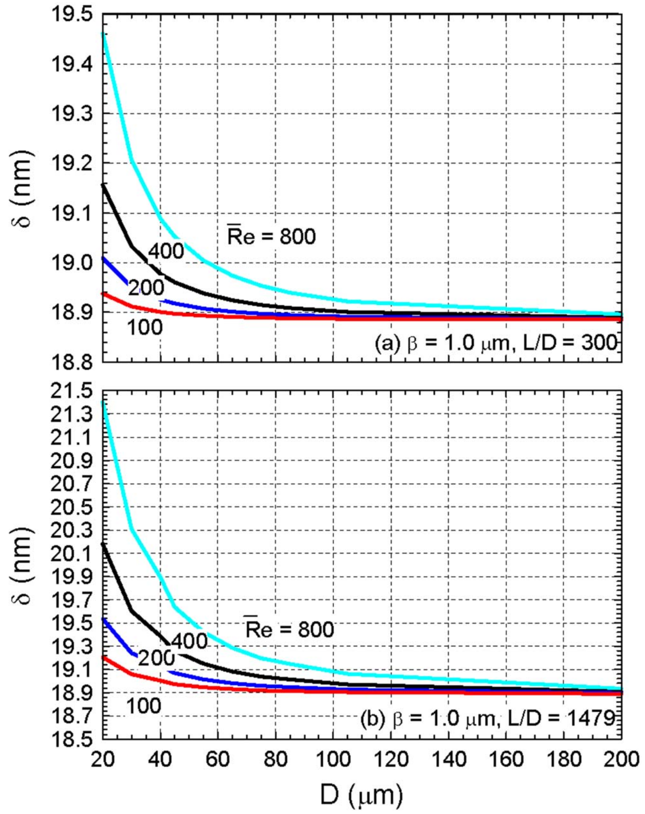

Fig. 15 Thickness of thin gas layer at microtube walls

$$(\delta + 0.5D)^2 = D(\mu_g/\mu_\ell)[0.25(\mu_l/\mu_g)D + \beta] \tag{16}$$

This equation is used to predict the thickness of the thin gas layer that may be separating the water flow from the wall of the microtubes in the experiments [1–3]. In these experiments, the deduced value of the slip length, β, in this paper are 1.0 μm and 0.7 μm, respectively (Figs. 4–8). Figure 15(*a*) presents the estimated thicknesses of the thin gas layer for laminar flows of water as a function of the diameter of the microtubes having $L/D=300$. The results in this figure are for different average Reynolds numbers $\bar{Re}$ and assumed slip length $\beta=1.0$ μm. Figure 15(*b*) presents similar results for microtubes with a larger aspect ratio, $L/D=1479$.

Results show that for the small aspect ratio, $L/D=300$, the thickness of thin gas layer at the wall of the microtubes with $D>100$ μm is estimated at ~18.9 nm and independent of the value of the average Reynolds number. For smaller diameters, the thickness of this layer slightly increases as the microtube diameter decreases and/or Reynolds number increases (Figs. 15(*a*) and 15(*b*)). For the microtubes with the larger aspect ratio, $L/D=1479$, the effect of Reynolds number extends to microtube diameters up to 200 μm (Fig. 15(*b*)). For large diameters, the estimated thickness of the thin gas layer is the same as in Fig. 15(*a*), $\delta=18.9$ nm, and almost independent of Reynolds number.

Figure 15(*b*) shows that an order of magnitude decrease in the microtube diameter to 20 μm increases the thickness of the thin gas layer at the wall by 2.5 nm and 1.3 nm to 20.2 nm and 21.4 nm, when $\bar{Re}=400$ and 800, respectively. For the same microtube diameter but the smaller aspect ratio, $L/D=300$, such increases in the thickness of the thin gas layer at the wall of the microtubes with decreased diameter or increased Reynolds number are <0.6 nm (Fig. 15(*a*)).

Summary and Conclusions

Viscous dissipation heating is important for laminar flows in microtubes and the friction number can be determined from either plotting the measured pressure drop or the rise in the fluid temperature in the microtubes due to the viscous heat dissipation versus the average Reynolds number. A semiempirical analytical expression for determining the friction number in microtubes is developed, which accounts for no-slip and slip at the wall and the effect of the thermal development of the flow at the inlet of microtubes.

The calculated values of the friction number as a function of the microtube diameter D and aspect radio L/D are in excellent agreement with those determined for the experimental data for water flows in glass and diffused silica microtubes ranging in diameter from 16 μm to 101 μm and are 0.02–0.1035 m long. The experimental values of the friction number are also in agreement with those determined from the numerical calculations for laminar water flows in microtubes at the same condition in the experiments. Such an agreement is suggestive of plausible slip in the experiments of water flow in microtubes.

The numerical calculations are performed using COMSOL MULTIPHYSICS 3.2A software at the same conditions in the experiments, namely, hydrodynamically fully developed but thermally developing inlet flow, adiabatic walls, and temperature dependent properties. These calculations investigated the effects of the thermally developing flow at the inlet of the microtubes and plausible slip at the wall on the values of the friction number. Results show that for $D<500$ μm the friction number for water flows in microtubes with a slip is much smaller than that of the classical Hagen–Poiseuille for smooth macrotubes (64), almost exponentially decreasing as the microtube diameter decreases.

The present results are suggestive of a plausible slip at the walls of the microtubes in the water flow experiments due to the highly stressed condition caused by the very high applied pressure that could exceed 120 MPa. The slip lengths of 0.7 μm and 1.0 μm, determined from the experimental data, decrease the friction number. For $L/D>1500$, the effect of the slip at the microtube wall on the friction number diminishes and when $D>400$ μm the value of the friction number approaches that of the classical Hagen–Poiseuille for smooth macrotubes of 64. For lower L/D, the friction number increases because of the thermally developing flow at the inlet of the microtubes exceeding that of the Hagen–Poiseuille for smooth macrotubes. This effect gradually diminishes as the diameter of the microtubes decreases, becoming negligible when $D<10$ μm and L/D approaches ~1500.

The presence of a slip at the microtube and microchannel walls is a subject of ongoing discussion. The results of recent investigations suggest that a nonslip boundary may not be valid in highly confined and stressed flows. Thus, it may be argued that a velocity slip in the water flow experiments investigated is plausible when the driving force overcomes the interfacial resistance, reducing viscous dissipation and the friction number. When this occurs, the presence of a nanometer-size layer between the flowing liquid and the wall is hypothesized.

Results show that the aspect ratio of the microtubes, L/D, slightly affects the thickness of the postulated thin layer at the wall of the microtubes. For the same diameter and Reynolds number, increasing L/D from 300 to 1479 increases the estimated thickness of the layer at the wall of the microtubes by as much as 2.5 nm. For $D>200$ μm, the layer thickness is almost constant and ~18.9 nm. Further investigations, however, are needed to confirm this hypothesis and determine the nature and the molecular composition of the nanometer-size layer.

Experimental results reported by numerous investigators indicate that the slip is a predictable and measurable effects for flow of highly confined liquids. Since liquid flow in microtubes and microchannels is highly confined, then it is appropriate to hypothesize that the same effect could be present. Experiments of liquid flow in microtube with hydrophobic wall have shown reductions in the pressure losses by as much as 20–40%. In this case, the lake of wetting of the wall results in a velocity slip, reducing the pressure losses and the viscous dissipation heating. In the case of a hydrophilic wall, the wetting of the liquid to the wall precludes the slip, except when the liquid is highly stressed. The arguments made in the paper, although based on a careful analysis of the experimental measurement, call for future investigation. The issue of a velocity slip in the highly confined flows in microtubes and microchannels invites future investigations using a combination of molecular dynamics and continuum flow calculations to determine the nature of the slip.

Acknowledgment

This research is supported by the University of New Mexico's Institute for Space and Nuclear Power Studies. The authors are indebted to Dr. G. P. Celata and his colleagues and students at ENEA Institute of Thermal Fluid Dynamics, Rome, Italy, for supplying the extensive listing of their experimental data for water flows in glass and diffused-silica microtubes.

Nomenclature

a = empirical coefficient, Eqs. (11) and (12)
C_p = liquid average heat capacity (J/kg K)
C_f = friction number or Poiseuille number
D = microtube inner diameter (μm)
D_h = hydraulic equivalent diameter (μm)
f = entrance correction factor, Eq. (11)
L = microtube length (m)
P = liquid pressure (Pa)
$\bar{\mathrm{Re}}$ = average Reynolds number $(\rho D\bar{v}_z/\bar{\mu})$
$\bar{\mathrm{Re}}^*$ = modified average Reynolds number, $\bar{\mathrm{Re}}(L/D)^3$
R = inner radius of microtube
r = radial coordinate
T = temperature (K)
v = liquid velocity (m/s)
$\bar{v}$ = liquid average velocity (m/s)
Z = axial coordinate

Greek Symbols

β = slip length at microtube wall (μm)
δ = thickness of gas layer at microtube wall, Eq. (13) (μm)
ΔP = pressure drop across a microtube (Pa)
ΔP^* = dimensionless pressure drop, $\Delta P/(\bar{\mu}^2/(1+8\beta/D)/(2\rho L^2))$
ΔT = liquid temperature rise across microtube (K)
ΔT^* = dimensionless temperature rise across microtube, $\Delta T/(\bar{\mu}^2/(2C_p\rho^2L^2))$
ℓ = characteristic length, Eq. (12) (μm)
$\bar{\mu}$ = liquid average dynamic viscosity (Pa/m)
ρ = liquid average density (kg/m^3)

Subscripts

f = friction
g = gas or air
in = inlet
ℓ = liquid
max = maximum at centerline of microtube
mod = modified
num = numerical
slip = at slip boundary near the microtube wall
tho = theory
z = in axial coordinate

References

[1] Celata, G. P., 2006, personal communications, ENEA Institute of Thermal Fluid Dynamics, Rome, Italy, Oct.
[2] Celata, G. P., Cumo, M., McPhail, S., and Zummo, G., 2006, "Characterization of Fluid Dynamic Behavior and Channel Wall Effects in Microtubes," Int. J. Heat Fluid Flow, **27**, pp. 135–143.
[3] Rands, C., Webb, B. W., and Maynes, D., 2006, "Characterization of Transition to Turbulence in Microchannels," Int. J. Heat Mass Transfer, **49**, pp. 2924–2930.
[4] Shah, R. K., and London, A. L., 1978, *Laminar Flow Forced Convection in Ducts: A Source Book for Compact Heat Exchanger Analytical Data*, Academic, New York.
[5] Xu, B., Ooi, K. T., Wong, N. T., and Choi, W. K., 2000, "Experimental Investigation of Flow Friction for Liquid Flow in Microchannels," Int. Commun. Heat Mass Transfer, **27**(8), pp. 1165–1176.
[6] Kandilkar, S. G., Joshi, S., and Tian, S., 2003, "Effect of Surface Roughness on Heat Transfer and Fluid Fllow Characteristics at Low Reynolds Numbers in Small Diameter Tubes," Heat Transfer Eng., **24**, pp. 4–16.
[7] Lelea, D., Nishio, S., and Takano, K., 2004, "The Experimental Research on Microtube Heat Transfer and Fluid Flow of Distilled Water," Int. J. Heat Mass Transfer, **47**, 2817–2830.
[8] Qu, W., Mala, Gh. M., and Dongqing, L., 2000, "Pressure-Driven Water Flows in Trapezoidal Silicon Microchannels," Int. J. Heat Mass Transfer, **43**, pp. 353–364.
[9] Churchill, S. W., 1977, "Friction-Factor Equation Spans All Fluid-Flow Regimes," Chem. Eng. J., **84**, pp. 91–92.
[10] Judy, J., Maynes, D., and Webb, B. W., 2002, "Characterization of Frictional Pressure Drop for Liquid Flows Through Microchannels," Int. J. Heat Mass Transfer, **45**, pp. 3477–3489.
[11] Baudry, J., Charlaix, E., Tonck, A., and Mazuyer, D., 2001, "Experimental Evidence for a Large Slip Effect at a Nonwetting Fluid-Solid Interface," Langmuir, **17**, pp. 5232–5236.
[12] Andrienko, D., Dunweg, B., and Vinogradova, O. I., 2003, "Boundary Slip as a Result of a Prewetting Transition," J. Chem. Phys., **119**, pp. 13106–13113.
[13] Bonaccurso, E., Butt, H.-J., and Craig, V. S. J., 2003, "Surface Roughness and Hydrodynamic Boundary Slip of a Newtonian Fluid in a Completely Wetting System," Phys. Rev. Lett., **90**(14), pp. 144501.
[14] Neto, C., Evans, D. R., Bonaccurso, E., Butt, H.-J., and Craig, V. S. J., 2005, "Boundary Slip in Newtonian Liquids: A Review of Experimental Studies," Rep. Prog. Phys., **68**, pp. 2859–2897.
[15] Tretheway, D. C., and Meinhart, C. D., 2004, "A Generating Mechanism for Apparent Fluid Slip in Hydrophobic Microchannels," Phys. Fluids, **16**(5), pp. 1509–1515.
[16] Gad-el-Hak, M., 1999, "The Fluid Mechanics of Microdevices—The Freeman Scholar Lecture," ASME J. Fluids Eng., **121**, pp. 5–33.
[17] Cieplak, M., Koplik, J., and Banavar, J. R., 2001, "Boundary Conditions at a Fluid-Solid Interface," Phys. Rev. Lett., **86**(5), pp. 803–806.
[18] Craig, V. S. J., Neto, C., and Williams, D. R. M., 2001, "Shear-Dependent Boundary Slip in an Aqueous Newtonian Liquid," Phys. Rev. Lett., **87**(5), 054504.
[19] Nagayama, G., and Cheng, P., 2004, "Effects of Interface Wettability on Microscale Flow by Molecular Dynamics Simulation," Int. J. Heat Mass Transfer, **47**, pp. 501–513.
[20] Zhu, Y., and Granick, S., 2001, "Rate-Dependent Slip of Newtonian Liquid at Smooth Surfaces," Phys. Rev. Lett., **87**(9), 096105.
[21] Zhu, Y. X., and Granick, S., 2002, "Limits of the Hydrodynamic No-Slip Boundary Condition," Phys. Rev. Lett., **88**(10), 106102.
[22] Maxwell, J. C., 1879, "On Stresses in Rarefied Gases Arising From Inequalities of Temperature," Philos. Trans. R. Soc. London, **170**, 231–256.
[23] Watanabe, K., Udagawa, Y., and Udagawa, H., 1999, "Drag Reduction of Newtonian Fluid in a Circular Pipe With a Highly Water-Repellent Wall," J. Fluid Mech., **381**, pp. 225–238.
[24] Morini, G. L., 2005, "Viscous Heating in Liquid Flows in Micro-Channels," Int. J. Heat Mass Transfer, **48**, pp. 3637–3647.
[25] Jiang, X. N., Zhou, Z. Y., Huang, X. Y., and Liu, C. Y., 1997, "Laminar Flow Through Microchannels Used for Microscale Cooling Systems," *Proceedings IEEE/CPMT Electronic Packaging Technology Conference*, pp. 119–122.
[26] Sharp, K. V., and Adrian, R. J., 2004, "Transition From Laminar to Turbulent Flow in Liquid Filled Microtubes," Exp. Fluids, **36**, pp. 741–747.
[27] Wu, H. Y., and Cheng, P., 2003, "Friction Factors in Smooth Trapezoidal Silicon Microchannels With Different Aspect Ratios," Int. J. Heat Mass Transfer, **46**, pp. 2519–2525.
[28] Weilin, Q., Mala, G. M., and Dongqing, L., 2000, "Pressure-Driven Water Flows in Trapezoidal Silicon Microchannels," Int. J. Heat Mass Transfer, **43**, pp. 353–364.

[29] Pfund, D., Rector, D., Shekarriz, A., Popescu, A., and Welty, J., 2000, “Pressure Drop Measurements in a Microchannel,” AIChE J., **46**(8), pp. 1496–1507.

[30] Park, H., Pak, J. J., Son, S. Y., Lim, G., and Song, I., 2003, “Fabrication of a Microchannel Integrated With Inner Sensors and the Analysis of Its Laminar Flow Characteristics,” Sens. Actuators, A, **103**, pp. 317–329.

[31] Hsieh, S.-S., Lin, C.-Y., Huang, C.-F., and Tsai, H.-H., 2004, “Liquid Flow in a Micro-Channel,” J. Micromech. Microeng., **14**, pp. 436–445.

[32] Hao, P.-F., He, F., and Zhu, K.-Q., 2005, “Flow Characteristics in a Trapezoidal Silicon Microchannel,” J. Micromech. Microeng., **15**, pp. 1362–1368.

[33] Hetsroni, G., Mosyak, A., Pogrebnyak, E., and Yarin, L. P., 2005, “Fluid Flow in Micro-Channels,” Int. J. Heat Mass Transfer, **48**, pp. 1982–1998.

[34] Li, Z.-X., Du, D.-X., and Guo, Z.-Y., 2003, “Experimental Study on Flow Characteristics of Liquid in Circular Microtubes,” Microscale Thermophys. Eng., **7**, pp. 253–265.

Particle Aspect-Ratio Effects on the Thermal Conductivity of Micro- and Nanoparticle Suspensions

Anna S. Cherkasova

Jerry W. Shan
e-mail: jshan@jove.rutgers.edu

Department of Mechanical and Aerospace Engineering,
Rutgers University,
Piscataway, NJ 08854-8054

The influence of particle anisotropy on the effective thermal conductivity of a suspension is experimentally investigated. Suspensions of micron-sized, silicon-carbide particles with varying aspect-ratio distributions were prepared and measured. It is shown that the conductivity of the silicon-carbide suspensions can be quantitatively predicted by the effective medium theory of Nan et al. (1997, "Effective Thermal Conductivity of Particulate Composites With Interfacial Thermal Resistance," J. Appl. Phys. ***81****(10), pp. 6692–6699), provided the volume-weighted aspect ratio of the particles is used. Recent experimental data on multiwalled-nanotube-in-oil suspensions by Yang et al. (2006, "Thermal and Rheological Properties of Carbon Nanotube-in-Oil Dispersions," J. Appl. Phys.,* ***99****(11), 114307) are also analyzed and shown to be in at least qualitative agreement with the effective-medium-theory prediction that the thermal conductivity of suspensions is enhanced by large aspect-ratio particles.* [DOI: 10.1115/1.2928050]

Keywords: thermal conductivity, suspension, aspect ratio, silicon carbide, effective medium theory

Introduction

Heat-transfer fluids can exhibit significant increases in thermal conductivity with the addition of highly conductive particles. Recent attention has focused on micro- and nano- particle suspensions because of their enhanced stability against sedimentation, reduction in potential for clogging a flow system, as well as the tantalizing possibility of unexpected enhancements in thermal conductivity. The latter has been spurred by reports of large increases in the thermal conductivity in very-low-volume-fraction nanoparticle and nanotube suspensions, for example, Cu nanoparticles in ethylene glycol [1], multiwalled carbon nanotubes (MWNTs) in oil [2], and silver nanoparticles in water and toluene [3], among others. In each case, the enhancement in thermal conductivity is reported to be greater than predicted by macroscopic theory for the given volume fraction and particle thermal conductivity. This has stimulated new theoretical and computational analysis [4–7] of the effective thermal conductivity of nanoparticle and nanotube suspensions.

The modeling of the effective conductivity of a composite material dates back to Maxwell [8], who derived the following expression for the conductivity of a two-component mixture with k_p and k_b as conductivities of suspended and suspending phases, respectively:

$$k = k_b\left(1 + \frac{3\varphi(\delta-1)}{2+\delta-\varphi(\delta-1)}\right) \tag{1}$$

In the above expression, φ is the volume fraction of suspended medium, $\delta = k_p/k_b$ is the ratio of conductivities, and it is assumed that (1) the suspended particles are spherical, (2) the particles are noninteracting, and (3) the interfacial resistance between the liquid and solid phases is negligible. There is considerable experimental evidence for the validity of the Maxwell model for thermal conductivities of non-nanoscale particulate suspensions. Despite the fact that the above expression was derived under the assumption of dilute suspensions, it agrees well with experimental data for spherical-particle suspensions with volume fraction less than approximately 10–20% when $\delta \gg 1$ [9]. At higher volume fractions, the particles cannot be considered to be isolated from each other, or they even can form a percolated network [10], causing the initial assumptions of the Maxwell model to fail.

A model for the effective thermal conductivity of a dilute suspension of spheroidal particles with aspect ratio a was developed by Fricke [11]. It can be written in the following form:

$$k = k_b\left(1 + \frac{n\varphi(\delta-1)}{(n-1)+\delta-\varphi(\delta-1)}\right) \tag{2}$$

Here, n is the dimensionless shape factor given by

$$n = \frac{\beta\delta-\beta}{(\delta-1)-\beta} \tag{3}$$

where

$$\beta = \frac{1}{3}(\delta-1)\left[\frac{2}{1+(\delta-1)L_{11}} + \frac{1}{1+(\delta-1)L_{33}}\right] \tag{4}$$

$$L_{11} = \frac{a^2}{2(a^2-1)} - \frac{a}{2(a^2-1)^{3/2}}\cosh^{-1} a \text{ and } L_{33} = 1 - 2L_{11} \tag{5}$$

Equation (2) was later generalized by Nan et al. [12] to include the effect of interfacial resistance in a form of an effective medium theory (EMT). Nan et al. [12] showed that for a dilute suspension of randomly orientated, spheroidal particles with radius r (along the short axis for a prolate spheroid) and interfacial (Kapitza) resistance R, the thermal conductivity is given by

$$k = k_b\left[1 + \frac{\varphi(2\beta_{11}+\beta_{33})}{3-\varphi(2\beta_{11}L_{11}+\beta_{33}L_{33})}\right] \tag{6}$$

where

Contributed by the Heat Transfer Division of ASME for publication in the JOURNAL OF HEAT TRANSFER. Manuscript received October 5, 2007; final manuscript received February 22, 2008; published online June 4, 2008. Review conducted by Yogendra Joshi.

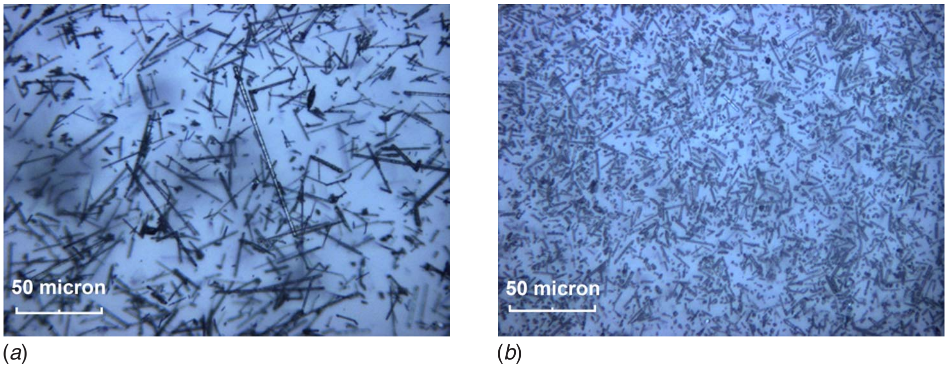
(*a*) (*b*)

Fig. 1 Image of SiC in EG suspension before (*a*) and after (*b*) 28 h of milling

$$\beta_{ii} = \frac{k_{ii} - k_b}{k_b + L_{ii}(k_{ii} - k_b)} \text{ and } k_{ii} = k_p + k_b(1 - L_{ii})(2 + 1/a)\alpha \quad (7)$$

Here, α is a dimensionless measure of the interfacial resistance, defined as

$$\alpha = \frac{Rk_b}{r} \quad (8)$$

with $\alpha=0$ denoting a perfect interface having no temperature jump.

For large-aspect-ratio particles, such as nanotubes, the Fricke/EMT prediction for effective thermal conductivity can greatly exceed that of the Maxwell model [13]. Experimental evidence for such an aspect-ratio effect on the thermal conductivity, particularly in fluid suspensions, is limited, however. Experimental measurements have been made in composite materials consisting of slightly prolate ($a=2$) or oblate ($a=0.5$) diamond particles in ZnS [14]; the measured conductivities were later found to be in good agreement with EMT [12]. For fluid suspensions, Xie et al. [15] measured the thermal conductivity of spherical and cylindrical silicon carbide (SiC) particles dispersed in water and ethylene glycol (EG). Substantially higher thermal conductivity enhancements were found for the cylindrical particles than the spherical ones. This is qualitatively consistent with EMT, but, unfortunately, no precise information was given about aspect ratio of the SiC whiskers. Yang and Han [16] studied the thermal conductivity of bismuth telluride (Bi_2Te_3) nanorods in perfluoronhexane (FC-72) and in hexadecane oil. The nanorods had an average diameter of 20 nm and the average length of 170 nm, giving an aspect ratio of 8.5. Measurements conducted at different temperatures showed higher thermal conductivities than predicted by the Maxwell theory for spherical particles, and were roughly consistent with EMT calculations. A slight enhancement in thermal conductivity above EMT predictions was attributed to the Brownian motion of the nanoparticles. No attempt was made to vary the aspect ratio of the nanorods.

In this paper, we report on a systematic study of the effect of particle aspect ratio on the effective thermal conductivity of particle-in-liquid suspensions. The conductivity of suspensions of micron-sized SiC particles of different shapes was measured and compared with EMT. The aspect ratio of the SiC cylinders was directly varying through milling. We analyze some recent data in the literature on the thermal conductivity of nanotube suspensions in light of the aspect-ratio effect predicted by EMT, and discuss additional factors that may affect the thermal conductivity of suspensions containing nanoscale particles.

Experimental Method

The thermal conductivity of various suspensions was measured using a transient hot-wire apparatus (KD-2 Thermal Properties Analyzer, Decagon Devices, Inc.). The hot wire measures the thermal conductivity and thermal resistivity from the rate of temperature increase of the probe for a constant heating rate. In the KD2, the hot wire is encapsulated in a needle to avoid problems, which can arise while measuring the thermal conductivity of electrically conductive fluids. The KD2 conforms to ASTM D5334 and IEEE 442-1981 standards for determining thermal conductivity, and, in our tests, reproduced literature values for the thermal conductivity of EG, mineral oil, and glycerin with error less than 5%, which is declared accuracy of KD2. All measurements were conducted at a temperature of $T=21.2°\text{C}$, which was maintained constant with the aid of temperature-controlled recirculating bath to avoid effects caused by natural convection. Temperature deviations did not exceed 0.5°C.

In this study, two types of micron-size SiC (Alfa Aesar Corp.) were dispersed in EG: (1) Spherical particles with diameters less than 40 μm and (2) whiskers 1.5 μm in diameter and nominally 18 μm in length. Samples of different solid volume fractions between $\varphi=0.01$ and $\varphi=0.05$ were prepared. We chose small volume fractions to ensure that the suspensions were dilute so that particles were unlikely to interact thermally with one another. The uncertainty in the solid-content volume fraction is estimated to be 0.001. This uncertainty comes from measurement of the volume of the suspending fluid and the mass of the suspended phase. After being mechanically stirred vigorously, all samples were further homogenized with the aid of bath sonicator for 30 min. Measurements performed before and after sonication indicated that the thermal conductivity was not affected by bath sonication. All samples were stable and no sedimentation occurred during the experiments. Each data point was obtained by taking five consecutive measurements, with 5 min intervals in between to allow the sample to reequilibrate with the water bath. We estimate the standard deviation of the mean conductivity to not to exceed 0.015 W/mK.

The actual aspect ratios of the SiC whiskers in suspension were determined from optical micrographs (Fig. 1). Particle-size analysis of 250 randomly chosen SiC whiskers in a diluted EG suspension showed a wide distribution of particle aspect ratios, with average volume-weighted aspect ratio of 9.6, calculated as

$$a_V = \frac{\Sigma_1^{250} a_i V_i}{\Sigma_1^{250} V_i} \quad (9)$$

where V_i is the volume for the particle with aspect ratio a_i of 9.6. The measured aspect-ratio distribution for SiC-EG suspension is shown in Fig. 2. For comparison, the average size of spherical particles was measured to be 32 μm. An optical micrograph of the spherical SiC particles and the measured particle size distribution from such micrographs are presented in Fig. 3.

To vary the aspect ratio of the SiC whiskers, the suspension at volume fraction of $\varphi=0.025$ was further processed in a ball mill. The ball mill, consisting of a rotating horizontal cylinder partially filled with a milling medium (in this case, ceramic balls), reduced

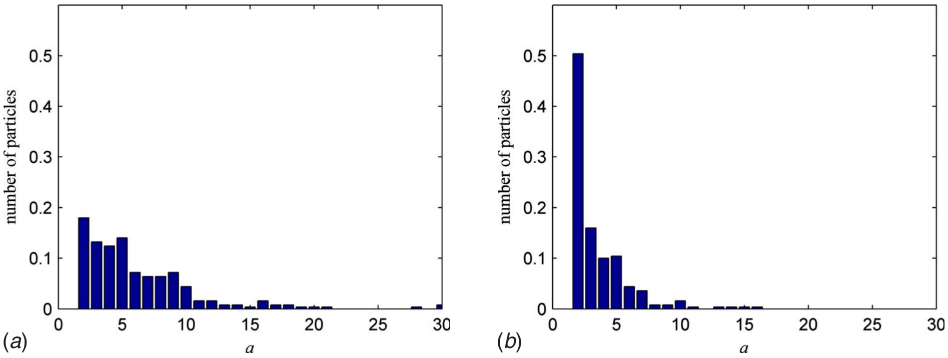

Fig. 2 Aspect-ratio distribution for SiC whiskers in EG before (*a*) and after (*b*) 28 h of milling

the whiskers' aspect ratio by grinding. The SiC whisker suspensions were processed for 4 h, 12 h, and 28 h, and the average volume-weighted aspect ratio of the whiskers was calculated after every step from images taken with an optical microscope (Fig. 1).

Figure 2 shows the distribution functions of whisker aspect ratios for the sample before and after 28 h of milling. It can be clearly seen that, after grinding, the fraction of very short particles is much higher, and the fraction of particles with an aspect ratio more than 10 decreased significantly. The values of the volume-weighted average aspect ratio and the corresponding grinding times are calculated from Eq. (9) and listed in Table 1. The volume-weighted average aspect ratio for the suspension changed gradually from 9.6 before milling to 4.8 after 28 h in the ball mill.

Results and Discussion

The measured thermal conductivities of suspensions of spherical and cylindrical SiC particles dispersed in EG at volume fraction up to $5 \pm 0.1\%$ are presented in Fig. 4. It can be clearly seen that suspensions containing cylindrical particles show significantly higher increase in thermal conductivity than suspensions with dispersed spherical particles. For the particle loading of 5% by volume, a thermal-conductivity enhancement of 85% was observed for suspensions containing dispersed whiskers, while the enhancement was only 15% for spheres. Over this low volume-fraction range, the thermal conductivity increase for both types of particles is nearly linear with volume fraction of solids.

In order to compare the experimental data obtained in this study with the Maxwell model and EMT predictions, the thermal conductivities of the base fluid and particles must be known. We have taken the thermal conductivities of EG and SiC to be $k_b = 0.25$ W/mK and $k_p = 360$ W/mK, respectively. The thermal conductivity of EG was measured directly, and the value used also is consistent with literature values [17]. As for thermal conductivity of SiC, no direct data for nano- and microparticles are available. Bulk SiC is a semiconductor that is considered to have a very high thermal conductivity. However, data reported for the thermal conductivity of SiC vary by almost four orders of magnitude, from 0.12 W/mK up to 490 W/mK at room temperature, with the actual value depending on the synthesis technique, impurity content, and material structure. The thermal conductivity of single crystal SiC has reported to be as high as 490 W/mK [18,19], but phonon scattering by electrically active impurities such as Al or N can significantly reduce thermal conductivity. At room temperature, the impurity concentration of 10^{20} cm^{-3} can decrease k by the factor of 20 [18]. The thermal conductivity of SiC polytypes has been measured to be up to 1100 W/mK for different temperatures. However, SiC thin films, which have an amorphous structure, typically have much lower thermal conductivities than that of the bulk material. Measurements [20] showed values of 1.44–1.49 W/mK for 500-nm-thick films fabricated at 20°C and 500°C, correspondingly. An even lower value of thermal conductivity, 0.12 W/mK was reported for optically thin SiC film [21]. The SiC particles used in the present study have a crystalline structure, hexagonal for the spherical particles and cubic for whiskers. Therefore, the thermal conductivity of a cubic SiC polycrystal at 300°C, $k_p = 360$ W/mK [18,22], is used as the thermal conductivity of the dispersed medium in Eqs. (1), (2), and (6).

Using these values for the thermal conductivities of EG and the SiC particles/whiskers, it is clearly seen in Fig. 4 that the Maxwell model for the thermal conductivity enhancement of spheres is in a good agreement with experimental data. The Maxwell model, Eq. (1), is insensitive to the thermal conductivity of the dispersed phase when the ratio, δ, of thermal conductivities of the dispersed and dispersing materials is greater than of order 100, so any possible error in thermal conductivity of SiC has minimal effect on the calculated conductivity. The EMT, Eq. (2), is much more sensitive with respect to the thermal conductivity of dispersed phase, k_p, but the results presented in Fig. 4 show a good agreement of

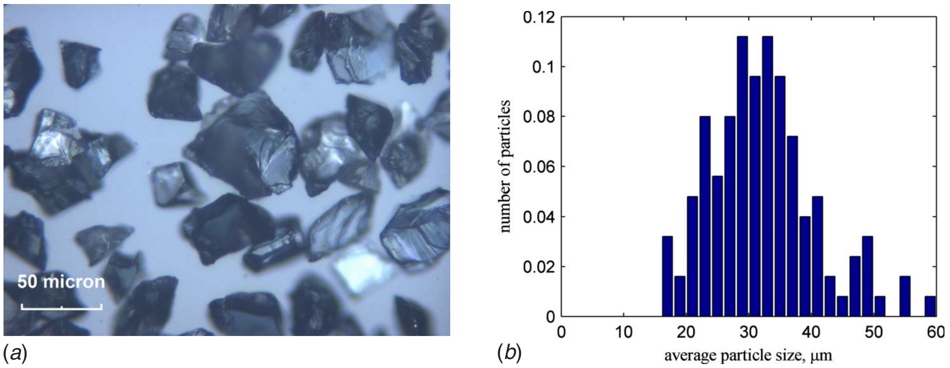

Fig. 3 Optical micrograph (*a*) and size distribution (*b*) for SiC spheres in EG

Table 1 Measured average volume-weighted aspect ratio of whiskers for suspensions containing 2.5% of solids by volume

Milling time, h	Average volume-weighted aspect ratio
0	9.6
4	8.2
12	6.1
28	4.8

SiC-whisker experimental data with the EMT calculations. For comparison, suspension thermal conductivities calculated using $k_p=100\ \mathrm{W/mK}$ and $k_p=500\ \mathrm{W/mK}$ are also plotted in Fig. 4. These limiting cases correspond to the small-grain and perfect, single-crystal SiC [18,23]. It can be seen that the EMT theoretical predictions fit the data well for any reasonable choice of thermal conductivities for the SiC whiskers. As previously discussed, the aspect ratio is taken as a volume-weighted average of $a=9.6$ for calculations.

The experimental data of Xie et al. [15] for suspensions of spherical and cylindrical SiC particles are also shown in Fig. 4 for comparison. For spherical particles, their data and ours match well. For the cylindrical particles, Xie et al. do not provide precise information about the exact particle size and shape. Thus, the differences seen in Fig. 4 between their data on cylindrical particles and ours most probably arise from the use of particles of different aspect ratios. Nonetheless, their measurements also show an increase in thermal conductivity above the Maxwell prediction when anisotropic particles are used. The thermal conductivities reported by Xie et al. can be fitted well by the EMT model if the suspension is assumed to contain SiC whiskers of aspect ratio 3.7, as seen in Fig. 4.

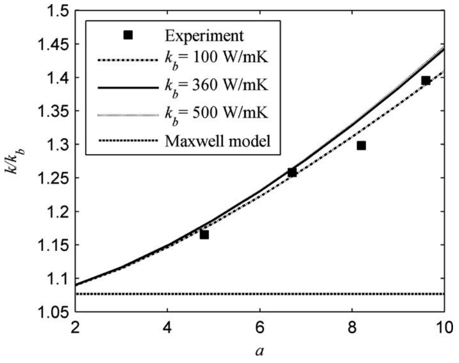

Fig. 5 Measured thermal conductivities of 2.5% volume suspensions of SiC in EG with whiskers of different aspect ratio. For comparison, the Maxwell model, and EMT predictions for different magnitudes of k_p, are shown.

To directly investigate the influence of particle aspect ratio on thermal conductivity, we further investigated the thermal conductivity of a suspension with fixed SiC volume fraction, but varying particle shape. As discussed previously, a sample containing 2.5% of SiC whiskers was processed in a ball milling machine to change the aspect ratio of particles in four steps. The measurements of the thermal conductivity of the suspension containing SiC whiskers of different aspect ratios are presented in Fig. 5. For a fixed volume fraction, the thermal conductivity enhancement goes from 16.5% up to 39.5% as the volume-averaged aspect ratio increases from 4.8 to 9.6. Comparison of the experimental data and the EMT prediction shows excellent agreement. Note that any possible contamination of the suspension by the grinding material itself should only increase the conductivity with grinding time, which is opposite to the observed trend.

As mentioned previously, the measured thermal conductivities in Figs. 4 and 5 were plotted versus the volume-weighted aspect ratio given in Eq. (9). However, it is not a priori obvious whether that is the appropriate aspect ratio to use in calculating the thermal conductivity of a suspension having a distribution of particle

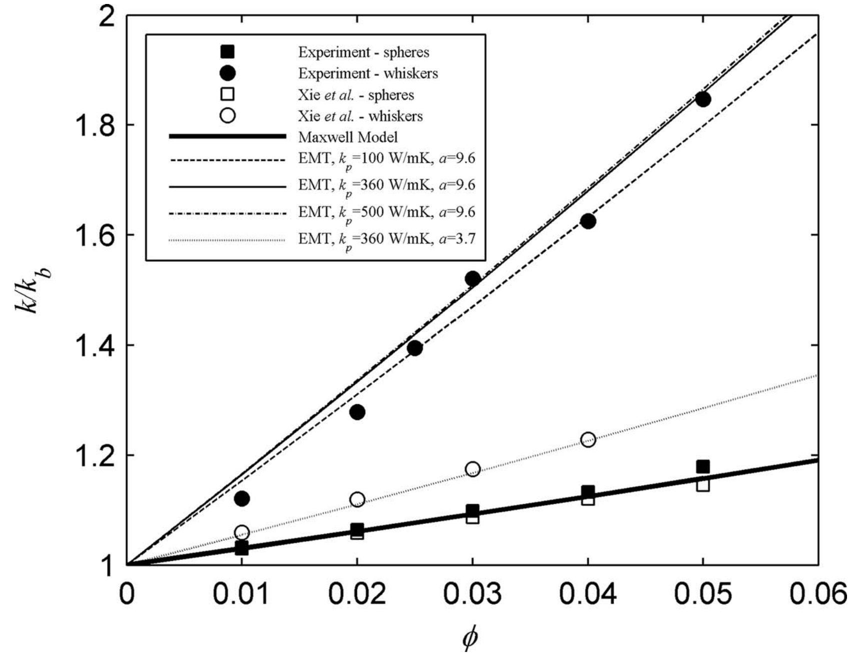

Fig. 4 Relative thermal conductivity enhancement in the suspensions containing SiC spherical particles (solid squares) and whiskers (solid circles) compared to the data calculated with the aid of Maxwell (dashed line) and EMT (solid line). Data by Xie et al. for spheres and cylinders are shown with hollow squares and circles correspondingly. EMT prediction for $a=3.7$ is shown with dotted line for comparison with the data on cylinders of Xie et al.

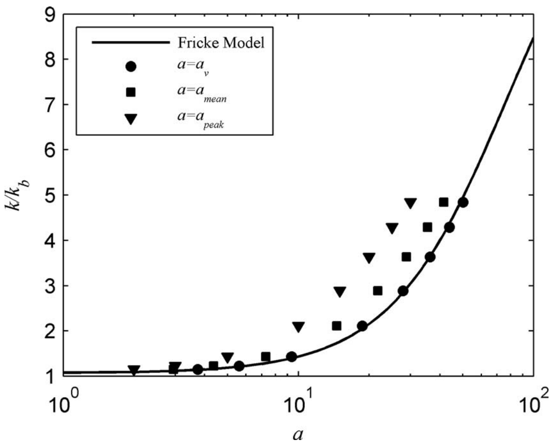

Fig. 6 Thermal conductivity of a 2.5% SiC-in-oil suspension with log-normal aspect ratio distribution (σ=0.5)

shapes. The particles' morphology could be characterized not only by the volume-weighted average aspect ratio but also by its peak (most probable), median, or mean value. To show that the volume-weighted aspect ratio is the correct measure to use, we can consider a suspension consisting of N particles of different aspect ratios. Following Fricke's approach, we obtain a modified formula for the parameter β:

$$\beta=\frac{1}{3}(\delta-1)\sum_{1}^{N}\frac{V_i}{\Sigma V_i}\left[\frac{2}{1+(\delta-1)L_{11}^{i}}+\frac{1}{1+(\delta-1)L_{33}^{i}}\right] \quad (10)$$

where the functions L_{11}^i and L_{33}^i are given by Eq. (5) for every particle. The outer summation in Eq. (10) can be replaced by an integral if an aspect-ratio distribution is given. Sample calculations for suspension of SiC whiskers in EG with a volume fraction of 0.025 are shown in Figs. 6 and 7. The particles were assumed to have a log-normal aspect-ratio distribution with logarithm standard deviations of either 0.5 or 2. Thermal conductivities calculated taking into account the entire aspect-ratio distribution (using Eq. (10)) are compared to those calculated using the peak (a_{peak}), mean (a_{mean}), and volume-weighted (a_V) aspect ratios. It can be seen that the conductivity calculated using the volume-weighted aspect ratio is most consistent with the full calculation. This result can be attributed to the fact that the thermal-conductivity contribution of the particles having a particular aspect ratio should depend on the total volume of such particles rather than on their number. Also, it should be noted that the distribution width affects the calculated thermal conductivity of the suspension; when σ increases, the thermal conductivity increases because the fraction of long particles, which contribute more to total thermal conductivity enhancement, is higher even though the peak (most likely) aspect ratio can stay the same. For a monodisperse suspension (delta-function distribution of particle aspect ratios), all three characteristic aspect ratios are the same and the thermal conductivity calculated using the distribution coincides with that predicted by Eq. (2). We note that, though these calculations were made for Fricke model, which assumes no interfacial resistance on the surface of the particle, the same approach can be applied to the more general model of Nan et al.

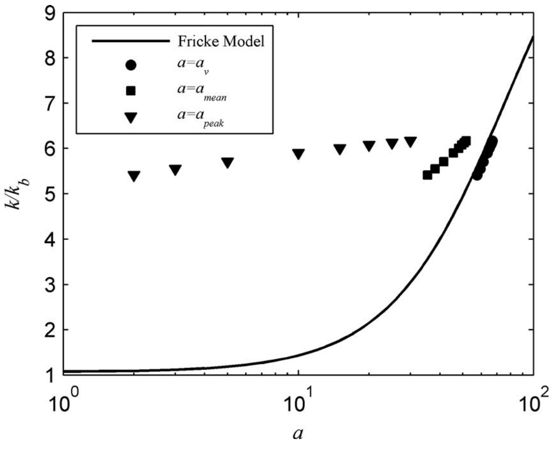

Fig. 7 Thermal conductivity of a 2.5% SiC-in-oil suspension with log-normal aspect ratio distribution (σ=2.0)

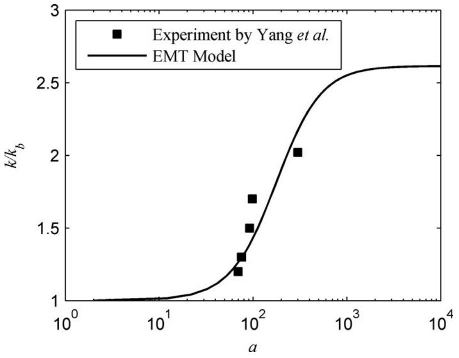

Fig. 8 Thermal conductivities of MWNTs in PAO with different aspect ratio of nanotubes. The solid squares indicate the measurements of Yang et al., while the solid line shows the EMT model.

Some recent data on the thermal conductivity of CNT suspensions can also be interpreted in light of the aspect-ratio dependence of thermal conductivity predicted by EMT. The axial thermal conductivity of single wall carbon nanotubes (SWNTs) is believed to be comparable with that of graphene (in-plane) and diamond, with predicted values in the range of 3000–6600 W/mK [24,25]. As noted by Nan et al., this conductivity, together with the very high aspect ratios of SWNTs, would cause EMT to predict thermal conductivity enhancements an order of magnitude greater than the highest increases that have been experimentally reported to date [13]. For individual MWNTs, a thermal conductivity of 300 W/mK has been reported [26]. We use this value to interpret the recent data by Yang et al. [27] that shows a dependence of thermal conductivity on the sonication time of a MWNT suspension. Yang et al. find that the thermal conductivity of MWNT/poly(α-olefin)-oil (PAO) suspensions at a volume fraction of $\varphi=0.0021$ decreases with sonication time. They also noted that the aspect ratio of the MWNTs was decreased by the intense ultrasonication that they used. Figure 8, which shows the measured thermal conductivities of Yang et al. plotted against the nanotubes' volume-weighted aspect ratio, obtained using their reported aspect-ratio distributions, shows that there is a very good qualitative agreement between the EMT and the experimental data. Although tempting to conclude that there is a quantitative agreement between the EMT and the data, it should be noted that, in the experiments of Yang et al., the reduction in aspect ratio with increasing sonication time was concomitant with a decrease in the size of large-scale nanotube agglomerates. Thus, it is not possible to separate the effect of decreasing particle aspect ratio from particle aggregation and other factors that may also affect the thermal conductivity. Nonetheless, the changes that Yang et al. observe in the thermal conductivity of the MWNT suspension are at least qualitatively consistent with the reduction in thermal conductivity brought about by decreasing aspect ratio that is predicted by EMT.

The lower limit of the thermal conductivity of a suspension is given by Eq. (1), which is that for spherical particles. However, there is an effective upper limit on the thermal conductivity enhancement with aspect ratio as well. Beyond an aspect ratio of about 100–500, depending on the solid/fluid thermal conductivities ratios, the further increase of particle aspect ratio does not significantly enhance the thermal conductivity. This is seen as a plateau for $a > 10^3$ in the EMT model line shown in Fig. 8.

We note that additional scale-dependent effects can enter into the thermal conductivity of nanoparticle and nanotube suspensions. Among these is the interfacial resistance between the solid-liquid interface, which becomes increasingly important due to the larger number of interfaces for a given volume fraction as the particle-size decreases. Within the framework of EMT, the importance of interfacial resistance is parametrized by the dimensionless variable α introduced in Eq. (8). For most liquid-solid interfaces, the Kapitza resistance is typically of order $10^{-8}\ \mathrm{m^2\,K/W}$ [28,29]. For SWNTs in water, Huxtable et al. [30] measured a thermal resistance of $R = 8.3 \times 10^{-8}\ \mathrm{m^2\,K/W}$, a value which is consistent with the $R = 4.52 \times 10^{-8} - 1.5 \times 10^{-7}\ \mathrm{m^2\,K/W}$ calculated by molecular dynamics simulations for SWNTs in liquid [31]. For the SiC spheres and whiskers used in the present experiments, interfacial resistance is negligible as it is estimated to be $\alpha = 2 \times 10^{-3}$ and $\alpha = 1 \times 10^{-2}$, respectively, in EG. For the MWNTs in PAO studied by Yang et al., interfacial resistance is not negligible, as $\alpha = 1$ assuming a diameter of 25 nm for the nanotubes made by catalytic decomposition of a ferrocene-xylene mixture [32]. Therefore, all calculations for MWNTs in oil suspension were made taking into account the interfacial resistance (Eq. (6)).

Other mechanisms have been hypothesized to influence the thermal conductivity of nanoparticle/nanotube suspensions: (1) interparticle clustering [4,33], (2) Brownian motion [34,35], and (3) ballistic phonon transport [36]. Of these, the most relevant for the MWNTs in PAO studied by Yang et al. is interparticle clustering, since the nanotubes were observed to form aggregates in suspension. As described by Prasher et al. [4], particles in suspension can cluster to form chains, which conduct heat along their backbone, thus significantly enhance the thermal conductivity of nanofluids. This is analogous to an aspect-ratio effect, since the particle chains can be viewed as large-aspect ratio particles. If the effective conductivity and volume fraction of the particle chains are known, then the conductivity of the suspension can be modeled using EMT of Nan et al., as done by Prasher et al.

Conclusions

In summary, we have experimentally validated the EMT prediction that the effective thermal conductivity of suspensions is enhanced by large aspect-ratio particles. For micron-sized SiC particles, where interfacial resistance is negligible, good quantitative agreement is seen between the measured thermal conductivities and EMT for volume fractions up to 0.05 (dilute suspensions) and volume-weighted aspect ratios ranging from 1 to 10. For recently reported data on MWNTs in PAO, the measured thermal conductivities at least qualitatively consistent with the aspect-ratio effect predicted by EMT; however, possible nanotube clustering in the suspension precludes us from drawing conclusions regarding quantitative agreement in this case. Nevertheless, the present data on SiC microparticles, together with the analysis of the data of Xie et al. and Yang et al. on nanoparticle and nanotube suspensions doubtlessly reveal the impact of filler shape on the effective thermal conductivity of particulate suspensions.

Acknowledgment

We thank A. E. Petersson for suggesting that we grind the SiC suspensions with a ball mill and Y. W. Lu for allowing us to use his microscope. This work was supported by the National Science Foundation through Grant No. CBET 0644719.

Nomenclature

φ = particle volume fraction
k = suspension thermal conductivity
k_p = suspended-medium thermal conductivity
k_b = base-fluid thermal conductivity
a = particle aspect ratio
a_V = volume-weighted-average aspect ratio
a_{peak} = most-probable aspect ratio
a_{mean} = mean aspect ratio
r = particle radius
V = particle volume
R = Kapitza resistance
σ = standard deviation of logarithm of particle-aspect-ratio distribution

References

[1] Eastman, J. A., Choi, S. U. S., Li, S., Yu, W., and Thompson, L. J., 2001, “Anomalously Increased Effective Thermal Conductivities of Ethylene Glycol-Based Nanofluids Containing Copper Nanoparticles,” Appl. Phys. Lett., **78**(6), pp. 718–720.
[2] Choi, S. U. S., Zhang, Z. G., Yu, W., and Grulke, E. A., 2001, “Anomalous Thermal Conductivity Enhancement in Nanotube Suspensions,” Appl. Phys. Lett., **79**(14), pp. 2252–2254.
[3] Patel, H. E., Das, S. K., Sundararajan, T., Sreekumaran, Nair A., George, B., and Pradeep, T., 2003, “Thermal Conductivities of Naked and Monolayer Protected Metal Nanoparticle Based Nanofluids: Manifestation of Anomalous Enhancement and Chemical Effects,” Appl. Phys. Lett., **83**(14), pp. 2931–2933.
[4] Prasher, R., Phelan, P. E., and Bhattacharya, P., 2006, “Effect of Aggregation Kinetics on the Thermal Conductivity of Nanoscale Colloidal Solutions (Nanofluid),” Nano Lett., **6**(7), pp. 1529–1534.
[5] Xue, Q. Z., 2006, “Model for the Effective Thermal Conductivity of Carbon Nanotube Composites,” Nanotechnology, **17**(6), pp. 1655–1660.
[6] Nan, C.-W., Liu, G., Lin, Y., and Li, M., 2004, “Interface Effect on Thermal Conductivity of Carbon Nanotube Composites,” Appl. Phys. Lett., **85**(16), pp. 3549–3551.
[7] Zhou, X. F., and Gao, L., 2006, “Effective Thermal Conductivity in Nanofluids of Nonspherical Particles With Interfacial Thermal Resistance: Differential Effective Medium Theory,” J. Appl. Phys., **100**(2), 024913.
[8] Maxwell, J. C., 1954, *A Treatise on Electricity and Magnetism*, Dover, New York.
[9] Heine, M. C., Vicente, J., and Klingenberg, D. J., 2006, “Thermal Transport in Sheared Electro- and Magnetorheological Fluids,” Phys. Fluids, **18**(2), 023301.
[10] Schueler, R., Petermann, J., Schulte, K., and Wentzel, H. P., 1998, “Agglomeration and Electrical Percolation Behavior of Carbon Black Dispersed in Epoxy Resin,” J. Appl. Polym. Sci., **63**(13), pp. 1741–1746.
[11] Fricke, H., 1924, “Mathematical Treatment of the Electric Conductivity and Capacity of the Dispersed Systems,” Phys. Rev., **24**(5), pp. 575–587.
[12] Nan, C.-W., Birringer, R., Clarke, D. R., and Gleiter, H., 1997, “Effective Thermal Conductivity of Particulate Composites With Interfacial Thermal Resistance,” J. Appl. Phys., **81**(10), pp. 6692–6699.
[13] Nan, C.-W., Shi, Z., and Lin, Y., 2003, “A Simple Model for Thermal Conductivity of Carbon Nanotube-Based Composites,” Chem. Phys. Lett., **375**(5–6), pp. 666–669.
[14] Every, A. G., Tzou, Y., Hasselman, D. P. H., and Raj, R., 1992, “The Effect of Particle Size on the Thermal Conductivity of ZnS/Diamond Composites,” Acta Metall. Mater., **40**(1), pp. 123–129.
[15] Xie, H., Wang, J., Xi, T., Liu, Y., and Ai, F., 2002, “Thermal Conductivity of Suspension Containing SiC Particles,” J. Mater. Sci. Lett., **21**(3), pp. 193–195.
[16] Yang, B., and Han, Z. H., 2006, “Temperature-Dependent Thermal Conductivity of Nanorod-Based Nanofluids,” Appl. Phys. Lett., **89**(8), 083111.
[17] 2005, *The CRC Handbook of Mechanical Engineering*, F. Kreith and D. Y. Goswami, eds., CRC, New York.
[18] Slack, G. A., 1964, “Thermal Conductivity of Pure and Impure Silicon, Silicon Carbide and Diamond,” J. Appl. Phys., **35**(12), pp. 3460–3466.
[19] Morelli, D., Heremans, J., Beetz, C., Woo, W. S., Harris, G., and Taylor, C., 1993, “Carrier Concentration Dependence of the Thermal Conductivity of Silicon Carbide,” *Proceedings of the Fifth Silicon Carbide and Related Materials Conference*, Washington, DC, Nov. 1–3, pp. 313–315.
[20] Choi, S. R., Kim, D., Choa, S.-H., Lee, S.-H., and Kim, H.-K., 2006, “Thermal Conductivity of AlN and SiC Thin Films,” Int. J. Thermophys., **27**(3), pp. 896–905.
[21] Henager, C. H., Jr., and Pawlewicz, W. T., 1993, “Thermal Conductivities of Thin, Sputtered Optical Films,” Appl. Opt., **32**(1), pp. 91–101.
[22] Goldberg, Y., Levinshtein, M., and Rumyantsev, S., 2001, “Silicon Carbide,” *Properties of Advanced Semiconductor Materials: GaN, AlN, InN, BN, SiC, SiGe*, M. E. Levinshtein, S. L. Rumyantsev, and M. S. Shur, eds., Wiley, New York, pp. 93–147.
[23] Snead, L. L., Nozawa, T., Katoh, Y., Byun, T.-S., Kondo, S., and Petti, D. A., 2007, “Handbook of SiC Properties for Fuel Performance Modeling,” J. Nucl. Mater., **371**(1–3), pp. 329–377.
[24] Berber, S., Kwon, Y.-K., and Tománek, D., 2000, “Unusually High Thermal Conductivity of Carbon Nanotubes,” Phys. Rev. Lett., **84**(20), pp. 4613–4616.
[25] Che, J., Cagın, T., and Goddard, W. A. III, 2000, “Thermal Conductivity of

Carbon Nanotubes," Nanotechnology, **11**(2), pp. 65–69.

[26] Choi, T.-Y., Poulikakos, D., Tharian, J., and Sennhauser, U., 2006, "Measurement of the Thermal Conductivity of Individual Carbon Nanotubes by the Four-Point Three-ω Method," Nano Lett., **6**(8), pp. 1589–1593.

[27] Yang, Y., Grulke, E. A., Zhang, Z. G., and Wu, G., 2006, "Thermal and Rheological Properties of Carbon Nanotube-in-Oil Dispersions," J. Appl. Phys., **99**(11), 114307.

[28] Ju, Y. S., 2005, "Impact of Nonequilibrium Between Electrons and Phonons on Heat Transfer in Metallic Nanoparticles Suspended in Dielectric Media," ASME J. Heat Transfer, **127**(12), pp. 1400–1402.

[29] Wilson, M. W., Hu, X., Cahill, D. G., and Braun, P. V., 2002, "Colloidal Metal Particles as Probes of Nanoscale Thermal Transport in Fluids," Phys. Rev. B, **66**(22), 224301.

[30] Huxtable, S. T., Cahill, D. G., Shenogin, S., Xue, L., Ozisik, R., Barone, P., Usrey, M., Strano, M. S., Siddons, G., Shim, M., and Keblinski, P., 2003, "Interfacial Heat Flow in Carbon Nanotube Suspensions," Nat. Mater., **2**(11), pp. 731–734.

[31] Shenogin, S., Xue, L., Ozisik, R., Keblinski, P., and Cahill, D. G., 2003, "Role of Thermal Boundary Resistance on the Heat Flow in Carbon-Nanotube Composites," J. Appl. Phys., **95**(12), pp. 8136–8144.

[32] Andrews, R., Jacques, D., Rao, A. M., Derbyshire, F., Qian, D., Fan, X., Dickey, E. C., and Chen, J., 1999, "Continuous Production of Aligned Carbon Nanotubes: A Step Closer to Commercial Realization," Chem. Phys. Lett., **303**(5), pp. 467–474.

[33] Prasher, R., Evans, W., Meakin, P., Fish, J., Phelan, P., and Keblinski, P., 2006, "Effect of Aggregation on Thermal Conduction in Colloidal Nanofluids," Appl. Phys. Lett., **89**(14), 143119.

[34] Prasher, R., Bhattacharya, P., and Phelan, P. E., 2005, "Thermal Conductivity of Nanoscale Colloidal Solutions (Nanofluids)," Phys. Rev. Lett., **94**(2), 025901.

[35] Krishnamurthy, S., Bhattacharya, P., Phelan, P. E., and Prasher, S. P., 2006, "Enhanced Mass Transport in Nanofluids," Nano Lett., **6**(3), pp. 419–423.

[36] Keblinski, P., Phillpot, S. R., Choi, S. U. S., and Eastman, J. A., 2002, "Mechanism of Heat Flow in Suspensions of Nano-Sized Particles (Nanofluids)," Int. J. Heat Mass Transfer, **45**(4), pp. 855–863.

Hybrid Full-Spectrum Correlated *k*-Distribution Method for Radiative Transfer in Nonhomogeneous Gas Mixtures

Gopalendu Pal

Michael F. Modest[1]
Fellow ASME
e-mail: mfmodest@psu.edu

Liangyu Wang

Department of Mechanical and Nuclear Engineering,
The Pennsylvania State University,
University Park, PA 16802

The full-spectrum k-distribution (FSK) approach is a promising model for radiative transfer calculations in participating media. FSK achieves line-by-line (LBL) accuracy for homogeneous media at a tiny fraction of LBL's high computational cost. However, inhomogeneities in gas temperature, total pressure, and component-gas mole fractions change the spectral distribution of the absorption coefficient and can cause inaccuracies in the FSK approach. In this paper, a new hybrid FSK method is proposed that combines the advantages of the multigroup FSK (MGFSK) method for temperature inhomogeneities in a single gas species and the multiscale FSK (MSFSCK) method for concentration inhomogeneities in gas mixtures. In this new hybrid method, the absorption coefficients of each gas species in the mixture are divided into M spectral groups depending on their temperature dependence. Accurate MGFSK databases are constructed for combustion gases, such as CO_2 and H_2O. This paper includes a detailed mathematical development of the new method, method of database construction, and sample heat transfer calculations for 1D inhomogeneous gas mixtures with step changes in temperature and species mole fractions. Performance and accuracy are compared to LBL and plain FSK calculations. The new method achieves high accuracy in radiative heat transfer calculations in participating media containing extreme inhomogeneities in both temperature and mole fractions using as few as $M=2$ spectral groups for each gas species, accompanied by several orders of magnitude lower computational expense as compared to LBL solutions. [DOI: 10.1115/1.2909612]

Keywords: thermal radiation, k-distribution method, inhomogeneous gas mixture, multiscale approach, global method

Introduction

Radiative transfer calculations in participating media can be most accurately evaluated by the line-by-line (LBL) approach, but, due to irregular gas phase absorption coefficients that rapidly vary across the spectrum, the radiative transfer equation (RTE) must be solved for up to 1×10^6 wavenumbers. Hence, the LBL approach is extremely time consuming and requires large computer resources. On the other hand, the absorption coefficient can be reordered into a monotonically increasing function, such that only a small number of quadrature point evaluations of the RTE is required [1,2], greatly reducing the computational cost. Several models have been proposed to apply the concept of reordering the absorption coefficient to the entire spectrum and these include the spectral-line-based weighted-sum-of-gray-gases (SLW) model [3,4], the absorption distribution function (ADF) method [5,6], and the recent full-spectrum *k*-distribution (FSK) method [7]. Whereas SLW and ADF methods are approximate schemes, in which the absorption coefficient is reduced to a few discrete values, the FSK method is an exact method for a correlated absorption coefficient using a continuous *k*-distribution over the entire spectrum. The FSK method achieves LBL accuracy for homogeneous media at a tiny fraction of LBL's computational cost. Since its introduction, the FSK method has undergone several major developments [7–10] and has become one of the most popular spectral models for radiative transfer calculations.

Although the FSK scheme is an exact method for radiative calculations in homogeneous media, its application in strongly inhomogeneous emitting-absorbing media challenges its accuracy. Inhomogeneities in total pressure, temperature, and component mole fraction (partial pressure) alter the local spectral behavior of the absorption coefficient, which is critical in the FSK reordering process. The effect of strong variations in total pressure along with negligible variation in temperature produces only a small change in the *k*-distribution as evidenced in meteorological applications [1,11,12]. On the other hand, varying temperature and gas concentrations have substantial effects on the accuracy of *k*-distribution and FSK methods [7,11,13–15].

In order to address the inhomogeneity problem, several strategies with different levels of sophistication and accuracy have been proposed in the literature. All the commonly used strategies include either the assumption of a correlated absorption coefficient or the scaling assumption. Details of these two approaches can be obtained from Modest [8]. The application of both the correlated and scaled approaches to the FSK method leads to the full-spectrum correlated *k*-distribution (FSCK) and scaled *k*-distribution (FSSK) methods, respectively. To alleviate the inaccuracies in inhomogeneous media, two different approaches have been proposed, namely, the fictitious gas (FG) [6] or multiscale [9] approach and the multigroup (MG) approach [10,16]. The concept behind these two approaches is to break up the gas absorption coefficients into pieces that are as correlated or scaled as possible. In the FG approach, the individual spectral lines comprising the absorption coefficient are placed into separate scales based on

---

[1] Corresponding author.

Contributed by the Heat Transfer Division of ASME for publication in the Journal of Heat Transfer. Manuscript received May 29, 2007; final manuscript received October 16, 2007; published online June 3, 2008. Review conducted by Walter W. Yuen.

their temperature dependence. In the MG approach, spectral positions, i.e., wavenumbers, are placed into several groups according to their dependence on temperature and partial pressure. Both approaches achieve increased correlation in the absorption coefficient within each FG or spectral groups and improve the accuracy of radiative calculations in inhomogeneous media. The multigroup FSK (MGFSK) method has been shown to achieve great accuracy for a single gas species with inhomogeneity in temperature [9,10,16], whereas the multiscale FSK (MSFSK) method can efficiently treat mixtures of absorbing gases with severe species inhomogeneity [17]. However, challenges still remain for radiative calculations in a gas mixture containing both temperature and species concentration inhomogeneities.

FSK calculations are very accurate and time efficient provided the required FSKs are known, which are tedious to compile from spectroscopic databases, such as HITRAN [18], HITEMP [19], and CDSD-1000 [20]. Several very approximate correlations have been generated by Denison and Webb [3,4] and Modest et al. [7,9,10,16]. However, to make accurate FSK calculations feasible for general engineering purposes, preassembled FSK must be available in the form of accurate and compact databases. Full-spectrum MG databases have been constructed by Zhang and Modest for carbon dioxide and water vapor from the HITEMP spectroscopic database [10,16]. The spectral positions of each gas were placed into 32 exclusive spectral groups depending on their temperature and partial pressure dependence. The absorption coefficients at the 32 group level satisfy the scaling approximation. The spectral groups from the databases are scalable, i.e., for better numerical efficiency, the spectral groups can be combined to obtain coarser numbers of groups. It has been reported that close-to-LBL accuracy can be achieved by considering only four such groups, within which the assumption of a correlated absorption coefficient holds.

In the current paper, a new hybrid multiscale multigroup FSK (MSMGFSK) method is proposed, which is capable of accurately handling radiative transfer in a gas mixture containing both temperature and partial pressure inhomogeneities with/without gray wall emission. The medium may also contain gray particles. However, mixtures containing nongray particles are beyond the scope of the present paper, because mixing of species for such case cannot be accurately performed at the full-spectrum level. This requires a narrow-band database and will be addressed in a follow up paper. The present MSMGFSK method resolves the absorption coefficient of an individual species in a mixture as one of its scales. Within each scale, the wavenumbers are placed into exclusive spectral groups according to their temperature dependence. Mixing of species is addressed by introducing an overlap parameter to approximate the effect of overlap among scales. In the MG databases created by Zhang and Modest [10,16], the absorption coefficients were obtained from the HITEMP spectroscopic database. Unfortunately, it has been observed that the HITEMP database is not accurate for CO_2 at temperatures higher than 1000 K [20,21]. Thus, also a new and better correlated database is constructed with spectral absorption coefficients for water vapor calculated from HITEMP 2000 and for carbon dioxide from CDSD-1000, which is considered more reliable. Since it had been found that radiative calculations using four groups can achieve close-to-LBL accuracy with faster computational times [10,22], MG databases are constructed with only four such groups. Sample calculations are performed for gas mixtures with temperature and partial pressure inhomogeneities. For all cases, results are compared to FSCK and LBL calculations.

Hybrid MSMGFSCK Approach

Although the multiscale multigroup full-spectrum correlated *k*-distribution (MSMGFSCK) method can be easily extended to include gray absorbing and scattering particles, for brevity, a medium consisting of a mixture of molecular gases is considered and the RTE for this medium can be written as [23]

$$\frac{dI_\eta}{ds} = \kappa_\eta(\underline{\phi})(I_{b\eta} - I_\eta) \tag{1}$$

subject to the boundary condition

$$\text{at } s = 0: \quad I_\eta = I_{w\eta} \tag{2}$$

Here, I_η is the spectral radiative intensity, κ_η is the absorption coefficient, $I_{b\eta}$ is the spectral blackbody intensity (or Planck function), and wavenumber η is the spectral variable. The term $\underline{\phi}$ is a vector of state variables that affect κ_η, which include temperature T, total pressure P, and gas mole fractions $\underline{x}$: $\underline{\phi}=(T,P,\underline{x})$. The boundary intensity $I_{w\eta}$ may be due to emission and/or reflection from the enclosure wall [24].

The total absorption coefficient κ_η is first separated into contributions from N component gases, e.g., CO_2 and H_2O, and then the spectral locations of the nth gas absorption coefficient are sorted into M exclusive spectral groups, i.e.,

$$\kappa_\eta = \sum_{n=1}^{N}\sum_{m=1}^{M_n}\kappa_{nm\eta}, \quad I_\eta = \sum_{n=1}^{N}\sum_{m=1}^{M_n} I_{nm\eta} \tag{3}$$

and the radiative intensity I_η is accordingly broken up. Note that the spectral locations constituting the mth group may not be consecutive. The RTE is then transformed into $\Sigma_{n=1}^{N} M_n$ component RTEs, one for each group of each gas or scale:

$$\frac{dI_{nm\eta}}{ds} = \kappa_{nm\eta}(\underline{\phi})I_{b\eta} - \kappa_\eta(\underline{\phi})I_{nm\eta}$$
$$\text{for } n = 1, \ldots, N, \quad m = 1, \ldots, M_n \tag{4}$$

It is observed, physically, that the intensity $I_{nm\eta}$ is due to emission from the mth group of the nth gas specie (the nmth group) but subject to absorption by all groups of other gases plus its own group. There is no overlap among groups of a single species and, therefore, there is no emission over wavenumbers where $\kappa_{nq\eta}(q \neq m)$ absorbs. Thus, in Eq. (4),

$$\kappa_\eta = \kappa_{nm\eta} + \sum_{l\neq n}^{N}\sum_{q=1}^{M_l}\kappa_{lq\eta} \tag{5}$$

We now apply the FSK scheme [23] to the RTE of each group: First, Eq. (4) is multiplied by Dirac's delta function $\delta(k_{nm}\text{-}\kappa_{nm\eta}(\underline{\phi}_0))$, followed by division with

$$f_{nm}(T_0,\underline{\phi}_0,k_{nm}) = \frac{1}{I_{b\eta}(T_0)}\int_0^\infty I_{b\eta}(T_0)\,\delta(k_{nm} - \kappa_{nm\eta}(\underline{\phi}_0))\,d\eta \tag{6}$$

where $\underline{\phi}_0$ and T_0 refer to a reference state. The resulting equation is then integrated over the entire spectrum, leading to

$$\frac{dI_{nmg}}{ds} = k_{nm}a_{nm}I_b - \lambda_{nm}I_{nmg} \quad \text{for } n = 1, \ldots, N, \quad m = 1, \ldots, M_n \tag{7}$$

where

$$I_{nmg} = \frac{\int_0^\infty I_{nm\eta}\delta(k_{nm} - \kappa_{nm\eta}(\underline{\phi}_0))d\eta}{f_{nm}(T_0,\underline{\phi}_0,k_{nm})} \tag{8}$$

$$g_{nm} = \int_0^{k_{nm}} f_{nm}(T_0,\underline{\phi}_0,k)dk \tag{9}$$

$$a_{nm} = \frac{f_{nm}(T,\underline{\phi}_0,k_{nm})}{f_{nm}(T_0,\underline{\phi}_0,k_{nm})} \tag{10}$$

$$\lambda_{nm}I_{nmg}=k_{nm}I_{nmg}+\frac{\int_0^\infty(\Sigma_{l\neq n}\Sigma_{q=1}^{M_l}\kappa_{lq\eta}(\underline{\phi}))I_{nm\eta}\delta(k_{nm}-\kappa_{nm\eta}(\underline{\phi}_0))d\eta}{f_{nm}(T_0,\underline{\phi}_0,k_{nm})} \tag{11}$$

Here, the absorption coefficient within each group has been assumed to be correlated. This implies that $k_{nm}=k_{nm}(T_0,\underline{\phi},g_{nm})$ is evaluated from the k-distribution of the local absorption coefficient of the nmth group weighted by the Planck function at the reference temperature [23]. The second term in Eq. (7) is due to the overlap of the absorption coefficient of the nmth group, $\kappa_{nm\eta}$, with groups of all other gases, and this overlap only occurs over part of the spectrum. Physically, the overlap coefficient λ_{nm} is a reordered absorption coefficient of the nmth group taking into account the overlap with groups of all other gases. Based on the MSFSK approach, the λ_{nm} can be approximately determined since the overlap effects between groups are relatively small. There are many ways of approximating λ_{nm}. Here, the approach used in the original MSFSK development is followed, that is, the overlap coefficient λ_{nm} is determined in such a way that the emitted intensity emanating from a homogeneous layer bounded by cold black walls is predicted exactly [9].

In Eq. (7), the reordering is performed in terms of $\kappa_{nm\eta}$ and the overlap coefficient between $\kappa_{nm\eta}$ and κ_η during the reordering process is lumped into λ_{nm}. In order to determine λ_{nm}, the reordering can also be performed in terms of κ_η, which, for a homogeneous layer at temperature T, leads to

$$\frac{dI^*_{nmg}}{ds}=\frac{k^*_{nm}I_b}{f(T,\underline{\phi},k)}-kI^*_{nmg}\quad \text{for } n=1,\ldots,N,\quad m=1,\ldots,M_n \tag{12}$$

where

$$f(T,\underline{\phi},k)=\frac{1}{I_b(T)}\int_0^\infty I_{b\eta}(T)\,\delta(k-\kappa_\eta(\underline{\phi}))d\eta \tag{13}$$

$$I^*_{nmg}=\frac{\int_0^\infty I_{nm\eta}\delta(k-\kappa_\eta(\underline{\phi}))d\eta}{f(T,\underline{\phi},k)} \tag{14}$$

$$k^*_{nm}=\frac{1}{I_b(T)}\int_0^\infty I_{b\eta}(T)\kappa_{nm\eta}\delta(k-\kappa_\eta(\underline{\phi}))d\eta \tag{15}$$

In Eq. (12), the interaction between $\kappa_{nm\eta}$ and κ_η is lumped into k^*_{nm}. The solutions to Eqs. (7) and (12) for a homogeneous layer at temperature T bounded by cold black walls can be analytically obtained, and the total exiting intensities at $s=L$, obtained from Eqs. (7) and (12), respectively, are

$$I_{nm}=\int_0^1 I_{nmg}dg=\int_0^\infty\frac{k_{nm}}{\lambda_{nm}}I_b[1-\exp(-\lambda_{nm}L)]f_{nm}(T,\underline{\phi},k_{nm})dk_{nm} \tag{16}$$

and

$$I^*_{nm}=\int_0^1 I^*_{nmg}dg=\int_0^\infty\frac{k^*_{nm}}{k}I_b[1-\exp(-kL)]dk \tag{17}$$

The spectrally integrated intensity, I_{nm}, must be equal to I^*_{nm}, and this requirement leads to

$$\lambda_{nm}=k\quad\text{and}\quad k_{nm}f_{nm}(T,\underline{\phi},k_{nm})dk_{nm}=k^*_{nm}(k)dk \tag{18}$$

or

$$k^*_{nm}(\lambda_{nm})d\lambda_{nm}=k_{nm}f_{nm}(T,\underline{\phi},k_{nm})dk_{nm} \tag{19}$$

Equation (19) provides the relationship between λ_{nm} and k_{nm} that is required to solve Eq. (7). One convenient way of determining λ_{nm} is by using the relationship [9]

$$\int_0^{k_{nm}}k'_{nm}f_{nm}(T,\underline{\phi},k'_{nm})dk'_{nm}=\int_0^{k'=\lambda_{nm}}k^*_{nm}(k')dk' \tag{20}$$

In wavenumber space, this can also be expressed as

$$\int_{\eta|\kappa_{nm\eta}\leq k_{nm}}\kappa_{nm\eta}I_{b\eta}(T)d\eta=\int_{\eta|\kappa_\eta\leq\lambda_{nm}}\kappa_{nm\eta}I_{b\eta}(T)d\eta \tag{21}$$

Equation (20) is an implicit relation for the $\lambda_{nm}-k_{nm}$ relationship. In practice, the left- and right-hand sides of Eq. (20) are evaluated for a set of predetermined k_{nm} and λ_{nm} values and the results are stored in two arrays. The corresponding λ_{nm} values for the k_{nm} values used in the RTE evaluations are determined by interpolation from the two arrays. The so-determined λ_{nm} will be a function of the state variables (i.e., temperature and gas species concentration) as well as k_{nm} (or g_{nm}).

Evaluation of Overlap Coefficient λ_{nm}

The left-hand side (LHS) of Eq. (20) can be readily evaluated since

$$\text{LHS}=\int_0^{g_{nm}(k_{nm})}k'_{nm}dg'_{nm} \tag{22}$$

and the k_{nm}–g_{nm} distribution of the nmth group can be obtained from the MG databases. The right-hand side (RHS) of Eq. (20) contains the k^*_{nm} term, which may be directly calculated from Eq. (15) using high resolution spectroscopic databases, if the spectral locations of each spectral group are known. This direct calculation, however, is extremely tedious and impractical for the solution of general problems. It is desirable to evaluate the RHS of Eq. (15) using databased MG k–g-distributions for faster and efficient computation. The MG database construction for combustion gases CO_2 and H_2O is discussed in detail in the following section.

In order to do so, the quantity Q_{nm} is considered for the nmth group:

$$Q_{nm}=\frac{1}{I_b}\int_0^\infty I_{b\eta}\kappa_{nm\eta}\exp(-\kappa_\eta L)d\eta \tag{23}$$

Physically, Q_{nm} is related to the emission from the nmth group, attenuated over path L by the groups of all other gases and itself. Q_{nm} can be rewritten as

$$\begin{aligned}Q_{nm}&=\frac{1}{I_b}\int_0^\infty I_{b\eta}\kappa_{nm\eta}\int_0^\infty\exp(-kL)\,\delta(k-\kappa_\eta)dkd\eta\\&=\int_0^\infty k^*_{nm}\exp(-kL)dk=\mathcal{L}(k^*_{nm})\end{aligned} \tag{24}$$

i.e., Q_{nm} is the Laplace transform of k^*_{nm}. Q_{nm} can also be written as

$$\begin{aligned}Q_{nm}&=\frac{1}{I_b}\int_0^\infty I_{b\eta}\kappa_{nm\eta}\exp(-\kappa_{nm\eta}L)\prod_{l\neq n}^{N}\exp(-\kappa_{l\eta}L)d\eta\\&\approx\frac{1}{I_b}\int_0^\infty I_{b\eta}\kappa_{nm\eta}\exp(-\kappa_{nm\eta}L)d\eta\\&\quad\times\prod_{l\neq n}^{N}\left(\frac{1}{I_b}\int_0^\infty I_{b\eta}\exp(-\kappa_{l\eta}L)d\eta\right)\end{aligned} \tag{25}$$

where $\kappa_{l\eta}$ is the total (all groups) absorption coefficient of the lth gas species. The second step follows by recognizing that the integration in the first step is a Planck function weighted averaging operator, together with the assumption that the absorption coefficients of the nmth group and all the other gases are statistically uncorrelated with each other. Since the mixing in Eq. (25) is at the full-spectrum level, it is expected to be somewhat less accurate than on a narrow-band level [25]. However, the uncorrelated assumption should be reasonable here since the nmth group not only comes from a different gas but also from scattered parts of the spectrum.

The k-distribution method can then be applied to Eq. (25), which is written as

$$\begin{aligned} Q_{nm} &\approx \int_0^1 k_{nm}\exp(-k_{nm}L)dg_{nm}\prod_{l\neq n}^{N}\left(\int_0^1 \exp(-k_l L)dg_l\right) \\ &= \int_{g_{nm}=0}^{1}\left(\int\cdots\int_{\substack{g_l=0\\ l\neq n}}^{1} k_{nm}(g_{nm}) \right. \\ &\qquad \left. \times\exp\left(-\sum_{l\neq n}k_l L - k_{nm}L\right)\prod_{l\neq n}^{N}dg_l\right)dg_{nm} \end{aligned} \tag{26}$$

Here, $k_l(g_l)$ is the k–g-distribution of the entire lth gas, obtained by combining all groups into one [10],

$$g_l(T,\underline{\phi},k) = \sum_{q=1}^{M} g_{lq}(T,\underline{\phi},k) - M + 1 \tag{27}$$

evaluated at any given k (same for all groups).

Equating Eqs. (26) and (24) leads to

$$\begin{aligned} \mathcal{L}(k^*_{nm}) &= \int_{g_{nm}=0}^{1}\left(\int\cdots\int_{\substack{g_l=0\\ l\neq n}}^{1} k_{nm} \right. \\ &\qquad \left. \times\exp\left(-\sum_{l\neq n}k_l L - k_{nm}L\right)\prod_{l\neq n}^{N}dg_l\right)dg_{nm} \end{aligned} \tag{28}$$

and the integral property of the Laplace transform gives

$$\begin{aligned} &\mathcal{L}\left(\int_0^{k=\lambda_{nm}} k^*_{nm}(k)dk\right) \\ &= \int_{g_{nm}=0}^{1}\left(\int\cdots\int_{\substack{g_l=0\\ l\neq n}}^{1} k_{nm}\times\frac{\exp(-\Sigma_{l\neq n}k_l L - k_{nm}L)}{L}\prod_{l\neq n}^{N}dg_l\right)dg_{nm} \end{aligned} \tag{29}$$

Finally, taking the inverse of the Laplace transformation results in

$$\begin{aligned} \text{RHS} &= \int_o^{k=\lambda_{nm}} k^*_{nm}(k)dk \\ &\approx \int_{g_{nm}=0}^{1}\left(\int\cdots\int_{\substack{g_l=0\\ l\neq n}}^{1} k_{nm}H\left(k-\sum_{l\neq n}k_l - k_{nm}\right)\prod_{l\neq n}^{N}dg_l\right)dg_{nm} \end{aligned} \tag{30}$$

where H is the Heaviside step function.

Table 1 Precalculated gas states and reference temperatures

Parameter	Sampling	Number of samples
Species	CO_2 and H_2O	2
Total pressure	0.1–0.5 bar every 0.1 bar; 0.7 bar; 1.0–14.0 bar every 1.0 bar; 15.0–30.0 bar every 5.0 bar	24
Local gas temperature	300–2500 K every 100 K	23
Mole fraction	0.0–1.0 every 0.25	5
Planck function temperature	300–2500 K every 100 K	23

By equating the LHS and RHS, a generic expression is obtained for the determination of the overlap coefficient λ_{nm} based on group k-distributions constructed from the MG databases, i.e.,

$$\begin{aligned} &\int_0^{g_{nm}(k_{nm})} k'_{nm}dg'_{nm} \\ &= \int_{g_{nm}=0}^{1}\left(\int\cdots\int_{\substack{g_l=0\\ l\neq n}}^{1} k_{nm}H\left(\lambda_{nm}-\sum_{l\neq n}k_l - k_{nm}\right)\prod_{l\neq n}^{N}dg_l\right)dg_{nm} \end{aligned} \tag{31}$$

The number of multiple integrals on the RHS of Eq. (31) is N, the number of component gases in the mixture.

Multigroup Database Construction

As stated earlier, accurate and compact databases of MGFSKs are constructed as a part of this work. The spectral absorption coefficients for water vapor are calculated from HITEMP 2000 and for carbon dioxide CDSD-1000 is used, which is considered more reliable than HITEMP for temperatures higher than 1000 K [20,21], as assembled by Wang and Modest [26]. The resulting MG k–g-distributions of the combustion gases are stored for various values of total pressure, local gas temperature, species mole fraction, and Planck function temperature and are summarized in Table 1.

Grouping of Wavenumbers. The wavenumbers of each gas species in 0.01 cm^{-1} intervals are grouped according to the temperature dependence of their absorption coefficients. Some typical results are shown in Figs. 1 and 2. Figure 1 corresponds to a few chosen spectral locations across the 4.3 μm band of CO_2 in a mixture with 10% CO_2 and 90% N_2, while Fig. 2 corresponds to a few chosen spectral locations across the 2.7 μm band of H_2O in a H_2O–N_2 mixture with 10% H_2O. It is observed that there are distinct behaviors of absorption coefficients with temperature, which are consistent for all spectral locations and gas species. This temperature dependence is classified into four categories and

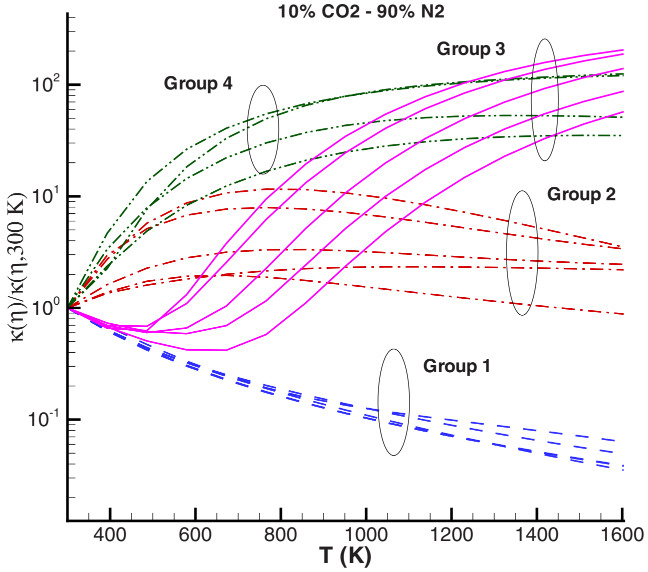

Fig. 1 Grouping of several spectral locations across 4.3 μm band of CO_2 in a CO_2–air mixture containing 10% CO_2

used for initial grouping of the spectral locations.

Step 1. As seen from Figs. 1 and 2, lines with decreasing κ_η with temperature at all temperatures are collected into Group 1, those which have increasing κ_η at low temperature but then decrease later on are placed into Group 2, lines that first decrease but later on wake up are placed into Group 3, and finally the lines that wake up at low temperature and continue to rise are collected into Group 4.

Step 2. After this initial grouping, each group is assigned an average k-profile, which is expressed as

$$k_{ij} = \frac{\sum_\eta [\kappa_\eta(T)/\kappa_\eta(T_{\rm ref})]\kappa_\eta(T_{\rm ref}) I_{b\eta}(T_{\rm ref})}{\sum_\eta \kappa_\eta(T_{\rm ref}) I_{b\eta}(T_{\rm ref})} = \frac{\sum_\eta \kappa_\eta(T) I_{b\eta}(T_{\rm ref})}{\sum_\eta \kappa_\eta(T_{\rm ref}) I_{b\eta}(T_{\rm ref})} \tag{32}$$

where i is the counter-indicating group and j is the temperature. Unlike the database constructed by Zhang and Modest [10,16], a weighted average of $\kappa_\eta(T)/\kappa_\eta(T_{\rm ref})$ is employed, using spectral emission $\kappa_\eta(T_{\rm ref})I_{b\eta}(T_{\rm ref})$ as the weight factor. In typical combustion applications, the maximum temperature is expected to vary between 500 K and approximately 1600 K, and for such temperature range, a value of $T_{\rm ref}$=850 K was found to give the best grouping results.

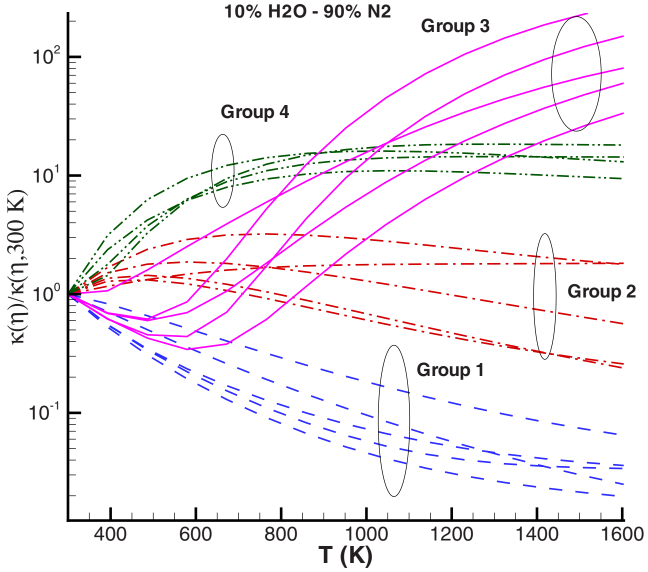

Fig. 2 Grouping of several spectral locations across 2.7 μm band of H_2O in a H_2O–air mixture containing 10% H_2O

The following are the steps used to optimize the grouping of wavenumbers:

Step 3. The group tag for each wavenumber is determined by minimizing the normalized departure of its relative temperature dependence from the average k-profile of the groups:

$$\sum_j \frac{(k_{ij} - C_{\eta i}\kappa_{\eta j})^2}{[\max(0.1\kappa_{\eta,\max}, k_{ij})]^2} = \varepsilon_{\eta i} \tag{33}$$

where

$$C_{\eta i} = \frac{\sum_j k_{ij}\kappa_{\eta j}}{\sum_j \kappa_{\eta j}^2} \tag{34}$$

In Eq. (33), the departure of the absorption coefficients from the average k-shape of the group is normalized in such a way that very low values of the absorption coefficient are given less importance. The numerator of Eq. (33) is the absolute departure of the absorption coefficient from the average k-shape, whereas the denominator normalizes that departure with respect to the average k-shape of the group. $C_{\eta i}$ is a constant optimized for each wavenumber, since the departure from the average k-shape is to be minimized, not departure from k itself. After calculating the total departure (ε_η) from the average k-shape, the spectral locations are assigned to that group for which the value of ε_η is minimum.

Step 4. After regrouping, the average k-profile of each group is updated based on Planck function weighted absorption coefficients:

$$k_{ij} = \frac{\sum_\eta w_{\eta j}\kappa_{\eta j} C_{\eta i}}{\sum_\eta w_{\eta j}} \quad \text{where } w_{\eta j} = \kappa_\eta(T_{\rm ref}) I_{b\eta}(T_{\rm ref}) \tag{35}$$

and the process is repeated until less than 1% of the total number of wavenumbers change groups.

Once all spectral locations are grouped, the full-spectrum $k-g$ distributions are calculated for each group and each gas species for the parameters presented in Table 1. When calculating FSKs for each group of a gas species, a set of nominal k-values between the group maximum and minimum k-values must be chosen at the local gas state. Here, a power law distribution of k-values is considered [26] and a total number of k-bins of N_k=2000. Details on the calculations of (MG) FSKs, and the weight function a from the absorption coefficients can be obtained from Zhang and Modest [7,10]. After calculating the initial k-distributions with 2000 k-bins, data compaction is performed using Gaussian quadrature schemes with a fixed-g concept as outlined by Wang and Modest [26]. The final database contains 128 k-distribution data points for each group. To eliminate the detrimental effect of noise in the stretch function a on quadrature efficiency, natural B-splines are used to smoothen the k–g-distributions by a small amount, resulting in better-behaved a-functions. Figure 3 shows the original and smoothened k–g-distributions and stretching functions a for Group 2 of a H_2O-N_2 mixture with 10% H_2O at 1500 K local gas temperature and 1000 K as the reference temperature. It is observed that a very small change (nearly indiscernible smoothening) in the k-distributions can result in a much smoother a-function.

The MG full-spectrum database is used to obtain the k–g-distributions for each group of each gas species. To obtain the k-distribution for an arbitrary state, interpolation is needed between precalculated states stored in the database. For a single gas species, the k-distribution is specified by total pressure (P), local gas temperature (T), mole fraction (x), and a Planck function temperature (T_0). Hence, for full-spectrum cases, four-dimensional

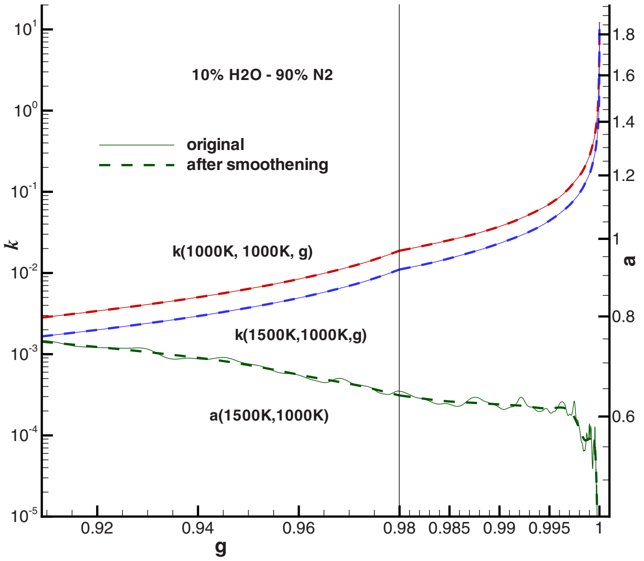

Fig. 3 Original and smoothed weight function *a* and cumulative *k*-distributions of Group 2 for 10% H_2O in H_2O–air mixture

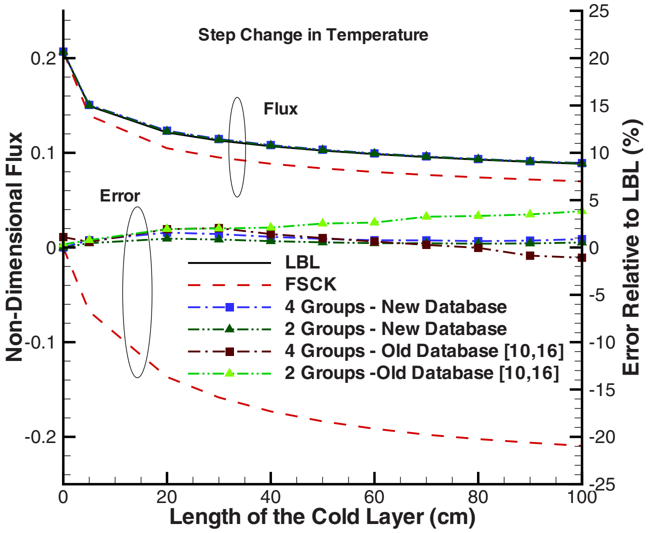

Fig. 4 Nondimensional heat flux leaving an inhomogeneous slab of 10% CO_2 and 20% H_2O at a total pressure of 1 bar with a step change in temperature: The hot left layer is at 1500 K and the cold right layer is at 300 K

interpolations in (P,T,T_0,x) are required. In order to achieve acceptable accuracy with small computational cost, a hybrid scheme is employed for database interpolation: 1D spline interpolation is used for P and trilinear interpolation for $T-T_0-\boldsymbol{x}$ as proposed by Wang and Modest [26]. The MG database containing four groups for each gas species has a total size of 500 Mbytes. For a given state, MG $k-g$-distributions can be obtained from the database in 20 ms on a Pentium Zeon 2.4 GHz computer.

The newly constructed MG database is scalable, i.e., for faster computation, the groups can be combined to obtain coarser groups. The k-g-distributions of the combined group can be calculated [10] from Eq. (27) as

$$1 - g_n(k) = \sum_m (1 - g_m(k)) \tag{36}$$

where g_n and g_m are the cumulative k-distributions for the same k-values of the combined groups and original groups, respectively. Details of group combination can also be obtained from Zhang and Modest [10]. When groups are combined to obtain a two-group $k-g$-distribution from four groups, the first two groups are combined into one group and the last two into second group, since the average characteristics of Groups 1 and 2 are similar (both of them contain lines with decreasing κ_η with increase in temperature at higher temperature). Groups 3 and 4 also have similarity in the sense that they contain lines with increasing κ_η at higher temperature.

Sample Calculations

To illustrate the performance of the newly created MG database in conjunction with the new hybrid MSMGFSCK method in handling inhomogeneous gas mixtures, a few sample calculations with extreme temperature and mole-fraction (partial pressure) inhomogeneities are performed. In all cases, a one-dimensional medium containing $CO_2-H_2O-N_2$ gas mixtures confined between cold black walls is considered. The mixture consists of two different homogeneous layers (denoted as left and right layers/columns) adjacent to each other. Two cases of total pressure, i.e., 1 bar and 10 bar, are considered. The left layer is at 1500 K and has a fixed width of 50 cm. The right layer is cold and at 300 K. The width of the cold layer is varied in the calculations. The radiative heat transfer leaving from the right layer is calculated using the LBL method, the single-scale FSCK method, and the hybrid MSMGFSCK method. For consistency, all three methods employ absorption coefficients obtained from CDSD-1000 and HITEMP for CO_2 and H_2O, respectively. In the MSMGFSCK calculations, the required $k-g$-distributions are obtained by interpolating the database, while in the single-scale FSCK calculations, the required $k-g$-distributions are directly calculated from the absorption coefficients without mixing k-distribution of species, i.e., the absorption coefficients are calculated for the mixture before the k-distributions are formed. For all k-distribution calculations, ten quadrature points (g-values) were employed. It was found that using more than ten quadrature points resulted in negligible improvement. Therefore, a total number of 10 (g-values)×2 (species)×2 or 4 (groups)=40 or 80 RTE evaluations was required for each case.

The LBL calculations serve as benchmark and the FSCK calculations serve to demonstrate the improvement made by the hybrid MSMGFSCK method.

Figure 4 compares the nondimensional radiative heat fluxes for the case of 1 bar total pressure and a step change in temperature only as calculated by several methods. The mole fractions of the component gases are kept uniform throughout the two-layer slab. The percentage errors of the MSMGFSCK and the single-scale FSCK calculations compared to LBL results are also shown in the figure. In order to compare accuracy of the new database with respect to the previous one, results are obtained from both the previous MG database created by Zhang and Modest [10,16] and the newly created MG database in this paper. For a temperature inhomogeneity of this magnitude (a drop from 1500 K to 300 K), the FSCK method gives more than 20% error as the cold layer length becomes larger than 80 cm, indicating the failure of the correlated absorption coefficient assumption. The errors of the MSMGFSCK method while using the new MG database, on the other hand, stay below 1.6% for any cold layer thickness. The number of the groups indicated in the figure is the number of groups into which each gas scale is separated. As can be seen from Fig. 4, the accuracy of the hybrid MSMGFSCK method is excellent, with the accuracy of the two-group case actually being better than for the four-group case, which apparently is due to the presence of compensating errors between grouping of absorption coefficients and mixing between two different absorbing gases. It has been shown by Modest and Riazzi [25] that for an isothermal layer of a gas mixture, the error incurred during heat transfer calculations is about 2% when the $k-g$-distributions are mixed at the full-spectrum level. Hence, a MG database of combustion

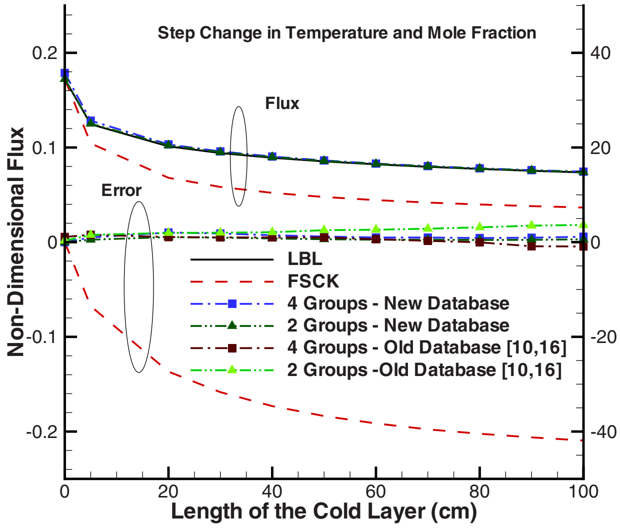

Fig. 5 Nondimensional heat flux leaving an inhomogeneous slab at a total pressure of 1 bar with step changes in temperature and mole fraction: The hot left layer contains 20% CO_2 and 10% H_2O at 1500 K and the cold right layer contains 10% CO_2 and 20% H_2O

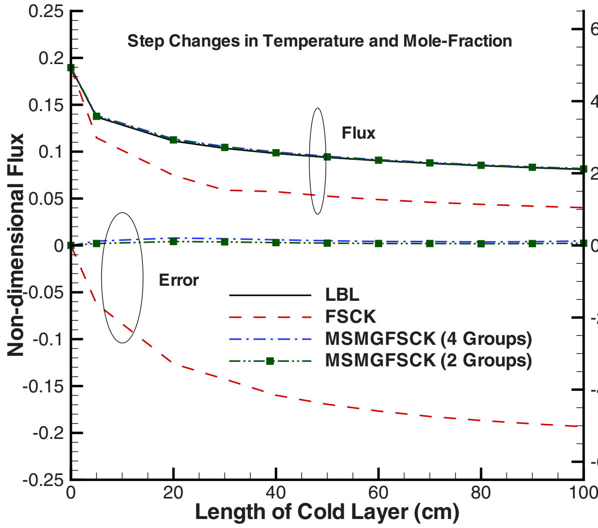

Fig. 6 Nondimensional heat flux leaving an inhomogeneous slab at a total pressure of 10 bar with step changes in temperature and mole fraction: The hot left layer contains 20% CO_2 and 10% H_2O at 1500 K and the cold right layer contains 10% CO_2 and 20% H_2O

gases with four or even two groups is sufficient to optimize between accuracy and numerical efficiency. Comparison with the data of Wang and Modest [22], in which the database created by Zhang and Modest [10,16] was used, verifies that the new MG database is superior, especially for the two-group case.

Figure 5 shows the results for a case including mole-fraction step changes in both CO_2 and H_2O in addition to a temperature step change as in Fig. 4. The left hot layer contains 20% CO_2 and 10% H_2O, and this composition is switched in the right cold layer. The total pressure of the gas mixture is 1 bar. The error of the FSCK method reaches more than 40% for this extremely inhomogeneous problem. On the other hand, the four- and two-group hybrid models provide excellent results with the maximum error remaining below 2%. Results from the new database are considerably more accurate than those of Wang and Modest [22] for the four-group case, and even more significantly for the two-group case.

Radiative calculations were also performed for a case of higher total gas pressure. Figure 6 shows the results for a case similar to the one in Fig. 5 except that the total gas pressure is raised to 10 bar. Again, it is observed that the MSMGFSCK formulation in conjunction with the new MG database predicts heat transfer calculations very accurately. The errors for the four- and two-group models remain limited to within 2%, whereas the FSCK methods produce more than 50% error. Hence, the results suggest that this new hybrid MSMGFSCK model together with the MG databases can efficiently perform over a wide range of gas states.

Conclusion

In this paper, a new FSK method was developed for radiative transfer in strongly inhomogeneous gas media. The method combines the advantages of the MSFSK method in handling the mixing problem and partial pressure inhomogeneities and those of the MSFSK method in handling temperature inhomogeneities. In this method, the absorption coefficient of the mixture is broken up into contributions from the gas components, and the absorption coefficient of each component gas is subsequently separated into exclusive correlated groups. The overlap between a group and all other gases is approximately treated. As the number of groups in each gas scale increases, the effect in the approximate treatment of the overlap becomes diminished. A new MSFSK database of improved accuracy has also been constructed for the most important combustion gases, carbon dioxide and water vapor. To optimize between computational efficiency and accuracy in radiative heat transfer calculations, this MG database contains four groups for each gas species. The accuracy of the new method was established by performing sample calculations for radiative transfer in strongly inhomogeneous media using the newly constructed database. It was found that the new method successfully handles extreme inhomogeneous problems with only two or four groups for each gas component.

Acknowledgment

This research has been supported by National Science Foundation under Grant No. CTS-0121573.

Nomenclature

a = nongray stretching factor for FSK method
f = k-distribution function, cm
g = cumulative k-distribution
H = Heaviside step function
I = radiative intensity, W/m^2 sr
k = absorption coefficient variable, cm^{-1}
k^* = overlap parameter defined in Eq. (15)
L = geometric length, cm
M = number of groups for a gas component
N = number of species/scales
P = pressure, bar
q = radiative heat flux, W/m^2
s = distance along path, cm
T = temperature, K
$x, \underset{\sim}{x}$ = mole fraction (vector)

Greek Symbols

η = wavenumber, cm^{-1}
$\underset{\sim}{\phi}$ = composition variable vector
δ = Dirac delta function
λ = overlap coefficient defined in Eq. (11), cm^{-1}
κ = absorption coefficient, cm^{-1}
σ = Stefan–Boltzmann constant, $=5.67 \times 10^{-8}$ $W/m^2 K^4$

Subscripts

0 = reference condition
b = blackbody emission
L = left layer
l = lth gas/scale
m = mth group
n = nth gas/scale
q = qth group
R = right layer
w = wall
η = spectral variable in wavenumber space
g = spectral variable in g-space

References

[1] Lacis, A. A., and Oinas, V., 1991, “A Description of the Correlated-*k* Distribution Method for Modeling Nongray Gaseous Absorption, Thermal Emission, and Multiple Scattering in Vertically Inhomogeneous Atmospheres,” J. Geophys. Res., **96**(D5), pp. 9027–9063.

[2] Goody, R. M., and Yung, Y. L., 1989, *Atmospheric Radiation: Theoretical Basis*, 2nd ed, Oxford University Press, New York.

[3] Denison, M. K., and Webb, B. W., 1993, “A Spectral Line Based Weighted-Sum-of-Gray-Gases Model for Arbitrary RTE Solvers,” ASME J. Heat Transfer, **115**, pp. 1004–1012.

[4] Denison, M. K., and Webb, B. W., 1995, “The Spectral-Line-Based Weighted-Sum-of-Gray-Gases Model in Nonisothermal Nonhomogeneous Media,” ASME J. Heat Transfer, **117**, pp. 359–365.

[5] Rivière, Ph., Soufiani, A., Perrin, M. Y., Riad, H., and Gleizes, A., 1996, “Air Mixture Radiative Property Modelling in the Temperature Range 10000–40000 K,” J. Quant. Spectrosc. Radiat. Transf., **56**, pp. 29–45.

[6] Pierrot, L., Rivière, Ph., Soufiani, A., and Taine, J., 1999, “A Fictitious-Gas-Based Absorption Distribution Function Global Model for Radiative Transfer in Hot Gases,” J. Quant. Spectrosc. Radiat. Transf., **62**, pp. 609–624.

[7] Modest, M. F., and Zhang, H., 2002, “The Full-Spectrum Correlated-*k* Distribution for Thermal Radiation From Molecular Gas-Particulate Mixtures,” ASME J. Heat Transfer, **124**(1), pp. 30–38.

[8] Modest, M. F., 2003, “Narrow-Band and Full-Spectrum *k*-Distributions for Radiative Heat Transfer-Correlated-*k* vs. Scaling Approximation,” J. Quant. Spectrosc. Radiat. Transf., **76**(1), pp. 69–83.

[9] Zhang, H., and Modest, M. F., 2002, “A Multi-Scale Full-Spectrum Correlated-*k* Distribution for Radiative Heat Transfer in Inhomogeneous Gas Mixtures,” J. Quant. Spectrosc. Radiat. Transf., **73**(2–5), pp. 349–360.

[10] Zhang, H., and Modest, M. F., 2003, “Scalable Multi-Group Full-Spectrum Correlated-*k* Distributions for Radiative Heat Transfer,” ASME J. Heat Transfer, **125**(3), pp. 454–461.

[11] Goody, R. M., West, R., Chen, L., and Crisp, D., 1989, “The Correlated *k* Method for Radiation Calculations in Nonhomogeneous Atmospheres,” J. Quant. Spectrosc. Radiat. Transf., **42**, pp. 539–550.

[12] Fu, Q., and Liou, K. N., 1992, “On the Correlated *k*-Distribution Method for Radiative Transfer in Nonhomogeneous Atmospheres,” J. Atmos. Sci., **49**(22), pp. 2139–2156.

[13] Rivière, P., Soufiani, A., and Taine, J., 1992, “Correlated-*k* and Fictitious Gas Methods for H_2O Near 2.7 μm,” J. Quant. Spectrosc. Radiat. Transf., **48**, pp. 187–203.

[14] Rivière, P., Scutaru, D., Soufiani, A., and Taine, J., 1994, “A New *c-k* Data Base Suitable From 300 to 2500 K for Spectrally Correlated Radiative Transfer in CO_2-H_2O Transparent Gas Mixtures,” *Tenth International Heat Transfer Conference*, Taylor & Francis, pp. 129–134.

[15] Rivière, P., Soufiani, A., and Taine, J., 1995, “Correlated-*k* and Fictitious Gas Model for H_2O Infrared Radiation in the Voigt Regime,” J. Quant. Spectrosc. Radiat. Transf., **53**, pp. 335–346.

[16] Zhang, H., and Modest, M. F., 2003, “Multi-Group Full-Spectrum *k*-Distribution Database for Water Vapor Mixtures in Radiative Transfer Calculations,” Int. J. Heat Mass Transfer, **46**(19), pp. 3593–3603.

[17] Wang, L., and Modest, M. F., 2005, “Narrow-Band Based Multi-Scale Full-Spectrum *k*-Distribution Method for Radiative Transfer in Inhomogeneous Gas Mixtures,” ASME J. Heat Transfer, **127**, pp. 740–748.

[18] Rothman, L. S., Barbe, A., Benner, D. C., Brown, L. R., Camy-Peyret, C., Carleer, M. R., Chance, K., Clerbaux, C., Dana, V., Devi, V. M., Fayt, A., Flaud, J.-M., Gamache, R. R., Goldman, A., Jacquemart, D. , Jucks, K. W., Lafferty, W. J., Mandin, J.-Y., Massie, S. T., Nemtchinov, V., Newnham, D. A., Perrin, A., Rinsland, C. P., Schroeder, J., Smith, K. M., Smith, M. A. H., Tang, K., Toth, R. A., Vander Auwera, J., Varanasi, P., and Yoshino, K., 2003, “The HITRAN Spectroscopic Molecular Database: Edition of 2000 Including Updates Through 2001,” J. Quant. Spectrosc. Radiat. Transf., **82**(1–4), pp. 5–44.

[19] Rothman, L. S., Camy-Peyret, C., Flaud, J.-M., Gamache, R. R., Goldman, A., Goorvitch, D., Hawkins, R. L., Schroeder, J., Selby, J. E. A., and Wattson, R. B., 2000, “HITEMP, the High-Temperature Molecular Spectroscopic Database,” Available Through http://www.hitran.com.

[20] Tashkun, S. A., Perevalov, V. I., Bykov, A. D., Lavrentieva, N. N., and Teffo, J.-L., 2002, “Carbon Dioxide Spectroscopic Databank (CDSD),” Available From ftp://ftp.iao.ru/pub/CDSD-1000.

[21] Modest, M. F., and Bharadwaj, S. P., 2002, “High-Resolution, High-Temperature Transmissivity Measurements and Correlations for Carbon Dioxide-Nitrogen Mixtures,” J. Quant. Spectrosc. Radiat. Transf., **73**(2–5), pp. 329–338.

[22] Wang, L., and Modest, M. F., 2005, “A Hybrid Multi-Scale Full-Spectrum *k*-Distribution Method for Radiative Transfer in Inhomogeneous Gas Mixtures,” *Proceedings of IMECE 2005*, Orlando, FL, ASME.

[23] Modest, M. F., 2003, *Radiative Heat Transfer*, 2nd ed., Academic, New York.

[24] Wang, A., and Modest, M. F., 2007, “An Adaptive Emission Model for Monte Carlo Ray-Tracing in Participating Media Represented by Statistical Particle Fields,” J. Quant. Spectrosc. Radiat. Transf., **104**(2), pp. 288–296.

[25] Modest, M. F., and Riazzi, R. J., 2004, “Assembly of Full-Spectrum *k*-Distributions From a Narrow-Band Database; Effects of Mixing Gases, Gases and Nongray Absorbing Particles, and Mixtures With Nongray Scatterers in Nongray Enclosures,” J. Quant. Spectrosc. Radiat. Transf., **90**(2), pp. 169–189.

[26] Wang, A., and Modest, M. F., 2005, “High-Accuracy, Compact Database of Narrow-Band *k*-Distributions for Water Vapor and Carbon Dioxide,” J. Quant. Spectrosc. Radiat. Transf., **93**, pp. 245–261.

Experimental Study on Fundamental Phenomena of Boiling Using Heat Transfer Surfaces With Well-Defined Cavities Created by MEMS (Effect of Spacing Between Cavities)

Takato Sato
e-mail: ad06002@ns.kogakuin.ac.jp

Yasuo Koizumi
e-mail: koizumiy@shinshu-u.ac.jp

Hiroyasu Ohtake
e-mail: at10988@ns.kogakuin.ac.jp

Department of Mechanical Engineering,
Kogakuin University,
2665-1 Nakano-machi, Hachioji-shi,
Tokyo 192-0015, Japan

Pool nucleate boiling heat transfer experiments were performed for water using heat transfer surfaces having unified cavities. Cylindrical holes of 10 μ*m in diameter and 40* μ*m in depth were formed on a mirror-finished silicon wafer of 0.525 mm in thickness using Microelectromechanical systems technology. The test heat transfer surface was heated by a semiconductor laser beam. Experiments were conducted in the range of up to* $4.54 \times 10^4\ W/m^2$*. The temperature of the back side of the heat transfer surface was measured by a radiation thermometer. When the spacing between cavities was* $S/L_c < 0.8$*, the horizontal and declining coalescence of bubbles on the neighboring cavities were dominant. Strong thermal and bubble coalescence interactions between nucleation sites were observed in this situation. This vigorous bubble coalescence created strong convection. The heat carried by this convection accounted for a large part of the heat transfer. As the cavity interval became wide,* $S/L_c \geq 1.2$*, the horizontal and the declining coalescence of the bubbles ceased. The coalescence was limited to the vertical or no coalescence. The thermal and bubble coalescence interactions between the nucleation sites became quite low, to the extent of being negligible. The bubbles themselves were key in carrying heat away from the heat transfer surface.* [DOI: 10.1115/1.2927399]

Keywords: nucleate boiling, bubble behavior, MEMS, artificial cavity

Introduction

Since boiling heat transfer has a high heat transfer coefficient, it has been used as a cooling technique for high-temperature bodies. The boiling phenomena have been investigated for more than 60–70 years. Even so, boiling phenomena have not yet been fully clarified.

Recently, it has become possible to produce artificial cavities using microelectromechanical systems (MEMS) technology. It is easy to create the cavities of various shapes, sizes, and depths using this technology.

Kenning and Yan [1] performed pool boiling experiments and examined the behavior of bubbles that were generated on the heat transfer surface. They reported that the heat transfer surface temperature fluctuation was caused by the effect of bubble growth and departure. Judd and Chopra [2] conducted boiling experiments using a glass plate as a heat transfer surface. They observed the bubble behavior through the glass plate and examined the relation between the cavity spacing and the interaction phenomena occurring at adjacent nucleation sites. Dhir [3] and Shoji et al. [4–7] performed pool boiling experiments using silicon wafer as the heat transfer surface. Dhir reported that the analytically predicted bubble shape agreed well with the measured bubble shape. Shoji et al. reported that the interaction between the nucleation sites was composed of bubble coalescence, thermal interaction, and hydraulic interaction.

The present study followed researches of Shoji et al. Pool nucleate boiling experiments using water were performed with the silicon wafer heat transfer surfaces. The relationship between the bubble coalescence and the cavity spacing, the temperature interaction between the nucleation sites, and the role of bubble movement were examined.

Experiments

Experimental Apparatus and Procedures. The arithmetical mean roughness of the silicon wafer was 2.2 nm. Single cavities and three cavities were created on the silicon wafer using MEMS technology. The thickness of the silicon plate was 0.525 mm. The cavities in the present study were cylindrical holes of $10 \pm 1\ \mu$m in diameter and $40 \pm 2\ \mu$m in depth [4–7]. The cavities in the three-cavity case were arranged in a straight line with a spacing of 1–4 mm, depending on the test conditions.

The experimental apparatus used in the present study is shown schematically in Fig. 1. The silicon plate of the heat transfer surface was adhered to a frame of polyimide resin, which was fixed at the bottom of a closed test vessel of 200 mm in width, 200 mm in depth, and 230 mm in height. The test vessel was made of brass and had a pair of view windows of Pyrex glass on opposing walls. It was sufficiently thermally insulated. The test container was partly filled with distilled water poured from a funnel. The distilled water was degassed by boiling before each experiment. A transparent polycarbonate square pipe was placed above the heat transfer surface to minimize the effect of bulk convection and water surface fluctuation. The state in the vessel was maintained at the saturated condition of 0.1 MPa using an electric heater and a water-cooled condenser. The heat transfer surface was heated by irradiating the back side of the heat transfer surface using a semiconductor laser beam. The diameter of the irradiated area ranged from 8 mm to 12 mm, depending on the cavity spacing. The back side of the silicon plate was colored with a black spray paint. The emissivity of the colored area was estimated to be 0.98. The back-side surface temperature was measured using a line-scan radiation thermometer with a temperature resolution of 0.08 K and a time resolution of 3 ms/line.

The intensity of the laser beam was increased stepwise in the experiments. The laser beam intensity, the temperature of the back-side surface of the heat transfer surface, and the temperature and pressure in the test container were recorded after the condition was fully stabilized at each step. The video recorder captured the bubble behavior synchronously with the back-side surface temperature measurement.

Derivation of Heat Flux. Laser beam power was measured before and after each step during the experiments by a commercial laser power meter within an uncertainty of ±3%. The average value of beam power before and after each step was defined as the

---

Contributed by the Heat Transfer Division of ASME for publication in the JOURNAL OF HEAT TRANSFER. Manuscript received August 1, 2006; final manuscript received March 5, 2008; published online May 29, 2008. Review conducted by Chang Oh. Paper presented at the fourth International Conference on Nanochannels, Microchannels and Minichannels (ICNMM2006), Limerick, Ireland, June 19–21, 2006.

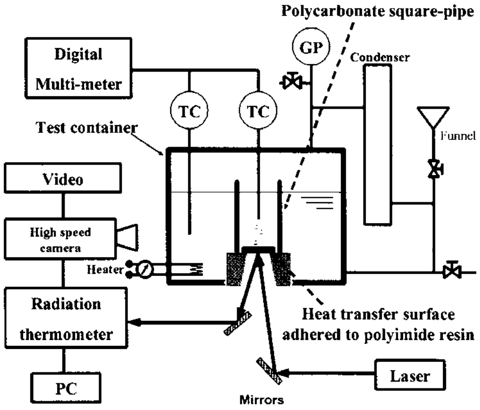

Fig. 1 Experimental apparatus

laser beam heating rate Q_{laser}.

The heat conduction rate through the silicon plate of thickness δ in the radial direction at the periphery r_{laser} of the irradiated area by the laser beam, which results in heat loss from the heated area Q_{loss}, is expressed as [5]

$$Q_{\text{loss}} = k\frac{\overline{T_{\text{in}}} - \overline{T_{\text{out}}}}{\Delta x}2\pi r_{\text{laser}}\delta \qquad (1)$$

where $\bar{T}_{\text{in}}$ and $\bar{T}_{\text{out}}$ are, respectively, the average temperatures for 4 s inside and outside the irradiated area periphery on the scanning line, Δx is the distance between these locations, and δ is the thickness of a heat transfer surface.

The net heating rate of the heat transfer surface was estimated as $Q_{\text{laser}} - Q_{\text{loss}}$, and the net heat flux of the heat transfer surface was derived by dividing this value by the irradiated area.

Experimental Results and Discussion

Thermal Interaction Between Nucleation Sites. The intensity of thermal interaction between the nucleation site and other positions, correlation coefficient of temperature fluctuation R_{cj}, is evaluated from the measured surface temperature fluctuations by calculating the correlation coefficient [5] as

$$R_{cj} = \frac{C_{cj}}{r_c r_j} \qquad (2)$$

where r is the standard deviation of the temperature fluctuation at a certain point. The subscripts c and j express the nucleation site and a certain position, respectively. The correlation function of temperature fluctuation C_{cj} is calculated as follows:

$$C_{cj} = \frac{\sum_{i=1}^{n}(T_c^i - \bar{T}_c)(T_j^i - \bar{T}_j)}{n} \qquad (3)$$

where T is the surface temperature and $\bar{T}$ is the time-averaged temperature. The letter n is the sampling number of temperature data by the radiation thermometer.

The standard deviation r is derived as

$$r = \sqrt{\frac{\sum_{i=1}^{n}(T^i - \bar{T})^2}{n}} \qquad (4)$$

Finally, the thermal interaction intensity between nucleation sites was defined as follows [6]:

$$\psi = \frac{\sum_{i=x1}^{x2} R_{ci} + \sum_{j=x2}^{x3} R_{cj}}{|X_3 - X_1|} \qquad (5)$$

where the denominator $|x_3 - x_1|$ is the distance between the nucleation sites, X_1 is the position of a certain nucleation site, X_3 is the position of a subjected nucleation site, and X_2 is the center position between these nucleation sites. Thermal interaction intensities calculated using Eq. (5) are shown in Fig. 2 for the three-cavity case. The spacing between cavities S is normalized with the Laplace length L_c in the figure as follows:

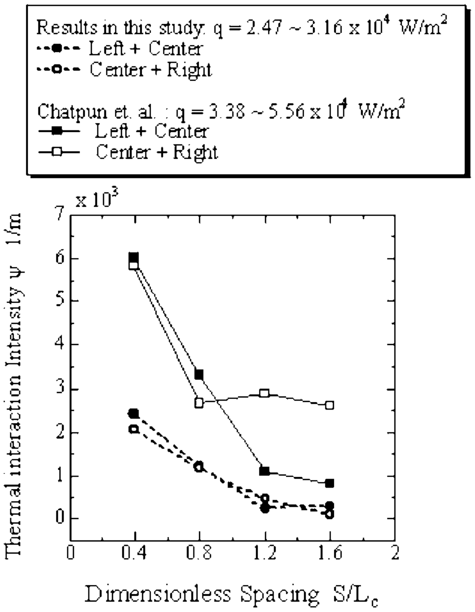

Fig. 2 Thermal intensity (three cavities)

$$S/L_c = S/\sqrt{\sigma/g(\rho_l - \rho_v)} \qquad (6)$$

The thermal interaction intensities decrease as the position moves away from the nucleation site. In the figure, the results of Chatpun et al. [6] are included for comparison. The thermal interaction intensity appears to saturate at around $S/L_c \cong 1.6$. The heat fluxes in the present study are in the range of 2.47–3.16 W/m^2. The heat flux is assumed to have some effect on the thermal interaction intensity. Further investigation is required on this.

Bubble Coalescence. Zhang and Shoji [5] classified the bubble coalescences into four categories. Normal lift is the case in which there is no coalescence. Vertical coalescence is the case in which a bubble on a nucleation site contacts a preceding bubble during the growth process of the bubble and then appears to be pulled away from the cavity and absorbed by the preceding bubble for an extremely short time period. Horizontal coalescence is the case in which two adjacent growing bubbles contact each other and then coalesce into one larger bubble. Declining coalescence is the case in which a growing bubble on a nucleation site coalesces with a bubble departing an adjacent nucleation site.

In Fig. 3, the bubble coalescence patterns are illustrated for the single cavity case and the three-cavity case. In Fig. 3, H, T, and C denote the hydraulic interaction, thermal interaction, and bubble coalescence interaction, which are the nucleation site interactions between nucleation sites (as defined by Zhang and Shoji). As the cavity spacing becomes $S/L_c \geq 1.2$, the horizontal coalescence decreases to zero, the declining coalescence also decreases, and the vertical coalescence and the normal lift increase.

Heat Transfer Role. The heat removal rate Q_{bubble} by a bubble itself is calculated as follows:

$$Q_{\text{bubble}} = V_{\text{bubble}}\rho_g h_{1g} f \qquad (7)$$

where V_{bubble} is the mean departure bubble volume, h_{lg} is the latent heat of distilled water, and f is the mean bubble departure frequency from the heat transfer surface. In the present study, in

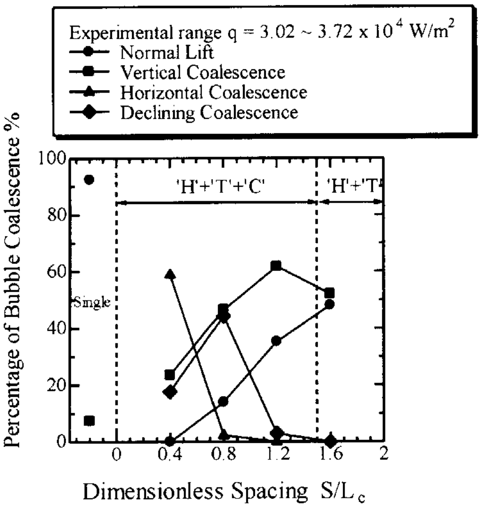

Fig. 3 Bubble coalescence

order to calculate V_{bubble}, it is assumed that the departing bubbles are spheres having mean departure bubble diameters.

The convection heat transfer coefficient of water is calculated in terms of Q_{laser}, Q_{loss}, Q_{bubble}, and the time-averaged heat transfer surface temperature $\bar{T}_w$ as follows:

$$h = \frac{Q_{\text{laser}} - Q_{\text{bubble}} - Q_{\text{loss}}}{(T_w - T_l)A} \tag{8}$$

where T_l is the water temperature and A is the area irradiated by the laser beam. The heat transfer coefficients obtained in this manner are normalized by the natural convection heat transfer coefficient h_0 of water for a horizontal mirror-finished plate: 2.27 $\times 10^3$ W/m^2 K. It was confirmed that boiling did not occur up to $\sim 4.54 \times 10^4$ W/m^2 in the case of no cavity, i.e., the mirror-finished surface. The results are shown in Fig. 4. When the cavity spacing S/L_c is less than 0.8, h/h_0 is approximately 1.75. Thus, convection is the primary component of the heat transfer, and the convection heat transfer is enhanced by the bubble agitation.

In Fig. 5, the ratios of Q_{bubble}/Q and Q_{conve}/Q are plotted with respect to the cavity spacing S/L_c. Here, Q is the net heating rate of the area irradiated by the laser beam, and Q_{conve} is the convection heat transfer rate from the area irradiated by the laser beam. It is clear that when the cavity spacing is narrow, i.e., $S/L_c < 0.8$, the convective heat transfer plays an important role in the heat transfer, and when the spacing is wide, i.e., $S/L_c \geq 1.2$, the boiling becomes key in the heat transfer.

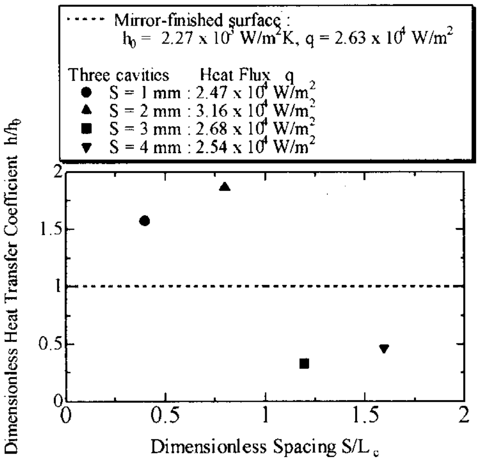

Fig. 4 Bubble agitation effect

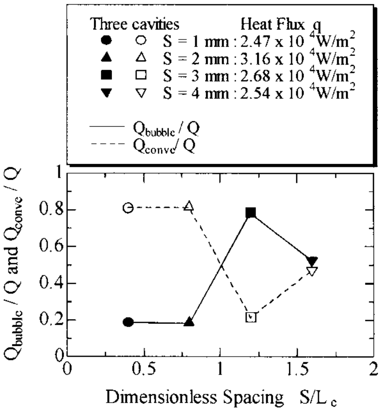

Fig. 5 Relation between phase change and convective heat transfer

Conclusions

Pool nucleate boiling heat transfer experiments were performed using water with heat transfer surfaces having unified cavities. Experiments were conducted in the range up to 4.54 $\times 10^4$ W/m^2. The following conclusions were obtained.

When the spacing between cavities was close, i.e., $S/L_c < 0.8$, the horizontal and the declining coalescence of bubbles on the neighboring cavities were dominant. Strong thermal and bubble coalescence interactions between nucleation sites were observed in this situation. This vigorous bubble coalescence created strong convection. The heat carried by this convection played an important role in heat transfer, when the cavities were close to each other.

As the cavity interval became wide, i.e., $S/L_c \geq 1.2$, the horizontal and declining coalescence of the bubbles ceased. The coalescence was limited to the vertical or no coalescence. The thermal and bubble coalescence interactions between the nucleation sites became quite low, to the extent of being negligible. In this situation, the bubble could grow large enough on the cavity and was able to absorb latent heat sufficiently. Bubbles themselves were the primary means of carrying heat away from the heat transfer surface.

Acknowledgment

The authors would like to thank Professor M. Shoji of Kanagawa University and Mr. M. Watanabe of the University of Tokyo for their valuable discussions and suggestions.

Nomenclature

g = gravitational acceleration, m/s^2
k = thermal conductivity, W/m K
Q = heating rate, W
q = heat flux, W/m^2

Greek Symbols

ρ = density, kg/m^3
σ = surface tension, N/m

Subscripts

bubble = bubble
g = gas
l = liquid
laser = laser beam
loss = heat loss

w = wall

References

[1] Kenning, D. B. R., and Yan, Y., 1996, "Pool Boiling Heat Transfer on a Thin Plate: Features Revealed by Liquid Crystal Thermography," Int. J. Heat Mass Transfer, **39**(15), pp. 3117–3137.

[2] Judd, R. L., and Chopra, A., 1993, "Interaction of the Nucleation Processes Occurring at Adjacent Nucleation Sites," ASME J. Heat Transfer, **115**(2), pp. 955–962.

[3] Dhir, V. K., 2001, "Numerical Simulations of Pool-Boiling Heat Transfer," AIChE J., **47**(4), pp. 813–834.

[4] Shoji, M., and Takagi, Y., 2001, "Bubbling Features From a Single Artificial Cavity," Int. J. Heat Mass Transfer, **44**(14), pp. 2763–2776.

[5] Zhang, L., and Shoji, M., 2003, "Nucleation Site Interaction in Pool Boiling on the Artificial Surface," Int. J. Heat Mass Transfer, **46**(3), pp. 513–522.

[6] Chatpun, S., Watanabe, M., and Shoji, M., 2004, "Nucleation Site Interaction in Pool Nucleate Boiling on a Heated Surface With Triple Artificial Cavities," Int. J. Heat Mass Transfer, **47**(14/16), 3583–3587.

[7] Chatpun, S., Watanabe, M., and Shoji, M., 2004, "Experimental Study on Characteristics of Nucleate Pool Boiling by the Effects of Cavity Arrangement," Exp. Therm. Fluid Sci., **29**(1), pp. 33–40.

Efficiency and Effectiveness of Heat Exchanger Series

Ahmad Fakheri
Professor
Department of Mechanical Engineering,
Bradley University,
Peoria, IL 61625
e-mail: ahmad@bradley.edu

The concept of heat exchanger efficiency is extended to the heat exchanger networks. General expressions that can be used for determining the overall efficiency and effectiveness of heat exchangers connected in series regardless of the heat exchanger type have been presented. A simple, accurate, approximate algebraic expression is provided for determining the efficiency of the heat exchanger. The approach presented is far more general compared to the traditional approaches, providing the designer the flexibility to select the efficiency of the individual heat exchangers, the overall system efficiency, the number of heat exchangers, as well as the type of heat exchanger to select, by utilizing a single equation. An expression is derived for determining the minimum number of shells, as a convenient alternative for the traditional methods currently in use. [DOI: 10.1115/1.2927404]

Keywords: heat exchangers, efficiency, heat exchanger efficiency, heat exchanger series, arithmetic mean temperature difference (AMTD), log-mean temperature difference (LMTD), effectiveness-NTU

1 Introduction

The concept of efficiency was recently introduced for heat exchangers [1,2]. The heat exchanger efficiency is defined as the ratio of the actual rate of heat transfer in the heat exchanger and the optimal rate of heat transfer, given by

$$\eta = \frac{q}{q_{\text{opt}}} = \frac{q}{UA(\bar{T} - \bar{t})} \tag{1}$$

where $\bar{T}$ and $\bar{t}$ are the arithmetic mean temperatures of the hot and cold fluids. The optimum heat transfer rate takes place in a balanced counterflow heat exchanger [1]. The efficiency of counterflow, parallel flow, single stream, and shell and tube heat exchangers is given by

$$\eta = \frac{\tanh(\text{Fa})}{\text{Fa}} \tag{2}$$

where the fin analogy number

$$\text{Fa} = \frac{\text{NTU}}{2N}(1 + mC_r^n)^{1/n} \tag{3}$$

is the nondimensional group that characterizes the performance of heat exchangers. In this equation, NTU is based on the total area of the heat exchangers and N is the number of heat exchangers connected in series. Equation (2) is identical to the efficiency of a constant area fin with insulated tip. It is also approximately valid for cross flow heat exchangers [3]. The values of m and n for different heat exchangers are shown in Table 1.

The simple closed form of Eq. (2) and its dependence on one parameter greatly simplify heat exchanger analysis. The concept of heat exchanger efficiency, as defined by Eq. (1), is based on the second law of thermodynamics [4]. Corresponding to each actual heat exchanger, there is an ideal heat exchanger that has the same UA, the same arithmetic mean temperature difference, and the same cold to hot fluid inlet temperature ratio. The ideal heat exchanger transfers the maximum amount of heat, equal to the product of UA, and the arithmetic mean temperature difference, and generates the minimum amount of entropy, making it the most efficient and least irreversible heat exchanger.

The concept of heat exchanger efficiency parallels that of isentropic efficiency defined for pumps, turbines, nozzles, etc., and results from the successful application of the second law of thermodynamics to nonadiabatic processes. Its application to heat exchangers has resulted in a simple general analytical expression for determining the heat exchanger efficiency as opposed to different charts or complicated equations for effectiveness or log-mean temperature difference (LMTD) correction factor, F. In the traditional approaches, the performance of heat exchangers is characterized by two parameters (NTU and C_r or P and R); the efficiency, on the other hand, depends on a universal nondimensional parameter, Fa. Additionally, the relevant driving temperature potential in heat exchangers appears to be arithmetic mean temperature difference, and not LMTD.

Below, the concept of heat exchanger efficiency is extended to heat exchanger networks composed of shell and tube and cross flow heat exchangers that are connected in series.

2 Analysis

The LMTD correction factor, the heat exchanger effectiveness, and heat exchanger efficiency are all derived from the same basic set of equations and therefore can be related to each other. For heat exchangers,

$$\begin{aligned} q &= UA\,\eta(\bar{T} - \bar{t}) = UAF\text{LMTD} = \varepsilon C_{\min}(T_1 - t_1) = C_h(T_1 - T_2) \\ &= C_c(t_2 - t_1) = C_{\min}\Delta T_{\min} \end{aligned} \tag{4}$$

To find a relation between F and ε,

$$\frac{UA}{C_{\min}} F\text{LMTD} = \varepsilon(T_1 - t_1) \tag{5}$$

which can be rearranged into

$$\text{NTU}F \frac{\dfrac{(T_1 - T_2)}{(t_2 - t_1)}\dfrac{(t_2 - t_1)}{(T_1 - t_1)} - \dfrac{(t_2 - t_1)}{(T_1 - t_1)}}{\ln\dfrac{(T_1 - t_2)}{(T_2 - t_1)}} = \varepsilon \tag{6}$$

Since

$$P = \frac{t_2 - t_1}{T_1 - t_1} = \frac{t_2 - t_1}{T_1 - t_1}\frac{C_c}{C_{\min}}\frac{C_{\min}}{C_c} = \frac{q}{q_{\max}}\frac{C_{\min}}{C_c} = \varepsilon\frac{C_{\min}}{C_c} \tag{7}$$

$$R = \frac{T_1 - T_2}{t_2 - t_1} = \frac{T_1 - T_2}{t_2 - t_1}\frac{C_h}{C_c}\frac{C_c}{C_h} = \frac{C_c}{C_h} \tag{8}$$

then Eq. (6) can be rearranged into

$$F = \frac{1}{\text{NTU}}\frac{\ln\dfrac{1 - \varepsilon C_r}{1 - \varepsilon}}{1 - C_r} \tag{9}$$

regardless of which fluid has the lower heat capacity. Heat exchanger efficiency is related to heat exchanger effectiveness through [2]

Contributed by the Heat Transfer Division of ASME for publication in the JOURNAL OF HEAT TRANSFER. Manuscript received February 11, 2007; final manuscript received February 26, 2008; published online May 29, 2008. Review conducted by S. A. Sherif.

Table 1 Fin analogy number for different heat exchangers

	m	n	Max error (%)
Counterflow	−1	1	0
Parallel	1	1	0
Single stream ($C_r=0$)	0	1	0
Single shell and tube	1	2	0
Cross flow			
$C_{\min}$ mixed $C_{\max}$ unmixed	1.2	4.4	<7.5
$C_{\min}$ unmixed $C_{\max}$ mixed	1.35	4.02	<3
Both mixed	1.2	2	<1.6
Both unmixed	−0.1	0.37	<8.4

$$\eta=\frac{1}{\mathrm{NTU}}\frac{1}{\frac{1}{\varepsilon}-\frac{(1+C_r)}{2}} \tag{10}$$

Equation (10) is a general expression that can be used to determine the efficiency of any heat exchanger, when its effectiveness is known. Eliminating effectiveness between Eqs. (9) and (10) results in the following expression relating F to heat exchanger efficiency:

$$\eta=\frac{\tanh\left[\frac{F\mathrm{NTU}(1-C_r)}{2}\right]}{\frac{\mathrm{NTU}}{2}(1-C_r)} \tag{11}$$

For example, for a counterflow heat exchanger, the LMTD correction factor $F=1$, and therefore Eq. (11) reduces to Eq. (2) for the efficiency of a counterflow heat exchanger.

2.1 Multishell and Tube. For a multishell and tube, Fakheri [5] provided the following general expression for determining, the F correction factor for a shell and tube heat exchanger having N shells as follows:

$$F_{N,2NM}=\frac{\frac{\sqrt{R^2+1}}{R-1}\ln\left[\frac{1-PR}{1-P}\right]^{1/N}}{\ln\frac{1+\left[\frac{1-PR}{1-P}\right]^{1/N}-\frac{\sqrt{R^2+1}}{R-1}+\frac{\sqrt{R^2+1}}{R-1}\left[\frac{1-PR}{1-P}\right]^{1/N}}{1+\left[\frac{1-PR}{1-P}\right]^{1/N}+\frac{\sqrt{R^2+1}}{R-1}-\frac{\sqrt{R^2+1}}{R-1}\left[\frac{1-PR}{1-P}\right]^{1/N}}} \tag{12}$$

where P and R are given by Eqs. (7) and (8). When the hot fluid has the smaller capacity,

$$P=\varepsilon C_r \tag{13}$$

$$R=\frac{1}{C_r} \tag{14}$$

Substituting into Eq. (12) and setting it equal to Eq. (9),

$$\frac{\frac{\sqrt{1+C_r^2}}{1-C_r}\ln\left[\frac{1-\varepsilon}{1-\varepsilon C_r}\right]^{1/N}}{\ln\frac{1+\left[\frac{1-\varepsilon}{1-\varepsilon C_r}\right]^{1/N}-\frac{\sqrt{1+C_r^2}}{1-C_r}+\frac{\sqrt{1+C_r^2}}{1-C_r}\left[\frac{1-\varepsilon}{1-\varepsilon C_r}\right]^{1/N}}{1+\left[\frac{1-\varepsilon}{1-\varepsilon C_r}\right]^{1/N}+\frac{\sqrt{1+C_r^2}}{1-C_r}-\frac{\sqrt{1+C_r^2}}{1-C_r}\left[\frac{1-\varepsilon}{1-\varepsilon C_r}\right]^{1/N}}}=\frac{1}{\mathrm{NTU}}\frac{\ln\frac{1-\varepsilon C_r}{1-\varepsilon}}{1-C_r} \tag{15}$$

which can be solved for the effectiveness and simplifies to

$$\varepsilon=\frac{1-\left\{\frac{1+\frac{1-C_r}{\sqrt{1+C_r^2}}\tanh\left[\frac{\mathrm{NTU}}{2N}\sqrt{1+C_r^2}\right]}{1-\frac{1-C_r}{\sqrt{1+C_r^2}}\tanh\left[\frac{\mathrm{NTU}}{2N}\sqrt{1+C_r^2}\right]}\right\}^N}{C_r-\left\{\frac{1+\frac{1-C_r}{\sqrt{1+C_r^2}}\tanh\left[\frac{\mathrm{NTU}}{2N}\sqrt{1+C_r^2}\right]}{1-\frac{1-C_r}{\sqrt{1+C_r^2}}\tanh\left[\frac{\mathrm{NTU}}{2N}\sqrt{1+C_r^2}\right]}\right\}^N} \tag{16}$$

The same equation is obtained, if the cold fluid has smaller capacity. The effectiveness of the individual shells of the heat exchanger is given by [6]

$$\varepsilon_1=\frac{2}{1+C_r+\frac{\sqrt{1+C_r^2}}{\tanh\left[\frac{\mathrm{NTU}}{2N}\sqrt{1+C_r^2}\right]}} \tag{17}$$

which can be substituted in Eq. (16) to yield

$$\varepsilon=\frac{1-\left\{\frac{1-\varepsilon_1 C_r}{1-\varepsilon_1}\right\}^N}{C_r-\left\{\frac{1-\varepsilon_1 C_r}{1-\varepsilon_1}\right\}^N} \tag{18}$$

This equation appears to be an original expression for the effectiveness of N identical shell and tube heat exchangers in series. Substituting Eq. (18) in Eq. (10), and simplifying, result in

$$\eta=\frac{2}{\mathrm{NTU}(1-C_r)}\frac{1-\left\{\frac{1-\frac{\mathrm{NTU}(1-C_r)}{2N}\eta_1}{1+\frac{\mathrm{NTU}(1-C_r)}{2N}\eta_1}\right\}^N}{1+\left\{\frac{1-\frac{\mathrm{NTU}(1-C_r)}{2N}\eta_1}{1+\frac{\mathrm{NTU}(1-C_r)}{2N}\eta_1}\right\}^N} \tag{19}$$

for the efficiency of multishell and tube heat exchangers, where the efficiency of each shell is given by

$$\eta_1=\frac{\tanh\frac{\mathrm{NTU}\sqrt{C_r^2+1}}{2N}}{\frac{\mathrm{NTU}\sqrt{C_r^2+1}}{2N}} \tag{20}$$

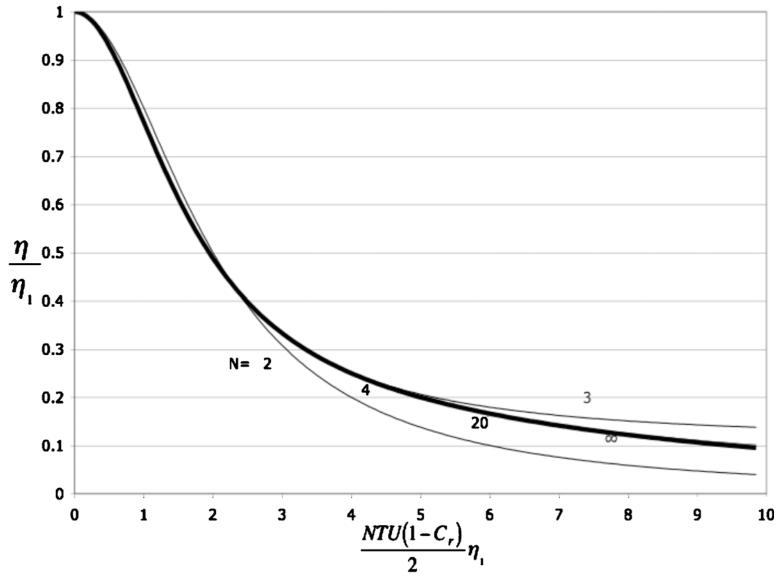

Fig. 1 Efficiency of heat exchanger network

2.2 Multipass Cross Flow Heat Exchangers. For cross flow heat exchangers connected in series where the overall behavior is counterflow and the individual heat exchangers have the same effectiveness (ε_1) and the fluids are mixed before entering the next heat exchanger, Kays and London [7] gave the following expression for the overall effectiveness of the system:

$$\varepsilon = \frac{1 - \left\{ \frac{1 - C_r \varepsilon_1}{1 - \varepsilon_1} \right\}^N}{C_r - \left\{ \frac{1 - C_r \varepsilon_1}{1 - \varepsilon_1} \right\}^N} \tag{21}$$

Note that this equation is identical to Eq. (18), which was derived for shell and tube heat exchangers connected in series. Therefore, Eq. (19) also applies to cross flow heat exchangers connected in series. Rearranging Eq. (19),

$$\frac{\eta}{\eta_1} = \frac{1}{\frac{\text{NTU}(1 - C_r)}{2}\eta_1} \frac{1 - \left\{ \frac{1 - \frac{\text{NTU}(1 - C_r)}{2N}\eta_1}{1 + \frac{\text{NTU}(1 - C_r)}{2N}\eta_1} \right\}^N}{1 + \left\{ \frac{1 - \frac{\text{NTU}(1 - C_r)}{2N}\eta_1}{1 + \frac{\text{NTU}(1 - C_r)}{2N}\eta_1} \right\}^N} \tag{22}$$

Figure 1 is a plot of Eq. (22). As can be seen, for four or more heat exchangers connected in series, all the results fall on the same curve.

Since

$$\lim_{N \to \infty} \frac{1 - \left\{ \frac{1 - Z/N}{1 + Z/N} \right\}^N}{1 + \left\{ \frac{1 - Z/N}{1 + Z/N} \right\}^N} = \tanh(Z) \tag{23}$$

the efficiency of the overall system is approximately equal to

$$\eta = \frac{\tanh\left[\frac{\text{NTU}(1 - C_r)}{2}\eta_1 \right]}{\frac{\text{NTU}(1 - C_r)}{2}} \tag{24}$$

Dividing both sides of Eq. (24) by η_1 results in

$$\frac{\eta}{\eta_1} = \frac{\tanh\left[\frac{\text{NTU}(1 - C_r)}{2}\eta_1 \right]}{\frac{\text{NTU}(1 - C_r)}{2}\eta_1} \tag{25}$$

Equation (25) provides the overall efficiency of a system made of a large number of heat exchangers connected in series. It is the limit of Eq. (22) as the number of heat exchangers approaches infinity. The curve labeled ∞ in Fig. 1 is a plot of Eq. (25) and as can be seen, it accurately approximates Eq. (22) for $N > 3$.

From Fig. 1, the overall efficiency of the network is less than the efficiency of its components. As the number of heat exchangers is increased, the NTU of the individual heat exchangers and thus their fin analogy number, Fa, decrease, bringing their efficiency close to 1, making the right hand side of Eq. (25) equal to that for a counterflow heat exchanger, or in the limit, the network behaves like that of a counterflow heat exchanger.

Equation (25) can also be used to arrive at an expression for the minimum number of heat exchangers needed in the network. From Eq. (4),

$$\frac{q}{C_{\min}(\bar{T} - \bar{t})} = \text{NTU}\,\eta = \frac{\Delta T_{\min}}{\bar{T} - \bar{t}} \tag{26}$$

Substituting for η from Eq. (26) into Eq. (24) and solving for NTU,

$$\text{NTU} = \frac{1}{\eta_1} \frac{2}{(1 - C_r)} \tanh^{-1}\left[\frac{\Delta T_{\min}}{\bar{T} - \bar{t}} \frac{(1 - C_r)}{2} \right] \tag{27}$$

Substituting for η_1 from Eq. (2) into Eq. (27) and rearranging the resulting equation lead to

$$\frac{\mathrm{Fa}}{N} = \tanh^{-1}\left\{ \frac{\mathrm{Fa}}{(\mathrm{NTU})N}\frac{2}{(1-C_r)} \tanh^{-1}\left[\frac{\Delta T_{\min}}{\bar{T}-\bar{t}}\frac{(1-C_r)}{2}\right]\right\} \tag{28}$$

In order for a solution to exist, the argument of the inverse hyperbolic function in Eq. (28) must be less than 1, resulting in

$$N > \frac{\mathrm{Fa}}{(\mathrm{NTU})}\frac{2}{(1-C_r)} \tanh^{-1}\left[\frac{\Delta T_{\min}}{\bar{T}-\bar{t}}\frac{(1-C_r)}{2}\right] \tag{29}$$

From this expression, the minimum number of heat exchangers needed to have a feasible design is the next integer higher than the value on the right hand side of Eq. (29).

The approach can be demonstrated by an example given in Ref. [8]. A hot stream is to be cooled from 410 to 110°C by another stream entering at 0°C and leaving at 360°C in a shell and tube heat exchanger. This problem is traditionally solved by trial and error, or by the graphical approach of “stepping off” [8], which results in a feasible solution of requiring three shells. From Table 1, for a shell and tube heat exchanger,

$$\mathrm{Fa} = \frac{\mathrm{NTU}}{2}\sqrt{1+C_r^2}$$

Using Eq. (28),

$$N > \frac{\sqrt{1+C_r^2}}{(1-C_r)} \tanh^{-1}\left[\frac{\Delta T_{\min}}{\bar{T}-\bar{t}}\frac{(1-C_r)}{2}\right]$$

$$N > \frac{\sqrt{1+\left(\frac{410-110}{360-0}\right)^2}}{\left(1-\frac{410-110}{360-0}\right)} \times \tanh^{-1}\left[\frac{360-0}{\frac{410+110}{2}-\frac{360+0}{2}}\frac{\left(1-\frac{410-110}{360-0}\right)}{2}\right] = 2.80$$

which also results in the feasible solution of three shells.

Therefore, for any type of heat exchanger connected in series, the overall effectiveness is given by Eq. (18), the overall efficiency by Eq. (19) exactly, and Eq. (23) approximately. Equation (25) is an approximate expression for the needed NTU to meet the design criteria. This approach is far more general compared to the traditional approaches, in that the designer has freedom to select the efficiency of the individual heat exchangers, the overall system efficiency, the number of heat exchangers, as well as the type of heat exchanger to select, by utilizing a single equation.

3 Conclusions

The heat exchanger efficiency is defined as the ratio of the actual heat transfer in a heat exchanger to the optimum heat transfer rate. The concept of heat exchanger efficiency is extended to the heat exchanger networks. General expressions that can be used for determining the overall efficiency and effectiveness of heat exchangers connected in series regardless of the heat exchanger type have been presented. Exact and approximate algebraic expressions are arrived at to determine the efficiency of the heat exchanger networks. An expression is also arrived at for determining the minimum number of heat exchangers in the network.

Nomenclature

A = total surface area, m^2
C = fluid heat capacity, $C=\dot{m}c_p$
c_p = specific heat
C_r = capacity rate ratio $C_r=C_{\min}/C_{\max}$
F = LMTD correction factor
Fa = fin analogy number
$\mathrm{LMTD}=[(\Delta T)_1-(\Delta T)_2]/\ln[(\Delta T)_1/(\Delta T)_2]$ = log-mean temperature difference
N = number of heat exchangers in series
NTU = overall number of transfer units $\mathrm{NTU}=UA/C_{\min}$
q = rate of heat transfer
q_{opt} = optimum heat transfer rate
T_1 = hot fluid inlet temperature
T_2 = hot fluid exit temperature
t_1 = cold fluid inlet temperature
t_2 = cold fluid exit temperature
$\bar{T}$ = arithmetic mean temperature of the hot fluid $\bar{T}=(T_1+T_2)/2$
$\bar{t}$ = arithmetic mean temperature of the cold fluid $\bar{t}=(t_1+t_2)/2$
U = overall heat transfer coefficient, $\mathrm{W/m^2\,K}$
ε = heat exchanger effectiveness $\varepsilon=q/q_{\max}$
η = heat exchanger efficiency $\eta=q/q_{\mathrm{opt}}$
$\Delta T_{\min}$ = temperature change of fluid with minimum capacity

References

[1] Fakheri, A., 2003, “Arithmetic Mean Temperature Difference and the Concept of Heat Exchanger Efficiency,” *Proceedings of the 2003 ASME Summer Heat Transfer Conference*, Las Vegas, Nevada, July 21–23, Paper No. HT2003-47360.

[2] Fakheri, A., 2003, “The Shell and Tube Heat Exchanger Efficiency and its Relation to Effectiveness,” *Proceedings of the 2003 American Society of Mechanical Engineers (ASME) International Mechanical Engineering Congress and Exposition (IMECE)*, Washington, D.C., Nov. 16–21.

[3] Fakheri, A., 2006, “Thermal Efficiency of the Cross Flow Heat Exchangers,” *Proceedings of the 2006 American Society of Mechanical Engineers (ASME) International Mechanical Engineering Congress and Exposition (IMECE)*, Chicago, IL, Nov. 5–10.

[4] Fakheri, A., 2007, “Heat Exchanger Efficiency,” ASME J. Heat Transfer, **129**(9), pp. 1268–1276.

[5] Fakheri, A., 2003, “A General Expression for the Determination of the Log Mean Temperature Correction Factor for Shell and Heat Exchangers,” ASME J. Heat Transfer, **125**, pp. 527–530.

[6] Incropera, F. P., and DeWitt, D., 2002, *Fundamentals of Heat and Mass Transfer*, 4th ed., Wiley, New York.

[7] Kays, W. M., and London, A. L., 1984, *Compact Heat Exchangers*, 3rd ed., Krieger Publishing Company.

[8] Ahmad, S., Linnhoff, B., and Smith, R., 1985, “Design of Multipass Heat Exchangers: An Alternative Approach,” ASME J. Heat Transfer, **110**, pp. 303–309.

Calculation Method for Thermal-Hydraulic System Simulation

Li Chenggong

Jiao Zongxia

School of Automation Science and Electrical Engineering,
Beihang University,
Beijing, 100083, China

This paper presents the fundamental approaches of modeling thermal-hydraulic component briefly. A set of lumped parameter mathematical models is developed, which are based on conservation of mass and energy. Subsequently, the connection rule for basic thermal-hydraulic components and the method to automatically generate the complete thermal-hydraulic system model are put forward. The integration methods for solving the cross-coupling thermal-hydraulic equations are also discussed for a position-controlled thermal-hydraulic system. Simulation results show the interaction between pressure and temperature. The simplified representations of thermal-hydraulic differential equations are also proposed in this paper, which can reduce simulation time. The validity of the simplified representations is judged by simulation. [DOI: 10.1115/1.2928006]

Keywords: thermal-hydraulic, simulation, modelling, method

1 Introduction

In hydraulic systems, the oil temperature mainly depends on the efficiency of some working components, such as pumps, motors, and valves. If the power losses of these components are large, the oil temperature will become undesirably high. Therefore, demands for thermal performance of some hydraulic systems are increasing. Modeling and simulation of thermal-hydraulic systems become very important.

Interest in the thermal consideration of hydraulic systems has surfaced through years. In the early 1970s, the Boeing Airplane Division (1970) and McDonnell Aircraft Company (1977) developed complex computer programs to predict the temperature changes in hydraulic components and systems [1]. In 1996, Sidders [2] has derived the basic formulas for modeling the thermal-hydraulic components at the University of Bath. In 1998, Storck [3] studied thermostatic temperature regulation in hydraulic systems in his Ph.D. thesis. These researches made it possible to predict the fluid temperatures of the thermal-hydraulic systems in the designing process. However, first, these articles mainly focused on the hydraulic component models and did not present the method to form the complete thermal-hydraulic system model. Second, no articles discussed the integration method to solve cross-coupling in thermal-hydraulic systems. Bad calculation method can lead to extremely long time for simulation.

This paper presents the fundamental functions for modeling thermal-hydraulic component briefly. Subsequently, the connection rule and the method for the thermal-hydraulic system models are introduced. By this method, the complete thermal-hydraulic system model can be generated automatically.

2 Basic Thermal-Hydraulic Modelling

Basic thermal-hydraulic components can be separated into two categories, resistive components and capacitive components. The resistive component can be assumed to have no fluid volume inside the component. So the resistive component can be described by a steady state model. The capacitive component can be assumed to have a fluid volume inside. It has two state variables: the temperature and the pressure.

2.1 Model for Basic Capacitive Component. The basic capacitive component is the volume in which the temperature and the pressure are computed. The conservation equations for mass and energy are the basic equations for thermal-hydraulic modeling of the capacitive component.

2.1.1 Flow Continuity Equation. The physical principle used to derive the continuity equation is conservation of mass. Mass neither can be created nor destroyed; if the flow rate of mass into a control volume exceeds the rate of flow out, mass will accumulate within the control volume [3]. The continuity equation for one-dimensional flow gives

$$\frac{dm}{dt} = \sum \dot{m}_{\text{in}} - \sum \dot{m}_{\text{out}} \tag{1}$$

The mass of liquid in the volume is given by

$$m = \rho \cdot V \tag{2}$$

where ρ is the mean fluid density in the control volume. It is possible to formulate the continuity equation from Eqs. (1) and (2) in terms of the density derivative as follows:

$$\frac{d\rho}{dt} = \frac{\dfrac{dm}{dt} - \rho \dfrac{dV}{dt}}{V} \tag{3}$$

The density being a thermodynamic property of the liquid is a function of pressure and temperature:

$$\rho = \rho(p,T) \tag{4}$$

By differentiating withrespect to temperature and pressure, Eq. (4) leads to

$$d\rho = \left(\frac{\partial \rho}{\partial p}\right)_T dp + \left(\frac{\partial \rho}{\partial T}\right)_p dT \tag{5}$$

From this equation, it is possible to write the continuity equation in terms of the pressure derivative as follows:

$$dp = \frac{1}{\left(\dfrac{\partial \rho}{\partial p}\right)_T}\left[d\rho - \left(\frac{\partial \rho}{\partial T}\right)_p dT\right] \tag{6}$$

Using the definition of the liquid properties and more particularly the isothermal bulk modulus β_T and the cubical expansion coefficient α_p, the pressure derivative with respect to time is given by:

$$\frac{dp}{dt} = \beta_T\left[\frac{1}{\rho}\frac{d\rho}{dt} + \alpha_p \frac{dT}{dt}\right] \tag{7}$$

Using Eqs. (3) and (7) leads to

$$\frac{dp}{dt} = \beta_T\left[\frac{1}{\rho \cdot V}\left(\frac{dm}{dt} - \rho\frac{dV}{dt}\right) + \alpha_p \frac{dT}{dt}\right] \tag{8}$$

where $\beta_T(p,T)=\rho/(\partial\rho/\partial p)_T$ is the isothermal fluid bulk modulus, and $\alpha_p(p,T)=-\frac{1}{\rho}(\partial\rho/\partial T)_p$ is the cubic expansion coefficient [4].

Combining Eq. (1) and Eq. (8) gives

$$\frac{dp}{dt} = \beta_T\left[\frac{1}{\rho \cdot V}\left(\sum \dot{m}_{\text{in}} - \sum \dot{m}_{\text{out}} - \rho\frac{dV}{dt}\right) + \alpha_p \frac{dT}{dt}\right] \tag{9}$$

Equation (9) will be referred to as the flow continuity equation.

Contributed by the Heat Transfer Division of ASME for publication in the JOURNAL OF HEAT TRANSFER. Manuscript received February 8, 2007; final manuscript received February 25, 2008; published online May 30, 2008. Review conducted by Louis C. Burmeister.

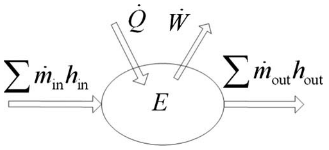

Fig. 1 Control volume

2.1.2 Energy Equation. The basic relationship for the thermal change of the fluid over a hydraulic component is the first law of thermodynamics applied to a flow process of the fluid volume [3]. The fluid volume is shown in Fig. 1. For a complete and more comprehensive mathematical survey, see Refs. [5,6]. The corresponding ordinary differential equation for fluid energy in a volume V is

$$\dot{Q} - \dot{W} = \sum \dot{m}_{\text{out}} h_{\text{out}} - \sum \dot{m}_{\text{in}} h_{\text{in}} + \dot{E} \tag{10}$$

where $\dot{W}$ is the rate of work except for the work required to push mass into and out of the control volume, which is taken care of by using enthalpies for the energy of fluid streams. The energy (E) in the control volume is the sum of the internal energy (U), the kinetic energy (KE), and the potential energy (PE): $E = U + \text{KE} + \text{PE}$. If the kinetic and potential energies are neglected, the time rate of change of the energy can be expressed according to

$$\frac{dE}{dt} = \frac{d(mu)}{dt} = m\frac{du}{dt} + u\frac{dm}{dt} \tag{11}$$

Since the fluids in this study do not change phase, the specific enthalpy can be expressed as a function of temperature T and pressure p, that is, $h = h(T,p)$. So the time derivative of h can be expressed as

$$\frac{dh}{dt} = \left(\frac{\partial h}{\partial T}\right)_p \frac{dT}{dt} + \left(\frac{\partial h}{\partial p}\right)_T \frac{dp}{dt} \tag{12}$$

The first term in Eq. (12) is recognized as the specific heat at constant pressure c_p,

$$\left(\frac{\partial h}{\partial T}\right)_p = c_p \tag{13}$$

The second term demands some rearranging using the so-called *Tds* equations [6]. It can be expressed as

$$\left(\frac{\partial h}{\partial p}\right)_T = \upsilon - T \cdot \left(\frac{\partial \upsilon}{\partial T}\right)_p = \upsilon - \upsilon \cdot \alpha_p \cdot T \tag{14}$$

where υ is the specific volume. Equation (12) can be rewritten as Eq. (15) by Eqs. (13) and (14) as follows:

$$\frac{dh}{dt} = c_p \frac{dT}{dt} + (1 - \alpha_p T)\upsilon \frac{dp}{dt} \tag{15}$$

The specific enthalpy is defined as

$$h = u + p\upsilon \tag{16}$$

After introducing Eqs. (15) and (16) into Eq. (11), Eq. (17) is obtained [7].

$$\frac{dE}{dt} = c_p m \frac{dT}{dt} - mT\alpha_p \upsilon \frac{dp}{dt} + h\frac{dm}{dt} - p\frac{dV}{dt} \tag{17}$$

Combining Eqs. (1), (10), and (17) gives

$$\frac{dT}{dt} = \frac{1}{c_p m}\left[\sum \dot{m}_{\text{in}}(h_{\text{in}} - h) + \sum \dot{m}_{\text{out}}(h - h_{\text{out}}) + \dot{Q} - \dot{W} + p\frac{dV}{dt} + mT\alpha_p \upsilon \frac{dp}{dt}\right] \tag{18}$$

In most thermal-hydraulic components, $\dot{W}$ represents the rate of boundary work and shaft work [8]. It can be written as

$$\dot{W} = \dot{W}_s + \dot{W}_b \tag{19}$$

where $\dot{W}_b$ is the rate of boundary work. It is calculated by

$$\dot{W}_b = p\frac{dV}{dt} \tag{20}$$

Introducing Eqs. (19) and (20) into Eq. (18) gives

$$\frac{dT}{dt} = \frac{1}{c_p m}\left[\sum \dot{m}_{\text{in}}(h_{\text{in}} - h) + \sum \dot{m}_{\text{out}}(h - h_{\text{out}}) + \dot{Q} - \dot{W}_s + T\alpha_p V \frac{dp}{dt}\right] \tag{21}$$

If it is assumed that the average enthalpy within the control volume equates to the leaving enthalpy regardless of the inlet conditions [2], Eq. (21) can be expressed as

$$\frac{dT}{dt} = \frac{1}{c_p m}\left[\sum \dot{m}_{\text{in}}(h_{\text{in}} - h) + \dot{Q} - W_s + T\alpha_p V \frac{dp}{dt}\right] \tag{22}$$

The change in specific enthalpy within the control volume is related to the change in pressure and temperature by

$$h_{\text{in}} - h = \bar{c}_p(T_{\text{in}} - T) + (1 - \bar{\alpha}_p \bar{T})\bar{\upsilon}(p_{\text{in}} - p) \tag{23}$$

Equation (23) has been derived by utilizing fundamental relationships between enthalpy, pressure, and temperature [2] and all fluid parameters are replaced with their mean values over the temperature and pressure range considered (indicated by barred notations).

2.2 Model for Basic Resistive Component. The basic resistive component represents the component in which there is no fluid volume. So there is no state variable (pressure and temperature) in this kind of component.

The mass flow rate through the resistive components can be described as

$$\dot{m} = k \cdot f(\Delta p) \tag{24}$$

The detailed expression depends on the concrete resistive component. For example, the standard orifice turbulent flow equation is used to represent the pressure flow characteristic as follows:

$$\dot{m} = C_d A \sqrt{2\rho(\Delta p)} \tag{25}$$

The power consumption can be calculated by

$$\dot{Q}_f = \frac{\Delta p \cdot \dot{m}}{\rho} \tag{26}$$

The input variables of resistive components are pressure and temperature, which can be calculated in capacitive components and the output variables of resistive components are mass flow rate and heat flow rate (power consumption), which can be used in capacitive components. So the resistive components must be connected by capacitive components and vice versa.

2.3 Heat Transfer Calculation. Usually, the basic resistive component is assumed to be adiabatic because there is no volume if it is small. The heat transfer model of the capacitive component consists of two nodes: a fluid node and a mass node. The fluid node represents the fluid in the component and the mass node represents the component's wall. The heat transfer between the

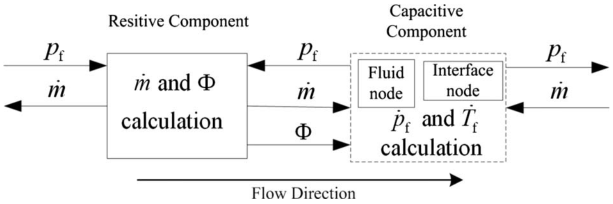

Fig. 2 Connection rule

fluid and the wall is dominated by convection.

The heat exchange from the fluid node to the mass node is given as

$$\dot{Q} = k_{fw}A(T_f - T_w) \tag{27}$$

where k_{fw} is the fluid/wall heat transfer coefficient, A is the heat transfer area inside the wall, T_f is the fluid temperature, and T_w is the wall temperature. So the energy equation for the fluid node is

$$\frac{dT_f}{dt} = \frac{1}{c_p m}\left[\sum \dot{m}_{\mathrm{in}}(h_{\mathrm{in}} - h_f) - k_{fw}A(T_f - T_w) + \dot{Q}_f - W_s + T_f \alpha_p V \frac{dp_f}{dt}\right] \tag{28}$$

where T_f is the fluid pressure. Equation (28) is the basic energy equation and Eq. (9) is the basic flow continuity equation for all the thermal-hydraulic components.

3 Modeling for Thermal-Hydraulic Systems

The capacitive components are the volumes in which the temperature and the pressure are computed. The temperature and pressure are computed from the enthalpy and mass flow rate inputs at ports of these components. The resistive components are the components in which the enthalpy and mass flow rates are evaluated from the temperature and pressure inputs at ports of these components. This implies that a thermal-hydraulic model is always built with resistive components connected by capacitive components, as shown in Fig. 2.

In Fig. 2, fluid nodes are treated as ideal capacitors and the resistance and inertia of the fluid nodes are not taken into account or added to the components connected. The interface node is composed of the volume of the hydraulic pipe and the idle volumes of the components connected.

In Fig. 2, the symbol Φ is defined by

$$\Phi = \sum \dot{m}_{\mathrm{in}}(h_{\mathrm{in}} - h_f) - k_{fw}A(T_f - T_w) + \dot{Q}_f - W_s \tag{29}$$

It is apparent that the calculation of Φ is dependent on the flow direction. For the upstream fluid node of the component Φ equals zero.

In Eq. (29), it can be seen that the liquid flowing out of the volume cannot affect the liquid temperature in the volume. That is, heat transfer is directional. So the calculation of Φ is used only in the downstream liquid node. According to this connection rule, the differential equations for the complete thermal-hydraulic system can be generated automatically.

4 Circuit Description

The thermal-hydraulic circuit simulated is a position control loop of a cylinder, as shown in Fig. 3. The hydraulic actuator moves a load and there is control using position feedback. The position error is subjected to the controller and the signal transferred to the servo valve.

Fast position change will lead to fast pressure change in chamber VA of the cylinder (noted in Fig. 3) and the temperature change can affect the system performance.

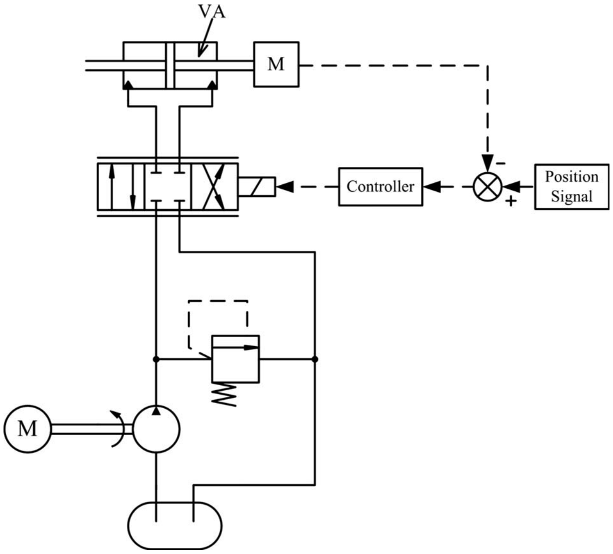

Fig. 3 Position-controlled system

5 Integration Methods

Equations (9) and (28) are the lumped parameter equations representing conservation of mass and energy. It is apparent that these two equations are cross coupled. Therefore, fast pressure transients will produce fast temperature transients and vice versa. For convenience, the following four symbols are defined:

$$a = \frac{\beta_T}{\rho \cdot V}\left(\sum \dot{m}_{\mathrm{in}} - \sum \dot{m}_{\mathrm{out}} - \rho \frac{dV}{dt}\right) \tag{30}$$

$$b = \frac{\beta_T \cdot \alpha_p}{\rho \cdot V} \tag{31}$$

$$c = \frac{1}{c_p m}\left[\sum \dot{m}_{\mathrm{in}}(h_{\mathrm{in}} - h_f) - k_{fw}A(T_f - T_w) + \dot{Q}_f - W_s\right] \tag{32}$$

$$d = \frac{T_f \alpha_p V}{c_p m} \tag{33}$$

where a represents the effect of the mass flow and b represents the effect of the temperature change; c represents the effect of heat flow and d represents the effect of the pressure change. So Eqs. (9) and (28) can be rewritten as

$$\frac{dp_f}{dt} = a + b\frac{dT_f}{dt} \tag{34}$$

$$\frac{dT_f}{dt} = c + d\frac{dp_f}{dt} \tag{35}$$

From these two equations, the cross coupling can be seen. It is easy to decouple these two differential equations by solving for each derivative to find

$$\frac{dT_f}{dt} = \frac{c + ad}{1 - bd} \tag{36}$$

$$\frac{dp_f}{dt} = \frac{a + bc}{1 - bd} \tag{37}$$

These two equations are explicit differential equations. There are many integration methods to solve them. For example, explicit Runge–Kutta methods are the easiest methods to implement.

The pressure and temperature change in the volume VA is shown in Fig. 4. It can be seen that fast pressure transients pro-

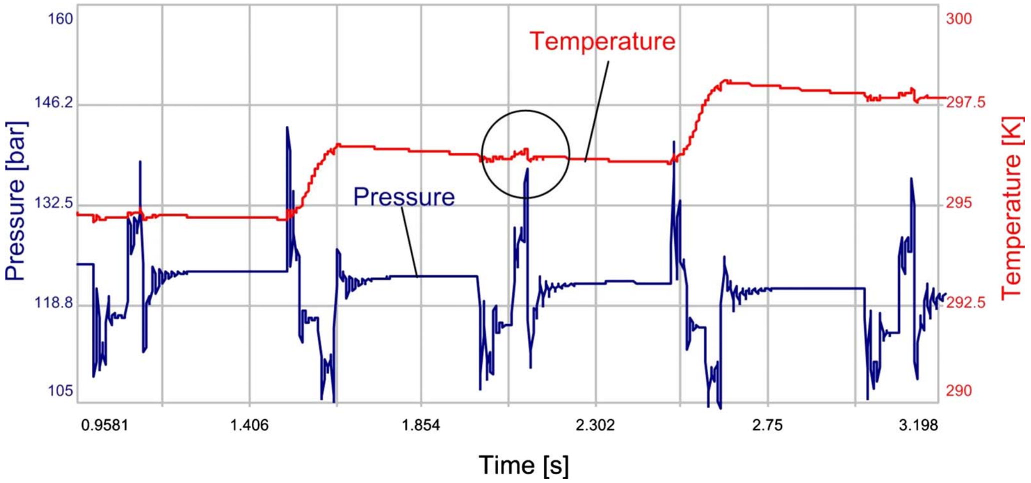

Fig. 4 Pressure and temperature response

duce fast temperature transients. Typical values of heat transfer coefficients can be obtained from correlations in Ref. [3]. More accurate coefficients need to be obtained by experiments, however. As is shown in Fig. 4, the vibration frequency of the pressure is very high. The pressure vibration produces temperature vibration, which is easily seen from the circled curves.

The expressions on the right hand side of Eqs. (36) and (37) are complex because the symbols $\{a,b,c,d\}$ are functions of pressure and temperature. So the expressions $\{(1-bd),ad,bc,c+ad,a+bc\}$ have to be calculated in each time step. This is time consuming because the integration step is very small (usually less than $\times 10^{-5}$ s) and the vibration amplitude of temperature is smaller than that of pressure: it can be assumed that the pressure derivative in step k is affected by the temperature derivative in step $k-1$ as follows:

$$\left.\frac{dp}{dt}\right|_{k} = a + b \left.\frac{dT}{dt}\right|_{k-1} \tag{38}$$

$$\left.\frac{dT}{dt}\right|_{k} = c + d \left.\frac{dp}{dt}\right|_{k} \tag{39}$$

The pressure and temperature change in the volume VA calculated by Eqs. (38) and (39) is shown in Fig. 5. It can be seen that there are almost no differences between Figs. 4 and 5. However, the calculation time for the right hand side of Eqs. (38) and (39) is less than that of Eqs. (36) and (37). So usually Eqs. (36) and (37) can be substituted by Eqs. (38) and (39) for thermal-hydraulic calculation.

However, in many cases, the temperature vibration affected by pressure transients is not important. The trend of temperature change in the whole working time is the main focus. In this kind of condition, the cross coupling of pressure and temperature can be neglected. Because b and d are much smaller than a and c (usually less than 1×10^{-7} s), the differential equation can be simplified as

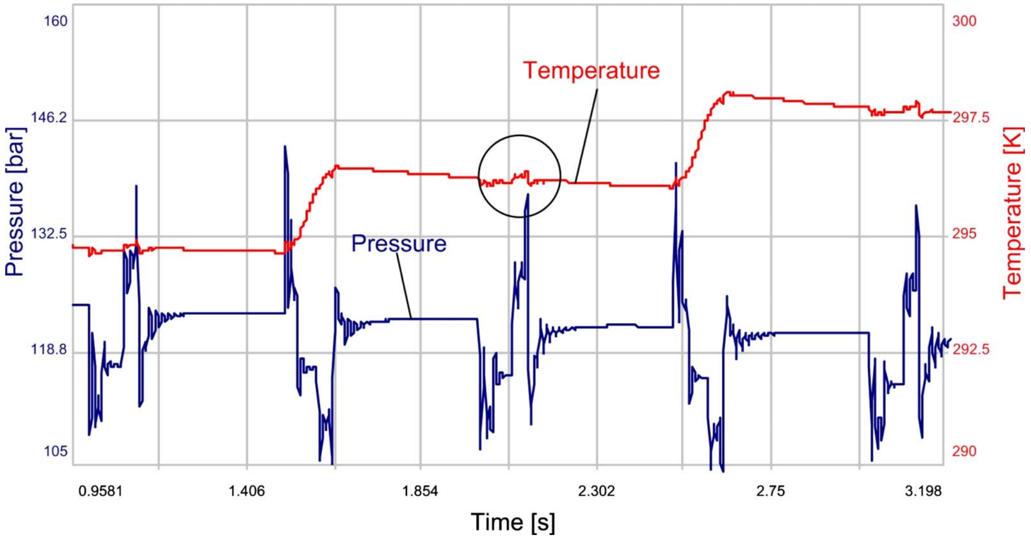

Fig. 5 Pressure and temperature response

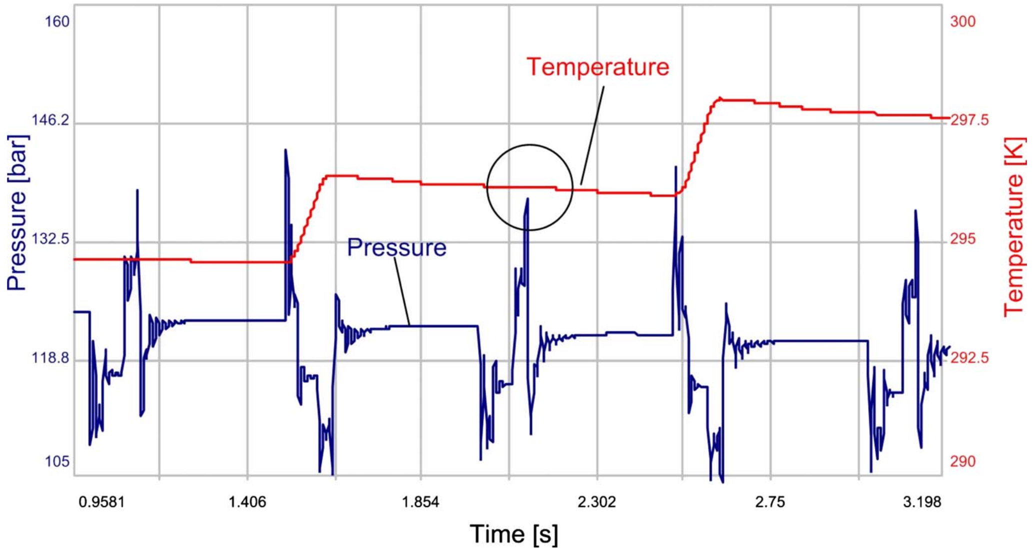

Fig. 6 Pressure and temperature response

$$\frac{dT}{dt} = c \tag{40}$$

$$\frac{dp}{dt} = a \tag{41}$$

The pressure and temperature change in the volume VA are shown in Fig. 6. It can be seen from the circled curves that fast pressure transients do not produce fast temperature transients. The cross coupling is not shown, but the temperature trend is the same as Fig. 4 or 5. The calculation time of this method is much reduced.

So if the thermal-hydraulic system is simulated, the above three calculation methods can be selected based on the research demand. The test results of elapsed physical time of 5 s are in Table 1. This test was done on a computer with an Intel CPU operating at 1.86 GHz with Windows XP operating system.

The values listed in Table 1 are only typical value references. They will vary according to the complexity of components' models and system configurations. Although it seems that there is not much difference in the elapsed time listed in the table, the simulation time is often very long (may be several hours) and so the difference of the elapsed time for simulation will be very much (may be hours).

Nomenclature

A = area
c_p = specific heat at constant pressure
C_d = flow coefficient
E = energy
U = internal energy
h = specific enthalpy

Table 1 Elapsed time for simulation

Applied equations	Eqs. (36) and (37)	Eqs. (40) and (41)	Eqs. (38) and (39)
Elapsed time (s)	36.928	32.719	33.250

k = heat transfer coefficient
m = mass
$\dot{m}$ = mass flow rate
p = fluid pressure
$\dot{Q}$ = heat flow rate
T = temperature
u = specific internal energy
V = fluid volume
$\dot{W}$ = rate of work
α_p = cubical expansion coefficient
β_T = bulk modulus
Δp = pressure difference
ρ = fluid density
υ = specific volume
η = dynamic viscosity
t = time

Subscripts

f = fluid
w = wall
fw = fluid/wall
in = inlet
out = outlet

References

[1] Engelhardt, J., 2000, "Thermal Simulation of an Aircraft Fluid Power System With Hydraulic-Electrical Power Conversion Units," *Proceedings of the First FPNI-PhD Symposium*, 435–448.
[2] Sidders, J. A., Tilley, D. G., and Chapple, P. J., 1996, "Thermal-Hydraulic Performance Prediction in Fluid Power Systems," Proc. Inst. Mech. Eng., IMechE Part I **210**(14), pp. 231–242.
[3] Storck, K., 1998, "Thermal System Analysis—Heat Transfer in Glass Forming and Fluid Temperature-Control Systems," Linköping University, Linköping, Sweden.
[4] Torben, O. A., and Michael, R. H., 2003, *Fluid Power Systems, Modeling and Analysis*, 2nd ed., Aalborg University, Denmark.
[5] IMAGINE S.A., 2000, *Thermal-Hydraulic Library User Manual*.
[6] Van Wylen, G. P., and Sonntag, R. E., 1985, *Fundamentals of Classical Thermodynamics*, 3rd ed., Wiley, New York.
[7] Sears, F. W., and Salinger, G. L., 1975, *Thermodynamics, Kinetic Theory and Statistical Thermodynamics*, 3rd ed., Addison-Wesley, Reading, MA.
[8] Chenggong, L., 2007, *Thermal-Hydraulic System Analysis for Aircrafts*, Beihang University, Beijing, China.

Exergy Analysis of Condensation of a Binary Mixture With One Noncondensable Component in a Shell and Tube Condenser

Y. Haseli
e-mail: yousef.haseli@mycampus.uoit.ca

I. Dincer[1]
e-mail: ibrahim.dincer@uoit.ca

G. F. Naterer
e-mail: greg.naterer@uoit.ca

Faculty of Engineering and Applied Science,
University of Ontario Institute of Technology,
2000 Simcoe Street North,
Oshawa, ON, L1H 7K4, Canada

The exergy (second-law) efficiency is formulated for a condensation process in a shell and one-path tube exchanger for a fixed control volume. The exergy efficiency η_{ex} is expressed as a function of the inlet and outlet temperatures and mass flow rates of the streams. This analysis is utilized to assess the trend of local exergy efficiency along the condensation path and evaluate its value for the entire condenser, i.e., overall exergy efficiency. The numerical results for an industrial condenser, with a steam-air mixture and cooling water as working fluids, indicate that η_{ex} is significantly affected by the inlet cooling water and environment temperatures. Further investigation shows that other performance parameters, such as the upstream mixture temperature, air mass flow rate, and ratio of cooling water mass flow rate to upstream steam mass flow rate, do not have considerable effects on η_{ex}. The investigations involve a dimensionless ratio of the temperature difference of the cooling water and environment to the temperature difference of condensation and the environment. Numerical results for various operational conditions enable us to accurately correlate both the local and overall exergy efficiency as linear functions of dimensionless temperature. [DOI: 10.1115/1.2909610]

Keywords: exergy efficiency, condensation, steam-air mixture, shell and tube condenser

1 Introduction

Exergy is a measure of the departure of the state of a system from that of the environment. It can be defined as the maximum obtainable work from the combination of the system and its environment. Unlike energy, exergy is not conserved; indeed, it is destroyed by irreversibilities. The exergy destruction during a process is proportionally related to the entropy generation due to these irreversibilities. Dincer [1] has conceptually discussed exergy from several perspectives and introduced an exergy analysis method as a useful tool for furthering the goal of more efficient energy-resource use.

Utilization of the exergy method in heat exchangers has been previously examined by different authors. Akpinar [2] experimentally studied the effects on heat transfer, friction factor, and dimensionless exergy loss by mounting helical (spring shaped) wires of different pitches in the inner pipe of a double-pipe heat exchanger. The effects of process parameters, such as mass flow rate and temperature, on the entropy generation and exergy loss were theoretically and experimentally investigated by Naphon [3] for a horizontal concentric tube heat exchanger. In the work of San and Jan [4] on a wet cross-flow heat exchanger, effectiveness, exergy recovery factor, and second-law efficiency of a wet heat exchanger were individually defined and numerically analyzed for various operating conditions. Additionally, the exergy-based thermoeconomic methodology has been developed in Refs. [5,6] for optimization purposes.

A detailed review of past literature indicates that past studies provide limited information about the second-law efficiency trends in a heat exchanger, particularly in condensers that are widely used in process and power industries. To the best knowledge of the authors, no post data have been presented with an exergy analysis for this type of heat exchanger. Therefore, the aim of this article is to assess the exergy efficiency for condensation of a pure vapor in a horizontal shell and tube condenser and evaluate its trend along the condensation path, particularly including the effects of a noncondensable gas on the heat and mass transfer.

2 Formulation of Exergy Efficiency

The objective of this section is to derive the exergy (second-law) efficiency for condensation of a vapor, taking into account the presence of noncondensing gas, in a shell and one-path tube condenser. The steady-state exergy rate balance for a control volume, shown in Fig. 1, can be written as (for details, see Ref. [7])

$$\dot{E}_d = \sum_{1} \dot{m}_1 e_1 - \sum_{2} \dot{m}_2 e_2 \tag{1}$$

The term $\dot{E}_d$ accounts for the time rate of exergy destruction due to irreversibilities within the control volume and e denotes the specific flow exergy. Subscripts 1 and 2 refer to the inlet and outlet, respectively. Hence,

$$\dot{E}_{\text{in}} = \sum_{1} \dot{m}_1 e_1 = \dot{m}_{v1} e_{v1} + \dot{m}_{g1} e_{g1} + \dot{m}_{c1} e_{c,1} \tag{2}$$

$$\dot{E}_o = \sum_{2} \dot{m}_2 e_2 = \dot{m}_{v2} e_{v2} + \dot{m}_{g2} e_{g2} + \dot{m}_{c2} e_{c2} + \dot{m}_{\text{cond}} e_{\text{cond}} \tag{3}$$

where $\dot{m}_{g1}=\dot{m}_{g2}=\dot{m}_g$ and $\dot{m}_{c1}=\dot{m}_{c2}=\dot{m}_c$.

In addition, with respect to the mass conversation of vapor, $\dot{m}_{v1}=\dot{m}_{v2}+\dot{m}_{\text{cond}}$, Eq. (1) becomes

$$\begin{aligned}\dot{m}_{v2}(e_{v1}-e_{v2}) + \dot{m}_g(e_{g1}-e_{g2}) + \dot{m}_{\text{cond}}(e_{v1}-e_{\text{cond}}) \\ = \dot{m}_c(e_{c2}-e_{c1}) + \dot{E}_d\end{aligned} \tag{4}$$

The second-law efficiency, i.e., exergy efficiency, can now be defined as

$$\eta_{\text{ex}} = \frac{E_o}{E_{\text{in}}} = \frac{\dot{m}_c(e_{c2}-e_{c1})}{\dot{m}_{v2}(e_{v1}-e_{v2}) + \dot{m}_g(e_{g1}-e_{g2}) + \dot{m}_{\text{cond}}(e_{v1}-e_{\text{cond}})} \tag{5}$$

Using standard thermodynamic relations, it can be shown that the flow exergy change in the coolant, vapor, and noncondensable gas in Eq. (5) can be formulated as follows:

$$e_{c2} - e_{c1} = c_{p,c}\left[(T_{c2}-T_{c1}) - T_o \ln\left(\frac{T_{c2}}{T_{c1}}\right)\right] \tag{6}$$

$$e_{v1} - e_{v2} = c_{p,v}\left[(T_{v1}-T_{v2}) - T_o \ln\left(\frac{T_{v1}}{T_{v2}}\right)\right] + T_o R_v \ln\left(\frac{P_{v1}}{P_{v2}}\right) \tag{7}$$

---

[1] Corresponding author.

Contributed by the Heat Transfer Division of ASME for publication in the Journal of Heat Transfer. Manuscript received May 11, 2007; final manuscript received August 29, 2007; published online June 2, 2008. Review conducted by Giulio Lorenzini.

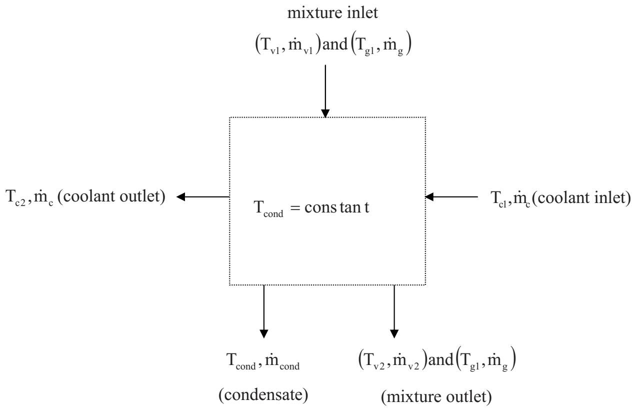

Fig. 1 An arbitrary control volume of the condenser, illustrating the inlet and outlet flows

$$e_{g1} - e_{g2} = c_{p,g}\left[(T_{g1} - T_{g2}) - T_o \ln\left(\frac{T_{g1}}{T_{g2}}\right)\right] + T_o R_g \ln\left(\frac{P_{g1}}{P_{g2}}\right) \tag{8}$$

In the bulk mixture, it is assumed that the temperature is uniform, so that vapor and noncondensable gas temperatures are the same in the inlet and outlet of the control volume, i.e., $T_{v1}=T_{g1}$ and $T_{v2}=T_{g2}$. Also,

$$e_{v1} - e_{\text{cond}} = h_{v1} - h_{\text{cond}} - T_o(s_{v1} - s_{\text{cond}}) \tag{9}$$

As condensation occurs at $T_{\text{cond}} \leqslant T_{v1}$, the difference between the inlet enthalpy of vapor at a temperature of T_{v1} and the condensate enthalpy is determined by the sum of heat transfer rates from cooling of the vapor from T_{v1} to T_{cond} and latent heat released at the condensation temperature. It may be written in the form of the following expression:

$$h_{v1} - h_{\text{cond}} = c_{p,v}(T_{v1} - T_{\text{cond}}) + h_{\text{fg}} \tag{10}$$

Furthermore, entropy of the inlet vapor, s_{v1}, may be expressed as the sum of the entropy difference due to the temperature difference $T_{v1}-T_{\text{cond}}$ at constant pressure P_{v1} and the entropy of saturated vapor at a temperature of T_{cond}, $s_{v|T=T_{\text{cond}}}$. Hence, the entropy difference in Eq. (9) can be written as

$$s_{v1} - s_{\text{cond}} = \Delta s_v + s_{v|T=T_{\text{cond}}} - s_{\text{cond}|T=T_{\text{cond}}} = c_{p,v} \ln\left(\frac{T_{v1}}{T_{\text{cond}}}\right) + s_{\text{fg}|T=T_{\text{cond}}} \tag{11}$$

Substituting Eqs. (10) and (11) into Eq. (9) yields

$$e_{v1} - e_{\text{cond}} = c_{p,v}\left[(T_{v1} - T_{\text{cond}}) - T_o \ln\left(\frac{T_{v1}}{T_{\text{cond}}}\right)\right] + h_{\text{fg}|T=T_{\text{cond}}} - T_o s_{\text{fg}|T=T_{\text{cond}}} \tag{12}$$

It should be noted that h_{fg} and s_{fg} are dependent on the saturation temperature. It is seen that the exergy efficiency in Eq. (5) can be expressed as a function of the inlet and outlet temperatures and mass flow rates of the streams.

3 Results and Discussion

This section presents a numerical evaluation of the exergy efficiency for a typical horizontal counter-current shell and one-path tube condenser, which is a TEMA "E" shell condenser of almost standard industrial design. The condenser has an exchange area of 30 m^2, with a 0.438 m diameter and 2.438 m length [8]. Table 1 gives the measured operational parameters with a steam-air mixture and cooling water as working fluids, resulting from a sample run.

Table 1 Inlet and outlet parameters of a typical condenser [8]

Quantity	Inlet	Outlet
Steam-air mixture temperature (°C)	125	29.30
Steam mass flow rate (kg/s)	1	0.01
Air mass flow rate (kg/s)	0.092	0.092
Cooling water temperature (°C)	10.50	20.05
Cooling water mass flow rate (kg/s)	62.5	
Condenser pressure (kPa)	18.2	

Equations (5)–(12) can be utilized to evaluate either exergy efficiency along the condensation path (local exergy efficiency) or the entire condenser (overall exergy efficiency). The results will be presented for both cases in the following sections. In the first case, one needs to obtain the variation of temperatures (including the shell side, tube side, and condensate) along the condensation path. For this purpose, the numerical model of Haseli and Roudaki [8], which uses heat and mass transfer equations of classical film theory, is utilized to determine the relevant parameters. The previous exergy methodology extends the past model of Haseli and Roudaki [8] to obtain the variation of exergy efficiency along the condenser. In order to determine the overall exergy efficiency of the condenser, one must use the outlet values of temperatures and mass flow rates, as well as the appropriate average condensation temperature resulting from the above mentioned model.

Figure 2 illustrates the variation of exergy efficiency η_{ex} along the condensation path at three different inlet cooling water temperatures and various environment temperatures. In Figs. 2(*a*)–2(*c*), a higher environment temperature at a constant inlet cooling water temperature results in a lower exergy efficiency along the condenser. In other words, as the temperature difference between the inlet cooling water and environment, i.e., $\Delta T = T_{c,\text{in}} - T_o$, decreases, then η_{ex} is reduced. It can also be seen that there are two types of curves. In the first group, η_{ex} decreases from the entrance of the steam-air mixture to the location after the midpoint in the condenser; a region around the fifth baffle space. Then, it starts to increase from this point to the outlet of the heat exchanger. In the second type of curves, however, η_{ex} continuously decreases along the condensation path (the lowest curves in Figs. 2(*b*) and 2(*c*)). It seems that there is a relation between the condensation heat transfer and η_{ex}. Past studies [8,9] have shown that from the region where exergy efficiency is a minimum, the condensation and heat transfer rates significantly diminish. Beyond this region, the relative role of sensible heat transfer increases.

As ΔT increases, η_{ex} becomes higher. This result agrees with the definition of exergy. When a system carries more exergy, it deviates more from the environment. Based on these results, it may be well understood why η_{ex} decreases from the entrance of the steam-air mixture to around the fifth baffle space, considering the configuration of the condenser in this study, which has a counterflow type. In other words, as cooling water flows in the opposite direction of the steam-air mixture, its temperature increases from the last baffle space to the first one where the mixture enters the heat exchanger. Thus, at a given environment temperature, the local $\Delta T = (T_c - T_o)$ will increase in the same direction. Except the region where the first group of curves of Fig. 2 has a positive slope, it seems that the local ΔT plays a dominant role in the variation of η_{ex}. It may be inferred that there exists another parameter that has a significant effect on the exergy efficiency.

Further investigation has been performed by evaluating the effects of other performance parameters, e.g., upstream mixture temperature, air mass flow rate, and the ratio of cooling water mass flow rate to the upstream steam mass flow rate. The variation of η_{ex} along the condenser at four different upstream mixture temperatures is represented in Fig. 3. Desuperheating the upstream mixture does not considerably affect the exergy efficiency. Since the condensation of steam is the predominant source of heat

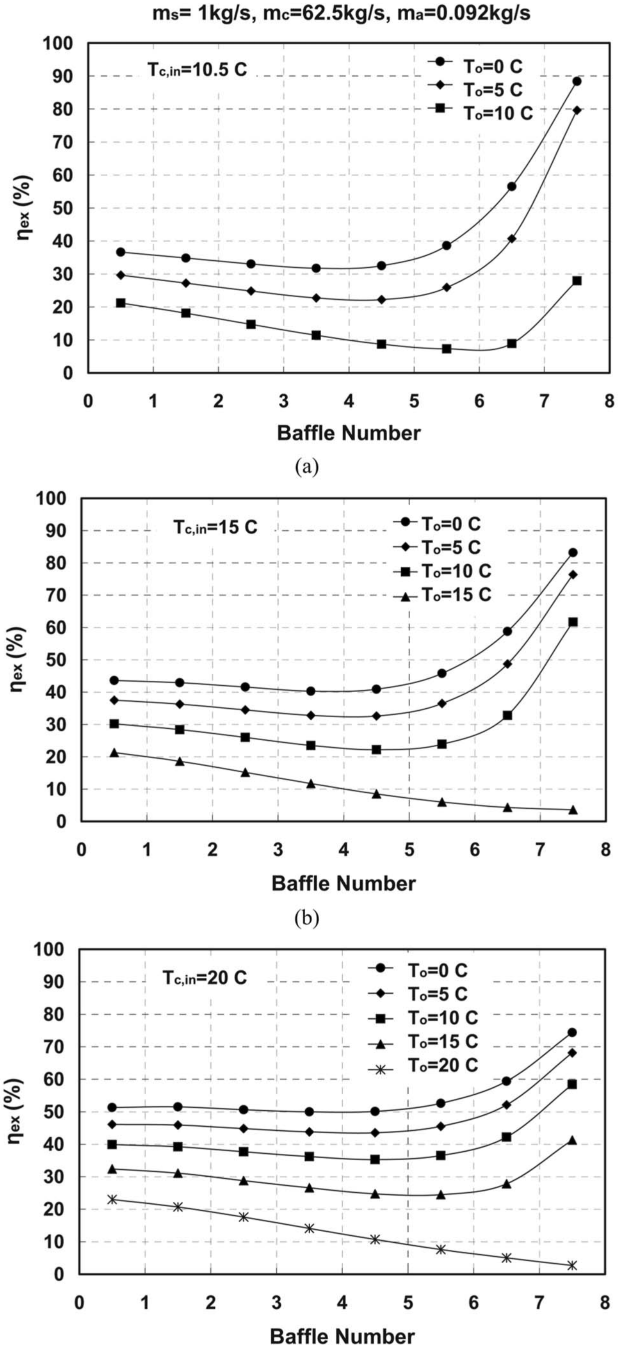

(a)

(b)

(c)

Fig. 2 Variation of exergy efficiency with environment temperature along the condensation path at different inlet cooling water temperatures: (*a*) 10.5°C, (*b*) 15°C, and (*c*) 20°C

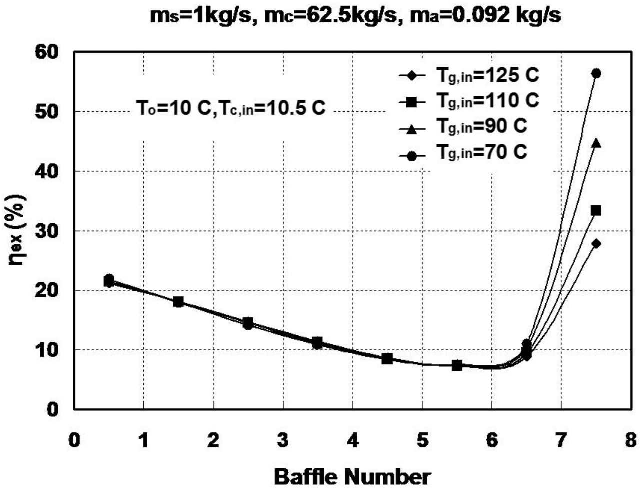

Fig. 3 Variation of exergy efficiency along the condensation path at different upstream steam-air mixture temperatures

transfer, a change in upstream mixture temperature does not have a significant effect on the heat transfer rate. Therefore, the temperature gradient of the cooling water does not significantly change. Likewise, an inconsistent result in the last baffle space is observed, which confirms that in addition to ΔT, there appears to be another factor that influences η_{ex}.

Figure 4 shows the effect of air mass flow rate on η_{ex} and it reveals that higher exergy efficiency may result from higher air leakage. The predicted outlet steam mass flow rates are also given in Fig. 4. Air is a noncondensable component that provides resistance to heat and mass transfer processes. Increasing the air mass flow rate leads to a lower heat transfer rate and condensation rate. Further discussion may be found elsewhere (such as Ref. [9]). A possible reason, which can now clarify the trend of the first group in Figs. 2 and 3, is that as long as all steam has not condensed, η_{ex} decreases along the condensation path. When condensation of steam almost finishes (usually by the last baffle space), η_{ex} tends to increase.

Figure 5 illustrates the effect of the ratio of the cooling water mass flow rate to the upstream steam mass flow rate R_m, on the exergy efficiency, in the range of 0.82–1.12 kg/s for the upstream steam mass flow rate. In accordance with the conservation of energy, a lower R_m causes a larger temperature gradient of cooling water. Thus, at a constant environment temperature, the corresponding exergy efficiency profile of the warmer cooling water (which carries more exergy) is higher. On the other hand, it is seen that the upstream mass flow rate of steam does not have a significant effect on η_{ex}. Nevertheless, the resulting graphs are not consistent in the last baffle space, whereby at a given ratio of mass flow rate, depending on the upstream steam mass flow rates, the exergy efficiency has a different value. The higher position of the process condition belongs to the lower upstream steam flow rate. This agrees with the earlier discussion of the previous paragraph.

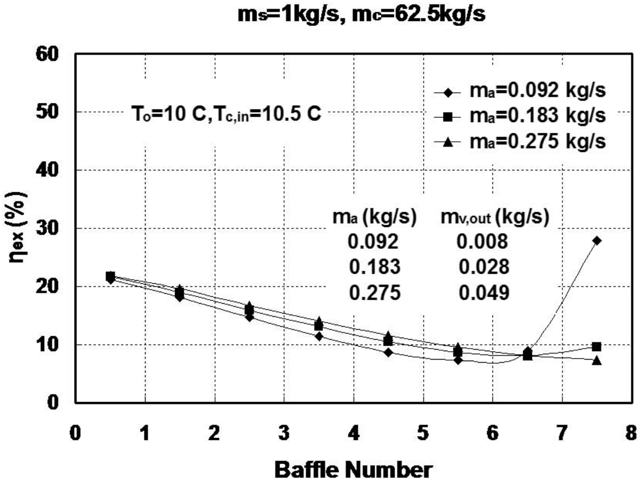

Fig. 4 Effect of air mass flow rate on exergy efficiency along the condensation path and predicted outlet steam mass flow rates

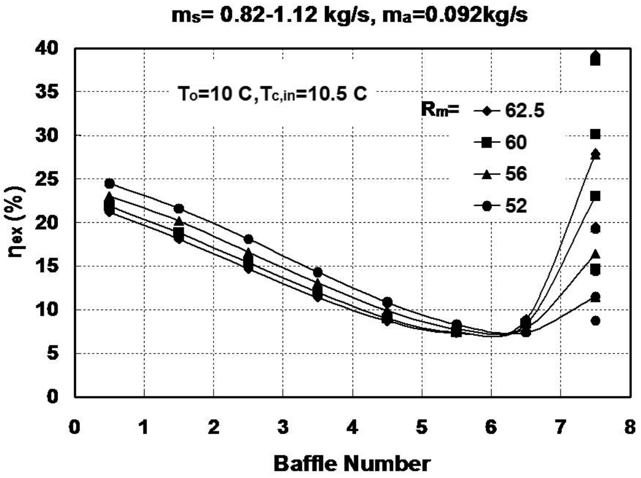

Fig. 5 Effect of the ratio of cooling water mass flow rate to upstream steam mass flow rate R_m on exergy efficiency

Based on these results, it may be inferred that the difference between cooling water and environment temperatures, as the first main factor, has a direct effect on the local exergy efficiency. Further numerical studies have been performed at different operational conditions to show that there is a consistent relation between the local exergy efficiency and dimensionless temperature θ defined as

$$\theta = \frac{T_{c1} - T_o}{T_{\text{cond}} - T_o} \tag{13}$$

where T_{cond} denotes the condensation temperature in the arbitrary control volume shown in Fig. 1.

The variation of η_{ex} versus θ is investigated for the following conditions, and the results are presented in Fig. 6: $m_a = 0.092-0.0275$ kg/s, $R_m = 52-62.5$, $T_{g,\text{in}} = 65-125°\text{C}$, and $T_{c,\text{in}} = 10-25°\text{C}$, respectively. A linear relation between η_{ex} and θ can be seen. The following correlation is proposed with less than 3% error:

$$\eta_{\text{ex}} = 1.2166\theta + 0.0075 \tag{14}$$

Furthermore, in order to observe the variation of overall exergy efficiency with dimensionless temperature, a similar investigation is performed at the following process situations: $m_a = 0.092-0.0275$ kg/s, $R_m = 52-62.5$, $T_{g,\text{in}} = 65-125°\text{C}$, and $T_{c,\text{in}} = 10-30°\text{C}$, respectively. Figure 7 shows the variation of $\eta_{\text{ex,overall}}$ against dimensionless temperature. The following correlation is obtained from the results, which predicts $\eta_{\text{ex,overall}}$ with less than 1% error:

$$\eta_{\text{ex,overall}} = 0.9677\theta + 0.1939 \tag{15}$$

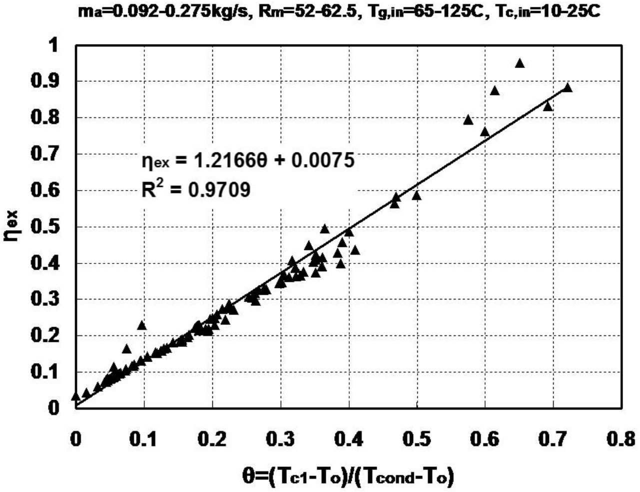

Fig. 6 Dependence of the local exergy efficiency on dimensionless temperature defined in Eq. (13)

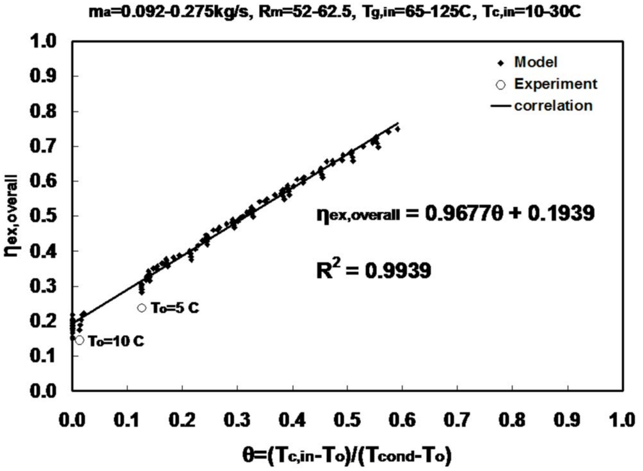

Fig. 7 Variation of overall exergy efficiency with dimensionless temperature

The real operating point of the system (based on Table 1) at two different ambient temperatures is located very close to the predicted values. In the limiting case of an ideal process without irreversibilities, i.e. $\dot{E}_d = 0$, the exergy efficiency is unity and the upper limits for θ are obtained as 0.816 and 0.833, respectively, from Eqs. (14) and (15).

4 Conclusions

The second-law (exergy) efficiency has been formulated for condensation of a binary mixture with one noncondensable component in a shell and one-path tube condenser. The exergy efficiency may be expressed as a function of inlet and outlet temperatures and mass flow rates of both streams across the boundary of a control volume, as well as the condensation temperature. Numerical results were obtained from an exergy formulation using some past data for an industrial scale countercurrent condenser, where condensation of steam occurs in the presence of air with cooling water as a coolant. The results show that temperature difference between cooling water and the environment has a dominant effect on the exergy efficiency. In addition, when the temperatures of the cooling water and environment are not equal, the exergy efficiency decreases along the heat exchanger, as long as condensation of steam occurs. Further investigations show a consistent relation between both local and overall exergy efficiencies and dimensionless temperature, which is defined as the ratio of the temperature difference of the cooling water and environment, to the temperature difference of the condensation and the environment.

Acknowledgment

The authors acknowledge the support provided by the Atomic Energy of Canada Limited and the Ontario Research Excellence Fund.

Nomenclature

c_p = specific heat, kJ/kg K
e = flow exergy, kJ/kg
$\dot{E}_d$ = exergy destruction rate, kW

$\dot{E}_{\text{in}}$ = input exergy rate, kW
$\dot{E}_o$ = output exergy rate, kW
h = enthalpy, kJ/kg
h_{fg} = condensation latent heat, kJ/kg
$\dot{m}$ = mass flow rate, kg/s
P = pressure, kP
R = gas constant, kJ/kg K
R_m = ratio of cooling water mass flow rate to upstream steam mass flow rate
s = entropy, kJ/kg K
s_{fg} = latent entropy, kJ/kg
T = temperature, °C
T_o = dead state/environment temperature, °C

Greek Letters

ΔT = difference between cooling water temperature at the inlet of control volume and environment temperature
θ = dimensionless temperature, Eq. (13)
η_{ex} = exergy efficiency
$\eta_{\text{ex,overall}}$ = overall exergy efficiency

Subscripts

c = coolant
cond = condensate
g = noncondensable gas
i = inlet
o = outlet
v = vapor

References

[1] Dincer, I., 2002, "The Role of Exergy in Energy Policy Making," Energy Policy, **30**, pp. 137–149.
[2] Akpinar, E. K., 2006, "Evaluation of Heat Transfer and Exergy Loss in a Concentric Double Pipe Exchanger Equipped With Helical Wires," Energy Convers. Manage., **47**, pp. 3473–3486.
[3] Naphon, P., 2006, "Second Law Analysis on the Heat Transfer of the Horizontal Concentric Tube Heat Exchanger," Int. Commun. Heat Mass Transfer, **33**, pp. 1029–1041.
[4] San, J. Y., and Jan, C. L., 2000, "Second-Law Analysis of a Wet Crossflow Heat Exchanger," Energy, **25**, pp. 939–955.
[5] Selbaş, R., Kızılkan, O., and Şencan, A., 2006, "Thermoeconomic Optimization of Subcooled and Superheated Vapor Compression Refrigeration Cycle," Energy, **31**, pp. 1772–1792.
[6] Accadia, M. D., Fichera, A., Sasso, M., and Vidiri, M., 2002, "Determining the Optimal Configuration of a Heat Exchanger (With a Two-Phase Refrigerant) Using Exergoeconomics," Appl. Energy, **71**, pp. 191–203.
[7] Moran, M. J., and Shapiro, H. N., 2004, *Fundamental of Engineering Thermodynamics*, 5th ed., Wiley, Hoboken, NJ..
[8] Haseli, Y., and Roudaki, S. J. M., 2004, "A Calculation Method for Analysis Condensation of a Pure Vapor in the Presence of a Non-Condensable Gas on a Shell and Tube Condenser," *Proceedings of the ASME Heat Transfer/Fluids Engineering Summer Conference*, Charlotte, NC, Vol. 3, pp. 155–163.
[9] Haseli, Y., and Roudaki, S. J. M., 2003, "Simultaneous Modeling of Heat and Mass Transfer of Steam-Air Mixture on a Shell and Tube Condenser Based on Film Theory," *Proceedings of the ASME Summer Heat Transfer Conference*, Las Vegas, NV, Vol. 2, pp. 251–259.

Heat Transfer Enhancement in Combined Convection Around a Horizontal Cylinder Using Nanofluids

E. Abu-Nada[1]
e-mail: eiyad@hu.edu.jo

K. Ziyad

M. Saleh

Y. Ali

Department of Mechanical Engineering,
Hashemite University,
Zarqa 13115, Jordan

Heat transfer enhancement in combined convection around a rotating horizontal cylinder using nanofluids is presented. The transport equations are solved numerically using a second-order finite volume scheme. Water-based nanofluid containing various volume fractions of different types of nanoparticles is used. The nanoparticles used are Cu, Ag, Al_2O_3, and TiO_2. In the region outside the plume, the Nusselt number increases by increasing the volume fraction of nanoparticles. However, in the plume region, the effect of the volume fraction of nanoparticles on the Nusselt number is less pronounced. [DOI: 10.1115/1.2909616]

Keywords: nanofluids, heat transfer enhancement, mixed convection, horizontal cylinder

1 Introduction

Heat transfer from a horizontal heated cylinder has many engineering applications such as heat exchangers, piping systems, solar collectors, and electric conductors. Some of these applications depend on natural convection as the main heat transfer mechanism, while others depend on forced convection for heat removal. It is important to understand the thermal behavior of such systems when both forced and natural convections simultaneously take place.

The geometrical shape of the cylinder creates nonuniformity in heat transfer around the cylinder surface. With a better understanding of the flow field behavior around the cylinder, it is possible to devise methods for heat transfer enhancement. An innovative technique for improving heat transfer, by using ultrafine solid particles in the base fluids, has been extensively used during the past decade. The term nanofluid refers to these kinds of fluids by suspending nanoscale particles in the base fluid [1,2]. Recently, Trisaksri and Wongwises [3] conducted a literature review on the general heat transfer characteristics of nanofluids. Daungthongsuk and Wongwises [4] performed a comprehensive review of convective heat transfer of nanofluids. Moreover, Wang and Mujumdar [5] conducted a review of heat transfer characteristics of nanofluids. Based on the mentioned reviews, the application of nanofluids in mixed convection applications is very limited. Therefore, the goal of this work is to study heat transfer characteristics of mixed convection around a horizontal heated rotating cylinder using different types of nanoparticles. The horizontal cylinder was selected as an example for studying the effect of nanoparticles in mixed convection application because there is a large variation in heat transfer rates around the cylinder surface in the tangential direction. Therefore, it is very useful to examine the effectiveness of nanoparticles in a medium that experience large variation in heat transfer (or temperature gradients). The problem will be investigated numerically by solving the Navier–Stokes and energy equations (NSE). Heat transfer characteristics will be analyzed for a wide range of volume fraction of nanoparticles using different types of nanoparticles.

2 Problem Description, Governing Equations, and Numerical Implementation

Figure 1 shows a schematic diagram of the cylinder and the physical flow field. Water-based nanofluid containing nanoparticles exists around the cylinder. The nanoparticles that are used are Cu, Ag, Al_2O_3, and TiO_2. The nanofluid is assumed incompressible, and the flow is assumed steady. It is assumed that the base fluid (i.e., water) and the nanoparticles are in thermal equilibrium and no slip occurs between them. Thermophysical properties of the nanoparticles can be found in Ref. [6]. The thermophysical properties of the nanofluid are assumed to be constant except for the density variation, which is approximated by the Boussinesq model. The cylinder surface is maintained at a constant temperature (T_w) higher than the ambient temperature (T_∞). The nondimensional governing equations for the laminar mixed convection around the cylinder in terms of stream function-vorticity formulation are as follows: vorticity equation:

$$\begin{aligned}\frac{\partial}{\partial\xi}\left(\omega\frac{\partial\Psi}{\partial\eta}\right)-\frac{\partial}{\partial\eta}\left(\omega\frac{\partial\Psi}{\partial\xi}\right) &= \frac{1}{\mathrm{Re}}\left[\frac{1}{(1-\varphi)^{0.25}\left((1-\varphi)+\varphi\dfrac{\rho_s}{\rho_f}\right)}\right]\left(\frac{\partial^2\omega}{\partial\xi^2}+\frac{\partial^2\omega}{\partial\eta^2}\right)\\ &\quad + E\frac{\mathrm{Gr}}{\mathrm{Re}^2}\left[\frac{1}{\dfrac{(1-\varphi)}{\varphi}\dfrac{\rho_f}{\rho_s}+1}\frac{\beta_s}{\beta_f}+\frac{1}{\dfrac{\varphi}{(1-\varphi)}\dfrac{\rho_s}{\rho_f}+1}\right]\\ &\quad \times\left(\frac{\partial T}{\partial\xi}\sin\eta+\frac{\partial T}{\partial\eta}\cos\eta\right)\end{aligned} \tag{1}$$

energy equation:

$$\frac{\partial}{\partial\xi}\left(T\frac{\partial\Psi}{\partial\eta}\right)-\frac{\partial}{\partial\eta}\left(T\frac{\partial\Psi}{\partial\xi}\right) = \frac{\lambda}{\mathrm{Re\,Pr}}\left(\frac{\partial^2 T}{\partial\xi^2}+\frac{\partial^2 T}{\partial\eta^2}\right)+\frac{1}{\mathrm{Re\,Pr}}\left[\frac{\partial T}{\partial\xi}\frac{\partial\lambda}{\partial\xi}+\frac{\partial T}{\partial\eta}\frac{\partial\lambda}{\partial\lambda}\right] \tag{2}$$

kinematics equation:

$$\Omega=-\frac{1}{E^2}\left(\frac{\partial^2\Psi}{\partial\xi^2}+\frac{\partial^2\Psi}{\partial\eta^2}\right) \tag{3}$$

where λ is given as

$$\lambda=\frac{\dfrac{k_{\mathrm{nf}}}{k_f}}{(1-\varphi)+\varphi\dfrac{(\rho c_p)_s}{(\rho c_p)_f}} \tag{4}$$

In Eqs. (1)–(3), the viscosity of the nanofluid is approximated as viscosity of a base fluid μ_f containing dilute suspension of fine spherical particles and is given by [7]

$$\mu_{\mathrm{nf}}=\frac{\mu_f}{(1-\varphi)^{2.5}} \tag{5}$$

The density of the nanofluid is expressed as

---

[1] Corresponding author.

Contributed by the Heat Transfer Division of ASME for publication in the JOURNAL OF HEAT TRANSFER. Manuscript received June 20, 2007; final manuscript received September 27, 2007; published online June 4, 2008. Review conducted by Sung Jin Kim.

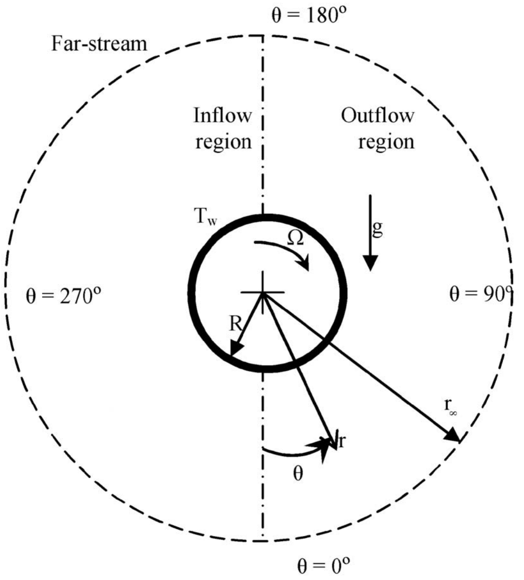

Fig. 1 Sketch of problem geometry

$$\rho_{\mathrm{nf}} = (1-\varphi)\rho_f + \varphi\rho_s \tag{6}$$

The heat capacitance of the nanofluid is expressed as [6]

$$(\rho c_p)_{\mathrm{nf}} = (1-\varphi)(\rho c_p)_f + \varphi(\rho c_p)_s \tag{7}$$

The effective thermal conductivity of the nanofluid is approximated by the Maxwell–Garnetts (MG) model [5,6]

$$\frac{k_{\mathrm{nf}}}{k_f} = \frac{k_s + 2k_f - 2\varphi(k_f - k_s)}{k_s + 2k_f + \varphi(k_f - k_s)} \tag{8}$$

The MG model is only restricted to spherical nanoparticles and does not take into account the shape of nanoparticles. It should be emphasized that macroscopic modeling of nanofluids is restricted to small temperature gradients [8]. Moreover, the MG model overestimates the enhancement in thermal conductivity for large concentration of nanoparticles. For high concentration of nanoparticles, the viscosity of the fluid increases and the assumption of constant fluid properties becomes less realistic. Besides, high values of Rayleigh numbers may not take place for dense and viscous mixture suspensions under a small temperature gradient.

Equations (1)–(3) are solved using the finite volume approach [9]. The diffusion term in the vorticity, energy, and kinematic equations is approximated by second-order central difference, which gives a stable solution. Furthermore, a second-order upwind differencing scheme is adopted for the convective terms. A fourth-order accurate formula for the vorticity boundary condition at the wall is adopted [10]. After solving Ψ, Ω, and T, further useful quantities are obtained. For example, Nusselt number can be expressed as

$$\mathrm{Nu} = -\frac{2}{\pi}\left(\frac{k_{\mathrm{nf}}}{k_f}\right)\frac{\partial T}{\partial \xi} \tag{9}$$

The average Nusselt number is evaluated as

$$\mathrm{Nu}_{\mathrm{av}} = \frac{\displaystyle\int_{\eta=0}^{\eta=2} \mathrm{Nu}(\eta)\,\mathrm{d}\eta}{2} \tag{10}$$

An extensive mesh testing procedure was conducted to guarantee a grid independence solution. Fourteen different mesh combinations were used for the case of Ri = 1.887 and Pr = 0.70. It was found that a grid size of 121 × 121 ensures a grid independence solution. The present numerical solution is validated by comparing the present code results using air, $\mathrm{Gr}_D/\mathrm{Re}_D^2 = 1.887$, and $\mathrm{Re}_D = 300$ to the experiment of Shimada et al. [11] and a good agreement is recorded.

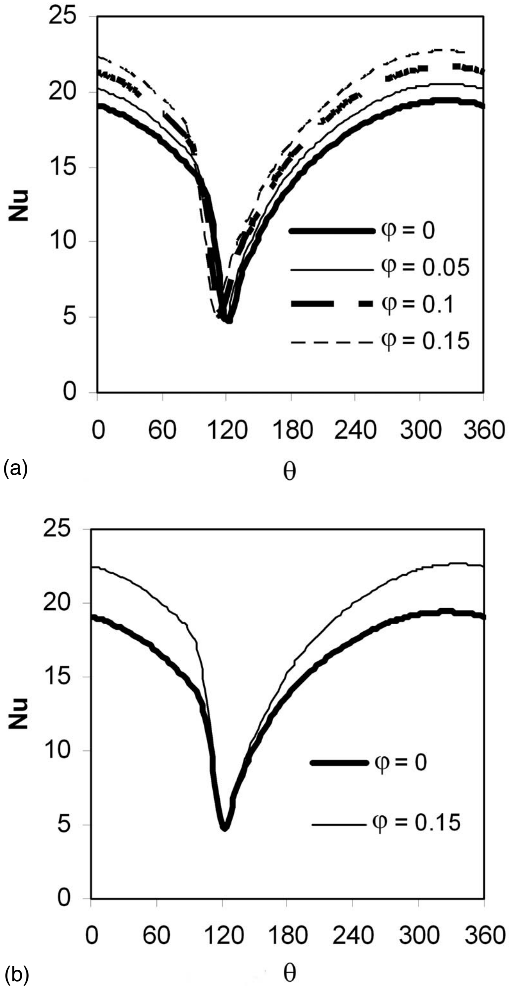

Fig. 2 (*a*) Nusselt number distribution around the cylinder surface using various volume fractions of Al_2O_3 nanoparticles: Pr = 6.2, Re_D = 300, and Ri = 1.887; (*b*) comparing the Nusselt number between pure water case and addition of 15% volume fraction of Al_2O_3 nanoparticles by overlapping plume regions in (*a*)

3 Results and Discussion

Figure 2(*a*) shows the variation of Nusselt number around the cylinder surface using various volume fractions of Al_2O_3 for the case of Ri = 1.887. It is shown that around the cylinder surface, and for any volume fraction of nanoparticles, there are places where the change in Nusselt number is moderate and places where the change is steep. The places with the steep change resemble the plume region. It is clear from Fig. 2(*a*) that the plume region is rotated in the clockwise direction by the presence of the nanoparticles and this rotation increases by increasing the volume fraction of the nanoparticles. As shown in Fig. 2(*a*), the case of $\varphi = 0.15$ is rotated by 12 deg from the pure water case in the clockwise direction. Also, Fig. 2(*a*) shows that in the region outside of the plume, the increase in volume fraction of the nanoparticles causes an increase in Nusselt number. However, within the plume region, the Nusselt is only shifted in the clockwise direction and its magnitude is almost not affected by the presence of the nanoparticles. This is clearly demonstrated in Fig. 2(*b*), where the two plume regions for the pure water case and $\varphi = 0.15$ are overlapped. This

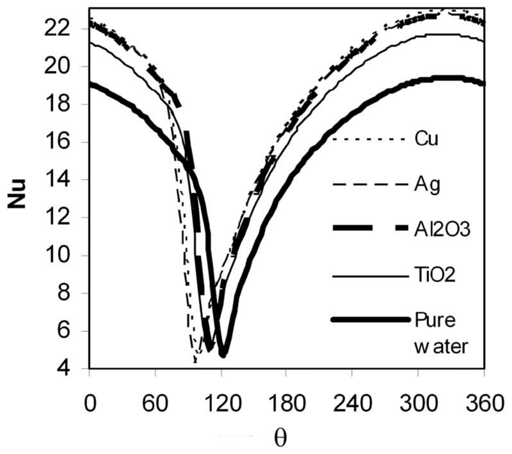

Fig. 3 Nusselt number distribution around the cylinder surface using various types of nanoparticles: $\varphi=0.15$, $Pr=6.2$, $Re_D=300$, and $Ri=1.887$

is done by rotating the curve of $\varphi=0.15$ by 12 deg in the counter clockwise direction. Figure 2(*b*) is very useful in characterizing places, where enhancements in heat transfer take place.

This behavior is furthermore explained by looking at Eq. (9). The equation shows that the Nusselt number is influenced by two parameters, which are the temperature gradient at the cylinder surface and the thermal conductivity ratio. As the percentage of the Al_2O_3 nanoparticles increases, the temperature gradient decreases. This decrease is due to the enhanced effective thermal conductivity of the nanofluid, which is accompanied by an increase in thermal diffusivity. The increase in thermal diffusivity causes a drop in the temperature gradients. The increase in thermal conductivity ratio is greater than the decrease in temperature gradient. Accordingly, the Nusselt number increases by increasing the volume fraction of the nanoparticles. However, within the plume region, the temperature gradient decrease becomes steeper for high volume fraction. This means that the reduction in temperature gradient becomes more pronounced and this reduction balances the enhancement in effective thermal conductivity, which explains the independency of the Nusselt number with the volume fraction of the nanoparticles in the plume region.

An interesting comparison between various nanofluids is presented in Fig. 3. It is interesting to note that on the cylinder surface, and outside the plume region, nanoparticles with high thermal conductivity experience high enhancements in heat transfer. Also, it is interesting to note that although Al_2O_3 has a low thermal conductivity, however, it still shows a comparable enhancement on heat transfer compared to the high thermal conductivity metals such as Cu or Ag. The thermal conductivity of Al_2O_3 is approximately one-tenth of Cu. However, the unique property that the Al_2O_3 poses (as well as TiO_2) is its low thermal diffusivity. The reduced value of thermal diffusivity means higher temperature gradients and therefore more enhancements in heat transfer. However, Cu and Ag have high values of thermal diffusivity and therefore this reduces temperature gradients, which will affect the performance of Cu and Ag nanoparticles. Therefore, to obtain a high Nusselt number requires a selection of nanoparticles that have high thermal conductivity as well as low thermal diffusivity. Low values of thermal diffusivity could be obtained by having high value of heat capacitance.

A careful inspection of Fig. 3 shows that for high thermal diffusivity nanoparticles, such as Cu, the plume size becomes larger; this means larger areas around the cylinder surface where the addition of nanoparticles becomes insignificant. By calculating the average Nusselt number around the cylinder surface, using Eq. (10), it is found that Al_2O_3 has an average Nusselt number almost exactly as Cu nanoparticles and even better enhancement than Ag nanoparticles. Therefore, the selection of nanoparticles in mixed convection application is not only dependent on the value of thermal conductivity but also depends on the value of thermal diffusivity.

4 Conclusions

For $Ri=1.887$ and outside the plume region, the Nusselt number increased by increasing the volume fraction of Al_2O_3 nanoparticles. The plume region is rotated in the clockwise direction by the presence of the Al_2O_3 nanoparticles and this rotation increases by increasing the volume fraction of the nanoparticles. However, in the plume region, the effect of the volume fraction on the Nusselt number was less pronounced. The nanoparticles need to have high thermal conductivity as well as low thermal diffusivity for good heat transfer enhancement in mixed convection applications. It is observed that nanoparticles with high thermal diffusivity have larger plume size, which affects the heat transfer enhancement of such nanoparticles. It was found that Al_2O_3 has an average Nusselt number almost exactly as Cu particles and even better enhancement than Ag nanoparticles due to the low thermal diffusivity of Al_2O_3 compared to the metal nanoparticles.

Nomenclature

c_p = specific heat at constant pressure
D = diameter of the cylinder
E = grid stretch parameter, $E=\pi e^{\pi\xi}$
Gr = grashof number, $Gr=g\beta(T_w-T_\infty)R^3/\upsilon_f^2$
Gr_D = Grashof number based on diameter, $Gr_D=g\beta(T_w-T_\infty)D^3/\upsilon_f^2$
g = gravitational acceleration
k = thermal conductivity
Nu = Nusselt number, $Nu=hD/k_f$
Pr = Prandtl number
R = radius of the cylinder
r = radial distance from cylinder surface, $r=e^{\pi\xi}$
Re = Reynolds number, $Re=\Omega D^2/\nu_f$
Re_D = Reynolds number based on diameter, $Re=\Omega D^2/\nu_f$
Ri = Richardson number, $Ri=Gr_D/Re_D^2$
T = dimensionless temperature, $T=T^*-T_\infty/T_w-T_\infty$

Greek Symbols

α = thermal diffusivity
β = thermal expansion coefficient
η = coordinates in computational plane, $(\eta=\theta/\pi)$
φ = nanoparticle volume fraction
λ = parameter defined in Eq. (4)
ν = kinematic viscosity
θ = angle measured from the lower plane
Ψ = dimensionless stream function
ψ = dimensional stream function
Ω = angular speed of the cylinder
ω = dimensionless vorticity
ρ = density
μ = dynamic viscosity
ξ = coordinate in computational plane

Subscripts

nf = nanofluid
f = fluid
s = solid
w = wall
∞ = farstream

References

[1] Choi, S. U. S., 1995, "Enhancing Thermal Conductivity of Fluids With Nanoparticles," *Developments and Applications of Non-Newtonian Flows*, D. A.

Siginer and H. P. Wang, eds., ASME, New York, Vol. FED-231/MD-66, pp. 99–105.

[2] Lee, S., Choi, S. U. S., and Eastman, J. A., 1999, “Measuring Thermal Conductivity of Fluids Containing Oxide Nanoparticles,” J. Heat Transfer, **121**, pp. 280–289.

[3] Trisaksri, V., and Wongwises, S., 2007, “Critical Review of Heat Transfer Characteristics of Nanofluids,” Renewable Sustainable Energy Rev., **11**, pp. 512–523.

[4] Daungthongsuk, W., and Wongwises, S., 2007, “A Critical Review of Convective Heat Transfer Nanofluids,” Renewable Sustainable Energy Rev., **11**, pp. 797–817.

[5] Wang, X.-Q., and Mujumdar, A. S., 2007, “Heat Transfer Characteristics of Nanofluids: A Review,” Int. J. Therm. Sci., **46**, pp. 1–19.

[6] Abu-Nada, E., 2008, “Application of Nanofluids for Heat Transfer Enhancement of Separated Flows Encountered in a Backward Facing Step,” Int. J. Heat Fluid Flow, **29**, pp. 242–249.

[7] Brinkman, H. C., 1952, “The Viscosity of Concentrated Suspensions and Solutions,” J. Chem. Phys., **20**, pp. 571–581.

[8] Shukla, R. K., and Dhir, V. K., 2005, “Study of the Effect of Thermal Conductivity of Nanofluids,” ASME International Mechanical Engineering Congress and Exposition, Orlando, FL.

[9] Patankar, S. V., 1980, *Numerical Heat Transfer and Fluid Flow*, Hemisphere, Taylor and Francis Group, New York.

[10] Weinan, E., and Liu, J.-G., 1996, “Vorticity Boundary Condition and Related Issues for Finite Difference Schemes,” J. Comput. Phys., **124**, pp 368–382.

[11] Shimada, R., Ohkubo, T., Kobayashi, T., and Kumagai, S., 1992, “Heat Transfer From a Rotating Cylinder With and Without Cross Flow,” Heat Transfer-Jpn. Res., **21**(2), pp. 109–122.

Steady State Performance of a Single Phase Natural Circulation Loop With End Heat Exchangers

N. M. Rao[1]
Rolta India Limited,
Rolta Technology Park,
MIDC, Andheri (E),
Mumbai 400093,
Maharashtra State, India
e-mail: nmuralidhararao@yahoo.com
e-mail: nakka.rao@rolta.com

B. Maiti
e-mail: bmaiti@mech.iitkgp.ernet.in

P. K. Das
e-mail: pkd@mech.iitkgp.ernet.in

Department of Mechanical Engineering,
Indian Institute of Technology,
Kharagpur 721302,
West Bengal, India

In the present investigation, the steady state performance of a rectangular single phase natural circulation loop (NCL) with end heat exchangers is studied. One-dimensional governing equations are considered in developing the mathematical model. Analytical expressions are derived for the circulation rate and temperature profile. However, the individual performance parameters are to be computed iteratively as the equations are strongly coupled. A suitable iterative procedure is given to evaluate the important loop parameters such as steady state flow rate, and riser and downcomer temperatures. Few special cases are discussed where analytical expressions for circulation rate and temperature distribution can be obtained directly without any iterative procedure. It is also shown that both the hot and cold end heat exchangers should have equal conductance (UA) for maximization of circulation rate. This feature of NCL is identical with heat power cycle and can be explained in light of equipartition principle.
[DOI: 10.1115/1.2928015]

Keywords: steady state, natural circulation loop, end heat exchangers, overall effectiveness, optimum allocation

Introduction

Both the steady and the transient behavior of natural circulation loops (NCLs) have been a subject of great interest for many decades because of their wide range of applications in engineering right from natural circulation boilers to large nuclear power plants. Most of the previous investigations are either considered a toroidal or a rectangular geometrical configuration especially with constant heat flux heating and cooling as boundary conditions [1,2]. For certain applications such as for nuclear plants, constant wall temperature cooling is an appropriate boundary condition [3]. In addition to the experimental investigations [1,3], various numerical studies are also available on toroidal loops [2,4] and rectangular loops [5]. However, almost all the studies considered constant heat flux heating, and either constant heat flux or constant wall temperature cooling as boundary conditions. Nevertheless, NCLs with constant finite heat capacity rate heating and cooling are encountered frequently in engineering applications such as waste heat recovery systems and systems in which the hot and cold fluids cannot be brought to close proximity due to the process requirement or limitation of plant design. Stability behavior of a rectangular loop with these boundary conditions is studied by Rao et al. [6].

The design of NCLs with end heat exchangers is to be done meticulously and their steady state performance is to be predicted with a higher level of confidence as these will further depend on the overall conductance of the individual units. As the resources are limited, it is important to find out the optimum allocation of the overall conductance between the two heat exchangers. Bejan [7] showed that the power from a heat engine cycle can be maximized when the total inventory of conductance $(UA)_t$ is equally distributed between the heat source and heat sink. However, such an exercise is so far not made for NCLs with end heat exchangers.

In the present study, it is intended to determine the circulation rate of the coupling fluid, spatial temperature distribution of coupling fluid, and external fluids as well as optimization of performance of system for a given fixed total inventory. It is shown that the overall effectiveness of the system is proportional to the square of the circulation rate of the coupling fluid for laminar flow and more than square for turbulent flow. The optimum allocation of the total conductance $(UA)_t$ between the end heat exchangers is achieved for maximizing the circulation rate, which in turn maximizes the overall effectiveness.

Mathematical Analysis

In the present work, rectangular NCL with end heat exchangers is considered. The inputs for the analysis are the loop geometry, heat exchanger characteristics and their geometry, hot and cold stream heat capacity rates, coupling fluid properties, and hot and cold stream inlet temperatures. Assumptions are made for analyzing the loop performance. The details on its working and assumptions can be obtained elsewhere [6].

Based on the physical model and assumptions, a steady state one-dimensional governing equation for the conservation of mass for single phase flow can be written as

$$\frac{du_{\mathrm{cf}}}{ds}=0 \tag{1}$$

where u_{cf} is loop fluid velocity and s is space coordinate running along the loop.

The integral loop momentum equation is expressed as

$$\oint \frac{2C_f\rho_{\mathrm{cf}}u_{\mathrm{cf}}^2}{D}ds+\sum_{i=1}^{n}\frac{2C_f\rho_{\mathrm{cf}}u_{\mathrm{cf}}^2}{D}L_{ei}+\oint \rho_{\mathrm{cfbuo}}g\,ds=0 \tag{2}$$

ρ_{cf} in first and second terms designates the constant density, whereas ρ_{cfbuo} in the third term represents variable density, used to determine frictional pressure drop and buoyancy head, respectively. D, L_{ei}, and C_f are loop diameter, equivalent length of various fittings, and friction factor, respectively.

Equation (2) can further be expressed considering the Boussinesq approximation as

$$\frac{32}{\pi^2}\frac{C_f\dot{m}^2}{\rho_0 D^5}\left[2(L_1+L_2)+\sum_{i=1}^{n}L_{ei}\right]=\rho_0 g\beta L_2(T_{\mathrm{cf2}}-T_{\mathrm{cf1}}) \tag{3}$$

where $\dot{m}$, L_1, and L_2 are loop mass flow rate, and horizontal loop length and height, respectively. T_{cf2} and T_{cf1} are loop fluid temperatures in adiabatic riser and downcomer, respectively. ρ_0 and β are reference density at its corresponding temperature T_0 and ther-

---

[1] Corresponding author.

Contributed by the Heat Transfer Division of ASME for publication in the JOURNAL OF HEAT TRANSFER. Manuscript received March 19, 2007; final manuscript received March 25, 2008; published online June 10, 2008. Review conducted by Yutaka Asako.

mal expansion coefficient of coupling fluid, respectively.

The friction factor C_f can be expressed as $C_f = a\,\mathrm{Re}^{-b}$, and substituting into Eq. (3) and neglecting the minor losses yield the following simplified loop momentum equation in terms of coupling fluid heat capacity rate, C_{cf}:

$$C_{\mathrm{cf}}^{2-b} = \frac{\pi^{2-b}}{2^{6-2b}a} \frac{\rho_0^2 g \beta D^{5-b} c_{\mathrm{cf}}^{2-b}}{\mu_{\mathrm{cf}}^{b}} \frac{L_2}{(L_1+L_2)} [T_{\mathrm{cf2}} - T_{\mathrm{cf1}}] \tag{4}$$

μ_{cf} and c_{cf} in Eq. (4) are viscosity and specific heat, respectively.

The following energy equations are used to determine the unknown downcomer temperature (T_{cf1}) and riser temperature (T_{cf2}) and derived from the elementary theory of heat exchangers. The simplified expressions are as follows:

$$T_{\mathrm{cf2}} = \left[T_{\mathrm{cf1}} \left(1 - \frac{C_{\min,h}}{C_{\mathrm{cf}}} \varepsilon_h \right) + T_{\mathrm{hi}} \left(\frac{C_{\min,h}}{C_{\mathrm{cf}}} \varepsilon_h \right) \right] \text{ hot end heat exchanger (HEHE)} \tag{5}$$

$$T_{\mathrm{cf1}} = \left[T_{\mathrm{cf2}} \left(1 - \frac{C_{\min,c}}{C_{\mathrm{cf}}} \varepsilon_c \right) + T_{\mathrm{ci}} \left(\frac{C_{\min,c}}{C_{\mathrm{cf}}} \varepsilon_c \right) \right] \text{ cold end heat exchanger (CEHE)} \tag{6}$$

T_{hi} and T_{ci} in the above equations are the hot and cold fluid inlet temperatures, respectively, and ε_h and ε_c are effectiveness of HEHE and CEHE, respectively. NTU_h and NTU_c for concentric tubes HEHE and CEHE are modified as $\mathrm{NTU}_h = (UA)^*(UA)_t/[1+(UA)^*]C_{\min,h}$ and $\mathrm{NTU}_c = (UA)_t/[1+(UA)^*]C_{\min,c}$, and these are derived by considering the product of total heat transfer coefficient and heat transfer area, $(UA)_t$, for the loop which is known a priori and also a constraint in the present study. One can write $(UA)_t$ is the summation of conductance of both HEHE and CEHE (Holmberg [8]) and is given below.

$$(UA)_t = (UA)_h + (UA)_c \tag{7}$$

Considering the ratio of $(UA)_h$ to $(UA)_c$ as $(UA)^*$, one gets the following relations from Eq. (7):

$$(UA)_h = \frac{(UA)^*(UA)_t}{[1+(UA)^*]} \quad \text{and } (UA)_c = \frac{(UA)_t}{[1+(UA)^*]} \tag{8}$$

Here, the focus is to replace both $(UA)_h$ and $(UA)_c$ in terms of $(UA)_t$ and $(UA)^*$ and the numerical value of $(UA)^*$, which is equal to 1.0, shows that both HEHE and CEHE conductances are equal to each other.

The substitution of boundary conditions, i.e., hot fluid inlet temperature, $\theta_{\mathrm{hi}} = 1.0$, and cold fluid inlet temperature, $\theta_{\mathrm{ci}} = 0$, yields the following nondimensionalized momentum and energy equations.

$$C_{\mathrm{cf}}^{\ *} = \left[N \mathrm{Gr}_D \frac{K_1}{(1+K_1)} [\theta_{\mathrm{cf2}} - \theta_{\mathrm{cf1}}] \right]^{1/(2-b)} \tag{9}$$

$$\theta_{\mathrm{cf2}} = \theta_{\mathrm{cf1}} + \left\{ [1 - \theta_{\mathrm{cf1}}] \frac{C_{\min,h}^{\ *}}{C_{\mathrm{cf}}^{\ *}} \varepsilon_h^{\ *} \right\} \tag{10}$$

$$\theta_{\mathrm{cf1}} = \theta_{\mathrm{cf2}} \left[1 - \frac{C_{\min,c}^{\ *}}{C_{\mathrm{cf}}^{\ *}} \varepsilon_c^{\ *} \right] \tag{11}$$

Equations (9)–(11) are coupled and to be solved simultaneously to determine the three variables, $C_{\mathrm{cf}}^{\ *}$, θ_{cf2}, and θ_{cf1}.

Once $C_{\mathrm{cf}}^{\ *}$, θ_{cf1}, and θ_{cf2} are known, the temperature variation along the loop as well as the hot and the cold streams can be obtained. The analytical expressions to determine the temperature profiles of hot, cold, and coupling fluids can be obtained elsewhere [6].

Although the general relationship among $C_{\mathrm{cf}}^{\ *}$, θ_{cf1}, and θ_{cf2} is highly implicit and cannot be determined analytically as depicted by Eqs. (9)–(11), one may think of some special cases where analytical solutions are possible.

Case I: $C_h^{\ *}$ and $C_c^{\ *}$ Tends to Infinity. For this case, the effectiveness of HEHE and CEHE, and downcomer and riser temperatures can be expressed as

$$\varepsilon_{h,c}^{\ *} = 1.0 \tag{12}$$

$$\theta_{\mathrm{cf2}} = 1.0 \tag{13}$$

$$\theta_{\mathrm{cf1}} = 0.0 \tag{14}$$

Therefore, loop flow rate can be expressed in explicit form as

$$C_{\mathrm{cf}}^{\ *} = \left[N\,\mathrm{Gr}_D \frac{K_1}{(1+K_1)} \right]^{1/(2-b)} \tag{15}$$

Case II: Approximation With Arithmetic Mean of Temperature Differences (AMTDs). Mathematical manipulation among heat transfer equations in terms of arithmetic mean temperature and equations related to heat carried away by hot, cold, and coupling fluids along with Eq. (9) with the substitution of input parameters, $\theta_{\mathrm{hi}} = 1.0$ and $\theta_{\mathrm{ci}} = 0$, yields the following simplified equation for coupling fluid flow rate in an explicit form.

$$C_{\mathrm{cf}}^{\ *(3-b)} = \frac{N\,\mathrm{Gr}_D \dfrac{K_1}{(1+K_1)}}{\left(\dfrac{1}{2C_h^{\ *}} + \dfrac{1}{2C_c^{\ *}} + \dfrac{1}{(UA)_h^{\ *}} + \dfrac{1}{(UA)_c^{\ *}} \right)} \tag{16}$$

Overall Effectiveness

Determining optimum loop flow rate through appropriate allocation of total conductance between two heat exchangers to maximize the heat transport (overall effectiveness) between hot and cold fluids was the crux of the forced flow indirect heat exchange systems. However, this is not the case with NCL where the loop flow rate is not known a priori. Deriving analytical expression for overall effectiveness of NCL is indeed necessary to know which parameters need to be optimized in order to maximize the overall effectiveness. Hence, the overall effectiveness of NCL is of relevance for the design and simulation of large systems of which NCL is a part. The overall effectiveness, ε_o, of NCL with end heat exchangers is defined (Holmberg [8]) as

$$\varepsilon_o = \frac{Q}{C_{\min,o}\Delta T_o} \tag{17}$$

where Q is the actual rate of heat transfer from hot fluid to cold fluid through coupling fluid whereas $C_{\min,o}\Delta T_o$ is the maximum possible heat transfer between hot and cold fluids. $C_{\min,o}$ is the minimum of hot and cold fluid heat capacity rates and ΔT_o is the temperature difference between hot and cold fluid inlet temperatures.

From the elementary theory of heat exchangers, Eq. (17) with the substitution of Eq. (9) can be written in nondimensional form as

$$\varepsilon_o^{\ *} = \frac{C_{\mathrm{cf}}^{\ *(3-b)}}{N\,\mathrm{Gr}_D \left(\dfrac{K_1}{(1+K_1)} \right) C_{\min,o}^{\ *} (\theta_{\mathrm{hi}} - \theta_{\mathrm{ci}})} \tag{18}$$

The above equation reveals that the overall effectiveness is solely a function of $C_{\mathrm{cf}}^{\ *}$ as the rest of the parameters are input to the system analysis. Therefore, maximum ε_o^* is achieved when C_{cf}^* is optimized. Hence, optimization of system is necessary and this can be achieved through optimum allocation of total available conductance.

Optimum Allocation of Total Conductance

The optimum design of any equipment aims at the reduction of the total cost, which comprises of equipment cost and the running cost over the stipulated life span. As there is no prime mover, the initial cost of the NCL has to be brought down adopting an optimum design. The initial cost of the indirect heat exchanger system will depend on the cost of HEHE and CEHE. Again, the cost of a heat exchanger depends on its surface area and type of surface augmentation technique used. The overall heat transfer coefficient (U) is dependent on the type of heat exchanger surface. In general, the cost of heat exchanger is then a function of UA.

Keeping the initial cost of the indirect heat exchanger system constant one can maximize the overall effectiveness by properly allocating UA between the CEHE and HEHE. In the previous section, it is shown that maximization of the overall effectiveness can be obtained by maximizing the C_{cf}^*. In the present exercise, C_{cf}^* is maximized keeping $(UA)_t$ constant.

Loop flow rate, from Eqs. (9)–(11), can be derived as a function of loop geometry, total conductance, $(UA)_t$, and $(UA)^*$. For a given loop geometry as well as total conductance, the equation corresponding to $\partial C_{\mathrm{cf}}^*/\partial(UA)^*=0$ is as follows:

$$\left\{\left[\frac{1}{C_{\min,h}^*}-\frac{1}{C_{\max,h}^*}\right]^2\frac{\bar{A}}{(1-\bar{A})^2} - \left[\frac{1}{C_{\min,c}^*}-\frac{1}{C_{\max,c}^*}\right]^2\frac{\bar{\mathbf{B}}}{(1-\bar{B})^2}\right\}=0 \qquad (19)$$

where

$$\bar{A}=e^{-(UA)_t^*(UA)^*/[1+(UA)^*][1/C_{\min,h}^*-1/C_{\max,h}^*]}$$

$$\bar{B}=e^{-(UA)_t^*/[1+(UA)^*][1/C_{\min,c}^*-1/C_{\max,c}^*]}$$

General Solution

The optimum allocation of $(UA)_t^*$ for the general case is obtained by calculating C_{cf}^* as a function of $(UA)^*$ by solving Eqs. (9)–(11), iteratively, by guessing θ_{cf1} and θ_{cf2} initially and updating C_{cf}^*, θ_{cf1}, C_{cf}^*, and θ_{cf2} sequentially.

The spatial temperature variation of coupling, hot, and cold fluids is determined using the above iterative procedure and can be obtained elsewhere [6]. Figure 1 depicts the variation of coupling fluid flow rate with $(UA)^*$ where C_{cf}^* reaches maximum at $(UA)^*=1.0$. The result shown in Fig. 1 is not a mere coincidence. It could be demonstrated for any combination of the operating and geometrical parameters; the NCL will have a maximum circulation rate when the total conductance $(UA)_t$ is equally distributed between the HEHE and CEHE.

In some special cases, one can analytically derive the optimum allocation. Such results are shown below.

Case I: C_h^* and C_c^* tend to infinity and Case II: $C_h^*=C_c^*$ and $C_{\mathrm{cf}}^*\neq C_h^*$. For both cases, Eq. (19) can be written as

$$\left[\frac{\bar{A}}{(1-\bar{A})^2}-\frac{\bar{B}}{(1-\bar{B})^2}\right]=0 \quad \text{where } \bar{A}<1.0 \text{ and } \bar{B}<1.0 \qquad (20)$$

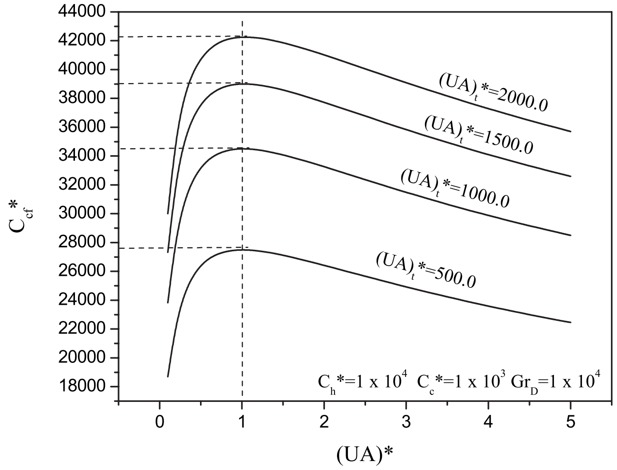

Fig. 1 Optimum allocation of $(UA)_t^*$

Equation (20) will have two solutions: one is ($\bar{A}=\bar{B}$) and the second one is $\bar{A}\bar{B}=1$.

Equating $\bar{A}$ and $\bar{B}$ gives rise to the following optimum condition:

$$(UA)^*=1.0 \qquad (21)$$

Equating $\bar{A}\bar{B}=1$, one can obtain the solution $(UA)^*=-1.0$, which is not feasible practically.

Case III: Use of Arithmetic Mean of Temperature Differences (AMTDs)

Equation (16) may be written for C_{cf}^* in terms of $(UA)_t^*$ and $(UA)^*$ as

$$C_{\mathrm{cf}}^{*(3-b)}=\frac{N\,\mathrm{Gr}_D\dfrac{K_1}{(1+K_1)}}{\left(\dfrac{1}{2C_h^*}+\dfrac{1}{2C_c^*}+\dfrac{(1+(UA)^{*2})}{(UA)_t^*(UA)^*}\right)} \qquad (22)$$

Differentiating Eq. (22) with respect to $(UA)^*$ and equate to zero gives the following optimum condition:

$$(UA)^*=1.0 \qquad (23)$$

Bejan [7] has shown that maximum power can be derived from a heat engine cycle when the total inventory of conductance $(UA)_t$ is equally distributed between the heat source and the heat sink, which is an example of equipartition principle. It is interesting to note that in case of a NCL, similar allocation of a fixed quantity of heat exchanger resource is required for maximizing the loop performance. A thermal power cycle and a NCL share a few common features. Both of these systems receive thermal energy from a high temperature source and rejects heat to a low temperature sink. The circulating fluid changes its property (sometime also the phase) as it passes through different parts of the cycle. In fact, NCL represents a limiting configuration of a thermal power cycle where the external work done is reduced to zero. The fact that both the systems need identical allocation of heat exchanger inventory for optimum performance emphasizes this similarity.

Examples of equipartition have been demonstrated in different engineering systems where equipartition of forces [9] and equipartition of thermal resistance [10] generated optimal designs. The optimal allocation of heat exchanger inventory between the hot and cold end of the NCL for maximum circulation (as well as maximum overall effectiveness) emphasizes the same principle.

Conclusion

The present study addresses some critical aspects of a rectangular single phase uniform cross-sectional NCL with end heat exchangers particularly related to loop circulation rate, overall effectiveness, and optimum allocation of total conductance. Circulation rate is obtained numerically for general case and analytically for few special cases. Overall effectiveness is derived as a function of loop circulation rate where it is proportional to ≥square of loop flow rate, loop geometry and inlet temperatures of both hot and cold streams. Equal allocation of total conductance $(UA)_t$ between HEHE and CEHE maximizes the loop flow rate, which in turn maximizes the overall effectiveness. The equal allocation of heat exchanger inventory to the hot and cold ends strengthens the macroscopic equipartition principle proposed by Bejan [7] for the maximum work output of heat engine cycles.

Nomenclature

$C_{\max}$ = larger heat capacity rate of the fluid, kW/K
$C_{\min}$ = smaller heat capacity rate of the fluid, kW/K
CR = $C_{\min}/C_{\max}$, dimensionless
g = gravitational acceleration, m^2/s
Gr_D = loop Grashof number, $\rho_0^2 g\beta(T_0-T_{\mathrm{ci}})D^3/\mu_{\mathrm{cf}}^2$, dimensionless
K_1 = ratio of vertical to horizontal loop length, L_2/L_1, dimensionless
n = number of fittings, dimensionless
N = constant, $(\pi^{2-b}/2^{6-2b}a)$
Re = Reynolds number $(\rho_{\mathrm{cf}}u_{\mathrm{cf}}D/\mu_{\mathrm{cf}})$, dimensionless
(UA) = product of overall heat transfer coefficient and heat transfer area, kW/K

Superscript

$*$ = nondimensionalized with $(\mu cD)_{\mathrm{cf}}$

Subscripts

c = cold fluid side
h = hot fluid side

References

[1] Creveling, H. F., De Paz, J. F., Baladi, J. Y., and Schoenhals, R. J., 1975, “Stability Characteristics of a Single Phase Free Convection Loop,” J. Fluid Mech., **67**, pp. 65–84..

[2] Greif, R., Zvirin, Y., and Mertol, A., 1979, “The Transient and Stability Behavior of a Natural Convection Loop,” ASME J. Heat Transfer, **101**, pp. 684–688.

[3] Vijayan, P. K., 2002, “Experimental Observations on the General Trends of the Steady State and Stability Behaviour of Single-Phase Natural Circulation Loops,” Nucl. Eng. Des., **215**, pp. 139–152.

[4] Jiang, Y. Y., and Shoji, M., 2003, “Flow Stability in a Natural Circulation Loop: Influences of Wall Thermal Conductivity,” Nucl. Eng. Des., **222**, pp. 16–28.

[5] Mousavian, S. K., Misale, M., D’Auria, F., and Salehi, M. A., 2004, “Transient and Stability Analysis in Single-Phase Natural Circulation,” Ann. Nucl. Energy, **31**, pp. 1177–1198.

[6] Rao, N. M., Maiti, B., and Das, P. K., 2005, “Stability Behaviour of a Natural Circulation Loop With End Heat Exchangers,” ASME J. Heat Transfer, **127**, pp. 749–759.

[7] Bejan, A., 1988, *Advanced Engineering Thermodynamics*, Wiley, New York.

[8] Holmberg, R. B., 1975, “Heat Transfer in Liquid-Coupled Indirect Heat Exchanger Systems,” ASME J. Heat Transfer, **97**, pp. 499–503.

[9] Sauar, E., Ratkje, S. K., and Lien, K. M., 1996, “Equipartition of Forces: A New Principle for Process Design and Optimization,” Ind. Eng. Chem. Res., **35**, pp. 4147–4153.

[10] Pramanick, A. K., and Das, P. K., 2005, “Heuristics as an Alternative to Variational Calculus for Optimization of a Class of Thermal Insulation Systems,” Int. J. Heat Mass Transfer, **48**, pp. 1851–1857.

Erratum: “Magnetohydrodynamic Flow Past a Vertical Plate With Radiative Heat Transfer” [Journal of Heat Transfer, 2007, 129(12), pp. 1708–1713]

S. Shateyi, P. Sibanda, and S. S. Motsa

In this paper there were a number of errors that we have corrected below.

2 Problem Formulation

There was a typing error in the last terms of the momentum equations (1*b*) and (1*c*) that ended up as an oversight. The correct form of the governing equations is

$$\frac{\partial u}{\partial x}+\frac{\partial v}{\partial y}=0 \tag{1a}$$

$$u\frac{\partial u}{\partial x}+v\frac{\partial u}{\partial y}=\nu\frac{\partial^2 u}{\partial y^2}+g\beta(T-T_\infty)-\frac{\sigma B_0^2}{\rho(1+m^2)}(u+mw) \tag{1b}$$

$$u\frac{\partial w}{\partial x}+v\frac{\partial w}{\partial y}=\nu\frac{\partial^2 w}{\partial y^2}-\frac{\sigma B_0^2}{\rho(1+m^2)}(w-mu) \tag{1c}$$

$$u\frac{\partial T}{\partial x}+v\frac{\partial T}{\partial y}=\alpha\frac{\partial^2 T}{\partial y^2}-\frac{1}{\rho c_p}\frac{\partial q_r}{\partial y} \tag{1d}$$

Consequently, the correct form of Eqs. (5*a*)–(5*d*) is

$$\frac{\partial F}{\partial \xi}+\frac{\partial G}{\partial \eta}=0 \tag{5a}$$

$$F\frac{\partial F}{\partial \xi}+G\frac{\partial F}{\partial \eta}=\theta+\frac{\partial^2 F}{\partial \eta^2}-\frac{M^2}{1+m^2}(F+mH) \tag{5b}$$

$$F\frac{\partial H}{\partial \xi}+G\frac{\partial H}{\partial \eta}=\frac{\partial^2 H}{\partial \eta^2}-\frac{M^2}{1+m^2}(H-mF) \tag{5c}$$

$$F\frac{\partial \theta}{\partial \xi}+G\frac{\partial \theta}{\partial \eta}=\frac{1}{\mathrm{Pr}}(1+N)\frac{\partial^2 \theta}{\partial \eta^2} \tag{5d}$$

The numerical calculations were made with the correct form of the equations and the conclusions drawn from the results therefore remain sound.

3 Results and Discussion

The incorrect temperature profiles in Figs. 2(*a*), 4, and 5 that were a result of small calculation domain used have been recomputed and the correct profiles are given below. All the figures were computed for $\xi=5$.

In the original paper there was a mix-up in the figures and captions for Figs. 6–8. The correct figures and captions are as follows:

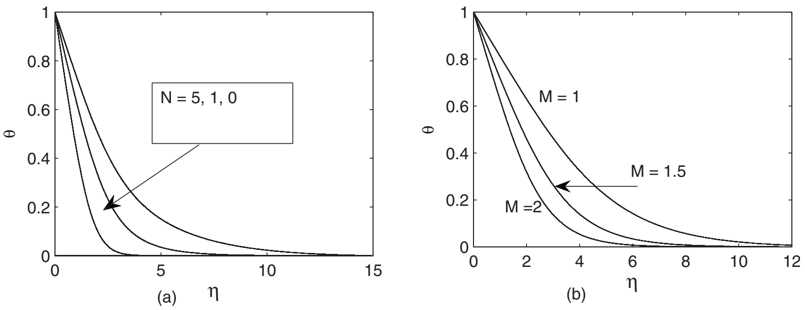

Fig. 2 The variation of temperature with (*a*) increasing radiation and (*b*) increasing magnetic field strength when $m=1$ and $\mathrm{Pr}=0.71$

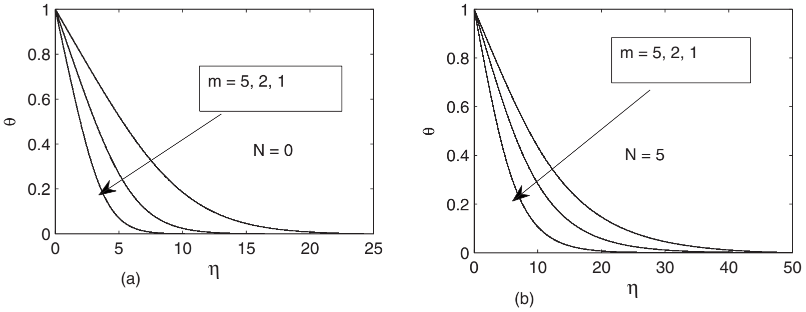

Fig. 4 The temperature distribution (*a*) without radiation effects and (*b*) with radiation for $M=1$ and $\mathrm{Pr}=0.71$

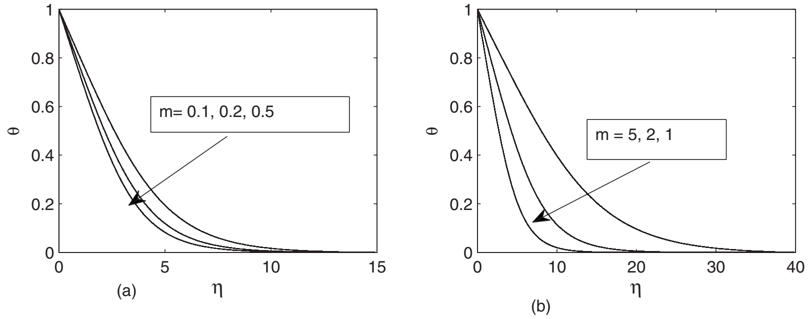

Fig. 5 **The temperature distribution for (*a*)$m<1$ and (*b*) $m\geq 1$ for $M=1$, $\Pr=0.71$ and $N=1$**

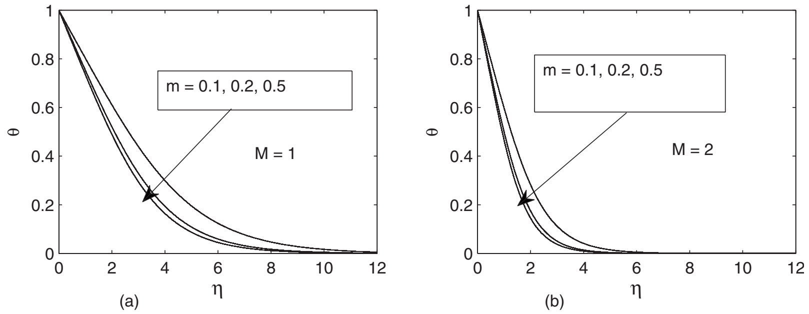

Fig. 6 **The variation of temperature with Hall parameter (*a*) $M=1$, (*b*) $M=2$ when $\Pr=0.71$ and $N=1$**

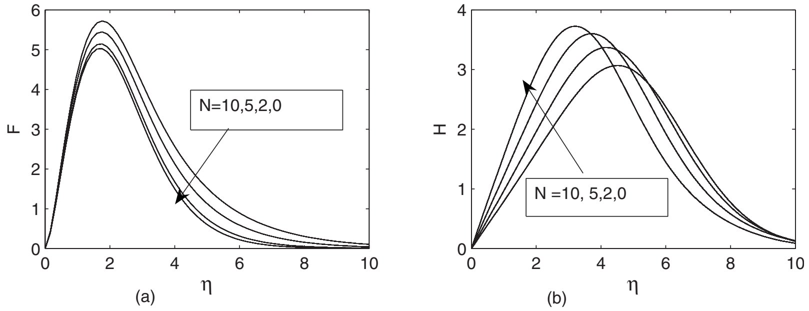

Fig. 7 **The variation of (*a*) tangential velocity and (*b*) lateral velocity distribution with increasing radiation. The tangential velocity decreases with radiation while the tangential velocity initially increases before reducing sharply to zero.**

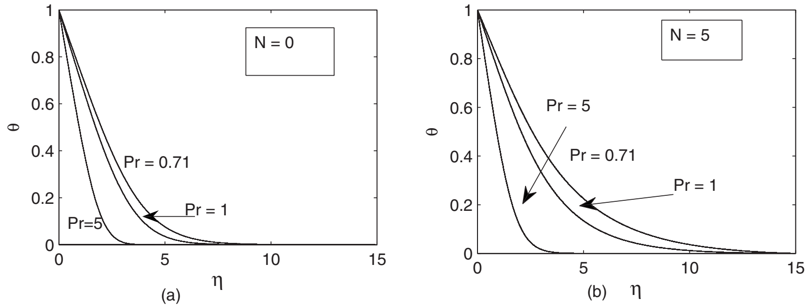

Fig. 8 **The variation of the temperature distribution with increasing Prandtl numbers (*a*) without radiation and (*b*) with radiation**